

BULGARIAN CHEMICAL COMMUNICATIONS

2016 Volume 48 / Special Edition F

*Journal of the Chemical Institutes
of the Bulgarian Academy of Sciences
and of the Union of Chemists in Bulgaria*

Modeling desalinization to reclamation of saline-sodic soils

M. Mohamadzadeh^{1*}, M. Homae², E. Pazira³

¹Department of Soil Science, Science and Research Branch, Islamic Azad University, Tehran, Iran

²Department of Soil Science Tarbiat Modares University, Tehran, Iran

³Department of Soil Science, Science and Research Branch, Islamic Azad University, Tehran, Iran

Received June 22, 2016; Revised December 16, 2016

Soil Salinity is one of the most important environmental factors limiting and agricultural hazard in arid and semi-arid regions. Accumulation of soluble salts within the root zone is one of the major problems because most of the crop plants are sensitive to salinity caused by high concentrations of salts in the soil. For prevail over this problem, leaching of accumulated salts and controlling soil salinity is necessary. The primary method of controlling soil salinity is to permit of the irrigation water to leach the soil, be drained and discharging through an appropriate drainage system. The objectives of this study were to introduce an empirical model to account for reclamation water and to compare the obtained results with some available models. Consequently, a large-scale field experiment was conducted in Jofeir region at south part of west Khuzestan plains, covering an area of 21285 ha with S3A3 and S3A4 salinity-sodicity classes. The intermittent pounding experiment was conducted with six double ring infiltrometers in a circular array. All experiments were accomplished by applying 100 cm of water in four-25 cm intervals. The leaching water was supplied from Karun rive. Four mathematical models were applied to the collected experimental data to derive a suitable empirical model. The results indicated that the proposed power model with maximum correlation coefficient of 0.88 and minimum standard error of 0.25 can provide reasonable estimates for leaching process compares to the previously proposed models.

Keywords: desalinization curve; saline-sodic soils; salt leaching; soil reclamation

INTRODUCTION

The accumulation of soluble salts in soil, affect the physical and chemical characteristic [1]. This effect may lead to the disorder of plants development or the complete stop of plants growth [2]. Soils become salty by natural way or human activities [3-6]. Low rainfall and high evaporation are two natural factors, which leads to salty soils. The numerous studies have been conducted because of the expansion of saline soils especially in arid and semi-arid regions in the world. Some of these studies have been done in terms of the survey of the salinity on the different operation of plants [4,7-9]. In addition, some of the researchers have been done the nutritional effects and saline soils fertility [3,10]. In some of the studies have been conducted around the plant response modeling to the salinity in different situations [11-12]

Regardless the salinity factor related to the natural or humanistic factors, the leaching action with or without the generation of drainage networks are the non-alternative solutions for saline soils desalinization [1,13]. The main purpose of leaching is the reduction of soli salinity in the certain level of root zone, unless internal drainage of soli is not appropriate or there is no way to build an artificial

drain [8, 14].The physical and chemical properties of soils are the main and determiner factors of required amount of water for leaching. The leaching curves are used in term of the detection of how much water need for salt leaching and reaching the balance level of salinity [14].

Leaching of soli soluble salts from the plants root zone have been done in two ways pounding irrigation (intermittent and Permanent) and sprinkler irrigation. In addition of leaching action, the salinity of irrigation water affected on crop yield and the fertile fields which becomes saline again [7-9, 15] In the case of irrigation by saline water, the decrease of performance is related to the soil and the type of water use [16]. In arid and semi-arid regions such as Iran, which water resources have high amount of soluble salts and soil texture almost is medium to heavy, the rainfall is not enough for natural removing of salts in soil profile. The application of required amount of water in terms of reduction of salts soils is very important.

In this case, many studies have been done in terms of estimation the amount of required water for leaching the soluble salts which results has been shown that for removing 80 percent of soluble salts from soils, the water volume should transmitted around 1.5 times of pore volume [17-18].

* To whom all correspondence should be sent:
E-mail maryam_mohamadzadeh@yahoo.com

The amount of required water for reclamation of 100 centimeter of soil in different condition of fields is about 0.30 to 2.58 meter [19].

The assessment of the required amount of water in terms of leaching of soluble salts from soils is the important stage in management of reclamation of saline soil. The depth of required water for leaching depends on some factors such as initial salinity, texture, soil depth and the way of leaching [19]. Leaching efficiency with unsaturated methods compare to permanent ponding because of emerges of unsaturated condition and as a result, water transmission from tiny mesh is higher [20]. For increasing the leaching efficiency, it is better; that soil humidity has been less than the saturated humidity [21] because the high amount of soluble salts leaching has done in this situation [22]. Before every leaching test, a question that is discussed is what amount of water should add to soil. For this reason, the simulation models are used for determine the amount of required water for leaching. There have done many studies around this subject. In one study, a new way of leaching for soil modification and leaching at a pistachio field in south of California has been applied [23]. In this survey, the required water was used in terms of salts transmission from trees root zone by means of mild flow way in multiple lines. These researchers reached a conclusion that proposed way for leaching and farm modification is appropriate. An economic assessment was done by Corwin et al. [24] for comparison of leaching ways. The results of this survey around salts transmission show that stable models are excel than unstable models. Rao and Leeds-Harrison [25] has cloned different irrigation ways with the aim of increasing the leaching efficiency in Haryana region of India and they applied the solved numerically Laplace equation to obtain the water flow models and a mass flow equation in terms of obtain the salt spatial distribution of soil. The results shown that, for soils modification of region; firstly soils should be ponding then taken into the intermittent irrigation. Because of spatial distribution of soil properties, the use of simulation models in field condition provides some problems. However, the uses of empirical models for soil modification programs are useful. Empirical models are provided by observational data and empirical measurements that are fitted on a mathematic relation. In this case, mathematical models were represented for determination of the pace of water absorb by plants in high level of soil salinity [11-26]. Empirical relations and leaching curves have used in the soil type, amount of salinity or the exchangeable

sodium percent in special depth of soil. Numerous empirical models are presented by researchers such as Reeve [27], Dieleman [28], Pazira and Kawachi [29] and Verma and Gupta [30]. The leaching tests were done in most of the Iran's Provinces that face with salinity problem [29]. Based on numerous tests and studies in central region of Khuzestan province, the empirical relation has been presented in the shape of hyperbola. In addition, Pazira and Keshavarz [31] have represented the estimation of required water for leaching in brine and sodium fields of Eastern south of Khuzestan province. Mohsenifar et al. [32] have done the application of leaching models types in two region of eastern west of Khuzestan province. The goal of this study was drawing of salinity curves, desodification and studying the effect of amendment material on salts leaching and exchangeable sodium in mentioned regions. In addition, the other aim of this study was the presentation of appropriate empirical relation for using in estimation of required water in terms of modification of neighborhood region. Rajabzadeh et al. [33] have done ponding way in a survey of middle fields of Khuzestan province. In this survey, empirical models have been presented for modifying and improving the brine and sodium soil in the studied region [33]. In addition, the other study because of estimation of required water for leaching the sodium and brine soils in south of Khuzestan province was done, the logarithm model compare to other prevalent models has the most efficiency with the application of leaching water in 4 frequency (0.25 meter) [1, 34]. The purpose of this study is the assessment of empirical leaching curves. In addition, in this study with apply of some models on field data, the new model was presented for desalinization of studied region soils.

MATERIAL AND METHODS

Leaching experiments carried out in three series of Jofeir region soil in south of Khuzestan plain. The annual height of region from sea level is 18 meter and has a very hot summers and moderate winters. This region based on the Amberjeh measurement is classified in mean warm desert climate. The annual rainfall is 223 millimeter and the measured amount of evaporation by pen evaporation-class A is 2169-millimeter year. This study carried out region in Khuzestan province that is a sedimentary plain that has been created by the sediments of Karun and Karkheh rivers. The quality of Karun and Karkheh Rivers has fluctuated in different seasons although with consideration on Wilcox diagram [35] in long term they are classified in $C_2 S_1$ and $C_3 S_1$ classes respectively.

In this study, Sableh, kushk and Salman soil series, with 3425, 5080 and 14845-Hectare area have been studied.

In terms of salinity and sodic are classified in class S_3A_3 , S_3A_3 and S_3A_4 class. Humidity and thermal regime of region are Aridic and Hyperthermic, respectively. The permability of these soils varying from average to slow. Sableh soils series based on the American classification is Fine, Carbonatic, Hyperthermic, Fluventic, Haplocambids. kushk soil series is fine, fine loamy, Carbonatic, typic haplosalids and Salman soil series is Fine, Carbonatic, Hyperthermic, Gypsic Haplosalids. Leaching of soluble salts from soil profile was done for desalination of soil.

The water required for leaching was supplied from Karun River with intermittent ponding [17] that has 1.47 ds/m electro conductivity. For survey of the possibility of desalination and desodification the intermittent ponding experiment was conducted with six double ring infiltrometers in circular array. All experiments were accomplished by Applying 100 cm of water in four-25 cm internal sampling was conducted rom 0-25, 25-50,50-75 75-100 and 100-150cm layers. Soil sample were collected before and after leaching and were measured the require analysis.

In every experiment were measured electro conductivity, soil reaction, Cation exchange capacity, sodium absorption Ratio, percentage of exchangeable sodium and lime, and gypsum percentage. Physical and chemical properties of different layers of soil profile for studied soil series were presented in Tables 1-3. For prevention of evaporation from soil surface during the sampling, the soil surface was covered by plastic sheets.

Tables 1 and 2 have shown that the soil texture of Sableh series is Loam to silty clay loam and in kushk series is clay loam to silty loam and Salman series is clay to silty clay loam (Table 1). The soil Bulk density in Sableh soil is between 1.48 to 1.52, 1.55 to 1.60 in kushk soil series and in Salman series is 1.55 to 1.60 g/cm³. This varies density depending on soil texture (Table 2).

The electro conductivity of saturation extract in Sableh Series was fluctuated between 16.00 to 26.60 and increase by depth. The same situation was seen in kushk and Salman Series. The amount of electro conductivity was fluctuated between 24.00 and 28.40 and between 30.80 and 24.10 ds/m in kushk and Salman series respectively (Table 2).

The changes of soil reaction are very low in every three series. These changes were also seen in calcium carbonate and gypsum in salman, kushk and sableh soils series.

Based on the Tables 1 and 2, the weight average of EC_e and ESP were computed. Because it is possible that all content of applied water didn't used in terms of the leaching salts from soil profile, and some portion of it, was used for compensation lack of soil humidity, in this case using amount of water, may not lead to soil chemical balance. It means that, the amount of soil equilibrium electro conductivity is a little more than electro conductivity of irrigation water. In this study, the equilibrium electro conductivity is calculated around 1.29 times higher than the salinity of irrigation water. Based on the amount of. EC_e , ESP, EC_{eq} and ESP_{eq} of different layers and according to tables 2, 3 and 4, the variable were define like these relations:

Table 1. Some physical properties of the soil layers before leaching

Soil series	Depth (cm)	soil moisture			Cumulative moisture deficit (cm)	Total porosity (%)	Bulk density (g/cm ³)	Soil particles			Soil texture
		Wilting point	Filed capacity	Before leaching				clay	silt	sand	
Sableh	0-25	15.5	26.00	8.94	6.48	41.54	1.52	40.00	38.00	22.00	C
	25-50	17.5	32.00	17.6	11.88	42.31	1.50	48.00	40.00	12.00	C
	50-75	15.5	33.00	19.6	17.04	43.08	1.48	54.00	38.00	8.00	C
	75-100	15.5	31.00	15.5	22.85	42.31	1.50	40.00	40.00	20.00	CL
	100-150	7.00	28.00	15.48	32.37	41.54	1.52	40.00	44.00	16.00	SiCL
Kushk	0-25	7.00	8.00	10.00	6.80	39.62	1.60	11.20	53.40	35.40	SiL
	25-50	7.00	23.00	2.70	14.67	40.38	1.55	15.20	59.40	25.40	SiL
	50-75	7.00	25.00	6.85	21.70	41.51	1.55	17.20	67.40	15.40	SiL
	75-100	8.00	16.00	5.88	25.62	41.51	1.55	11.20	47.40	41.40	L
	100-150	5.00	14.00	8.70	29.73	41.51	1.55	7.20	31.40	61.40	SL
Salman	0-25	12.00	21.00	10.26	4.16	41.51	1.55	38.00	42.00	20.00	CL
	25-50	13.00	24.00	12.64	8.56	41.51	1.55	34.00	48.00	18.00	SiCL
	50-75	13.00	24.00	14.60	12.21	41.51	1.55	36.00	42.00	22.00	SiCL
	75-100	13.00	20.00	17.40	13.23	40.38	1.58	30.00	48.00	22.00	SiCL
	100-150	7.00	22.00	18.93	15.69	39.62	1.60	24.00	54.00	22.00	SiL

$$x = \frac{D_{lw}}{D_s}, y = \frac{EC_f - EC_{eq}}{EC_i - EC_{eq}} \quad (1)$$

$$x = \frac{D_{lw}}{D_s}, y = \frac{ESP_f - ESP_{eq}}{ESP_i - ESP_{eq}} \quad (2)$$

That EC_i and EC_f are the electro conductivity of soil saturation extract before and after of leaching

(ds/m) respectively. EC_{eq} is the electro conductivity of soil saturation extract in equilibrium condition (ds/m), ESP_i and ESP_f are the exchangeable Sodium percentage of before and after leaching in equilibrium condition respectively, ESP_{eq} is the exchangeable Sodium percentage in equilibrium condition, D_w is the depth of practical leaching water (cm). D_{lw} is the depth of leaching water (cm)

Table 2. Soil chemical properties before leaching in soil series

Soil series	Depth (cm)	Electro conductivity (dS/m)	ESP * (%)	(SAR) (Meq/lit) ^{0.5}	Ex.Na Meq/100gr	C.E.C Meq/100gr	gypsum (%)	Calcium Carbonate (%)	(pH)
Sableh	0-25	16.00	19.67	10.12	2.65	13.50	1.86	44.62	7.70
	25-50	18.91	27.30	12.51	4.75	17.40	1.65	46.40	7.80
	50-75	13.70	29.08	19.70	4.74	16.30	6.74	39.10	7.70
	75-100	19.00	28.74	19.55	5.00	17.40	4.90	42.30	7.50
	100-150	26.60	30.49	30.72	4.97	16.30	2.49	41.52	7.60
	Avg	18.84	27.05	18.54	4.42	16.18	3.53	42.78	7.66
Kushk	0-25	15.40	10.09	8.20	0.83	8.20	3.97	47.57	7.60
	25-50	18.40	10.69	11.10	0.83	8.70	12.48	48.87	7.40
	50-75	15.00	8.32	5.80	0.90	10.80	30.90	46.00	7.50
	75-100	14.00	5.22	3.90	0.43	8.20	15.80	46.80	7.70
	100-150	14.20	4.21	3.90	0.26	6.20	7.48	48.90	7.40
	Avg	15.40	7.70	6.58	0.67	8.42	13.96	47.62	7.52
Salman	0-25	30.8	42.86	12.90	5.31	12.40	8.89	44.02	7.40
	25-50	29.5	41.59	13.10	4.97	12.00	4.98	45.60	7.30
	50-75	28.2	34.68	14.20	4.45	12.80	2.62	44.65	7.20
	75-100	24.1	33.64	11.80	3.70	11.00	4.24	46.37	7.40
	100-150	28.6	35.00	18.91	3.50	10.00	0.80	48.10	7.30
	Avg	28.24	37.55	14.18	4.38	11.64	4.30	58.61	7.32

*ESP = Ex.Na+×100/CEC

Table 3. Soil chemical properties after leaching in soil series

Soil series	Depth (cm)	Electro conductivity (dS/m)	ESP * (%)	(SAR) (Meq/lit) ^{0.5}	Ex.Na Meq/100gr	C.E.C Meq/100gr	gypsum (%)	Calcium Carbonate (%)	(pH)
Sableh	0-25	1.88	5.05	4.15	0.68	13.50	2.52	-	7.70
	25-50	5.20	6.90	3.33	1.20	17.40	4.54	-	7.80
	50-75	10.23	12.94	14.14	2.11	16.30	4.77	-	7.60
	75-100	16.73	25.57	12.71	4.45	17.40	1.18	-	7.70
	100-150	23.73	23.68	36.26	3.86	16.30	2.25	-	7.40
	Avg	11.55	12.83	14.12	2.46	16.18	3.05	-	7.64
	Diff	- 7.29	-14.22	- 4.42	- 1.96	0	-0.50	**n.d	-0.02
Kushk	0-25	2.33	8.54	2.27	0.70	8.20	4.56	-	7.70
	25-50	4.85	10.46	6.00	0.91	8.70	6.57	-	7.50
	50-75	5.68	7.96	4.68	0.86	10.80	26.01	-	7.10
	75-100	4.50	3.29	3.49	0.27	8.20	5.49	-	7.40
	100-150	4.63	5.32	3.88	0.33	6.20	4.58	-	7.50
	Avg	4.39	7.11	4.06	0.61	8.42	11.88	-	7.44
	Diff	-21.01	-0.59	-2.52	-0.06	0	- 2.08	**n.d	-0.08
Salman	0-25	4	8.72	8.73	1.08	12.40	8.50	-	7.60
	25-50	14.87	8.03	15.10	0.96	12.00	9.50	-	7.70
	50-75	13.07	6.39	3.20	0.82	12.80	14.30	-	7.50
	75-100	11.17	4.73	2.30	0.52	11.00	13.50	-	7.70
	100-150	17.515	32.60	40.30	3.26	10.00	4.20	-	7.20
	Avg	12.12	12.02	13.92	1.33	11.64	10.00	-	7.54
	Diff	-16.12	-25.53	-0.26	-3.05	0	- 1.64	**n.d	+ 0.22

- represent decreasing + represent increasing *ESP = Ex.Na+×100/CEC n.d* not determination

and D_s is the depth of soil layer (cm). The reduction of EC_{eq} and ESP_{eq} from numerator and denominator the fractions of 1 and 2 equation lead to the results become independent from the effects of external factors such as the amount of evaporation, condition of international soil drainage, the quality of leaching water and the condition of applying the experiment. In this way, in fact, function is changed from explicit to the implicit function [36]. Analysis was done by SPSS, Curve Expert and Excel soft wars. Then four mathematical models fitted to values. The best empirical model was selected for every series of soils. Then with combination of all results, the best empirical model was obtained for studied region. These models were analysis in 1% significant level with some statistic criteria such as correlation coefficient and standard error. Then the appropriate model was determined for desalination.

RESULTS AND DISCUSSION

The amount of EC_e in soil has decreased after applying the leaching water (Table 3). Because of removing salts from surface to depth is the inversion of salts distribution before the leaching. After the leaching the sharp decrease was seen in EC_e and ESP in all of the layers.

This decrease was higher in surface layers specially the layer 0- 25 cm. after leaching, soil ESP has decreased and this reduction was higher in the layer 0-25 cm. Since, the secondary factor of soil salinity is sodium chloride, by increasing the concentration and as a result, increase the salinity the amount of sodium is rising (Table 3).

However, because of high solubility, this salt is removed easily from the soil. Overall, after leaching the amount of in Sableh, kushk and Salman have decreased to 7.29, 21.01, and 16.12 respectively. Similarly, ESP has had this trend in mentioned regions around 14.22, 0.59, and 25.53 respectively (Table 3).

By using data, obtained from two variables, X and Y, and according to analysis, four mathematical models were fitted to them. Exponential model with correlations coefficient of 0.9098 and standard error of 0.29 in significant level 1 percent was derived as a best model for kushk series that showed following:

$$Y = 0.854e^{-0.294x} \quad (3)$$

The most appropriate estimated model of sableh series was exponential model with correlations coefficient of 0.9172 and error standard of 0.40 in significant level 1 % achieved like this:

$$Y = 0.9172 e^{-0.444x} \quad (4)$$

One of the advantages of exponential model is that, it is possible to add leaching correlations coefficient into mentioned model like that:

$$Y = 0.854e^{-0.296x(\frac{f}{\theta_v})} \quad (5)$$

$$Y = 0.9172. \exp^{-0.444.x.(\frac{f}{\theta_v})} \quad (6)$$

F is a leaching efficiency quantity without distance and depends on soil texture (volumetric soil moisture). The leaching efficiency can be achieved by using empirical relations:

$$f = \frac{r.EC_w}{EC_{eq}} \quad (7)$$

$$r = \frac{Dw}{D_s} \quad (8)$$

By using relations 5 and 6 the leaching efficiency for sableh and kushk series was calculated 0.34 and 0.54 respectively that is in line with soil texture of region.

Logarithm model showed the best result in Salman series. The correlations coefficient and standard error in significant level 1% were 0.9107 and 0.34 respectively. The following relations were derived:

$$Y = 0.3181 + (0.144) \ln x \quad (9)$$

Based on relations 5 and 6 the leaching efficiency of Karkheh and Salman series were calculated 0.36 that it is consistent with soil texture.

Four mathematical models were applied to the collected experimental data to derive a suitable empirical model. The proposed exponential model with maximum correlation coefficient of 0.8821 and minimum standard error of 0.747 Can provide reasonable estimates for leaching process. The following relations were derived:

$$Y = 0.1107e^{-1.025} \quad (10)$$

If the variables were clear, water depth for required leaching in terms of soil modifications by using relations 10 can calculate:

$$D_{iw} = D_s. \left[\ln. \frac{\frac{EC_f - EC_{eq}}{EC_i - EC_{eq}}}{0.7898} \right] (1.025. \frac{f}{\theta_v}) \quad (11)$$

By applying relations 3, 4 and 9 the desalination curves for soil series of region are derived. The results are shown in Figure 1.

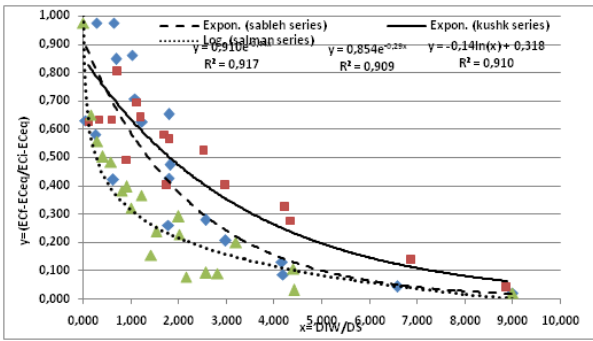


Fig. 1. Soil desalination curves in soil series in case study.

As seen in Figure 1 salt leaching of Karkheh, Sableh and Salman were easy, average and hard respectively. In addition, these three curves shown that, leaching of Salman series needs more water compare to Karkheh and Sableh series.

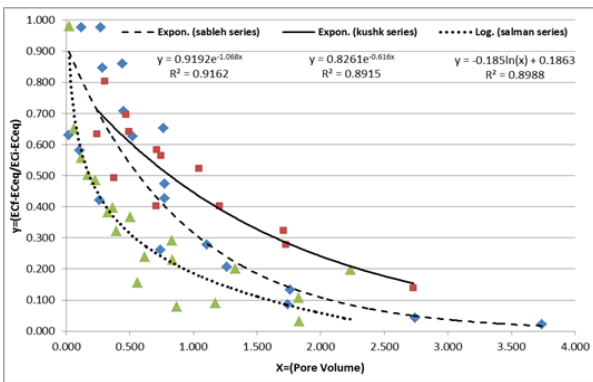


Fig. 2. Soil desalination curves in soil series in case study.

Desalination express based on pores volume compare to D_{lw}/D_s (Figs. 1&2) can be presenting better the salt leaching from soil layers. In fact, this hypothetic is not existence in the nature. However, the pore volume is the volume that leaching water passing toward it. The achieved correlation coefficients based on pore volume are less than toward water to soil, although the amounts were more real and more appropriate in assessment of the soil salinity changes (Fig. 2). Achieved desalination curves based on the relation 9 for soils of region that shown in Figure 3. By using of this curve, the last soil electrical conductivity (EC_f) and pure depth of required water for reclamation actions (D_{lw}) can estimate (Fig. 3). It should be considered for estimating all amount of required water for leaching, moisture reduction of the soil layer, evaporation from water and soil surface, and the level of rainfall. Furthermore, these factors should considered into calculation and leaching planning.

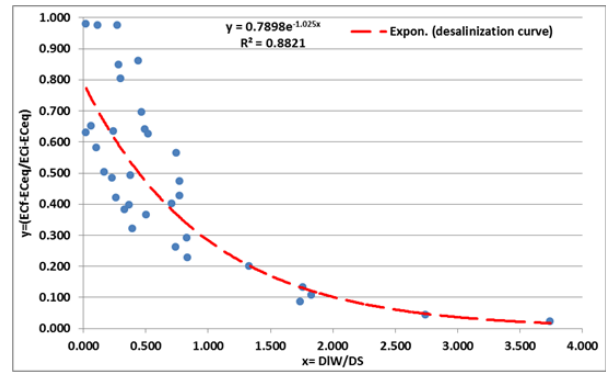


Fig. 3. Soil desalination curves in case study

It should attend that the application of these curves in the soil of case study in primary amount is in 13.70 to 30.8 ds/m of electro conductivity and 4.21 to 42.86 of sodium changes. By using figures of weight average, soil EC_e was calculated by applying tests and following relations of the percentage of removing initial salts and the percentage of leftover initial salts.

$$Y = \frac{EC_f}{EC_i} \times 100 \quad (12)$$

$$Y' = 100 - \left(\frac{EC_f}{EC_i} \times 100 \right) \quad (13)$$

$$Y' = 100 - \left(\frac{EC_f}{EC_i} \times 100 \right) \quad (14)$$

D_w is the depth of applied leaching water (cm), Y is the percentage of leached salts, Y' residual initial salt content, P.V is a pore volume and n is pores. Figures 4-6 show the relation of leached initial salt content with pore volume.

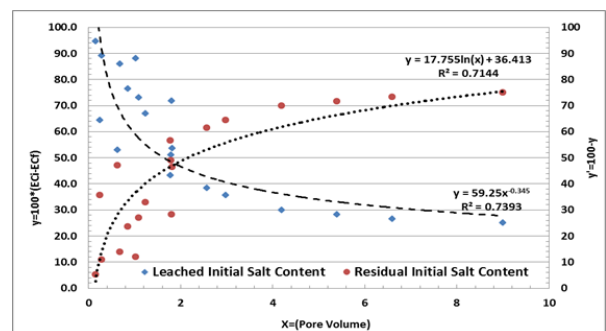


Fig. 4. Soil desalination curve and fraction of excess salts removed in sableh series.

By applying 100 cm water in Sableh soil series, which results in the leaching of 75.5, 73.30, 64.43, 48.95 and 32.98 percent of initial salts that equaling by 9.20, 6.60, 2.98, 1.80 and 1.23 unit of pore water in mentioned layers (Fig. 4).

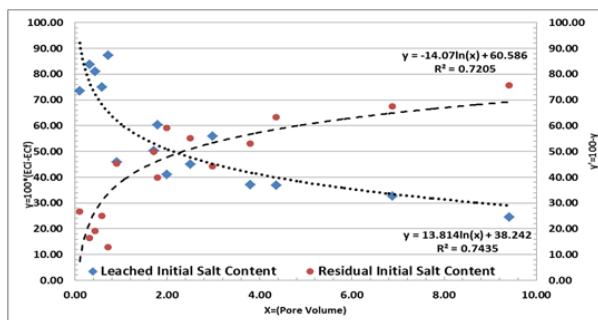


Fig. 5. Soil desalination curve and fraction of excess salts removed in kushk series.

According to results that shown in figure 5, applying 100 cm depth of leaching water in kushk series leads to the removing of 75.67, 67.41, 53.01, 44.20 and 39.82 percent of initial salts of soil layers that are equaling by 9.41, 6.88, 3.80, 2.99 and 1.79 unit of pore water for those layer (Fig. 5).

The survey of figure 6 show that the application of 100 cm water in Salman series leads to leaching of 86.04, 85.39, 81.26, 57.63 and 68.00 percent of initial salts of 25 cm layers. These data are equal by 9.24, 6.83, 4.41, 2.02 and 1.21 unit of pore volume for soil layers respectively (Fig. 6).

By considering the results in Figures 4-6 it is seen that in Sableh soil series the salts are removed around 35% for one unit of pore volume and around 58% for two unit of pore volume (Fig. 4).

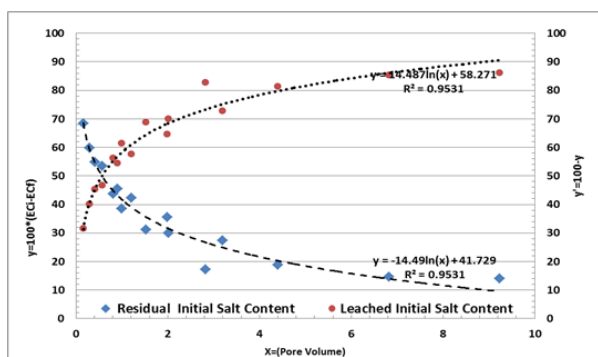


Fig. 6. Soil desalination curve and fraction of excess salts removed in salman series.

This trend also is seen in kushk series soil for unit of pore volume about 45% and for two unit of pore volume around 60% of salts are removed (Fig. 5). While, for one and two unit of pore volume of salman series around 65 and 78% of initial soils are removed (Fig. 6). The results of this study agree with of some researcher. Based on Neilson and Biggar [21] theory, for each of pore volume and two unit of this volume around 50 and 80 % of salts should remove. In addition, some researchers have reported that about 75% salts in sandy loam soils are transferred from unit of pore volume. Van der Molen [37] showed that 50% of soluble salts are

removed for applying per unit of pore volume from soil profile. In addition, there is a need for 120 cm leaching water that equaling by 35 unit of pore volume [38].

As a result, this study has shown that leaching efficiency of kushk series higher than Salman and Sableh series. This difference is associated with physical characteristics of soil and distribution of soil pores. In the case of soil texture, kushk, Sableh and Salman series have light to average, average to heavy and heavy to very heavy respectively.

Because of preferential flow, in heavy texture soil a part passed of water from cracks, penetrate to down ward without passing the real path of soil pores, as a result leaching efficiency are less than moderate and light texture soils.

The other factor that can mention is infiltration. Infiltration is impressing by sustainable and large pores. The existence of intensive structures in soil leads to soil infiltration is more affected by the relative frequency soil particles. Therefore, the water permeability of heavy soils is slow. In addition, number and continuity of large pores of soils have the high influence on the rate of water permeability to soil. Large soil pores are affected by type of soil structure. Therefore, variables such as bulk density and soil pores as an index represented soil structure that effective on the water permeability to the soil.

In this condition, the effect of some soil characteristics such as capillary power affected by relative frequency of soil particles has decreased and large pores (number, arrangement and continuity) characteristics, water permeability to soil and as a result the better salt leaching from soils become inhibits.

The results in Table 4 showed that, the sharp decrease around 4 ds/m or less of initial electro conductivity needs significant pure leaching water. Furthermore, 2645 m³ leaching water is need for decreasing the initial soil electro conductivity from 46 to 32 ds/m. Similarly, for decreasing the electro conductivity from 32 to 16, 16 to 8 and 8 to 4 ds/m, 2720, 2885 and 4160 m³ leaching water is require respectively. For analyzing the presented desalination model (relation 9), the comparison between presented model, and some empirical leaching models was done (Table 4).

That Initial soil electro conductivity until 150 cm of depth, the final soil electro conductivity, and the equilibrium of electro conductivity are considered 46.4 and 1.29 ds/m respectively.

The result show that Verma and Gupta model [30], Pazira and Keshavarz [31], Asadi et al. [39], Dieleman [28], and Hoffman [40] are estimating

Table 4. Required desalinization water for gradual decreasing of initial soil salinity from 46 ds/m to 4 ds/m

Initial soil salinity (ds/m)	Soil depth(cm)				Initial soil salinity (ds/m)	Soil depth(cm)			
	0-25	0-50	0-100	0-150		0-25	0-50	0-100	0-150
6.00	0.10	0.19	0.38	0.576	28.00	0.40	0.40	1.61	2.416
8.00	0.16	0.32	0.63	0.948	30.00	0.42	0.42	1.66	2.493
10.00	0.20	0.41	0.82	1.224	32.00	0.43	0.43	1.71	2.565
12.00	0.24	0.48	0.96	1.443	34.00	0.44	0.44	1.76	2.633
14.00	0.27	0.54	1.08	1.625	36.00	0.45	0.45	1.80	2.696
16.00	0.30	0.59	1.19	1.781	38.00	0.46	0.46	1.84	2.756
18.00	0.32	0.64	1.28	1.916	40.00	0.47	0.47	1.88	2.813
20.00	0.34	0.68	1.36	2.037	42.00	0.48	0.48	1.91	2.866
22.00	0.36	0.71	1.43	2.145	44.00	0.49	0.49	1.95	2.918
24.00	0.37	0.75	1.50	2.243	46.00	0.49	0.49	1.98	2.967
26.00	0.39	0.78	1.56	2.333					

Table 5. Comparison of require desalinization water for different available models and newly proposed model

Model	Water require for desalinization(cm)				Needed water (weighted mean) (m)	Rank
	0-25	0-50	0-100	0-150		
Reeve [27]	0.61	1.23	2.45	3.68	1.61	8
Dielman [28]	0.40	0.80	1.60	2.40	1.05	4
Leffelaar & Sharma [41]	0.54	1.08	1.62	2.16	1.42	7
Hoffman [40]	0.80	1.59	3.19	4.78	2.10	9
Verma & Gupta [30]	0.31	0.62	1.25	1.87	0.82	2
Pazira & Keshavarez [31]	0.31	0.63	1.26	1.88	0.83	3
Pazira & Kawachi [29]	0.48	0.96	1.91	2.87	1.26	5
Rajabzade et al. [33]	1.72	3.44	6.88	10.32	4.53	10
Asadi et al. [39]	0.26	0.52	1.05	1.57	0.69	1
new model (2013)	0.49	0.99	1.98	2.97	1.30	6

the amount of leaching water for soils less than new model. Pazira and Kawachi [29] and Reeve [27] model estimate the amount of soils leaching water a little more than new model. Rajabzadeh et al. [33] and Leffelaar and Sharma [41] models compare to the final model are not enough appropriate for estimating the required water in terms of modification the soil region. Some cause of this lack of appropriateness that can mention involving the differences among chemical and physical properties of tested soils and the leaching applied way. The similar results are reported by other researchers [31] (Table 5).

RESULTS

The study of the percentage of leached salt in soil profile of all three case studies soil series showed that by considering the application of two-unit pore water volume as a leaching water, the differences of soil texture and the effect of soil texture of washing the soluble salts can associated as a causes. So that, when soil texture becomes lighter, it leads to increase the removing percentage of soluble salts and because of the existence of natural calcium resources in soils, there was no

tendency to sodiomic and this important subject indicates the lack of necessity of applying the amendment materials.

REFERENCES

1. S. A. Kapourchal, M. Homae, E. Pazira, *Int. J. Agric. Sci. Res.*, **1**, 25 (2011).
2. V. R. Jalali, M. Homae, In: Proc. 19th Worl. Cong. Soil. Sci, Australia, p 50 (2010).
3. Y. M. Hosaini, N. A. Homae, N. A. Karimian, S. Saadat, *J. Plant. Pro*, **3**, 91 (2009).
4. V. R. Jalali, M. Homae, Proceedings of XXXIII CIOSTA Conference, Italy, p.1283 (2009).
5. V. R. Jalali, M. Homae, S. Taherizadeh. Proceedings of XXXIII CIOSTA Conference, Italy, p.1289 (2009).
6. V. R. Jalali, M. Homae. Proceedings of XXXIII CIOSTA Conference, Italy, p.1283 (2009).
7. A. R. Kiani, M. Mirlatif, M. Homae, Effect of different irrigation regimes and salinity on wheat yield in Gorganregion. Agricultural Engineering Conference, Belgium (2004).
8. A. R. Kiani, M. Mirlatif, M. Homae, Wheat production function under salinity and water stress, Agricultural Engineering Conference, Belgium (2004).

9. A. R. Kiani, A. Asadi, M. Homaeae, M. Mirlatifi, Proceedings of MTERM International Conference, AIT, Thailand (2004).
10. E. Esmaili, S. Asadi-Kapourchal, M. J. Malakouti, M. Homaeae. *Plant Soil Environ*, **56**, 537 (2008).
11. M. Homaeae, C. Dirksen, R.A. Feddes, *Agric. Water Manag.*, **57**, 89 (2002).
12. M. Homaeae, U. Schmidhalter, *Irrigation Sci.*, **27**, 83 (2008).
13. A. A. Norozi, M. Homaeae, A. Farshad. *Iran Environ. Sci.*, **8**, 59 (2012).
14. E. Pazira, M. Homaeae, Proceedings of the XVIIth World Congress of the International Commission of Agricultural Engineering (CIGR), Canada, p. 1(2010).
15. A.R. Kiani, G. A. Roshani, M. Homaeae. Proceedings of Second International Salinity Forum, Adelaide Convection Centre, Australia (2008).
16. A. Ben-Gal, E. Ityel, L. Dudley, S. Cohen, U. Yermiyahu, E. Presnov, L. Zigmond, U. Shani, *Agric. Water Manag.*, **95**, 587 (2008).
17. H. A. Loáiciga, H. Allison, *J. Hydrol. Eng.*, **12**, 109 (2007).
18. W. R. Gardner, R. H. Brooks, *Soil Sci.*, **83**, 295 (1957).
19. R.K. Gupta, Proceedings of International American Salinity and Water Management, Mecxico, p. 49 (1992).
20. C.M. Cote, K.L. Bristow, P.J. Rose, *J. Contam. Hydrol.*, **43**, 191 (2000).
21. D. R. Nielsen, J. W. Biggar, *Soil Sci. Soc. Am. J.*, **215**, 1 (1961).
22. W. R. Gardner, M. Fireman, *Soil*, **5**, 244 (1958).
23. C. M. Burt, B. Isabel, *Am. Soc. Agric. Eng.*, **12**, 14 (2005).
24. D. L. Corwin, J. D. Rhoades, J. Simuner, *Agric. Water Manag.*, **90**, 165 (2007).
25. K. V. G. K. Rao, P. B. Leeds-Harrison, *Agric. Water Manag.*, **19**, 303 (1991).
26. M. Homaeae, C. Dirksen, R. A. Feddes, *Agric. Water Manag.*, **57**, 111 (2002).
27. R. C. Reeve, Third Congress of International Commission on Irrigation and Drainage Transaction, Part 5, p.10.175 (1957).
28. P. J. Dieleman, Veenman, Wageningen, p.175 (1963).
29. E. Pazira, T. Kawachi, *J. Integ. Agric. Water Use Fresh Res.*, **6**, 39 (1981).
30. S. K. Verma, R. K. Gupta, *J. Ind. Soc. Soil Sci.*, **37**, 803 (1989).
31. E. Pazira, A. Keshavarz, International Workshop on the Use of Saline and Brackish-Water for Irrigation, Indonesia, p. 328 (1998).
32. K. Mohsenifar, E. Pazira, P. Najafi, *J. Res. Agric. Sci.*, **2**, 73 (2006).
33. F. Rajabzadeh, E. Pazira, M. H. Mahdian, S. H. Mahmoodi, M. Heidarizadeh, *J. Appl. Sci.*, **22**, 4020 (2009).
34. S. A. Kapourchal, M. Homaeae, E. Pazira, *J. Basic Appl. Sci. Res.*, **3**, 774 (2013).
35. L. A. Richards, In: Agricultural Handbook No. 60, USDA, Washington (1954).
36. M. Mohamadzadeh, M. Homaeae, E. Pazira, *Int. J. Agric. Sci. Res.*, **3**, 45 (2013).
37. W. H. Van der Molen, *Soil Sci.*, **81**, 19 (1956).
38. T. Talsma, *Aust. J. Soil Res.*, **5**, 37 (1966).
39. S. A. Kapourchal, M. Homaeae, E. Pazira, *J. Conserv. Water Soil. Res.*, **2**, 65 (2012).
40. G. J. Hoffman, Proceedings of International American Salinity and Water Management, Technical Conference, Mecxico, PP: 49, 64 (1980).
41. P. A. Leffelaar, P. Sharma, *J. Hydrol.*, **32**, 203 (1977).

Anthracene biodegradation by *Pseudomonas aeruginosa* isolated from Babolrood River estuary in Mazandaran province

M. Sasani¹, S. Khoramnejadian^{1*}, R. Safari²

¹Department of Environment, Damavand branch, Islamic Azad University, Damavand, Iran

²Ecological academy of Caspian Sea, Department of Aquatic Biotechnology, Sari, Iran

Received February 17, 2016; Revised December 26, 2016

A wide variety of polycyclic aromatic hydrocarbons (PAHs) is found in the environment as a result of the incomplete degradation of organic substances or by many anthropogenic activities, such as the petrochemical industry and oil refining. In these activities, PAHs are existing in the effluent as complex compounds of low bioavailability that are highly limiting for conventional biodegradation techniques. These compounds are mutagenic and carcinogenic for human and animals. Biodegradation is one of the most important methods for decreasing of environmental pollutants. This process was done using different microorganism particularly bacteria and fungi. Various parameters such as pH, temperature, time, biotic and abiotic factors influence on biodegradation. Anthracene is three rings aromatic and exists in petroleum oil contaminated sites. Some of bacteria, owing to degrader enzymes production, are capable to degrade of anthracene. The aim of this study was isolation of anthracene biodegrading bacteria from Babolrood River estuary and evaluation of the biodegradation process in bench scale. Sampling was done from river estuary sediment and had cultured in Minimal Salt Medium (MSM). *Pseudomonas aeruginosa* was one of the isolated bacteria from river sediment that identified by molecular technique. In next step, influence of pH, temperature and concentration of anthracene were surveyed on anthracene biodegradation by *P. aeruginosa* during zero, 24 and 48 hours. The results showed that the optimized condition for biodegradation included pH= 7.5, 35 °C and 150 ppm of anthracene. Bacterial degradation of anthracene was increased with prolong of incubation time. Efficiency of *P. aeruginosa* for decomposition of anthracene was more than 50% during 48 hours. As regards to high ability of *P. aeruginosa* and also its survival in improper condition this bacteria can be used as biological tools for degradation of anthracene in oil contaminated regions.

Keywords: *Pseudomonas aeruginosa*, Anthracene, Babolrood River, PAHs.

INTRODUCTION

Growth population, urbanization and industrial development and enhance the standard levels of living, cause increase needing to new resources and the arrival of new compounds to human life cycle leading to contamination of water resources. High doses of chemical pollutants via industrial wastewater and municipal wastewater and industrial enter to the environment and natural water resources [1]. High volumes of organic waste production as a result of urbanization and necessity to manage different organic waste at low-input must be mentioned as well as eco-friendly basis [2].

Polycyclic aromatic hydrocarbons (PAHs) are recognized as carcinogenic and mutagenic compounds [3]. These compounds are often found as complex mixtures in the environment and rarely seen in single form. These compounds are usually

colorless (white or light yellow color) and used in the painting, making plastics, pesticides and asphalt roads [4]. Although some of the PAHs compounds in natural conditions were decayed by the indigenous microbial population but this process usually takes time [5] and requires using of techniques with high performance which is able to carry out this process in a shorter time. Some physical methods such as flotation has a no high efficiency and common chemical methods such as using of surfactants was usually costly and have a lot of limitations. One effective method to reduce the PAHs compounds is use of biological methods that microbes individually or in combination in order to complete decomposition of pollutants were used. Research on biodegradation of petroleum compounds show that this method is one of the most economic and effective methods to hydrocarbon removal from aqueous environments [3]. In the process of biodegradation some microorganisms should be used that are indigenous in the infected area and are not included manipulated organism [6]. Ability of bacteria in

* To whom all correspondence should be sent:
E-mail khoramnejad@damavandiau.ac.ir

soil, water or sediment to biodegradation of PAHs depends on the complexity of the chemical structure of substances and compatibility enzyme producing bacteria in the environment of pollutants. Generally, two-ring PAHs are readily biodegradable and various bacteria are capable of degrading these compounds and used them as a source of carbon and energy [7]. Degradation of compounds containing benzene rings hardly was done and only bacteria have indicator enzymes was able to do this process. Anthracene including tricyclic aromatic compounds is less studied. According to the few studies on indigenous bacteria in Caspian region in northern Iran, the main objective of this study was biodegradation of polyaromatic hydrocarbons (anthracene) by *Pseudomonas aeruginosa*, isolated from sediments of estuaries Babolrood River and identification of secondary metabolites by GC-MS analysis.

MATERIAL AND METHODS

All tests were done based on standard methods described in the Examination of Water and Wastewater [8]. All chemicals were purchased from Merck Company (Germany).

Sampling

In this study, Babolrood estuarine sediment in Mazandaran province was used as a bacteria isolation medium. Samples were conducted using the Grp from sediment Babol River at several points of the estuary. In order to prevent the death of bacteria in the sediment, samples placed on plastic containers and transferred to the central laboratory in the shortest time with low temperature.

Obtain pure samples of anthracene degrading bacteria

Generally, the medium contain the pollution index compound was used to isolate the bacteria with desired properties as a selector agent. For this purpose, after transferring the samples to laboratory and preparation serial dilution, culture was conducted at MSM medium. After adjusting the pH in the range of 7, disinfection process was carried out at 120 °C for 15 m and after arriving medium temperature to 50 °C, sterilized Anthracene with 0.45 micron filter Millipore as a source of carbon (50 mg/l) was added. After incubation at 30 °C for 5 days and growth of cultured bacteria (the appearance of opacity). Subsequently culture was conducted at MSM agar contain anthracene and samples were incubated at 30 °C for 72 h. After growth of anthracene degrading colonies, to

subculture and purifying colonies index was action [9-10].

Molecular study

Polymerase chain reaction (PCR) was applied for identification of isolated bacteria [11]. Two pairs of primers were designed based on the nucleotide sequences of the 16s rRNA gene [11-13] of *P. aeruginosa* include: F: (5'-CCAGTTTGATCMTGGCTCAG -3') and R: (5'-AGAGTTTGATCMTGGCTCAG -3) in order to identify the *P. aeruginosa*. Primers were synthesized by Cinna Gen Company (Tehran, Iran). DNA extracted according the method described by Samaei et al. (2013) and polymerase chain reaction was repeated in 30 cycles [11] under the following conditions: 30 s min at 94 °C (1 Hz), 1 min at 64 °C, 1 min at 58°C, 1.5 min at 72 °C (35 Hz) and finally, PCR was completed with the final extension step at 72 °C for 8 min. Distilled water was used as a negative control in each PCR reaction.

Sequencing of PCR product

For each sample 30 µl of PCR products and 20 µl of each forward and reverse primers (Concentration of 20 µmol) were transferred in a separate tubes to the BIONEER Company (South Korea). After receiving the results of sequencing using Sanger assay and BLAST in the GenBank NCBI, unknown bacteria were identified [11].

Preparation of bacteria to inoculate the broth media to evaluate the decomposition process

At first, the primary cultured bacteria carried in TSB medium and after incubation at 30 °C for 24 h, medium was centrifuged at 13,000 rpm for 5 min and after discarding the supernatant, 10 ml of saline solution was added to the remaining sediment and after mixing, opacity suspension was compared with McFarland standard tubes (0.5 McFarland equivalents 1.5×10^8 CFU/ ml) [9].

Biodegradation of anthracene in broth media

Anthracene biodegradation test were performed in 500 ml Erlenmeyer flasks containing 200 ml of MSM media. Studied parameters, including concentration of anthracene (150, 200 ppm), incubation time (0, 24, and 48 h), pH (6.5 and 7.5) and temperature (25 and 35 °C). Samples was put in a shaking incubator at 120 rpm and tryptic soy agar (TSA) was used to assess the process of growth bacteria and the number of colonies was determined. The high-performance liquid chromatography device (HPLC, KNAUER,

Germany) was used to measure the concentration of anthracene residue after decomposition by bacteria [5]. Acetonitrile solvent and water with ratio of 90 to 10 as a mobile phase with a flow rate of 1 mL per minute, C18 column and UV detector were used [12-14]. All experiments were conducted With 3 replications.

Statistical analysis

The obtained data were subjected to two-way analysis of variance using SPSS statistical software, release 18.0. Duncan's new multiple range test was performed to determine the significant differences between means at the 5% probability level ($P < 0.05$).

RESULTS

Isolated bacteria

Biochemical tests and PCR assay confirmed *P. aeruginosa*. After PCR assay, DNAs extracted from isolated bacteria gave the expected 357 bp PCR fragment of 16S rDNA sequences, which is specific for *P. aeruginosa* which shown in Fig. 1.

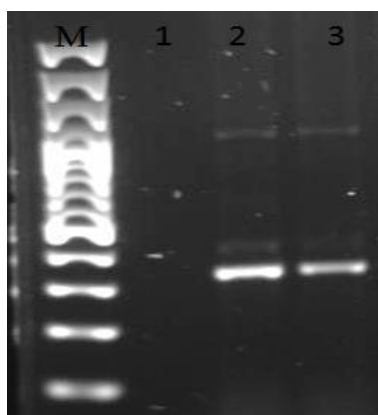


Fig. 1. Electerophoretic analysis (2% agarose gel) of DNA amplified fragments from 3 isolates in this experiment (M: Marker, Lan 1: negative control, Lan 2: positive control, Lan 3: positive isolate).

The effect of initial concentration of anthracene on the removal efficiency

Results of Tables 1 and 2 showed that by increasing the concentration of anthracene process of growth of *P. aeruginosa* was decreased. On the other hand, anthracene reduction in the concentration of 200 mg/l at 24 and 48 hours has been very slowly. Changes in the number of bacteria and concentrations of anthracene was significant after 24 and 48 h ($P < 0.05$). The number of *P. aeruginosa* shown in table 1. Concentration changes of anthracene in the presence of *P. aeruginosa* in 150 and 200 mg/l were shown in table 2.

The effect of initial pH on the removal efficiency

The concentration of 150 mg/l has a better effect on bacterial decomposition. Therefore, 150 mg/l concentrations were considered as the optimum concentration for next study. Results of Tables 3 and 4 showed that pH=7.5 had a better bacterial decomposition compared to pH of 6.5. The number of *P. aeruginosa* (log) at pH= 6.5 and 7.5 were shown in table 3. Table 4 shown the Concentration changes of anthracene in the presence of *P. aeruginosa* at pH= 6.5 and 7.5.

Table 1. The number of *P. aeruginosa* (log) in 150 and 200 mg/l concentration of anthracene.

Incubtion time (h)	Concentration (mg/l)	
	200 mg/l	150 mg/l
0	7.00 ±0.2 aC	7.02 ±0.33 aC
24	8.25 ±0.03 bB	8.48 ±0.03 aB
48	8.41 ±0.07 bA	9.25 ±0.07 aA

*Different small and capital superscript letters within each row and column, respectively, represent significant differences ($p < 0.05$).

Table 2. Concentration changes of anthracene in the presence of *P. aeruginosa* in 150 and 200 mg/l concentration.

Incubtion time (h)	Concentration (mg/l)	
	200 mg/l	150 mg/l
0	200.00 ±4.25 A	150.00 ±1.45 A
24	165.00 ±4.89 B	120.00 ±3.26 B
48	150.00 ±2.30 C	73.00 ±4.11 C

*Different capital superscript letters within column, represent significant differences ($p < 0.05$).

Table 3. The number of *P. aeruginosa* (log) at pH= 6.5 and 7.5 (in 150 mg/l concentration of anthracene)

Incubtion time (h)	pH	
	7.5	6.5
0	7.04 ±0.08 aC	7.01 ±0.12 aC
24	8.68 ±0.04 aB	8.52 ±0.03 bB
48	9.52 ±0.07 aA	9.18 ±0.07 bA

*Different small and capital superscript letters within each row and column, respectively, represent significant differences ($p < 0.05$).

Table 4. Concentration changes of anthracene in the presence of *P. aeruginosa* at pH= 6.5 and 7.5

Incubtion time (h)	pH	
	7.5	6.5
0	150.00 ±1.11 aA	150.00 ±1.21 aA
24	121.00 ±4.17 aB	119.00 ±3.42 aB
48	73.00 ±3.26 aC	70.00 ±1.82 aC

*Different small and capital superscript letters within each row and column, respectively, represent significant differences ($p < 0.05$).

The effect of temperature on the removal efficiency

The effect of temperature on decomposition of anthracene are shown in Tables 5 and 6. Most bacterial decomposition at 35 °C was observed. Observed changing in the number of bacteria and 150 anthracene concentrations in both 25 and 35 °C at 24 and 48 hours was significant ($P < 0.05$).

Table 5. The number of *P. aeruginosa* (log) in 25 C° and 35 C° at pH= 7.5 and 150 mg/l concentration of anthracene)

Incubtion time (h)	Temperature	
	25 C°	35 C°
0	7.00 ±0.09 aC	6.98 ±0.06 aC
24	8.50 ±0.06 bB	8.73 ±0.09 aB
48	9.35 ±0.20 bA	9.85 ±0.28 aA

*Different small and capital superscript letters within each row and column, respectively, represent significant differences ($p < 0.05$).

Table 6. Concentration changes of anthracene (150 mg/l concentration) in the presence of *P. aeruginosa* in 25 and 35 °C at pH= 7.5

Incubtion time (h)	pH	
	25 C°	35 C°
0	150.00 ±1.45 aA	150.00 ±1.34 aA
24	120.00 ±2.12 aB	122.00 ±3.20 bB
48	71.00 ±3.25 aC	75.00 ±1.84 aC

*Different small and capital superscript letters within each row and column, respectively, represent significant differences ($p < 0.05$).

Survey the removal efficiency in optimum condition

Based on the results, the best conditions to decomposition of anthracene was pH=7.5, 35 °C temperature and 150 mg/l of anthracene concentration. In this condition, the removal efficiency was more than 50 percent.

Identification of secondary metabolites producing from the decomposition of anthracene

In figure 2, different secondary metabolites producing from the biodegradation of anthracene was shown. The highest peak of the secondary metabolite was 2,3-dehydroxy naphthalene followed by catechol and phthalate. These metabolites are recognized as intermediate terminal products and represent a relatively complete biodegradation of anthracene by *P. aeruginosa*. isolats. Based on the figure 2, a lot of metabolites with very low values were produced that immediately affected by microbial degradation and turn into the next metabolite. Among the most important of these compounds can be mentioned to

Anthracene cis 1,2-dihydroxy DL, 1,2-dihydroxy Anthracene, Cis 4, 2-oxobut enoic acid.

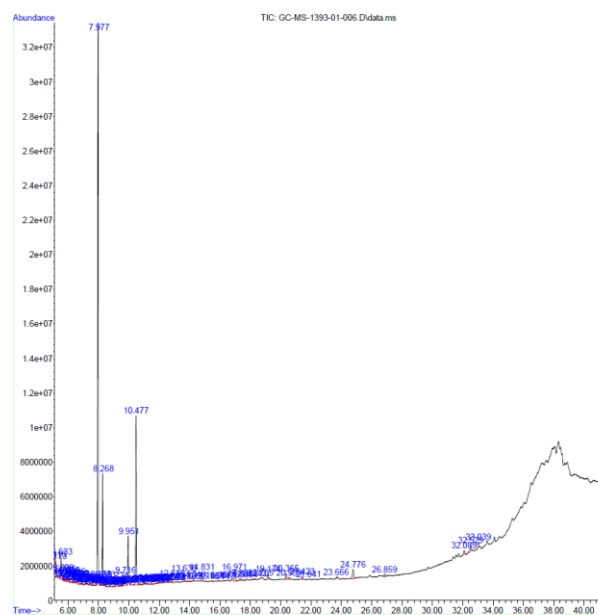


Fig. 2. Chromatograms showing degradation of the PAH by *P. aeruginosa*.

DISCUSSION

Isolated bacteria

In Jacques et al. (2005) study, *P. aeruginosa* was recognized as indicator bacteria isolated from soils contaminated with petroleum which was able to biodegradation of anthracene in high concentrations [15]. In Simarro et al. (2013) survey, *Pseudomonas* sp., was able to biodegradation of anthracene and naphthalene at different concentrations [16]. Prakash et al. (2014) reported that *Pseudomonas* sp., *Bacillus* sp. and *Micrococcus* sp. were the dominant genera isolated from contaminated areas with petroleum that able to biodegradation of benzene, toluene, anthracene, naphthalene and gasoline. Results showed when these bacteria were used in combination forms, significant decline of petroleum compounds were observed [14]. In Safahieh et al. (2010) study, *P. aeruginosa* and *Pseudomonas putida* was recognized as bacteria with high ability in biodegradation of naphthalene in Khor Moosa and the rate of degradation of naphthalene by these bacteria after 120 h were 96% and 91%, respectively [17]. In these mention study, different species of *Pseudomonas* were able to growth in different conditions and capable to biodegradation of petroleum compounds. These bacteria because of producing the different enzymes and have a spore form have a high efficacy to reduce the different environmental pollutants.

The effect of initial concentration of anthracene on the removal efficiency

The results indicate that by increasing concentrations of anthracene the trend of biodegradation was slower that related to toxicity of PAHs in high concentrations of bacteria [18]. Some works reported that *P. aeruginosa* and *P. putida* isolated from soils contaminated with petroleum capable to biodegradation of anthracene in high concentrations after 120 h. Ability of bacteria to biodegradation of petroleum compounds was depend on the genus and species of bacteria, ability of bacteria to producing of biodegradation enzymes and finally to period time of incubation [15]. In current study the period of incubation time was 48 h which has been relatively little time for biodegradation of bacterial and bacteria need the more time for adaptation to the new conditions and biodegradation of petroleum compounds. In some studied, this time was 5 days. In current study *P. aeruginosa* were able to biodegradation of anthracene at a concentration of 150 mg/l during 48 hours with efficacy more than 50%. Although in other studies, during 6 to 10 days the efficiency of biodegradation was between 55 to 65% [15-17]. Therefore, it is expected that with increasing the incubation time, the efficiency of biodegradation of anthracene was increased by *P. aeruginosa*.

The effect of initial pH on the removal efficiency

Study of Simarro et al. (2013) showed that *Pseudomonas* species capable to biodegradation of Polycyclic aromatic hydrocarbons at pH=7 and relatively high temperature (30 °C), in this study biodegradation of naphthalene was faster than anthracene [16]. Results of Jacques et al. (2005) study indicated that *P. aeruginosa* isolated from contaminated soil able to biodegradation of anthracene at pH 6.5, 7 and 7.5 with 28.2, 32.5 and 34.5 during 5 days which reflects the high efficiency of biodegradation at pH=7.5. These results were similar to our study and confirmed it [15]. Most environmental bacteria has optimum activity at pH=7.5. Also, in lower or higher pH were able to growth and proliferation.

The effect of temperature on the removal efficiency

In other work Research of Jacques et al. (2005) proved that *P. aeruginosa* isolated from contaminated soil able to biodegradation of anthracene at 20, 25, 30, 35 and 40 ° C with 46.8, 59.6 and 64% during 5 days. These results indicated high efficiency of this bacterium to biodegradation of anthracene at 20 and 30 °C, in our study highest efficiency of *P. aeruginosa* to

biodegradation of anthracene was observed in 30 °C. Some Studies showed that different species of *Pseudomonas* capable to biodegradation of naphthalene and anthracene at 35 °C and used them as a source of carbon and energy. Different bacteria depending on their natures (thermophilic, psychrophilic and mesophilic) has been able to grow and reproduce at different temperatures and has a minimum, maximum and optimum temperatures of growth [16].

The removal efficiency in optimum condition

Studies by other researchers confirmed the results of the present study and in most study pH=7.5 and 35 °C temperature provide the optimum conditions for biodegradation bacteria, So in mention condition some bacterial species able to adapted to higher concentrations of petroleum compounds and eventually biodegradation them. In other studies, the incubation time was between 6 to 10 days or even more, although in present study the incubation time was 2 days. However, in this period time the efficiency was more than 50 percent which reflects the high ability of *P. aeruginosa* to biodegradation of anthracene.

Identification of secondary metabolites producing from the decomposition of anthracene

In our study similar to Arab and Salim (2010) survey, intermediate compounds was produce due biodegradation of anthracene by *P. aeruginosa* isolated from contaminated soil [15]. Various metabolites due biodegradable of aromatic ring compounds was identified and compared with each for quality and quantity properties [18-19]. The presence of phthalates indicating that the bacteria action through the phthalate metabolite and anthracene was converted to phthalate. In this assay the number of generated metabolites was low [20]. The presence of catechol indicated that Anthracene affected by bacterial decomposition was converted to the secondary metabolites and finally to catechol that is different from the phthalate metabolite pathway [21].

CONCLUSION

Results of current study indicated that *P. aeruginosa* isolated from estuarine sediments of Babolrood River had the high potential and ability to biodegradation of Anthracene and in the optimum condition (temperature and pH) able to biodegradation more than 50% of Anthracene in *in vitro* condition. So, after complete and additional studies and confirmed the ability biodegradation of Aromatic compounds by *P. aeruginosa* and achieve

to reasonable results, *P. aeruginosa* for native to the climatic conditions of Mazandaran province could be used to clean up oil spills in polluted areas.

REFERENCES

1. W. Christopher, R. Bentham, *Appl. Environ. Soil Sci.*, **46**, 171 (2011).
2. H. Radnezhad, S. H. Khalili Arjaqy, F. Mortazaeinezhad, M. Foroughi Abari, M. Sadeghi, *J. Pure Appl. Microbiol.*, **9**, 2203 (2015).
3. G. Coral, S. Karagoz, *Ann. Microbiol.*, **55**, 255 (2005).
4. D. Boyle, C. Wiesner, R. A. Ichardson, *Soil Biol. Biochem.*, **30**, 873 (1998).
5. A. Arab, B. Salim, *J. Am. Sci.*, **10**, 1237 (2010).
6. M. Emtiazjo, S. Sedighi, *Int. J. Sci. Environ. Tech.*, **11**, 258 (2009).
7. A. Sharon, L. Churchil, P. Jenniffer, R. Harpe F. Perry, *Appl. Environ. Microbiol.*, **65**, 52 (1999).
8. APHA/AWWA/WEF Standard Methods for the Examination of Water and Wastewater, 20 ed. Washington DC, (1998).
9. R. Safari, Z. Yaghobzadeh, *J. Mar. Sci. Tech.*, **3**, 35 (2006).
10. C. Cerniglia, *Biodegradation*, **3**, 331 (1992).
11. M. R. Samaei, S. B. Mortazavi, *Fresen Environ. Bull.*, **22**, 1304 (2013).
12. M. Barret, H. Carre, *Water Res.*, **44**, 3797 (2010).
13. C. Kazunga, M. Aitken, *Appl. Environ. Microbiol.*, **66**, 1917 (2000).
14. A. Prakash, S. Bisht, J. Singh, *Turk J. Eng. Environ. Sci.*, **38**, 41 (2014).
15. R. J. S. Jacques, E. C. Santos, F. M. Bento, M. C. R. Peralba, P. A. Selbach, E. L. S. Sa', A. O. Flavio Camargo, *Int. Biodeterior. Biodegr.*, **56**, 143 (2005).
16. R. Simarro, N. Gonzalez, F. L. Bautista, C. M. Molina, *FEMS Microbiol. Ecol.*, **83**, 438 (2013).
17. S. Bisht, P. Pandey, A. Sood, *Braz. J. Microbiol.*, **41**, 922 (2010).
18. C. Cripps, A. John, B. Steven, D. Aust, *Appl. Environ. Microbiol.*, **56**, 1114 (1990).
19. C. E. Cerniglia, *Adv. Appl. Microbiol.*, **30**, 31 (1984).
20. A. Safahieh, F. Mojodi, H. Zolgharnin, *Int. J. Environ. Stud.*, **58**, 149 (2010).
21. S. Bajkic, B. Vasiljevic, *Arch. Biol. Sci.*, **63**, 1057 (2011).

Choline reduces the hepatocyte nuclear factor-4 α (HNF-4 α) in HepG2 cells

A.Mohammadi^{1,2}, M.R. Baneshi³, T. Khalili^{1,*}

¹Department of Clinical Biochemistry, Afzalipour School of Medicine, Kerman University of Medical Sciences, Kerman, Iran.

²Physiology Research Center, Kerman University of Medical Sciences, Kerman, Iran

³Modeling in Health Research Center, Institute for Futures Studies in Health, Department of Biostatistics and Epidemiology, School of Public Health, Kerman University of Medical Sciences, Kerman, Iran

Received February 25, 2016; Revised November 12, 2016

Choline is a semi-essential nutrient that is required to make main membrane phospholipids including phosphatidylcholine and sphingomyeline. The liver is the most important organ for metabolism dietary choline and phosphatidylcholine. The liver is enriched transcription factors of genes that are preferentially expressed in this tissue. Hepatocyte nuclear factor-4 α (HNF-4 α) is known as a master regulator of liver-specific gene expression. The activity of HNF-4 α may be regulated by dietary components. In this study, to investigate the effects of choline and lecithin on HNF-4 α expression, the HepG2 cells were treated with several concentrations of these compounds, including concentration of 11.25 μ M, 22.5 μ M, 35 μ M for choline and 0.23 mg/ml and 0.46 mg/ml for lecithin, at three time intervals 6, 12 and 24 hours. Then expression of HNF-4 α at mRNA level was assessed by real-time PCR. The results showed a 50% decrease in HNF-4 α mRNA levels when HepG2 cells were treated with choline chloride at concentration 35 μ M for 24 hours.

Keywords: Phosphatidylcholine, Real-time PCR, gene expression, DNA methylation, lecithin

INTRODUCTION

Choline is a semi-essential nutrient that is found in dietary sources such as egg yolk, meat, liver, nuts and soybean. It functions as a methyl group donor [1-2] and is involved in many physiological processes, including metabolism and transport of lipids, methylation reactions, and neurotransmitter synthesis [1]. The majority of choline in our body is found in phospholipids such as phosphatidylcholine and sphingomyelin. Phosphatidylcholine (lecithin) is the most abundant choline species in mammalian tissues that accounts for 95% of the total choline pool [2-3]. It is a major structural component of membrane bilayers and lipoproteins, and thereby it participates in signaling and transport across membranes [3-5]. Phosphatidylcholine is the important choline metabolite that is necessary for packaging and export of triglycerides in VLDL (very low density lipoprotein) and solubilization of bile salts for secretion [6-7]. Liver is an important site for choline metabolism and storage and also, it requires choline for proper function, so that choline deficiency causes abnormal deposition of fat in the liver and results in fatty liver disease [6]. In human, choline deprivation causes liver cell death and Hepatosteatosis. The spectrum of effects choline in the liver and several mechanisms for these effects has been identified [8-10].

The liver is enriched transcription factors of genes that are preferentially expressed in this tissue. Hepatocyte nuclear factor-4 α (HNF-4 α) is a highly

conserved member of the nuclear receptor superfamily that regulates the expression of genes involved in fatty acid, cholesterol and glucose metabolism [11-13]. The study with liver-specific HNF-4 α knockout (KO) has shown that inactivation of HNF-4 α leads to abnormal deposition glycogen and of lipid in the liver. Lipid accumulation and fatty liver phenotype in this animal are indicated the role of HNF-4 α in the regulation of genes involved in fatty acid metabolism [11, 14]. It can influence the levels and activity of HNF-4 α but it is not known if HNF-4 α may be affected by choline, as an endogenous factor and also a component of dietary. Thus, the objective of this study was an investigation of the effects of choline and also lecithin on HNF-4 α expression.

MATERIALS AND METHODS

Cell culture

HepG2 cells were prepared from the Stem cell Research Center of Kerman University of Medical Sciences. After thawing and cell recovery in Dulbecco's Modified Eagle Medium (DMEM) containing fetal bovine serum (at ratio 1:10 as 1ml from thawed cells and 9ml medium), the cells were cultured in DMEM supplemented with 10% of FBS and 1.5% of penicillin/streptomycin and were maintained at 5% CO₂ and temperature of 37°C. The medium was changed every 3-4 days. Each T-25 flask of Cultures was split (1:4) when it reached to 80-90% Confluency using 1ml trypsin/EDTA (0.05% trypsin, 0.5mM EDTA). For treatment, cells were plated at a seeding density of 1.5-2 \times 10⁶ cells

* To whom all correspondence should be sent:
E-mail: taherehkh2131@yahoo.com

per each 60 mm petri dish in medium and after 24 hours, the medium was replaced with medium containing choline (11.25 μ M, 22.5 μ M, 35 μ M) or lecithin (0.23 mg/ml and 0.46 mg/ml) and the cells were incubated at 37°C and 5% of CO₂ for 6, 12 or 24 hours. At the end of treatment period, the cells were washed twice with phosphate buffered saline (PBS) and then were detached by scraping in Tripure reagent (Roche applied science, Switzerland) for RNA extraction. The samples were frozen at -80 °C until RNA isolation could be carried out.

RNA extraction

Total RNA was extracted from HepG2 cells using Trizol reagent (Roche applied science, Switzerland) according to the manufacturer's instructions. The quality and integrity of RNA were checked by electrophoresis on 1% agarose gel. The concentration of total RNA was quantified spectrophotometrically at 260 nm using a ND-1000 nanodrop (Thermo Scientific).

Reverse Transcription and Real-time PCR

First-strand cDNA was synthesized from 1 μ g of total RNA using Revert Aid First Strand cDNA synthesis kit (Thermo Scientific, USA) according to the manufacturer's protocol. In brief, the reverse transcription reaction mixture was prepared in a final

volume of 20 μ l containing 4 μ l reaction buffer (5X), 2 μ l dNTP mix (10mM), 1 μ l random Hexamer (100 μ M), total RNA (1 μ g) and nuclease-free water. Thermal program for cDNA synthesis was as follows: first step incubation at 25 °C for 5 min, then one cycle incubation at 42 °C for 60 min that terminated by heating at 70 °C for 5min. The cDNAs were stored at -20 °C until use. Real time PCR were performed with 3 μ l cDNA and specific primers (Table 1) for HNF-4 α (hepatocyte nuclear factor-4 α), ChDH (Choline dehydrogenase), BHMT1 (Betaine-homocysteine methyltransferase1) genes and HPRT (Hypoxanthine phosphoribosyl transferase) gene as a reference gene using 2 μ l from RealQ Plus 2x Master Mix Green, high ROX (Ampliqon, Denmark), 1 μ l forward and 1 μ l revers primers (500nM), 3 μ l cDNA and water to final volume of 20 μ l in StepOne Real-time PCR System (Applied Biosystems). The thermal conditions were used as follows: initial incubation at 95 °C for 5min, followed by 40 cycles at 95 °C for 10 sec, annealing temperature (55-58 °C) for 30 sec and 72°C for 30sec. The relative levels of mRNAs were calculated by Delta-Delta CT ($2^{\Delta\Delta Ct}$) method as $\Delta\Delta Ct = (Ct_{\text{target gene}} - Ct_{\text{HPRT}})_{\text{treated}} - (Ct_{\text{target gene}} - Ct_{\text{HPRT}})_{\text{control}}$ [15] that target genes are HNF-4 α , ChDH and BHMT1 and HPRT is an internal reference gene.

Table 1. The primer sequences used in real-time PCR experiments

Gene symbol	Forward Primer	Reverse Primer	Product size (bp)	Accession numbers	Reference
HNF-4 α ^a	5' TGCCTACCTCAAAGCCATC 3'	5'ATGTAGTCCCTCCAAGCTCA C 3'	111	NM_000457.4	Designed
BHMT1 ^b	5' CGTGGACTTCTTGATTGCAG 3'	5'AATCTCCTTCTGGGCCAAT G 3'	122	NM_001713.2	[21]
CHDH ^c	GCAAGGAGGTGATTCTGAGTG G 3'	5'GGATGCCCAGTTTCTTGAG GTC 3'	99	XM_017006799	[21]
HPRT ^d	GACCAGTCAACAGGGGACAT 3'	5'GTCCTTTTCACCAGCAAGC T 3'	182	XM_011531328	[23]

^a Hepatocyte nuclear factor-4 α , ^b Betaine-Homocysteine methyltransferase1, ^c Choline dehydrogenase,

^dHypoxanthine phosphoribosyl transferase.

Statistical analysis

Statistical analysis was performed using SPSS 22 software. To investigate of changes of HNF-4 α mRNA levels in treatment groups (choline chloride, lecithin and control) we used one way ANOVA test that followed by post hoc Scheffe test. Comparison of ChDH and BHMT1 mRNA levels between treated cells with choline chloride and control group was done with an unpaired t-test. The statistical significance was considered at P < 0.05.

RESULTS AND DISCUSSION

Nutritious diet has been effective to possess various biological activities such as antimutagenic, hypolipidaemic, antioxidant, antitumour, anti-fungal and hepatoprotective [16]. To investigate the effects of choline and lecithin on HNF-4 α expression, the human hepatoma cell line, HepG2, was used. The HepG2 cell line is similar to hepatocytes in term of biological responsiveness. In addition, these cells are relatively easier than hepatocytes to maintain in

culture so that they are used widely for in vitro studies [12, 17]. In this study, HepG2 cells were treated with choline chloride and L- α -lecithin and then relative levels of HNF-4 α mRNA were measured by real-time PCR. The results were shown that choline chloride exposure decreases mRNA levels of HNF-4 α . Different concentrations of choline chloride reduced the expression of mRNA in a dose-dependent manner.

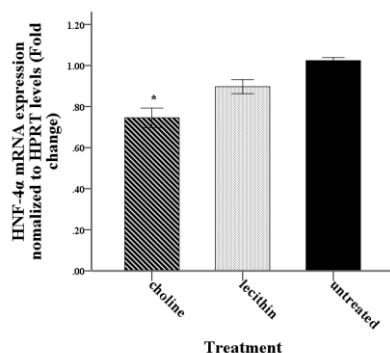


Fig. 1. The expression of HNF-4 α mRNA in HepG2 cells after treatment with choline chloride and lecithin. The relative mRNA levels of HNF-4 α were measured using SYBR Green quantitative real-time PCR and according to $\Delta\Delta C_t$ method using HPRT as an endogenous control. Data analysis was performed by one-way ANOVA followed by post hoc Scheffe test. n=4; error bars represent mean \pm SEM. * P < 0.002.

Figure 1 shows the expression of HNF-4 α mRNA in HepG2 cells after treatment with choline chloride and lecithin, and concentration effects of choline on mRNA levels of HNF-4 α were shown in Figure 2. As it can be seen, the concentrations of 11.25 μ M, 22.5 μ M and 35 μ M from choline had reduced HNF-4 α mRNA to 10, 20, and 50%, respectively that it was only statistically significant at concentration 35 μ M. The change of HNF-4 α mRNA levels in 35 μ M concentration from choline chloride was investigated at three time intervals of 6, 12, and 24 hour treatment. The expression of HNF-4 α mRNA decreased after 12 and 24 hours of exposure to choline chloride that it was only significant after 24 hours It was shown in Figure 3.

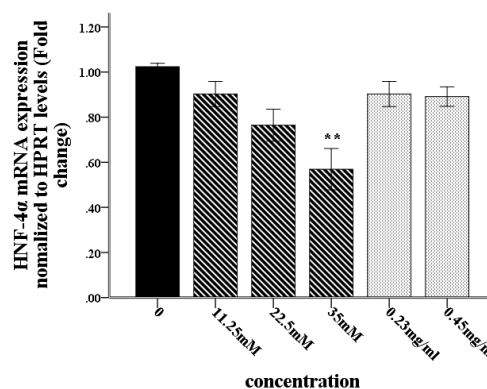


Fig. 2. The concentration effects of choline chloride and L- α -lecithin on mRNA levels of HNF-4 α . The HepG2 cells were treated with Choline chloride at three concentrations (11.25, 22.5 and 35 μ M) and L- α -lecithin at two concentrations (0.23 and 0.46 mg/ml). The relative mRNA levels HNF-4 α were quantified using of real-time PCR. Changes of HNF-4 α mRNA expression were only significant at 35 μ M of choline chloride. Data represents mean \pm SEM from four independent cultures **P < 0.0001.

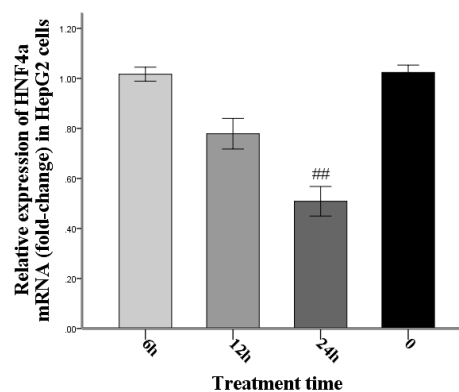


Fig. 3. The change of mRNA levels of HNF-4 α after exposure to 35 μ M concentration of choline chloride at three interval times 6, 12, and 24h. A decrease of HNF-4 α expression was approximately 20% at 12 hour treatment and that was 50% at 24 hours and it was only significant at the letter. Data represents mean \pm SEM from four independent cultures, ## P < 0.05.

Previous studies have been shown that diet can influence the levels and hence the activity of HNF-4 α . For example, despite of that HNF-4 α is known as a nuclear receptor that does not require the addition ligand in order to activation [18-19], it is found that in livers of mice, linoleic acid (C18:2 ω 6) is bound to HNF-4 α [19]. Choline is an essential nutrient for proper function of nearly every cell. It contributes to epigenetic modification via its role as a source of methyl-groups [20]. For this purpose, choline is first oxidized to betaine by choline dehydrogenase (ChDH) enzyme and then betaine denoted its methyl group to homocysteine for

remethylation to methionine, that this reaction is catalyzed by betaine-homocysteine methyltransferase1 (BHMT1).

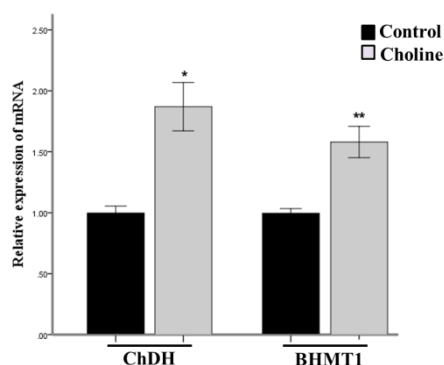


Fig. 4. The expression of ChDH (choline dehydrogenase) and BHMT1 (Betaine-Homocysteine methyltransferase1) mRNA in HepG2 cells after treatment with choline chloride at 35 μ M concentration and 24 hours exposure. An unpaired t-test analysis was used to compare mean differences between treatment and control groups. Data represents mean \pm SEM from four independent cultures. * P <0.0001 and ** P <0.003.

Finally, methionine is converted to methyl donor S-adenosylmethionine and it is ready for methylation reactions [21-22]. The study of Jiang et al. (2016) has been shown that in the HepG2 cells, choline supplementation increases global DNA methylation. They also observed overexpression of ChDH and BHMT1 enzymes at mRNA level after choline exposure [21]. In the present study, we assessed mRNA expression of enzymes ChDH and BHMT1 by real-time PCR. Figure 4 indicates expression of ChDH and BHMT1 mRNA after utilization of choline chloride at 35 μ M concentration for 24 hours. As it can be seen, choline exposure increased mRNA levels of both enzymes. This observation is consistent with findings of Jiang X et al. (2016). It is possible that choline treatment caused DNA methylation in HepG2 cell and hence it changed HNF-4 α expression [23]. However, we did not investigate that whether the reduction in HNF-4 α is resulted from up-regulation of DNA methylation specific genes (such as ChDH and BHMT1 genes that increased) in HepG2 cells. The decrease of HNF-4 α expression may influence on cell function and expression a large number of genes, because HNF-4 α is the nuclear receptor that exerts its function via both direct transcriptional effects on its target genes and indirectly with positive or negative regulation of other transcription factors, each of which regulates numerous downstream targets [12]. The study by Wang et al (2011) has indicated that when HNF-4 α expression is suppressed in HepG2 cells by the technique of RNA interference, a large number of genes (approximately 3088 of genes) are

up-regulated. Although, this study did not explain about the underlying causes, but, their observations suggest that HNF-4 α directly or indirectly regulates many liver specific genes [12].

Another study on mice with disrupted HNF-4 α gene in liver, has indicated that HNF4 α is central to the maintenance of hepatic function and it is a major in vivo regulator of genes involved in the control of lipid homeostasis, so that the mice lacking hepatic HNF-4 α display decreased expression of essential gene for VLDL (very low density lipoprotein) secretion and they have accumulation of lipid in hepatocytes [11]. In the present study, the decrease of HNF-4 α mRNA level was observed after treatment of HepG2 cells with choline. Considering the above study [11], it can be concluded that choline may cause lipid accumulation in liver, but this effect has not been observed so far. Further studies are required for understanding the mechanisms by which choline influence on liver function, and also to know how decreased HNF-4 α expression affects the liver.

CONCLUSION

The conclusion that choline as a semi-essential nutrient, is able to change gene expression. Choline is mainly metabolized in the liver. The present study showed that choline affects the expression of hepatic specific transcription factor, HNF-4 α . The possible mechanism by which choline reduces HNF-4 α expression may involve increased DNA methylation that it should be investigated by further experiments. Up-regulation of genes involved in formation of active methyl group, ChDH and BHMT1, can suggest the possibility of DNA methylation.

REFERENCES

1. J. W. E. Jr, I. A. Macdonald, S. H. Zeisel, Present Knowledge in Nutrition. Choline, John Wiley & Sons, Inc, (2012).
2. S. V. Konstantinova, G. S. Tell, S. E. Vollset, O. Nygard, O. Bleie, P. M. Ueland, *J. Nutr.*, **138**, 914 (2008).
3. P. M. Ueland, *J. Inherit. Metabo. Dis.*, **34**, 3 (2011).
4. C. Kent, P. Gee, S. Y. Lee, X. Bian, J. C. Fenno, *Mol. Microbiol.*, **51**, 471 (2004).
5. S. Robertson, Choline chloride, SIDS Initial Assessment Report For SIAM 19. UNEP PUBLICATIONS, (2004) .
6. K. D. Corbin, S. H. Zeisel, *Curr. Opin. Gastroen.*, **28**, 159 (2012).
7. Z. Li, L. B. Agellon, D. E. Vance, *J. Biol. Chem.*, **280**, 37798 (2005).

8. A. R. Johnson, C. N. Craciunescu, Z. G. Teng, R. J. Thresher, J. K. Blusztajn, *FASEB J.*, **24**, 2752 (2010).
9. A. A. Noga, Y. Zhao, D. E. Vance, *J. Biol. Chem.*, **277**, 42358 (2002).
10. K. A. Waite, N. R. Cabilio, D. E. Vance, *J. Nutr.*, **132**, 68 (2002).
11. G. P. Hayhurst, Y. -H. Lee, G. Lambert, J. M. Ward, F. J. Gonzalez, *Mol. Cell Biol.*, **21**, 1393 (2001).
12. Z. Wang, E. P. Bishop, P. A. Burke, *BMC Genomics.*, **12**, 1 (2011).
13. C. A. Wiwi, M. Gupte, D. J. Waxman, *Mol. Endocrinol.*, **18**, 1975 (2004).
14. C. P. Martinez-Jimenez, I. Kyrmizi, P. Cardot, F. J. Gonzalez, I. Talianidis, *Mol. Cell Biol.*, **30**, 565 (2010).
15. A. Mohammadi, M. R. Baneshi, Z. Vahabzadeh, T. Khalili, *Biosci. Biotechnol. Res. Asia*, **13**, 1797 (2016).
16. C. Ge, H. Radnezhad, M. F. Abari, M. Sadeghi, G. Kashi, *Appl. Ecol. Env. Res.*, **14**, 547 (2016).
17. L. Guo, S. Dial, L. Shi, W. Branham, J. Liu, J. L. Fang, *Drug Metab. Dispos.*, **39**, 528 (2011).
18. W. W. Hwang-Verslues, F. M. Sladek, *Curr. Opin. Pharmacol.*, **10**, 698 (2010).
19. X. Yuan, T. C. Ta, M. Lin, J. R. Evans, Y. Dong, E. Bolotin, *PloS one*, **4**, e5609 (2009).
20. S. Lao, The University Of North Carolina At Chapel Hill, p. 42 (2013).
21. X. Jiang, E. Greenwald, C. Jack-Roberts, *Nutr. metab. insights*, **9**, 11 (2016).
22. Y. W. Teng, M. G. Mehedint, T. A. Garrow, S. H. Zeisel, *J. Biol. Chem.*, **286**, 36258 (2011).
23. J. Zhang, J. R. Cashman, *Drug Metabl. Dispos.*, **34**, 19 (2006).

Assessment of the contributions of the highest NO₂ concentrations by industrial sources using AERMOD dispersion model

M.F. Abari¹, S. M. Zarandi^{2*}, N. Mansouri¹

¹ Department of Environment and Energy, Science and Research Branch, Islamic Azad University, Tehran, Iran

² Department of Environmental Health Engineering, Health Faculty, Shahid Beheshti University of Medical Sciences, Tehran, Iran

Received June 17, 2016; Revised November 21, 2016

The Environmental Protection Agency (EPA) recently announced a 1-hour NO₂ standard based on the multiyear average of the 98th percentile of the annual distribution of daily maximum 1-hour values, not exceeding 188 µg/m³. The AERMOD-the EPA's preferred dispersion model for near-field applications was recently modified to fully support the form of the 1-hour NO₂ National Ambient Air Quality Standard (NAAQS), which contains three different NO-to-NO₂ conversion methods for estimating the ambient concentrations of NO₂. The prevalence of nitrogen oxide (NO_x) emissions from the Esfahan Oil Refinery Complex, petrochemical and power plant is in the form of nitric oxide (NO) rather than NO₂. NO gases in the emission plume mix with the atmosphere and react with ozone and other oxidants to oxidize a portion of the NO to NO₂. In this study, the contribution of industrial groups in randomly selected receptors in all the directions within three, six and 30 kilometres from the centre point were determined in relation to the screening approach of Tier I, assuming full conversion of NO to NO₂. The results showed that the cumulative first highest max daily contribution 1-hour value averaged over 1 year (2012) equalled 26.7 and 25.8%, calculated from total NO₂ ground level concentration of 590.7 and 571.973 µg/m³ in the West and South receptors(3km). Contributions of 15.5 and 10.6% were devoted to the receptors located within 6km and 30 km respectively. While 36 and 50% SE receptor first-highest max concentration were portioned to the petrochemical and refinery, the total of cumulative apportionment in the SW receptor was released from the power plant. The cumulative first-highest max daily contribution of 1-hour value during 2012 reached to 2218.329 (µg/m³); that highest one 88.6% (1966.4 µg/m³) was related to the refinery. As well as, the rank of 50 highest 1-hour NO₂ that indicated the exceeding the values of EPA's Standards only distributed in 34 receptors in south and 16 receptors in west over year throughout the domain. The max 1-hour concentration of NO₂ in Esfahan city receptor was 73.7 (µg/m³) that was below the standard level.

Keywords: EPA, Cumulative, industrial groups, receptor, 1-hour NO₂

INTRODUCTION

Rapid increase in industrialization, urbanization, communication and transport systems have been well recognized as one of the major issues impact on environmental pollution which concern the quality of life in urban areas across the globe. Investigations has made it clear that noise pollution [1], as well as groundwater high nitrate concentration from agricultural activates [2] has reached to a hazardous level over the years.

Among pollution issues, poor air quality attracts a high level of interest within the scientific community and engages public opinion because of the known relationship between exposure to many air pollutants and increased adverse short- and long-term effects on human health [3-9]. In fact, poor air quality is generally result of increasing levels of gaseous pollutants, which are mainly considered toxic for humans and other living organisms due to their extensive natural or anthropogenic activities [10]. The NO_x gases are

an important type of these gaseous pollutants and usually emitted by fuel combustion sources in the form of nitric oxide (NO), and in smaller quantities as NO₂ gas [11]. The NO gases in the emission plume mixes with the atmosphere and reacts with ozone and other oxidants to oxidize a portion of the NO to NO₂. There are numerous other atmospheric reactions of NO_x species; these include further oxidation of NO₂ to nitrate radical (NO₃) and nitric acid (HNO₃), as well as photo-dissociation of NO₂ back to NO through the absorption of UV radiation during the daytime [12]. However, during the early stages of the dispersion of a NO_x emission plume (i.e., at distances ranging from approximately 0.1 to 10 km over time intervals of 10-300 min), the principal NO_x reaction is NO oxidation by ozone to form NO₂ [13]. In reference to these issues, EPA has promulgated a 1-hour average National Ambient Air Quality Standard (NAAQS) for NO₂, and major sources of NO_x emissions must estimate their NO₂ air quality impacts as part of EPA's air quality permitting programs. The AERMOD (The American Meteorology Society-Environmental Protection Agency Regulatory Model) dispersion model has been

* To whom all correspondence should be sent:

E-mail smotesaddi@sbmu.ac.ir

developed by EPA for these air quality impact analyses, and AERMOD contains three different NO to NO₂ conversion methods for estimating the ambient concentrations of NO₂ [14]. EPA's "Guideline on Air Quality Models" (GAQM), 40 CFR Part 51 Appendix W, describes a three-tiered screening approach to calculating NO₂ concentrations based on dispersion model predictions of NO_x concentrations (NO_x is modeled as if it is a conserved or non-reactive tracer). The three tiers, arranged in order from simplest to most refined, are:

Tier 1 – Assume full conversion of NO to NO₂, so that the NO_x predicted by AERMOD is 100 % NO₂

Tier 2 – Ambient Ratio Method (ARM), where model predicted NO_x concentrations are multiplied by a NO₂/NO_x ambient ratio, derived from ambient monitoring data

Tier 3 – More detailed methods that account for the plume dispersion and chemistry may be considered on a case-by-case basis, including the Ozone Limiting Method (OLM) and the Plume Volume Molar Ratio Method (PVMRM) [15].

The Total Conversion Method assumes 100 percent conversion of NO to NO₂. This is the simplest and most conservative method of evaluating NO₂ impacts from NO_x sources. Due to the conservative nature of the method, no justification is needed for its use and it is often applied as the screening method for the assessment of NO₂ impacts (Level 1 assessment) in various jurisdictions [16].

In Maptaphut area, AERMOD had been utilized by several studies. Chusai *et al.* (2012) used AERMOD to evaluate dispersion of NO₂ and SO₂ and relative roles of emission sources over this area. It was found that predicted data of both pollutants were under-estimated when compared with those observed data [17]. Results also indicated that petrochemical industry played the major contribution in annual average area-wide concentrations of NO₂ and SO₂ in this area. As well as a study of AERMOD tiering approach for NO₂ prediction in this industrial area was conducted by [18]. Three methods were tested for their performance in modelling NO₂ concentrations (Tier I: total conversion of NO_x to NO₂; Tier II: NO₂/NO_x ratio of 0.60 and Tier III: ambient O₃ concentrations were used for calculation using the plume volume molar ratio method (PVMRM)). The results indicated that Tier 1 provided less bias with those measured data as compared with other tiers. It also performed very well in predicting the extreme end of NO₂ concentrations. This study

recommended that Tier 1 was appropriate for prediction of the average as well as in determining the maximum ground level concentration of NO₂ in the Maptaphut industrial area [18].

In reference to these findings and given that the expansion and establishment of several industrial plants, including oil refineries, petroleum products, and power plant are major emission sources of NO_x particularly in the industries areas. Well as scientific researches focus on the analysis of the relative contributions from different activities to air quality reported that it is very important because such data are necessary to determine the types of sources that are most effective on average air pollutant concentrations in industrial complexes [19]. Specifically, air quality models have proven useful for determining the spatio-temporal distribution of air pollutants and for developing emission control policies that allocate limits to air pollutant emissions [20-22]. Furthermore, dispersion modeling describes the transport and dispersion of air pollutants, as well as chemical and physical processes within the plume. Such data enable researchers to better analyze air pollutant concentrations in various areas [19]. According to the statement contained and taking into consideration the fact that the establishment and development Oil Companies by ministry of petroleum in Isfahan has led to the construct complex dependent industries that cause NO_x pollutants cumulative release. Whereas AERMOD is the preferred model for dispersion of a wide range of application such as determination of the daily contribution 1-hour average NO₂ concentration, in this research in order to reach this goal Tier 1 applied to the 1-hour NO₂ contribution without any additional justification.

This study aims to (i) estimate, first of all, the highest maximum daily contribution 1-hour NO₂ values averaged over 1-year for source groups, including the refinery, power plant, and petrochemical and dependent industries for 13 randomly selected receptors, (ii) determine temporal and spatial distribution of 50 highest 1-hour NO₂ ground-level concentrations in all receptors during 2012, and (iii) compare 1-hour NO₂ concentrations using 1-year meteorological data with NAAQS (188 µg/m³).

MATERIALS AND METHODS

Esfahan oil companies

Esfahan Oil Refining Company (E.O.R.C.) started its activities in the refining of raw oil and production of oil-related products on 1980 and now

produces more than 22% of each of the oil-related internal products. E.O.R.C. supplies light lube cut fee to Sepahan Oil, vacuum bottom to JEI Oil, platformate to Esfahan Petrochemical and straight-run kerosene to L.A.B, which is located to the northwest of Esfahan city, at an altitude of 1,685 metres above the sea, in an area of about 340 hectares along the Esfahan-Tehran highway. The Esfahan refinery has seen much progress in crude oil refining per day-there were so many products in the early 1990s-and the crude oil refining capacity of the company increased 85% compared to the design capacity of 200,000 barrels per day, which has increased to more than 375,000 barrels [23].

Esfahan Shahid Montazeri Power Plant is located above the Esfahan Refinery on 2.2 million m² land, while L.A.B is located on the western side of the power plant. Esfahan Petrochemical is the first producer of the aromatic line of chemicals in an area of 170 hectares, located to the south of Esfahan refinery.

AERMOD model

AERMOD is a steady-state Gaussian plume model that contains algorithms to simulate plume rise and turbulent atmospheric mixing and dispersion processes [14]. It is recommended by the US EPA to examine the effects of sources on receptor that are generally within 50 km of the source [24] (US EPA, 2004). AERMOD is the current preferred model for 'a wide range of regulatory applications in all types of terrain' for purposes of estimating ambient concentrations of NO₂, based on NO_x emissions, under Tiers 1 and 2 and 3 [25].

Two pre-processors-AERMAP and AERMET-are required in order running AERMOD. AERMAP is a terrain pre-processor that characterizes the terrain and generates receptor grids, discrete receptors, and elevation for AERMOD. In AERMOD, when specifying discrete receptors, it is necessary to specify the position of a source relative to which the receptor is assigned [26]. Gridded terrain data are used to calculate a representative terrain-influenced height (hc), associated with each receptor location, and to calculate the dividing streamline height. The gridded data needed by AERMAP is selected from digital elevation model (DEM) data [27].

The surface and profile meteorological data, used in this study, were derived from NOAA/ESRL pre-processed meteorological data. Data periods read from meteorological data files were started on the first hour of 1st January to the 24th hour of 31st December 2012. The gridded data required by

AERMAP were selected from Digital Elevation Model (DEM) data and the terrain data were collected during the Shuttle Radar Topography Mission (SRTM). In this study, a comprehensive Uniform Cartesian grid-extending to 30 km from the centre of the emission source-was used in the AERMOD model. Also, the number of 13 Cartesian discrete receptors was selected randomly in all directions, at distances of 3, 6, and 30 km away from the centre-point, and the Esfahan receptor was chosen as a representative of the highest population point. In this study, Tier 1-full conversion of NO_x to NO₂ (100% conversion)-was used as an assumption for NO₂ prediction.

Emission data

Emission data were obtained from (DOE) database, measured by a reliable laboratory. These data were reported by each factory annually for air pollution monitoring. This study classified industry into six source groups: 1) Linear Alkyl Benzene (L.A.B), 2) JEI Oil, 3) Sepahan Oil 4) Petrochemical industry, 5) Power plant and 6) Refinery. In toto, there were 74 stack data, which were located in this industrial area. Characteristics of stack emission source were as summarized in Table 1.

RESULTS

The output of the pre-processors

The AERMET pre-processor presented the wind rose, which shows the frequency of occurrence of winds as well as their strength and direction. The wind rose depicts whether the predominant wind direction is respectively from the West, North West and South West. Calm winds comprised 55% of the total winds (Fig. 1). Terrain contours were processed by the AERMAP (Fig. 2) and showed elevation dense isoclines located in the west to west north of the study area. In general, isoclines of altitude varied from 1,539 to 2,527 metres.

Contributions of 1-hour average concentration of Source Groups

The first highest maximum daily contribution 1-hour values averaged over 1-year of emission sources assessed by AERMOD in this connection-the contribution of emission sources were determined in the receptor groups in the four directions at a distance of approximately 3 km (North, East, South and West), 6km (North2, East2, South2, and West2), 30 km (NE, SE, SW, and NW) and Esfahan (Table 2). Hence, in the table, it can be seen that total 1-hour average concentrations were 184.69 µg/m³ in north receptor, with contributions

Table 1. Characteristics of stack emission sources by Mean+S.D.

Stack emission group	Number of stack	Stack height (m)	Stack diameter,(m)	Stack exit Temperature,(°C)	Stack exit Velocity, (m/s)	NO _x Emission rates (g/s)
Petrochemical Refinery	8	27±9.33	1.5±0.44	255.69±226.6	10.4±5.13	1.5±1.74
Power plant	49	59.6±13	2.4±0.99	420±153	7.9±1.9	11.5±11.3
JEI Oil	8	210±0	3.1±0	171.5±50	19.3±1.24	43.97±14.6
Sepahan Oil	2	38.5±2.12	1.2±0	686 ±22.12	15±0	1.72±0.14
LAB	3	35±2	1.45±0.25	344.8±90.6	15±0	6.97±2.1
	4	59.75±5.44	1.87±0.62	344.85±47.3	15±0	5.2±2

S.D. = Standard deviation

Table 2. First highest maximum daily contribution 1-hour values averaged over 1-year for all source groups

Discrete Receptor (Group Name)	X (m)	Y(m)	Elevation (ZELEV)	Hill Heights (ZHILL)	CONT JEI OIL [µg/m ³]	CONT L.A.B [µg/m ³]	CONT PETRO [µg/m ³]	CONT PLANT POWER [µg/m ³]	CONT REF [µg/m ³]	CONT SEPAHAN OIL [µg/m ³]	CONT ALL [µg/m ³]	%
North	546925.5	3630332	1640.29	2526	0.23561	0.04735	11.3748	0	165.780	7.25565	184.694	8.3
East	546925.5	3630332	1640.29	2526	3.15125	1.50935	0.36899	0.00825	209.243	9.43619	222.773	10
South	547120.7	3624085	1794.42	2526	0.0001	0.00468	15.8384	0	555.088	1.04225	571.973	25.8
West	544414	3626636	1807.19	2526	0.38789	0.00893	0.02263	0	579.938	10.30572	590.663	26.7
North2	547110.7	3638536	1616.74	1616.7	0.58976	0.27812	17.6655	0	58.6756	5.60856	82.8176	3.7
East 2	558065.1	3626728	1576.95	1576.9	0.84557	1.67287	5.43941	0.04105	70.4750	3.94699	82.4209	3.7
South 2	558065.1	3626728	1576.95	1576.9	0.84557	1.67287	5.43941	0.04105	70.4750	3.94699	86.24	4.1
West 2	534875.8	3626159	1946.52	2505	0.49562	0.86692	3.90764	1.46207	75.8932	3.6684	86.2938	4
Isfahan	560483.6	3619188	1573.05	1573.0	0.58413	2.51605	12.0487	0.00133	53.6184	4.94582	73.7145	3.1
NE	572979	3653737	1669.94	1669.9	0.42388	1.36825	5.82224	0.11335	51.7918	2.5278	62.0473	2.7
SE	575570.7	3600175	1544.06	1717	0.63363	1.62129	20.0115	0	27.8567	5.66221	55.7855	2.5
SW	519244.6	3600866	1997.95	2421	1.00E	0.00092	0.00443	50.6914	0.01218	0.0013	50.7102	2.3
NW	519244.6	3654773	1841.35	2473	0.23313	2.30216	6.73962	5.3768	51.0010	2.54016	68.1928	3.1
TOTAL					7.95	13.2	111.7	58.3	1966.4	60.6	2218.329	
%					0.36	0.59	5	2.6	88.6	2.7	100	
Average					0.62298	1.0167	8.5946	4.48624	151.266	4.6652	170.6407	

Standard concentration =188 µg/m³

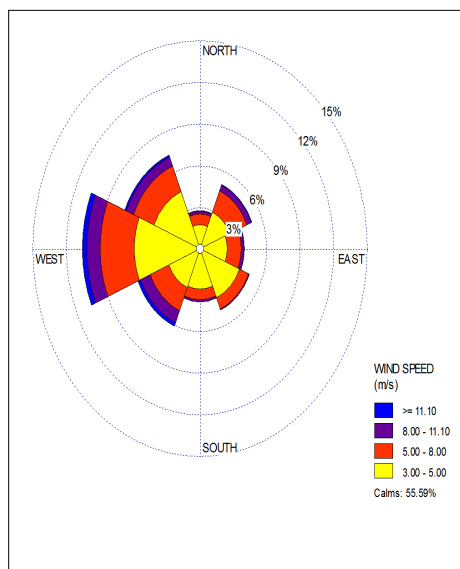


Fig. 1. Wind rose of meteorological data.

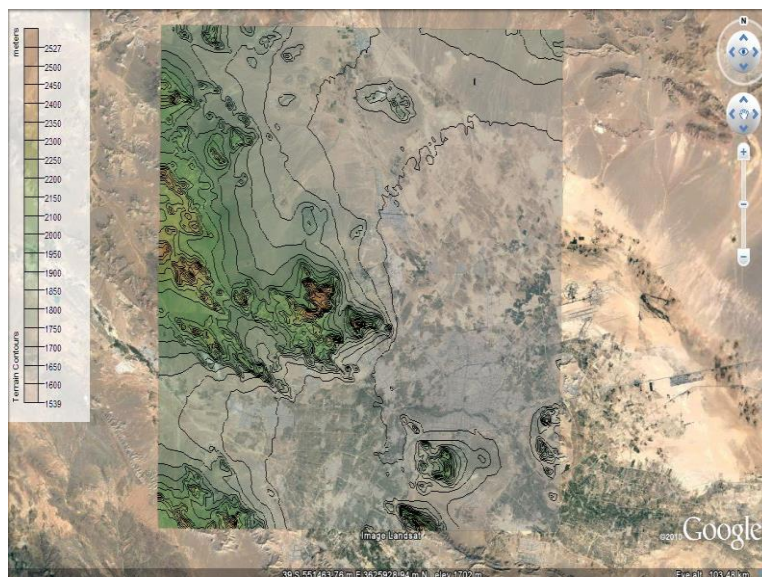


Fig. 2. Terrain contours by the AERMAP.

of 8.3%. NO₂ ground-level concentrations of Eastern receptor, portioned by 10%, were equal to 222.8 µg/m³. Moreover, the south receptors had a 25.8% contribution from total NO₂ ground-level concentration and equalled 571.97 µg/m³. The highest predicted concentration of NO₂ related to the west receptor up to 590.7 µg/m³ and, consequently, the total contribution of this receptor

was 26.7%. All four receptors (distance of 6 km of centre-point) and receptors located 30 kilometres away from centre-point were contributed by 15.5% and 10.7% (respiratory). The more than 99% concentration in SW recaptures (30 km) caused by power plant and 2.5% total contribution of SE receptor divided to 36 and 50% of Petrochemical and refinery respectively.

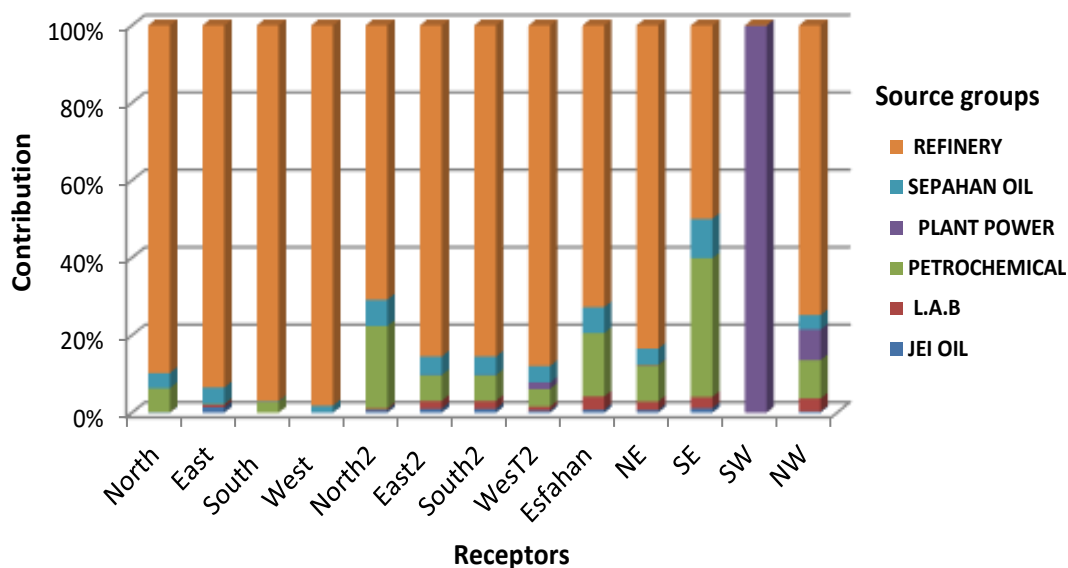


Fig. 3. The contribution of source groups in each receptor.

In relation to the predicted results, the refinery with NO₂ ground-level concentration equalling 1,966.4 µg/m³ had the highest contribution. The other corresponding source for SE receptor concentrations was Petrochemical. About 99% of the predicted concentration was contributed by emission of power plant in SW receptor. Also, the power plant did not have any effect on receptor groups in the four directions at a distance of approximately 3 km (North, South and West), North2 and SE. Total source group concentrations indicated highest to lowest polluted industries by respectively the refinery, Petrochemical, Sepahan Oil, power plant, L.A.B and JEI Oil (Table 2 and Fig. 3).

Temporal-spatial distribution of maximum 1-hour NO₂ from 1 to 50

As can be deduced from Table 3, 50 maximum highest 1-hour NO₂ ground-level concentrations were ranked for all receptors located only in South and West receptors. The highest concentration ranges for South receptor equalled 571.9739 µg/m³ to 268.011µg/m³ accrued in 34 cases. Also, 16 cases of ground level concentrations were corresponded to by the West receptor. Regarding Fig. 4, the temporal distribution maximum ranked concentrations explained that the south receptor throughout the months of a year received maximum 1-hour NO₂, with the highest frequency in March and October. However, this state was not observed in April, June, September, November and December for the West receptor. Overall, the greatest frequency of the highest 1-hour NO₂ occurred in March, October and February respectively.

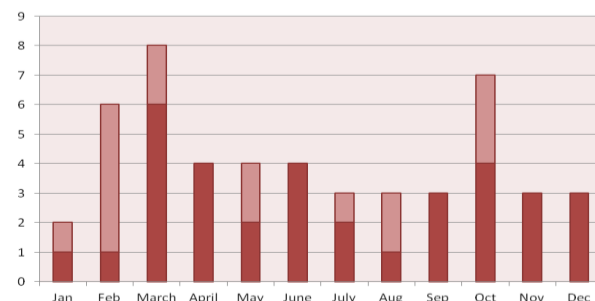


Fig. 4. Temporal-Spatial distribution of 50 cases of highest 1-hour NO₂ in all receptors.

Also, it was emphasized that the West receptor was mainly responsible for 50 highest 1-hour NO₂ this year.

Comparison with EPA standard

Based on comprehensive uniform Cartesian receptors grid extending 30km, the range of highest daily 1-hour values was between 16 and 1080 µg/m³, illustrating some exceeding 1-hour concentrations in 2012. In fact, Fig. 5 represented that the maximum 1-hour NO₂ ground-level concentrations is 5.7 times more than EPA standard 188 (µg/m³) that occurred in the vicinity of the centre-point. With regard to the predicted values, the refinery corresponded to 3.1, 2.95 and 1.1 times exceeding first maximum concentration 1-hour more than the EPA standard in West, South and East receptors respectively (Table 2). According to Table 3, all 50 first maximum 1-hour NO₂ values exceeded 188 µg/m³ in West and South receptors as well with violation of 3 to 1.4 times more than standard. For the Esfahan receptor, total concentration was acceptable, and so it did not have any effect on the resident population in this area.

Table 3. Temporal-spatial distribution of 50 cases of highest 1-hour NO₂ in all receptors

RANK	CONC [µg/m ³]	(YYMMDDHH)	Receptor	RANK	CONC [µg/m ³]	(YYMMDDHH)	Receptor
1	571.9739	12022021	S	26	365.811	12110217	S
2	525.0401	12032924	W	27	363.4813	12110323	S
3	500.4069	12120319	W	28	360.0639	12022204	S
4	481.108	12121617	W	29	358.0189	12060922	S
5	476.112	12102102	W	30	355.9894	12021218	S
6	451.2863	12092620	W	31	355.5398	12102805	W
7	448.8831	12032304	S	32	347.6009	12030322	S
8	447.6141	12032520	W	33	344.8019	12052701	W
9	438.6483	12011102	S	34	344.0498	12031918	W
10	427.841	12100623	S	35	340	12103122	S
11	423.7533	12082701	S	36	336.9673	12091901	S
12	423.4426	12022124	W	37	315.2369	12041005	S
13	411.571	12122007	S	38	307.0502	12040202	S
14	410.1798	12070104	W	39	296.8948	12030521	W
15	406.9648	12081923	S	40	296.4295	12022320	W
16	403.5412	12021720	S	41	295.4345	12042701	S
17	403.2453	12080404	S	42	290.1612	12072202	W
18	398.2622	12050622	S	43	287.7539	12011822	S
19	393.9638	12101222	S	44	283.7877	12062804	S
20	386.7081	12050423	S	45	272.786	12100805	S
21	384.4575	12061322	S	46	270.9455	12040319	S
22	380.131	12031320	W	47	269.5393	12100919	S
23	378.2883	12031322	W	48	268.8437	12061001	S
24	371.6585	12090702	S	49	268.295	12052420	S
25	366.0983	12073101	S	50	268.011	12111607	S

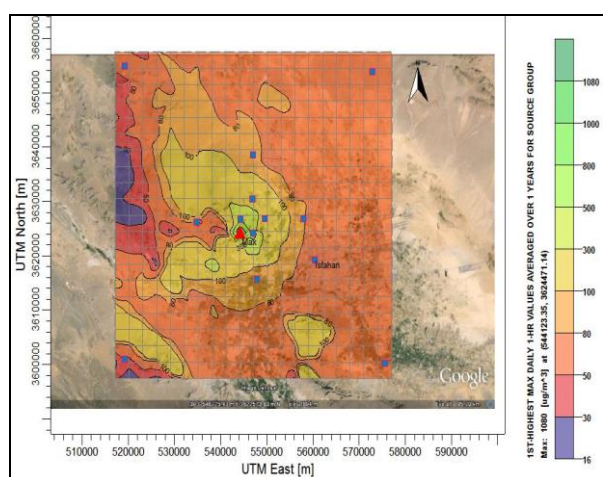


Fig. 5. Simulation of first Maximum 1-hour NO₂ concentration (blue squares represent location of receptors).

DISCUSSION

In this study, the highest maximum daily contribution 1-hour NO₂ associated with the emission rates of petroleum industrial sources was estimated. The contributions of discrete receptors that were located within approximate distances of 3, 6 and 30 km (receptor groups) keep away from a centre-point determined by AERMOD modelling. The results revealed that the cumulative 1-hour NO₂ concentrations (all sources) decline with increasing distance from the sources; however, the largest number of locations with the highest

concentrations was in the West and South receptors as well as more concentration of SE receptor affected by the Petrochemical and the refinery, while power plants had a 99% contribution in the SW receptor. However, the contribution of the refinery in the other receptors was more than 80%. Even though the power plant had an emission rate (43.97±14.6) greater than that of the refinery (11.5±11.3). According to Table 1, it can be the cause of the number of stacks and their heights.

However, the power plant corresponded to about 100% of NO₂ concentration in SW receptor. It is clear that tall stacks exert a great influence on the dispersion of pollutants. Based on some works, the contributions of the Petrochemical industry to annual concentrations of SO₂ and NO₂ were larger than the power plant, even though its emissions were almost four times lower than the emissions of power plant factory. They supported the scientific arguments that the taller stacks of the power plant group enhanced the dilution abilities of emissions from power plants, reducing concentrations of air pollutants at the ground surface level. Furthermore, plumes emitted may travel longer distances before reaching the ground level [28].

Also, the spatial distribution revealed that of 50 maximum highest 1-hour NO₂ ground-level concentrations, only governed by South and West receptors, all of them exceeded the EPA standard. In the interpretation of this result, it can be said that though the main wind direction is from the West,

North West and South West, it is, however, recognized that the highest concentration by prevailing winds do not match necessarily (Fig. 1, 5). In this type of prediction, the maximum highest 1-hour ground level concentrations in different spaces are considerable, and it can-in some cases-be different with the prevailing wind in our area. Furthermore, the results discovered that the higher concentrations can be seen at the place where the terrain begins to elevate at the feet of mountains (Figures 2 and 5). In this regard, referring to the behaviour of the plume, the pollutants can be trapped around the mountains such as that which occurred for south and west receptors, especially when calm winds occurred more than 50% in most cases. In Esfahan city, calm winds included 55% of the total winds [29]. According to the overall most temporal frequency of the highest 1-hour NO₂ occurred in March, October and February, it may be justified through the meteorological parameters and seasonal changes over a year.

Generally, the refinery with 88.6% values NO₂ ground level concentration had the most and Sepahan Oil, JEI Oil and L.A.B industries made the least contributions in the whole area. Concentrations in Esfahan receptor as a dense population point did not have any concern about special NO₂ effects on health.

CONCLUSIONS

The majority of the emissions of the oxides of nitrogen (NO_x) from emission sources are in the form of nitric oxide (NO). The NO gases in the emission plume mix with the atmosphere and react with ozone and other oxidants to oxidize a portion of the NO to NO₂. EPA describes a three-tiered screening approach to calculate NO₂ concentrations, based on dispersion model predictions of NO_x concentrations. Tier 1 approach, which assumes full conversion of NO to NO₂, could be overly conservative in many cases, and may also be prone to reflecting source-oriented impacts from nearby industrial sources located in a single corporate area.

Based on the use of AERMOD modelling, the total source group's concentrations indicated highest to lowest polluted industries by the refinery, Petrochemical, Sepahan Oil, power plant, L.A.B and JEI Oil respectively. Therefore, efforts should be more focused on NO_x emissions advanced control instruments for refinery. The AERMOD model is also a useful tool for identifying emission and contribution sources by discrete receptors.

To conclude, it can be supposed that the ranking of 50 highest 1-hour NO₂ ground-level

concentrations used in this survey showed some cases with maximum concentrations, which can help decision-makers, identify the most polluted receptors. Also, the determination of receptor contributions on different sides is important because in some receptors, corresponding pollutant sources are diverse, such as the SW receptor in this study.

REFERENCES

1. H. Radnezhad, M. Moshtaghi, M. Sadeghi, *J. Mater. Environ. Sci.*, **6**, 2703 (2015).
2. H. Radnezhad, M. Foroughi Abari, M. Sadeghi., *Biol. Forum*, **7**, 75 (2015).
3. J. Schwartz, *Epidemiol.*, **8**, 371 (1997).
4. J. Valdés-González, J. Boll, *Open J. Air Pollut.*, **4**, 208 (2015).
5. B. Brunekreef, S. Holgate, *Lancet*, **360**, 1233 (2002).
6. M. Kampa, E. Castanas, *Environ. Pollut.*, **151**, 362 (2008).
7. R. Maynard, In: R. E. Hester, R. M. Harrison, (Eds.), *Issues in Environmental Science and Technology*, 108-128 (2009).
8. W. Yang, S. Omaye, *Mutat. Res.*, **674**, 45 (2009).
9. R. Rückerl, A. Schneider, S. Breitner, J. Cyrys, A. Peters, *Inhal. Toxicol.*, **23**, 555 (2011).
10. R. Harrison, R. M. Harrison, *Pollution: Causes, Effects and Control, 4th ed. Cambridge* (2001).
11. EPA, *Integrated Science Assessment for Oxides of Nitrogen e Health Criteria* (2008).
12. R. M. Harrison, (Eds: Harrison RM). *The Royal Society of Chemistry, Cambridge, UK.* 69-192 (2001).
13. P. Karamchandani, A. Koo, C. Seigneur, *Environ. Sci. Technol.*, **32**, 1709 (1998).
14. M. Podrez, *Atmos. Environ.*, **103**, 163 (2015).
15. U.S. EPA, *Guideline on Air Quality Models (GAQM) as codified in 40 CFR 51, Appendix W.* (2005).
16. A. Todoroski, P. Henschke, M. Yu, *NSW Environ. Protect. Authority*, 1-50 (2015).
17. C. Chusai, K. Manomaiphiboon, P. Saiyasitpanich, S. Thepanondh, *J. Air Waste Manag. Assoc.*, **62**, 932 (2012).
18. S. Tunlathorntham, S. Thepanondh, *Environ. Sci. Inform. Appl. Technol.*, 229 (2015).
19. H. D. Lee, J. W. Yoo, M. K. Kang, J. S. Kang, J. H. Jung, K. J. Oh, *Atmos. Pollut. Res.*, **5**, 664 (2014).
20. N. Holmes, L. Morawska, *Atmos. Environ.*, **40**, 5902 (2006).
21. Y. Zhang, X. Liu, K. Olsen, W. Wang, B. Do, G. Bridgers, *Atmos. Environ.*, **44**, 2767 (2010).

22. J. Ma, H. Yi, X. Tang, Y. Zhang, Y. Xiang, L. Pu, *J. Environ. Sci.*, 1608 (2013).
23. A. Khosravanie, Guidance to environmental engineering in oil refinery, *Nioc Publication, Tehran*, p. 78 (2001).
24. US EPA. *User's Guide for the AMS/EPA Regulatory Model-AERMOD* (2004).
25. *Research Triangle Park, NC 27711*, 1-23 (2010).
26. U.S. EPA (United States Environmental Protection Agency), *Research Triangle Park, NC: Office of Air Quality Planning and Standards*, (2004).
27. D. Macintosh, J. Stewart, T. Myatt, *Atmos. Environ.*, **44**, 262 (2010).
28. L. Khamyingkert, S. Thepanondh, *Environ. Asia*, **9**, 28 (2016).
29. H. Ataei, H. Shahidinia, *Second National Conference on Planning and Environmental Protection* (2013).

Applications and attributes of nickel (II) schiff base complexes derived of phenylenediamine

A. Sahraei, H. Kargar*, M. Hakimi

Department of Chemistry, Payame Noor University , P.O.BOX 19395-3697, Tehran, I. R. Iran.

Received September 12, 2016; Revised December 26, 2016

The first-row transition metals have been found to constitute a major part of ligands. Nickel that is one of the transition metals has numerous ligands associated with it. The Schiff bases are useful to design coordination compounds with notable structural, magnetic, biomimetic, electrochemical and photophysical properties. This review focuses on Ni²⁺ cation coordination with the Schiff base derivatives of phenylenediamine properties and the most their applications, including Polymerisation, catalytic, Nonlinear optical (NLO), Electrochemical, Magnetic, Photophysical and antibacterial properties.

Keywords: Schiff base, phenylenediamine, Applications

INTRODUCTION

One of the most important stereochemical models in transition metal coordination chemistry are Schiff base complexes, with ease of preparation and structural variations. One of the Structural characters of a Schiff base is a nitrogen analog of an aldehyde or ketone in which the carbonyl group (C=O) has been replaced by an imine or azomethine [1-2].

Sahraei et al. was synthesized tetradentate N₂O₂ donor Schiff base ligand by adding 6-methoxy-salicylaldehyde to a solution of 4,5-dimethyl-1,2-phenylenediamine in ethanol. This ligand was characterized by ¹H NMR, IR and elemental analysis and its solid state structure was determined using single crystal X-ray diffraction [3].

Sahraei et al. have synthesized and determined crystal structure of the nickel (II) complexes by using single crystal X-ray diffraction (Fig. 1) [4].

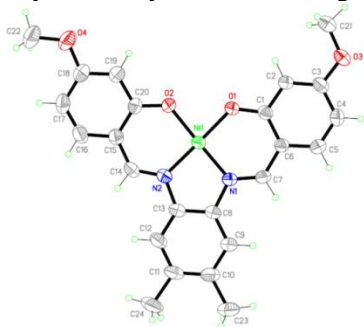
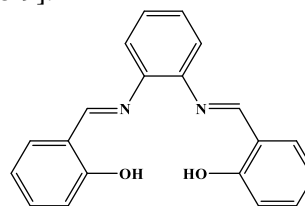


Fig. 1. crystal structure of the nickel (II) complex.

There are a lot of reports on their applications in homogeneous and heterogeneous catalysis in recent

years. Schiff base metal complex-catalyzed oxidation of organic compounds is a topic that has been investigated comprehensively many years ago [5-6]. Encapsulation in nanoporous solids such as zeolite is an interesting technique for heterogenization, when the complex is confined exclusively in the zeolite pore, we will not observe any leaching [7].

We determine Schiff base complexes (e.g., salophen 1, Scheme 1) as building blocks of new conjugated polymers and supramolecular structures. A lot of attention has been paid to these molecules as they are known to catalyze oxidation and epoxidation reactions and they have been used highly as luminescent molecules for LED applications [8-9].



Scheme 1. N,N'-Bis(salicylidene)-1,2-phenylene diamine (salophen).

One of the most famous symmetrical tetradentate ligand is N'-Bis(salicylidene)-1,2-phenylenediamine (salophen), that makes complexes with metal ions and organic compounds [10]. The investigation of complexation reactions of this ligand in nonaqueous matrices can be used as a suitable method to design the analytical systems like, potentiometric sensors [11–13], bulk liquid membrane transport [14], optical sensors [15], solid phase extraction [16] and biochemistry scope [17]. Schiff base complexes have been used as drugs and they possess a wide variety of antimicrobial

* To whom all correspondence should be sent:
E-mail: h.kargar@pnu.ac.ir

activities against bacteria, fungi and specific type of tumors. Some medicines prevent from the growth of tumors when administrated as metal chelated [18].

POLYMERISATION PROPERTIES

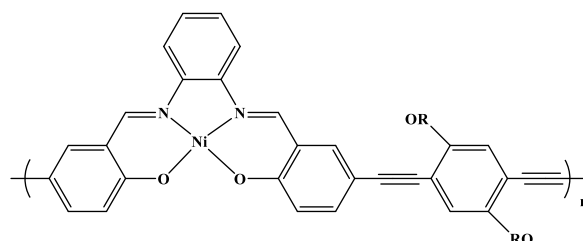
Polymers including transition metals in the backbone are been a topic for intensive researches since these polymers gives properties which are different from their separate organic and inorganic components [19]. Recent researches show that metal-containing polymers may be applicable as catalysts, sensors, and ceramic precursors [20-22].

A series of Schiff base Polymers 1-2 were prepared and characterized (Schemes 2-3) the first examples of soluble poly(salphenyleneethynylene)s. polymers 1 can be soluble in THF as our work in this field has revealed that rigid, metal-containing polymers are difficult to dissolve. The synthesis of polymers 1 was repeated based on the method in a published paper through Pd(0)-catalyzed Sonogashira cross-coupling of bromo- or iodosalphen complexes with 1,4-dialkoxy-2,5-diethynylbenzene [23]. On the other hand, the polymers were insoluble in THF. Actually, when we turned the substituents from octyl in **a** to hexadecyl in **b**, the obtained polymers were almost insoluble in THF. It is probable that luminescence which was reported in this paper is due to the existence of the oligomers or remaining

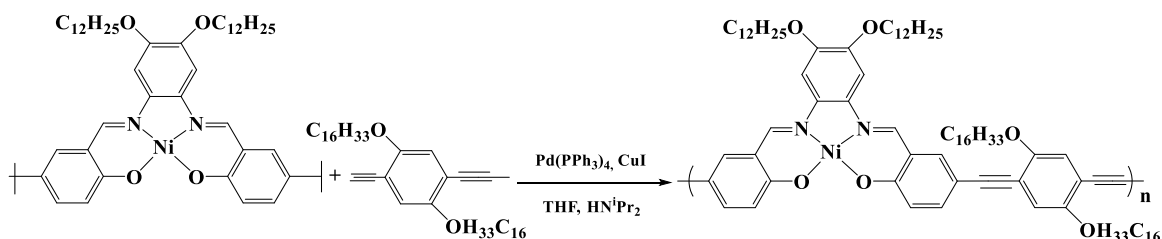
dibromosalphen complex. Despite the supplementary alkoxy substituents polymers 2 were very soluble in THF and they were still insoluble in other solvents such as chloroform and toluene. By multiple precipitations from THF into methanol and acetone the polymers were purified. This polymer is amorphous that shows only an amorphous halo centered at $20^\circ 2\theta$.

Preliminary investigations of these polymers show that they are not a suitable candidates for LED applications, but they have been useful for modern chemical sensors or assembling into nanogrids and other supramolecular structures [24].

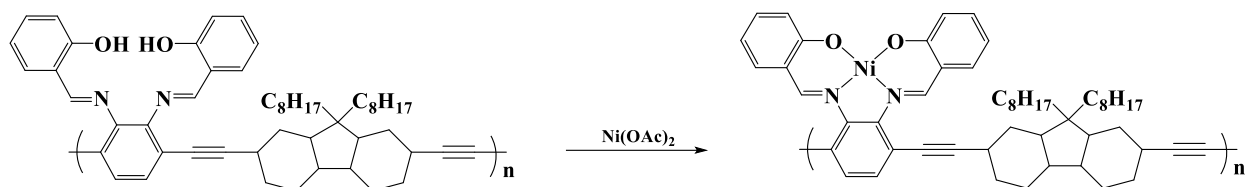
New π -conjugated poly(aryleneethynylene)s polymers including of salophen (Poly-1) and Ni-salophen (Poly-1-Ni) units were achieved in high yields by Pd-catalyzed polycondensation. Poly-1 reacted to Ni^{2+} to give a 1:1 Ni complex quantitatively (Scheme 4). Both the Ni-free and Ni-containing polymers were electrochemically active in the reduction and oxidation areas, and CV (cyclic voltammetry) scans of the polymers indicated a reduction peak of the salophene unit at about -2.2 V vs Ag^+/Ag and an oxidation peak of the salophene unit at about 0.8 V vs Ag^+/Ag . π -Conjugated polymers with immobilized salophen-metal complexes will expand the domain of polymer chemistry and coordination chemistry [25].



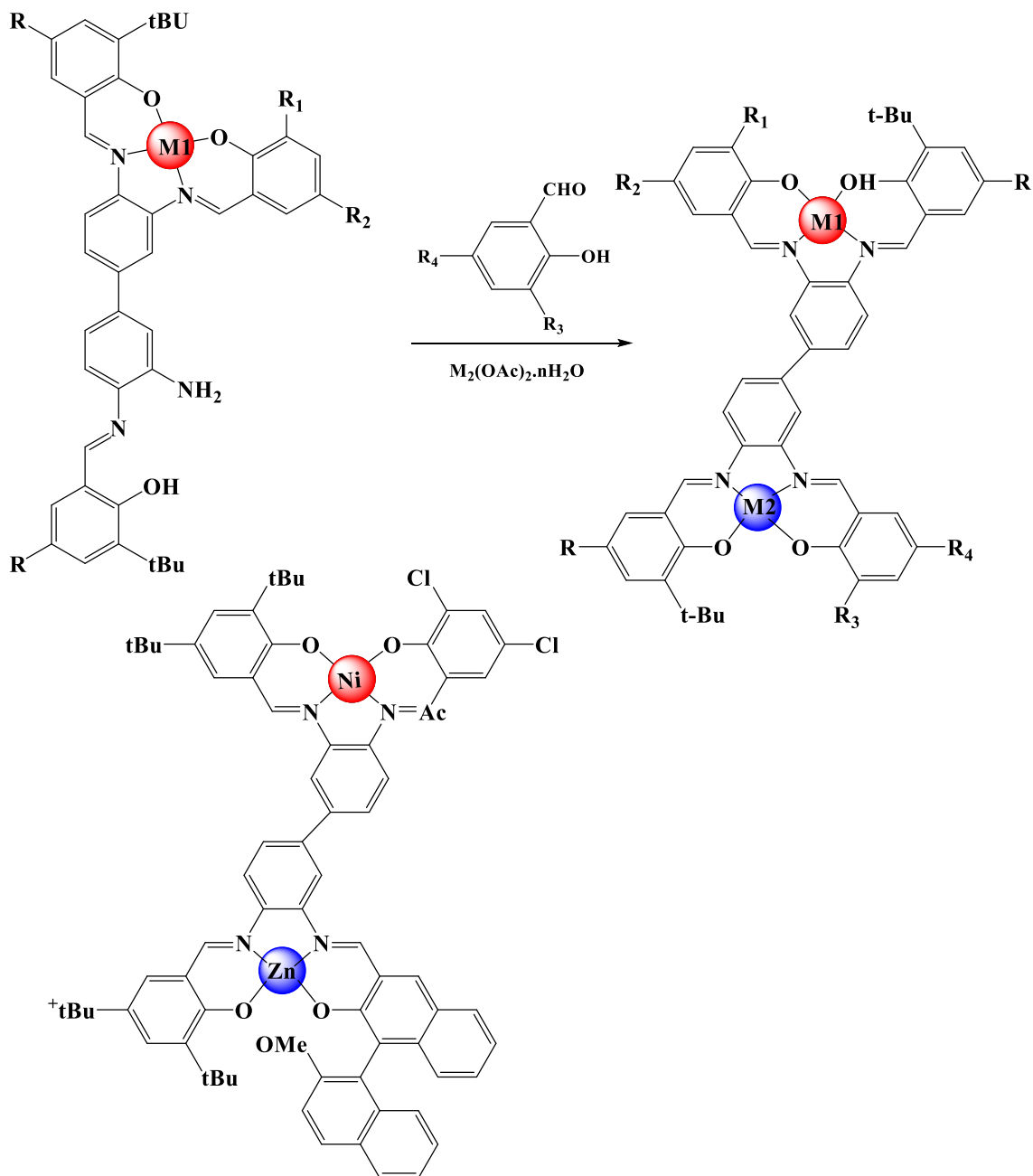
Scheme 2. Synthesis of Polymer 1 ($R_a = \text{OC}_8\text{H}_{17}$, $R_b = \text{OC}_{16}\text{H}_{33}$).



Scheme 3. Synthesis of Polymer 2.



Scheme 4. Polymerisation of salophen (Poly-1) and Ni-salophen (Poly-1-Ni).

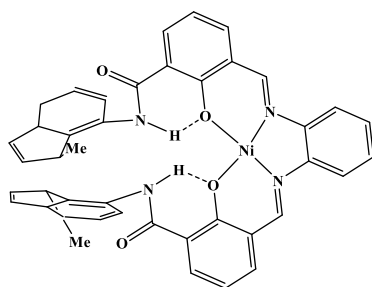


Scheme 5. Synthesis of heterobimetallic complexes.

CATALYTIC PROPERTIES

In recent years, the focus has expanded to the use of (metallo)salen building blocks for applications including (cooperative) multimetallic catalysis [26]. In order to create the multifunctional materials where both metal ions indicate different complementing functions like in the case of a determination and catalytic position, two various complexed ions could be useful. According to our information a direct and selective method for preparation of hetero-multimetallic salen structures was not priority and could have great potential in the domain of homogeneous catalysis and specially in cascade or tandem processes. Castilla et al. have presented a modular synthetic strategy for the formation of heterobimetallic salophen complexes that uses accessible monometallic triimine precursors synthetically [27] (Scheme 5).

A new field of metal foldamers has been determined in which small end groups control the sense of helical folding, even in a case where the helical bias of the end group is a mismatched relation to the internal diamine. It will be necessary to utilise analogues in order to design foldamers so that they can be used in catalysis, and the metal center is not blocked by the ends of the helices. However, the large amount of the chiroptical properties indicates that the (P)-helix is the thermodynamically dominant conformation for a compound (Scheme 6) in solution [28].



Scheme 6. A case of the helical bias of the end group.

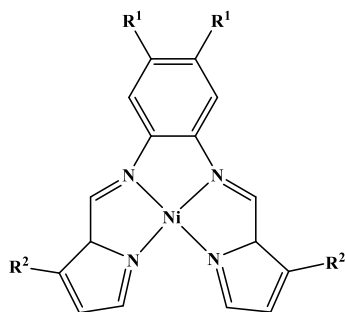
Ren et al. introduced a well-defined homogeneous Ni(salophen) catalyst as a “metallo-ligand” in a porous MOF (metal-organic framework). The Ni(salophen) units and coordinatively unsaturated Cd active sites accessible through the open MOF channels were used to produce an efficient heterogeneous catalyst for the coupling reactions of CO₂ with epoxides under relatively mild situations. The MOF catalyst features a high local density of cooperative layer Ni(salophen) motifs, indicating improved catalytic application in relation to the monomeric homogeneous catalyst. This solid catalyst is

recyclable easily and it is used again without any clear loss of catalytic activity even after being used three times. This work is a basis for a new strategy in the logical design of effective self-supported MOF catalysts for CO₂ absorption and insitu fixation based on functional metallosalens or metalloporphyrins [29].

NONLINEAR OPTICAL (NLO) PROPERTIES

Molecular-based second-order nonlinear optical (NLO) chromophores have been paid a lot of attention because of their potential applications in showing optoelectronic technologies. Polling chromophores into high T_g polymer lattices has become the most probable approach toward molecular-based NLO instruments. The important prerequisites to design suitable candidates are large $\mu \times \beta$ product and high thermal stability. In addition to organic NLO chromophores, the development of organometallic chromophores [30], that provides very large NLO responses [31] is hampered by moderate thermal stabilities. On the other hand, large hyperpolarizabilities have recently been investigated in long-range conjugated push pull metalloporphyrin complexes [32]. The crystal structure, the synthesis, electronic and second-order nonlinear optical (NLO) properties of a new bis(salicylaldiminato) -nickel(II) Schiff-base complex are shown by Nakatani et al. The compound crystallizes in the space group $P\bar{1}$. They can determine the NLO properties by electric field induced second harmonic (EFISH) and by INDO/SCI-SOS calculation. This compound has been obtained by condensation of 4-(diethylamino)salicylaldehyde and 1,2-diamino-4,5-dinitrobenzene in the presence of nickel(II) chloride that shows the largest second-order NLO response reported for this family of bis(salicylaldiminato)nickel(II) metal complexes, with $\mu \times \beta$ value of $1530 \times 10^{-48} \text{ cm}^5 \text{ esu}^{-1}$. Also, a thermal stability up to 300 °C, represents potential uses of metal salen derivatives in poled polymers matrix with high T_g [33].

The synthesis, thermal stability, optical spectroscopic, electronic structure, and second-order nonlinear optical (NLO) properties of a new class of materials, based on planar [N₄]Ni(II) complexes, are reported by Bella et al. The unsubstituted derivative shows the efficiency of urea in second-harmonic generation at 1.9 μm is 1.2 times. INDO/SCI-SOS quantum-chemical calculations can predict a sizeable molecular response and a considerable octupolar contribution to optical nonlinearity [34] (Scheme 7).



Scheme 7. Synthesis of $[Ni_4]Ni(II)$ complexes

5. Electrochemical properties

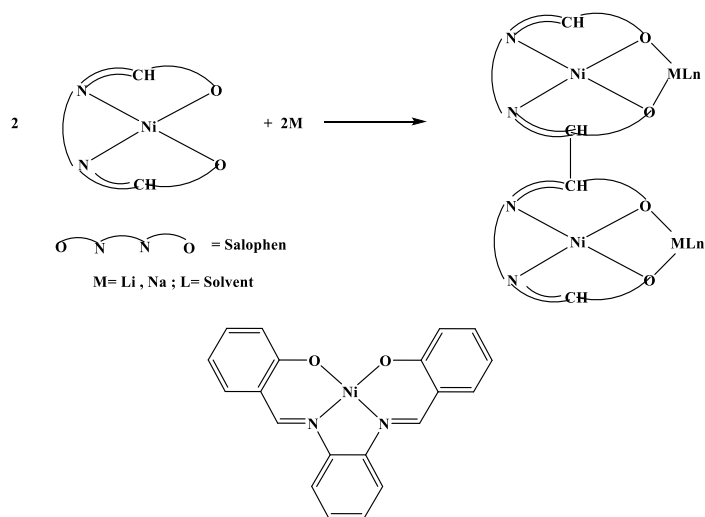
Transition metal complexes have an important participation in many electrochemical catalytic processes [35]. By cyclic voltammetry and controlled potential electrolysis, The electrochemical reduction mechanism of Ni(II)(salophen), Ni(L), in DMF has been investigated by Isse et al. The complex represents several redox processes. The first electron uptake, a ligand-based one-electron transfer at $E^\circ = -1.39$ V vs sce, will result in the formation of a nickel(II) radical anion, $[Ni(II)(L)]^-$, which dimerizes quickly, giving rise to a product which consists of two Ni(L) units joined through a C-C bond. The dimer $[Ni(II)(L)]_2^{2-}$ undergoes a nickel-centred reversible reduction process that happens at $E^\circ = -2.25$ V vs sce to give $[Ni(I)(L)]_2^{4-}$. The dianion dimer can also be oxidized irreversibly at ca -0.8 V to restore the original Ni(L) complex. At the highest sweep rates dimerization is hampered so it allows the reversible reduction of the primary radical anion to $[Ni(I)(L)]^{2-}$ be observable [36].

The electrochemical reduction of the Schiff base ligands N,N'-1,2-ethylenebis-(salicylideneimine) and N,N'-1,2-phenylenebis(salicylideneimine) were studied in DMF by cyclic voltammetry, controlled potential electrolysis and coulometry by Isse et al. The process includes a self-protonation mechanism whereby the two-electron reduction product, a cyclic derivative, are formed together with the conjugate base of the substrate, as a result of proton transfer from the substrate itself to the basic intermediates [37]. This study has shown that the peculiar electrochemical behaviour of Ni(salophen), that is considerably different from other nickel Schiff base complexes [38-39] and it can be interpreted so that the first electron uptake of $Ni^{II}L$ consists of the ligand instead of the metal center, so that a Ni(II) radical anion $[Ni^{II}L]^{*-}$ is constructed. The latter dimerizes rapidly in order to give a di-nickel(II) dimer in which two salophen units are joined by a carbon-carbon bond [40] (Scheme 8).

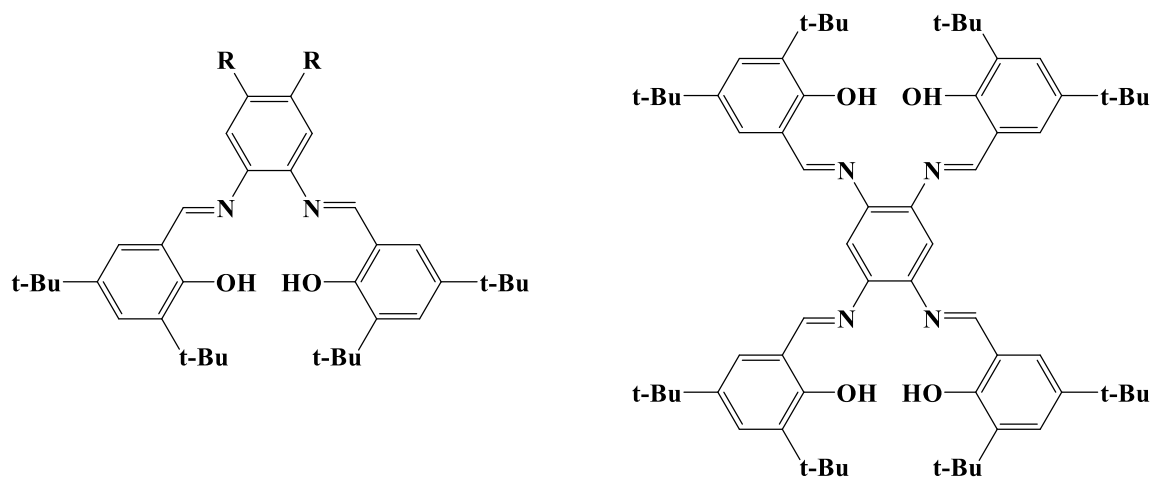
Rotthaus et al. have synthesized and determined crystal structure of The nickel(II) complexes of the mono and di-nuclear Schiff base ligands H_2L^{OMe} , $H_2L^{NO_2}$ and H_4L^{bis} . Cyclic voltammetry curves show that the electrochemical communication is considerably influenced by the substituent and the solvent. One of the one-electron oxidized species $[Ni(L^{OMe})]^+$ in CH_2Cl_2 is Phenoxy radical with partial delocalization of the spin density on a metal orbital (contribution of 6.8%) while $[Ni(L^{NO_2})]^+$ was found to disproportionate once it is generated. In the dinickel(II) complex of H_4L^{bis} , like $[Ni_2(L^{bis})]$, the phenylene spacer creates an electronic communication between the two metallic sites. Single oxidation of $[Ni_2(L^{bis})]$ gives the delocalized phenoxy radical $[Ni_2(L^{bis})]^+$, whose EPR signature is close to that of $[Ni(L^{OMe})]^+$. Double oxidation provides the bis- $\{Ni^{II}$ -delocalized radical $\}$ species $[Ni_2(L^{bis})]^{2+}$. Each radical is located at a different metallic site but a weak and an important magnetic interaction will be between the paramagnetic centers. In the presence of pyridine, a complex including two ferromagnetically coupled nickel(III) ions will be obtained. The magnetic coupling has been calculated to 3.7 cm⁻¹, whereas the zero field splitting parameters are $|D| = 0.012$ cm⁻¹ and $E = 0$. They are in accordance with the large intermetallic distance (7.7 Å) and they are weak which are observed in the neutral precursor $[Ni_2(L^{bis})]$ [41] (Scheme 9).

Vegelet al. have been investigated the electrochemical properties of the complexed transition-metal cations in the heterodinuclear complexes and mono-transition-metal cation complexes by polarography and cyclic voltammetry. The half-wave potential relies on the nature of the transition-metal cation and the mode of coordination. The changes of the half-wave potential depends on the ring size and rigidity of the polyether cavity. The nickel complex (Scheme 10) undergo a one-electron reduction [42].

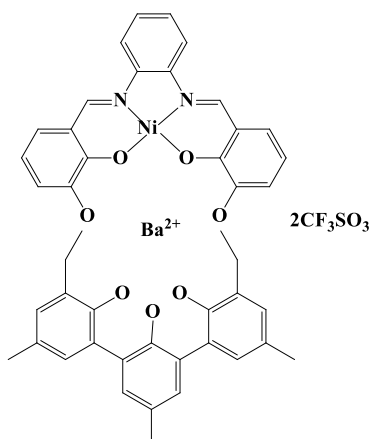
Schley et al. prepared several monometallic salen complexes derived from O-functionalized diamines and used them as metalloligand in the synthesis of heterobimetallic complexes. Reactions of the conjugated nickel(II) salen complex 2a with metallocene derivatives provided soluble di- and trinuclear heterobimetallic complexes that depend on the use of stoichiometry. Cyclic voltammetric experiments on 2a, 5a (Scheme 11) indicated the electron-withdrawing effect of the Tp^*_2La fragment. For all tested complexes, the catalytic activity in the epoxidation of the styrene was low.



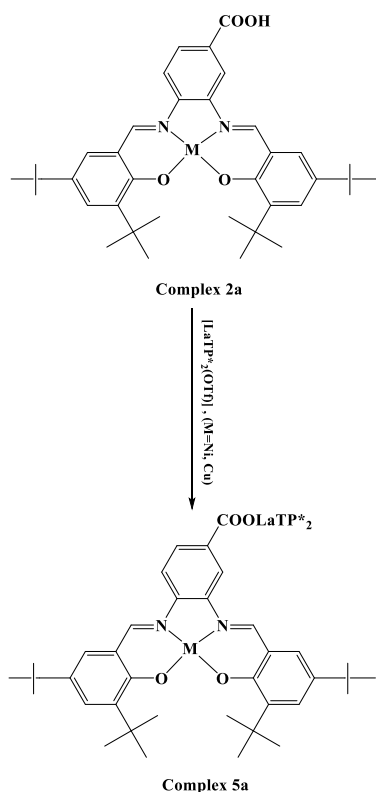
Scheme 8. Studied of the electrochemical reduction of Ni(salophen) with alkali metals.



Scheme 9. Mono and di-nuclear Schiff base ligands.



Scheme 10. Heterodinuclear complexes and mono-transition-metal cation complexes.



Scheme 11. Synthesis of several monometallic salen complexes derived from O-functionalized diamines.

The cyclic voltammogram of the mononuclear nickel(II) complex 2a in dichloromethane represents two quasi-reversible signals at $E_{1/2} = 1.10$ V and $E_{1/2} = 1.39$ V (vs. SCE) that were determined as $\text{Ni}^{\text{II}}/\text{Ni}^{\text{III}}$ and $\text{Ni}^{\text{III}}\text{L}/\text{Ni}^{\text{III}}\text{L}^+$ (L = salenligand). The analogous signals of the heterobimetallic complex 5a will be observed at $E_{1/2} = 1.09$ V and $E_{1/2} = 1.44$ V (vs. SCE). The difference between equivalent redox potentials of the mono- and heterobimetallic complexes is rather small and only is significant in the case of $E_{1/2}(\text{Ni}^{\text{III}}\text{L}/\text{Ni}^{\text{III}}\text{L}^+)$. The redox potential $E_{1/2}(\text{Ni}^{\text{III}}\text{L}/\text{Ni}^{\text{III}}\text{L}^+)$ of the heterobimetallic complex 5a is 50 mV higher than the monometallic equivalent 2a, that shows a small electron-withdrawing influence caused by the early transition metal [43].

Mononuclear and heterodinuclear complexes of the salen-type ligand H_2LH_2 [$\text{H}_2\text{LH}_2 = 2,2'$ -[1,2-dihydroxy-benzene-4,5-diylbis(nitrilomethylidene)]

bis(3,5-di-tert-butylphenol)] were prepared by Schley et al. Also cyclic voltammetric investigations were done to determine the effect of the second transition metal complex fragment $[\text{ZrCp}^*_2]^{2+}$ on the metallo salen ligand. The cyclic voltammograms of $[\text{NiLH}_2]$ and $[\text{NiL}(\text{ZrCp}_2)]$ are described in Fig. 2. Moreover, the complexes were controlled in the catalytic epoxidation of styrene. The experiments revealed that the heterobimetallic complexes always display lower activity than the corresponding monometallic complexes, in accordance with further surveys in our group. When PhIO was used the decreased catalytic activity in the heterobimetallic complexes may be caused by more facile oxidation and decomposition. If the heterobimetallic complex is retained in solution, a steric effect of the bulky $[\text{ZrCp}^*_2]^{2+}$ fragment may play a role in the catalytic process. Both the tert-butyl groups and the ZrCp^*_2 fragment shield the catalytically active transition metal and can decrease the catalytic activity [44].

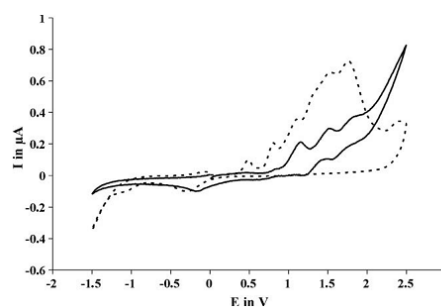
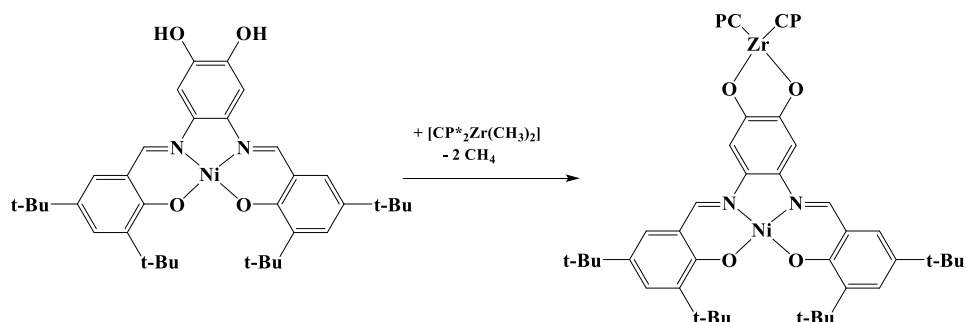


Fig. 2. Cyclic voltammograms of $[\text{NiLH}_2]$ (—) and $[\text{NiL}(\text{ZrCp}_2)]$ (···) in dichloromethane.

Zeolite-encapsulated complexes have interesting catalytic potential specially considering the activity for partial oxidation and stability. By a suitable choice of guest and host material, we can have further scope to design efficient catalyst systems. Salavati-Niasari et al. understood that their geometry and the steric environment of the active sites will have an effect on catalytic properties of the complexes. HGNM (Host-Guest Nano composite Materials) are stable enough to be reused and are suitable to be used as partial oxidation catalysts [45].



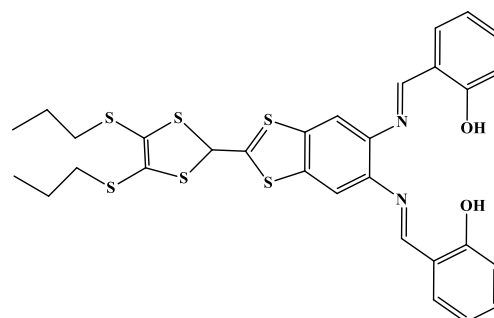
Scheme 12. Synthesis of Mononuclear and heterodinuclear complexes of the salen-type ligand H_2LH_2 [$H_2LH_2 = 2,2'$ -[1,2-dihydroxy- benzene-4,5-diylbis(nitrilomethylidene)] bis(3,5-di-tert-butylphenol)].

MAGNETIC AND PHOTOPHYSICAL INVESTIGATIONS

Cosquer et al. have invented two simple synthetic steps permitted access to two TTF-based ligands, L^1 (Scheme 13), and L^2 . The former led to six heterobimetallic dinuclear complexes of the formula $[(L^1)MLn(hfac)_3]$ (where $M=Cu^{II}$, Ni^{II} ; $Ln=Y^{III}$, Er^{III} , Yb^{III}). The UV-visible absorption properties have been investigated in a chloroform solution and rationalized by DFT and TD-DFT calculations. Upon oxidation, intramolecular SOMO \rightarrow LUMO (20800 cm^{-1}) and SOMO- $n \rightarrow$ SOMO (11350 cm^{-1}) charge transfers have been observed, but the HOMO \rightarrow LUMO charge transfers (20750 cm^{-1}) disappear. Through electrochemistry and absorption properties and the reducing agent, the reversibility of the oxidation has been confirmed. A ligand-centered fluorescence at 14450 cm^{-1} is Created by Irradiation at the HOMO \rightarrow LUMO charge transfer energy of the dinuclear complex $[(L^1)NiY(hfac)_3]$ [46].

BIOLOGICAL ACTIVITIES

We can observe the better antibacterial activity among Schiff base of pyrolidone, pyridone with *O*-phenylenediamine and their metal complexes [47]. Recently, the increase of microbial resistance to antibiotics which are used causes the more search for new compounds with potential effects against pathogenic bacteria. When heterocyclic compounds played an important role in regulating biological activities the most considerable advances will happen in medicinal chemistry. It is said that a lot of Schiff bases are important medicinally and we can use them to design medicinal compounds [48]. The derivatives of Schiff bases including nitro and halo have antimicrobial and antitumor activities [49]. Also the Antimicrobial and antifungal activities of different Schiff bases have been reported [50]. Fungi toxicity of some Schiff bases have been investigated by Sahu et al.[51]. The high antimicrobial activities of some Schiff bases were reported by Gawad et al [52].



Scheme 13. Formula of the ligands L^1 Synthesis by Cosquer.

Akila et al. prepared the symmetrical mixed ligand Schiff bases by condensing *o*-phenylenediamine with salicylaldehyde, *o*-phenylenediamine with benzaldehyde and their use to prepare mononuclear Schiff base mixed ligand complexes have been shown in this article. The results of the biological screening of the ligands and their metal complexes demonstrated that the antibacterial activities of the chelated ligands increase as compared to the free ligands [53].

Raman et al. synthesized and characterized of Schiff base ligand(L) derived from β -ketoanilide and furfural with *o*-phenylenediamine and diethylmalonate. The in vitro antimicrobial activity of the complexes of the ligand and its ligand was investigated by disc diffusion method.The results that were obtained from antifungal and antibacterial tests indicated that all the complexes are more active towards fungi than bacteria. It became clear that complexes have higher antimicrobial activity than that of free ligand [54].

A tetraaza macrocyclic Schiff base (L), synthesized from 1,2-(diimino-4' -antipyrynyl)-1,2-diphenylethane and *o*-phenylenediamine by Raman et al. acts as a tetradentate ligand and forms solid cationic complexes with Ni(II) salts in ethanol. All the synthesized compounds were describedthrough microanalytical data, magnetic susceptibility measurements, IR, UV-Vis., 1H NMR, ^{13}C NMR, ESR and mass spectral techniques. The investigated compounds and

uncomplexed metal salts were experimented against bacteria like *Staphylococcus aureus*, *Bacillus subtilis*, *Klebsiella pneumoniae*, *Salmonella typhi*, *Pseudomonas aeruginosa* and *Shigella flexneri*. The activity of the metal salts is higher than the metal chelates and the free ligand [55].

The antibacterial activities of the Schiff base derived from N,N'-1,2-phenylene-bis(2-hydroxy-1-naphthaldimine) were investigated by Prakash et al. biologically, these complexes are active against bacteria fungus viz. *E. coli* and *S. aureus* *C. albicans* so these may be considered as suitable antibacterial agents and fungicides [56].

Halli et al. synthesized and characterized complexes Ni(II) derived from E-N'-(3,4,5-trimethoxybenzylidene)benzofuran-2-carbohydrazone and ortho-phenylenediamine/ 2,6-diamino-pyridine, The antifungal and antibacterial activities of the complexes and ligands have been screened against bacteria *Escherichia coli* and *Staphylococcus aureus* and against fungi *Aspergillus niger* and *Aspergillus flavus* [57].

Sherif and Abdel-Kader have synthesized Schiff bases derived from condensation of 1,4-phenylenediamine and benzopyrone derivatives. By using *Escherichia coli* and *Staphylococcus capitis* the antibacterial activity was screened but by using *Aspergillus flavus* and *Candida albicans*, the antifungal activity was investigated. The results showed that the tested complexes have antibacterial properties [58].

The complexes of the Schiff base including Ni(II), Co(II), Cu(II) and Zn(II) were derived from vanillinidene-4-aminoantipyrine and *o*-phenylenediamine were synthesized and characterized by Sivasankaran Nair and Arish. The in vitro biological screening effects of the synthesized compounds were tested against the bacterial species, *Escherichia coli*, *Bacillus subtilis*, *Pseudomonas aeruginosa* and *Staphylococcus aureus*; fungal species, *Aspergillus niger*, *Aspergillus Candida albicans* and *flavus* by using the disc diffusion method and the results show that the metal complexes are more biological active than the ligand [59].

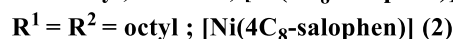
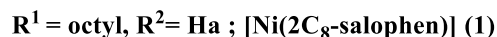
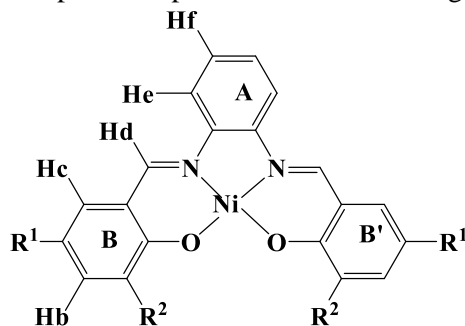
MISCELLANEOUS PROPERTIES

Joshaghani et al. have investigated the complexation reaction between Cu^{2+} , Co^{2+} and Ni^{2+} metal cations with N,N'-bis(salicylidene)-1,2-phenylenediamine (salophen), in three nonaqueous polar solvents such as: dimethyl sulfoxide (DMSO), acetonitrile (AN), methanol (MeOH) and two binary mixtures of AN:MeOH and AN:DMSO at 25 °C by conductometric and spectrophotometric

methods. By considering the temperature dependence on stability constants and the results for all metal ion complexes, the values of the thermodynamic parameters (ΔH° , ΔS° and ΔG°) for complexation reactions were obtained. So the value of ΔH° , ΔS° and ΔG° are solvent dependent [60].

Tamaki et al. have reported that the change in the surface alignment of [Ni(salophen)] substituted by different number of alkyl groups on HOPG. The increase in the number of substituted long alkyl groups caused the increase of the solubility of the complex toward organic solvent, but the tendency of the decrease is to aggregate. This influence is considered as a reason to explain why 2 with four alkyl groups covered HOPG surface with monomers, while 1 with two alkyl groups covered with dimers [61] (Scheme 14).

A series of metal complexes with salophen and salen derivatives as ligands Schiff bases has been prepared and fully characterized, including three X-ray crystal structures by Arola-Arnal et al. The interactions of these complexes with duplex and human telomeric quadruplex DNA have been investigated by fluorescence resonance energy transfer (FRET), fluorescent intercalator displacement tests, and in one case of circular dichroism. These researches have shown the square-planar metal complexes to be the most suitable quadruplex DNA stabilizers, specially the planar nickel(II) salophen complexes 3 and 4 are the best quadruplex DNA binders and telomerase inhibitors. Also the FRET competition investigations have shown the complexes to have a high degree of selectivity for the DNA quadruplex versus duplex DNA. These findings have permitted us to establish the most important properties that metal complexes should have to interact with quadruplex DNA selectively. This will have the value of determining the best strategy to prepare metal complexes as potential anticancer drugs [62].



Scheme 14. Structure of [Ni(salophen)] substituted by different number of alkyl groupson HOPG.

L-Ascorbic acid (Vitamin C) is an antioxidant, preventing color changes and alterations of aroma and flavor as well as expanding the storage time of the products [63]. This vitamin is among the compound of major biological significance, it has a key role in the protection against biological oxidation processes, the treatment and prevention of common cold, mental diseases and infertility, the treatment and prevention of Scurvy, but it is also important in the regulation of the immunological system and in tissue reconstruction, which is useful for the formation of collagen. Potentiometric membrane sensors for periodate based on amodern synthesized and well characterized Ni(II)-Schiff bases with high sensitivity and good selectivity were developed and was used in batch and hydrodynamic modes of operation. The sensors have the advantages of rapid response, logical selectivity, low cost and possible interfacing with computerized and automated systems. Interfacing the sensor in a flow injection analysis system gives sufficient speed of analysis, good reproducibility, high sample throughput and excellent response characteristics. Direct analysis of ascorbic acid was possible under static and hydrodynamic condition of operations with a linear range 2.0–13gmL⁻¹ with a sample rate ~50–55 sample h⁻¹ [64]. Some of the analytical properties of improved method were compared with other techniques based on different methods, this process is simple and inexpensive because Most of these methods, use the expensive instruments, [65–69], there is no selectivity [69-71], involving careful control of the reaction situations or derivatization reactions [69-70,72-73], and they need time-consuming pretreatment steps that are not easily applied to turbid or colored samples and affect their usefulness for routine analysis [69-70].

Acknowledgments : Payame Noor University, for providing necessary facilities to carry out the work is gratefully acknowledged.

REFERENCES

1. H. Kargar, R. Kia, M. N. Tahir, A. Sahraei, *Acta Crystallogr., Sect. E.*, **66**, 1246 (2010).
2. A. Adabiardakani, M. Hakimi, H. Kargar, *World Appl. Programming*, **2**, 472 (2012).
3. A. Sahraei, H. Kargar, R. Kia, I. U. Khan, *Acta Crystallogr., Sect. E.*, **67**, o636 (2011).
4. A. Sahraei, H. Kargar, R. Kia, M. N. Tahir, *Acta Crystallogr., Sect. E.*, **67**, m82 (2011).
5. R. A. Sheldon, W. C. E. Arends, A. Dijkman, *Catal. Today*, **57**, 157 (2000).
6. R. A. Sheldon, R. S. Downing, *Appl. Catal. A: Gen.*, 189 (1999).
7. J. C. Medina, N. Gabriunas, A. Paez-Mozo, *J. Mol. Catal. A. Chem.*, **115**, 233 (1997).
8. M. Palucki, P. J. Pospisil, W. Zhang, E. N. Jacobsen, *J. Am. Chem. Soc.*, **116**, 9333 (1994).
9. S. M. Kim, J. S. Kim, B. C. Sohn, Y. K. Kim, Y. Y. Ha, *Mol. Cryst. Liq. Cryst.*, 371 (2001).
10. K. Bergstad, H. Grennberg, J. E. Backvall, *Acta Chem. Scand.*, **59**, 741 (1999).
11. M. B. Gholivand, F. Ahmadi, E. Rafiee, *Electroanalysis*, **18**, 1620 (2006).
12. M. K. Amini, J. H. Khorasani, S. S. Khaloo, S. Tangestaninejad, *Anal. Biochem.*, **320**, 32 (2003).
13. M. R. Al-Saraj, S. M. Saadeh, M. S. Abdel-Latif, *Anal. Lett.*, **36**, 2417 (2003).
14. M. B. Gholivand, F. Ahmadi, E. Rafiee, *Separ. Sci. Technol.*, **41**, 315 (2006).
15. M. B. Gholivand, P. Niroomandi, A. Yari, M. Joshaghani, *Anal. Chim. Acta*, **538**, 225 (2005).
16. M. B. Gholivand, F. Ahmadi, E. Rafiee, *Separ. Sci. Technol.*, **42**, 897 (2007).
17. S. Kashanian, M. B. Gholivand, F. Ahmadi, A. Taravati, A. Hosseinzadeh-Colagar, *Spectrochim. Acta Part A.*, **67**, 472 (2007).
18. K. H. Reddy, P. S. Reddy, P. R. Babu, *Transition Met. Chem.*, **25**, 154 (2004).
19. I. Manners, *Science*, **294**, 1664 (2001).
20. V. Chandrasekhar, A. Athimoolam, *Org. Lett.*, **4**, 2113 (2002).
21. D. T. McQuade, A. E. Pullen, T. M. Swager, *Chem. Rev.*, **100**, 2537 (2000).
22. M. J. MacLachlan, M. Ginzburg, N. Coombs, T. W. Coyle, N. P. Raju, J. E. Greedan, G. A. Ozin, I. Manners *Sci.*, **287**, 1460 (2000).
23. O. Lavastre, I. Illitchev, G. Jegou, P. H. Dixneuf, *J. Am. Chem. Soc.*, **124**, 5278 (2002).
24. A. C. W. Leung, J. H. Chong, B. O. Patrick, M. MacLachlan, *Macromolecules*, **36**, 5051 (2003).
25. H. Fukumoto, K. Yamane, Y. Kase, T. Yamamoto, *Macromolecules*, **43**, 10366 (2010).
26. G. M. Sammis, H. Danjo, E. N. Jacobsen, *J. Am. Chem. Soc.*, **126**, 9928 (2004).
27. A. M. Castilla, S. Curreli, E. C. Escudero-Adan, M. Martinez Belmonte, J. Benet-Buchholz, W. A. Kleij, *Org. Lett.*, **11**, 22 (2009).
28. Z. Dong, J. N. Plampin, G. P. A. Yap, J. M. Fox, *Org. Lett.*, **12**, 18 (2010).
29. Y. Ren, Y. Shi, J. Chen, S. Yang, C. Qi, H. Jiang, *RSC Adv.*, **3**, 2167 (2013).
30. N. J. Long, *Angew. Chem., Int. Ed.*, **34**, 21 (1995).
31. I. R. Whittall, M. G. Humphrey, A. Persoons, S. Houbrechts, *Organometallics*, **15**, 1935 (1996).

32. S. M. Lecours, H-W. Guan, S. G. Dimagno, C. H. Wang, M. J. J. Therien, *J. Am. Chem. Soc.*, **118**, 1497 (1996).
33. K. Nakatani, I. Maltey-Fanton, A. Delaire, *J. Chem. Mater.*, **11**, 995 (1999).
34. S. D. Bella, I. Fragal, A. Guerri, P. Dapporto, K. Nakatani, *Inorg. Chim. Acta*, **357**, 1161 (2004).
35. O. N. Efimov, V. V. Strelets, *Coord. Chem. Rev.*, **99**, 15 (1990).
36. A. A. Isse, A. Gennaro, E. Vianello, *Electrochim. Acta.*, **37**, 113 (1992).
37. A. A. Isse, A. Cennaro, E. Vianello, *Electrochim. Acta.*, **42**, 2065 (1997).
38. C. Gosden, J. B. Kerr, D. Pletcher, R. Rosas, *J. Electroanal. Chem.*, **117**, 101 (1981).
39. P. Zanello, A. Cinauanti, *Transition Met. Chem.*, **10**, 370 (1985).
40. A. A. Isse, A. Gennaro, E. Vianello, *Electrochim. Acta.*, **37**, 113 (1992).
41. O. Rotthaus, O. Jarjayes, C. Philouze, C. P. Del Valleband, F. Thomas, *Dalton Trans.*, 1792 (2009).
42. F. C. J. M. v. Veggel, S. Harkema, M. Bas, W. Verboom, C. J. van Staveren, G. J. Gerritsma, D. N. Reinhoudt, *Inorg. Chem.*, **28**, 1133 (1989).
43. M. Schley, S. Fritzsche, L. P. onnecke, E. Hey-Hawkins, *Dalton Trans.*, **39**, 4090 (2010).
44. M. Schley, P. Lönnecke, E. Hey-Hawkins, *J. Organomet. Chem.*, **694**, 2480 (2009).
45. M. Salavati-Niasari, M. Shakouri-Arani, F. Davar, *Microporous Mesoporous Mater.*, **116**, 77 (2008).
46. G. Cosquer, F. Pointillart, B. L. Guennic, Y. L. Gal, S. Golhen, O. Cador, L. Ouahab, *Inorg. Chem.*, **51**, 8488 (2012).
47. S. Gaur, *Asian J. Chem.*, **15**, 250 (2003).
48. S. K. Chakraborti, De. B. Kumar, *J. Indian Chem. Soc.*, 137 (1973).
49. T. D. Chaudhari, S. S. Subnis, *Bull. Haskins Inst.*, **4**, 85 (1986).
50. S. Shah, R. Vyas, R. H. Mehta, *J. Indian Chem. Soc.*, **69**, 590 (1992).
51. K. Sahu, R. K. Behera, R. C. Pathaik, A. Nayak, G. B. Behera, *Indian J. Chem.*, **18B**, 557 (1979).
52. M. Abdul-Gawad, Y. M. Issa, S. M. Abd-Alhamid, *Egypt J. Pharm. Sci.* 34 (1993) 219.
53. E. Akila, M. Usharani, S. Vimala, R. Rajavel, *Chem. Sci. Rev. Lett.*, **1**, 181 (2012).
54. R. Natarajan, J. A. Ramaraj, J. Jeyasekaran, *J. Iran Chem. Res.*, **3**, 83 (2010).
55. N. Raman, A. Kulandaisamy, K. Jeyasubramanian, *Synth. React. Inorg. Met-Org. Chem.*, **34**, 17 (2004).
56. D. Prakash, C. Kumar, K. R. R. P. Singh, *Indian Chem. Soc.*, **85**, 371 (2008).
57. M. B. Halli, V. B. Patil, M. Kinni, R. B. Sumathi, *J. Coord. Chem.*, **64**, 651 (2011).
58. O. E. Sherif, N. S. Abdel-Kader, *Spectrochim. Acta Part A*, 519 (2014).
59. M. S. Nair, D. Arish, *Trans. Indian Inst. Met.*, **64**, 287 (2011).
60. M. Joshaghani, M. B. Gholivand, F. Ahmadi, *Spectrochim. Acta Part A*, **70**, 1073 (2008).
61. Y. Tamaki, K. Tomono, Y. Hata, N. Saita, T. Yamamoto, K. Miyamura, *Bull. Chem. Soc. Jpn.*, **85**, 592 (2012).
62. A. Arola-Arnal, J. Benet-Buchholz, S. Neidle, R. Vilar, *Inorg. Chem.*, **47**, 11910 (2008).
63. M. W. Davey, M. Van Montagu, D. Inze, M. Sanmartin, A. Kanellis, N. Smirnoff, I. J. J. Benzie, J. J. Strain, D. Favell, J. Fletcher, *Sci. J. Food Agric.*, **80**, 825 (2000).
64. A. A. Aziz, A. H. Kamel, *Talanta*, **80**, 1356 (2010).
65. A. Rodríguez-Bernaldo de Quirós, M. Fernández-Arias, J. López-Hernández, *Food Chem.*, **116**, 509 (2009).
66. A. Balaguer, A. Chisvert, A. Salvador, *J. Sep. Sci.*, **31**, 229 (2008).
67. Y. Peng, Y. Zhang, J. Ye, *J. Agric. Food Chem.*, **56**, 1838 (2008).
68. T. Wu, Y. Guan, J. Ye, *Food Chem.*, **100**, 1573 (2007).
69. T. R. L. C. Paixao, M. Bertotti, *J. Pharm. Biomed. Anal.*, **46**, 528 (2008).
70. D. G. Themelis, P. D. Tzanavaras, F. S. Kika, *Talanta*, **55**, 127 (2001).
71. A. Abbaspour, A. Khajehzadeh, A. Noori, *Anal. Sci.*, **24**, 721 (2008).
72. Y. Peng, Y. Zhang, J. Ye, *J. Agric. Food Chem.*, **56**, 1838 (2008).
73. T. Wu, Y. Guan, J. Ye, *Food Chem.*, **100**, 1573 (2007).

Potential of phytoremediation for the removal of petroleum hydrocarbons in contaminated soils associated with *Rhodococcus erythropolis*

E. Mirzakhani¹, F. Mortazaeinezhad^{1*}, A. Tahmorespour², H. Radnezhad³,

¹Department of Horticulture, Isfahan (Khorasgan) Branch, Islamic Azad University, Isfahan, Iran.

²Department of Basic Medical Science, Isfahan (Khorasgan) Branch, Islamic Azad University, Isfahan, Iran.

³Department of Environmental Sciences, Isfahan (Khorasgan) Branch, Islamic Azad University, Isfahan, Iran.

Received February 12, 2016; Revised December 26, 2016

Degradation of petroleum hydrocarbons of the contaminated soils from the region of Isfahan refinery in colonized and un-colonized soils with the *Cynodon dactylon* and *Poa pratensis* plant species associated with *Rhodococcus erythropolis* Bacteria was investigated during 90 days in experiment greenhouse. It was in a completely randomized design with 12 treatments in 3 replications. On 90th day, the rate of decline of petroleum hydrocarbons in soil was measured by the EPA41 8 / 1 method. Statistical analysis was carried out using SPSS software as a regular and factorial means compared with LSD tests at $P < 0.01$ for the effect of the bacteria, species and the interaction effect of them. The highest average rate of reduction was observed for the effects of species of *Cynodon dactylon* as well as the effects were caused by the bacteria in the ideal level. However the higher impact obtained by bacteria inoculation. The *Cynodon dactylon* treatments inoculated with bacteria showed the higher impact for removal petroleum hydrocarbons in the contaminated soils. Although both plants and their associated microorganisms presented a potential for removal of petroleum hydrocarbons in contaminated soils, results highlighted that potential may be distinct among plant species, which should be accounted for when designing cleanup strategies.

Keywords: Contaminated soils, *Cynodon dactylon*, petroleum hydrocarbons, *Poa pratensis*, Region of Isfahan Refinery, *Rhodococcus erythropolis*.

INTRODUCTION

Organic compounds, released in the environment by various human activities, are posing serious threat to the environment due to their toxicity, hydrophobic nature and persistence in the environment for a longer period of time. The presence of organic compounds in soil, such as hydrocarbons, polyaromatic hydrocarbons, polychlorinated biphenyls, phenols, chlorophenols, toluene, trinitrotoluene, benzene, herbicides and pesticides, inhibits growth and metabolic activities of soil-associated microbes, even at very low concentrations [1-4]. Furthermore, organic compounds can enter the food chain, and due to their toxic nature they can cause mutagenicity and carcinogenicity in animals and humans [5-7]. Therefore, the removal of these organic compounds from soil and water is one of the main issues in the field of environmental sciences and engineering [8-11].

Recently, the focus of the studies is to investigate the pollutants removal in soil using the organic and inorganic methods [12].

Phytoremediation is a promising technology for the removal of hydrocarbons from polluted soil and

it depends on synergistic relationships between plants and their associated rhizosphere microbial communities [13]. The root system of the plant is one of the most important factors. Plants can indirectly influence degradation by altering the physical and chemical conditions of the soil [14]. Plant roots exude organic and inorganic substances to their neither exterior during normal metabolism. Root exudates act as substrates for soil microorganisms, thereby enhancing the degradation of toxic organic chemicals [15-16]. showed that some tropical grasses and legumes are resistant to petroleum pollution, and root surface was increased in the graminoids *Brachiaria brizantha*, *Cyperus aggregatus*, and *Eleusine indica* in petroleum-polluted soils. In addition, bioremediation is using plants and microorganisms to remove or detoxify environmental contaminants. Bioremediation has been intensively studied over the past two decades, driven by the need for a low-cost, in situ alternative to more expensive engineering-based remediation technologies [17-19]. Under petroleum-polluted conditions, plants or plant-associated microflora can convert hydrocarbons (HCs) to non-toxic forms. Bioremediation has been applied to remove crude oil [20-21], motor oil [22-23] from soil.

The remediation processes include treating the petroleum pollutants with hydrocarbon-degrading microorganisms [24]. such as *Rhodococcus*

* To whom all correspondence should be sent:
E-mail: mortazaeinezhad@khuisf.ac.ir

erythropolis. *R. erythropolis* cells possess various kinds of enzymes that allow them to biodegrade different pollutants [25]. mainly utilizing different types of monooxygenases and dioxygenases to degrade pollutants and also facilitate cell growth [26]. The biodegradability of *R. erythropolis* is related somewhat to the tolerance to the toxic substrates and solvents. It was reported that *R. erythropolis* tolerates both water-miscible, such as ethanol and butanol up to 50% (v/v), and water-immiscible solvents such as dodecane and toluene (5%, v/v). Tolerance mechanisms to the hydrocarbons involve the adaption of the cell surface to the environment [27]; (e.g. more mycolic acids or fatty acids in the cell surface) and thus to enhance the direct contact between cells and oil pollutants for a better biodegradation rate [28]. Iran is the world's fourth largest producer of crude oil and oil pollution is therefore widespread in this region during production and transport activities. Biological methods such as enhanced microbial degradation and phytoremediation are promising green and cost effective tools for large scale remediation [29-31]. However, the time span for biological methods is often long and the techniques are less efficient on highly polluted sites and for remediation of heavier oil products [32-34]. Therefore, finding new approaches to enhance efficiency of bioremediation is desired. The aim of this study is to determine the most efficient short term strategy for phytoremediation of severely oil contaminated soils from Isfahan refinery region in Iran. So that, (i) examined the potential of the phytoremediation the *Cynodon dactylon* and *Poa pratensis* (ii) The assessment of the bioremediation efficiency was based on *Rhodococcus erythropolis* inoculation on the *Cynodon dactylon* and *Poa pratensis* (iii) evaluated the effect of species interactions and bacteria in removal of petroleum hydrocarbons.

MATERIALS AND METHODS

Sampling

Samples were randomly collected from locations in several soil samples in the area of the depot of sulfur in Isfahan Refinery region. The non-contaminated soil was randomly sampled from the closest locate to the soil contaminated with petroleum hydrocarbons.

Sample processing

Each soil sample was crushed, thoroughly mixed then sieved through a 2 mm pore size sieve (RETSCH, Germany) to get rid of large debris. The

sieved soil was then mixed with 50% garden soil and soil analysis was conducted to determine the physical and chemical characteristics of the soil (Table 1).

Table 1. Chemical and physical characteristics of the soil

Name	Unit	measure
EC	ds/m	11.5
pH		7.9
Lime	%	18.5
Gypsum	%	0.25
Total nitrogen	%	0.061
Organic carbon	%	0.56
Available phosphorus	mg/kg	17
Available Potassium	mg/kg	230
Clay	%	22
Sand	%	37
Silt	%	41
Soil texture	Loamy	-
Petroleum hydrocarbons in non-contaminated soil	g/kg	0.2
Petroleum hydrocarbons in contaminated soil	g/kg	4

The electrical conductivity (EC) measured of the saturated extract. Acidity (pH) was determined in saturation mud. The gypsum measured by EDTA, soil organic carbon by Nelson method and total nitrogen in soil by Kejedal, restorable phosphorus by Olsen method were measured. Hydrometer method was used to determine soil texture. As well as minimum and maximum levels of petroleum hydrocarbons in contaminated soil and normal soil (non-contaminated control soil) was selected and the concentration of petroleum hydrocarbons was measured in both cases by EPA418 /1.

Soil sterilization

To remove the microorganisms of soil, 1.5 kg of soil contaminated with petroleum hydrocarbons was transferred to the 15 bags of polypropylene moisture resistant and autoclave at 121 degree and was maintained for 20 minutes under these conditions.

Preparation of the used materials

Rhodococcus erythropolis strain PTCC 1767 was purchased from the collection of fungus and bacteria Regional Center of Industrial Research Organization of Iran. Material culture medium, the antibiotic kanamycin, N-hexane, naphthalene, anthracene and phenanthrene 1 and 10 with 99% purity was purchased from Sigma-Aldrich Company.

Preparation of the stocks

Stoke antibiotic kanamycin was prepared at a concentration of 150 ppm in the water solvent, and the stocks of naphthalene, anthracene and phenanthrene 1 and 10 were each prepared separately by the solvent n-Hexane at a concentration of 10 ppm.

Preparation of BHI culture medium

Preparation of BHI culture medium (Table 2) was performed to the volume 1 liter with combinations of enzymatic digestion of animal tissues, extract of calf brain without water, glucose, sodium chloride, and disodium hydrogen phosphate in grams per liter. Then it was adjusted to pH 7 and at 110 °C for 20 minutes was autoclaved, and after the cooling the stock kanamycin the concentration of 150 ppm at a rate of 10 cc by the syringe filter 0.22 µm, filtered and added to culture medium.

Preparation of BH specific solid culture medium

BH specific solid culture medium (Table 3) was prepared to the volume of 1 liter with the compounds of magnesium sulfate, calcium chloride, monopotassium phosphate, diammonium phosphate, potassium nitrate, ferric chloride and glucose in grams per liter. The pH was adjusted to 7, agar added and the medium was autoclaved at 110 °C for 20 minutes. After cooling the stock

kanamycin with the 150 ppm concentration, 10 cc of it was filtered by the syringe filter 0.22 µm, and added to the culture medium. Before closing of agar, 20 cc of the culture medium was poured into petri dish.

Preparation of NA general solid culture medium

General solid culture medium NA was prepared to the volume of 1 liter of peptone, meat extract expressed in grams per liter. The pH was adjusted to 7, agar (gr/l) added to the culture medium and the medium was autoclaved at 110 °C for 20 minutes. After cooling the stock kanamycin with the 150 ppm concentration, 10 cc of it was filtered by the syringe filter 0.22 µm, and added to the culture medium. Before closing of agar, 20 cc of the culture medium was poured into petri dish (Table 4).

Preparation of MSM liquid culture medium

Liquid culture medium MSM (Table 5) was prepared to the volume of 1 liter with compounds of ammonium nitrate, potassium dehydrogenate phosphate, magnesium chloride, calcium chloride and zinc chloride in grams per liter. The pH was adjusted to 7, and the medium was autoclaved at 110 °C for 20 minutes. After cooling the stock kanamycin with the 150 ppm concentration, 10 cc of it was filtered by the syringe filter 0.22 µm, and added to the culture medium. Before closing of agar, 20 cc of the culture medium was poured into petri dish. After cooling the stocks kanamycin the concentration 150 ppm the amount 10cc by the syringe filter 0.22 µm filtered. Moreover 20 cc from each of naphthalene stoke, anthracene and phenanthrene 1 and 10 with 100 ppm concentration were filtered by the syringe filter 0.44 µm and as the carbon source added to the culture medium.

Table 2. Preparation of BHI culture medium

Animal tissue of enzymatic digested	Extract of calf brain without water	Glucose	Disodium hydrogen phosphate	Kanamycin
(gr/L)				(cc)
10	12.5	4	2.5	10

Table 3. Preparation of BH solid culture medium

magnesium sulfate	calcium chloride	monopotassium phosphate	diammonium phosphate	potassium nitrate	ferric chloride	glucose	agar	Kanamycin
(gr/l)								(cc)
0.2	0.02	0.1	1	1	0.5	2	15	10

Table 4. Preparation of NA solid culture medium

Peptone	Meat extracts	Agar	Kanamycin
	gr/l		(cc)
5	3	15	10

Table 5. Preparation of MSM liquid culture medium

Ammonium nitrate	Potassium dihydrogen phosphate	dipotassium hydrogen phosphate	MgCl ₂ .6H ₂ O	CaCl ₂ .6H ₂ O	MnCl ₂ .6H ₂ O	ZnCl ₂ .6H ₂ O	Kanamycin	Naphthalene	Anthracene	phenanthrene
			(gr/l)					(cc)		
1	2	7	2	1	0.1	0.1	10	20	20	20

Morphology of the Rhodococcus erythropolis bacteria

Linear *Rhodococcus erythropolis* bacteria culture was carried out in tow medium of specific solid culture of Hess Bushnell and general nutrient agar. Petri dish was transferred into the incubator at 30 °C for 48 hours, and then gram staining was carried out on colonies of *Rhodococcus erythropolis* bacteria. The purple color of colonies of *Rhodococcus erythropolis* bacteria under a light microscope was observed.

Transfer of Rhodococcus erythropolis bacteria to the suspension of inoculation

After activating bacteria in liquid culture medium BHI, 1 cc of deposits with bacterial cells was prepared by centrifugation of 3000 rpm for 20 minutes, and was transferred to the liquid culture medium of MSM to the volume of 1 liter and then was placed in an incubator shaker with 30 °C temperature and 180 rpm for 12 hours.

Inoculation of bacteria to the contaminated soil

1cc of liquid culture medium MSM with bacterial colonies in the centrifuges 3000 rpm for 20 minutes was taken and the centrifugation was transferred to the 12 petri dish containing 10 grams of contaminated soil sterile.

Preparation of seeds

First the impurities were isolated from the seeds of the plant species of Bermuda grass (*Cynodon dactylon*) and Kentucky bluegrass (*Poa pratensis*) to sterilize the seeds. In the second stage the seeds were washed 5 times with tap water, the seeds were soaked in 75% ethanol solution for 30 seconds. In the fourth stage were washed three times with distilled water for 10 minutes. In the fifth stage the seeds were soaked for 15 minutes with 25% sodium hypochlorite. In the final stage (stage six) the seeds were washed 3 times with distilled water each time for 10 minutes. The amount of 0.1 gr seed annual

meadow grass species and 0.1 gr of seed of Bermuda grass species was added to the pots.

The seeds were added to the 36 pots with 1.5 kg of soil contaminated with petroleum hydrocarbons. The contaminated soil with inoculation suspension of Bactria was mixed with soil of 12 pots; 0.1 grams the seed of the each species was added to these pots.

Implementing the plan

The experiment was carried out as factorial and ordinary in a completely randomized design with 12 treatments and 3 replications (Table 6). Two species Bermuda grass (*Cynodon dactylon*) and annual meadow grass (*Poa pratensis*), the bacterium *Rhodococcus erythropolis* on 2 levels the bacterial inoculation and without inoculation, ordinary soil and soil contaminated with petroleum hydrocarbons completely (100% contaminated) made the experimental treatments. The treatments were carried out in the two levels of sterile and non-sterile for 90 days in research greenhouse of Islamic Azad University Isfahan (Khorasgan). Rate reduction of petroleum hydrocarbons were measured at 90 days.

Measuring the concentrations of petroleum hydrocarbons

To measure the concentrations of petroleum hydrocarbons, sampling was done of the soil contaminated with petroleum hydrocarbons and uncontaminated soil, each in three replications of the treatments. Concentration of petroleum hydrocarbons was measured according to the Global Environment Facility 418.1 and IR spectrophotometer Jackv model 450. Concentrations of petroleum hydrocarbons were also measured in ordinary soil.

Extractable petroleum hydrocarbons

Petroleum hydrocarbons were extracted based on the method by ultrasonic EPA 35 / 50C and the solvent for 3 times. 1 gram of contaminated soil and ordinary soil was solved in 10 cc of fluorine

carbon chloride solvent by sonic ultrasonic tour, soil particles became micron droplets then at 3000 rpm were centrifuged for 2 minutes to obtain a homogeneous extract. Cleaning and separation of polar compounds by combining 1.0 grams of silica gel was carried out in a homogeneous extract by Vertex. The extract obtained by Whatman filter paper was smooth. Dilution of the extract was carried out by the solvent fluorocarbon 1, 1, and 3 according to the concentration of each sample if necessary. The extract was filtered by the syringe filter 0.22 µm.

The data were analyzed by SPSS software and data means were compared using the least significant difference at 1%, and charts' drawing was done by SPSS software.

RESULTS

The effect of treatments on the mean concentration of petroleum hydrocarbons of contaminated soils

Analysis of variance of the concentration of petroleum hydrocarbons in contaminated soils

Table 6. The experimental treatments

Row	Treatments	Symptom
1	Soils contaminated sterilized uncultivated	T1
2	Non-sterilized soils contaminated without cultivation	T2
3	Sterilized soils contaminated inoculated with bacteria <i>Rhodococcus erythropolis</i> + <i>Poa pratensis</i>	S+P+B
4	Sterilized soils contaminated without inoculation of bacteria <i>Rhodococcus erythropolis</i> + <i>Poa pratensis</i>	S+P+NB
5	Non-Sterilized soils contaminated inoculated with bacteria + <i>Poa pratensis</i>	NS+P+B
6	Non-Sterilized soils contaminated without inoculation of bacteria <i>Rhodococcus erythropolis</i> + <i>Poa pratensis</i>	NS+P+NB
7	Sterilized soils contaminated inoculated with bacteria <i>Rhodococcus erythropolis</i> + <i>Cynodon dactylon</i>	S+C+B
8	Sterilized soils contaminated without inoculation of bacteria <i>Rhodococcus erythropolis</i> + <i>Cynodon dactylon</i>	S+C+NB
9	Non-Sterilized Soils contaminated inoculated with bacteria <i>Rhodococcus erythropolis</i> and <i>Cynodon dactylon</i>	NS+C+B
10	Non-Sterilized soils contaminated without inoculation of bacteria <i>Rhodococcus erythropolis</i> + <i>Cynodon dactylon</i>	NS+C+NB
11	Ordinary soil + <i>Cynodon dactylon</i>	C1
12	Ordinary soil + <i>Cynodon dactylon</i>	C2

Table 7. Analysis of variance of the average concentration of petroleum hydrocarbon soil contaminated treatments in day 90.

Sources of variation	Df	Mean square
Petroleum hydrocarbons (gr/kg)		
Species	1	**0.29
Error	16	0.1
CV%		6.73

ns, * and ** symbolize not significant and significant at the 5% and 1% levels of probability, respectively.

indicated the significant effect ($p= 0.01$) of *Cynodon dactylon* species on the average concentration of petroleum hydrocarbon of the soil contaminated treatments in day 90 (Table 7).

Comparing the means with LSD post hoc tests at $P < 0.01$ indicated a statistically significant effect in the reduction of the petroleum hydrocarbons by *Cynodon dactylon* plant species compared with *Poa pratensis*. The maximum reduction in petroleum hydrocarbons (mean 65.1 gr/kg) related to *Cynodon dactylon* species (Fig. 1).

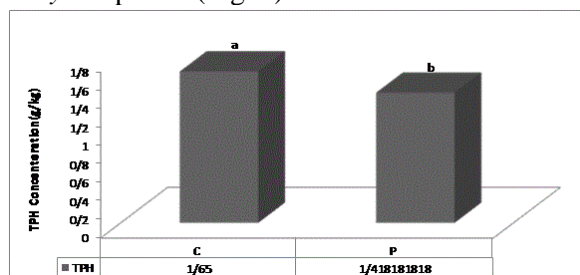


Fig. 1. The effect of the species of *Cynodon dactylon* and *Poa pratensis* on the average concentration of petroleum.

Hydrocarbons of contaminated soils

Means comparison of concentration by LSD post hoc tests at $P < 0.01$ showed that the average decrease of hydrocarbon petroleum is in the ideal level by the treatments of inoculated with bacteria and without inoculated bacteria. So that the concentration was reduced in the inoculated with bacteria treatment with mean of 1.57 gr/kg and the mean of reduction in without inoculation of bacteria treatment was 1.5 gr/kg (Fig. 2).

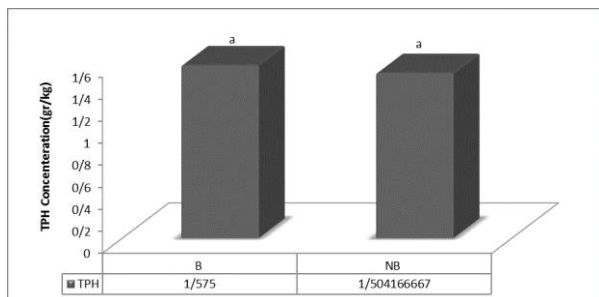


Fig. 2. The effect of inoculation and without inoculation of bacteria treatments on the average concentration of petroleum.

The average concentration of petroleum hydrocarbons were compared by the LSD post hoc tests at $P < 0.01$ of the simultaneous effect the species of *Cynodon dactylon* and *Poa pratensis* with soil. Significant differences were observed between the soil treatment and *Cynodon dactylon* specie with *Poa pratensis* specie and soil. The specie of *Cynodon dactylon* reduced concentrations of petroleum hydrocarbons in ideal level, so that the average reduction of 1.56 gr/kg related to the treated sterile soil with *Cynodon dactylon*, and the mean of petroleum hydrocarbons reduction was 65.1 gr/kg in non-sterile conditions (Fig. 3).

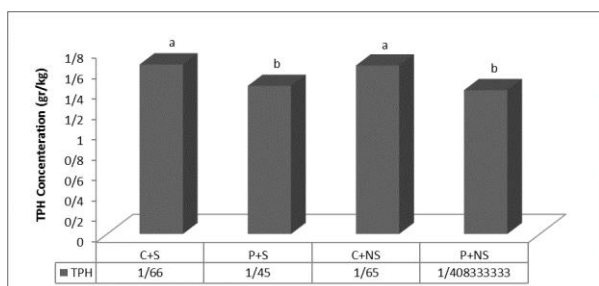


Fig. 3. The effect of treatments with *Cynodon dactylon* and sterile soil, *Poa pratensis* and sterile soil, *Cynodon dactylon* and non-sterile soil and *Poa pratensis* with non-sterile soil on the average concentration of petroleum.

In order to evaluate the simultaneous effect of species and bacteria, the average concentrations of petroleum hydrocarbons were compared based on

the LSD post hoc tests test at $P < 0.01$. The test showed no significant difference in the simultaneous effect of species and bacteria.

However 1.7 gr/kg mean rate of decline obtained in the treatment of *Rhodococcus erythropolis* inoculated with the *Cynodon dactylon*, the rate mean of decline was 1.6 gr/kg in the treatment without inoculating *Rhodococcus erythropolis* with the *Cynodon dactylon*.

DISCUSSION

Phytoremediation has now emerged as a promising strategy for removal of a variety of soil contaminants [35-37]. The effect of planting plants on contaminated soil for refined petroleum hydrocarbons revealed the highest mean rate of decline is related to the *Cynodon dactylon* specie. This can be caused by the more stimulate of the roots of *Cynodon dactylon* to grow compared with *Poa pratensis* specie (Fig. 1). The efficiency of phytoremediation relies on the establishment of active plants with sufficient biomass growth, active root proliferation and/or root activities that can support a flourishing microbial consortium assisting phytoremediation in the rhizosphere [38-41]. It is reported that planting plants in areas contaminated with petroleum hydrocarbons may increase the rate of production of metabolites of the enzyme degrading effect. Therefore they require more source of carbon for bacteria to increases the decomposing process and reduce the average concentration of petroleum hydrocarbons. The diversity of root morphology amongst plant species may explain some of this variability. For example, species from *Poaceae* are often chosen due to their high rooting density which is capable of supporting large microbial communities [42-45].

Bioremediation of petroleum-contaminated soil is mainly based on biodegradation in the rhizosphere [46-47]. Bioremediation uses microbes or other biological systems to degrade environmental pollutants [48-54]. In this study, performance *Rhodococcus erythropolis* bacteria in the soil contaminated with petroleum hydrocarbons revealed the ideal level of the average rate of decline of petroleum hydrocarbons in both inoculation and without inoculation bacteria. However, the highest rate of decline obtained of the inoculated treatment with *Rhodococcus erythropolis*. *Rhodococcus erythropolis* inoculation in the soil may be modified the providing of nutrients for plants. Rhizoremediation, which can be used at the final stages of polluted soil re-cultivation, is based on the use of microorganisms

to utilize environmental pollutants as carbon and energy source and leads to the destruction of organic pollutants by microorganisms associated with plant roots [55-56].

Phytoremediation associated with microbial bioremediation led to a more successful remediation method of contaminants, particularly organic compounds [57]. The mechanism of combination plants and bacteria in contaminated soil for refined petroleum hydrocarbons (Fig.3) showed that the rate of decline of Petroleum hydrocarbons is in the ideal level for the interaction of bacteria and specie and it obtained of *Cynodon dactylon* specie for inoculation and without inoculation bacteria. The highest effect was related to the inoculated treatments. The action of good root-colonizing and pollutant-degrading bacterial strains can result in efficient cleaning of polluted soils. It has been reported that root systems of some plants such as tall fescue, sorghum, maize, alfalfa, ryegrass, Bermuda grass, and rice contain highly potent hydrocarbon-degrading microorganisms. [58]. it is stated that perennial plant species (*Lolium perenne*) with degrading bacteria *Rhodococcus erythropolis* to the removal of soil contaminated with petroleum hydrocarbons in soil is one of the most effective methods (Fig. 4).

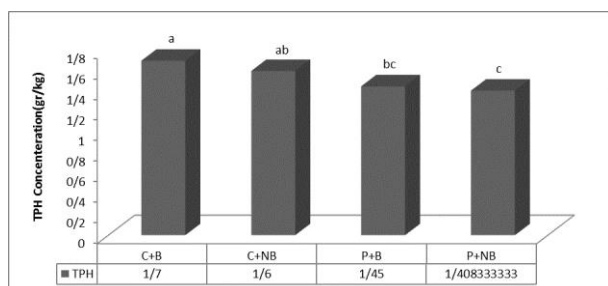


Fig. 4. The effect of treatments with *Cynodon dactylon* and inoculated Bacteria, *Cynodon dactylon* and without inoculated Bacteria, *Poa pratensis* and inoculated Bacteria and *Poa pratensis* without inoculated Bacteria on the average concentration of petroleum hydrocarbons

CONCLUSION

Degradation of hydrocarbons in 100% soils during the study was negligible, regardless of the applied treatments. Low percentages of hydrocarbon degradation, suggesting that a longer time period may be required. Phytoremediation proved to be an effective strategy for hydrocarbon removal, and colonized soils showed high rates of degradation in most experiments. So that the presence of plants clearly enhanced hydrocarbon degradation compared to un-colonized soils, significant

hydrocarbon degradation was found in *Cynodon dactylon* specie and also significant *Cynodon dactylon* potential for hydrocarbons.

Phytoremediation seems to depend on root system development. Overall results point that *Cynodon dactylon* and *Poa pratensis* and their associated microorganisms present a potential for phytoremediation of petroleum hydrocarbons in contaminated soils, but the response to bioremediation treatments varied with plant species. In general the information obtained in this study may be useful for the decision on which phytoremediation strategies to apply to a specific contaminated soil. One of the most important mechanisms for remediation of hydrocarbons contaminated soil seems to be based on the synergy of plant roots of *Cynodon dactylon* and microorganisms. Therefore, due to the hard seed germination of this species in contaminated soils needs to be the seeds germinated in the out of soils contaminated and then transferred to contaminated soil. This makes the plant to seamlessly cover the entire surface the contaminated soil and creates a uniform root mass.

REFERENCES

1. P. Oleszczuk, *J. Chemosphere*, **65**, 1616 (2006).
2. F. Porteous, T. Moore, B. Barac, L. Borremans, J. Oeyen, D.C.D. Vangronsveld van der Lelie, B. Moore, *J. Syst. Appl. Microbiol.*, **29**, 539 (2006).
3. G. MacKinnon, H. J. Duncan, *J. Chemosphere*, **90**, 952 (2013).
4. J. L. Sun, H. Zeng, H. G. Ni, *J. Chemosphere*, **90**, 1751 (2013).
5. B. Mahanty, K. Pakshirajan, V.V. Dasu, *J. Environ. Sci. Technol.*, **41**, 1697 (2011).
6. H. Guo, J. Yao, M. Cai, Y. Qian, Y. Guo, H.H. Richnow, R.E. Blake, S. Doni, B. Ceccanti, *J. Chemosphere*, **87**, 1273 (2012).
7. M. Havelcová, A. Melegy, S. Rapant, *J. Chemosphere*, **95**, 63 (2014).
8. R. A. Cameselle, K. R. Chirakkara, *J. Chemosphere*, **93**, 626 (2013).
9. C. Chigbo, L. Batty, R. Bartlett, *J. Chemosphere*, **90**, 2542 (2013).
10. J. Wei, X. Liu, Q. Wang, C. Wang, X. Chen, H. Li, *J. Chemosphere*, **97**, 92 (2014).
11. X. Zhu, X. Ni, J. Liu, Y. Gao, *J. Clean-Soil Air Water*, **42**, 306 (2014).
12. H. Radnezhad, M. Foroughi Abari, M. Sadeghi, *Biol. Forum*, **7**, 75 (2015).
13. S. Khan, M. Afzal, S. Iqbal, M.S. Mirza, Q. M. Khan, *J. Chemosphere*, **91**, 663 (2013).
14. S. D. Cunningham, T. A. Anderson, P.A. Schwab, F. C. Hsu, *J. Adv. Agron.*, **56**, 44 (1996).
15. T. A. Anderson, E. A. Guthrie, B. T. Walton, *J. Environ. Sci. Technol.*, **27**, 2630 (1993).

16. N. Merkel, R. Schultez-Kraft, C. Infante, *J. Water Air Soil Pollut.*, **165**, 235 (2005).
17. N. Merkel, R. Schultez-Kraft, *J. Appl. Bot. Food Qual.*, **78**, 185 (2004).
18. A. Chehregani, B. Malayeri, *J. Agric. Biol.*, **9**, 462 (2007).
19. A. Chehregani, F. Mohsenzade, F. Vaezi, *J. Environ. Chem.*, **72**, 1349 (2009).
20. C. C. Wiltse, W. L. Rooney, Z. Chen, A. P. Schwab, M. K. Banks, *J. Environ. Qual.*, **27**, 169 (1998).
21. S. S. Radwan, H. Al-Awadhi, N. A. Sorkhoh, I. M. El-Nemer, *J. Microbiol. Res.*, **153**, 247 (1998).
22. E. Dominguez-Rosado, J. Pichtel, *J. Environ. Eng. Sci.*, **21**, 169 (2004).
23. C. H. Chaineau, J. L. More, J. Oudot, *J. Environ. Qual.*, **29**, 568 (2000).
24. F. Solano-Serena, R. Marchal, J. P. Vandecasteele, *J. Appl. Microbiol.*, **97**, 629 (2004).
25. C. C. C. R. De Carvalho, M. M. R. Da Fonseca, *J. Appl. Microbiol. Biotechnol.*, **6**, 715 (2005).
26. M. J. Larkin, L. A. Kulakov, C.C.R. Allen, *J. Curr. Opin. Biotechnol.*, **16**, 282 (2005).
27. D. H. Pieper, W. Reineke, *J. Curr. Opin. Biotechnol.*, **11**, 262 (2000).
28. M. Bouchez-Naitali, H. Rakatozafy, R. Marchal, J. Y. Leveau, J. P. Vandecasteele, *J. Appl. Microbiol.*, **86**, 421 (1999).
29. W. F. M. Roling, M. G. Milner, D. M. Jones, F. Fratepietro, R. P. J. Swannell, F. Daniel, I. M. Head, *J. Appl. Environ. Microbiol.*, **70**, 2603 (2004).
30. S. K. Brar, M. Verma, R. Y. Surampalli, K. Misra, R. D. Tyagi, N. Meunier, J. F. Blais, *J. Waste Manage.*, **10**, 59 (2006).
31. M. Soleimani, M. Afyuni, M. A. Hajabbasi, F. Nourbakhsh, M. R. Sabzalian, J. H. Christensen, *J. Chemosphere*, **81**, 1084 (2010).
32. P. Fernandez-Alvarez, J. Vila, J. M. Garrido, M. Grifoll, G. Feijoo, J. M. Lema, *J. Hazard. Mater.*, **147**, 914 (2007).
33. Y. Liang, X. Zhang, D. Dai, G. Li, *J. Int. Biodeterior. Biodegrad.*, **63**, 80 (2009).
34. V. P. Beškoski, C. Takić, M. C. J. Milić, C. Ilić, G. Gojgic-Cvijović, C. Jovancević, C. Vrvic, M. M. B, *J. Serb. Chem. Soc.*, **75**, 1605 (2010).
35. T. Macek, M. Mackova, J. Kas, *J. Biotechnol. Adv.*, **18**, 23 (2000).
36. L. A. Newman, C. M. Reynolds, *J. Curr. Opin. Biotechnol.*, **15**, 225 (2004).
37. M. L. W. Åslund, B. A. Zeeb, A. Rutter, K. J. Reimer, *J. Sci. Total Environ.*, **374**, 1 (2007).
38. W. W. Wenzel, *J. Plant Soil*, **321**, 385 (2008).
39. Z. D. Parrish, M. K. Banks, A. P. Schwab, *J. Environ. Pollut.*, **137**, 187 (2005).
40. A. Yateem, T. Al-Sharrah, A. Bin-Haji, *J. Soil Sed. Contam.*, **16**, 269 (2007).
41. P. Nichols, R. Leeming, V. Latham, M. Rayner, In: Preprints of Papers Presented at 2 12th American Chemical Society National Meeting, Orlando, FL., **36**, p. 175 (1996).
42. G. Adam, H. Duncan, *J. Environ. Pollut.*, **120**, 363 (2002).
43. O. Barrutia, C. Garbisu, L. Epelde, M. C. Sampedro, M. A. Goicolea, J. M. Becerril, *J. Sci. Total Environ.*, **409**, 4087 (2011).
44. S. E. Gaskin, R. H. Bentham, *J. Sci. Total Environ.*, **408**, 3683 (2010).
45. S. Lee, W. Lee, C. Lee, J. Kim, *J. Hazard Mater.*, **153**, 892 (2008).
46. C. M. Frick, R. E. Farrell Germida, In: Assessment of Phytoremediation as an In-Situ Technique for Cleaning Oil-Contaminated Sites. Petroleum Technology Alliance Canada, Calgary, p35 (1999).
47. R. L. Tate, In: Soil Microbiology. Wiley, New York. 143, p.59 (1995).
48. R. M. Atlas, *J. Chem. Technol. Biotechnol.*, **52**, 149 (1991).
49. R. M. Atlas, M. C. Atlas, *J. Curr. Opin. Biotechnol.*, **2**, 440 (1991).
50. M. Dua, A. Singh, N. Sethunathan, A. K. Johri, *J. Appl. Microbiol.*, **2**, 22 (2002).
51. H. J. Heipieper, *J. Nato Sci. Series IV, Earth Environ. Sci.*, **76**, 1 (2007).
52. M. Owsianiak, A. Szulc, L. Chrzanowski, P. Cyplik, M. Bogacki, A. K. Olejnik-Schmidt, A. K. Heipieper, *J. Appl. Microbiol. Biotechnol.*, **84**, 545 (2009).
53. H. G. Song, X. P. Wang, R. Bartha, *J. Appl. Environ. Microbiol.*, **56**, 652 (1990).
54. X. P. Wang, R. Bartha, *J. Soil Biol. Biochem.*, **22**, 501 (1990).
55. K. E. Gerhardt, X-D. Huang, B. R. Glick, B. M. Greenberg, *J. Plant Sci.*, **176**, 20 (2008).
56. I. Kuiper, E. L. Lagendijk, G. V. Bloemberg, B. J. Lugtenberg, *J. Mol. Plant Microbe Interact.*, **17**, 6 (2004).
57. I. A. Al-Baldawi, S. R. Sheikh Abdullah, N. Anuar, F. Suja, I. Mushrifah, *J. Ecol. Eng.*, **74**, 463 (2015).
58. R. S. Hedge, J. S. Fletcher, *J. Chemosphere*, **32**, 2471 (1996).

Effects of choline, TMA, and TMAO on the expression of flavin-containing monooxygenases 3 and 5 in mice

A. Mohammadi^{1,2}, M. R. Baneshi³, T. Khalili^{1,*}

¹Department of Clinical Biochemistry, Afzalipour School of Medicine, Kerman University of Medical Sciences, Kerman, Iran.

²Physiology Research center, Kerman University of Medical Sciences, Kerman, Iran.

³Modeling in Health Research Center, Institute for Futures Studies in Health, Department of Biostatistics and Epidemiology, School of Public Health, Kerman University of Medical Sciences, Kerman, Iran

Received February 12, 2016; Revised December 20, 2016

Choline and trimethylamine N-oxide (TMAO) have been considered as factors associated with cardiovascular disease (CVD). TMAO is produced from trimethylamine (TMA) oxidation by flavin-containing monooxygenase 3. Flavin-containing monooxygenases (FMOs) are enzymes that catalyze oxygenation of a wide range of compounds and drugs. Human and mouse livers, are included other members of FMO family, FMO4 and FMO5. Expression of FMO5 in our liver is approximately equal to FMO3 expression. FMO3 and FMO5 enzymes are known to be involved in lipids and glucose metabolism. In this study, we investigated the effects of choline, TMA and TMAO on FMO3 and FMO5 expression. For this purpose, these compounds were injected to female NMRI mice as intraperitoneally and then liver tissues were collected to evaluate of FMO3 and FMO5 expression. Trimethylamine administration resulted in 8-fold ($P < 0.0001$) increase in FMO3 mRNA levels and a 2.5-fold ($P < 0.0001$) increase in FMO3 protein compared to controls (mean different equal to 6.87 for mRNAs and 1.67 for protein). A significant decrease (approximately 45% ($P < 0.05$)) in FMO3 mRNA was observed following choline administration (mean difference of FMO3 mRNA levels between treatment and control groups equal to 0.576). FMO5 mRNA levels were decreased to 50% than to controls ($P = 0.003$) after TMA treatment. Overall, our data indicate that FMO3 and FMO5 expression is influenced by TMA and choline.

Keywords: Flavin-containing monooxygenase, Gene expression, mouse, Real-time PCR, trimethylamine-N-oxide

INTRODUCTION

Flavin-containing monooxygenases (FMOs) are microsomal enzymes that catalyze the oxygenation of a wide variety of nitrogen- and sulfur-containing compounds [1] as well as drugs and xenobiotics [2]. In mammals, FMOs are expressed in tissue-specific and developmental-dependent manner [3]. In human, five FMO genes encode functional proteins and are on the long arm of chromosome 1 of which FMO1-4 are located in one of cluster at q23-25 and FMO5 is in the region 1q21.1 [3-4]. A second cluster containing 5 pseudogenes was also detected on chromosome1. The mouse genome contains nine FMO genes that FMO1-4 and FMO6 are clustered on chromosome1 and FMO5 is on chromosome1 and FMO5 is on chromosome3 [5]. FMO3 is the most important isoform of FMO enzymes that was expressed in adult human liver [3] and in the liver of adult female mice [6]. The importance of FMO3 is because of its role in the processing of some drugs (e.g. cimetidine), chemicals in cigarette (nicotine) [7] and dietary derived trimethylamine (TMA) [8].

Trimethylamine, as a FMO3 specific substrate, is converted to trimethylamine N-oxide (TMAO) by this enzyme. Most people excrete 95% or more of TMA as TMAO [3]. FMO5 is expressed in the liver and can be detected easily at the protein level in all studied species. Both in vitro and in vivo studies have shown that liver FMO (FMO3) was affected by exogenous factors such as diet [9] and endogenous factors as hormones [10], obesity and genetic [11]. More recent studies have shown that some members of FMO family play the important physiological roles [12-15]. For example, it is known that FMO5 regulates changes metabolic associated ageing by up-regulation of cholesterol biosynthesis and also promoting the expression of enzymes involved in glycolysis/gluconeogenesis [12]. Recently, it has been found that FMO3 through a gut flora-dependent pathway, TMA/FMO3/TMAO, plays a very important role in the regulation of cholesterol metabolism [15-16]. Following intake of foods containing choline, lecithin, or L-carnitine, these compounds are metabolized by gut enterobacteria to produce TMA. Trimethylamine is readily absorbed from the gastrointestinal tract and subsequently oxidized by liver FMO3 to form TMAO [14, 17-18]. It has been suggested that TMAO is associated with

* To whom all correspondence should be sent:
E-mail: taherehkh2131@yahoo.com

atherosclerosis and cardiovascular disease (CVD) [14, 16, 19]. Trimethylamine N-oxide can result in up-regulation of scavenger receptors such as CD36 and SRA1 which have been linked to atherosclerosis [20-21]. Although TMAO, as a product of FMO3 function, is considered as a potent predictive factor of atherosclerosis in human and is associated with CVD risk [14, 17], however the studies have shown that changes of FMO3 expression have profound effects on lipid and glucose metabolism [15, 22]. In addition, TMA, as a FMO3 specific substrate, is a compound that likely is involved in the regulation of cholesterol through FMO3 function [15]. Therefore, it is important to study of possible effective factors on FMO3 expression (substrates and products of FMO3) because it contributes to understanding the function of FMO3 in lipid metabolism. In this study, the main objective was to investigate the changes of FMO3 expression in mouse liver after administration TMA (specific substrate), TMAO (FMO3 product) and choline (as a precursor of TMA and a diet component). The addition, FMO5 expression was evaluated as a member of FMO family that is involved in lipid metabolism.

MATERIALS AND METHODS

Chemicals and Reagents

Choline chloride, Trimethylamine hydrochloride and Trimethylamine N-oxide (TMAO) obtained from Sigma-Aldrich (Germany). Primary antibodies including anti-FMO3, anti-FMO5, goat anti-rabbit IgG-HRP conjugated were from Abcam Biotech Company (Cambridge, UK). Anti-GAPDH and goat anti-mouse secondary antibody were from Novus Biological (Littleton, USA) and R&D Systems Europe (Abingdon, UK), respectively. The cDNA Synthesis kit was from Thermo Scientific (USA) and Real-time PCR kit was obtained from Bio-Rad Laboratories (Hercules, California). All other materials used in this study were of molecular grade.

Animals and treatments

Experiments were performed on 8-9 weeks old female NMRI mice (20-25 gr). Thirty five mice were divided into 5 groups. Animals were kept at 12h light: 12 h dark cycle and chow diet as *ad libitum*. To determine the appropriate time to study, we performed pilot experiments in two series as following. In the first series, the animals were divided into four group including: three groups for treatment with choline, TMA and TMAO that received each of these as intraperitoneal, once-daily for 4 days and one group with distilled water injection as a control. In second series, four groups of animals were considered for each treatment. The compound was administered on first day and animals

along with time-matched controls were sacrificed at time intervals of 24, 48, 72, and 96 hours after injection. The time points for TMA were 12, 24, 48, and 72 hours. The chosen time-point was based on the largest changes at FMO3 mRNA levels. Maximum changes in the FMO3 mRNA were observed at 12 h after injection for TMA, and 48h after injection of TMAO or choline. These time periods were therefore selected for subsequent experiments.

In mice, the 50% lethal dose (LD50) of choline for Ip administration is 225 mg/kg according to "Organization for Economic Cooperation and Development" [23]. We chose 1mmol/kg or 139.6mg/kg for choline, to ensure that the animals do not die and according to previous studies [24]. Also, according to "Acute Exposure Guideline Levels (AEGLS) for trimethylamine", LD50 has been reported as 95-148mg/kg for TMA and 2240-3350 mg/kg for TMAO [25]. The selected doses were 1mmol/kg For TMA and 3000mg/kg For TMAO. Twelve hours after injection of TMA and 48h after injection of choline and TMAO, animals were sacrificed by high concentrations of CO₂, their livers were removed and snap frozen in liquid nitrogen and stored at -80 °C until use. The protocol was approved by the Ethics Committee of Kerman University of Medical Sciences.

RNA extraction

Total RNA from liver tissues, approximately 20-30 mg, was extracted using Trizol reagent (Roche applied science, Germany) according to manufacturer's instructions. The quality and purity of extracted RNA were assayed spectrophotometrically using a ND-1000 nanodrop (Thermo Scientific, USA), also the integrity of RNA was evaluated by electrophoresis on 1% agarose gel.

Revers Transcription-QPCR

First-strand complementary-DNA (cDNA) was synthesized from 1000 ng of total RNA using Revert Aid First Strand cDNA synthesis kit (Thermo Scientific) according to the manufacturer's instruction and was used as the template for real-time PCR experiments. Synthesized cDNAs were stored at -20 °C until use. Real-time PCR was performed using specific primers (Table 1) for FMO3, FMO5, and HPRT (hypoxanthine phosphoribosyl transferase) as a reference gene, and iQ-SYBR Green Supermix (BioRad) in StepOne Real-time PCR System (Applied Biosystems). Reaction mix was included the SYBR supermix 1X of kit (SYBR® Green I dye, iTaq DNA polymerase; 25 U/ml, dNTPmix with 0.2 mM each deoxynucleosid-5'-triphosphates, Tris-HCl; 20 mM,

MgCl₂; 3 mM, KCl; 50 mM fluorescein; 10mM and stabilizer), Rox dye (500 nM), 300-500 nM primers, 2-4 µl from cDNA and H₂O in final volumes 20µl. Thermal program was as follows: starting point 95 °C for 10 min that was followed by 45 cycles at 95 °C for 10s, annealing temperature for each primer pair (Table1) for 30s and extension temperature at 72 °C for 30s, at the end was used one step collecting melting curve data at 55-95 °C with ramping rate of 0.3 °C/s. Relative levels of FMO3 and FMO5 mRNAs were determined after data normalization against hypoxanthine phosphoribosyl transferase (HPRT) as a reference and was calculated by delta-delta Ct (2^{ΔΔCt}) method with ΔΔCt = (Ct_{target gene} - Ct_{HPRT})_{treated} - (Ct_{target gene} - Ct_{HPRT})_{control} that target genes are FMO3 or FMO5, and control is untreated sample.

Western blotting

For protein extraction, approximately 30-40mg of hepatic tissues was homogenized in 750-1000µl ice-cold RIPA buffer (Tris-HCl; 50mM pH =7.5, NaCl; 150mM, SDS; 0.01%, Na-deoxycholate; 0.5%, NP-40; 1% and EDTA; 1mM) containing 1mM phenylmethylsulfonyl fluoride, PMSF (Sigma Aldrich, Germany), and 1X protease inhibitor cocktail (Santa Cruz, USA). Lysates were centrifuged at 12000 g for 15 min at 4 °C. Total protein concentration was determined by a bicinchoninic acid assay method using a BCA kit (Santa Cruz) according to manufacturer's protocol. Twenty mg of liver proteins was separated on 10% SDS-acrylamide gels. Separated proteins were transferred to a PVDF (Polyvinylidene Fluoride) membrane (0.2 µm, BIO-RAD, USA) using a Bio-Rad apparatus (USA). The membrane was blocked for 1 hour in 5% skim milk in TBST (Tris-buffered saline with 0.5% tween -20) and incubated for 1-1.5 h with primary antibodies as follows: Anti-FMO3 (Abcam-ab126790) was diluted 1/3000 in TBST buffer and anti-FMO5 (Abcam-ab103973) was diluted 1/5000 in TBST buffer. Membranes were then washed 3 times for 20 min each time, with

TBST buffer and then were incubated at room temperature for 1.5h with goat anti-rabbit IgG conjugated to horseradish peroxidase (HRP) (Abcam-ab97051) at 1/20000 dilution in TBST buffer. Mouse anti-GAPDH antibody (Novus Biological-NB300-328) was used for normalization of protein levels. Anti-GAPDH antibody was diluted at 1/8000 (in TBST buffer) and membrane was incubated for 1.5 h at room temperature. After washing the membrane 3 times (at 20 min each time) with TBST, PVDF was incubated with goat anti-mouse IgG conjugated to HRP antibody (R&D system-HAF007) diluted 1/5000 (in TBST buffer) for 2 h at room temperature. Finally, the enhanced chemiluminescence substrate (Perkin Elmer, USA) was added to the membranes according to the manufacturer's protocol followed by exposure to X-Ray film. The films were developed and protein bands were measured semi-quantitatively using an Image J software version 1.48.

Statistical analysis

Statistical analysis was performed using SPSS 22 software. The comparison between control(s) and treatment groups was made by one-way ANOVA followed by post hoc Scheffe test or Student's t-test where appropriate. Results are expressed as mean ± standard error of mean (SEM). P <0.05 were considered statistically significant.

RESULTS

Effects of choline, TMA and TMAO on FMO3 expression in mice livers

In the present study, choline, TMA and TMAO were administrated to animals as a single dose of intraperitoneal injection based on preliminary experiment results. Relative expression of FMO3 mRNA from these experiments was represented in Table 2. As data shows, maximum changes (decreasing) in FMO3 mRNA were caused at 48 hour after choline and TMAO treatment, and also at 12 hour after TMA administration. We performed experiment in these time points.

Table 1. The primer sequences and conditions used in real-time PCR

Gene	Forward/Revers Primer sequence	Product size(bp)	Accession numbers	Tm ^d	References
mFMO3 ^a	5'-CACCCTGAAAAGCACGGTA-3' 5'-CTTATAGTCCCTGCTGTGGAAGC-3'	151	NM_008030.1	57	[41] and designed
mFMO5 ^b	5'-ATCACACGGATGCTCACCTG-3' 5'-GCTTGCCTACACGGTTCAAG-3'	234	NM_001161763.1	58	[41]
mHPRT ^c	5'-AGCTACTGTAATGATCAGTCAAC-3' 5'-AGAGGTCCTTTTCACCAGCA-3'	198	NM_013556.2	57	[41]

^a mouse flavin-containing monooxygenases 3, ^b mouse flavin-containing monooxygenases 5 and ^c mouse hypoxanthine phosphoribosyl transferase. ^d Annealing temperature (Tm) for each primer pair.

Table 2. Relative expression of FMO3 mRNA in mice livers after pilot experiments

Treatment	Relative expression of FMO3 mRNA at time points (hour)				
	24(or 12 for TMA)	48	72	96	Daily course
Choline (n=3)	0.736 ± 0.12	0.517 ± 0.143	0.751 ± 0.27	1.304 ± 0.24	0.685 ± 0.19
TMA (n=2)	7.934 ± 0.21	3.526 ± 0.22	1.45 ± 0.09	0.89 ± 0.07	6.489 ± 0.49
TMAO (n=2)	0.64 ± 0.065	0.21 ± 0.56	0.427 ± 0.045	0.943 ± 0.13	0.482 ± 0.025

The abundance of FMO3 mRNA was determined by Real-time-PCR. Values are presented as means ± S.E.

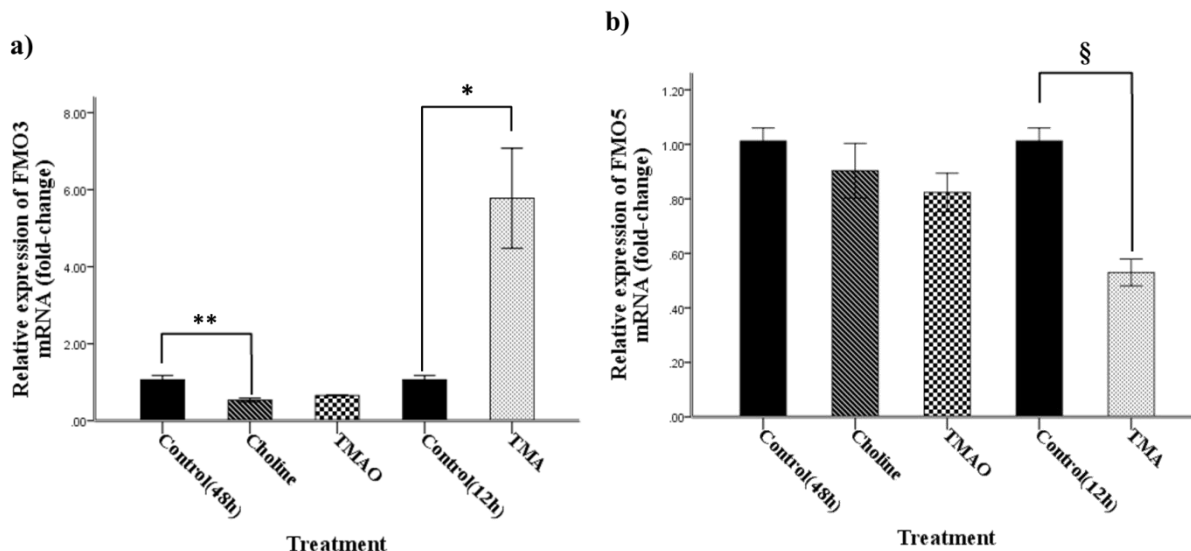


Fig. 1. Relative expression of FMO3 and FMO5 mRNAs in liver mice. Animals received choline (139 mg/kg), trimethylamine N-oxide (3 g/kg) or trimethylamine hydrochloride (95.6 mg/kg) as intraperitoneal injection and were killed after 48h or 12h, and their livers were removed. mRNA expressions were measured by real-time PCR. Hypoxanthine phosphoribosyl transferase (HPRT) mRNA levels were measured and were used as a reference gene. a) FMO3 mRNA levels that normalized with HPRT mRNA. b) FMO5 mRNA levels that were normalized with HPRT. Values present means ± SEM of 6-7 mice per group *: P < 0.0001, **: P < 0.05, §: P < 0.003 compared to controls.

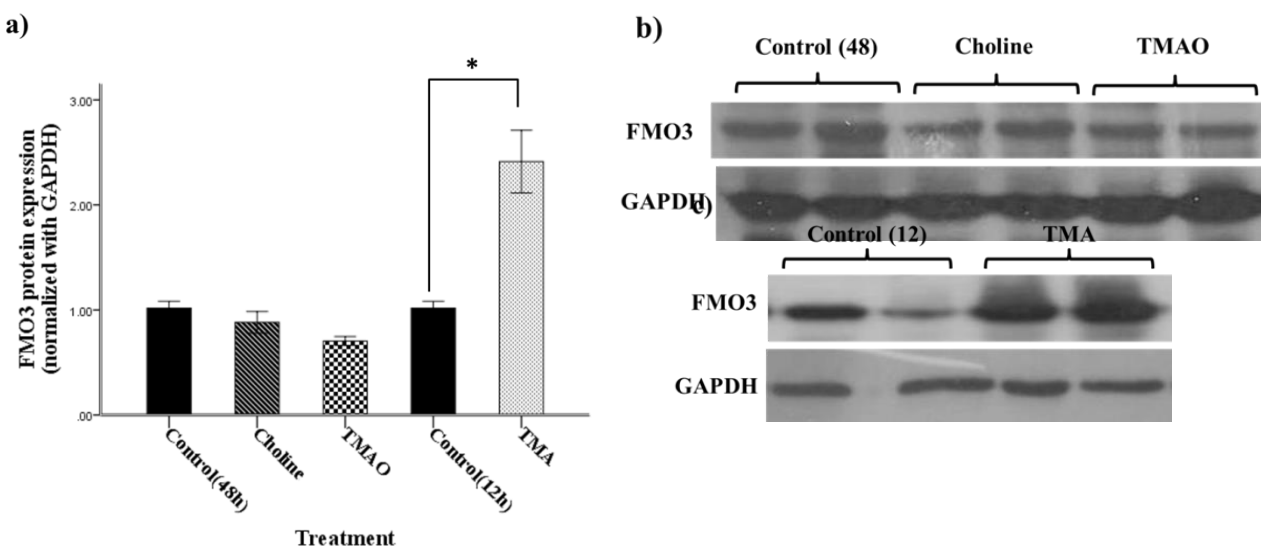


Fig. 2. Analysis of western blot bands for FMO3 protein after densitometry analysis by image J software and normalization with GAPDH protein bands. Relative expression was calculated by a) dividing (FMO3/GAPDH) protein ratio from each sample (treated) to (FMO3/GAPDH) protein ratio from control. Plotted bars represent means ± SEM of 6-7 mice b) Western blot bands of FMO3 and GAPDH proteins in liver samples from mice treated with choline, trimethylamine N-oxide (TMAO) and control 48h (water received as IP injection). c) Western blot bands of FMO3 and GAPDH proteins in liver samples from mice treated with trimethylamine (TMA) and control 12h (water received as IP injection). *: P < 0.0001 compared to respective controls.

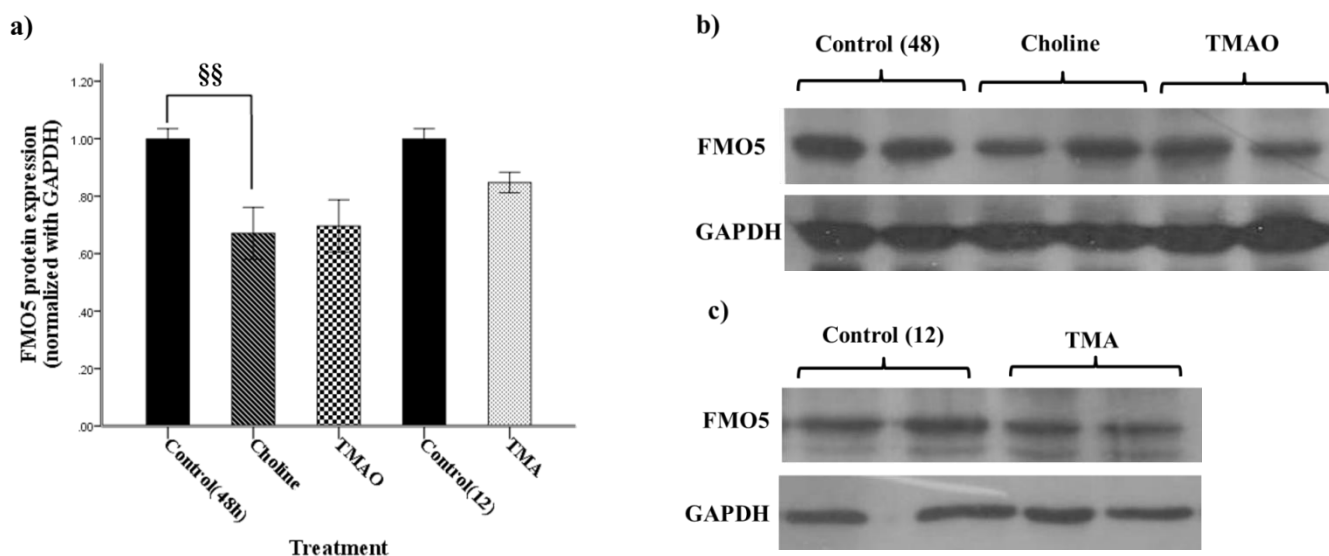


Fig. 3. Relative amounts of FMO5 protein. Western blot bands of FMO5 protein were analyzed after by image J software and normalization with GAPDH protein bands. Relative expression was calculated by **a)** dividing (FMO5/GAPDH) protein ratio from each sample (treated) to (FMO5/GAPDH) protein ratio from control. Plotted bars represent means \pm SEM of 6-7 mice. **b)** Western blot bands of FMO5 and GAPDH proteins in liver samples from mice treated with choline, trimethylamine N-oxide (TMAO) and control 48h (water received as IP injection). **c)** Western blot bands of FMO3 and GAPDH proteins in liver samples from mice treated with trimethylamine (TMA) and control 12h (water received as IP injection). §§: $P=0.018$ compared to respective controls.

The relative expression of FMO3 mRNA was shown in Figure 1. As it can be seen, FMO3 mRNA level shows a remarkable change after treatment with choline and TMA (Figure 1a). TMA administration was caused an increase in mRNA expression of FMO3 to approximately 8-fold ($P < 0.0001$) compared to controls. Relative levels of FMO3 protein were also increased about 2.5-fold ($P < 0.0001$) after exposure with TMA compared to time-matched controls (Figure 2a and 2c). The results indicated a decrease of FMO3 mRNA expression of 45% compared to the control group (controls 48 h) when mice were treated with choline that it was significant statistically ($P < 0.05$). The changes at the protein level were presented in Figures 2a and 2b. FMO3 protein levels only decreased 12% compared to controls after choline treatment that was not significant. Analysis of FMO3 mRNA expression by real-time PCR, although was shown a decrease approximately 20% in mice TMAO treated relative to the controls, but there was no significant difference statistically between treated mice and control group ($P = 0.34$) (Figure 1a). Also, no significant difference was detected at protein level between animals TMAO

treated and respective control (control 48h) as can be seen in Figure 2a and 2b ($P = 0.086$).

Effects of choline, TMA and TMAO on FMO5 expression in mice livers

Analysis of real-time PCR results and western blots for FMO5 did not show correlation between FMO5 mRNA levels and its protein levels. When mice were treated with TMA, FMO5 mRNA expression decreased to 50% ($P = 0.003$) than to control group that was statistically significant (Figure 1b) but decrease of FMO5 protein levels was only 10% compared to controls ($P = 0.35$) (Figure 3a and 3c). In contrast, after treatment with choline, FMO5 mRNA did not change significantly ($P = 0.55$) (Figure 1b), However, a significant decrease ($P < 0.018$) was observed in FMO5 protein levels in mice treated with choline relative to animal control (Figures 3a and 3b). FMO5 expression at mRNA and protein levels were decreased after administration of TMAO to mice but these changes was not significant statistically Figures 1b, 3a and 3b.

DISCUSSION

Recent studies have demonstrated that some members of flavin-containing monooxygenase (FMO) family not only metabolize drugs, but also play important physiological roles in intermediary metabolism [12, 22, 26]. FMO3 is a member of FMO family that oxidizes trimethylamine (TMA) to trimethylamine-N-oxide (TMAO) [16]. It has been found that despite of directly biochemical relation of FMO3 and TMAO, FMO3 enzyme and TMAO product impact lipid metabolism through distinct mechanisms. In fact, transcription control of FMO3 has been raised as an important regulatory key for cholesterol metabolism so that subtle changes in FMO3 expression can perturb lipid metabolism significantly [15, 22]. In this regard, the present study attempted to investigate impacts choline, TMA and TMAO on FMO3 expression in mouse liver after intraperitoneal administration these compounds. Our experiments showed increase significantly of FMO3 expression after exposure to TMA and a significant decrease after choline administration. Therefore, it can be considered that TMA and choline are metabolites with the ability to change FMO3 expression. A number of studies have described the impact of various factors on FMO3 expression. Hepatic FMO activity is greatly affected by the foods [9, 16]. For example, the intake of foods containing indols (e.g. Vegetables) inhibits FMO3 activity [27]. Also, in mice fed with cholic acid-rice diet were observed the increase in FMO3 mRNA and protein expression [16]. The increased FMO3 expression as a result of TMA may influences on lipid and glucose metabolism, since the recent study conducted by Diana M. Shih (2015) [22] using Hep3B cells which had overexpression of FMO3 resulting from adenovirus mediated gene transduction, showed increased glucose production (gluconeogenesis) and lipogenesis. It is possible that TMA affects lipid metabolism through both increasing TMAO levels (as a proatherogenic metabolite) and increase in FMO3 expression that should be investigated by further experiments. The results of the current study showed a significant decrease in FMO3 mRNA levels after choline administration to mice. However, changes in protein levels were not significant. The liver and kidneys are responsible for rapid clearance of choline from circulation [28]. In liver choline's net uptake is result from two processes, one is concentration dependent and transfers choline by a non-saturable mechanism and the other depicts a saturable mechanism. At high concentrations, approximately 60% of choline is metabolized to betaine by choline oxidase system (composed of choline dehydrogenase and betaine-

aldehyde dehydrogenase), 30% is metabolized to phosphorylcholine and lecithin and 10 % remains as free choline. At lower concentrations, phosphorylcholine and lecithin constitute approximately 70% of the choline metabolites [29]. Decreased FMO3 mRNA levels on the second day (48 hours) after administration of a single dose of choline (as seen in current study) may be result of the influence of choline metabolites, phosphorylcholine and lecithin. Given that in a previous study, we did not observe any change in FMO3 expression with lecithin [30], it is possible that the decreased FMO3 after choline administration resulted from another choline metabolite, phosphorylcholine, or from increased free choline. A study conducted by Cashman et al [31] revealed that in rats administered Total Parenteral Nutrition (TPN) for 5 days, adding choline to TPN (TPN + choline) increased hepatic FMO activity. They observed a 1.6 fold increase in FMO3 protein, which was not significantly different, compared to controls. Our results, however, showed a decrease in FMO3 protein, although this difference was also not significant. This difference between Dr Cashman study and our result might be due to the production of different metabolites in periods longer than 2 days that we used in our study. We can therefore conclude that choline does not affect FMO3 protein levels significantly.

Analysis of hepatic FMO5 expression in mice treated with TMA showed a significant decrease in FMO5 mRNA levels. This is interesting because TMA is not a substrate for FMO5. It has been found that only two members of the FMO family, FMO1 and FMO3, metabolize TMA, with FMO3 being the more active isoform [16]. In human and mouse liver, mRNA levels of FMO5 are higher than other FMOs [8, 32] but, this enzyme has no activity than to typical substrates of FMOs such as trimethylamine and benzydamine [33-34]. Despite this, FMO5 was affected by a number of compounds and chemicals. For example, in primary human hepatocytes, rifampin induces FMO5 expression [35], also FMO5 was induced by lipoic acid in female mouse hepatocytes [36]. Possible implications of changes in FMO5 expression should be investigated. It appears to be important, because the repression of FMO5 gene expression has been observed in liver samples of patients with type-2 diabetes [37]. Results from our study did not show any correlation between the expression FMO5 at mRNA and protein levels. This is in agreement with an Overby's study [38] that showed variability in protein and mRNA expression for hepatic FMOs (FMO3 and FMO5). Gene

expression is regulated at many levels from DNA to protein. Several processes influence protein levels in the cell: mRNA export from nucleus to cytoplasm, degradation of some mRNA molecules, and selecting mRNAs for translation by ribosomes [39]. There are also several reasons for the poor correlation between the levels of mRNA and protein. The first is, existence complicated and varied post-transcriptional mechanisms involved in turning mRNA into protein that have not defined. Second is, differences in *in vivo* half-life of proteins; and final is, being significant amount of error and noise in both protein and mRNA experiments that limit our ability to get a clear picture. It is unknown about FMO family, whether the regulation at transcription level or post-translation alteration is determinant for amounts of protein. Therefore, it is difficult to determine factor(s) that resulted in poor relation between mRNA and protein in FMO5.

In summary, the experiments this study showed the increase of FMO3 expression (at mRNA and protein levels) by TMA and the decrease of FMO3 mRNA levels by choline. FMO5 mRNA amounts were also decreased by TMA, although TMA is not a substrate for FMO5. Understanding of the mechanisms involved in the changes of FMO3 and FMO5 expression requires further experiments [39-41].

Acknowledgments: The authors thank the head of the department of physiology and Vida Naderi, Ph.D student of physiology, of the Afzalipour School of medicine, Kerman University of medical sciences for their contribution of animal treatment and valuable assistance.

REFERENCES

1. P. E. Hlavica, L. A. Damani, N-oxidation of Drugs: biochemistry, pharmacology, toxicology, 1st ed., Springer, Netherlands, (1991).
2. B. A. Palfey, C. A. McDonald, *Arch. Biochem. Biophys.*, **493**, 26 (2010).
3. S. K. Krueger, D. E. Williams, *Pharmacol. Ther.*, **106**, 357 (2005).
4. R. R. McCombie, C. T. Dolphin, S. Povey, I. R. Phillips, E. A. Shephard, *Genomics.*, **34**, 426 (1996).
5. D. Hernandez, A. Janmohamed, P. Chandana, I. R. Phillips, E. A. Shephard, *Pharmacogenet.*, **14**, 117 (2004).
6. J. G. Falls, B. L. Blake, Y. Cao, P. E. Levi, E. Hodgson, *J. Biochem. Toxicol.*, **10**, 171 (1995).
7. J. R. Cashman, S. B. Park, C. E. Berkman, L. E. Cashman, *Chem-biol. Interact.*, **96**, 33 (1995).
8. J. R. Cashman, J. Zhang, *Annu. Rev. Pharmacol.*, **46**, 65 (2006).
9. A. Dixit, T. E. Roche, *Arch. Biochem. Biophys.*, **233**, 50 (1984).
10. J. G. Falls, D.-Y. Ryu, Y. Cao, P. E. Levi, E. Hodgson, *Arch. Biochem. Biophys.*, **342**, 212 (1997).
11. K. Jeong-Hyeon, L. Tong-Joo, P. Chang-Shin, J. Eun-Hee, O. Yun-Mi, K. Ju-Hee, *Mol. Cell Toxicol.*, **4**, 5 (2008).
12. S. G. Gonzalez Malagon, A. N. Melidoni, D. Hernandez, B. A. Omar, L. Houseman, S. Veeravalli, F. Scott, D. Varshavi, J. Everett, Y. Tsuchiya, J. F. Timms, I. R. Phillips, E. A. Shephard, *Biochem. Pharmacol.*, **96**, 267 (2015).
13. S. Veeravalli, B. A. Omar, L. Houseman, M. Hancock, S. G. Gonzalez Malagon, F. Scott, *Biochem. Pharmacol.*, **90**, 88 (2014).
14. Z. Wang, E. Klipfell, B. J. Bennett, R. Koeth, B. S. Levison, B. Dugar, A. E. Feldstein, E. B. Britt, X. Fu, Y. M. Chung, Y. Wu, P. Schauer, J. D. Smith, H. Allayee, W. H. Tang, J. A. DiDonato, A. J. Lusis, S. L. Hazen, *Nature.*, **472**, 57 (2011).
15. M. Warriar, D. M. Shih, A. C. Burrows, D. Ferguson, A. D. Gromovsky, A. L. Brown, *Cell Rep.*, **10**, 326 (2015).
16. B. J. Bennett, T. Q. de Aguiar Vallim, Z. Wang, D. M. Shih, Y. Meng, J. Gregory, H. Allayee, R. Lee, M. Graham, R. Crooke, P. A. Edwards, S. L. Hazen, A. J. Lusis, *Cell metab.*, **17**, 49 (2013).
17. R. A. Koeth, Z. Wang, B. S. Levison, J. A. Buffa, E. Org, B. T. Sheehy, E. B. Britt, X. Fu, *Nature Med.*, **19**, 576 (2013).
18. A. Q. Zhang, S. C. Mitchell, R. L. Smith, *Food Chem. Toxicol.*, **37**, 515 (1999).
19. W. W. Tang, Z. Wang, B. S. Levison, R. A. Koeth, E. B. Britt, X. Fu, Y. Wu, S. L. Hazen, *New Engl. J. Med.*, **368**, 1575 (2013).
20. A. Mohammadi, A. G. Najjar, M. M. Yaghoobi, Y. Jahani, Z. Vahabzadeh, *Inflammation*, **39**, 393 (2016).
21. A. Mohammadi, A. G. Najjar, M. M. Yaghoobi, Y. Jahani, Z. Vahabzadeh, *Cell Mol. Biol.*, **61**, 94 (2015).
22. D. M. Shih, Z. Wang, R. Lee, Y. H. Meng, N. Che, S. Charugundla, H. Qi, J. Wu, C. Pan, J. M. Brown, T. Vallim, B. J. Bennett, M. Graham, S. L. Hazen, A. J. Lusis, *J. Lipid Res.*, **56**, 22 (2015).
23. OECD, Organization for Economic Cooperation and Development SIDS initial assessment report for SIDM, Berlin, Germany, (2004).
24. A. K. Mehta, N. Arora, S. N. Gaur, B. P. Singh, *Reg. Toxicol. Pharmacol.*, **54**, 282 (2009).
25. <http://www.epa.gov/aegl/trimethyl-amine-results-aegl-program>
26. J. Miao, A. V. Ling, P. V. Manthena, M. E. Gearing, M. J. Graham, R. M. Crooke, K. J. Croce, R. M. Esquejo, C. B. Clish, D. Vicent, S. B. Biddinger, *Nat. Commun.*, **6**, 6498 (2015).
27. J. R. Cashman, Y. Xiong, J. Lin, H. Verhagen, G. van Poppel, P. J. van Bladeren, S. Larsen-Su, D. E. Williams, *Biochem. Pharmacol.*, **58**, 1047 (1999).
28. J. Blish, *J. Physiol.*, **120**, 53 (1953).

29. S. H. Zeisel, D. L. Story, R. J. Wurtman, H. Brunengraber, *P. Natl. Acad. Sci. USA.*, **77**, 4417 (1980).
30. A. Mohammadi, M. R. Baneshi, Z. Vahabzadeh, T. Khalili, *Biosci. Biotechnol. Res. Asia.*, **13**, 1797 (2016).
31. J. R. Cashman, V. Lattard, J. Lin, *Drug Metab. Dispos.*, **32**, 222 (2004).
32. A. Janmohamed, D. Hernandez, I. R. Phillips, E. A. Shephard, *Bioch. Pharmacol.*, **68**, 73, (2004).
33. D. H. Lang, A. E. Rettie, *Brit. J. Clin. Pharmacol.*, **50**, 311 (2000).
34. D. H. Lang, C. K. Yeung, R. M. Peter, C. Ibarra, R. Gasser, K. Itagaki, R. M. Philpot, A. E. Rettie, *Biochem. Pharmacol.*, **56**, 1005 (1998).
35. J. M. Rae, M. D. Johnson, M. E. Lippman, D. A. Flockhart, *J. Pharmacol. Exp. Ther.*, **299**, 849 (2001).
36. L. Houseman, Flavin-containing monooxygenases: regulation, endogenous roles and dietary supplements, University of London, (2008).
37. T. Takamura, M. Sakurai, T. Ota, H. Ando, M. Honda, S. Kaneko, *Diabetologia.*, **47**, 638 (2004).
38. L. H. Overby, G. C. Carver, R. M. Philpot, *Chem-Biol. Interact.*, **106**, 29 (1997).
39. B. Alberts, D. Bray, K. Hopkin, Essential cell biology, fourth ed., Garland science, Taylor & Francis group, p. 261 (2014).
40. D. Greenbaum, C. Colangelo, K. Williams, M. Gerstein, *Genome Biol.*, **4**, 117 (2003).
41. L. K. Siddens, M.C. Henderson, J.E. Vandyke, D.E. Williams, S.K. Krueger, *Biochem. Pharmacol.*, **75**, 570 (2008).

Prokaryotic pico- and nanoplankton community structure in the hypersaline lakes of the Qaidam Basin

L. Chu^{1, 2}, J. Wang^{1, 3}, F. Wang^{1*}, M. Chen¹, Z. Liu⁴

¹State Key Laboratory of Simulation and Regulation of Water Cycle in River Basin, China Institute of Water Resources and Hydropower Research, Beijing, 100038, China

²College of Hydrology and Water Resource, Hohai University, Nanjing, 210098, China

³Institute of Shandong River Wetlands, Laiwu, 271100, China

⁴Institute of Microbiology, Chinese Academy of Sciences, Beijing, 100101, China

Received July 13, 2016; Revised December 13, 2016

Pico- and nanoplankton were the main drivers of the biogeochemical cycles over large areas of the world's waters, play key ecological roles in aquatic ecosystems. We performed a comprehensive analysis of the genetic diversity (16S rDNA gene) of the prokaryotic pico- and nanoplankton communities (PPNC, a size of member in PPNC range 0.2-20 μm) and the whole prokaryotic plankton community (WPPC, a size of member in WPPC $>0.2 \mu\text{m}$) in three hypersaline lakes located in the Qaidam Basin. Most of the 16S rDNA gene sequences obtained of the PPNC in Lake Gahai were closely related to Proteobacteria phylum. The most abundant sequences of the PPNC, however, primarily represented Euryarchaeota (78.60%) in Lake Gasikule. An obvious divergence between the structure of the PPNC and the WPPC was observed. The most common group of WPPC was assigned as unclassified prokaryotes in Lake Gahai, accounting for 23.27% of the total number of sequences. Altitude, temperature and TDS (total dissolved solids) were significantly correlated with the distribution of the PPNC. This study also shows important gaps in the current knowledge about PPNC inhabiting hypersaline lakes, highlighting the need for future, more detailed investigations to develop active conservation strategies to preserve the microbial biodiversity in these areas.

Keywords: Prokaryotic pico- and nanoplankton community, Hypersaline lake, Qaidam Basin.

INTRODUCTION

Inland saline lakes represent approximately 5% of modern drylands [1]. These water bodies are numerous and distributed worldwide in semi-arid or arid areas [2]. Studies have shown that salinity plays a dominant role in regulating the composition of prokaryotic plankton in inland waters [3-4]. The bacterial communities of freshwater and hypersaline lakes show only small taxonomic overlap [5]. Soda lake environments are good examples of extreme environments [6]. Studies of soda lakes have improved our understanding of the biology of extreme environments and have resulted in the identification of novel microorganisms and enzymes (extremozymes) with potential for biotechnological applications [7]. These enzymes are stable at high pH values, salt concentrations, or temperatures [8-9].

Prokaryotic pico- and nanoplankton is the smallest size fraction of prokaryotic plankton. Picoplanktonic cell sizes range from 0.2 to 2.0 μm [10] (i.e., cells that can pass through a 3- μm pore-size filter [11]). Nanoplankton are ubiquitous protozoan zooplankton in a size range of 2 to 20 μm , play key ecological roles in aquatic ecosystems [12]

. In contrast to the macroscopic organisms studied for centuries, the microscopic prokaryotes have only received adequate attention in the last forty years. A number of studies have provided evidence that picoplankton are the most abundant organisms in the ocean, often dominating the planktonic biomass and primary production. Most studies [13-14] have almost entirely focused on marine members. However, only a few genomes are available from non-marine prokaryotic picoplankton and nanoplankton.

More recently, prokaryotic picoplankton members in both the summer and the winter communities in central European hypersaline lakes have been identified using molecular biological techniques, including denaturing gradient gel electrophoresis (DGGE) and sequence analysis [15]. These molecular analyses (16S rDNA gene and *cpcBA*-IGS region) have identified a dominant group of picocyanobacteria belonging to the *Cyanobium gracile* cluster (group A) of the picophytoplankton clade in shallow alkaline lake (Lake Fertő, Neusiedlersee) in April. The bacterial community is largely dominated by halophilic and halotolerant microorganisms in Isabel lake [6]. Molecular tools in prokaryotic picoplankton have substantially increased our knowledge of microbial community structures [16]; Our current knowledge

* To whom all correspondence should be sent:
E-mail: wangf@iwhr.com

on microorganisms isolated in culture, however, does not completely represent the microbial diversity in saline systems[17-20].

The Qaidam Basin, a large intermountain depression with an arid to semi-arid continental climate, is located in the northeastern margin of the Tibetan Plateau, China [21] and is surrounded by the Qilian, Kunlun, and Aejin mountains. This basin contains dozens of freshwater to hypersaline lakes at high elevations from 2700 to 3200 m above sea level. The hypersaline lakes located in the Qaidam Basin represent a peculiar environment, increasing the potential of identifying previously undescribed halophilic species or isolates with interesting biochemical features[22-23]. In the present study, a massive 454 tag-based sequencing approach targeting the V3, V4 and V5 region of the 16S rDNA gene was used to obtain an overview of the prokaryotic pico- and nanoplankton community (PPNC, a size of member in PPNC range 0.2-20 μm) structure in the hypersaline lakes of the Qaidam Basin. The whole prokaryotic plankton community (WPPC, a size of member in WPPC >0.2 μm) were also analyzed. We also evaluated the distribution patterns of the PPNC along gradients of salinity and other physicochemical parameters.

EXPERIMENTAL

Materials

Analytical methods

Sample collection and DNA extraction

Three lakes located in the Qaidam Basin at elevations ranging from 2,853 to 3,170 m above sea level were investigated (Figure 1; Table S1). The selected lakes covered a TDS gradient from 93.60 to 466.00 g/L. Water samples were collected from surface waters (top 30 cm) using a 5 L Schindler sampler in August 2013 and were immediately filtered through a 20- μm mesh sieve to remove most of the mesozooplankton and large particles. Plankton samples (2000–2500 ml water) for the next-generation sequencing (NGS) analyses were collected on 0.2- μm pore-size Isopore filters using a hand pump at a pressure of less than 15 mmHg. Water temperature, pH and dissolved oxygen levels were measured using a Hydrolab sensor (Austin, TX, USA). Overall, five samples were analyzed (Table S1). The concentrations of the six major ions sodium (Na^+), calcium (Ca^{2+}), magnesium (Mg^{2+}) and sulfate (SO_4^{2-}), and the concentration of total nitrogen (TN) were measured according to standard methods [24] after transporting the samples to the laboratory. The total dissolved solids (TDS) of the

investigated habitats were determined using a conventional conductivity meter (Table S1). Filters for DNA extraction were stored in liquid nitrogen during the field campaign and transported to the laboratory. The DNA was extracted after the cetyltrimethylammonium bromide extraction procedure [18].

16S rDNA Gene Sequencing

PCR was performed using 454 sequencing adaptor-linked primers flanking V3, V4 and V5 region of the 16S rDNA gene by GeneWiz, Inc. (Beijing, China). The quality and the quantity of DNA were examined by agarose gel electrophoresis and spectrophotometrically quantified by Nano Drop ND 2000 (Thermo Scientific, DE, USA). Then the DNA was used as the template for amplifying 16S rDNA genes. PCR mixtures (50 μl) were prepared in duplicate and each contained 2 μl of DNA template, 5 μl of $10 \times$ PCR buffer (50 mm KCl, 10 mm Tris-HCl and 1.5 mm MgCl_2), 200 μM of dNTP, 0.2 μM of each primer and 2.5 U Taq polymerase (Promega, Madison, WI, USA). The PCR thermal regime consisted of an initial denaturation of 3 min at 94 $^\circ\text{C}$, followed by 30 cycles of 30 s at 94 $^\circ\text{C}$, 30 s at 60 $^\circ\text{C}$, 1 min at 72 $^\circ\text{C}$ and a final cycle of 5 min at 72 $^\circ\text{C}$. PCR products were pooled and purified with the Qiaquick gel purification kit according to the manufacturer's instructions (Qiagen, Hilden, North Rhine-Westphalia, Germany). DNA concentration and quality were determined with a NanoDrop 1000 spectrophotometer (Wilmington, DE, USA).

Data Preprocessing

Paired-end reads were assigned to samples based on their unique barcode and truncated by cutting off the barcode and primer sequence. Paired-end reads were merged using FLASH (V1.2.7, <http://ccb.jhu.edu/software/FLASH/>) [25], a very fast and accurate analysis tool, which was designed to merge paired-end reads when at least some of the reads overlap the read generated from the opposite end of the same DNA fragment, and the splicing sequences were called raw tags. Quality filtering on the raw tags were performed under specific filtering conditions to obtain the high-quality clean tags [26] according to the QIIME (V1.7.0, <http://qiime.org/index.html>) [27] quality controlled process. The tags were compared with the reference database (Gold database, http://drive5.com/uchime/uchime_download.html) using UCHIME algorithm (UCHIME Algorithm, http://www.drive5.com/usearch/manual/uchime_algo.html) [28] to detect chimeric sequences, and then

the chimeric sequences were removed[29]. Then the Effective Tags finally obtained.

OTU Clustering and Taxonomy Assignment

Sequences analysis were performed by Uparse software (Uparse v7.0.1001, <http://drive5.com/uparse/>)[30]. Sequences with s were performed by Uparse software (Uparse v7.0.1001, <http://drive5.com/uparse/>) high-quality clean tagsrlap the read genFor each representative sequence, the Green Gene Database (<http://greengenes.lbl.gov/cgi-bin/nph-index.cgi>) [31] was used based on RDP.classifier(Version 2.2, <http://sourceforge.net/projects/rdp-classifier/>)algorithmto annotate taxonomic information.

Microbial Diversity and Statistical Analysis

OTUs abundance information were normalized using a standard of sequence number corresponding to the sample with the least sequences. Subsequent analysis of alpha diversity and beta diversity were all performed basing on this output normalized data. Alpha diversity is applied in analyzing complexity of species diversity for a sample through 6 indices, including Observed-species, Chao1, Shannon, PD-whole tree rarefaction. The Chao1 estimator (<http://www.mothur.org/wiki/Chao1>); Two indices were used to identify Community diversity: The Shannon index Shannon (<http://www.mothur.org/wiki/Shannon>); The Simpson index Simpson (<http://www.mothur.org/wiki/Simpson>); One indice to characterized Sequencing depth: The Good's coverage (<http://www.mothur.org/wiki/Coverage>).

Other statistical analyses

For statistical analysis, the environmental parameters were transformed to avoid skewed data distributions: ion concentrations were arcsine transformed, other chemical parameters were log10 transformed; and the pH, elevation, and latitude were not transformed. Significant marginal effects were analyzed after running a separate canonical correspondence analysis (CCA) on the OTU using square root transformation for each of the environmental factors (i.e., ion percentages, pH, elevation, total phosphorus(TP), total nitrogen (TN), and (TDS). We ran a CCA on the OTU and selected the three most important factors based on automatic forward selection(i.e., TDS, Cl, and Na) of the CANOCO program. The data set generated in this study has been deposited at GenBank's Short Read Archive(SRA) under Accession No. SRA178606.

RESULTS

Characteristics of the studied lakes

Gahai (TDS, 92-96 g/L), Xiaochaidan (TDS, 94-99 g/L) and Gasikule (TDS, 317-344 g/L) are typical hypersaline lakes situated in the Qaidam Basin of the Qinghai-Tibet Plateau, China. The salt lake Gasikule is located in the northwestern part of the Qaidam Basin at an elevation of approximately 2858 m above sea level, where less precipitation and high evaporation have resulted in the highest salinity (Figure 1). Gahai Lake is situated in the eastern part of the Qaidam Basin at an elevation of approximately 2853 m above sea level and is a hypersaline lake with abundant biological resources of *Artemia* (brine shrimp). The TDS of Gahai Lake has been stable in past years. Xiaochaidan Lake is a newly developed lake located in the northeastern part of the Qaidam Basin at an elevation of approximately 3170 m above sea level. Over the last century, the water area of Xiaochaidan Lake has increased two times. As a result, the TDS of Xiaochaidan Lake was 339.10 g/L in the 1970s, but was 94-99 g/L in 2013. Although these three lakes are all located in the Qaidam Basin of the Qinghai-Tibet Plateau, Xiaochaidan Lake and Gahai Lake are largely separated from Gasikule (408 and 603 km, respectively) (Figure 1). Five sample sites were investigated in the present study. TDS and certain physiochemical parameters varied widely along the spectrum from the Gahai sample site to the Gasikule sample site. Table S1 lists the sampling sites, the samples collected and the physicochemical parameters measured.

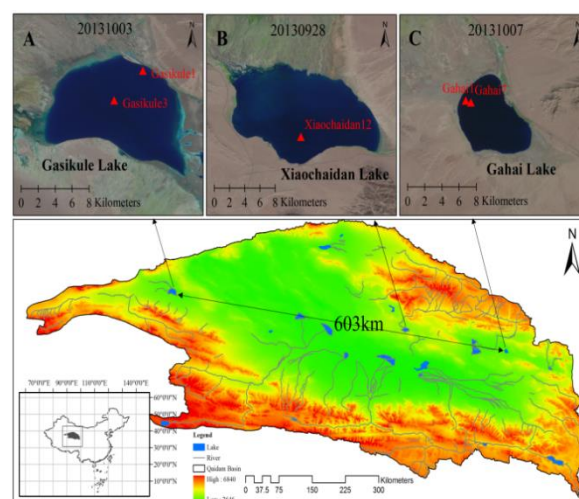


Fig. 1. Locations of three hypersaline lakes in Qaidam Basin. A, Gasikule Lake; B, Xiaochaidan Lake; C, Gahai Lake.

Composition and diversity of the PPNC

After quality filtering and preprocessing, 609,154 reads were obtained, with an average read length of 480 bp from the five sequenced samples examined in the present study; approximately forty-three percent, or a total of 260,201 reads, were assigned to prokaryotic pico- and nanoplankton assemblages. Sequencing yielded highly variable results among the samples, ranging from 85,336 to 153,144 total reads per sample site (Table 1). 97% sequence identity was considered a consensus threshold for reads belonging to the same OTU. The 16S rDNA gene sequences were distributed among nine high-rank taxonomic groups and matched 18 known prokaryote classes.

Table 1. Statistics of Taxonomic Composition in three hypersaline lakes of Qaidam Basin

Samples	Valid	TNR*	Phylum	Class	Order	Family	Genus	Other (ratio)
Gahai1	12827648901	13	24	46	81	150	4.20%	
Gahai7	15177270250	12	25	49	90	152	55.50%	
Xiaochaidan12	15314474351	11	21	49	96	154	15.50%	
Gasikule1	8533628873	11	21	38	62	103	0.70%	
Gasikule3	9062637826	13	23	41	66	114	5.00%	

*TNR Total number of reads

Composition and diversity of the PPNC

After quality filtering and preprocessing, 609,154 reads were obtained, with an average read length of 480 bp from the five sequenced samples examined in the present study; approximately forty-three percent, or a total of 260,201 reads, were assigned to prokaryotic pico- and nanoplankton assemblages. Sequencing yielded highly variable results among the samples, ranging from 85,336 to 153,144 total reads per sample site (Table 1). 97% sequence identity was considered a consensus threshold for reads belonging to the same OTU. The 16S rDNA gene sequences were distributed among nine high-rank taxonomic groups and matched 18 known prokaryote classes.

The 16S rDNA gene sequences were distributed among eight high-rank taxonomic groups in hypersaline Gahai Lake. *Proteobacteria* was the most common phylum in Gahai Lake, accounting for 33.60% of the total number of sequences (Figure 2A). *Bacteroidetes* was the second most prevalent phylum, accounting for 24.40% of the total number of sequences in Gahai Lake. *Cyanobacteria* was the third most prevalent phylum, accounting for 22.20% of the total number of sequences in Gahai Lake. Unexpectedly, *Cyanobacteria* accounted for only 0.05% and 6.10% of the total sequences in Gasikule Lake and Xiaochaidan Lake, respectively (Figure 2A). The 16S rDNA gene sequences were distributed

among eight high-rank taxonomic groups in hypersaline Xiaochaidan Lake. Most sequences from the Xiaochaidan Lake sample were affiliated with *Proteobacteria* (56.40%) (Figure 2A). *Actinobacteria* was the next most prevalent phylum in the Xiaochaidan Lake samples, accounting for 20.20% of all sample sequences. The most abundant sequences in Gasikule Lake were primarily represented by *Euryarchaeota* (76.75%). The 16S rDNA gene sequences were distributed among nine high-rank taxonomic groups in hypersaline Gasikule Lake (Figure 2A). *Bacteroidetes* was the second most prevalent phylum, accounting for 11.60% of the total number of sequences in Lake Gasikule (Figure 2A). *Proteobacteria* was the third most prevalent phylum, accounting for 10.55% of the total number of sequences in Gasikule Lake. There were approximately 2.10%, 1.30%, and 0.10% sequences defined as unclassified prokaryotic pico- and nanoplankton clusters in Lakes Gahai, Xiaochaidan, and Gasikule, respectively.

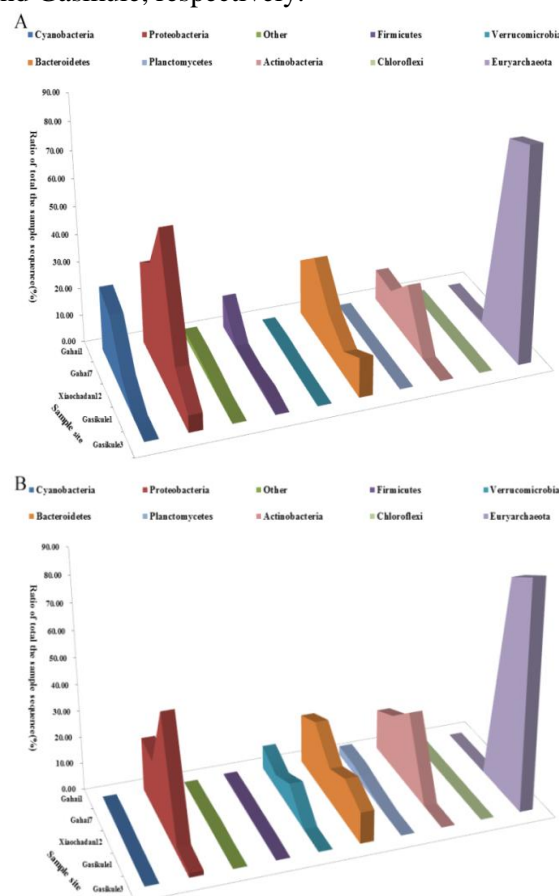


Fig. 2. The taxonomic composition of prokaryotic pico- and nanoplankton communities in three hypersaline lakes in Qaidam Basin. A, Prokaryotic pico- and nanoplankton community (a size range of 0.2-20 μm) of investigated sample site. B, prokaryotic plankton community (a size range >0.2 μm) of investigated sample site.

Compare the composition and diversity of the PPNC with WPPC

The diversity of the WPPC in the same sample site was significantly different from the diversity of the PPNC. As shown in Figure 2B, the most common group of WPPC was assigned as unclassified prokaryotes in Lake Gahai, accounting for 23.27% of the total number of sequences. *Bacteroidetes* was the second most prevalent Phylum, accounting for 20.67% of the total number of sequences in Gahai Lake. *Proteobacteria* was the third most prevalent phylum, accounting for 19.39% of the total number of sequences in Gahai Lake. *Euryarchaeota* was the most common phylum in Lake Gasikule, accounting for 82.85% of the total number of sequences (Figure 2B). *Bacteroidetes* was the second most prevalent phylum, accounting for 14.01% of the total number of sequences in Gasikule Lake. *Proteobacteria* was the third most prevalent phylum, accounting for 2.07% of the total number of sequences in Gasikule Lake.

Table 2. The most abundant taxa in in three hypersaline lakes of Qaidam Basin.

Sample site	Taxa	Ratio (%)
Gahai1	Bacteria;Cyanobacteria;Cyanobacteria;Chloroplast;Chlorophyta;Other	23.30
	Bacteria;Proteobacteria;Alphaproteobacteria;Rhodobacteriales;Rhodobacteraceae;Other	18.50
	Bacteria;Firmicutes;Bacilli;Lactobacillales;Lactobacillaceae;Lactobacillus	11.80
Gahai7	Bacteria;Cyanobacteria;Cyanobacteria;Chloroplast;Chlorophyta;Other	18.50
	Bacteria;Proteobacteria;Gammaproteobacteria;Other;Other	11.90
	Bacteria;Proteobacteria;Alphaproteobacteria;Rhodobacteriales;Rhodobacteraceae;Other	11.30
*XCD12	Bacteria;Actinobacteria;Actinobacteria;Actinomycetales;Microbacteriaceae;Other	18.60
	Bacteria;Proteobacteria;Alphaproteobacteria;Rhodobacteriales;Rhodobacteraceae;Other	16.50
	Bacteria;Proteobacteria;Betaproteobacteria;Burkholderiales;Alcaligenaceae;Other	13.10
**GSK1	Archaea;Euryarchaeota;Halobacteria;Halobacteriales;Halobacteriaceae;Haloquadratum	43.00
	Archaea;Euryarchaeota;Halobacteria;Halobacteriales;Halobacteriaceae;Other	31.00
	Bacteria;Bacteroidetes;Sphingobacteria;Sphingobacteriales;Rhodothermaceae;Salinibacter	7.60
GSK3	Archaea;Euryarchaeota;Halobacteria;Halobacteriales;Halobacteriaceae;Haloquadratum	47.90
	Archaea;Euryarchaeota;Halobacteria;Halobacteriales;Halobacteriaceae;Other	29.90
	Bacteria;Bacteroidetes;Sphingobacteria;Sphingobacteriales;Rhodothermaceae;Salinibacter	13.40

*XCD, Xiaochadan12 Lake; **GSK, Gasikule Lake

Most abundant taxa of PPNC in different sampling sites

Table 2 shows the habitat distribution of abundant taxa at or below the phylum rank in different sampling sites, based on amplicon sequencing. Unclassified prokaryotic taxa (belonging to the class Cyanobacteria) exhibited the highest

proportion in the Gahai1 Lake sample point, accounting for 18.60% of the total number of sequences (Table 2). The most common taxa in the Xiaochadan12 sampling point belong to the class *Actinobacteria*, accounting for 39.79% of the total number of sequences. These taxa have not been well studied and cannot be clearly classified into any genus. At the Gasikule1 and Gasikule3 sampling sites, the prokaryote communities primarily consisted of microorganisms of the genus *Haloquadratum*. The next most abundant sequences were affiliated with unclassified species, accounting for 31% and 29.90% of the total number of sequences, respectively. Unclassified pico- and nanoplankton accounted for significant components of the investigated samples.

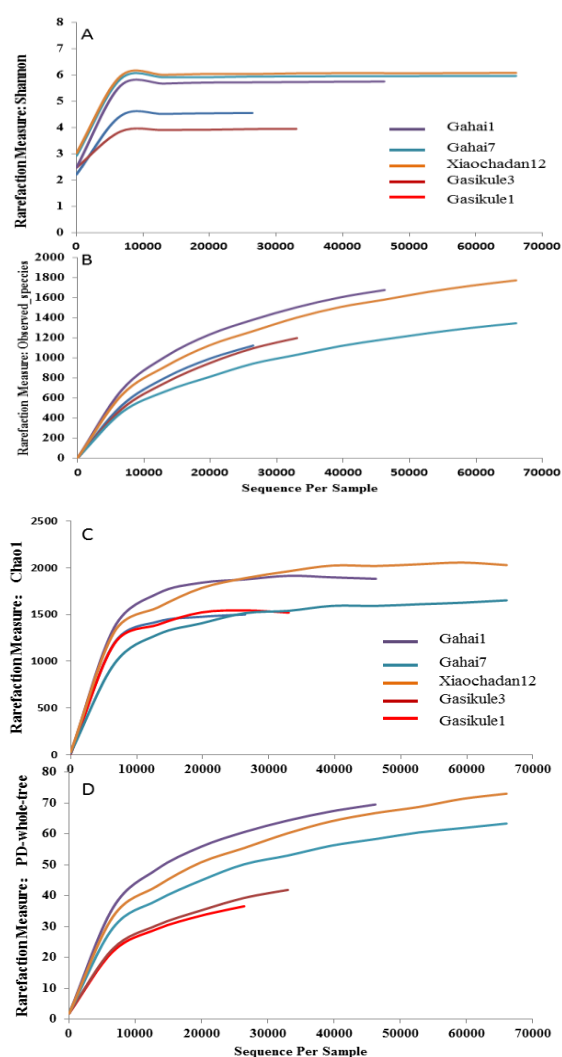


Fig. 3. Estimating species richness of three hypersaline lakes in Qaidam Basin. A, Shannon rarefaction curves; B Observed, species rarefaction curves; C, chao1 rarefaction curves; D PD-whole tree rarefaction curves.

Alpha diversity of the PPNC

Abundance OTU tables were used to calculate the Shannon's diversity index and Simpson's evenness. The Shannon rarefaction analysis (Figure 3) revealed exhaustive sequencing, even for the smallest dataset. As shown in Figure 3, the estimated number of observed species varied between 1124.80 and 1347.40. The highest diversity index was observed in Gahai7 (Observed Species = 1347.40), and the lowest diversity index was observed in Lake Gasikule1 (Observed Species = 1124.80). The Chao1 estimator was calculated to predict the total number of OTUs (richness) in the water samples from the studied lakes at a 97% similarity cutoff. The taxonomic richness levels estimated for the five samples were 1882.108, 1651.577, 2028.465, 1500.107, and 1520.658 for Lakes Gahai1, Gahai7, Xiaochaidan12, Gasikule1 and Gasikule3, respectively (Figure 3). Considering the mean estimated richness in DNA datasets, the Xiaochaidan 12 sample site was the most diverse lake, closely followed by the Gahai1 sample site.

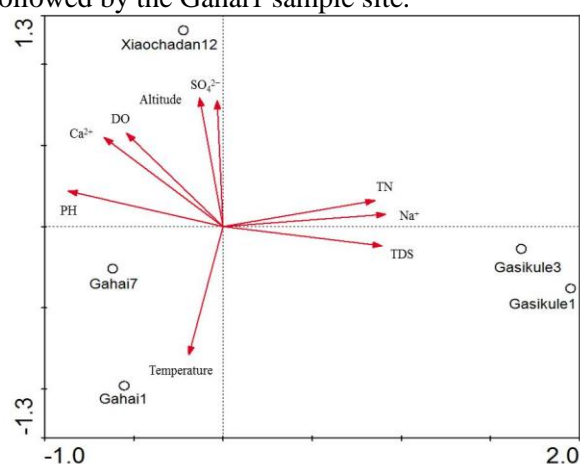


Fig. 4. CCA biplots based on OTU and geographical or selected chemical parameters. DO, dissolved oxygen, TN total nitrogen; TDS total dissolved solid.

Influence of physicochemical and chemical parameters on the diversity of PPNC

To analyze the influence of the prokaryotic pico- and nanoplankton community structure and other measured physicochemical parameters, a distinct CCA was generated from pooled habitat datasets. Three parameters showed significant correlations with this CCA: Altitude, temperature and TDS. These parameters were also significantly correlated with the CCA generated from unmerged datasets, and the fitted vectors are shown in Figure 4. The CCA analysis of chemical variables yielded three clusters (Figure 4), primarily separated according to elevation, temperature and TDS. The first cluster contained Gahai Lake sample points (Gahai1,

Gahai7); the second contained large Xiaochaidan Lake sample points (Xiaochaidan 12); and the third cluster contained Gasikule Lake sample points (Gasikule1 and Gasikule3). Elevation affected the PPNC structure in Xiaochaidan Lake, whereas temperature was a major factor in Gahai Lake. calcium (Ca^{2+}) and sulfate (SO_4^{2-}) were also the factors that influence of the PPNC structure in Xiaochaidan Lake. TDS was the most important factor influencing the distribution of PPNC assemblages in Gasikule Lake (Figure 4).

DISCUSSION

The development of pyrosequencing as a technique for the deep sequencing of microbial communities has contributed a tremendous amount of new information to the current understanding of the diversity of these systems [32]. Extreme environments contain less diverse communities [33]. However, all hypersaline lakes examined in the present study harbored remarkably diverse microbial communities considering the high salinity of these water bodies (Figure 2). Microorganisms that inhabit these lakes are potentially valuable "gene reservoirs" for future biotechnological applications, particularly those involving saline conditions (e.g., microbial treatment of saline or high-salt waste water). Investigations of the community taxon diversity (microdiversity) of the bacterioplankton at higher salinities are necessary for understanding the patterns of the global distribution of microbial diversity.

Picocyanobacteria were prevalent in Gahai Lake

PPNC in the hypersaline lakes were dominated with bacteria, except for Gasikule lake, which was dominated with archaea at a proportion of 74.9-78.6% (Figure 2A). The competitive advantage of archaea over bacteria in extreme environments is associated with the degree of energetic [34] or salinity stress [35-36] experienced by microbes in lakes and the physiological adaptations of the two groups for dealing with such stresses.

Notably, the most prevalent class in the investigated sample site of Gahai Lake was picocyanobacteria, while only a few organisms were detected in Gasikule Lake. Although there were no obvious discrepancies in the TDS between Gahai Lake and Xiaochaidan Lake, the ratios of picocyanobacteria in PPNC showed obvious differences (22.20% and 6.10%, respectively). Cyanobacteria of picoplanktonic cell size (0.2 to 2.0 μm) are globally important primary producers in freshwater, brackish, and marine ecosystems [14]. Picocyanobacteria contribute as much as 70% of the

total primary production in lakes, particularly in oligotrophic high mountain lakes[37-38]. Furthermore, Picocyanobacteria incorporate dissolved organic matter (DOM) into the food web[39]. Because of the small size of picocyanobacteria, these organisms comprise the main food source of nanoplanktonic protozoans: Ciliata, Flagellata and larger zooplankton[40]. The differences among the compositions of the PPNC in the investigated lakes revealed that there were fewer food sources in Gasikule Lake and Xiaochaidan Lake. Moreover, as the primary producer in the ecosystem, picocyanobacteria play important roles in the material cycle and energy flow in hypersaline lakes. These results contributed to the explanation of why *Artemia* prevail in Gahai Lake but not in other hypersaline lakes situated in the Qaidam Basin of the Qinghai-Tibet Plateau.

Influences of TDS and Altitude on PPNC

Salinity might be the strongest stress factor limiting microbial diversity[17,41]. Our result confirmed that TDS is an environmental factor that strongly influences the taxonomic composition of prokaryotic picoplankton assemblages in inland waters[18]. Recent reports have suggested that salinity and oxygen are important factors that shape the microbial composition in aquatic habitats[18,42-43,46-48]. As we know, the mechanisms controlling primary production might involve many factors, such as nutrient limitations, toxicity, or trophic interactions[44]. In the present study, CCA analysis revealed that temperature was significantly correlated with the distribution of prokaryotic picoplankton and assemblages in Gahai Lake, whereas altitude was a major factor influencing the taxonomic composition of prokaryotic pico- and nanoplankton assemblages in Xiaochaidan Lake (Figure 4). When compared with TDS, Gasikule Lake had the the highest levels. As expected, the prokaryotic pico- and nanoplankton assemblages in Gasikule Lake were significantly different than the two lakes. The results of the present study revealed that TDS defines distinct prokaryotic pico- and nanoplankton assemblages among lakes, whereas other factors affect the distribution of prokaryotic pico- and nanoplankton assemblages within one lake.

The obvious divergence between the structures of the PPNC and WPPC

The sequence length obtained through 454 pyrosequencing, originally of 100 bp, now exceeds 400 bp (Titanium chemistry, 454 Life Sciences, Basel, Switzerland), enabling a more precise

taxonomic classification of the reads[45]. The most common group of prokaryotic communities in Lake Gahai was assigned as unclassified prokaryotes, accounting for 23.27% of the total number of sequences[23]. However, the results of our study suggest that Proteobacteria was the most common phylum in Lake Gahai, accounting for 33.60% of the total number of sequences. As shown in Figure 2B, Proteobacteria was the third most prevalent phylum (20.67% of the total number of sequences) among the WPPC in Gahai Lake. Unexpectedly, our results revealed that Picocyanobacteria was the third most prevalent phylum of PPNC in Gahai Lake (22.20%). These results confirm that caution must be taken before making conclusions regarding the geographic restriction of novel clades, reflecting the biases of the methods used, i.e., data search or taxon under-sampling. One should consider that diversity analyses based on single genes require a more careful interpretation of the results (e.g., phylogenetic resolution of the region analyzed or the possibility of horizontal gene transfer). These studies also reveal important gaps in the current knowledge concerning planktonic microbial inhabitants in hypersaline water bodies.


Most saline lakes are defined according to endorheic drainage basins in dry areas world wide. Considering the scarcity of water in arid lands, temporary water has greater ecological significance in arid regions compared with in wet regions. The results of the present study showed that hypersaline lakes in the Qaidam Basin most likely contain a significant number of novel species, which must be cultured for detailed ecophysiological studies. The present study is the first attempt to characterize picoprokaryotic diversity in the hypersaline lakes of the Qaidam Basin, setting the basis for future studies describing new bacterial species or isolates with biotechnological applications and stressing the need to preserve extreme ecosystems with undescribed diversity.

CONCLUSION

Proteobacteria were the common phylum of PPNC in Lake Gahai. The most abundant sequences, however, primarily represented Euryarchaeota (78.60%) of PPNC in Lake Gasikule. An obvious divergence between the structure of the PPNC and the WPPC was observed. The most common group of WPPC was assigned as unclassified prokaryotes in Lake Gahai. *Bacteroidetes* was the second most prevalent Phylum, accounting for 20.67% of the total number of sequences in Gahai Lake. Altitude, temperature and TDS(total dissolved solids) were

significantly correlated with the distribution of the PPNC.

Acknowledgements: The authors would like to thank Lanping Zhou, Qiang Zhang and Peng Zhang for their assistance with the collection of samples from the waters of saline lakes. This work was financed through a grant from the Independent Study Project of the State Key Laboratory of the Simulation and Regulation of the Water Cycle in a River Basin (NO.2013ZY06), a Pre-project of The Qinghai Department of water resources, The Self-Regulation Project of State Key Laboratory of Simulation and Regulation of Water Cycle in River Basin, China Institute of Water Resources and Hydropower Research, Grant(NO. 2016TS01), the Open Research Fund of State Key Laboratory of Simulation and Regulation of Water Cycle in River Basin, China Institute of Water Resources and Hydropower Research, Grant(NO. IWHR-SKL-201620), The National Natural Science Funds Fund(NO.51309247).

Supporting Information: One files containing The geographical, physical, and chemical characteristics of three hypersaline lakes in Qaidam Basin are available as supplemental materials at Online. Table S1 The geographical, physical, and chemical characteristics of three hypersaline lakes in Qaidam Basin. 

REFERENCES

1. R.G. Bryant, *International J of Remote Sensing.*, **17**, 315 (1996).
2. W.D. Williams, *Verh Internat Verein Limnol.*, **26**, 61 (1996).
3. S. Benlloch, A. López-López, E.O. Casamayor, L. Øvreås, V. Goddard, F.L. Daae, G. Smerdon, R. Massana, I. Joint, F. Thingstad, C. Pedrós-Alió, F. Rodríguez-Valera, *Environ. Microbiol.*, **4**(6), 349 (2002).
4. H. Jiang, H. Dong, B. Yu, G. Lv, S. Deng, Y. Wu, M. Dai, N. Jiao, *FEMS Microbiol Ecol.*, **67**, 268 (2009).
5. Q.L. Wu, G. Zwart, M. Schauer, Kamst-van, M.P. Agterveld, M.W. Hahn, *Applied & Environm. Microbiol.*, **72**(8), 5478 (2006).
6. J.F. Aguirre-Garrido, H.C. Ramírez-Saad, N.Toro, F. Martínez-Abarca, *Microb. Ecol.*, **71**(1), 68 (2016).
7. C.D. Litchfield, *Meteorit Planet Science.*, **33**, 813 (1998).
8. E.B. Hollister, A.S. Engledow, A.J. Hammett, T.L. Provin, H.H. Wilkinson, T.J. Gentry, *Isme Journal.*, **4**(6), 829 (2010).
9. C.M. De, M. Staiano, M. Rossi, S. D'Auria, *Journal of the Royal Society Interface.*, **4**(13), 183 (2007).
10. J.M. Sieburth, V. Smatacek, J. Lenz, *Limnol and Oceanography.*, **23**, 1256 (1978).
11. M.I. Viprey, L. Guillou, M. Ferréol, D. Vaultot, *Environm Microbiol.*, **10**(7), 1804 (2008).
12. N. Das, A. Pandey, *International Letters of Natural Sciences.*, **43**, 38 (2015).
13. O. Zhaxybayeva, W.F. Doolittle, R.T. Papke, J. Gogarten, *Genome Biol and Evolu.*, **1**, 325 (2009).
14. D.J. Scanlan, M. Ostrowski, S. Mazard, A. Dufresne, L. Garczarek, W.R. Hess, A.F. Post, M. Hagemann, I. Paulsen, F. Partensky, *Microbiol & Molecular Biol R.*, **73**(2), 249 (2009).
15. Z.G. Keresztes, T. Felföldi, B. Somogyi, G. Székely, N. Dragoş, K. Márialigeti, C. Bartha, L. Vörös, *Extremophiles.*, **16**(5), 759 (2012).
16. J. Handelsman, *Microb and molecular biol reviews.*, **68**, 669 (2004).
17. A. Oren, B.K. Baxter, B.C. Weimer, *Natural Resources & Environmental Issues*, Iss 1 (2009).
18. Q.L. Wu, A. Chatzinotas, J. Wang, J. Boenigk, *Micro Ecol.*, **58**, 569 (2009).
19. X. Triadó-Margarit, E.O. Casamayor, *Fems Microb ecol.*, **85**, Early View. doi: 10.1111/1574-6941.12095 (2013).
20. E.O. Casamayor, *FEMS microbiol ecol.*, **85**, 503 (2013).
21. M.P. Zheng, X.F. Liu, *Aquat Geochem.*, **15**, 293 (2009).
22. J.L. Wang, F. Wang, L.M. Chu, H. Wang, Z. Zhong, Z. Liu, J. Gao, H. Duan, *Plos One.*, **9**(11), e112812 (2014).
23. Z.P. Zhong, Y. Liu, L.L. Miao, F. Wang, L.M. Chu, J.L. Wang, Z.P. Liu, *Applied & Environ Microbiol.*, **82**(6), 1846 (2016).
24. A.E. Greenberg, L.S. Clesceri, A. DEaton, *American Public Health Association.*, Washington (1992).
25. T. Magoč, S.L. Salzberg, *Bioinformatics.*, **27**(21), 2957 (2011).
26. N.A. Bokulich, S. Subramanian, J.J. Faith, D. Gevers, J.I. Gordon, R. Knight, D.A. Mills, J.G. Caporaso, *Nature Methods.*, **10**(1), 57 (2013).
27. J.G. Caporaso, J. Kuczynski, K. Bittinger, F.D. Bushman, E.K. Costello, N. Fierer, A.G. Peña, J.K. Goodrich, J.I. Gordon, G.A. Huttley, S.T. Kelley, D. Knights, J.E. Koenig, R.E. Ley, C.A. Lozupone, D. McDonald, B.D. Muegge, M. Pirrung, J. Reeder, J.R. Sevinsky, P.J. Turnbaugh, W.A. Walters, J. Widmann, T. Yatsunenko, J. Zaneveld, R. Knight, *Nature Methods.*, **7**(5), 335 (2010).
28. R.C. Edgar, B.J. Haas, J.C. Clemente, C. Quince, R. Knight, *Bioinformatics*, **27**(16), 2194 (2011).
29. B.J. Haas, D. Gevers, A.M. Earl, D.V. Ward, G. Giannoukos, D. Ciulla, D. Tabbaa, S.K. Highlander, E. Sodergren, B. Methé, T.Z. DeSantis, J.F. Petrosino, R. Knight, B.W. Birren, *Genome Research.*, **21**(3), 494 (2011).
30. R.C. Edgar, *Nature Methods.*, **10**(10), 996 (2013).
31. T.Z. Desantis, P. Hugenholtz, N. Larsen, M. Rojas, E.L. Brodie, K. Keller, T. Huber, D. Dalevi, P. Hu, G.L. Andersen, *Greengenes, Applied & Environm Microbiol.*, **72**(7), 5069 (2006).
32. L.J. Yan, M.P. Zheng, Z.J. Yuan, *Mineral Deposits.*, **33**(5), 921 (2014).
33. A. Sengupta, W.A. Dick, *Microb. Ecol.*, **70**(3), 1 (2015).

34. M.J. Fawley, K.P. Fawley, M.A. Buchheim, *Microb Ecol.*, 48,489 (2004).
35. A. Oren, *Microbiol and molecular boil reviews.*, **63**, 334 (1999).
36. D.L. Valentine, *Nature Reviews Microbio.*, **5**, 316 (2007).
37. Q.L. Wu, P. Xing, W.T. Liu, *Micro Ecol.*, **59**, 614 (2010).
38. T. Weisse, and A. Schweizer, *Verh Internat Verein Limnol.*, 24, 821 (1991).
39. C. Ruiz-González, R. Simó, R. Sommaruga, J.M. Gasol, *Frontiers in Microbiol.*, **4**(4), 131 (2013).
40. N. Jakubowska, E. Szelaż-Wasielewska, *Marine Drugs.*, **13**(3), 1497 (2015).
41. T.N. Zhilina, D.G. Zavarzina, A.N. Panteleeva, G.A. Osipov, N.A. Kostrikina, T.P. Tourova, G.A. Zavarzin, *International Journal of Systematic and Evolutionary Microbiol.*, **62**, 1666 (2012).
42. D.P. Herlemann, M. Labrenz, K. Jürgens, S. Bertilsson, J.J. Waniek, A.F Andersson, *Isme Journal.*, **5**, 1571 (2011).
43. A. Barberán, and E.O. Casamayor, *Microb Ecol.*, **61**, 465 (2011).
44. G.A. Zavarzin, T.N. Zhilina, Kluwer Academic Publishers., 2000, p.191.
45. C. Bachy, J.R. Dolan, P. López-García, P. Deschamps, D. Moreira, *Isme J.*, **7**(2), 244 (2012).

Study on gas recognition and determination based on gas sensors

Li Yajie*

School of Science, Beijing University of Posts and Telecommunications, Beijing, 100876, China

Received February 12, 2016; Revised December 26, 2016

Study on odor sources with help of gas sensors is of important theoretical value and practical significance. Study of electronical nose is greatly helpful to gas recognition and determination. Study of gas sensor arrays has become more and more popular. We can identify phytochemical volatiles with gas sensors. We can do explore analysis to the data with cluster analysis method without using training samples. Thus, it is widely applied in gas sensor array mode recognizing. In this article, we used the comprehensive grey cluster algorithm with certain choosing principle to recognize gas sensors array models and did description and data analysis and sorting. The result shows that we can use the improved method to recognize different volatile chemical constituents more effectively.

Keywords: Odor Recognition System, Cluster Analysis, Choosing Principle, Factor Analysis

INTRODUCTION

Odor is a sort of phytochemical floating in the air that can generally be sensed by living organisms. However, there are some locations not suitable for living organisms to detect. Study how to imitate the olfactory behavior of living organisms and integrate the olfactory technology with electronic products has great theoretical value and practical significance in identifying the odor sources. This study result could be used in environmental disaster prevention like explosive substance searching, post-disaster-searching and rescuing, detecting and identifying poisonous gas, etc. Results of some scientific studies showed that the faster the odor appearances or the faster it gets stronger the serious the accident is. In current time, scientist from many countries sees Rn, He, H₂, Hg, CO₂ etc as the signs for earthquakes. So these types of gas have become study target for gas recognition and determination.

The odor source recognition methods are methods in which we can use sensors to detect the material construction and the concentration distribution of the odor and use some certain method to determine the odor's type and its location. There are two types of methods to determine the odor sources. One is static detecting method; the other is the active searching method work with mobile robots. Studying of electronic nose is of great help to odor sources recognition. More and more study related to gas sensor has been published in chemistry literatures [1,2,3,4]. The main purpose of studying the gas sensor array is to find a system that can imitate the breathing system to effectively recognize the gas chemistry types and to determine their concentration [5,6,7]. The sensor array can supply multi-aspect information and its

changeable response models can generate large amount of data. Model recognizing method is the main tool to process the gas sensor data and recognizing different phytochemical volatiles has always been a hot study topic in gas sensor array.

Many model recognizing methods like cluster analysis method, discriminatory analysis method, artificial neural network method, support vector machine have been applied in gas sensor study [8]. In these methods, we do not require training sample to do the exploratory classifying to the data in cluster analysis method. It is widely applied in recognizing the gas sensor array models. Correlation analysis, factor analysis and some other statistical methods have been applied in chemistry study. Through factor analysis, we can reduce the high dimension data's dimension to make the data easy to study. In this way, we can also find the latent variables thus to find the data structure to get the useful chemistry information. We have improved the cluster analysis method and make it comprehensive cluster algorithm by applying certain choosing principles. We use the comprehensive cluster algorithm in gas sensor array recognizing. The gas sensor data were sorted and the result shows that the improved algorithm can help us to recognize different phytochemical volatile component effectively.

MATERIAL AND METHODS

Gas Sensor

According to the sensor mechanism, gas sensor methods could be sorted into chemical sensor method, gas chromatographic method and absorption spectrum analysis method. Materials used in chemistry study are usually electrolyte, metallic ox-

* To whom all correspondence should be sent:
E-mail lyj7712@163.com

ide (ceramics or semiconductor) and macromolecular polymeric film.

Following are the sensors usually used to make chemical gas sensor array: metal oxide semiconductor sensor (MOS), metal oxide field effect transistor sensor (MOSFETS), Quartz Crystal piezo transistor sensor (QCM), surface acoustic wave sensor (SAW), Chemresistor, and optical sensor, etc [9]. Seiyama was the first person that used semiconductor effect of SnO₂ to determine the air composition in 1964. Later in 1968, a company in Japan has started to make SnO₂ sensors for business reason. Currently, SnO₂ is used as the main material for most metallic oxide gas sensors. People make each type of gas sensors by mixing SnO₂ with other components to determine the composition and concentration of the tested gases. SnO₂ gas sensors are widely used in our daily life and in industrial production activities for their high sensitivity, short response and recovery time, their good performances and low cost. SnO₂ gas sensors' structure is described in figure below (Figure 1). Usually a gas sensor is formed by a foundation, the electrode leads and its sensitive materials and the heating units.

We usually have to test the gas of very low concentration when we do gas determination. We could improve the catalytic activity on surface of the SnO₂ semiconductors by mixing SnO₂ with some kinds of metals or metallic oxide and then improve the sensors' sensitivity and selectivity thus to extend the fields the sensors can be applied in. Maekawa and Suzuki and some others has make serial gas sensors by coating different metallic oxides catalyst on SnO₂ film mixed with PbO_x.

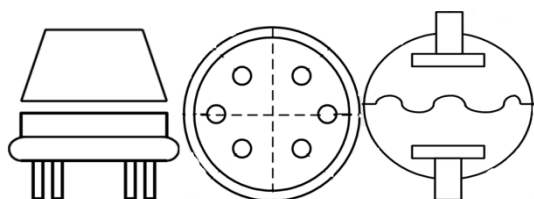


Fig. 1. SnO₂ Gas sensor architecture.

They made the SnO₂ sensors with and without catalyst coating into a MOS gas sensors array of high selectivity. This gas sensors array were used and have helped us determined 40 phytochemical volatiles. The sensors data in this article was quoted from reference articles [10,11]. There were sensitivities data from SnO₂ film with 7 metallic coating and an original SnO₂ film with no coating. Here below we call it M-S data. Since we cannot cite all the data, we listed part of the data in chart below (Table 1).

Method

We mark the original data matrix of the gas sensors sensitivity $S = (S_{ij})$. In the matrix, $S_{ij}, i = 1, \dots, 8, j = 1, \dots, 40$, stands for the sensitivity of the gas sample ranked I that is acquired by the gas sensor ranked j . Sensitivity is the ratio of the resistant value in the oxygen environment (or we say in the air) and the resistant value in the chemical atmosphere. To make it easy to record, we use abbreviations for the variables' names. For example, we use W for W/Al₂O₃, and we make an analogy in the same pattern for the other names.

Descriptive data analysis is a method we present the data in a form easy for people to understand. It might be a chart, a figure or an index. For example, from the mean value and variance of the data we can see the data's characteristics with descriptive data analysis method in chart (Table 2). Deductive data analysis is a method using a statistical model to predict and test the data's regularity. We want to find the specialty of each method, so we used box plots, see figure (Figure 2), in this article.

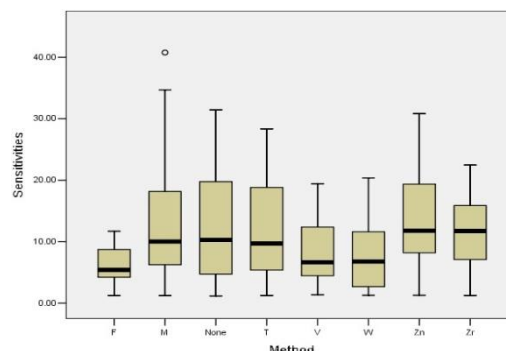


Fig. 2. Box Plots.

Compare the original data and the mean value, we can see that ZnO method and Mo/SiO₂ method have higher sensitivity in their mean value. We see that the gas sensitivity has been improved 75% from the original data. The Fe-Mo-O_x method is more stable. Its variance is smaller and we can see that none of the skewness or kurtosis of the data is in normal distribution. We can intuitively see the mean value and the variance of the data in figure 2 and at the same time there are some exceptional values in the Mo/SiO₂ method.

We can make the scatter diagram from the connection between different methods, see figure (Figure 3). We can intuitively see the positive linear relationship between the original film method and the ZnO, V/SiO₂, TiO₂, Mo/SiO₂ methods. In fact, we can calculate and get the Pearson correlation coefficient of None & TiO₂, None & Mo/SiO₂, None & Fe-Mo-O_x.

Table 1. Sensitivities to odor gases for sensors with various catalytic layers.

Sample	Measured object	Catalytic layer							
		None	W/Al ₂ O ₃	ZnO	ZrO ₂	Mo/SiO ₂	V/SiO ₂	TiO ₂	Fe-Mo-O _x
1	CH ₃ OH	5.18	6.04	6.33	4.95	4.92	5.28	5.38	4.24
2	C ₂ H ₅ OH	9.38	1.5	10.6	8.84	7.76	6.71	9.65	5.69
3	<i>n</i> -C ₃ H ₇ OH	16.44	2.81	20.34	16.06	15.89	11.5	17.9	9.18
4	<i>i</i> -C ₃ H ₇ OH	12.61	2.16	11.62	10.5	8.53	6.63	12.83	6.95
...
39	CH ₃ SCH ₃	1.16	4.9	1.57	1.49	1.33	1.39	1.35	1.47
40	CH ₃ SSCH ₃	2.65	4.91	2.39	2.4	1.71	2	2.32	1.78

Table 2. Statistics

Statistics	None	W	Zn	Zr	M	V	T	F
Mean	12.3273	8.138	14.025	11.657	13.037	8.296	11.959	6.3945
Median	10.275	6.77	11.785	11.725	10.01	6.655	9.695	5.4
Std. Deviation	8.67725	5.65767	8.33631	5.87563	9.83588	5.0191	8.05339	2.99782
Skewness	0.61	0.744	0.646	-0.073	1.142	0.661	0.555	0.185
Kurtosis	-0.828	-0.482	-0.535	-0.787	0.593	-0.693	-0.987	-1.094

Table 3. T Test

		Paired Differences		t	df	Sig. (2-tailed)
		Mean	Std. Deviation			
Pair 1	None - Zn	-1.69775	3.89068	-2.76	39	0.009
Pair 2	None - M	-0.70975	5.94538	-0.755	39	0.455
Pair 3	None - F	5.93275	6.01628	6.237	39	0.000

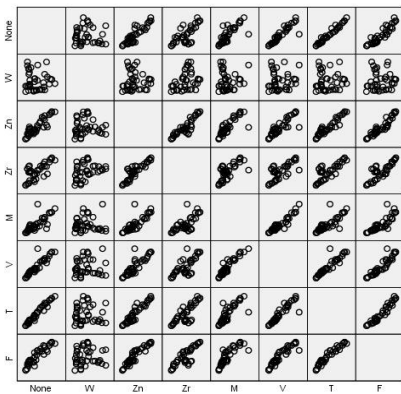


Fig. 3. Scatter Diagram.

We did T test of the data to find the differences between each method. Here we cited results of 3 groups of compared data in the chart below (Table 3).

From the chart we can see that there are big differences between the mean values of None & TiO₂ and the mean values of None & Fe-Mo-O_x. However, there were no significant differences between the mean values of None & Mo/SiO₂.

We proposed the choosing principle based on the above data analysis after consideration of practical problems and the numbers of variables. When the number of the variables is bigger than K, the

choosing principle is: 1. Choose the variables of higher sensitivity which have variable mean values compared with the original film data. 2. Choose the variables with sensitivity that are positively correlated to the original film data.

This means the variables we analyzed thereafter are marked as X_i , $\{i | i \in I_1, i \in I_2, i \geq K\}$. In the data:

$$I_1 = \begin{cases} 1, \mu_i - \mu_1 \geq 0 \\ 0, \mu_i - \mu_1 < 0 \end{cases}, I_2 = \begin{cases} 1, \rho_{i1} \geq 0 \\ 0, \rho_{i1} < 0 \end{cases} \quad (1)$$

When the numbers of the variables is smaller than K, we try to use as much variables as we can because the variables here are not easy to obtain. In this condition, the choosing principle is: Choose the variables with sensitivity that are positively correlated to the original film data.

Now the variables are still marked as X_i , $\{i | i \in I_2, i < K\}$, and in the data:

$$I_2 = \begin{cases} 1, \rho_{i1} \geq 0 \\ 0, \rho_{i1} < 0 \end{cases} \quad (2)$$

The value of K should be supplied by gas sensors specialists. In this article, we value K 50 based on the statistical understanding of number magnitude. M-S data is in this condition. We can get the qualified X_i . The coefficient of W/Al₂O₃ method is negative value, so these values will not be used in this article. We

REFERENCES

1. J. Park, W.A. Groves, E.T. Zellers, A. Chem, *Analytical Chemistry*, **71**, 3877 (1999).
2. J. Janata, M. Josowicz, P. Vanysekand, D.M. Devaney, *AnalChem*, **70**, 179R (1998).
3. A.N. Chaudry, T.M. Hawkinsand, P.J. Travers, *Sensors & Actuators B Chemical*, **69**, 236 (2000).
4. M. Rapp, J. Reibel, A. Voigt, M. Balzerand, O. Bülow, *Sensors & Actuators B Chemical*, **65**, 169 (2000).
5. J.W. Gardner, P.N. Bartlett, *Sensors & Actuators B Chemical*, **18**, 210 (1994).
6. M. Holmberg, F. Winqvist, I. Lundström, J.W. Gardnerand E.L. Hines, *Sensors & Actuators B Chemical*, **27**, 246 (1995).
7. K. Persaudand, G. Dodd, *Nature*, **299**, 352 (1982).
8. C. Distante, N. Ancona, P. Siciliano, *Sensors & Actuators B Chemical*, **88**, 30 (2003).
9. P.C. Jurs, G.A. Bakkenand, H.E. Mcclelland, *Chemical Reviews*, 100, 2649 (2000).
10. T. Maekawa, K. Suzuki, T. Takada, T. Kobayashi, M. Egashira, *Sensors & Actuators B Chemical*, **80**, 51(2001).
11. J. W.Gardner, *Sensors & Actuators B Chemical*, **4**, 109 (1991).
12. B. L. Villarreal, J.L.Gordillo, *Pattern Recognition*, **7914**, 126 (2013).
13. P. Sepideh, A.J. Lilienthal, T. Marco, *Sensors*, **12**, 16404 (2012).

Preparation of acrylamide/2-ethylhexyl acrylate copolymer and calculation of monomer reactivity ratios

M. Tian, Y.J. Xu*

School of Chemistry and Chemical Engineering, Harbin Institute of Technology, Harbin 150001, China

Received February 12, 2016; Revised December 26, 2016

Recently, available petroleum resources on the earth are being exhausted gradually while its consumption is increasing. To improve oil recovery yield, a new profile control agent has been developed and reported here for scientific and application concerns. Acrylamide (AM)/2-Ethylhexyl acrylate (2-EHA) copolymer is an inexpensive profile control agent, but it is not facile to regulate the controllable factors during the preparation of AM/2-EHA copolymer. Hence, it is necessary to clarify the copolymerization mechanism which are related to the monomer reactivity ratio. The copolymerization of AM and 2-EHA by free radical copolymerization method was studied. Based on the copolymer composition obtained by FT-IR method reactivity ratio was determined by Yezrielev-Brokhina-Roskin method. The result indicates that the reactivity ratios of AM and 2-EHA are 0.913 and 0.477 respectively. The effect of temperature on the reactivity ratios was also discussed. It can be a significant quantitative reference for industrial production.

Keywords: Reactivity Ratio, FT-IR, Acrylamide, Copolymer

INTRODUCTION

Recently, available petroleum resources on the earth are being exhausted gradually while its consumption is increasing. The necessity for enhancing oil recovery becomes imperative [1, 2]. Acrylamide (AM)/2-Ethylhexyl acrylate (2-EHA) copolymer is an inexpensive profile control agent with properties of thermal stability, alkali tolerance and salt resistance [3, 4], but it is not facile to regulate the controllable factors during the preparation of AM/2-EHA copolymer. In this paper, a new profile control agent fabricated by AM and 2-EHA was synthesized by free radical copolymerization. Reactivity ratio[5-7], which is an important parameter for free radical copolymerization, was also optimized. The monomer reactivity ratio can be calculated by Q-e scheme[8, 9] from some handbooks but it is not universal constants decided by the species of radical and monomer. The monomer reactivity ratio is also affected by the environment such as polymerization temperature, solvent, polarity, calculation method and so on. Hence, the results will be quite different. In this paper, AM/2-EHA copolymer was synthesized with varied AM-2-EHA feeding molar ratios and the monomer conversion is less than 10 wt %. Copolymer composition was determined by FT-IR method. The reactivity ratios of AM and 2-EHA were calculated using Yezrielev-Brokhina-Roskin (YBR) calculative method [10, 11]. The

effect of temperature on the monomer reactivity ratios was also discussed. Due to the calculations of reactivity ratios at different temperature, the relations between the monomer reactivity ratios and temperature were also obtained respectively. This was beneficial to industrial production in mass.

MATERIAL AND METHOD

Materials

Monomer. Acrylamide (AM) and 2-Ethylhexyl acrylate (2-EHA) ; Initiator. Benzoyl Peroxide (BPO); Solvent. Ethyl Alcohol and Ethyl Acetate. AM (99.9%) and 2-EHA (99.9%) were used for the copolymerization without any purification. All the solvents were freshly distilled before use. Benzoyl peroxide (BPO, 99%) was recrystallized from the chloroform solution.

Preparation of AM/2-EHA copolymer

AM/2-EHA copolymer was prepared using a solution polymerization technique as follows: AM and 2-EHA, 20g; BPO, 0.4 mol% of total monomers; and solvents ethyl alcohol and ethyl acetate, 50 ml respectively, were mixed in a four-necked flask under a nitrogen atmosphere. The reaction mixture was stirred at 60°C. The four-necked flask was equipped with a centigrade thermometer and a water condenser and placed in a thermostat which was maintained at the desired temperature. Termination of free radical chain took place in a constant temperature bath (0°C). The monomer conversion is less than 10 wt % in weight. The reaction mixtures, after polymerization, were poured into an excess of

* To whom all correspondence should be sent:

E-mail: xuyongjun1218@126.com

ethyl alcohol to precipitate out the product. The product was Soxhlet-extracted with water to remove polyacrylamide. The copolymer was dried in vacuo overnight at room temperature to a constant weight and used for characterization and monolayer studies.

Characterization of AM/2-EHA copolymer

Fourier transforms infrared spectroscopy (FT-IR) Fourier transform infrared spectra recorded on a Perkin-Elmer infrared spectrometer using KBr pellets. The spectra were collected over a range of 400-4000 cm^{-1} and each sample was measured for thrice.

$^{13}\text{C-NMR}$ $^{13}\text{C-NMR}$ spectra were run on a Bruker 400 MHz spectrometer using benzene and CDCl_3 as solvents. It allows the identification of carbon atoms in an organic molecule.

The calculation of monomer reactivity ratios

The standard samples were prepared by AM and 2-EHA homopolymers at different molar ratio of two monomers. The reaction conditions of AM homopolymer and 2-EHA homopolymer are the same as that of copolymer. The blend samples were prepared to 20 wt % toluene solution. The solution samples were tested in coating method by FT-IR at the same spectral slit width. FT-IR spectra of blend samples synthesized at 60°C was shown in Fig.1(b). The absorption of C-N and C-O-C were the characteristic peaks of AM and 2-EHA respectively and the relative peak areas were obtained. The standard curve was plotted between the blend ratio and the peak area ratio of the characteristic absorption crests, see Fig.2. The copolymer samples were prepared to 20 wt% toluene solution in the same way. The solution samples were tested in coating method by FT-IR at the same spectral slit width and the peak area ratio of the characteristic absorption crests was obtained respectively. The molar ratio of two monomers in the copolymer was ascertained by the standard curve.

RESULTS AND DISCUSSION

FT-IR analysis

The FT-IR spectrum of copolymer was shown in Fig.1(a). The absorption band at 2872 cm^{-1} and 2962 cm^{-1} were due to symmetrical and antisymmetrical stretching vibration of C-H in primary alkyl.

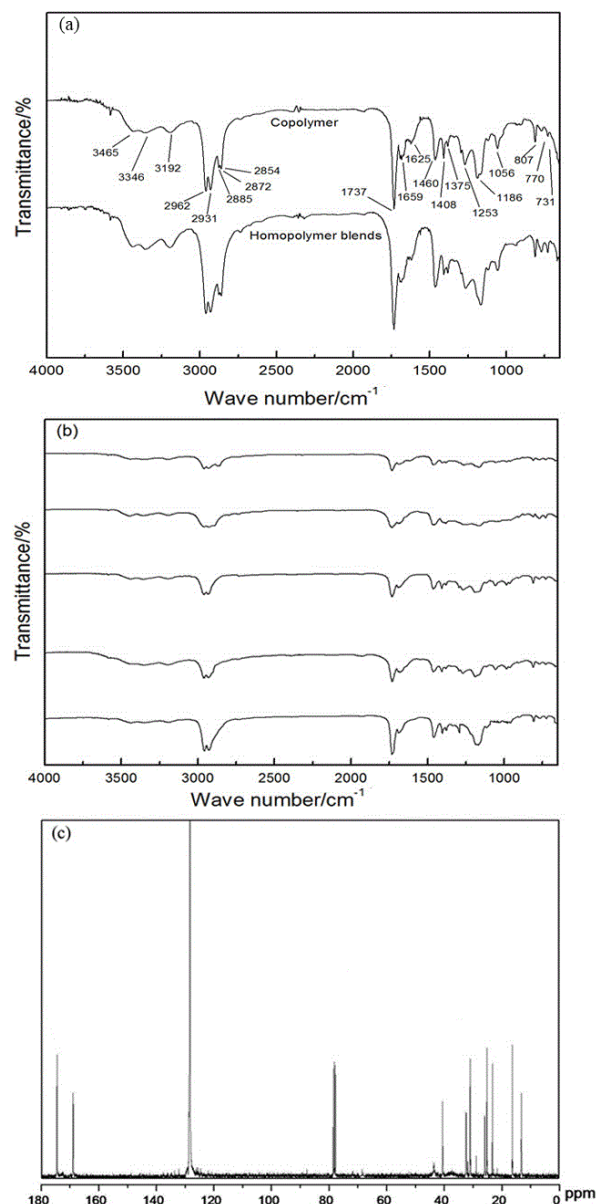


Fig.1. Characterization of Copolymer and Homopolymer blends.(a) FT-IR spectra of Copolymer and Homopolymer blends;(b) FT-IR spectra of Copolymer and Homopolymer blends; (c) The ^{13}C NMR of Copolymer.

The absorption band at 2854 cm^{-1} and 2931 cm^{-1} were due to symmetrical and antisymmetrical stretching vibration of C-H in secondary alkyl. The absorption band at 2885 cm^{-1} was assigned to symmetrical stretching vibration of C-H in tertiary alkyl. The absorption band at 1375 cm^{-1} and 1460 cm^{-1} were due to symmetrical and antisymmetrical bending vibration of C-H in primary alkyl. The absorption band at 1253 cm^{-1} was assigned to bending vibration of C-C in alkyl. The absorption band at 3192 cm^{-1} and 3346 cm^{-1} were due to symmetrical and antisymmetrical stretching vibration of N-H in $-(\text{CO})\text{NH}_2$. The absorption band at 1659 cm^{-1} was assigned to stretching vibration of

C=O in-(CO)NH₂. The absorption band at 1625 cm⁻¹ was assigned to bending vibration of C-N in-(CO)NH₂. The absorption band at 1408 cm⁻¹ was assigned to stretching vibration of C-N in-(CO)NH₂. The absorption band at 807 cm⁻¹ was assigned to bending vibration of N-H in-(CO)NH₂. The absorption band at 1737 cm⁻¹ was assigned to stretching vibration of C=O inR₁(CO)OR₂. The absorption band at 1056 cm⁻¹ and 1186 cm⁻¹ were due to symmetrical and antisymmetrical stretching vibration of C-O-C in R₁(CO)OR₂. The absorption band at 3465 cm⁻¹ was assigned to stretching vibration of C=O overtones absorption peak inR₁(CO)OR₂. There is no absorption peak at 3100 cm⁻¹~3000 cm⁻¹ of C-H in double bonds. Consequently, AM and 2-EHA had reacted completely and AM/2-EHA copolymer had been prepared.

¹³C-NMR analysis

The ¹³C-NMR spectrum of copolymer was shown in Fig.1 (c). Signals due to the carbons of long alkyl side chains were observed in the region 10-40 ppm. The signal at 175 ppm is due to ester carbonyl carbon. The signal at 169 ppm is due to Amide Groups. There was only one signal (at δ=129) when δ was between 100 and 150 and we could infer that double bonds had reacted completely. The results of ¹³C-NMR showed that AM and 2-EHA were in copolymerization.

The calculation of monomer reactivity ratios

The standard samples and the copolymer samples were prepared at 60°C respectively.

The standard samples were prepared by AM homopolymer and 2-EHA homopolymer at different molar ratio. The blend samples were prepared to 20

wt% toluene solution. The solution samples were tested in coating method by FT-IR (see Fig.1 (c)). The absorption of C-N (1408cm⁻¹) and C-O-C (1056 cm⁻¹) were the characteristic peaks of AM and 2-EHA respectively, and the relative peak areas A₁/A₂ were obtained (see Fig. 2). To minimize deviation the data in Table 1 were treated by least square method. The standard curve can be obtained, see Fig. 2.

The copolymer samples were prepared to 20 wt % toluene solution. The solution samples were tested in coating method by FT-IR and the peak area ratio of the characteristic absorption crests was obtained respectively. The molar ratio of two monomers in the copolymer were ascertained by the standard curve, see Table 1. The monomer reactivity ratios of AM and 2-EHA were calculated by YBR calculative method. R stands the mole fraction of AM to 2-EHA in feed, ρ stands the mole fraction of AM to 2-EHA in copolymer, r₁ and r₂ are the reactivity ratio of two monomers.

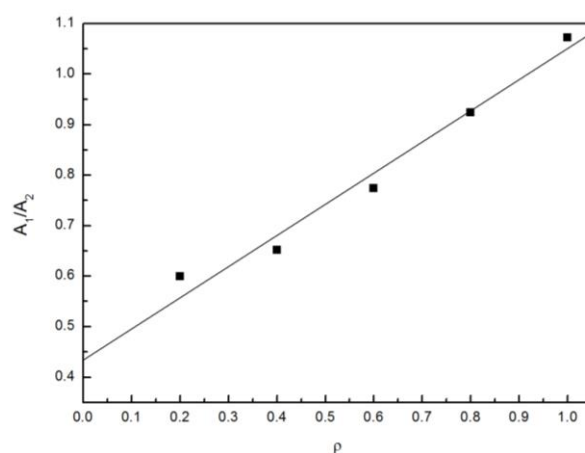


Fig.2. The Standard Curve.

Table 1. The copolymer compositions at different temperatures*

R	323.15K		333.15K		343.15K		353.15K		363.15K	
	ρ	Y	ρ	Y	ρ	Y	ρ	Y	ρ	Y
0.1	0.1896	7.6	0.1841	4.7	0.1823	5.2	0.181	3.7	0.1758	5.1
0.2	0.3942	1.2	0.3657	6.1	0.3458	3.6	0.3349	4.1	0.3145	2.6
0.4	0.6258	3.5	0.6148	3.3	0.5985	6.1	0.5842	5.0	0.5433	9.1
0.6	0.9287	6.8	0.9247	8.4	0.9245	4.2	0.9241	7.3	0.9103	4.8
0.8	1.0215	2.5	1.0246	7.5	1.0387	7.6	1.0458	6.4	1.0549	5.7

*Y is 'Yeild' and the unit is '%'

Table 2. The relative data for the calculation of r_1 and r_2 . **

T/K	T'/K	r_1	r_1'	r_1^*	$r_1'^*$	E_a	A	r_2	r_2'	r_2^*	$r_2'^*$	E_b	B
323.15	333.15	0.863	0.913	0.872	0.901	2931.70	2.60	0.446	0.477	0.450	0.470	3871.29	1.90
323.15	343.15	0.863	0.926	0.872	0.929	2926.00	2.59	0.446	0.488	0.450	0.490	3901.18	1.92
323.15	353.15	0.863	0.967	0.872	0.956	2924.10	2.59	0.446	0.507	0.450	0.509	3911.14	1.93
323.15	363.15	0.863	0.973	0.872	0.983	2923.14	2.59	0.446	0.529	0.450	0.528	3916.13	1.93
333.15	343.15	0.913	0.926	0.901	0.929	2919.94	2.59	0.477	0.488	0.470	0.490	3932.92	1.94
333.15	353.15	0.913	0.967	0.901	0.956	2919.94	2.59	0.477	0.507	0.470	0.509	3932.92	1.94
333.15	363.15	0.913	0.973	0.901	0.983	2919.94	2.59	0.477	0.529	0.470	0.528	3932.92	1.94
343.15	353.15	0.926	0.967	0.929	0.956	2919.94	2.59	0.488	0.507	0.490	0.509	3932.92	1.94
343.15	363.15	0.926	0.973	0.929	0.983	2919.94	2.59	0.488	0.529	0.490	0.528	3932.92	1.94
353.15	363.15	0.967	0.973	0.956	0.983	2919.94	2.59	0.507	0.529	0.509	0.528	3932.92	1.94
AVG						2922.46	2.59					3919.73	1.93

** r_1, r_1', r_2 and r_2' are the monomer reactivity ratios of AM and 2-EHA calculated by YBR method while $r_1^*, r_1'^*, r_2^*$ and $r_2'^*$ are the monomer reactivity ratios of AM and 2-EHA by regression treatment.

The FR method can be expressed by the following:

$$\rho = R(r_1 R + 1) / (r_2 + R), \quad (1)$$

YBR method is the combination of FR equation and least square method. For instance, eq (1) is multiplied by $R^{-1}\rho^{-1/2}$ to give the following [12]:

$$(R/\rho^{1/2}) r_1 - (\rho^{1/2}/R) r_2 + (1/\rho^{1/2} - \rho^{1/2}) = 0, \quad (2)$$

Taking into account least square method, eq (3) is given by:

$$r_1 A_1 - r_2 n = B_1, \quad (3)$$

And

$$-r_1 n + r_2 A_2 = B_2, \quad (4)$$

$$\text{Where, } A_1 = \sum_{i=1}^n \frac{R_i^2}{\rho_i}, \quad B_1 = \sum_{i=1}^n R_i \left(1 - \frac{1}{\rho_i}\right),$$

$$A_2 = \sum_{i=1}^n \frac{\rho_i}{R_i^2}, \quad B_2 = \sum_{i=1}^n \frac{\rho_i}{R_i} \left(\frac{1}{\rho_i} - 1\right); n: \text{ the number of experimental data.}$$

Consequently,

$$r_1 = (A_2 B_1 + n B_2) / (A_1 A_2 - n^2), \quad (5)$$

$$r_2 = (A_1 B_2 + n B_1) / (A_1 A_2 - n^2), \quad (6)$$

Eq (5) and eq (6) are the YBR method. Accordingly, reactivity ratios of AM and 2-EHA are 0.913 and 0.477 respectively.

The effect of temperature on the monomer reactivity ratios

The reactivity ratio is defined as :

$$r_1 = k_{11}/k_{12}, \quad (7)$$

and with Arrhenius equation defined as:

$$k_{11} = A_{11} \times e^{-E_{11}/(8.314 \times T)}, \quad (8)$$

$$k_{12} = A_{12} \times e^{-E_{12}/(8.314 \times T)}, \quad (9)$$

Another form of equation (7) is:

$$r_1 = k_{11}/k_{12} = (A_{11}/A_{12}) \times e^{-(E_{11}-E_{12})/(8.314 \times T)} = A \times e^{-E_a/(8.314 \times T)}, \quad (10)$$

Where, $A = A_{11}/A_{12}$, $E_a = E_{11} - E_{12}$, A_{11} 、 A_{12} are collision factor, E_{11} is the activation energy of chain propagation reaction in self-polymerization while E_{12} is the activation energy of chain propagation reaction in copolymerization. When r_1 is less than 1, k_{11} is less than k_{12} and E_{11} is more than E_{12} . When r_1 is more than 1, k_{11} is more than k_{12} and E_{11} is less than E_{12} .

r_2 can also be obtained as:

$$r_2 = k_{21}/k_{22} = (A_{21}/A_{22}) \times e^{-(E_{21}-E_{22})/(8.314 \times T)} = B \times e^{-E_b/(8.314 \times T)}, \quad (11)$$

Where, $B = B_{21}/B_{22}$, $E_b = E_{21} - E_{22}$

The monomer reactivity ratios were calculated by YBR method at 50, 60, 70, 80, 90°C respectively, and the composition in feed was shown Table 1. As the results shown in Table 2, the monomer reactivity ratios increase as temperature goes up, but only a little. Each two sets of data treated by least square method was used to calculate the equations of r_1 and r_2 by Eq (10) and Eq (11). The relative data for the calculation of r_1 and r_2 was shown in Table 2. r_1 and r_2 can be obtained as:

$$r_1 = (2.59 \pm 0.01) \times e^{-2922.46 \pm 9.24/(8.314 \times T)} = (2.59 \pm 0.01) \times e^{-351.51 \pm 1.11/T}$$

$$r_2 = (1.93 \pm 0.03) \times e^{-3919.73 \pm 48.44/(8.314 \times T)} = (1.93 \pm 0.03) \times e^{-471.46 \pm 5.83/T}$$

DISCUSSION

There is not much difference between FT-IR spectra of AM/2-EHA copolymer and that of the blend composed of homopolymers of AM and 2-EHA (see Fig.1(a)). The wave numbers of absorption peaks did not change but absorption intensity changed. The characteristic peaks in homopolymer blends behaved the same absorption effect as that in copolymer(see Fig.1(b)). As a result the standard curve obtained by homopolymer blends can be used to calculate the molar ratio of two monomers in the copolymer.

The monomer reactivity ratios of AM and 2-EHA are 0.913 and 0.477 respectively. It is noted that both of the monomer reactivity ratios r_1 and r_2 , even r_1r_2 , are <1 , which implies that: (1)The copolymerization of AM and 2-EHA is non-ideal and has azeotropic copolymerization point. Namely, the concentration of monomer in solution equals that in copolymer at the azeotropic copolymerization point. (2) AM and 2-EHA are prone to alternating copolymerization because terminal groups of the copolymer tend to polymerize heterogeneous monomer, i.e. alternating copolymerization.

CONCLUSION

AM/2-EHA copolymers were synthesized by free radical copolymerization using benzoyl peroxide (BPO) under nitrogen atmosphere at different temperatures and characterized by FT-IR and ^{13}C -NMR method. The results showed that AM and 2-EHA were in copolymerization. The monomer reactivity ratios of AM and 2-EHA were calculated by YBR calculative method. The copolymer compositions were obtained by FT-IR.

The standard curve was obtained by homopolymer blends and the molar ratios of two monomers in the copolymer were ascertained by the standard curve. The absorption of C-N (1408cm^{-1}) and C-O-C (1056cm^{-1}) were the characteristic peaks of AM and 2-EHA respectively. Peak area ratio of two characteristic peaks was used in the calculation of the molar ratio of two monomers in the copolymer and homopolymer blends. The reactivity ratios of

AM and 2-EHA were calculated, by YBR method, to be 0.913 and 0.477 respectively. It can be inferred that Random copolymerization occurred in the copolymerization of AM and 2-EHA and there are many alternating units in the copolymer chain. The effect of temperature on the monomer reactivity ratios for AM and 2-EHA was also discussed. As temperature goes up, the monomer reactivity ratios increase, but only a little. The relations between r_1 , r_2 and T were also obtained respectively. It is simple and reliable to calculate the monomer reactivity ratios for AM and 2-EHA in free radical copolymerization by FT-IR spectroscopy. The method can be used to calculate the monomer reactivity ratios which have the separate characteristic peaks in the copolymer. The monomer reactivity ratios can be a significant quantitative reference for industrial production.

REFERENCES

1. J. Li, T. Wu, G. Feng, *GuangDong Chem. Ind.*, **39**, 53 (2012).
2. C. Kang, H. Wang, C. Liu, C. Zhang, *Biochem. Eng. J.*, **11**, 197 (2002).
3. M. Tian, Y.J. Xu, *Adv. Mater. Res.*, **602-604**, 732 (2013).
4. D. A. Z. Wever, F. Picchioni, A. A. Broekhuis, *Ind. Eng. Chem. Res.*, **52**, 16993 (2013).
5. D. A. Z. Wever, F. Picchioni, A. A. Broekhuis, *Prog. Polym. Sci.*, **36**, 1558 (2011).
6. N. Pekel, N. Şahiner, O. Güven, Z. M.O. Rzaev, *Eur. Polym. J.*, **37**, 2443 (2001).
7. F. M. Lewis, C. Walling, W. Cummings, E. R. Briggs, F. R. Mayo, *J. Am. Chem. Soc.*, **70**, 1519 (1948).
8. R. Chujo, H. Ubara, A. Nishioka, *Polym. J.*, **3**, 670 (1972).
9. K. Nariyoshi, T. Teiji, F. Junji, *Bull. Chem. Soc. Jpn.*, **36**, 905 (1963).
10. T. Sumiyoshi, W. Schnabel, *Macromol. Chem. and Phys.*, **186**, 1811 (1985).
11. M. Lartey, M. Gillissen, B.J. Adzima, K. Takizawa, D. R. Luebke, H. B. Nulwala, *J. Polym. Sci. Pol. Chem.*, **51**, 3359 (2013).
12. A. O. Moughton, T. Sagawa, W. M. Gramlich, M. Seo, T. P. Lodge, M. A. Hillmyer, *Polym. Chem., Polym. Chem.*, **4**, 166 (2013).
13. A. J. Yezrielev, E. L. Brokhina, *Vys. Soed.*, **A11**, 1670 (1969).

Quantitative analysis of the relationship between permeability and microstructure of solidified dredger fill

H. Liu, W. Liu*, Y. Cui

School of Ocean Science and Engineering, Shanghai Maritime University, Shanghai P. R. China 201306

Received February 12, 2016; Revised December 26, 2016

The dredger fill of Shanghai Hengsha Island Dongtan is solidified by self-made curing agent, and the permeability of Solidified dredger fill is measured by the indoor penetration test. The microstructure of the solidified dredger fill and unsolidified dredger fill is observed by using Scanning Electron Microscope (SEM). The microscopic image of dredger fill is processed and analysed by using IPP, and the microstructure parameter was calculated that include mean equivalent particle diameter D_p , mean equivalent pore diameter D_b , plane porosity n . The Quantitative analysis of the relationship between permeability and microstructure of Solidified dredger fill is done. The research results show that the permeability of solidified dredger filled creases with the increase of mean equivalent particle diameter D_p and the decrease of mean equivalent pore diameter D_b and plane porosity n ; Under the same age, the permeability coefficient K has a good linear relationship with mean equivalent particle diameter D_p , mean equivalent pore diameter D_b and plane porosity n ; The effect of plane porosity on the permeability of solidified dredger fill is larger than the mean equivalent particle diameter and mean equivalent pore diameter.

Key words: Solidified dredger fill, curing agent, permeability coefficient, microstructure SEM.

INTRODUCTION

The rapid development of China's coastal economy promotes the construction of port and waterway dredging, which produced a lot of dredger fill. 2010 to 2015, in process of the Yangtze River waterway dredging, 80 million cubic meters of dredger fill is produced each year; In the Pearl River Delta region, the amount of dredger fill is about 80 million cubic meters [5]. In 2013, the amount of dredger fill is 1 billion 600 million in china. In 2016, it will be 3 billion cubic meters in china. The water content of the dredger fill is very high, and the engineering quality is very poor. The water content and the engineering properties can be improved by adding the curing agent to the dredger fill. The permeability of solidified soil is an important index of its mechanical properties, and the permeability coefficient is one of the decisive factors in the selection of static and dynamic drainage consolidation method and the determination of its technological parameters[6]. At present, the research on the permeability of soil is mostly focused on the structure of soil, the consolidation stress and the influence of saturation on the permeability[2,7,8]. Many scholars have discussed the relationship between the permeability and microstructure of bentonite, contaminated soil and so on[9,12]. The micro aspect of the soil is the research process of the material from the internal

mechanism to the external performance, which can reflect the real situation of the soil.

EXPERIMENTAL

Test materials

The dredger fill is from Hengsha Island of Shanghai. The physical indexes of the dredger fill are tested by the laboratory test and the data are shown in Tab.1. The curing agent used in the experiment is a mixture of various materials, which accounts for the main components of the material for cement and lime, the minor components mainly include lignin sulfonate, acrylamide and so on.

Test method

In this experiment, the water content of the soil is 56%, the amount of curing agent is 0%, 4%, 8%, 12%. The high of cutting ring is 40mm, the diameter of cutting ring is 61.8mm. Curing temperature is $20 \pm 2^\circ\text{C}$, Curing humidity is 90%. Permeability test and scanning electron microscope test were carried out for 7 days, 14 days, 21 days and 28 days respectively.

Permeability test is done by South TST - 55 type osmometer, the test procedure and calculation method is in accordance with 《Standard For Soil Test Methods》 [3], specific operating procedures in this won't repeat them.

* To whom all correspondence should be sent:
E-mail: liuw8848@163.com

Table. 1. Physical properties of the soil specimens.

Specific gravity	Gravity kN/m ³	Water content(%)	Liquid limit	Plastic limit	Internal friction angle	Cohesion (kPa)
2.75	18.3	45	30.43	27.91	35.64	0.917

Scanning electron microscope test is done by field emission scanning electron microscope(ERSEM)that made in japan in the Analysis and Testing Center of Shanghai Jiao Tong University. Dehydration and drying method for samples is oven drying method. The dried sample is cut into small pieces with a knife slowly. The size of small pieces is 6*6*20mm. The small pieces is broken carefully and the plane of break is used for scanning electron microscope test. Image-Pro Plus

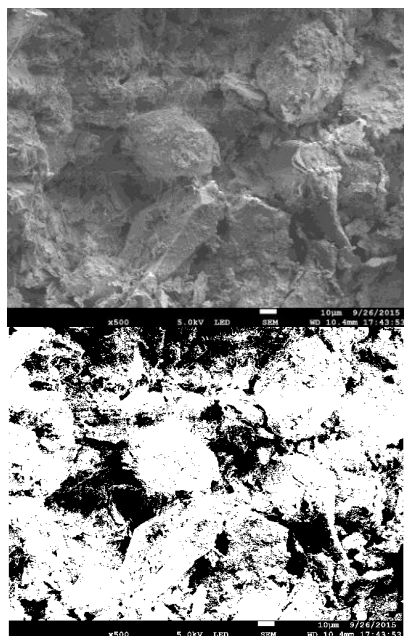


Fig. 1. Microscopic image and binary image of dredger fill

The micro image of solidified dredger fill is processed and analysed by using the Image-Pro Plus. Main operating procedures include Image segmentation, image morphological processing, the calibration of the measuring unit, the selection of measurement parameters and data analysis and finishing. Huang li [4], zhang jiru [13], zheng zhiheng [14], cui yongtao [1], xurijing [10,11] have done a detailed introduction, not tired in words here.The microscopic imageand binary image of dredger fill is showed in Fig.1. The Microscopic image and binary image of solidified dredger fill is showed in Fig.2.

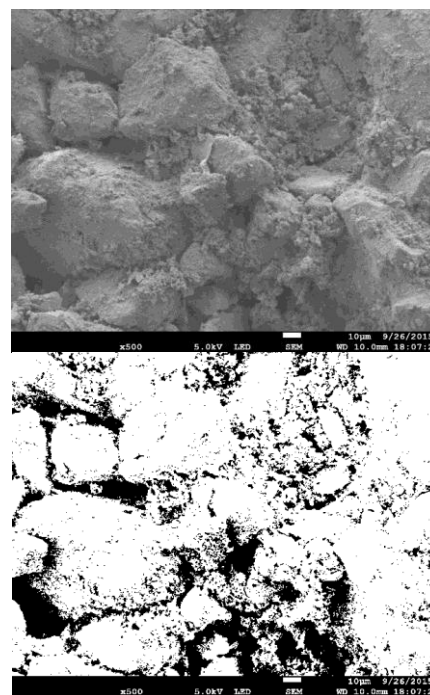


Fig. 2. Microscopic imageand binary image of solidified dredger fill

TEST RESULT

Permeabilitytest result

The permeability coefficient of solidified dredger fill under different age and different curing agent content is showed in Tab.2. The relationship between the permeability coefficient and curing period is showed in Fig.3.The relationship between the permeability coefficient and curing agent content is showed in Fig.4.

Table. 2. The permeability coefficient of Solidified dredger fill.

curing period T(d)	curing agent content λ/%			
	0	4	8	12
0	7.319	7.315	7.308	7.299
7	7.331	4.867	3.546	1.903
14	7.208	2.782	1.859	0.611
21	7.351	2.091	0.813	0.416
28	7.119	1.325	0.575	0.201

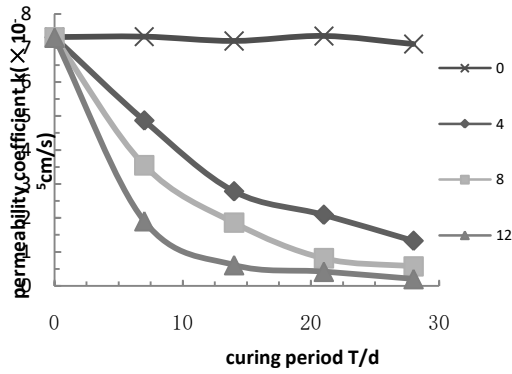


Fig. 3. Relationship between the permeability coefficient and curing period.

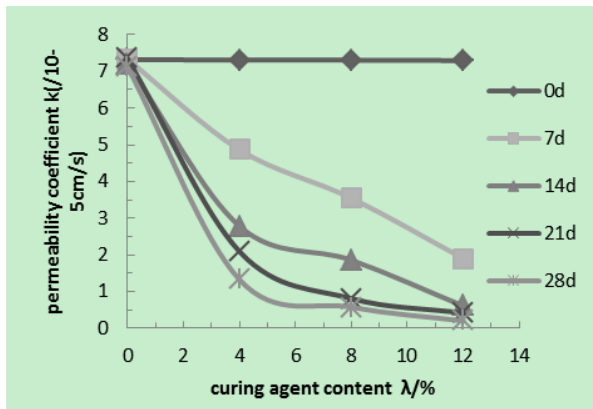


Fig. 4. Relationship between the permeability coefficient and curing agent content.

Fig. 3 shows that along with the curing period growth, the permeability coefficient of solidified dredger fill is getting smaller; The permeability coefficient decreased very significantly before 14 days, and the permeability coefficient tended to be stable after 14 days; the permeability coefficient of solidified dredger fill that curing agent content is 8%, 12% and curing period is 28 days is close to, which indicates that the curing agent for the improvement of permeability of dredger fill has been fully played when the curing agent content is 8%.

Fig.4 shows that along with the curing agent content growth, the permeability coefficient of solidified dredger fill is getting smaller under the same curing period; The difference of the permeability coefficient of solidified dredger fill is very big when the curing period is 7 days and it is not big when the curing period is 14 days, 21 days and 28 days

Image analysis results

The micro image of solidified dredger fill is processed and analyzed by using the Image-Pro Plus. Data extracted from the image is analyzed.

mean equivalent particle diameter D_p , mean equivalent pore diameter D_b and plane porosity n are quantitatively analyzed.

Mean equivalent particle diameter D_p is the mean value of the equivalent diameter of all the particles in the analyzed area, that is the size of particles from the statistical significance. Mean equivalent particle diameter D_p is equal to the diameter of the equivalent circle that is equal to the area of the particles unit, which can approximately represent the size of a single particle.

$$D_p = \sum \frac{d_i}{n} \quad (1)$$

Error! Reference source not found. (2)

Where: Error! Reference source not found. Error! Reference source not found.—the diameter of the equivalent circle that is equal to the area of the particle unit

Error! Reference source not found.—the area of the particle unit

Error! Reference source not found.—the number of particles in the analyzed area.

The mean equivalent particle diameter of Solidified dredger fill under different age and different curing agent content is showed in Tab.3. The relationship between the mean equivalent particle diameter and curing period is showed in Fig.5. The relationship between the mean equivalent particle diameter and curing agent content is showed in Fig.6.

Table. 3. the mean equivalent particle diameter of solidified dredger fill

Curing period T(d)	Curing agent content λ /%			
	0	4	8	12
7	1.83	2.11	2.61	2.71
14	1.83	2.35	2.88	2.94
28	1.83	2.69	2.94	3.25

Fig. 5 shows that along with the curing period growth, the mean equivalent particle diameter increases linearly under different curing agent content and the linear correlation coefficients are above 0.95. Fig. 6 shows that along with the curing agent content growth, the mean equivalent particle diameter increases linearly under different curing period and the linear correlation coefficients are above 0.91. It is proved that the mean equivalent particle diameter increases gradually during the solidification process.

Mean equivalent pore diameter D_b is the mean value of the equivalent diameter of all the pores in the analyzed area, that is the size of pores from the statistical significance. Mean equivalent pore diameter D_b is equal to the diameter of the equivalent circle that is equal to the area of the structural unit, which can approximately represent the size of a single pore.

$$D_b = \sum \frac{d_i}{N} \quad (1)$$

Error! Reference source not found. (2)

Where:**Error! Reference source not found.**—the diameter of the equivalent circle that is equal to the area of the pore unit

Error! Reference source not found.—the area of the pore unit

Error! Reference source not found.—the number of pores in the analyzed area.

The mean equivalent pore diameter of Solidified dredger fill under different age and different curing agent content is showed in Tab.4. The relationship between the mean equivalent pore diameter and curing period is showed in Fig.7. The relationship between the mean equivalent pore diameter and curing agent content is showed in Fig.8.

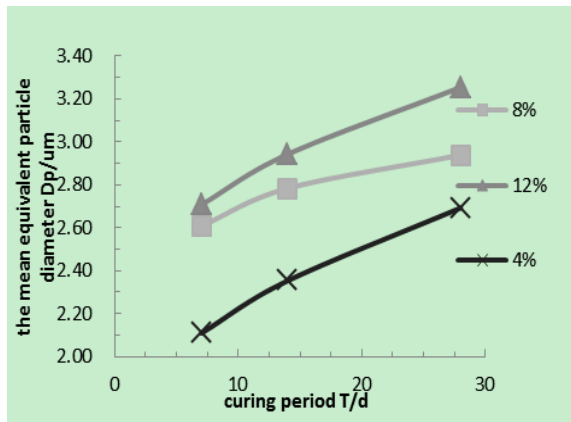


Fig. 5. Relationship between the mean equivalent particle diameter and curing period.

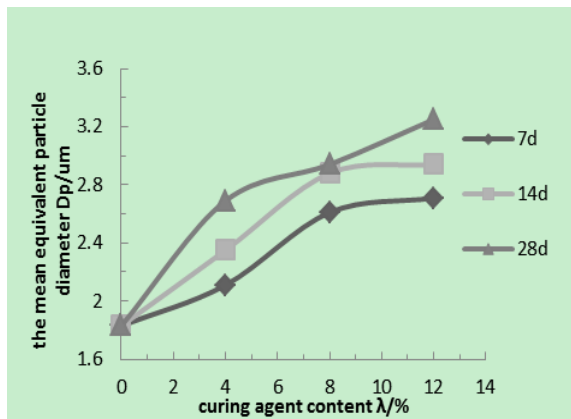


Fig. 6. Relationship between the mean equivalent particle diameter and curing agent content.

Table 4. The mean equivalent pore diameter of Solidified dredger fill.

Curing period T(d)	Curing agent content lambda/%			
	0	4	8	12
7	4.44	2.03	1.52	1.26
14	4.44	1.56	1.15	1.09
28	4.44	1.48	1.06	0.98

Fig. 7 and Fig.8 show that along with the curing period and curing agent content growth, the mean equivalent pore diameter gradually decrease. Compared with the mean equivalent particle diameter, the rate of decrease of the mean equivalent pore diameter is faster than the rate of increase of the mean equivalent particle diameter, which indicates that due to the presence of grain resistance (friction, cohesion, etc.), the size, shape and position of soil particles will change when the cementing effect of the curing agent is fully played and overcome grain resistance.

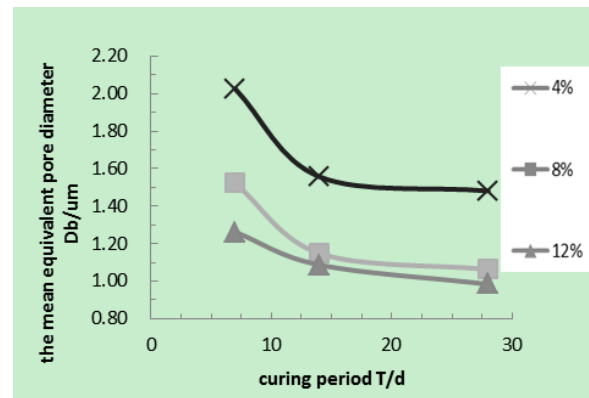


Fig. 7. Relationship between the mean equivalent pore diameter and curing period.

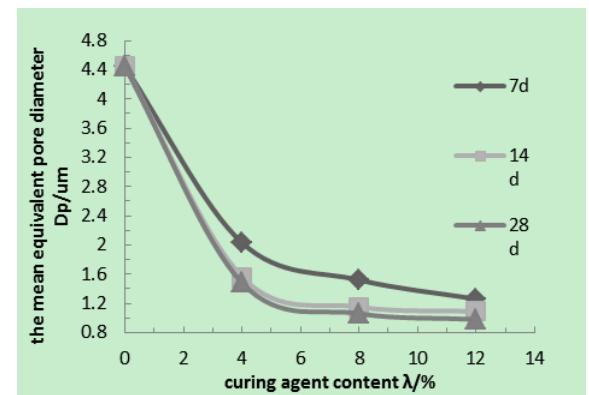


Fig. 8. Relationship between the mean equivalent pore diameter and curing agent content.

Fig. 7 shows that the difference of the mean equivalent pore diameter is not obvious when the curing agent content is 8% and 12%, and both are smaller than the mean equivalent pore diameter that curing agent content is 4%. This analysis is similar to the analysis of Fig. 3, which indicates that the permeability of solidified dredger fill is closely related to the mean equivalent pore diameter.

Plane porosity n is the pore area percentage of the whole analyzed area. The calculation formula is as follows:

$$n = \frac{S_b}{S} \times 100\% \quad (5)$$

Where: n —Plane porosity

Error! Reference source not found.—pore area in the analyzed area

S —the whole analyzed area.

The plane porosity of solidified dredger fill under different age and different curing agent content is showed in Table. 5. The relationship between the plane porosity and curing period is showed in Fig. 7. The relationship between the plane porosity and curing agent content is showed in Fig. 8.

Table. 5. the plane porosity of Solidified dredger fill.

Curing period T(d)	Curing agent content λ /%			
	0	4	8	12
7	33.37	23.09	18.30	17.86
14	33.37	18.51	17.71	13.77
28	33.37	14.50	13.75	13.36

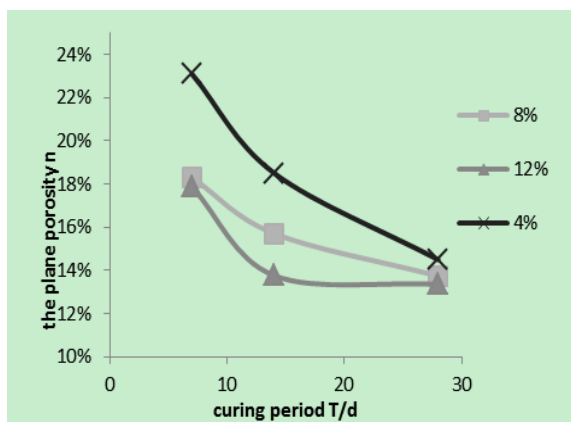


Fig. 9. Relationship between the plane porosity and curing period.

Fig. 9 and Fig. 10 show that along with the curing period and curing agent content growth, the

plane porosity gradually decrease. Compared with the mean equivalent pore diameter D_b , the variation law of the two is very similar, which indicates that the permeability of solidified dredger fill is closely related to the plane porosity.

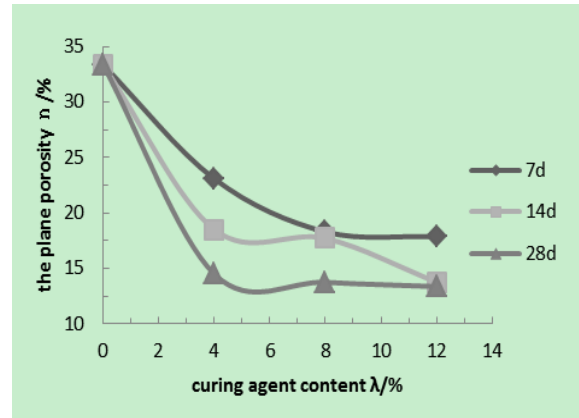


Fig. 10. Relationship between the plane porosity and curing agent content.

Quantitative analysis of relationship between permeability coefficient and microstructure

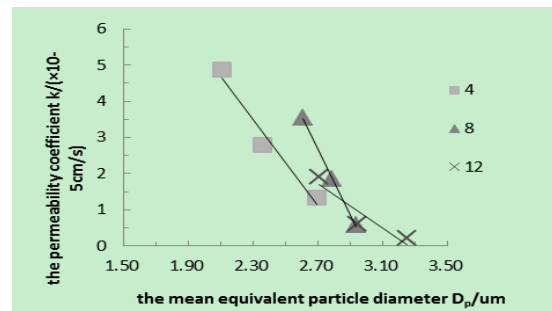


Fig. 11. Relationship between the permeability coefficient and mean equivalent particle diameter.

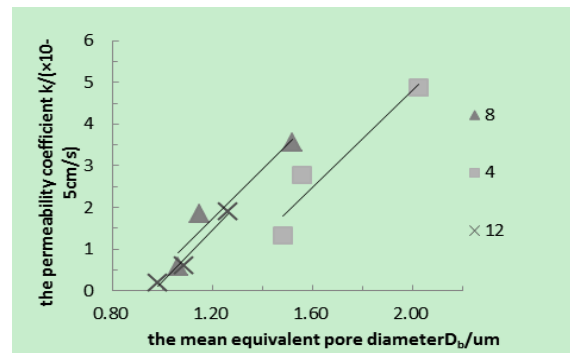


Fig. 12. Relationship between the permeability coefficient and mean equivalent pore diameter

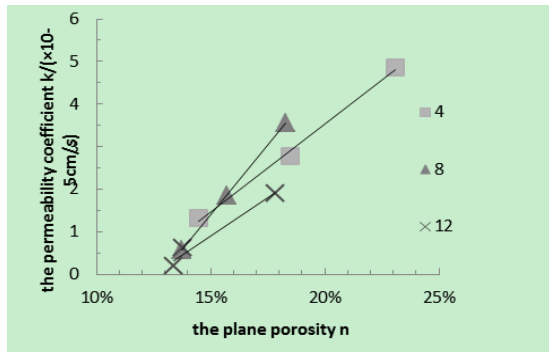


Fig. 13. Relationship between the permeability coefficient and plane porosity.

The relationship between the permeability coefficient and the mean equivalent particle diameter is showed in Fig. 11. Fig. 11 shows that along with the mean equivalent particle diameter increases, the permeability coefficient gradually decrease. In the solidification process of the dredger fill, the micro aspect is the increase of the mean equivalent particle diameter, the macroscopic aspect is the decrease of the permeability coefficient. The change of macroscopic and microscopic show that in the solidification process of the dredger fill, small particles gradually gather large particles due to the cementation of hydration products, the contact force between particles is enhanced, the soil structure become denser, integrity is improved, and permeability is improved.

The relationship between the permeability coefficient and the mean equivalent pore diameter is showed in Fig. 12. Fig. 12 shows that along with the mean equivalent pore diameter decrease, the permeability coefficient gradually decrease. In the

solidification process of the dredger fill, the micro aspect is the decrease of the mean equivalent pore diameter, the macroscopic aspect is the decrease of the permeability coefficient. The change of macroscopic and microscopic show that in the solidification process of the dredger fill, the smaller the mean equivalent pore diameter, the greater the flow resistance is., and the lower the permeability coefficient is.

The relationship between the permeability coefficient and the plane porosity is showed in Fig. 13. Fig. 13 shows that along with the plane porosity decrease, the permeability coefficient gradually decrease. The change of macroscopic and microscopic show that in the solidification process of the dredger fill, the lower the plane porosity, the More compact structure is., and the lower the permeability coefficient is.

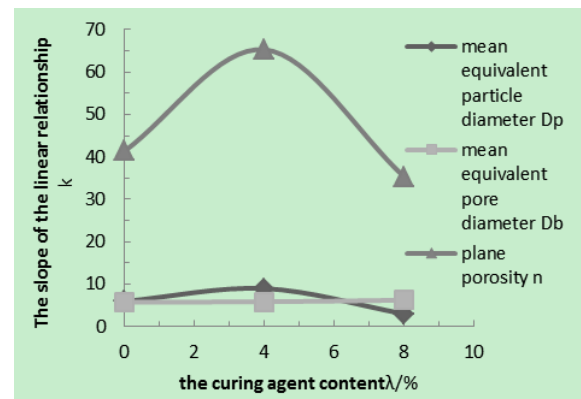


Fig. 14. The slope of the linear relationship of microstructure parameters and permeability coefficient under different content of curing agent.

Table. 6. Linear relationship between permeability coefficient and microstructure of Solidified dredger fill.

Microscopic parameter	Curing agent content λ/%	The linear relationship between permeability coefficient k and microstructure	R ²	Slope K
mean equivalent particle diameter D _p	4	k= -5.9631D _p + 17.215	0.9624	5.9631
	8	k= -8.9982D _p + 26.979	0.9981	8.9982
	12	k= -3.0179D _p + 9.8619	0.8681	3.0179
mean equivalent pore diameter D _b	4	k= 5.7832D _b - 6.7695	0.9166	5.7832
	8	k= 5.8814D _b - 5.3245	0.9295	5.8814
	12	k= 6.2588D _b - 6.0475	0.9801	6.2588
plane porosity n	4	k = 41.342x - 4.7395	0.9960	41.342

8	$k= 65.284x - 8.3987$	0.9991	65.284
12	$k= 35.309x - 4.3905$	0.9772	35.309

The linear relationship between permeability coefficient and microstructure of Solidified dredger fill is showed in Table. 6. It can be seen from the table 6 that there is an excellent linear relationship between the permeability coefficient and the three micro structure parameters, which indicates that the permeability coefficient K is strongly correlated with the mean equivalent particle diameter Dp, mean equivalent pore diameter Db and plane porosity n.

The slope of the linear relationship of microstructure parameters and permeability coefficient under different content of curing agent is showed in Fig. 14. It can be seen from the figure 14 that the slope of the linear relationship between the permeability coefficient and the mean equivalent particle diameter Dp and the mean equivalent pore diameter Db is very small, which is below 10, and the slope of the linear relationship between the permeability coefficient and the plane porosity n is above 35, which is 8-10 times of the former under the same conditions. So compared with the mean equivalent particle diameter Dp and the mean equivalent pore diameter Db, The effect of the plane porosity on permeability of solidified soil is greater.

CONCLUSION

The permeability of solidified dredger fill is measured by the indoor penetration test. The microstructure of the solidified dredger fill and unsolidified dredger fill is observed by using Scanning Electron Microscope (SEM). The microscopic image of dredger fill is processed and analyzed by using IPP, and the microstructure parameter is calculated that include mean equivalent particle diameter Dp, mean equivalent pore diameter Db, plane porosity n. The Quantitative analysis of the relationship between permeability and microstructure of Solidified dredger fill is done. The research results show that:

1) Self-made curing agent can effectively reduce the permeability of dredger fill, the permeability coefficient decrease with the growth of the age and the increase of the content of curing agent. The permeability coefficient decreased very intense before 14 cured days, and the permeability coefficient tends to be stable after 14 days. So in

order to improve the permeability of the dredger fill, it can be taken to increase the amount of curing agent.

2) The quantitative analysis of the particles of the solidified dredger fill shows that the mean equivalent particle diameter Dp has a linear correlation with the curing period T, and the correlation coefficient is above 0.95.

3) The quantitative analysis of the pores of the solidified dredger fill shows that the difference of the mean equivalent pore diameter is not obvious when the curing agent content is 8% and 12%, and both are smaller than the mean equivalent pore diameter that curing agent content is 4%. Compared with the mean equivalent particle diameter, the rate of decrease of the mean equivalent pore diameter is faster than the rate of increase of the mean equivalent particle diameter.

4) The quantitative analysis of the plane porosity of the solidified dredger fill shows that the plane porosity of original dredger fill is 66.63%. The plane porosity of solidified dredger fill decreases with the increase of the curing agent and the growth of the curing period. When the curing period is 28 days, the plane porosity of the solidified dredger under three different content of curing agent is little difference and tends to be stable.

5) The quantitative analysis of the relationship between permeability coefficient and microstructure of the solidified dredger fill shows that the larger the mean equivalent particle diameter Dp is, and the smaller the mean equivalent pore diameter Db and plane porosity n are, the lower the permeability coefficient is. The mean equivalent particle diameter Dp, mean equivalent pore diameter Db, plane porosity n have a good linear relationship with the permeability coefficient k, and the correlation coefficient K is above 0.9, compared with the mean equivalent particle diameter Dp and the mean equivalent pore diameter Db, The effect of the plane porosity on permeability of solidified soil is greater.

Acknowledgments: Financial support for this study was provided by the National Natural Science Foundation of China (51078228) and the National Marine public welfare industry research special funds of China (201105024-5) and the Graduate

innovation fund of Shanghai Maritime University (2016ycx025).

REFERENCES

1. Y.T. Cui, W.B. Liu, B.Q. Xu, *Science Technology and Engineering*, **05**, 260 (2016).
2. Z.W. Gu, B.N. Sun. Dong Yining, *Chinese Journal of Rock Mechanics and Engineering*, **22**(3), 505 (2003).
3. GB/T 50123-1999 Standard For Soil Test Methods.
4. L. Huang, Quantitative Analysis of Micro-Porosity of Saturated Soft Clay and Its Fractal Description, Wuhan University of Technology, 2007.
5. B. Ji, X.M. Xiao, Z. Li, *Safety and Environmental Engineering*, **02**, 54 (2010).
6. M.C. Jia, L. Wang, J. Zhou, *Journal of Tong Ji University(natural science)*, **4**, 493 (2010).
7. Y.Y. Li, B.J. Liu, Y.L. Xie, *Journal of Rock Mechanics and Engineering*, **25**(S2), 3587 (2004).
8. K.H. Xie, Y.C. Zhuang, X.B. Li, *Journal of Geotechnical Engineering*, **27**(5), 591 (2005).
9. C. Xu, D. Li, L. Huang, *Journal of Tong Ji University(natural science)*, **06**, 819 (2011).
10. R. Q. Xu, W. W. Deng, B. Xu, J. P. Lai, X. Q. Zhan, L. Y. Xu, J. Y. Lu, *Journal of Earth Science and Environment*, **3**, 104 (2015).
11. R.Q. Xu, L.Y. Xu, W.W. Deng, Y. H. Zhu, *Journal of Zhejiang University(Engineering Science)*, **8**, 1417 (2015).
12. Z.H. Zhang, H.Y. Li, Y.M. Shi, *China Civil Engineering Journal*, **47**(12), 122 (2014).
13. J.R. Zhang, J. Zhu, L. Huang, W.J. Huang, *Journal of Wuhan University of Technology*, **4**, 80 (2008).
14. Z.H. Zhen, J.W. Gao. *Transportation Science and Technology*, **8**, 124 (2015).

Study of hydraulic performance and pressure pulsation characteristics of the grinder pump in case of clogging

X. Wang, Y. Lu*, R. Zhu, Q. Fu, W. Zhong

National Research Center of Pumps, Jiangsu University, Zhenjiang, Jiangsu 212013, China

Received February 12, 2016; Revised December 26, 2016

In order to study the variation rule of head, efficiency and the shaft power of the non-blocking submersible grinder pump, as well as the influence of the static cutter runner clogging on its pressure pulsation when the static cutter runner is clogged, this study adopts, on the basis of experiments, RNG k-Epsilon turbulence model to carry out steady and unsteady calculation about the computational domain of the grinder pump. By analyzing 28 different clogging cases of the static cutter runner, it is found that with the clogging degree of the static cutter runner increasing, the head changes in shape of a parabola, the maximum efficiency point of the grinder pump deflects to low flow point, and the high efficiency area of the pump narrows. In the low flow area, the throttling action between the dynamic cutter and static cutter is the most important factor that affects the pump characteristics variation rule, whereas, in the high flow area, the throttling action between the dynamic cutter and static cutter, the clearance cavitation at the radial clearance, and the vortex-type cavitation on the edge of the impeller outlet together affect the pump characteristics variation rule of the submersible grinder pump; inside of the submersible grinder pump, when the static cutter runner is clog-free or part of the runner is not completely clogged, the passing frequency of the dynamic cutter is the most important factor that affects the pressure pulsation, whereas, when part of the static cutter runner is completely clogged, the dynamic-static interaction effect between the dynamic cutter and static cutter is the most important factor that affects the pressure pulsation.

Key words: Submersible Grinder Pump, turbulence model, Channel blockage, pressure pulsation, cavitation.

INTRODUCTION

With the rapid development of industry and agriculture, more and more sewage thus generated contains fiber and other impurities, ordinary sewage pump is prone to be clogged during the run time so that it is unable to meet the requirement of discharging substance with high fiber impurities, as a result, sewage pump with auxiliary cutting or grinding device is more and more widely used. Therefore, the submersible grinder pump is widely used in industries such as municipal, sewage treatment, environmental protection, light industry, mining, study making, water conservancy and chemical industry, etc.

Scholars both at home and abroad have made a deep study into the submersible pump, among which for the first time in 1979, Kratzer A [1] systematically summarized design and model selection issues of the sewage pump, and emphatically analyzed the lossless performance of various pump when discharging materials; J.A. Escobar [2] studied safety of the submersible pump by analyzing submersible pump system breakdown caused by stress corroded fitting bolt through X-ray fluorescence spectrum; Parviz Ali-Zadea [3] carried

out study on submersible pump noise, analyzed the relations between interference level and noise level and provided a noise elimination plan; Hernandez - Solis, A and Carlsson, F [4] studied the relation between submersible centrifugal pump cavitation and motor power capacity, diagnosing cavitation and impeller damage of the submersible centrifugal pump by monitoring motor power capacity and current flow; Liu, Yingyuan [5] mainly studied the cavitation flow characteristics of the rotor pump and discussed several factors affecting the cavitation, including rotation speed, pressure difference and gap size and inlet pressure; Lee, Kyoung - Hoon [6] carried out experiments on the effects of cavitation flow instability of the double-blade axial inducer and observed the internal asymmetric cavitation and cavitation phenomenon of the inducer; Cudina [7] established correlation with pump cavitation through noise spectrum generated by cavitation, so as to test the cavitation; Domestic scholars Wang Songlin [8] and Wang Yushi [9], etc. verified the feasibility of the RNG k- ϵ model and the transport equation cavitation model through experiment, finding that pressure pulsation intensity under cavitation condition was 2 times as much as that under non-cavitation condition, and pressure pulsation under low flow condition was about 5 times as much as that under design condition; Zhu

* To whom all correspondence should be sent:

Rongsheng and Wang Zhenwei [10, 11], etc. studied the effects on the external characteristics of the non-blocking submersible grinder pump with or without grinding device and the clearance between dynamic cutter and static cutter. It can be found that few scholars both at home and abroad studied the submersible pump performance of all aspects under clogging condition.

This study carries out simulation studies on submersible grinder pump static cutter on the basis of experiment, mainly studies the head, power capacity and efficiency variation rule and internal flowing characteristics of the static cutter runner under different clogging conditions, and analyses frequency domain and time domain characteristics of the internal pressure pulsation of the pump when static cutter runner is clogged, so as to learn the internal flow characteristics of the non-blocking submersible grinder pump and to provide theory basis for the optimization design of grinder pump.

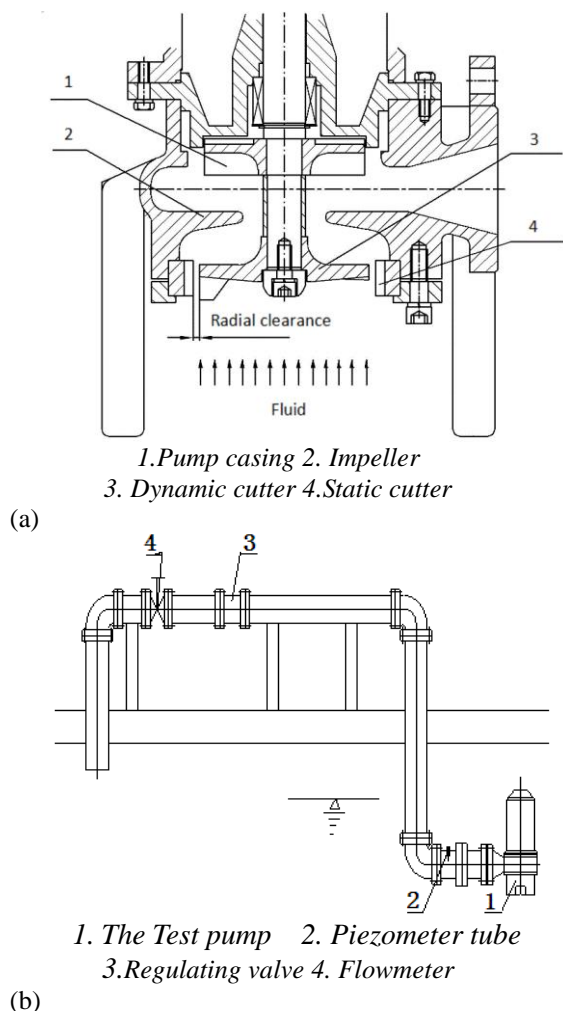


Fig. 1. Structure sketch and diagram of the test device.

NUMERICAL SIMULATION AND EXPERIMENTAL PART

Experiment table and Experiment method

Use GSP-22 non-clogging submersible grinder pump as the experimental pump, with clean water as the transmission medium. The pump performance test is carried out at the open test bed in Jiangsu University's National Water Pump and System Engineering Technology Research Center. The entire test system consists of GSP-22 non-clogging submersible grinder pump, outlet piping, comprehensive experiment table, TPA-3 pump product parameter measuring instrument, FLK1151 pressure transmitter, and NSKYLWGY liquid turbine flowmeter, etc. In order to verify the pressure pulsation characteristics of the CFD simulation, use CY301 high-precision high-speed intelligent pressure sensor to collect the pressure pulsation data at both static cutter and volute outlet. As the submersible grinder pump works underwater during the experiment, use D28 hose to provide waterproof protection to CY301, the structure sketch of pump and test device diagram, static cutter models with different partial clogging degrees and the experiment site as shown in figure 1(a),1(b), 2,3



Fig. 2. Static cutter models with different partial clogging degrees



Fig. 3. Experiment site

This experiment is divided into two parts, including pump external characteristic experiment and pump pressure pulsation characteristic experiment. The pump external characteristic experiment includes 8 kinds of static cutter runner

clogging schemes with 13 flow point tests for each scheme. The experiment is started by the shutoff valve. Changing the real-time flow capacity (0 ~ 35 m³/h), the pump test system can record inlet and outlet pressure and shaft power of the centrifugal pump, and automatically calculate the head, shaft power and efficiency of the pump. Pump pressure pulsation experiment and pump external characteristic experiment are carried out simultaneously. Set the collecting zero point in the data-collecting software NetSensor before start the pump, set the sampling frequency as 2000 Hz, sampling time 30s, then collect data respectively at flow capacity points of 0.5Q, 0.7Q, 1.0Q, 1.2Q and 1.5Q.

Numerical methods

This study uses the software Pro/E to make model and adding a segment of water body in front of cutter inlet and at volute outlet, so as to guarantee higher stability of the simulation results. The entire model included water inlet, dynamic cutter water body, static cutter and rear runner water body, impeller water body, volute water body and water outlet, as shown in figure 4.

This study uses the ANSYS-CFX 14.5 to conduct numerical simulation, including steady calculation and unsteady calculation. As the static cutter of non-blocking submersible grinder pump is composed of multiple narrow half-round runner, and structured grid can take better control over the grid number than unstructured grids, and easy to converge. Therefore, use meshing software ICEM to make structured mesh division to all water body parts, and make unstructured mesh division to static cutter and rear runner water body. The grid qualities of minimum angle of each water body part are shown in Table 1.

As the grid quality directly affects the result of numerical simulation, it is only when the increase of grid number has little influence on the results that the accuracy of simulation calculation can be determined. In order to determine whether the grid number and quality of the computational domain meet the practical requirements, independence inspection on the grid of the model is carried out based on Standard k- ϵ and RNG k- ϵ turbulence models respectively. Dividing the model on the

basis of different mesh density, the calculation shows that when the grid number reaches 12037.56 million, the design-point head variation range of grinder pump is below 5%, and when the grid number reaches up to 15832.73 million, the design-point head variation range of grinder pump is below 1%, indicating that the calculation results has nothing to do with the grid number. Considering the accuracy and efficiency of calculation, numbers are finally determined as follows: inlet water body grid number 334656, dynamic cutter water body grid number 1619.04 million, static cutter and rear runner water body grid number 4832.16 million, impeller water body grid number 4092 million, volute water body grid number 2100.5 million, outlet water body grid number 623.1 million, and the total model grid number 16613.36 million.

As the CFX has introduced a large number of turbulence models, it can run simulation of most of the hydraulic rotating machinery. In order to make the simulation result closer to reality, this study chooses the RANS two-equation model of Standard k-Epsilon model and RNG k-Epsilon model, the Shear Stress Transport model, the BSL model and k-Omega model. Big difference exists among the velocity distribution at different locations of the whole water domain. Calculation shows that the minimum Reynolds number at the pump inlet is and the maximum Reynolds number at the static cutter runner is , in which the Reynolds number range applies to the 5 kinds of turbulence model above.

Comparing the above 5 kinds of turbulence model simulation results (head variation curve and efficiency variation curve) and experimental data, it is found that in the low flow area (0 ~ 0.6 Q), the k-w model coincides best with the experimental data, followed by BSL > RNG k- ϵ > SST > Standard k- ϵ ; around the design point (0.7 ~ 1.2 Q), the RNG k- ϵ model coincides best with the experimental data, followed by SST > k-w > BSL > k- ϵ ; in the high flow area (1.2 ~ 2.0 Q), BSL model coincides best with the experimental data, followed by RNG k- ϵ > k-w > Standard k- ϵ > SST, as shown in figure 5.

Table 1. Grid quality of each part.

Grid	Water inlet	Dynamic cutter water body	Static cutter water body	Impeller	Volute	Water outlet
Quality	0.70	0.43	0.41	0.57	0.45	0.72
Min angle	48	29	23	38	33	53

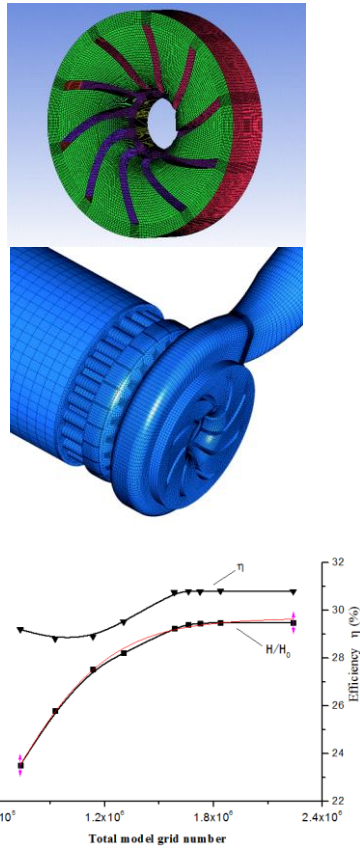


Fig. 4. Grid and grid-independent test

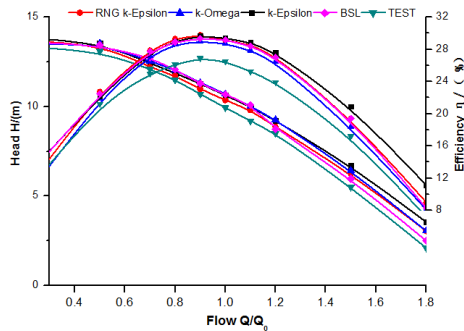


Fig. 5. Comparison of different turbulence models.

Through comprehensive analysis, the RNG $k-\epsilon$ model is selected as the main turbulence model of this calculation and SIMPLE algorithm is adopted to couple pressure and velocity; based on the finite volume method of finite element to discrete equations, the dynamic and static coupling surface between impeller and volute, as well as between dynamic cutter and static cutter water body uses Frozen Rotor interface, of which the convection term of the equation uses High resolution scheme, whereas the diffusion term uses central difference scheme, with the reference pressure being 1101 325 Pa.

In order to make the calculation of the flow field closer to reality, pressure inlet and quality outlet are used to set the boundary conditions during

calculation. Based on submersible depth of non-clogging submersible grinder pump in actual work field, set the inlet pressure as 200 000Pa; set the wall roughness as $10\mu\text{m}$; and use non-slip boundary conditions at the solid sidewall. Convergence scheme selects Root Mean Square Residual (RMS) of all control volumes in the computational domain, and set the convergence precision of RMS as 10^{-5} .

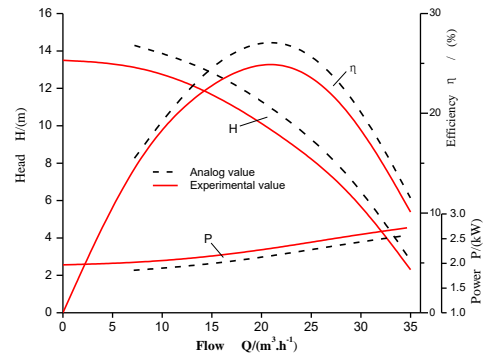


Fig. 6. Comparison of simulation prediction and experiment results.

Figure 6 shows the comparison between the experiment of the submersible grinder pump with grinding device and simulation of external characteristic curve. It can be seen that: there is certain deviation between submersible grinder pump simulation value and model machine performance experiment value, with head deviation less than 6% and efficiency deviation less than 8%. The CFD simulation calculates that the overall performance is better than the experiment performance of model machine, but the overall curve trend is consistent with better match degree. As the numerical simulation calculates only the hydraulic efficiency of fluid calculation domain and considers only the hydraulic loss of the calculation domain, whereas, except for the hydraulic loss, a lot of losses, such as leakage loss and mechanical loss, as a result, numerical simulation of the submersible grinder pump external characteristic using CFD software has certain accuracy and reliability. Whereas, the collecting data of pressure pulsation experiment verifies that the passing frequency of the dynamic cutter is the most important frequency affecting pressure pulsation when the static cutter runner is clog-free. When $1/8$, $1/6$, $1/4$, $1/3$ and $1/2$ of the static cutter runner is clogged, the dynamic-static interference frequency of the dynamic and static cutter is the most important frequency that affects the pressure pulsation.

RESULTS AND DISCUSSION

Calculation model uses the GSP-22 non-clogging submersible grinder pump, with the design parameters of the model shown in table 2.

This study mainly studies the effects of the long and narrow runner blockage of grinder pump static cutter, on the hydraulic performance and pressure pulsation characteristics of grinder pump. There are two kinds of research conditions about static cutter runner clogging: research 1 studies the effect of different number of runner clogging on grinder pump external characteristics; and as part of the static cutter runners are not completely clogged, research 2 studies effects of different clogging degree on grinder pump external characteristics.

Effects of different number of grinder pump static cutter runner blockages on hydraulic performance of the grinder pump

As the grinding device runner of submersible grinder pump is both narrow and long, clogging in part of the runner often happens in actual operation. The grinding device runner number in this model is 24. In order to study the effects of clogging degree of the grinding device on grinder pump external characteristics, analog computation is carried out on pump external characteristics of water body models with different clogging number of static cutter runners. In this study, a total number of 28 static cutter water body models are set up, respectively are 3 non-clogging water body models (large runner, small runner and combination of large runner and small runner), 2 two-clogged runner water body models, 2 four-clogged runner, 3 six-clogged runner water body models, 5 eight-clogged runner water body models, 2 ten-clogged runner water body models, 5 twelve-clogged runner water body models, 2 fourteen-clogged runner water body models, 2 sixteen-clogged runner water body models, and 2 partly not completely clogged runner. Mainly analyze the effect laws of runner clogging degree on grinder pump head, efficiency and shaft power.

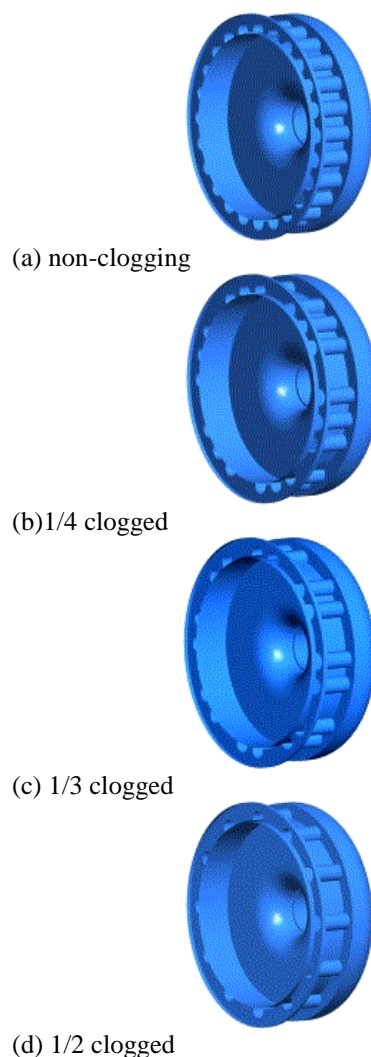


Fig. 7. Static cutter water body models with different partial clogging degrees.

Analysis of the effects of static cutter runner clogging on grinder pump head

This section mainly analyzes the effects of static cutter runner clogging degree on grinder pump head characteristics at flow capacity of 0.7Q, 1.0Q and 1.2Q, and verifies hydraulic models respectively with static cutter runner clogging degree of 0, 1/2, 1/3, 1/4 by experiments. Figure 8 shows the simulation results of head characteristics, in which it can be found that with the increase of static cutter runner clogging degree, head varies in shape of a parabola.

Table 2. Design parameters of experimental pump

Design point flow $Q/m^3 \cdot h^{-1}$	Design point head, H/m	Rotational speed $n/r \cdot min^{-1}$	Specific rotational speed, n_s	Impeller outside diameter, D_2/mm	Impeller outlet width, b_2/mm	Impeller hub diameter, d_h/mm	Blade outlet angle, β_2	Blade number, Z
22	10	2900	147.1	112	16	39	63	10

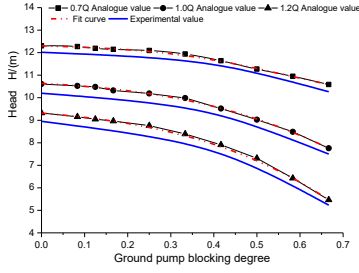


Fig.8. Effects of static cutter runner clogging on grinder pump head.

Comparison of head curves respectively at flow capacity of 0.7Q, 1.0Q and 1.2Q shows that static cutter runner clogging has greater impact on the head under high flow working condition. In order to study effect laws of static cutter runner clogging degree on the head under different flow capacity conditions, linear fits the head analog data on the basis of least square method. Carry out tendency prediction comparative analysis on the data respectively by three schemes of linear regression, polynomial regression and exponential regression, of which the quadratic polynomial fitting scheme is optimal, as shown in figure 5. It can be seen in the figure that the fitting effect is quite ideal, with the black fine lines representing the analog variation curves of the grinder pump with different clogging number, the red lines representing the tendency fitting line of head variation rules, and the blue lines showing the actual experimental variation curves of head. The equations of relations between grinder pump and clogging degree variation rules of static cutter runner at flow capacity of 0.7Q, 1.0Q and 1.2Q are as follows:

$$H = -3.72\left(\frac{n}{24}\right)^2 + H_{0.7Q}, \quad R^2 = 0.9371,$$

$$H' = -7.44\left(\frac{n}{24}\right); \quad (1)$$

$$H = -6.30\left(\frac{n}{24}\right)^2 + H_{1.0Q}, \quad R^2 = 0.9689,$$

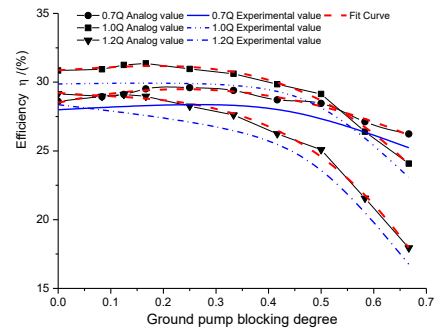
$$H' = -12.60\left(\frac{n}{24}\right); \quad (2)$$

$$H = -8.259\left(\frac{n}{24}\right)^2 + H_{1.2Q}, \quad R^2 = 0.9967,$$

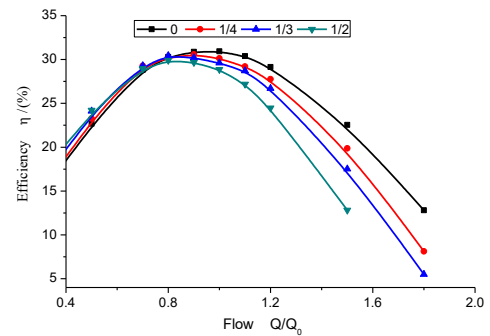
$$H' = -16.52\left(\frac{n}{24}\right); \quad (3)$$

In the equations above, $H_{0.7Q}$, $H_{1.0Q}$ and $H_{1.2Q}$ represent respectively the heads at flow capacity of 0.7Q, 1.0Q and 1.2Q under non-clogging static cutter runner condition, R^2 represents the variance of simulation data corresponding to the head fitting equation. The head variation rule equation H' shows that the effect of grinder pump static cutter clogging on pump head at flow capacity of 1.2Q is

2.5 times as much as the effect at flow capacity of 0.7Q. On the one hand, it is because as flow capacity increases, flow velocity at the clearance increases, the contraction and diffusion loss at the clearance increases significantly, the throttling action of dynamic and static cutter radial clearance becomes more obvious, and the throttling action of radial clearance is not obvious with a correspondingly reduced hydraulic loss because of the small flow velocity under low flow working condition. On the other hand, it is because as the flow velocity of the fluid between dynamic cutter and static cutter increases, pressure drops caused by clearance cavitation and more serious cavitation. The static cutter runner clogging degree is in direct proportion to flow area of the dynamic and static cutter. Combined with the head variation rule equation H , the pump head variation is in direct proportion to the square of dynamic and static cutter flow area, that is, the throttling action at the clearance is in direct proportion to the square of the fluid flow velocity. Whereas, without grinding device, the flow area at the pump inlet has little impact on pump head, with no obvious regularity.



(a)



(b)

Fig. 9. Effects of static cutter runner clogging on grinder pump efficiency.

Analysis of the effects of static cutter runner clogging on grinder pump efficiency

Figure 9 (a) is the effect curve of static cutter runner clogging degree on grinder pump efficiency characteristics, with the black fine lines representing the analog variation curves of the

grinder pump efficiency, the blue lines representing the actual experimental variation curves of efficiency, and the red lines representing the tendency fitting lines of efficiency variation rules. It can be found that the variation tendencies of efficiency curve at flow capacity of $0.7Q$, $1.0Q$ and $1.2Q$ are completely different. When flow capacity is $0.7Q$, the efficiency curve of grinder pump shows a tendency of ascending firstly then descending with the static cutter runner clogging degree, with grinder pump efficiency being 28.6% under non-clogging condition and pump efficiency being 26.23% when clogging degree reaching $2/3$.

It is thus clear that the static cutter clogging has little impact on pump efficiency at low flow capacity point. When the flow capacity is $1.0Q$, partial clogging (with clogging degree under 0.4) of the static cutter runner has little impact on pump efficiency, then decreases significantly. When clogging degree exceeds 0.55, the pump efficiency is lower than the efficiency at flow capacity of $0.7Q$ under the same working condition. When flow capacity is $1.2Q$, the efficiency curve of grinder pump descends significantly with static cutter runner clogging degree, especially when clogging degree exceeds $1/2$. Combined with figure 9 (b), it can be seen that the maximum efficiency point of the grinder pump shifts to low flow capacity point and the high efficiency area of the pump narrows with the variation of the static cutter runner clogging degree of the grinder pump. This is mainly because that under high flow working condition, fluid flow velocity increases, pressure decreases, serious cavitation intensifies the static cutter runner clogging, as a result, the performance of the submersible grinder pump at high flow area is seriously affected by runner clogging.

To sum up, as the static cutter runner clogging degree varies, the throttling action between dynamic cutter and static cutter at low flow area is the most important factor affecting the pump characteristics variation rule, whereas, the throttling action between dynamic cutter and static cutter, clearance cavitation at the radial clearance as well as the vortex-type cavitation at the impeller outlet at high flow area together affect the pump characteristics variation rule of the submersible grinder pump.

Study on the effect of static cutter runner clogging degree on the pressure pulsation characteristics of submersible grinder pump

As the static cutter runner clogging degree increases, more unstable factors appear inside the submersible grinder pump, such as the existence of

eddy current and reflux of fluid at the static cutter affected by cavitation, vortex inside the bladeless cavity, and pressure pulsation of high strength and high frequency caused by the collapse of cavitation bubbles, etc. Through the analysis of pressure pulsation frequency domain, factors that affect the unstable flow inside the pump can be found by the relations between pressure pulsation intensity and frequency. As a result, this section mainly analyzes the pressure pulsation frequency domain of the submersible grinder pump. In order to monitor the variation rule of pressure, respectively set up 8 pressure monitoring points evenly along the peripheral direction at the half-round runner outlet of the static cutter and 4 at the wall of the volute outlet, take samples of the pressure data at a fixed time interval t within time T , with the sampling frequency greater than twice the highest signal frequency.

Figure 10 shows the time domain charts of pressure pulsation at the static cutter runner outlet after deducting the inlet static pressure in different clogging schemes, with the abscissa representing 2 periods of rotation and ordinate representing the pressure intensity P . It can be observed from figure 12(a), 12(b), 12(c) and 12(d) that the period of waveform variation rule of time domain is $0.5T$. Each period has 12 small fluctuations under non-clogging and partly not completely clogged conditions, 4 large fluctuations and 4 small fluctuations with $1/3$ clogged, and 6 large fluctuations with $1/2$ clogged. Sequence diagram periodic fluctuation is mainly caused by the rotation of the two-blade dynamic cutter, whereas, small fluctuations in the period is caused by the dynamic-static interaction effect between the dynamic cutter and static cutter, and the range of small fluctuation increases with the increase of clogging degree becoming the main component of the pulse. With the increase of flow capacity, pressure at the static cutter runner outlet drop significantly, pulsation amplitude increases significantly. At flow capacity of $0.7Q$, the maximum pulsation amplitudes with $1/3$ and $1/2$ of the static cutter runner clogged are 17706 Pa and 23018 Pa, respectively as 1.20 times and 1.56 times of the pulsation amplitudes under non-blocking condition.

Figure 11 is the pressure pulsation frequency domain characteristic diagram at the static cutter runner outlet under different clogging degrees of the grinder pump static cutter runner. In this model, amplitudes and frequency-domain characteristics at different monitoring points under different working conditions of grinder pump are obtained through

fast Fourier transform of monitoring point pressures, with the rotational speed of grinder pump $n = 2900 \text{ r. min}^{-1}$. As a result, the rotation frequency of the impeller is $f_0 = 48.33 \text{ Hz}$, the dynamic cutter blade number is 2, impeller blade number is 10, tooth passing frequency $f = 2 f_0 = 96.66 \text{ Hz}$, and blade passing frequency $f = 10 f_0 = 483.33 \text{ Hz}$. By observing figure 11 (a), 11 (b) and 11 (c), it can be found that the pressure pulsation frequencies are distributed at 96.66 Hz ($2 f_0$) and at multiples of this frequency. Figure 11 (a) representing non-clogging static cutter runner and figure 11(b) representing partly not completely clogged runner, the maximum pulsation amplitude in both figures are at the frequency of 193.33 Hz ($4 f_0$), and the pulsation amplitude at the frequency of 1160 Hz ($24 f_0$) is obviously higher than the amplitude of adjacent harmonic frequency. Figure 11 (c) and 11 (d) representing conditions of $1/3$ and $1/2$ clogged static cutter runner, the maximum pulsation amplitudes of the two figures are respectively at the frequency of 386.66 Hz ($8 f_0$) and 580 Hz (f_0), with the maximum pulsation amplitude about 1.74 times as much as that of the non-clogging static cutter runner, and the second largest pulsation amplitude at the frequency of

193.33 Hz ($4 f_0$), with the pulsation amplitude close to that of non-clogging static cutter runner.

Figure 12 is the pressure pulsation at the volute outlet in different clogging schemes. It can be seen that under both non-clogging and partly not completely clogged conditions, the maximum pulsation amplitude at the volute outlet is the passing frequency of the dynamic cutter and the second largest pulsation amplitude is the passing frequency of the impeller blade. When $1/3$ and $1/2$ static cutter runner is clogged, the maximum pulsation amplitudes of both conditions are at the dynamic-static interference frequency, and the second largest pulsation amplitude frequency is the passing frequency of the impeller blade. The above analysis shows that inside of the entire submersible grinder pump, when the static cutter runner is clog-free or partly not completely clogged, the passing frequency of the dynamic cutter is the most important factor affecting the pressure pulsation; when part of the static cutter runner is completely clogged, the dynamic-static interaction effect of the dynamic and static cutter is the most important factor affecting the pressure pulsation and being verified in the pressure pulsation experiment.

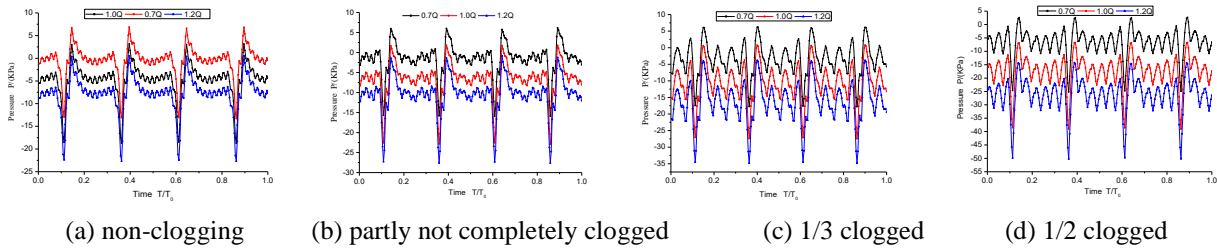


Fig. 10. Time domain diagram of pressure fluctuation at the static cutter runner.

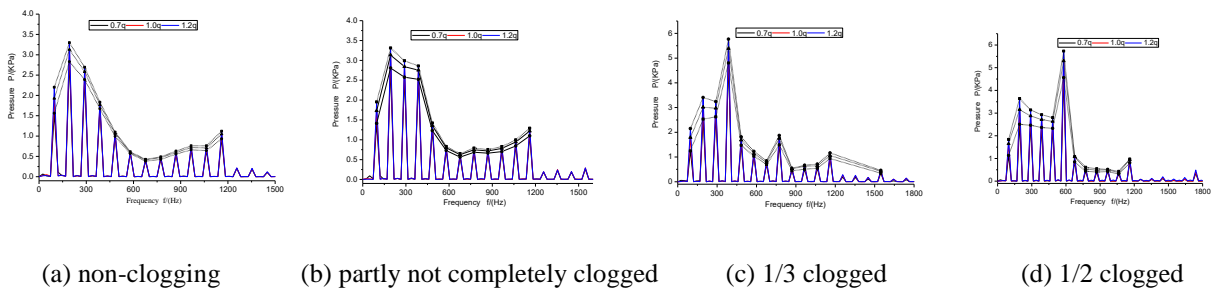


Fig. 11. Frequency domain diagram of pressure fluctuation at the static cutter runner

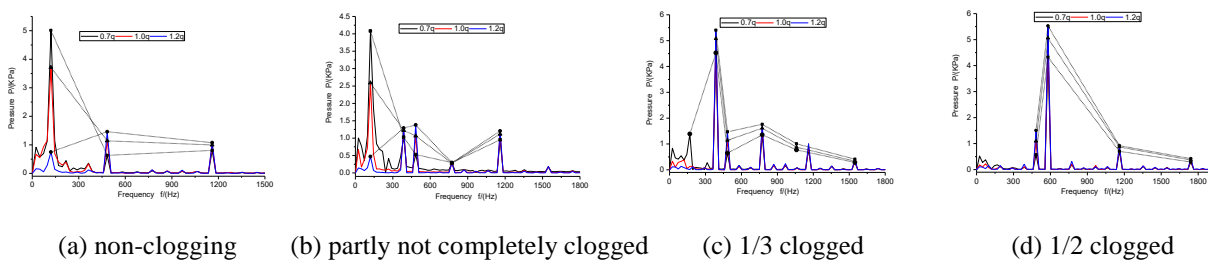


Fig. 12. Frequency domain diagram of pressure fluctuation at the volute outlet.

CONCLUSIONS

(1) By the 28 established static cutter water body models with different clogging degrees, it is found that as the static cutter runner clogging degree increases, the head declines in shape of a parabola, the maximum efficiency point of the grinder pump shifts to low flow capacity point, and the high efficiency area of the pump narrows. The throttling action between dynamic cutter and static cutter at low flow area is the most important factor affecting the pump characteristics variation rule, whereas, the throttling action between dynamic cutter and static cutter, clearance cavitation at the radial clearance as well as the vortex-type cavitation at the impeller outlet at high flow area together affect the pump characteristics variation rule of the submersible grinder pump.

(2) Through analysis of the time domain and frequency domain of inlet and outlet pressure pulsation of the submersible grinder pump in different clogging schemes, it can be found that in the submersible grinder pump, when the static cutter runner is clog-free or partly not completely clogged, the passing frequency of the dynamic cutter is the most important factor affecting the pressure pulsation; when part of the static cutter runner is completely clogged, the dynamic-static interaction effect of the dynamic and static cutter is the most important factor affecting the pressure pulsation.

Acknowledgments: This research was financially supported by: (1)National Natural Science Foundation of China (51379091); (2)A science and technology program funded by Natural Science Foundation of Jiangsu Province (BK20130516); (3)National Youth Natural Science

Foundation of China (51509112); (4) Key R & D programs of Jiangsu Province of China (BE2015129 AND BE2016160); (5)Prospective joint research project of Jiangsu Province (BY2016072-02); (6)Supported by the Open Research Fund of Key Laboratory of ministry (provincial), (Xihua University) , szjj2016-070; (7)Jiangsu Province ordinary university graduate student research innovation project (KYLX16_0894)

REFERENCES

- 1.F. Aschenbach, *World Pumps*, **355**, 42 (1996).
- 2.J.A. Escobar, A.F. Romero, J. Lobo-Guerrero, *Engineering Failure Analysis*, **60**, 1 (2015).
- 3.P. Ali-Zadea, C. Hajiyevb, U. Hajiyevac, M. Yilmazd, *Journal of Petroleum Science and Engineering*, **110**, 109 (2013).
- 4.A. Hernandez-Solis, F. Carlsson, *European Power Electronics and Drives*, **20**(1), 58 (2010).
- 5.L. Yingyuan; W. Leqin; Z. Zuchao. *Journal of Mechanical Engineering Science*, **229**(14), 2626 (2015).
- 6.L. Kyoung-Hoon; Y. Joo-Hyung; K. Shin-Hyung. *Journal of Mechanical Science And Technology*, **23**(9), 2350 (2009).
- 7.M. Cudina,; J. Prezelj, *Applied Acoustics*, **22**(4), 540 (2009).
- 8.W. Songlin, T. Lei, W. Yuchuang, *Journal of Vibration and Shock*, **32**(22), 168 (2013).
- 9.W. Yuchuang, T. Lei, C. Shuliang, Z. Baoshan, *Journal of Mechanical Engineering*, **50**(10), 163 (2014).
- 10.Z. Rongsheng, W. Zhenwei, L. Peng, W. Xiuli, *Journal of agricultural mechanization research*, **5**, 179 (2013).
- 11.Z. Weiguo, L. Ming, L. Yi, S. Jianping, S. Qice. *Journal of Drainage and Irrigation Machinery Engineering*, **12**, 1033 (2015).

Analysis on stability of slope in a typical cold region based on thermo-mechanical coupling

M. Li*, Y. Song, F.Chen

Wuhan University of Technology, Wuhan, China

Received December 12, 2016; Revised February 26, 2016

Factors which affect slope stability in cold regions are more complex than in normal temperature region. Physical and mechanical properties of rock and soil vary greatly in the process of freezing and thawing cycle. And the slope stability also changed with this. In this paper, the numerical simulation method was used to analysis temperature distribution of rock and soil in cold area and the displacement of slope affected by temperature based on phase transition of rock and soil in cold regions. The paper also analysis the change of slope stability in the different freeze-thaw cycles, freeze-thaw depth and water content of slope by establish a stability analysis model.

Keywords: stability analysis; stability of slope; thermo-mechanical coupling; cold regions

INTRODUCTION

As a typical representative of the cold regions, the slope stability of Tibet is influenced drastically by temperature. The physic-mechanical properties and initial properties of geotechnical material after freezing and thawing cycle changes to some extent. And the stability of the slope depends largely on the physic-mechanical properties of rock-soil mass [1]. So the damage and frost heaving of rock-soil mass in cold regions engineering affected by temperature amplitude, alternating frequency, moisture content and its mechanical properties, etc [2,3].

The stability of slope in cold regions is closely related to the temperature distribution. External temperature effects the temperature field distribution inside the slope. At the same time, we also need to consider the effect of heating and phase change process on the slope [4]. Besides, freezing and melting process have a great influence on the stability of slope as well. So the stability conditions have great difference with normal temperature region [5, 6]. In this case, it is significant to study the slope stability in cold regions.

THE FORM OF SLOPE FAILURE IN ALPINE REGION

Thaw slump. Thaw slump is the unique form of instability in permafrost region [7]. It is generally occurred in the excavation disturbance. The thermal equilibrium state of shallow slope is rapidly destroyed in a human disturbance conditions. Shear strength and cohesion of melting soil dramatic decrease for its saturated state in the

condition that the quickly enrichment of water after melting. So the melting soil will slide along the frozen layer under itself weight in this condition. This type of landslide often happens in the summer melt season. Its specific form is as shown in figure 1.

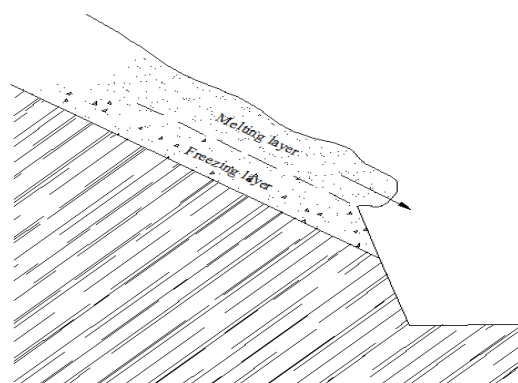


Fig. 1. Sketch map of thaw slump.

The collapse of rock slope. Freeze-thaw collapse usually occurred in rock slope [8]. That is because the crack of rock slope growth for its volume expansion after the rain penetrated into the primary pores and freeze, then the slope will collapse in the freeze-thaw cycle. The instability process is as shown in figure 2.

Slope stability is closely related to the temperature field distribution. Soil slope failures are usually happed at the melting period and their stability are closely related to the melting depth. But the major form of rock slope failures is shallow collapse which is related to the depth of the freeze-thaw cycle effect. So if we want to analyze slope stability, the first thing we need to determine is the influence of temperature on geotechnical engineering.

* To whom all correspondence should be sent:

E-mail mayshine-1988@163.com (Mo-Xiao Li)

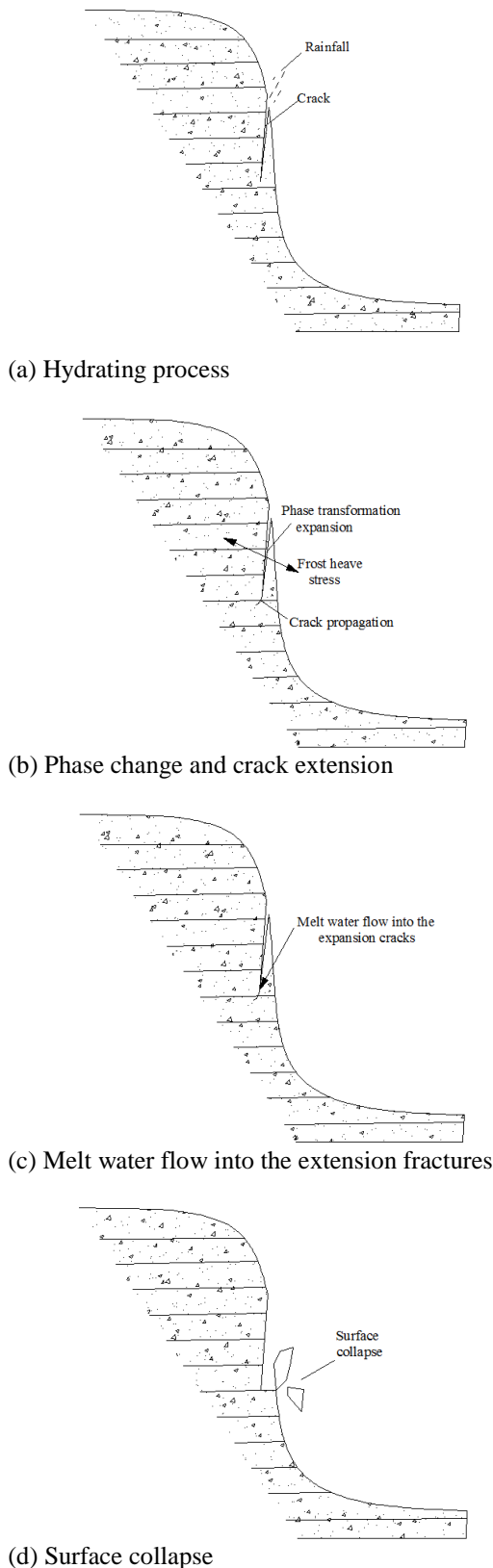


Fig.2. Sketch map of freeze-thaw collapse.

THE THERMO-MECHANICAL COUPLING ANALYSIS OF SLOPE

A slope of hydropower in Tibet was chosen as an example to research. The rock of slope mainly contains the unweathered diorite porphyries and strongly weathered diorite porphyries, and its surface is soil-rock-mixture covering layer which thickness is 3-6m. The slope model is set up based on these dates. The thickness of covering layer of model is select 5m. Slope profile is as shown in figure 3 and the finite element mesh is as shown in figure 4.

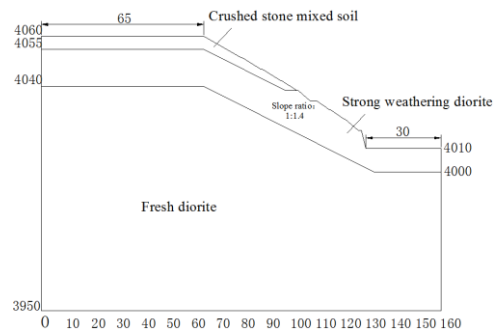


Fig.3. Sketch map of slope profile.

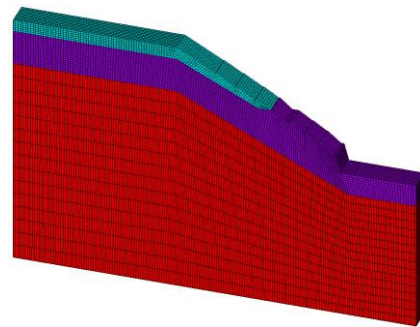


Fig.4. The finite element mesh.

The setting of temperature boundary conditions is important to analyze the temperature. It is the drive to make heat transfer occurrence and development. There are three kinds of thermal boundary conditions.

(1) The value of temperature on boundary surface is given and the value is a function of time and space.

(2) Define the heat flux density on boundary surface as a known function.

(3) Define the state of heat convection on boundary surface.

The surface of slope is mainly influenced by air temperature. The periodic change of external environment temperature cause the change of slope surface temperature, and this main performance is the convection heat transfer between slope surface and air. According to the above classification boundary conditions and the establishment of the geometric model, the surface and plain stage of slope choosing the first boundary condition which the temperature changed with time was given based on

the local climatic conditions. Both sides of the model chose the adiabatic boundary conditions for the slope temperature changes have little effect on the temperature outside the slope angle. And bottom boundary is input constant temperature.

Climate of Lhasa is semi-arid plateau temperate monsoon climate zone and its annual sunshine has 3000 hours. So the temperature changes can be simplified into the following trigonometric formula according to its features.

$$T(t) = T_0 + A_0 \sin\left(\frac{2\pi}{365}t + B\right)$$

T_0 is the average temperature of slope surface

and its value is 1°C based on the climate data. A_0 is the temperature amplitude and its value is 16°C based on the climate data. B is the initial phase for calculation.

The first step to solve the temperature field is to determine the initial temperature field. And the initial formation temperature field determines the accuracy of the unsteady temperature field analysis. Thermal analysis parameters are in Table 1. The initial temperature distribution is as shown in Figure 5.

The temperature field distribution inside slope changes with ambient temperature. That means the heat will be passed out from the high temperature to low temperature due to the temperature gradient. Surface temperature began to decline when it is higher than the ambient temperature and the shallow section begins freezes in this time. Figures 6 to 11 are the temperature contours of the freezing (Nov.,

Dec. and Jan.) and thawing (Mar., Apr. and May.) period.

As it can be seen from figures 6 to 8, depth of freezing increased over time in freeze period. The changes of slope surface temperature are more obvious than the changes of deep rock mass which reason is that freeze is only in a certain degree of shallow part. And figures 9 to 11 show that when the surface temperature of the frozen section rises, the shallow part firstly began to melt and there are still frozen in the center of the freezing layer.

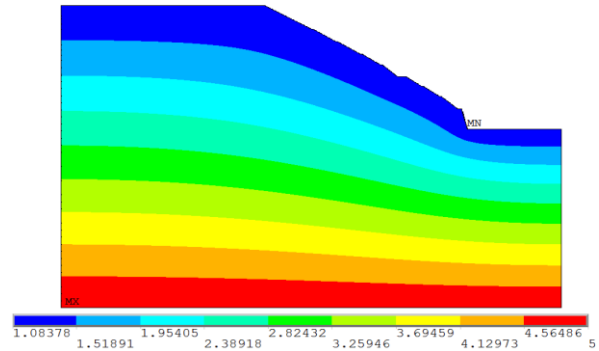


Fig. 5. The initial temperature field contours.

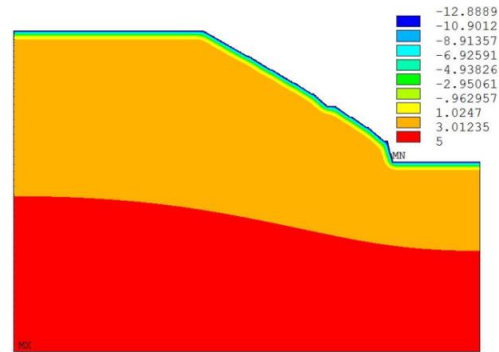


Fig.6. Temperature field contours of Nov.

Table 1. Thermal analysis parameters

sample	status	specific heat capacity J/(Kg·k)	thermal conductivity W/(M·k)	enthalpy $10^7 J / m^3$
gravel	freeze	1833	1.95	2.762
mixed soil	melt	2043	1.72	3.329
strongly weathered	freeze	1109	1.99	2.901
diorite	melt	1235	1.83	3.521
unweathered diorite	freeze	1077	1.98	2.698
	melt	1140	1.90	3.281

Take a temperature of characteristic point every 1 meter along the normal direction inside slope from the top of the hill covering layer and strongly weathered layer until 5 meter. Then the changes

trends of freezing and melting temperature with depth are plotted in Figures 12 and 13.

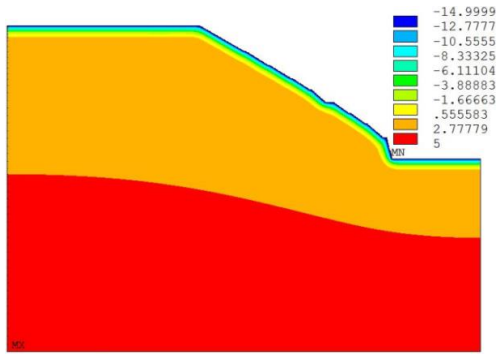


Fig. 7. Temperature field contours of Dec.

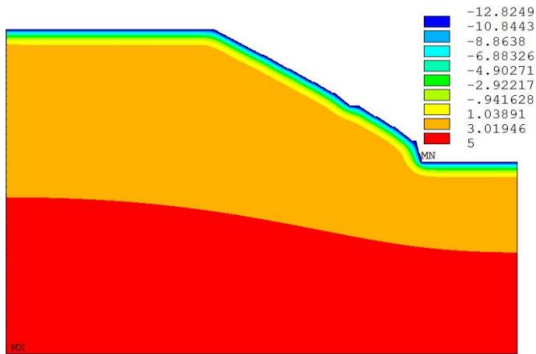


Fig. 8. Temperature field contours of Jan.

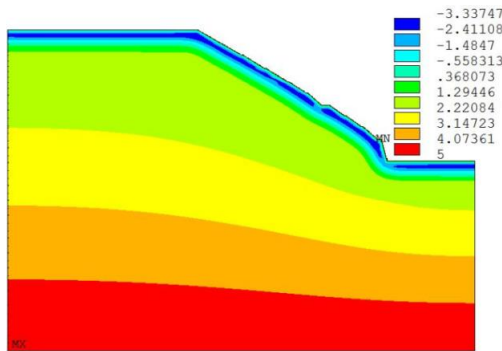


Fig. 9. Temperature field contours of Mar.

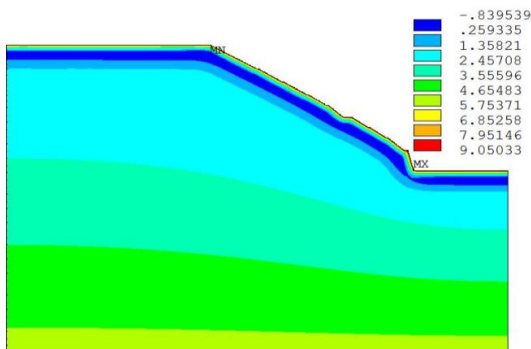


Fig. 10. Temperature field contours of Apr

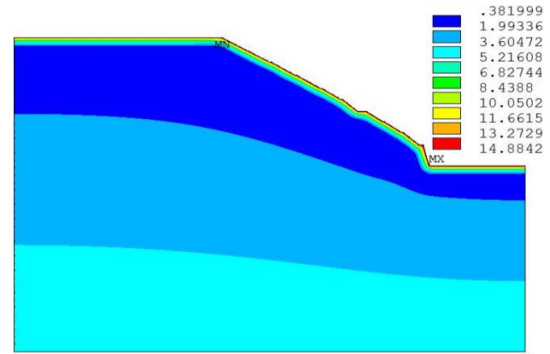


Fig. 11. Temperature field contours of May.

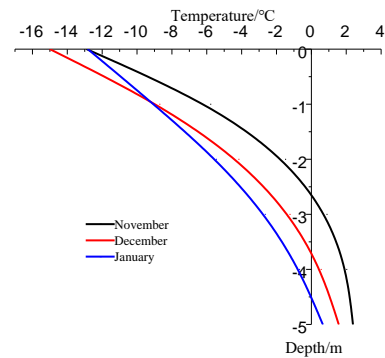


Fig. 12. Changes of temperature in freezing period

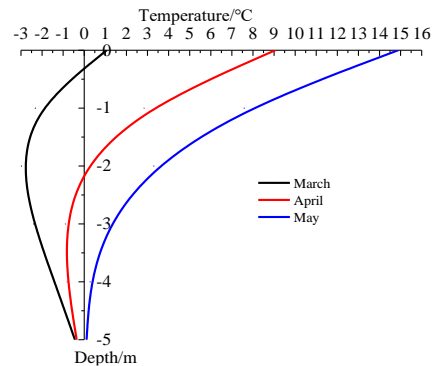


Fig. 13. Changes of temperature in melting period.

From the figures 12 and 13 we can find that the change of the depth is more hysteresis than the shallow's. That means effect of temperature on the deep rock mass is much smaller. Apparent from the figure the temperature of melt in the vertical direction have two times to cross over the phase-change interval. So in the slope, the freezing and thawing times of rock and soil vary from different depths.

In view of the rock and soil in cold regions affected severe by temperature, the figure 14 and 15 are the change of rock displacement simply caused by thermal effects. And the figure 16 is a tendency of rock displacement caused by frost heave and thawing-settlement.

In figure 14 and 15 the trends of vertical displacement of the slope versus time consistent with the change of ambient temperature. Because the magnitude of displacement is closely related to temperature loads. When the temperature changed in the same, the displacement generated by the thermal expansion is less than the displacement of gravel mixed soil.

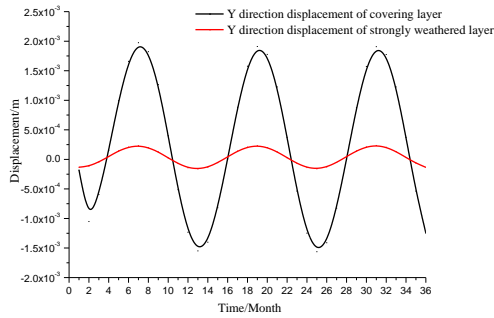


Fig. 14. Vertical displacement versus time curve of surface in different properties of rock and soil slope.

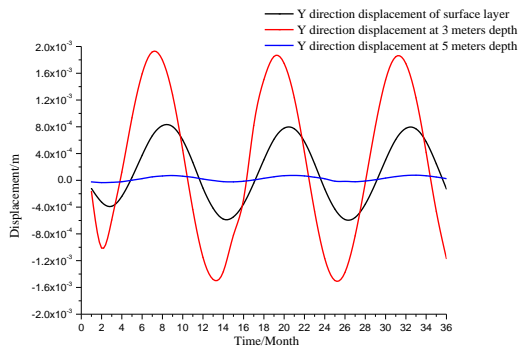


Fig. 15. Vertical displacement versus time curve under different overburden depth.

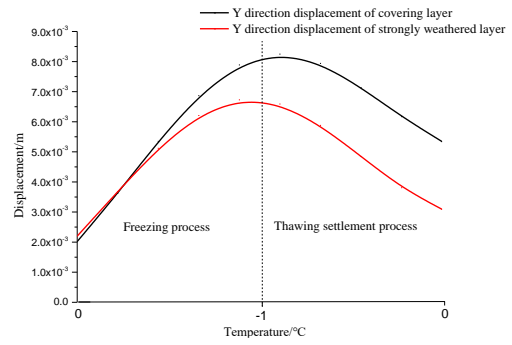


Fig. 16. Vertical displacement versus time curve of surface in different properties of rock and soil slope considered frost heave and thawing-settlement.

That is because the thermal expansion coefficient of diorite is less than the coefficient of thermal expansion of cement mixed soil. As it can be seen from Fig. 16, the displacement of rock and soil caused by phase transition in slope has the opposite trend with the change of temperature. When the temperature drops, unfrozen water phase becomes ice and its volume expansion. When the temperature rises, the ice melted and its volume decreases. Since the coefficient of linear expansion of the freezing and thawing process is so great that the shift change during the phase transition is more intense than it simply caused by the heat.

THE SLOPE STABILITY ANALYSIS

The slope stability analysis is to the rock slope and the soil slope, and the materials partitions of these slopes shows in the figure 17 and 18. The calculation parameters are as show in the table 2 and 3.

Table 2. Physical and mechanical parameters of the rock slope.

sample	density(kN/m ³)		shear(breaking) Strength				elastic modulus	Poisson's ratio
	dry	saturation	air-dry		saturation			
			C(KPa)	ψ(°)	C(KPa)	ψ(°)	E(GPa)	μ
strongly weathered diorite	24.9	25.6	100	37	40	35	3	0.34
unweathered diorite	26	26.3	130	49	50	47	40	0.26

Table 3. Physical and mechanical parameters of the soil slope.

soil type	water content	severe (KN/m ³)	elastic modulus (MPa)	Poisson's ratio	cohesion (KPa)	angle of internal friction (°)
thawed soil	11.80%	18.00	5	0.38	15.20	28.70
	13.06%	18.20	5	0.38	12.93	28.49
	14.17%	18.38	5	0.38	11.02	28.40
	15.40%	18.58	5	0.38	9.52	28.21
	16.80%	18.80	5	0.38	7.74	28.10
normal temperature soil	-	17.00	6	0.35	28.00	30.00
frozen soil	-	18.00	30	0.32	40.00	28.00

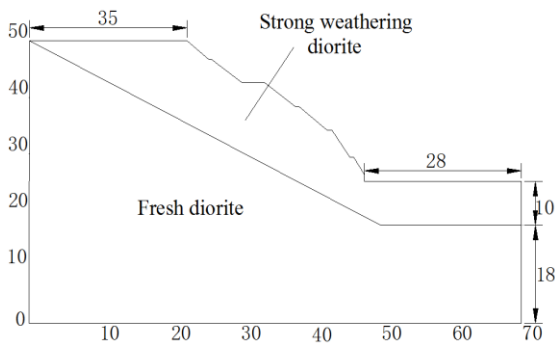


Fig. 17. Model of the rock slope.

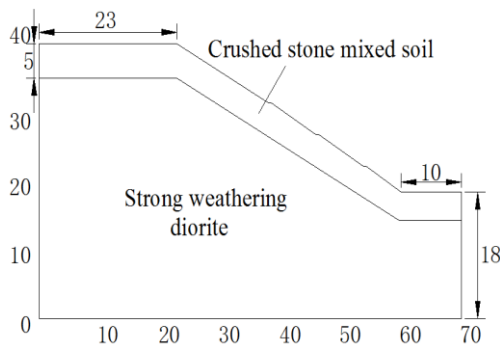


Fig. 18. Model of the soil slope.

For the rock slope, the temperature field of the shallow slope is mainly affected by the temperature change in the cold regions. The rock intensity of the shallow slope moves down in a certain degree as the thawing depth and the Freezing-thawing cycles increase. To explore the impact of freezing-thawing on the slope stability, the freezing-thawing deterioration is set as 10% and using the strength reduction method analyses the stability in the different freezing-thawing thickness(0m, 1m, 2m, 3m and 4 m). The safety factor and the shear strain increment cloud of 2m freezing-thawing thickness

show in the figure 19. Figure 20 shows the variation of the safety factor.

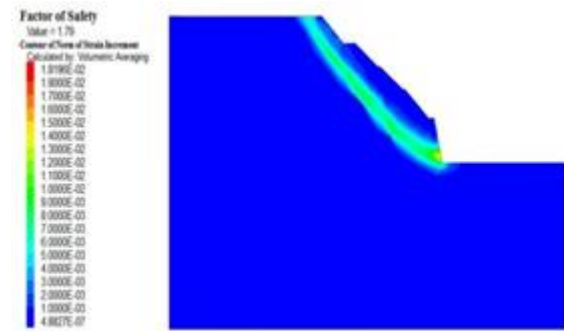


Fig. 19. Safety factor and shear strain increment cloud.

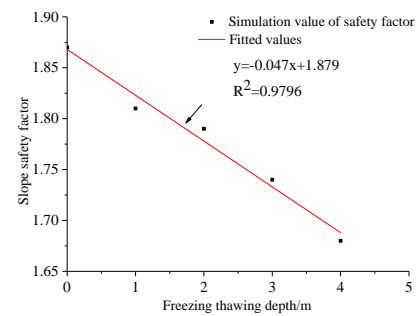


Fig. 20. Relations of the freezing-thawing thickness and safety factor.

Figure 20 shows that the safety factor of the slope is 1.87 in normal state (the freezing-thawing thickness is 0m). The safety factor linearly moves down as the freezing-thawing depth increases. The safety factor is only 1.68 when the freezing-thawing thickness is 4m, and the safety factor decreased by 10%. Therefore, with the expansion of the temperature, the stability of the rock slope decreases.

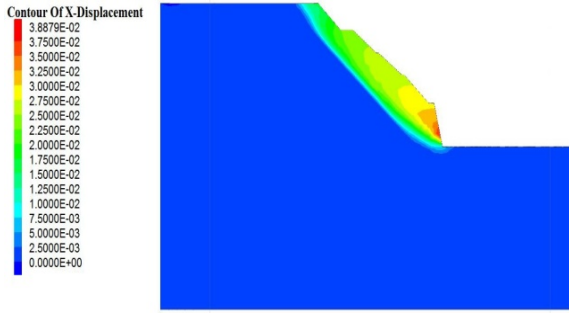


Fig. 21. Displacement vector in x direction of thaw layer which thickness is 2m.

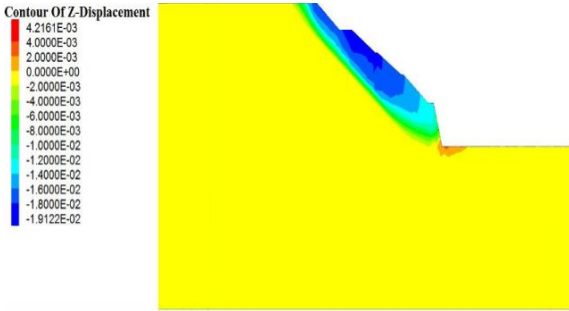


Fig. 22. Displacement vector in z direction of thaw layer which thickness is 2m.

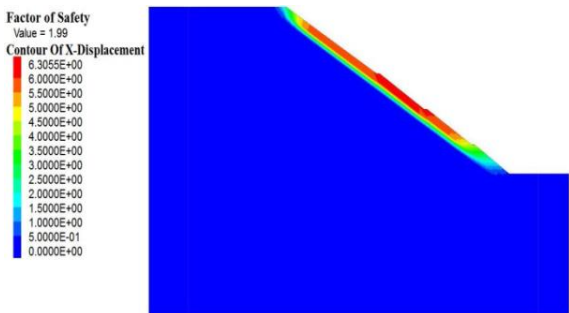


Fig. 23. Displacement contour under the critical state of slope (the water content: 11.80%, the thawing depth: 2m)

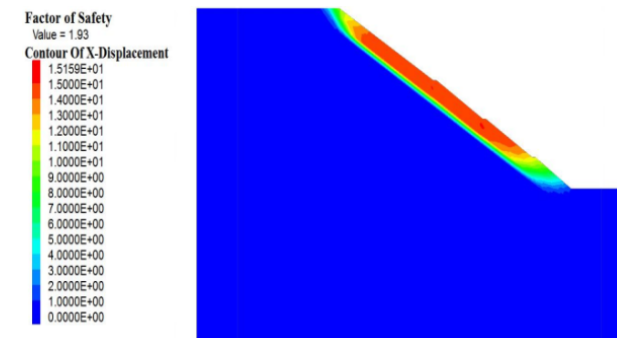


Fig. 24 Displacement contour under the critical state of slope (the water content: 11.80%, the thawing depth: 3m).

As can be seen from figure 21, X direction of displacement gradually increase along the slope downward and obvious stratification at 2m freeze-thaw unstable situation at the critical layer thickness. The maximum displacement in the x direction is located at the foot of the slope, which is located at

the node level of destruction toe. As can be seen from figure 22, the vertical displacement of rock slope mainly concentrated in the top of the hill and gradually reduced along the top of the hill down gradually. Due to the slope of the upper rock mass has a negative displacement, when slope toe will be squeezed, positive displacement in the slope toe.

For soil slope, the melting depth and water content is closely related to the stability of the slope. In order to study moisture content and melting depth effect on the stability of soil slope, the slope stability safety coefficient F_s is obtained by using the strength reduction in moisture content is 11.80%、13.06%、14.17%、15.40%、16.80% and the melting layer thickness in 1-4 m.

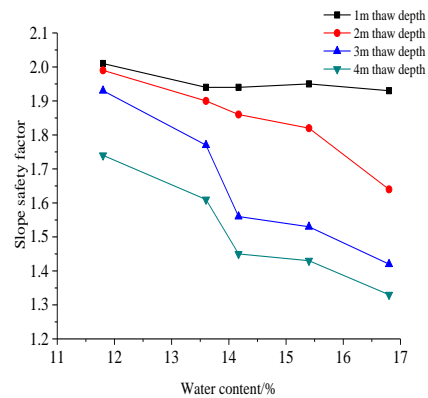


Fig. 25. Relations of the water content and the slope safety factor.

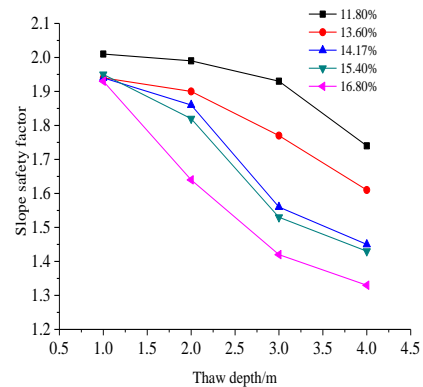


Fig. 26. Relations of the thawing depth and the slope safety factor.

Figure 23 and 24 show that the failure of the soil slope usually occurs in the shallow parts of soil and the slip surface located in the thawing interface. The slip surface gradually moves down as the thawing depth increases. The slipping body in a critical state is a ribbon and some parts of the soil at the foot of the slope has upward trend when the slope is in a thawing state. The reason is that the bottom of the slipping body is arcuate and the soil under the arc gradually moves up due to the pressure of the soil

above the arc. This is consistent with the actual situation of the slipping slope in the hot-thawing state.

Figure 25 shows that the safety factor decreased as the water content increases. However, the variation of the safety factor is not obvious when the thawing depth is 1m. The safety factor is 1.93 and 2.01 when the water content of the slope is 16.80% and 11.80%, and the safety factor decreased by only 4%. Therefore, the slope stability and the water content are less relevant. The impact of the water content to the slope stability becomes obviously as the thawing depth increases. The safety factor is 1.74 and 1.33 when the water content is 11.80% and 16.80%, and the safety factor changed 24%.

Figure 26 shows that the safety factor changed 13.4% when the water content is 11.80% and the thawing depth goes from 1m to 4m. The safety factor changed 31.1% when the water content is 16.80%. The impact of the thawing depth on the slope stability becomes significant as the water content increases. The angle of internal friction and cohesion is mainly determined by the thawing depth and the water content. And the cohesion changed 49% when the water content goes from 11.80% to 16.80% and the angle of internal friction is close. Therefore, the decrease of the cohesion is the essential reason for the slope collapse.

CONCLUSION

This paper makes some research on the slope stability condition under the effect of temperature in cold regions, drawing the following conclusions:

The main influence of external temperature on the temperature field of the slope is shallow part, the shallow part of the temperature cycle changes significantly and the deep part of the temperature field is consistent of the initial temperature field.

In the non phase transition region, the displacement of the slope is similar to that of the change of the environment temperature; Compared to the strong weathered layer, the change of the displacement of the cover layer is more significant.

In the phase transition region, the change of slope displacement is opposite to the change of environment temperature. And under the same temperature change, the deformation of the non phase transformation zone is smaller than that of the phase change region. In the cold regions, the phase transition caused by freezing and thawing cycle is the primary factor causing the deterioration of rock mass.

The stability condition in rock slope and the effect range of freeze-thaw cycle are closely related to the number of freeze-thaw cycles. With the deepening of the freeze-thaw depth, the slope stability safety factor decreased significantly, the influence range of freezing and thawing is closely related to the temperature peak value and the number of freeze-thaw cycles is related to the temperature change cycle. So the lower of the temperature and more frequent changes in the temperature, the worse the slope stability. The stability of soil slope is closely related to water content, and when the water content is lower and the melting depth is lower, the slope stability is not changed much with the normal temperature slope and as the increase of the water content and the depth of melting, the stability of the slope decreases rapidly.

REFERENCES

1. W.Lei, L. Xi-bing, Y. Yan-bo, G.Li. *J. Glaciol. Geocryol.*, **36**(3), 632 (2014).
2. C. Tian-cheng, W. Bing-qian, *J. N.W. Hydroelec. Pow.*, **19**(3), 5 (2003).
3. E.M. Winkler, *Eng. Geo.*, **2**(5), 315 (1968).
4. Y. Kang, Q. Liu, S. Huang, *Col. Reg. Sci. Tech.*, **95**, 19 (2013).
5. Z. You-Wu, G.Dong-Xin, *J. Glaciol. Geocryol.*, **01**, 1,95 (1982).
6. C. Yu-Chao, Y. Gen-She, F. Jian-Bin, *S.X. Archi.*, **32**(14), 82 (2006).
7. N. Fu-Jun, C.Guo-Dong, L. Yuan-Ming, J. De-Wu. *Chi. J. Geotech. Eng.*, **26**(3): 402 (2004).
8. Y.Yan-Xia, Z.Yan-Bo, L. Cai, Y. Hong-ming. *Yangtze Riv.*, **43**(2), 46 (2012)..

Direct synthesis of Mg/Al layered double hydroxide films with different oriented hexagonal platelets via vapor phase transport and hot water treatment

L.-Y. Luan^{1,*}, L.-H. Wang¹, L.-X. Zhao¹, Z.-H. Wang¹, J. Li¹, D.-J. Sun^{2,*}

¹Shandong Provincial Analysis and Test Center, Shandong Academy of Science, Jinan 250014, China.

²Key Laboratory for Colloid and Interface Chemistry of the Education Ministry, Shandong University, Jinan 250100, China

Received February 12, 2016; Revised December 26, 2016

Layered double hydroxide (LDH) films with different oriented LDH platelets have been obtained by vapor phase transport and hot water treatment with amorphous precursors, respectively. The effect of preparation conditions, such as varying the crystal growth temperature, crystal growth time and nucleation method is discussed. Furthermore, the mechanisms of the formation of LDH film are also proposed.

Keywords: Layered double hydroxide (LDH) film, Vapor phase transport, Hot water treatment

AIMS AND BACKGROUND

Layered double hydroxides (LDHs), also known as anionic clays or hydrotalcite-like compounds, are attracted intensive attention because of their potential applications in wide areas, such as catalysts, catalyst supports and nanocomposites [1, 2]. Structurally, LDHs can be characterized as containing brucite-like layers, where some divalent metal cations have been partially substituted by trivalent metal cations to form positively charged sheets. The charge is compensated by exchangeable anions and water molecules in the interlayers [3, 4]. Owing to their structural anisotropy, new techniques have been recently used to prepare crystalline LDH films. If high quality LDH films can be obtained, their unique electronic, optical and magnetic properties will lead to potential applications in optics, membrane and sensors devices [5]. Pinnavaia et al. [6] have reported that transparent LDH films can be formed by the colloidal LDH suspensions provided through hydrolysis of alkoxide-intercalated LDH derivatives. By the sol-gel process and hot water treatment with the amorphous mixed metal oxides, Yamaguchi et al. have prepared LDH films with high transparency [7, 8]. However, most of the obtained LDH films were not well oriented because these methods were hard to control the orientation of the LDH crystals. In addition, these investigations were only focused on the surface morphologies and properties of the obtained films, but not related to the crystal growth process in course of the formation of LDH films. To explore the crystal growth mechanism of LDH platelets or to observe the

assembly of nanosized inorganic particles on solid surface, high quality oriented LDH films originated from amorphous precursors directly is favorable. The preparation method developed in this study for fabricating well oriented LDH thin films including a low temperature deposition (a sol-gel transition) followed by hot water treatment (dissolution-precipitation) and vapor phase transport (VPT). According to Xu et al. [9, 10], who first proposed to produce crystalline zeolite by vapor phase transport via the introduction of a vapor mixture with an amorphous dry gel, we tried to vary the nucleation conditions by replacing the hot water with water vapor. Amazingly, these two kinds of treatments with amorphous LDH precursors gave rise to LDH films with different oriented hexagonal platelets.

EXPERIMENTAL PART

Preparation of amorphous precursors

The synthesis of colloidal Mg₂Al-LDH was carried out by a non-steady coprecipitation method [11]. As contrast, we replaced the room temperature deionized water by ice water (3-5 °C). The pH of an aqueous solution of mixed magnesium and aluminium chlorides (total metal concentration 0.5 M, Mg/Al molar ratio 2:1) was raised to 9.5 by adding diluted aqueous ammonia (1:4 (v/v)) under vigorous stirring. The obtained precipitate was aged in ice bath for 45 min. After filtration, the filter cake was washed thoroughly with ice water to pH about 7.5, and then collected, diluted to 2 wt% and dripped on glass and mica substrates for XRD and SEM measurements, respectively. The coated substrates were dried at the same temperature as the precipitates prepared. After that, one part of the coated substrates were immersed in hot water at 65

* To whom all correspondence should be sent:

E-mail sdilly916@126.com, djsun@sdu.edu.cn

°C and 80 °C, respectively, and the others were placed on the supporter of the autoclave whose bottom was filled with deionized water. The autoclave was closed in an oven at 80 °C, 90 °C and 110 °C, respectively. The water vapor forms during heating. After an enough crystallization time of 24h, the substrates were taken out of the reactor and dried at room temperature.

Characterization

Powder X-ray diffraction patterns (XRD) were collected using a Rigaku D/MAX-rA X-ray diffractometer with Cu K α radiation ($\lambda = 1.54184 \text{ \AA}$). The surface morphologies of the Mg₂Al-LDH film were characterized by a JSM-6700F field emission scanning electron microscope (FE-SEM) under the following conditions: accelerating voltages (V_{acc}) of 0.5 kV, and emission current of $10 \times 10^{-6} \text{ A}$, a probe current of $7 \times 10^{-12} \text{ A}$ and the samples were all treated by performing conductive over-coating of Pt.

RESULTS AND DISCUSSIONS

Figure 1 shows the XRD patterns of Mg₂Al-LDH film formed at different preparation conditions on the glass substrates. The characteristic peaks of crystalline LDH cannot be found in the XRD pattern (Figure 1a), which indicates the amorphous nature of the freshly prepared samples from coprecipitation with ice water. However, two weak peaks are observed in the freshly prepared samples with room temperature water (Figure 1b), most likely because a slow crystal growth occurs under room temperature in time scale (45 min). These results indicate that amorphous nanoparticles are formed instead of crystalline LDH platelets in the coprecipitation and aging processes, especially when the crystal growth temperature is reduced to about zero. This is important for the investigation of the crystal growth mechanisms from an amorphous precursor. After hot water and VPT treatment (Figure 1c-1g), all the samples have three sharp diffraction peaks corresponding to the diffraction planes of (003), (006) and (009) respectively, typical of hydroxide-like compounds. The basal spacing is 0.785 nm, which agrees well with the published value for Mg₂Al-LDH [12]. The absence of (011) reflections indicates that the samples have high stacking fault density [12], which was not affected by the hot water and VPT treatment. It can be also seen that the intensity of the peak is enhanced while the full width at half maximum is decreased with the increasing of the crystal growth temperature, indicating the crystallinity of LDH platelets is improved.

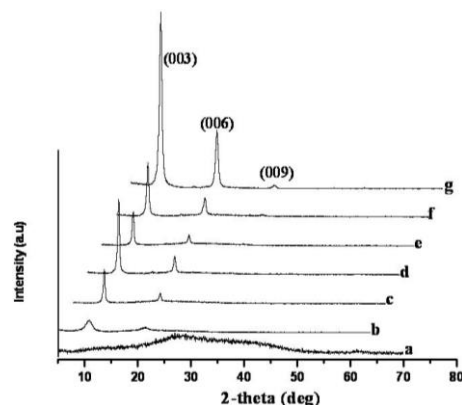


Fig. 1. XRD patterns of Mg₂Al-LDH film formed on glass substrates of freshly prepared LDH with (a) ice water and (b) room temperature water; the same samples as (a) were hot water treatment at: (c) 65 °C, (d) 80 °C for 24h and VPT treatment at: (e) 80 °C; (f) 90 °C; (g) 110 °C for 24h, respectively.

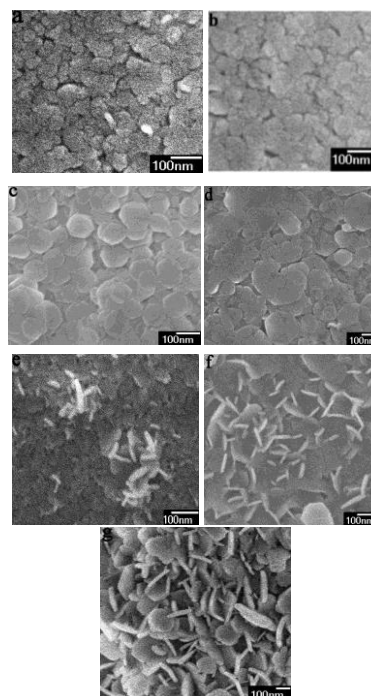


Fig. 2. SEM micrographs of the surface of Mg₂Al-LDH film formed on mica substrates formed of freshly prepared LDH with ice water (a) and room temperature water (b); the same samples as (a) were hot water treatment at: (c) 65 °C, (d) 80 °C for 24h and VPT treatment at: (e) 80 °C; (f) 90 °C; (g) 110 °C for 24h, respectively.

The SEM images of LDH films obtained under different crystal growth temperature and time are shown in figure 2, which also confirmed the crystal growth processes of amorphous Mg₂Al-LDH nanoparticles formed after hot water and VPT treatment. The surface morphologies of LDH films formed by the freshly prepared Mg₂Al-LDH precipitates with ice water (Figure 2a) show that they are amorphous aggregates of many ultrafine

nanoparticles. When the coprecipitation and aging processes were carried out under room temperature (Figure 2b), the nanoparticles become larger and much closer to hexagonal in shape, suggesting the slow nucleation and growth of LDH nanoparticles under room temperature. Obviously, for the investigation of the crystal growth process of LDH films, hot water and VPT treatment with the amorphous film (a) is favorable and useful. After crystallization directly in situ on the substrates by immersing the coated substrates in hot water at 65 °C and 80 °C for 24h, as shown in Figure 2c and 2d, regular hexagonal platelets and well oriented films were formed. As the crystallization temperature increases, the obtained hexagonal LDH platelets become larger with an arrangement of ab-faces parallel to the substrates.

Surprisingly, when the coated substrates were treated with water vapor at 80 °C for 24h, hexagonal platelets were also formed. But the orientation of partial LDH platelets becomes ab-faces vertical to the substrates, as characterized by the “bright areas” in Figure 2e. Furthermore, when the temperature of the water vapor is increased to 90 °C and 110 °C (Figure 2f and 2g), more and more hexagonal platelets on the surfaces of the obtained Mg₂Al-LDH film are vertical to the substrates and form obvious flowerlike structures. This is consistent with the XRD patterns of the obtained LDH films. Such an orientation with ab-faces vertical and the c-axis parallel to the substrates were observed in Ni-Al LDH films, but in their studies the substrates were pre-treated and the nucleation method was hot water treatment [13,14].

Previously, the formation of crystalline LDH platelets was found to occur in the coprecipitation process, as the fast coprecipitation under room temperature led to a number of uniform nuclei. The following hydrothermal treatment was to improve the crystallinity of the LDH particles and to disperse the initial LDH aggregates into colloidal suspensions [15]. Obviously, crystallization in this way is conflict with our original intention to explore the crystal growth mechanisms of LDH platelets from amorphous precursors. Therefore, we reduce the crystallization temperature to about zero (3-5 °C), under which we consider the crystal growth to be frozen, and thus gives rise to amorphous LDH precipitates during coprecipitation and aging processes. In the same way, the initial films on the

substrates prepared by the deposition and drying processes with a sol-gel transition are also regarded as amorphous.

The process of Mg₂Al-LDH film formation on mica substrates with hot water treatment and vapor phase transport are respectively shown in Figure 3. In the early stage of hot water treatment, the particles firstly experience disaggregation, namely the dissolution of amorphous LDH precursor. After that, the growth of the LDH individual crystallites takes place via Ostwald ripening (the so-called 3-D process including dissolution, deposition and diffusion). Small crystallites dissolve and the Mg and Al species deposit onto the bigger crystallites. Meanwhile, the cations diffuse within the hydroxide layers to reduce the lattice defect and form a better crystallized LDH particle. So we can imagine that a stable monodispersed LDH suspension is formed within the vessel, and thus the particles on the surface of the obtained LDH films are uniform. This indicates that hot water treatment at 65 °C for 24h is enough to make the amorphous LDH precursors fully crystallize. However, when the hot water treatment temperature is up to 80 °C, the particles become unhomogeneous because the growth of LDH platelets is increased and reaggregation takes place at higher temperatures. The orientation of hexagonal LDH platelets with ab-faces parallel to the substrates can be attributed to the intrinsic preference of maximum face-to-face contact between the substrates and LDH platelets as well as the adherence of the substrates.

For VPT treatment, the amorphous LDH precursors on the surface of the substrates are actually closed in the water vapor formed during heating, but not brought into contact with the water directly. The water vapor condenses within the dry gel micropores, and thus the upper particles of the amorphous precursors firstly dissolve and crystallization occurs due to a dissolution-reprecipitation process. As a result, the nanoparticles grow outward from the surface of the films with an arrangement vertical to the substrates, which maybe related to the spatial competition between LDH platelets [13]. Although the crystal growth mechanisms under VPT treatment are unclear, these results make us believe that the water vapor has played an important role in controlling the orientations of LDH platelets.

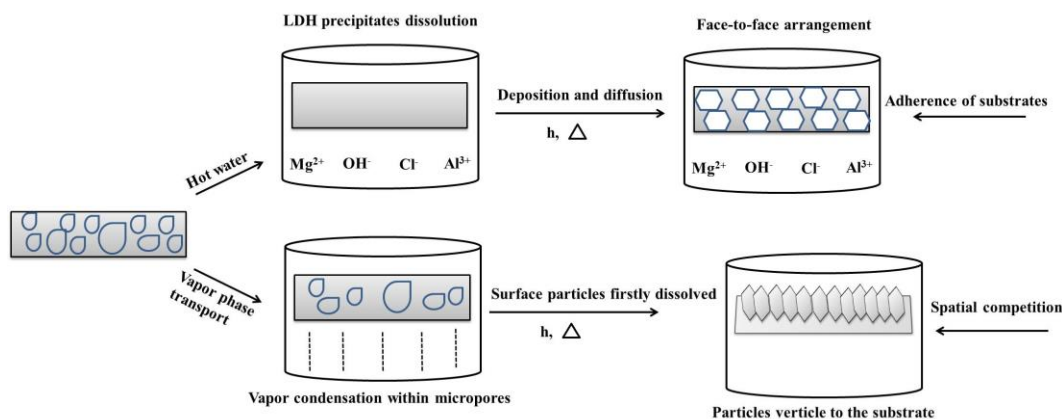


Fig. 3. Schematic of Mg₂Al-LDH film formation on substrates with hot water treatment and vapor phase transport, respectively.

So far as I know, there are rarely reports on the preparation of Mg₂Al-LDH films with VPT treatment from amorphous precursors. However, there are some questions need to be figured out, such as why hot water and VPT treatment result in different arrangement of the hexagonal platelets, how the VPT treatment controls the orientation of the LDH particles? Nevertheless, we provide simple and novel methods to prepare LDH films with different oriented hexagonal platelets. And these questions will be resolved in our further studies.

CONCLUSION

For the applications of LDHs, low costs to manufacturing are very important. Here, we report simple methods to fabricate different oriented Mg₂Al-LDH films via a low-temperature coprecipitation followed by hot water or VPT treatment. The surface morphologies of the produced films are a complex function of many factors, such as crystal growth mechanism, crystallization temperature and crystallization time as well as nucleation and growth environment. For the theoretical studies, the formation of the LDH films can be regarded as the growth of the LDH nanocrystals immobilized on the substrates, which is significant for the investigation of the crystallization process from amorphous precursors. In our further studies, we plan to investigate the optical and magnetic properties of the well oriented LDH films to expand their applications.

Acknowledgment: We acknowledge the financial support from the National Nature Science Foundation of China (21603124) and Shandong Provincial Analysis and Testing Center.

REFERENCES

1. H.C. Greenwell, S. Stackhouse, P.V. Coveney, W. Jones, *J. Phys. Chem. B*, **107**, 3476 (2003).
2. S.P. Newman, S.J. Williams, P.V. Coveney, W. Jones, *J. Phys. Chem. B*, **102**, 6710 (1998).
3. F. Cavani, F. Trifiro, A. Vaccari, *Catal. Today*, **11**, 173 (1991).
4. V. Rives, Ed. Layered Double Hydroxides: Present and Future, Nova Science Publishers: New York, 2001.
5. X.D. Lei, L. Yang, F.Z. Zhang, D.G. Evans, X. Duan, *Chemistry Letters*, **34**, 1610 (2005).
6. E. Gardner, K.M. Huntoon, T.J. Pinnavaia, *Adv. Mater.*, **13**, 1263 (2001).
7. N. Yamaguchi, T. Nakamura, K. Tadanaga, A. Matsuda, T. Minami, M. Tatsumisago. *Crystal Growth & Design*, **6**, 1726 (2006).
8. N. Yamaguchi, D. Ando, K. Tadanaga, M. Tatsumisago, *J. Am. Ceram. Soc.*, **90**, 1940 (2007).
9. W.Y. Xu, J. X. Dong, J.P. Li, J.Q. Li, F. Wu. *J. Chem. Soc. Chem. Commun.*, **8**, 755 (1990).
10. S.G. Thoma, T.M. Neno. *Microporous and Mesoporous Materials*, **41**, 295 (2000).
11. L.Y. Luan, W. Li, S.Y. Liu, D.J. Sun, *Langmuir*, **25**(11), 6349 (2009).
12. M. Bellotto, B. Rebours, O. Clause, J. Lynch, D. Bazin, E. Elkaim, *J. Phys. Chem.*, **100**, 8527 (1996).
13. Z. Lv, F.Z. Zhang, X.D. Lei, L. Yang, D.G. Evans, X. Duan, *Chem. Eng. Sci.*, **62**, 6069 (2007).
14. H.Y. Chen, F.Z. Zhang, T. Chen, S.L. Xu, D.G. Evans, X. Duan, *Chem. Eng. Sci.*, **64**, 2617 (2009).
15. Z.P. Xu, G.S. Stevenson, C.Q. Lu, G.Q. Lu, P.F. Bartlett, P.P. Gray, *J. Am. Chem. Soc.*, **128**, 3 (2006).

Chemical gas leakage source determination using distributed EM algorithm with Gaussian mixture model

Z. Yong^{1,2}, Z. Liyi^{1,2*}, W. Li³, H. Jianfeng², B. Zhe²

¹*School of Electronic Information Engineering, Tianjin University, Tianjin 300072, China*

²*The College of Information, Tianjin University of Commerce, Tianjin 300134, China*

³*The College of Information, Hebei University of Technology, Tianjin 300401, China*

Received February 12, 2016; Revised December 26, 2016

Chemical gas leakage source determination with sensor networks has become a research significance in the pollution environmental monitoring and security protection fields, which also known as gas leakage source parameters estimation. In this paper, we proposed a distributed EM algorithm for the chemical gas leakage source determination, and which was based on Gaussian Mixture model. Simulation results show that the proposed EM algorithm could determinate the gas leakage source localization and emission rate, Compare to the central EM algorithm, the distributed EM method was suggested because it can balance the accuracy performance and energy consumption in the sensor network, and it will get a significant reduction in the required numbers of sensor nodes and less energy to achieve the desired performance with less time, all of that was based on the dynamical adjusting scheme for computing sensor nodes selection.

Keywords: Chemical Gas Leakage Source Determination; Sensor Networks; Gaussian Mixture Model

INTRODUCTION

With the development of chemical industry, the hazardous chemical leakage, especially toxic gas leakage accidents occur occasionally. The leakage source's position and intensity determination has become the key problem to be solved urgently in the emergency rescue. Leakage source detection and determination generally means the process of discovering and tracking the spread of plume and finally determine the location and related parameters of the gas source, usually with "active" searching by sensor networks or mobile robots [1]. The research involves fundamental problems in information processing in sensor networks, detection and estimation, stochastic process, information entropy, artificial intelligence search and node routing planning in the field of information and automation [2-4]. And biomimetic olfaction and computational fluid dynamics and other studies are also related closely [5-7].

Scholars have made unremitting efforts and explorations on the study of leakage sources determination for many years, and achieved some research results. The results were mainly based on the stochastic process theory and probabilistic statistical estimation method, in which, the basic idea is to estimate the occurrence probability of the related leakage accidents. The accident occurred probability determination problem in the designated

location, also generally known as dangerous leakage reconstruction [8,9]. The common methods such as Bayesian inference [10], minimum relative entropy (MRE) [11,12] and statistic induction were often used in the reconstruction of leakage accident inversion. Bayesian inference is the main research method of leakage accident reconstruction and source parameter determination.

At first, the Bayesian inference method makes use of the prior information of the likelihood function and the parameter to get the posterior probability distribution based on the known prior probability distribution. Secondly, the measurement result should be obtained to fit the posterior probability density function distribution, and finally the estimated value of the parameters to be obtained by sampling method. The current research mainly combines the Bayesian inference method with the stochastic Monte Carlo sampling method (MC) or the Markov chain Monte Carlo sampling method (MCMC) to achieve the estimation of source parameters [13,14].

Monte Carlo method was usually easy to converge to local optimal solution, especially when the initial value selected far away from the true value. The limitation is more serious in large-scale spatial hazardous chemical leakage determination studies, which will increase the difficulty of the method [15]. However, when the Bayesian inference method combining with the Monte Carlo method or the Markov chain Monte Carlo method with (the former is abbreviated as BMC, the latter is BMCMC), the probability distribution of iterative updating

* To whom all correspondence should be sent:
E-mail: zhangyong@tjcu.edu.cn

parameters could overcome the Monte Carlo method insufficient. The Markov chain Monte Carlo method (MCMC) extends the application of Bayesian inference to parameter inverse calculation. The Markov chain can be obtained by means of random search, so that the limit distribution of the Markov chain is the posterior probability density function [16,17]. Markov chains of sufficient length can guarantee that the sampling results close to the posterior distribution. Senocak [18], Chow[19] and Kosovic [20] realized that the combination of Bayesian inference and MCMC method can estimate the parameters of the release source with a set of concentration observations, and the parameters estimation results will be reached based on the obtained posterior probability density function of the source parameters (position and intensity) by MCMC sampling. Since MCMC sampling usually takes several thousand iterations to converge to the posterior probability distribution, it is computationally intensive and computationally time-consuming, which is usually not sufficient in an accident contingency.

Keats[21-23], Yee[24] used the convective diffusion equation with the MCMC method to describe the source-receiver association to determine the likelihood function, which resulted in a significant increase in computational efficiency.

Keats [21] used BMCMC method to estimate the location and intensity of the source in a complex urban environment. The results show that the convective diffusion equation and the MCMC sampling method can be used to obtain accurate values of four parameters within a reasonable time. Keats[22] combine the inverse Lagrangian stochastic model with Eulerian type concomitant convection-diffusion equation further, and the source parameters can also be solved in BMCMC under non-conservation conditions quickly. Yee [24] established an adjoint model for Eulerian and Lagrangian type diffusion equations, respectively, in which, the concentration distribution can be calculated directly when the distribution of the source is given, and the computational efficiency can be improved significantly. Yee [25] deduces the source location and intensity with unknown number of leak sources. Guo [29] used an unsteady concomitant transfer model and an advanced numerical scheme (finite volume method) based on adaptive mesh encryption to perform the reconstruction of leakage source in a three-dimensional urban environment. Numerical results show that the application of the unsteady state transfer equation and the MCMC method is very effective, and the introduction of the non-stationary

inversion method can significantly improve the accuracy of the leakage source location in the wind direction.

Because of the time-varying nature of the sensor data and the instability of the initial concentration field, it is necessary to perform a real-time determination method for the leakage source. For example, Johannesson [27] proposed a sequential Monte Carlo (SMC), The Monte Carlo (SMCMC) method to inverse the unstable dynamic system, which further extends the application of Bayesian inference method in the leakage source parameters determination problem. Chinese scholars were also use probability and statistics methods to fulfill the leakage source determination related research. Zhu [28] proposed a method based on Bayesian estimation theory, the ensemble Kalman smoothing and Kalman filtering method for the inverse problem of leakage source. Guo [29] used Bayesian inference combined with Markov chain Monte Carlo sampling method to calculate the gas source in urban area.

The Bayesian-Monte Carlo method has been widely used in the study of leakage source determination of various scales, but it needs to know the prior distribution of parameters at first, and the sampling process of parameter posterior distribution is extremely time consuming, so that the computational efficiency of the determination algorithm should be improved in the event of an happened emergency [30].

The inverse theory has been widely used in the source determination research of groundwater sources [31], earthquake sources [32], sound sources [33], heat sources [34]. In addition, most of the current research has been focused on the application of methods, and the analysis of diffusion patterns and its impact on the real-time and applicability of leakage source determination is seldom involved. Most of them used the static plume Gaussian model with a constant flow conditions, however, the actual flow is more time-varying and dynamic, and the static Gaussian model also has some limitations[35,36], so the real time performance was usually not meet the practical requirements.

Therefore, in this paper, we propose an integrated method for the gas leakage sources rapid determination problem based on the information processing technology of sensor network and the theoretical analysis of mixed Gaussian model. The proposed distributed EM algorithm with Gaussian Mixture models was considered for the distributed determination implementation because of the highly nonlinear diffusion model and the heavily noise corrupted sensor node's measurements. On the other hand, we also gave a computing sensor nodes

modification method for the estimation performance improving and the energy consumption reducing.

The following structure: Section 2, the problem description is given. we analyzed the gas leakage diffusion Gaussian Mixture Model, proposed an distributed EM algorithm for chemical gas leakage source determination. In section 3, we compare the distributed EM method with the central EM method and analyze the simulation results. Section 4, conclusion.

PROBLEM DESCRIPTION

The gas leakage concentration information measured by sensor nodes in the sensor network is generally consistent with a diffusion model. Gaussian model and the model based on turbulent diffusion theory are usually used in the existing gas leakage source determination. Gas leakage concentration diffusion model usually can be described as a stochastic process and the source determination problem can also be known as a gas leakage diffusion model reconstruction problem.

In this paper, we assume that the flow environment is consistent with the Gaussian model distribution and based on the following application of turbulent gas diffusion model.

(1) The positive direction of the x axis is considered as the direction of the wind direction, without considering the obstruction of the obstruction and other effects, assuming that the flow environment is a stable and uniform airflow field;

(2) The main study is to determinate a gas source parameters of source coordinates $\mathbf{r}_s = (x_s, y_s)$ and the estimated value \hat{q} of the source emission rate

(3) A rate of gas release from the gas source;

(4) N sensor nodes were used with a simple dynamic topology distributed in the square area, the location of each node itself was known.

The main goal is to design a determination method to achieve the gas leakage source parameters vector θ estimation via stochastic process information processing and the estimator defined as:

$$\hat{\theta} = [\hat{x}_s, \hat{y}_s, \hat{q}]$$

Where $[\hat{x}_s, \hat{y}_s]$ means the estimator of source coordinates, and \hat{q} is the source emission rate estimator.

Gas Leakage Diffusion Model

In this paper, an approximate analytic model that adapted proposed by Ishida [10] was used:

$$c(\mathbf{r}_i, t) = \frac{q}{2\pi K} \frac{1}{d} \exp\left[-\frac{U}{2K}(d - \Delta x)\right] \quad (1)$$

Where $c(\mathbf{r}_i, t)$ is the concentration at $\mathbf{r}_i = (x_i, y_i)$

and time t ; q is the gas diffusion rate; K is the turbulent diffusion coefficient; U is the wind speed;

$d = \sqrt{(x_i - x_s)^2 + (y_i - y_s)^2}$ is the distance from any point to the gas source, and $\mathbf{r}_i = (x_i, y_i)$ is the current sensor node position.

$\Delta x = (x_s - x_i) \cos \alpha + (y_s - y_i) \sin \alpha$, α is the upwind direction angle with x-axis.

If we take the x-axis as the downwind direction, the equation (1) can be rewritten as:

$$c(\mathbf{r}_i, t) = \frac{q}{2\pi K} \frac{1}{x_i - x_s} \exp\left[-\frac{U}{2K}(d - (x_i - x_s))\right] \quad (2)$$

Figure 2 shows the two-dimensional gas diffusion model under different wind speed and direction. Since the static model based on turbulent diffusion theory introduces the wind direction consideration, and more in line with the simulated environmental conditions. So in this paper, the gas source determination algorithm is mainly based on the Gaussian model and its Mixture models.

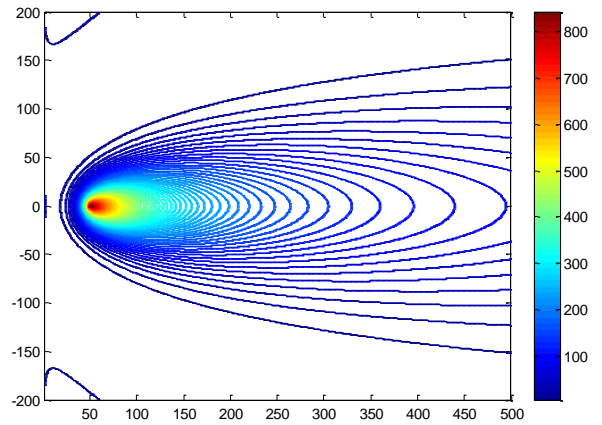


Fig. 1 Gas concentration diffusion in a 400m×500m rectangle area

Figure 1 shows the gas diffusion with equation (2), the gas leakage source location is (50, 0) m, the color bars stand for the diffusion concentration (unit is ppm). And figure 2 gives the diffusion with different wind speed and direction in the field.

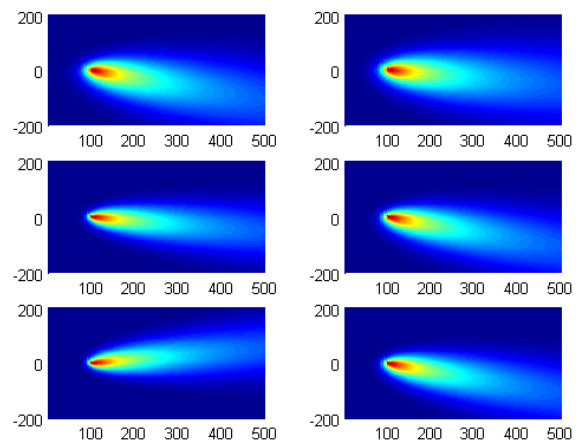


Fig. 2 Diffusion shape with different direction and speed

calculations with the simplicity, thus a complex maximization problem into a series simple maximization problem.

Let $\hat{\theta}_k$ to be the k-th estimator of the maximum likelihood estimate of the representation θ , EM iterative algorithm can be achieved by the following two steps:

Step E: Determine the average log likelihood function for the complete data set z_c :

$$Q(\theta, \hat{\theta}_k) = \int \log p(\theta|z, z_c) p(z_c|\hat{\theta}_k, z) dz_c \quad (10)$$

Step M: Find the largest θ with log-likelihood function of complete data

$$\hat{\theta}_{k+1} = \arg \max_{\theta} Q(\theta, \hat{\theta}_k) \quad (11)$$

The E and M steps are iteratively calculated to obtain the estimated sequence $\hat{\theta}_1, \hat{\theta}_2, \dots, \hat{\theta}_k$ of unknown parameters θ . The final convergence value of the sequence is the maximum likelihood estimator of the unknown parameter θ .

EM algorithm is an iterative algorithm to maximize the expected value, which can be divided into two categories: centralized EM algorithm and distributed EM algorithm. It mainly used in the following two cases:

(1) The observation data is not complete, which due to the limitations of the observation process;

(2) The likelihood function does not resolve, or likelihood function expression is too complex, which will result in maximum likelihood function of the traditional estimation method failure.

As for the second one, the centralized EM algorithm is usually used. Although the method can get more accurate results in the actual calculation, the entire sensor network carries a lot of data communications. Its communication bandwidth and energy have higher requirements, or easily lead to partial network paralysis, especially the sink node and its neighbor nodes. On the other hand, a large number of data traffic congestion will also increase the response time and reduce network efficiency. Therefore, in this paper, we introduce a distributed EM algorithm to effectively solve the problems.

Distributed EM algorithm is an improvement on the centralized EM algorithm, whose main purpose is to reduce the energy consumption of the whole network without affecting the positioning accuracy. The maximum energy consumption in sensor network was the communication cost, the number of nodes involved in the calculation and the inter-node traffic will be reduced with the use of distributed computing method, thus the entire network time life will extend. We proposed the distributed EM algorithm to estimate the maximum likelihood point

to achieve the leakage source, which is based on the leak gas diffusion Gaussian Mixture Model. The algorithm can be divided into two steps: solving the maximum likelihood function and the distributed EM algorithm:

(1) The maximum likelihood function

The process of solving the log-likelihood function is described as follows:

$$p(z|\theta) = \prod_{n=1}^N (\alpha_1 p_1(z|\theta) + \alpha_2 p_2(z|\theta)) \quad (12)$$

take a logarithm on the formula (12):

$$\log p(z|\theta) = \log \alpha_1^N + \sum_{n=1}^N p_1(z_n|\theta) + \log \alpha_2^N + \sum_{n=1}^N p_2(z_n|\theta) \quad (13)$$

The estimated value of θ can be get from the solution of Partial Differential Equation:

$$\frac{\partial \log p(z|\theta)}{\partial \theta_i} = 0 \quad (14)$$

It is difficult to obtain the estimator of θ directly from Eq.(14), so we use the distributed EM algorithm to estimate the unknown parameters in the GMM model. According to Eq. (12) and Eq. (13), the EM iterative algorithm for Gaussian Mixture model parameters is:

$$\hat{\alpha}_{m,i+1} = \frac{1}{N} \sum_{n=1}^N \alpha_i(\theta_m|z_n) = \frac{1}{N} \sum_{n=1}^N \frac{\alpha_m p_m(z_n|\theta_m)}{\sum_{m=1}^2 \alpha_m p_m(z_n|\theta_m)} \quad (15)$$

$$\hat{\theta}_{m,i+1} = \frac{\sum_{n=1}^N \alpha_i(\theta_m|z_n) z_n}{\sum_{n=1}^N \alpha_i(\theta_m|z_n)} \quad (16)$$

Where $\alpha(\theta_m|z) = \frac{\alpha_m p_m(z|\theta_m)}{\sum_{m=1}^2 \alpha_m p_m(z|\theta_m)}$ is the

posteriori probability based on Bayesian theory and $\alpha(\theta_1|z) + \alpha(\theta_2|z) = 1$.

By choosing the reasonable initial value, the maximum likelihood estimation can be obtained using Eqs. (15) and (16). EM algorithm is essentially an iterative algorithm, so two issues should be considered in the estimation of parameters:

(1) the convergence of parameter estimation;

(2) the convergence rate of parameter estimation.

To ensure the convergence of the EM algorithm, it is necessary that the iteration estimate value of the parameters should ensure the likelihood function to be monotonic. The convergence rate of the EM algorithm is usually related to the allowable error level of the initial value and the estimated value. The

chosen initial value α_1, α_2 is a uniformly distributed random number.

Since the observation noise set can be decomposed into the diffusion environmental noise and the turbulence noise, the weighting coefficient satisfies the condition $\alpha_1 + \alpha_2 = 1$.

Therefore, we can improve the iteration of the weighting coefficient by choosing the distribution of $\alpha_1 \sim U(0,1)$, and $\alpha_2 = 1 - \alpha_1$, for the mean and variance convergence rate improvement can be found in the literature [8], simulation shows that this simplification can effectively reduce the number of iterations and improve operational efficiency than traditional EM algorithm.

Distributed EM algorithm is different from the centralized EM algorithm, it does not require all the network nodes to participate in the calculation at the same time, but select the appropriate number of nodes involved in the operation according to the accuracy of the algorithm performance needed, the selected node is called running node set. In this paper, we assume that the N-1 operation node sends $\hat{\theta}_{k-2}$ and $\hat{\theta}_{k-1}$ to node N by communication, and if θ does not converge, it moves on to the next cycle, otherwise, the calculation will stop when the convergence is out of the loop.

Because the EM algorithm has the convergence, as for the distributed EM algorithm, we can say that it also has the convergence. However, due to the limited computing number of nodes and the noise interference, the convergence may be slow in the real calculation. There are two solutions: the number of sensor nodes can be adjusted in real time to improve the convergence rate, such as the use of four nodes involved in the calculation, if not converged in the next cycle, we can use five or six nodes involved in the calculation. This computing nodes increasing method can effectively increase the convergence speed, but also it will increase the energy consumption of the entire network; the other method is the threshold adjusting method, which means that you can increase the threshold to end the calculation if the operation has not converged for a long time. In this paper, the former method is used to solve the slow convergence problem. From the view of communication, the node with information in distributed method only communicates with the neighbor node, while the centralized method needs to communicate all the location information to sink, the former has great advantage in reducing the communication energy consumption. In the simulation experiment, the convergence of the distributed method is obvious and fast, and the problem of the slow convergence is only

theoretically analyzed.

It can be seen that distributed EM algorithm is an effective method for the determination of leakage source, which can reduce the energy consumption of the whole network while ensuring high positioning accuracy with great significance for practical applications.

SIMULATION RESULTS AND VALUATION

It is assumed that the Gaussian Mixture Model distribution is composed of N1 (0, 0.5) and N2 (0, 4) two Gaussian noise random variables, the mixed weighting coefficients are $\alpha_1 = 0.75$ and $\alpha_2 = 1 - 0.75 = 0.25$. Since no Gaussian mixture distribution function is provided in the Matlab tool box, we use the Bernoulli test method to generate the observed data of the GGM model according to Eq. (9). In this paper, the simulation data length is $N = 128$ and the number of iterations is 20. GGM model parameters, after 20 iterations with (16), the estimated values are $\alpha_1 = 0.7493$ and $\alpha_2 = 0.2507$, it is clear that we get a good mixture of the weighted coefficients of the estimated value by the EM estimation.

In order to generate realistic environmental concentration data of the 2-D sensor field, We designed a simulation environment with MATLAB and VC++. As shown in Figure 3 and in Figure 4 the wind speed and direction in the fluent field was given.

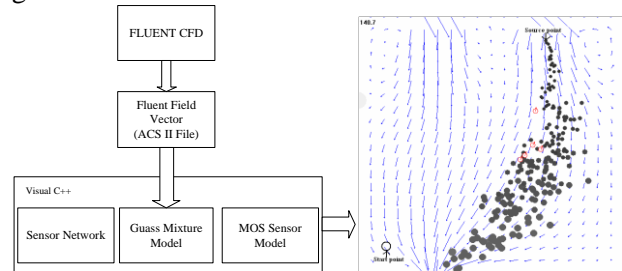


Fig. 3 The realistic environmental of 2-D sensor field

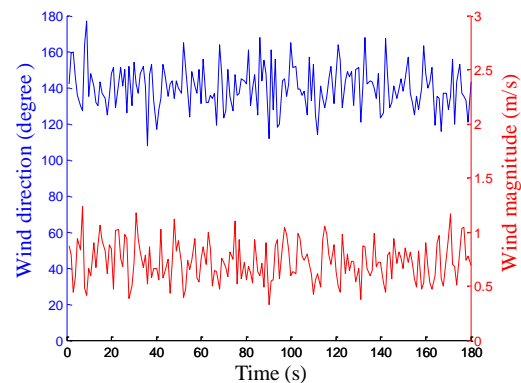


Fig. 4 The fluent field of wind speed and direction data

Figure 4 shows several typical moments of the gas leak source search and determination process in the indoor turbulence environment where the gas leak source is located at (7m, 9m). A red circle with a red arrow indicates the position and attitude of the sensor nodes. The length and direction of the blue arrows indicate the intensity and direction of the wind, respectively. After the gas leak source releases 100s (the number in the upper left corner of each subgraph indicates the time), the sensing node begins to diverge in different directions in the vicinity of the position (1m, 1m). When any node detects the gas concentration, the gas leakage source determination started. In Figure 5, the determination process with four time were provided

In order to analyze the performance of the distributed EM method, we compare to the central EM algorithm with the estimation errors of chemical gas leakage source's coordinates and emission rate, and the determination speed is also considered.

The trajectories of the chemical gas leakage source determination process with the distributed EM and central EM algorithms were given in Figure 6. The blue points represented the selected nodes that computed the parameters, and the circle with different radius surrounding means the sensor measurement. The source determination process could be started at any sensor node (such as the pink node) and iteratively move to the source field, until the final gas source determination was reached, (68,-45) of the central EM method and (52, 13) of the distributed EM method, which represented by the black star and the green triangle independently.

As for Figure 6, the distributed EM method was better than central EM method with less sensor nodes, faster speed and lower communication in the same time step.

In order to compare the two algorithms more clearly between the determination accuracy and the selected sensors number, we give the performance of the distributed EM and central EM in Figure 7. The determination error of the gas leakage source coordinates and the emission rate with the execution time was shown respectively. The determination accuracy of the distributed EM were higher than the central EM with the same sensor nodes, but the execution time speed was not improved because that the sensor nodes selected was confirmed at each time step.

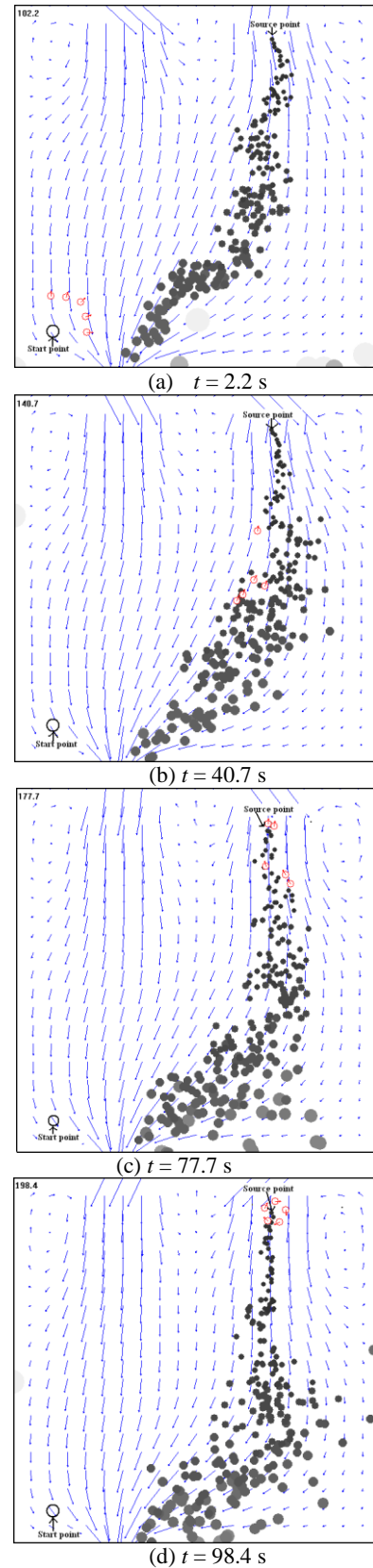
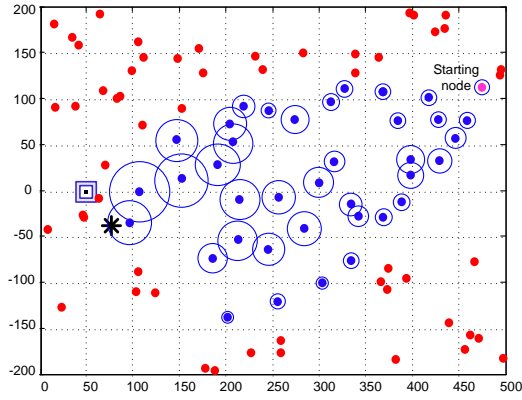
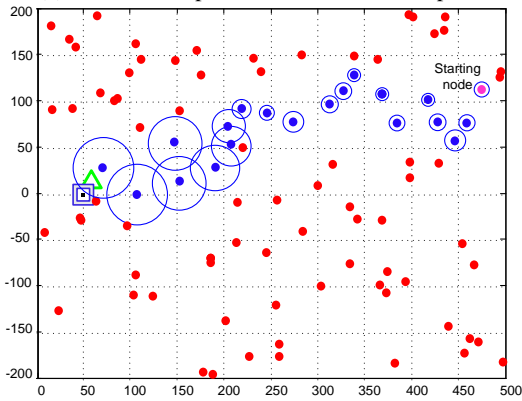


Fig. 5 The determination process



(a) Central EM parameter determination process



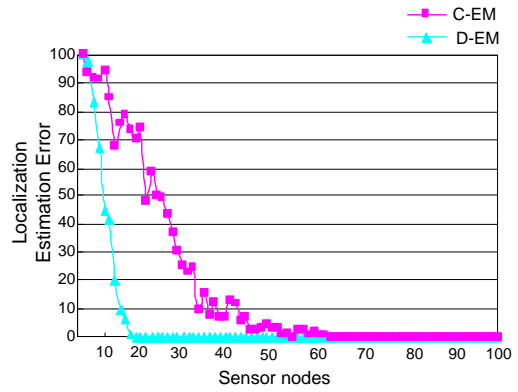
(b) Distributed EM parameter determination process

Fig. 6. An example of the distributed estimation algorithm

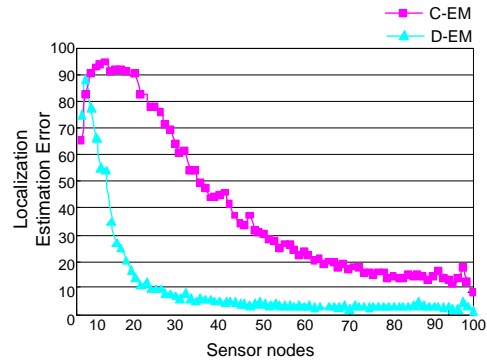
At last, we compared the different approach method with the energy consumption considering, the energy remaining results was shown with the sensor node selected numbers adjusting pattern in the Figure 8.

CONCLUDING

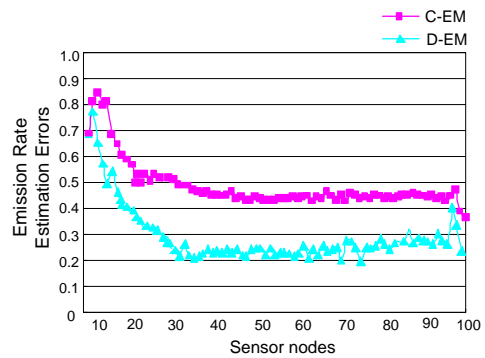
We have presented the distributed EM parameter determination method with Gaussian Mixture model analysis. At the same time, a dynamically adjusting method of sensor nodes selected based on the estimation covariance value was given for the balance of the determination performance and the sensor network consumption. The analysis of the two algorithms had presented with the simulation results. We can see that the distributed EM algorithm was better than central EM method and the nodes number affects the energy consumption and the bias estimation.



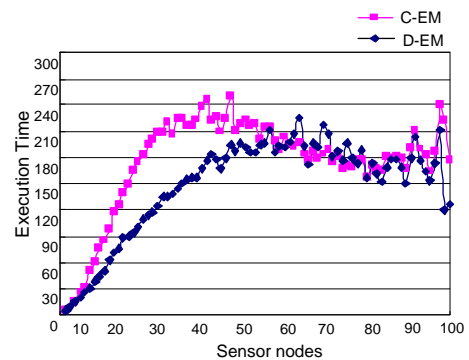
(a) X localization estimation error of the chemical source



(b) Y localization estimation error of the chemical source



(c) The emission rate estimation errors of the chemical source



(d) The execution time of the methods

Fig. 7 Determination error of coordinates and emission rate with the execution time

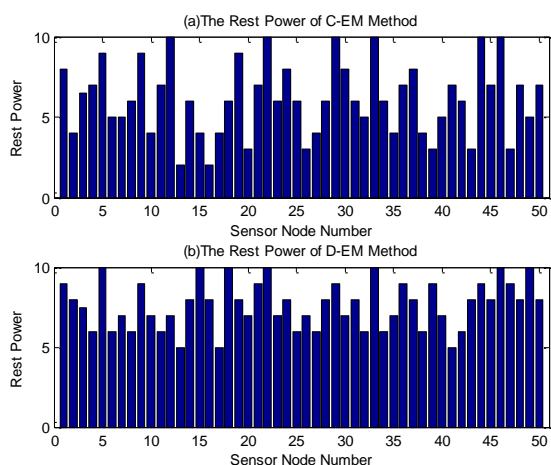


Fig. 8 The energy remaining results of different method

Acknowledgment: The authors wish to thank for the financial support of Natural Science Foundation of China (61573253, 61271321), Tianjin Science and Technology Project (16YFZCGX00360), Tianjin Natural Science Foundation (16JCYBJC16400), The National Training Programs of Innovation and Entrepreneurship for Undergraduates (201610069007), National Natural Science Foundation Foster Project of Tianjin University of Commerce. The corresponding author is Professor Zhang Liyi.

REFERENCES

1. A. Keats, E. Yee, F. S. Lien, *Environmental Modelling and Software*, **25**, 1000 (2010).
2. S. Mitra, S. P. Duttagupta, K. Tuckley, *IEEE International Conference on Industrial Technology*, 349(2012).
3. H. Ruhi, J. Charles, L. Ray, *Environmental Science & Technology*, **46**, 1739 (2012).
4. J. G. Li, Q. H. Meng, Y. Wang, *Autonomous Robots*, **30**(3), 281 (2011).
5. D. Q. Gao, W. Chen, *Sensors and Actuators B*, **120** (2), 584 (2007).
6. M. Ortner, A. Nehorai, A. Jeremic, *IEEE Transactions on Signal Processing*, **55**(6), 2520 (2007).
7. S. Balasubramanian, J. Amamcharla, Panigrahi S, *Food and Bioprocess Technology*, **5**(4), 1206 (2012).
8. D. Ucinski, M. Patan, *International Journal of Applied Mathematics and Computer Science*, **20**(3), 459(2010).
9. S. Capasso, P. Iovino, S. Salvestrini, *Chemosphere*, **73**(4), 614 (2008).
10. K. S. Rao, *Atmospheric Environment*, **41**(33), 6964 (2007).
11. A. D. Woodbury, T. J. Ulrych, *Water Resources Research*, **32**(9), 2671(1996).
12. A. Woodbury, E. Sudicky, T. J. Ulrych, *Journal of Contaminant Hydrology*, **32**(1-2), 131 (1998).
13. X. P. Zheng, Z. Q. Chen, *Chinese Journal of Safety Science*, **20**(5), 29 (2010).
14. X. P. Zheng, Z. Q. Chen, *Journal of Loss Prevention in the Process Industries*, **24**(4), 293 (2011).
15. G. Cervone, P. Franzese, *Computers & Geosciences*, **36**(7), 902 (2010).
16. M. D. Sohn, M. J. Small, *Journal of Environmental Engineering*, **126**(10), 893 (2000).
17. S. S. Qian, C. A. Stow, M. E. Borsuk, *Ecological Modelling*, **159**(2-3), 269 (2003).
18. I. Senocak, N. W. Henuartner, M. B. Short, *Atmospheric Environment*, **42**(33), 7718 (2008).
19. F. K. Chow, B. Kosovic, S. Chan, *Journal of Applied Meteorology and Climatology*, **47**(6), 1553 (2008).
20. B. Kosovic, G. Sugiyama, S. Chan, *9th Annual George Mason University Conference on Atmospheric Transport and Dispersion Modeling*, 2005
21. A. Keats, E. Yee, F. S. Lien, *Atmospheric Environment*, **41**(3), 465 (2007).
22. A. Keats, E. Yee, F. S. Lien, *Ecological Modeling*, **205**(3-4), 437(2007).
23. A. Keats, E. Yee, *Atmospheric Environment*, **43**(3), 510 (2009).
24. A. Keats, F. S. Lien, *Journal of Wind Engineering and Industrial Aerodynamics*, **96**(10-11), 1805 (2008).
25. E. Yee, *Boundary-Layer Meteorology*, **127**(3), 359 (2008).
26. S. D. Guo, R. Yang, H. Zhang, *International Journal of Heat and Mass Transfer*, **52**(17-18), 3955 (2009).
27. G. Johannesson, B. Hanley, J. Nitao, *US: Lawrence Livermore National Laboratory*, 2004
28. J. Zhu, P. Wang, *Atmospheric Science*, **30**(05), 871 (2006).
29. S. D. Guo, R. Yang, *Journal of Tsinghua University (Science and Technology)*, **49**(05), 629 (2009).
30. A. Keats, E. Yee, F. S. Lien, *Environmental Modelling & Software*, **25**(9), 1000 (2010).
31. N. Tian, J. Sun, *Inverse Problems in Science and Engineering*, **19**(2), 181 (2011).
32. P. Mandal, U. Dutta, *Bulletin of the Seismological Society of America*, **101**(4), 1719(2011).
33. A. Levy, S. Gannot, *IEEE Transactions on Audio, Speech, and Language Processing*, **19**(6), 1540 (2011).
34. N. Tian, J. Sun, W. B. Xu, *International Journal of Heat and Mass Transfer*, **54**(17-18), 4110 (2011).
35. J. Matthes, L. Groll, H. B. Keller, *IEEE Transactions on Signal Processing*, **53**(5), 1711 (2005).
36. P. Shuo, J. A. Farrell, *IEEE Transactions on System, Man, and Cybernetics, Part B*, **36** (5), 1068 (2006).

Spatial dynamics of bacterial communities in rural household biogas digesters in different climatic regions of Yunnan plateau, China

B. Yang^{1,2,3}, Q. Li^{1,2,3}, Y. Wu⁴, G. Tian^{1,2,3}, M. Dong⁴, F. Yin^{1,2,3}, X. Zhao^{1,2,3}, Y. Wang⁴, W. Xiao⁴, W. Zhang^{1,2,3*}, X Cui^{4*}

¹Yunnan Research Center of Biogas Technology and Engineering, Yunnan Normal University, Kunming 650500, People's Republic of China

²Engineering and Research Center of Sustainable Development and Utilization of Bioenergy, Ministry of Education, Yunnan Normal University, Kunming 650500, People's Republic of China

³Yunnan Key Laboratory of Rural Energy Engineering, Yunnan Normal University, Kunming 650500, People's Republic of China

⁴Yunnan Institute of Microbiology, State Key Laboratory for Conservation and Utilization of Bio-Resources in Yunnan, Yunnan University, Kunming 650091, People's Republic of China

Received February 12, 2016; Revised December 26, 2016

In order to reveal correlations between spatial dynamics, metabolic pathways and environmental factors of bacterial communities present in household biogas digesters in different climatic regions of Yunnan Plateau, bacterial communities were characterized based on phylogenetic analysis of 16S rRNA sequences and redundancy analysis (RDA) from 4 representatives of the biogas digesters located in 4 different climatic regions. Four 16S rRNA gene clone libraries were constructed from sampled activated sludges, which resulted in a total of 14 bacterial phyla, dominated by *Firmicutes*, *Bacteroidetes*, *Chloroflexi* and *Proteobacteria*. These are responsible for completion of hydrolysis, fermentation, hydrogenesis and acetogenesis in the fermentation metabolic process. RDA analysis identified a positive correlation between the abundances of bacterial communities and environmental temperatures as well as volatile solid contents of the four samples. The results demonstrate that biogas digesters were promoted in tropical and subtropical regions, while organic wastes containing a high VS were utilized as raw materials, because under these conditions the most diverse bacteria are predicted to improve the efficiency of the biogas fermentation system.

Keywords: biogas digester, bacterial community, 16S rRNA gene clone library, spatial dynamic, redundancy analysis (RDA), metabolic pathway.

INTRODUCTION

The biogas fermentation technology has become increasingly popular for mitigation of environmental, agricultural and energy issues [16]. An investigation by the authors towards development and investments in the biogas industry in Yunnan, China, showed that up to 2013, about 3,000,000 rural households made use of a biogas digester, illustrating the increasing role of biogas fermentation for solving rural environmental issues [18], prevention of deforestation [14] and increasing the rural energy supply [3].

The fermentation process to produce biogas depends on microbial activity, with a large fraction of uncultured bacteria typically present in a biogas fermentation system [6], which makes the process a bit like a “black box” [5]. Limited knowledge is available about the basic ecology such as microbial composition, population structure and metabolic pathways of the bacterial communities. The

correlations between bacterial community and environmental factors also remain largely obscure, which makes optimization of the fermentation process difficult, for instance by selection of the right bacterial groups and environmental factors. Traditional microbiological technologies based on growth of pure cultures failed to reveal the typical biological processes of biogas fermentation [19]. Although in recent years microbiologists have utilized methods and technologies traditionally applied to molecular ecology to study the basic principles of biogas fermentation to design high-efficiency systems [25], the understanding of the basic ecological issues of bacterial communities in a biogas fermentation system remains largely unknown, and the biogas digesters of the Yunnan Plateau, which are subject to a variable local climate, are no exception.

Here, for the first time the 16S rRNA gene library technology was utilized to study the diversity and metabolic pathways of bacterial communities in rural household biogas digesters in the Yunnan Plateau. Four samples were analyzed at depth, taken from digesters located in four different climatic regions. A redundancy analysis (RDA) was

To whom all correspondence should be sent:
E-mail: wootichang@163.com; xlcuiynu@aliyun.com

performed to analyse the relationship between the detected bacterial communities and environmental factors. The resulting data present a theoretical basis for design of high-efficiency rural household biogas fermentation systems in Yunnan Plateau.

MATERIALS AND METHODS

Sampling locations

Sampling was performed in four counties of the Yunnan Plateau with different local climates: Jinghong County represents a north tropical tropic climate zone, Jianshui County is south subtropical, Yulong County is in the south temperate zone and Shangri-La County is located in a northern temperate climatic region. In all these four zones, initially activated sludges were sampled from a total of 26 plateau rural household biogas digesters in July and August, 2012. The digesters re-sampled 3 times and samples were stored in 50mL sterile sampling tubes at -80°C in the laboratory prior to analysis.

Pilot experiments assessed the diversity of prokaryotic micro-organisms by denaturing gradient gel electrophoresis (DGGE), which showed that differences in the microbial diversity were not significant for various samples within every climatic region. Therefore, one biogas digester was selected to represent each climate zone, and the active sludge samples of these four digesters were used to construct four 16S rRNA gene clone libraries. Details of these four sampling sites are provided in Table 1.

Analysis of abiotic factors (physical and chemical parameters)

The following physical and chemical parameters of the collected samples have been determined and given in Table 2: pH; total solid (TS) and volatile solid (VS) content as determined by weight [22]; total phosphorus (TP) content measured by the vanadium ammonium molybdate spectrophotometric method [12]; ammonia nitrogen (NH₃-N) content by Nessler's reagent colorimetric method [21]; and chemical oxygen demand (COD) by the potassium dichromate method [9].

DNA extraction, PCR amplification and purification

Total bacterial DNA was extracted from the samples by using the PowerSoil[®] DNA Isolation Kit (MoBio Laboratories, Carlsbad, USA) [27] following instructions of the manufacturer. For PCR amplification of the bacterial 16S rRNA gene, forward primer 27F [24] and reverse primer 1541R [11] were used. The amplification reaction contained 5µL 10×PCR buffer (including 1.5mmol/L Mg²⁺), 4µL dNTP mix (2.5mmol/L each), 5µL BSA (0.1%), 2µL primer 787F (with GC clips, 10pmol/L), 2µL primer 1059R (10pmol/L), 2.5 U Taq DNA polymerase (5 U/µL) and 3µL DNA solution in a total volume of 50µL. The PCR amplification conditions were as follows: pre-degeneration at 94°C for 5 min, followed by 16 cycles of 45 s at 94°C, 45 s at 60-52°C (steps of 0.5°C decrease per cycle), 2 min at 72°C followed, by 9 cycles with 1 min at 94°C, 1 min at 55°C and 1 min at 72°C. A final extension was performed for 10 min at 72°C.

Table 1. Geographical data of the four sampled rural household biogas digesters in Yunnan Plateau, China.

Sample No.	Sampling site	Annual mean temperature (°C)	Longitude	Latitude	Elevation (m)
YN1	Jinghong County	21.9	101°6'E	22°51'N	840
YN2	Jianshui County	18.4	102°89'E	23°70'N	1296
YN3	Yulong County	12.6	100°14'E	26°85'N	2451
YN4	Shangri-La County	5.5	99°77'E	37°78'N	3218

Table 2. Physical and chemical parameters of 4 rural household biogas digesters samples in Yunnan Plateau.

Sample No.	pH	TS (%)	VS (%)	TP (mg/L)	NH ₃ -N (mg/L)	COD (mg/L)
YN1	7.37	11.18	75.10	190.19	231.9	6989.4
YN2	7.68	8.33	74.14	260.15	265.77	17172
YN3	7.27	3.32	68.35	320.63	167.90	13356
YN4	7.63	9.68	53.73	433.28	249.85	25948.8

Amplicons were analysed using DNA gels, excised and purified with SanPrep DNA Gel Extraction Kit (Sangon Biotech, Shanghai, China) according to the manufacturer's instructions.

Construction of 16S rRNA gene clone library

Purified PCR amplification products were ligated into pMD[®] 19-T Vector (TaKaRa, Dalian, China) using a cloning kit and transformed into competent *E. coli* DH5 α [4]. A total of 500 white colonies from each sample were selected randomly for sequence analysis, which was performed by Sangon Biotech (Shanghai) Co., Ltd.

Sequence analysis

Detection of possible chimeras was carried out utilizing Mallard software [1]. Operational Taxonomic Units (OTU) were attributed using DOTUR software [26] with a similarity cutoff $\geq 97\%$ within an OTU. Sequences were then aligned with the best hit found in the GenBank database by Blast [23]. The coverage rate was used to evaluate the sequencing depth of the clone library, which was calculated by utilizing SPADE software [10].

Analysis of the correlation between bacterial communities and environmental factors

A redundancy analysis (RDA) was carried out to

determine correlations between bacterial communities and environmental factors by use of Canoco software [2].

RESULTS

The number of sequences, OTUs, and coverage rate of the samples are presented in Table 3. A total of 1285 bacterial sequences were obtained, which could be divided into 430 OTUs. The average coverage rate of the library was 82.6%. This high coverage indicates that the sequencing depth was sufficient to cover the majority of bacteria present, allowing an indepth analysis of the main bacterial populations present. The results indicate that clear geographical spatial differences exist between the 4 samples.

The obtained sequences were used to query the GenBank database by BLAST. The highest proportion of sequences that could be attributed to a bacterial group was found for YN1; this sample also contained the most diverse population, from which 13 different bacterial phyla were detected, compared to 10 phyla from YN2, 6 from YN3 and 7 from YN4. Approximately 10 to 25% of the sequences could not be attributed to a known phylum (unclassified bacteria). The results are summarized in Table 4

Table 3. OTU identification in the four samples.

Sample No.	Sequence number	OTU number	Coverage rate (%)
YN1	330	108	81.5
YN2	350	127	77.9
YN3	269	80	84.4
YN4	336	115	86.6
Total	1285	430	82.6 (mean)

Table 4. Abundance of bacterial phyla detected in the four samples.

Bacterial phylum	YN1 (%)	YN2 (%)	YN3 (%)	YN4 (%)
<i>Bacteroidetes</i>	23.62	16.88	11.5	11.1
<i>Chloroflexi</i>	21.50	26.07	3.4	0.5
<i>Firmicutes</i>	13.94	13.76	27.5	65.5
<i>Proteobacteria</i>	8.76	10.61	9.1	4.4
<i>Armatimonadetes</i>	2.12	1.44	ND	ND
<i>Synergistetes</i>	1.81	1.44	ND	ND
<i>Planctomycetes</i>	1.20	3.46	ND	3.8
<i>Actinobacteria</i>	1.20	0.57	0.7	1.9
<i>Thermotogae</i>	0.60	0.86	ND	ND
<i>Spirochaetes</i>	ND	0.29	2.6	2.5
<i>Chlorobi</i>	0.30	ND	ND	ND
<i>Verrucomicrobia</i>	0.30	ND	ND	ND
<i>Fusobacteria</i>	0.30	ND	ND	ND
<i>Deinococcus-Thermus</i>	0.30	ND	ND	ND
Unclassified bacteria	24.23	24.92	45.4	10

ND: not detected

The major bacterial phyla detected in all four samples were *Firmicutes*, *Bacteroidetes*, *Chloroflexi* and *Proteobacteria*, which were found in all four samples and also were the most abundant. In total the phylum *Firmicutes* was the most abundant bacterial group detected and included the most OTUs (148), accounting for 34.42% of the total OTUs. However, their relative numbers were only highest for YN3 and YN4. *Firmicutes* are typical inhabitants of anaerobic digested sludge, wastewater treatment bioreactors and faeces [13]. They are responsible for cellulose degradation, hydrolysis of organic matter and degradation of long-chain fatty acid, and often act together with methanogens in anaerobic digestion processes as they produce acetate on which methanogens feed to produce CH₄[13]. The abundance of *Firmicutes* in YN3 and YN4 particularly suggests that the anaerobic process with production of CH₄ based on acetate metabolism occurs in these rural household biogas digesters.

Bacteroidetes were the second most abundant bacteria in the samples. They were the most abundant detected bacteria in this phylum in YN1 and YN2. These organisms are typical for anaerobic environments such as seabeds, intestines and anaerobic reactors where they are responsible for degradation of acids from macromolecular carbohydrates [7]. The third major bacteria detected belonged to the phylum *Chloroflexi*, though their

abundance was only high in YN1 and YN2. *Chloroflexi* use carbohydrates such as glucose and co-occur with hydrogenotrophic methanogens (to which the *Chloroflexi* supply hydrogen)[15]. In turn, these hydrogenotrophic methanogens can produce CH₄ from H₂ and CO₂[15]. It is likely that similar process, resulting in a net reaction of 4H₂ + CO₂→CH₄ + 2H₂O occurs in the sampled rural household biogas digesters YN1 and YN2.

The phylum *Proteobacteria* was the fourth major bacterial group, which are primarily isolated from soil, faeces, anaerobic activated sludge, etc [17]. They are responsible for hydrolysis of starch, long-chain fatty acids, amino acids and so on[17].

DISCUSSION

Metabolic pathways for dominant bacterial groups

The metabolic degradation of organic matter in a typical biogas fermentation process can be divided into 3 stages [24]. During the first stage, bacteria are responsible for hydrolysis and fermentation of organic macromolecules; the second stage is responsible for hydrogenesis and acetogenesis for which other bacteria are responsible, while during the third stage methanogenesis is performed by methanogens [22]. In view of this “3-stage theory” the metabolic pathways for the dominant bacteria detected in the rural household biogas digesters were predicted, as shown in Figure 1.

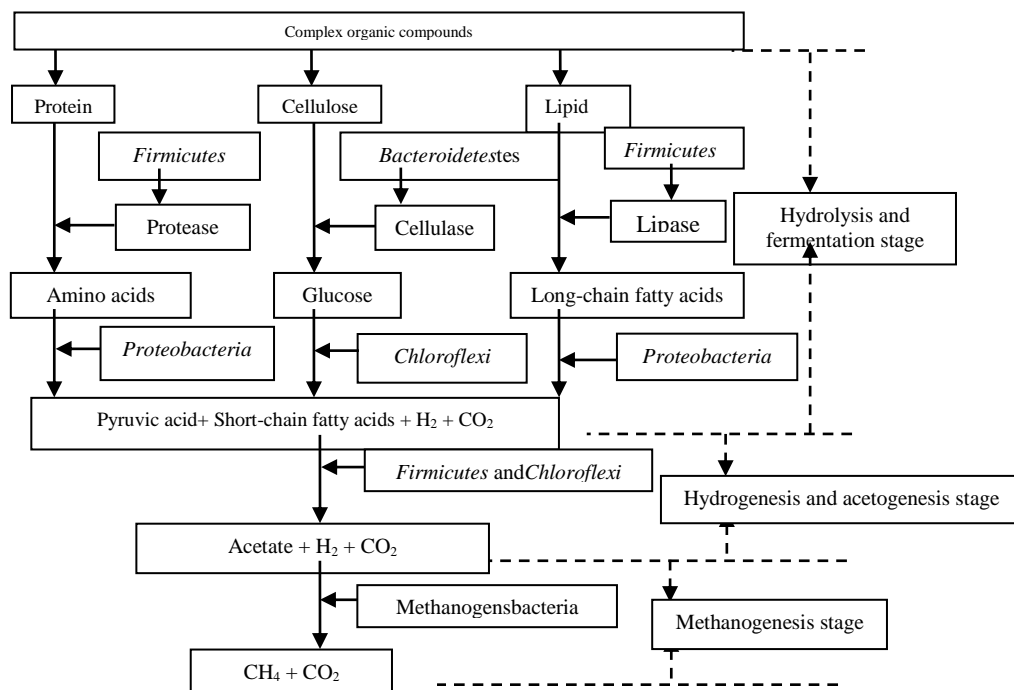


Fig. 1. Predicted metabolic pathways for dominant bacterial groups in rural household biogas digesters in Yunnan Plateau.

The figure illustrates that the fermentation process is complex and depends on multi-flora

cooperative metabolism to completely decompose organic matter into CH₄ and CO₂. Those dominant

bacteria detected in the rural household biogas digesters in Yunnan Plateau are mainly responsible for degradation of complex organic matter in the first stage (hydrolysis and fermentation) and the second stage (hydrogenesis and acetogenesis). These processes would supply the necessary substrates, such as acetate, H₂ and CO₂, for biogas (CH₄) production by methanogens.

Correlation between bacterial communities and environmental factors

A redundancy analysis (RDA) was performed and the findings were biordered with respect to physical and chemical characteristics of the samples, producing a diagram as shown in Figure 2. Now it can be seen that of the 14 detected bacterial phyla, 10 phyla (*Bacteroidetes*, *Chloroflexi*, *Proteobacteria*, *Armatimonadetes*, *Synergistetes*, *Thermotogae*, *Chlorobi*, *Verrucomicrobia*, *Fusobacteria* and *Deinococcus-Thermus*) positively correlated to the annual mean temperature as well as to VS content. The abundance of *Firmicutes* and *Spirochaetes* positively correlated with the TP content as well as to the elevation of the sampled digesters. Further, two phyla (*Actinobacteria* and *Planctomycetes*) positively correlated with COD, pH, TS and NH₃-N content. Restricting the findings to the 4 major bacteria groups, a strong positive correlation was found between abundance of *Bacteroidetes*, *Chloroflexi* and *Proteobacteria* with annual mean temperature as well as VS, while a strong negative correlation existed between the abundance of *Firmicutes* and temperature and VS. The detected correlations between bacterial groups and environmental factors shows that, of the

analysed parameters, atmospheric temperature and VS are the major environmental factors influencing compositions of bacterial communities in rural household biogas digesters in Yunnan Plateau.

Metabolic activities of bacterial groups in biogas digesters are closely related to the local atmospheric temperature [20]. The higher this temperature is, the more robust the metabolism of bacterial groups in a certain temperature range would be [20]. At higher temperatures, growth and enrichment of various bacteria will be stimulated, which could explain the high number of 13 phyla in YN1, which was situated in the tropics (annual mean atmospheric temperature: 21.9°C) compared to 10 phyla in YN2 (from subtropical Jianshui County with an annual mean temperature of 18.4°C) and relatively few phyla from the digesters located in temperate zones. The abundance of various bacterial groups may effectively improve the efficiency of any biogas fermentation system. Thus, we suggest that biogas digesters should be promoted in regions in the tropics and subtropics.

The VS are organic substances found in the raw materials, which support the catabolism of bacterial groups [8]. A high content of VS may promote growth and enrichment of various bacteria groups [8]; it seems to have resulted in more abundant bacterial groups in YN1 and YN2 (VS content 75.10% and 74.14%, respectively), compared to YN3 and YN4 (VS content 68.35% and 53.73%, respectively). Thus, we suggest that biogas fermentation raw materials with a high VS content are optimal for biogas digesters.

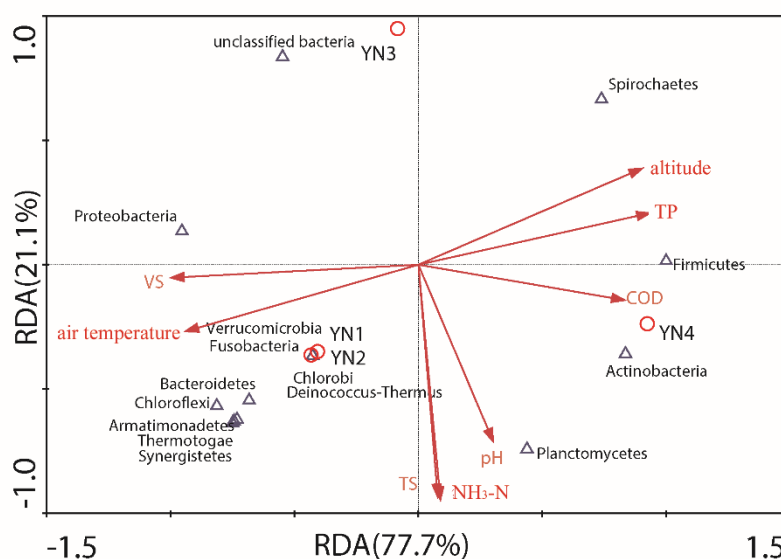


Fig. 2. RDA biordered diagram of the correlation between bacterial groups and environmental factors.

CONCLUSION

The bacterial groups detected in rural household biogas digesters in four different climatic regions of Yunnan Plateau belong to 14 bacterial phyla, of

which *Firmicutes*, *Bacteroidetes*, *Chloroflexi* and *Proteobacteria* are dominant. However, a considerable proportion of detected bacterial sequences belonged to unclassified bacteria. Geographical spatial differences correlated with observed diversities of bacterial groups; the bacterial diversity was significantly higher in samples obtained from digesters located in the northern tropics and southern subtropics than from the south and north temperate zones. In a biogas fermentation microecological system, *Firmicutes*, *Bacteroidetes*, *Chloroflexi* and *Proteobacteria* are the dominant bacterial groups, which are mainly responsible for the hydrolysis and fermentation stage and the hydrogenesis and acetogenesis stage. The atmospheric temperature and VS content were found to be the major environmental factors that influence composition and diversity of bacteria in rural household biogas digesters in Yunnan Plateau.

Acknowledgements: We are thankful for grants from the National Natural Science Foundation of China (NSFC; 31160123/C0309 and 51366015), the Yunnan Provincial Sciences and Technology Platform Promotion Plan (2013DH041), the Specialized Research Fund for Doctoral Program of Universities (20135303110001), Yunnan Province Key Fund of Applied Basic Research (2014FA030), Open Fund from Yunnan Key Laboratory of Rural Energy Engineering (2015KF07) and the Doctoral Candidate Academic Newcomer Award of Yunnan Province. We are also grateful to the staff of the Forestry Bureaus of Jinghong County, Jiangshui County, Yulong County and Shangri-La County.

REFERENCES

1. L.I. Blake, A. Tveit, L. Øvreås, I.M. Head, N.D. Gray, *PLoS ONE*, **10**(6), e0129733 (2015).
2. G.C.D. Carvalho, R.J.D. Sá-Neto, F. Barros, *Scientometrics*, **105**(1), 593 (2015).
3. Y. Chen, G. Yang, S. Sweeney, Y. Feng, *Renew. Sust. Energ. Rev.*, **14**(1), 545 (2010).
4. M. Dong, Y. Wu, Q. Li, G. Tian, B. Yang, Y. Li, L. Zhang, Y. Wang, W. Xiao, F. Yin, X. Zhao, W. Zhang, X. Cui, *Curr. Microbiol.*, **70**(5), 679 (2015).
5. G. Collins, S. Kavanagh, S. McHugh, S. Connaughton, A. Kearney, O. Rice, C. Carrigg, C. Scully, N. Bhreathnach, T. Mahony, P. Madden, A.M. Enright, V. O'Flaherty, *J. Environ. Sci. Heal. A*, **41**(5), 897 (2006).
6. J. Hofman-Bang, D. Zheng, P. Westermann, B.K. Ahring, L. Raskin, *Adv. Biochem. Eng. Biotechnol.*, **81**(81), 151 (2003).
7. K. Kampmann, S. Ratering, T. Kramer, M. Schmidt, W. Zerr, S. Schnell, *Appl. Environ. Microbiol.*, **78**(7), 2106 (2012).
8. A. Khalid, M. Arshad, M. Anjum, T. Mahmood, L. Dawson, *Waste Manage.*, **31**(8), 1737 (2011).
9. E. Orlofsky, N. Bernstein, M. Sacks, A. Vonshak, M. Benami, A. Kundu, M. Maki, W. Smith, S. Wuertz, K. Shapiro, O. Gillor, *Agr. Ecosyst. Environ.*, **215**, 140 (2016).
10. W.J. Liu, Z.H. Sun, Y.B. Zhang, C.L. Zhang, Menghebilige, M. Yang, T.S. Sun, Q.H. Bao, W. Chen, *J. Dairy Sci.*, **95**(3), 1064 (2012).
11. N. Massalha, A. Brenner, C. Sheindorf, I. Sabbah, *Water Res.*, **63**(7), 42 (2014).
12. J.J. Maynard, R.A. Dahlgren, A.T. O'Geen, *Ecol. Eng.*, **47**(5), 221 (2012).
13. T. Narihiro, T. Terada, K. Kikuchi, A. Iguchi, M. Ikeda, T. Yamauchi, K. Shiraishi, Y. Kamagata, K. Nakamura, Y. Sekiguchi, *Microbes Environ.*, **24**(2), 88 (2009).
14. A. Ni, *China Health Rev.*, **3**, 7 (2012).
15. P.B. Pope, V. Vivekanand, V.G.H. Eijsink, S.J. Horn, *3 Biotech*, **3**(5), 407 (2013).
16. J. Popp, Z. Lakner, M. Harangi-Rákos, M. Fári, *Renew. Sust. Energ. Rev.*, **32**(32), 559 (2014).
17. G. Rastogi, D.R. Ranade, T.Y. Yeole, A.K. Gupta, M.S. Patole, Y.S. Shouche, Novel methanotroph diversity evidenced by molecular characterization of particulate methane monooxygenase A (pmoA) genes in a biogas reactor, *Microbiol. Res.*, **164**(5), 536 (2009).
18. G.V. Rupf, P.A. Bahri, K. Boer, M.P. McHenry, *Renew. Sust. Energ. Rev.*, **52**, 468-476 (2015).
19. J.L. Sanz, T. Köchling, *Process Biochem.*, **42**(2), 119 (2007).
20. F.A. Shah, Q. Mahmood, M.M. Shah, A. Pervez, S.A. Asad, *Shah. World J. 2014*, Article ID 183752 (2014).
21. Q. Xu, X. Jin, Z. Ma, H. Tao, J.H. Ko, *Bioresour. Technol.*, **168**(3), 92 (2014).
22. Z.J. Zhang, J. Zhu, *Agr. Ecosyst. Environ.*, **105**(1), 115 (2005).
23. M.J. Rivera, C. Rodriguez-Saona, A. Egizi, D.M. Fonseca, D.E. Jennings, A.M. Koppenhöfer, *Agr. Ecosyst. Environ.*, **222**, 148-155 (2016).
24. S.T. DuPont, S.W. Culman, H. Ferris, D.H. Buckley, J.D. Glover, *Agr. Ecosyst. Environ.*, **137**(1), 25 (2010).
25. G. Tian, Q. Li, M. Dong, Y. Wu, B. Yang, L. Zhang, Y. Li, F. Yin, X. Zhao, Y. Wang, W. Xiao, X. Cui, W. Zhang, *Environ. Sci. Pollut. Res.*, **23**(11), 11137 (2016).
26. L. Zhou, Y. Wang, X.E. Long, J. Guo, G. Zhu, *FEMS Microbiol. Lett.*, **360** (1), 33 (2014).
27. J. Wang, D. Zhang, L. Zhang, J. Li, W. Raza, Q. Huang, Q. Shen, *Agr. Ecosyst. Environ.*, **216**, 116 (2016).

Numerical simulation analysis of flow and heat transfer of supercritical LNG in the IFV condenser

Y. Shouguang^{1*}, X. Wenjie¹, Y. Yong², Z. Lianwei²

¹ Jiangsu University of Science and Technology, Zhenjiang 212003, China

² CSSC Shenghui Equipment CO., LTD, Zhangjiagang 215600, China

Received February 12, 2016; Revised December 26, 2016

With the development of the technology of storage, transportation and utilization of liquefied natural gas (LNG), the effective and energy-saving gasification equipments had become research hotspot. In order to obtain the characteristics and laws of the flow and heat transfer process of LNG in the intermediate fluid vaporizer (IFV) condenser and provide theoretical basis for optimal design and operation of IFV condenser, Fluent software was used to numerically simulate the flow and heat transfer process of supercritical LNG in IFV condenser. The influences of LNG mass flow rate and operating pressure on the heat transfer process were analyzed emphatically. Simulation results showed that the heat transfer process could be enhanced in the critical region, but it was not conducive to the convective heat transfer in supercritical state. It appeared the phenomenon of heat transfer deterioration in the second half of the heat exchange tube, especially under the condition of low mass flow rate. Increased mass flow rate could enhance heat transfer, which effectively improved the phenomenon of heat transfer deterioration. The average surface heat transfer coefficient was improved by 13.56%, which was caused by the increase of the average mass flow rate of 0.01 kg/s. Increased operating pressure made the average surface heat transfer coefficient lower, and the average surface heat transfer coefficient was decreased by 1%, which was caused by the increase of the average operating pressure of 0.5 MPa. When the operating pressure was greater than 7.0 MPa, the phenomenon of heat transfer enhancement in the critical region disappeared, and the surface heat transfer coefficient decreased continuously.

Keywords: supercritical fluid; IFV; numerical simulation; LNG

INTRODUCTION

Natural gas (NG), a kind of clean energy, is gradually into the public eyes. The large quantity of NG transportation and storage can be realized by liquefied natural gas (LNG), which means that it is necessary to solve the problem of LNG storage and gasification before large scale applications. Therefore, the effective and energy-saving gasification equipments have become research hotspot. Intermediate fluid vaporizer (IFV), a kind of vaporizer with the intermediate heat transfer medium, is mainly composed of three heat exchangers, namely, evaporator, condenser and thermolator. LNG will transform into supercritical fluid when the temperature of LNG exceeds the critical temperature under supercritical pressure in the IFV condenser. Under the supercritical state, the physical parameters of fluid will change sharply, which will have great effects on the heat transfer process. So, the core heat exchange process of IFV is gasification process of LNG under supercritical pressure, which will directly affects the overall heat transfer efficiency of vaporizer and the transmission efficiency of NG. Therefore, it is very

important to analyze the flow and heat transfer process of LNG in the IFV condenser. Pu et al. [1] used different heat transfer correlations to handle three heat transfer processes of IFV, and the influences that mass flow rate of seawater, inlet pressure of LNG and mass flow rate of LNG on the heat transfer process of IFV under various operating conditions were obtained by compiling program and calculation. Liu et al. [2] made the structural optimization design for the existing IFV and proposed a kind of heat exchange tube structure of spiral wound, which contributed to the increase of the compactness and pressure bearing capacity of heat exchange tube bundles. Lee et al. [3] further studied the phase-change heat transfer characteristics of hydrocarbon refrigerants, and the experimental research results of hydrocarbon refrigerants were analyzed comparing with the results of R22. Song et al. [4] carried out the simulation research of the heat transfer process of sub-cooled intermediate fluid by Fluent and studied the influence of different inclination angles of heat exchange tube on the heat transfer process.

Currently, the research on the heat transfer process of supercritical fluid is mainly focused on carbon dioxide and water, but the research on supercritical LNG is relatively few. S. M. Liao and T. S. Zhao [5] studied the flow and heat transfer

* To whom all correspondence should be sent:
E-mail zjyaosg@126.com

process of supercritical carbon dioxide in vertical micro channel by numerical simulation. The velocity field, temperature field and drag coefficient of fluid in the pipe with four different diameters were analyzed respectively under the condition of gravity, heating and cooling. The results showed that the influence of buoyancy on heat transfer process is very large, and it could not be ignored in the simulation process. Yang et al. [6] studied the convective heat transfer of supercritical carbon dioxide in different inclined angles by numerical simulation. Considering the effects of buoyancy on the heat transfer process, through the analysis of temperature field, secondary flow, surface heat transfer coefficient and other parameters, the conclusion that the surface heat transfer coefficient decreased with the increase of the inclination angles of the heat exchange tubes was drawn. Li et al. [7] used Fluent software to simulate the flow and heat transfer process of supercritical LNG in vertical circular tube and analyzed the heat transfer performance of methane under different heat exchange tubes. The flow and heat transfer correlations of supercritical methane in different structures were obtained.

Based on the above research, this paper took the single heat exchange tube in IFV condenser as the research object. The numerical simulation and analysis of the flow and heat transfer process of LNG were carried out by Fluent. Taking into account the effects of gravity and buoyancy, the influences of mass flow rate of LNG and operating pressure on the heat transfer process of IFV condenser were studied respectively, and the characteristics and laws of the flow and heat transfer process of LNG were obtained, which provided theoretical basis for optimal design and operation of IFV condenser.

ESTABLISHMENT OF ANALYSIS MODEL

Physical model

To get the physical model of the IFV condenser, this paper made the following assumptions and simplifications:

- (1) The flow of the fluid in the heat exchange tube was stable, and the pressure loss was ignored.
- (2) The number of heat exchange tubes in the condenser is numerous, but the flow and heat transfer process of the fluid in each tube is basically similar. Therefore, this paper took single heat exchange tube of the condenser as the research object.
- (3) The saturated propane steam of condenser releases latent heat of condensation to heat the

LNG in the heat exchange tubes. Therefore, it can be considered that the outer wall of the heat exchange tube is a uniform wall temperature boundary condition [8].

The simplified physical model is shown in Fig. 1. The design parameters of IFV were chosen in the literature [9]. The length of the heat exchange tube is 6000 mm. The outside diameter is 19 mm, and the inside diameter is 15 mm, and the straight tube spacing is 38 mm.

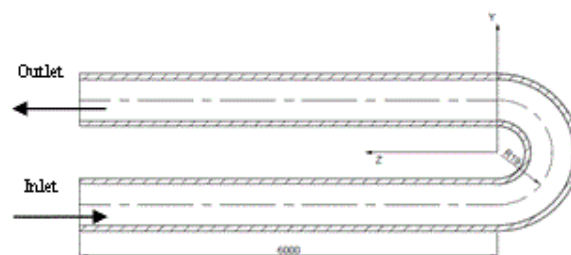


Fig. 1. Sketch map of physical model.

Physical property setting

LNG is a multicomponent mixture, mainly composed of methane, ethane, propane and nitrogen, and methane has the highest percentage of the total [10]. Therefore, this paper used methane to replace LNG in numerical simulation, and the error was within the allowable range of the project [7]. The change of the physical properties of methane under the supercritical pressure was described by linear interpolation function (piecewise-linear) of Fluent. The concrete expression formula of linear interpolation function is as follows:

$$\phi(T) = \phi_n + \frac{\phi_{n+1} - \phi_n}{T_{n+1} - T_n} (T - T_n) \quad (1)$$

Contrast the calculation results of the physical properties of methane by linear interpolation functions with the calculation results by RefProp software. The relative error of the calculated value was less than 2% [11], which can satisfy the engineering precision.

Mathematical model

According to the basic governing equations of fluid flow and heat transfer [12, 13, 14], the RNG k-ε turbulence model with high numerical accuracy for supercritical fluid was adopted in the numerical simulation [15]. For the near wall region, enhanced wall function was used to solve the problem of the computational error due to the high Reynolds number model [16].

In the boundary condition, in order to avoid the influence of the temperature change of LNG at the

entrance on the inlet velocity, mass flow inlet was selected as inlet boundary condition, and the inlet temperature was 111.15 K [9]. Because the pressure and temperature at the outlet were unknown, the boundary condition of outlet was set to be free flow condition. The outer surface of the heat exchange tube was set to be the uniform wall temperature boundary condition, and the inner wall of the heat exchange tube was set to be the non slip and fixed wall surface. The annular walls between the inner and outer diameter of the heat exchange tube at the inlet and outlet were set to be adiabatic walls.

Mesh generation and numerical methods

The structured grid was used to divide the whole computation domain. According to the flow field characteristics of the research object, the computation domain was divided into solid and fluid domains, and the fluid-solid coupling treatment was carried out on the contact surface of the solid and fluid domains, so as to realize the fluid-solid coupled heat transfer. The axial and radial grid distributions of the heat exchange tube are shown in Fig. 2 and Fig. 3 respectively. Grid distribution was uniform, and there was no grid distortion. Besides, the grid connection was tight at the junction of the straight pipe and the elbow. The total number of meshes was 3460000, and the worst mesh quality was 0.625.

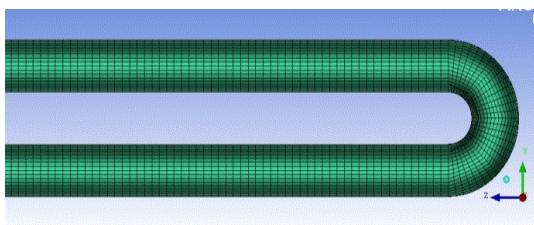


Fig. 2. The axial grid distribution.

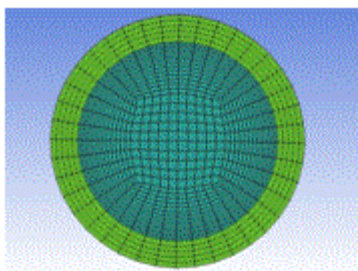


Fig. 3. The radial grid distribution.

The separation algorithm based on pressure of Fluent was chosen to solve the three-dimensional steady flow. The governing equations were discretized by the finite volume method, and the first order upwind scheme was adopted in the discretization scheme. Implicit method was used for the linearization of the equation. The standard

pressure interpolation scheme was used, and the SIMPLE algorithm was used for the pressure-velocity coupling algorithm.

CALCULATION RESULTS

Influence of mass flow rate on the heat transfer process

Under the operating pressure of 6.0 MPa, the influences of four kinds of inlet mass flow rate (0.02 kg/s, 0.03 kg/s, 0.04 kg/s and 0.05 kg/s) on the heat transfer process of methane in the tube were studied respectively, and 0.02 kg/s was the actual working conditions. According to the calculation results of physical properties of methane by the REFPROP software, the results show that the specific heat of methane increased with the increase of temperature under supercritical pressure and appeared maximum value near the critical point, and then decreased with increasing temperature, and finally tended to be stable [11]. In order to facilitate the research and description, the region near the critical point was referred to as critical region, and the region between the critical point and the extreme point of specific heat was defined as critical region.

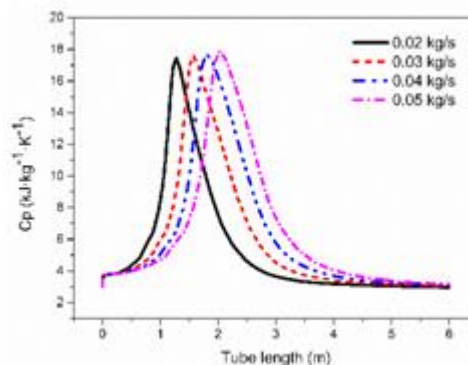


Fig. 4. Curves of specific heat of the fluid near the wall.

Fig. 4 shows the curves of the specific heat of the fluid near the wall inside the tube under four different inlet mass flow rate. As it can be seen, with the increase of mass flow rate, the position of extreme point of specific heat went backwards along the length direction of the tube, but the extreme value did not change. That is because the change of mass flow rate does not affect the physical parameters of methane and only affect the distribution of the physical parameters. It also shows the position of the critical region of methane went backwards with the increase of mass flow rate.

The curves of surface heat transfer coefficient under different mass flow rate are shown in Fig. 5. The comparison of Fig. 4 and Fig. 5 shows that the

position of extreme point of specific heat was very close to the position of extreme point of surface heat transfer coefficient under the same mass flow rate. In the monotonically decreasing region of specific heat, methane was completely transformed into supercritical fluid, and the surface heat transfer coefficient decreased sharply. Even in the second half of the heat exchange tube, it appeared the phenomenon of heat transfer deterioration, especially under conditions of low mass flow rate. With the increase of the inlet mass flow rate, surface heat transfer coefficient at the same position of the tube was significantly improved. The position of heat transfer deterioration went backwards, and the range of heat transfer deterioration became smaller.

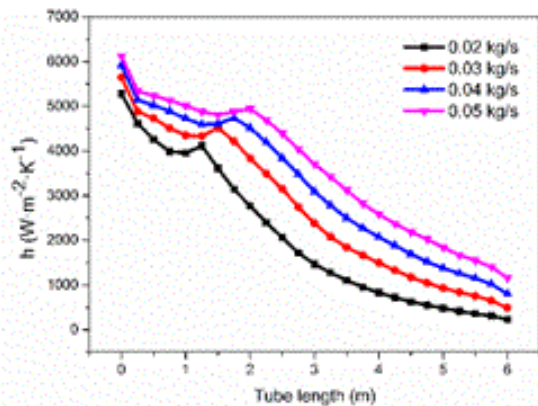


Fig. 5. Curves of surface heat transfer coefficient.

Influence of operating pressure on the heat transfer process

Under the inlet mass flow rate of 0.05 kg/s, the influences of four kinds of operating pressures (6.0 MPa, 6.5 MPa, 7.0 MPa and 7.5 MPa) on the heat transfer process of methane in the tube were studied respectively.

Fig. 6 shows the curves of the specific heat of the fluid near the wall inside the tube under four different operating pressures. It is known that the extreme value of specific heat of methane decreased with the increase of operation pressure. The position of extreme point of specific heat went backwards along the length direction of the tube, and the peak range became larger. This indicates that the critical region of methane went backwards with the increase of the operating pressure.

The curves of surface heat transfer coefficient under different operating pressures are shown in Fig. 7. The comparison of Fig. 6 and Fig. 7 shows that the extreme point of surface heat transfer coefficient was very close to the extreme point of specific heat under the same operating pressure when the operating pressure was less than 7.0 MPa.

In the monotonically decreasing region of specific heat, the surface heat transfer coefficient was decreased continuously, which was not conducive to the convective heat transfer. When the operating pressure was greater than 7.0 MPa, the surface heat transfer coefficient decreased along the tube, and there was no extreme value in the curve of surface heat transfer coefficient.

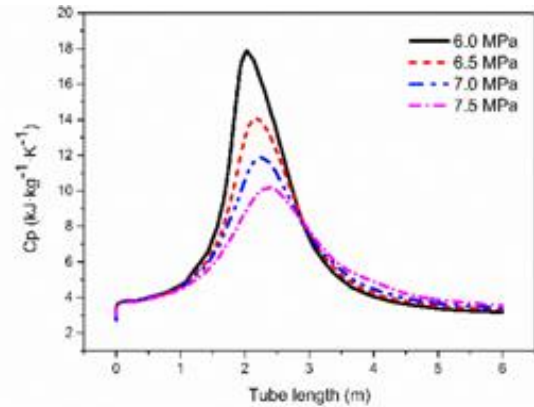


Fig. 6. Curves of specific heat of the fluid near the wall.

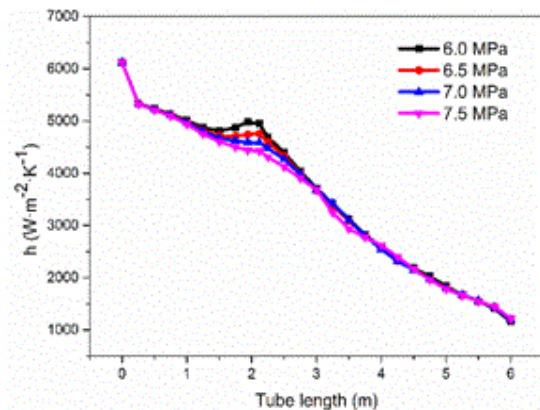


Fig. 7. Curves of surface heat transfer coefficient.

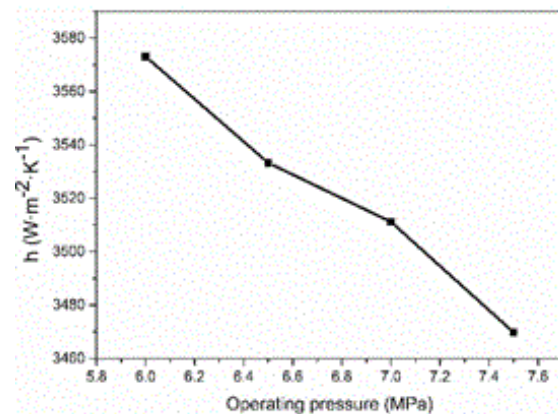


Fig. 8. The curve of average surface heat transfer coefficient.

The comparison of Fig. 6 and Fig. 7 also shows that the surface heat transfer coefficient near the extreme point of specific heat decreased with the

increase of operating pressure, and the surface heat transfer coefficient was little affected by the operating pressure in the region away from the extreme point of specific heat. Because of the differences of the surface heat transfer coefficient under different operating pressures near the extreme point of specific heat, the average surface heat transfer coefficient was decreased with the increase of the operating pressure, as shown in Fig. 8.

DISCUSSION AND ANALYSIS

Main results and findings

In order to obtain the characteristics and laws of the flow and heat transfer process of LNG in the intermediate fluid vaporizer (IFV) condenser, this paper took the single heat exchange tube in IFV condenser as the research object, and Fluent software was used to numerically simulate the flow and heat transfer process of LNG in the three dimensional heat transfer tube. The following main results and findings are obtained:

1) The maximum point of surface heat transfer coefficient was near the extreme point of specific heat of methane. In the monotonically decreasing region of specific heat, the surface heat transfer coefficient was decreased continuously. It appeared the phenomenon of heat transfer deterioration in the second half of the heat exchange tube, especially under conditions of low mass flow rate.

2) Increasing the inlet mass flow rate of LNG made the surface heat transfer coefficient at the same position of the tube significantly improved. The position of heat transfer deterioration went backwards, and the range of heat transfer deterioration became smaller.

3) There was no maximum point in the curve of surface heat transfer coefficient when the operating pressure was greater than 7.0 MPa. The surface heat transfer coefficient near the extreme point of specific heat decreased with the increase of operating pressure, and the operating pressure had little effect on the surface heat transfer coefficient in the region away from the extreme point of specific heat.

Analysis and comparison of the results

According to the Heat Transfer [8], the calculation formulas of Reynolds number, Nusselt number, Prandtl number and mass flow rate are as follows:

$$Re = \rho u d / \mu \quad (2)$$

$$Nu = h d / \lambda \quad (3)$$

$$Pr = \mu c_p / \lambda \quad (4)$$

$$q_m = \rho A u \quad (5)$$

According to the Dittus-Boelter formula, the heat transfer correlation of forced convection heat transfer is as follows when the LNG is heated in tube:

$$Nu = 0.023 Re^{0.8} Pr^{0.4} \quad (6)$$

Formula (2), (3), (4), (5) and (6) formed the simultaneous equations, which can obtain the relation between surface heat transfer coefficient and physical property parameters of fluid, and the relation is expressed as:

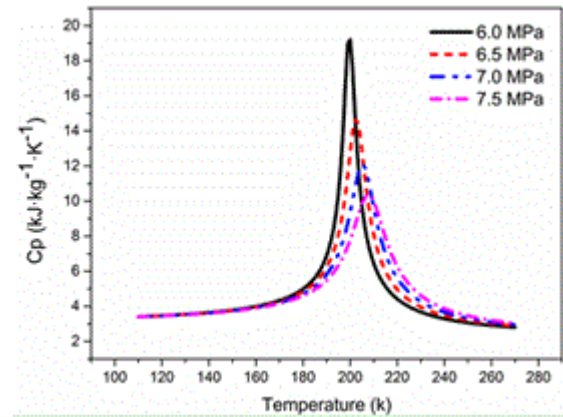
$$h = 0.0279 \lambda^{0.6} \cdot d^{-1.8} \cdot \mu^{-0.4} c_p^{0.4} \cdot q_m^{0.8} \quad (7)$$

It was known that the surface heat transfer coefficient was affected by thermal conductivity, pipe diameter, viscosity, specific heat and mass flow rate by formula (7). However, the surface heat transfer coefficient was only affected by thermal conductivity, viscosity and specific heat when the pipe diameter and mass flow rate were constant. Fig. 9 shows the curves of specific heat, thermal conductivity and viscosity of methane under four kinds of operating pressures. Thermal conductivity and viscosity of methane decreased sharply in the critical region but the specific heat increased sharply in the critical region, as shown in Fig. 9. When the operating pressure was less than 7.0 MPa, the specific heat in the critical region increased by an order of magnitude, however, the viscosity and thermal conductivity decreased within the same order of magnitude. According to the formula (7), in the critical region, specific heat was the main factors that affected the surface heat transfer coefficient under the same mass flow rate. Because of the changing trends and characteristics of specific heat near the extreme point, the surface heat transfer coefficient increased in the critical region and appeared the maximum point near the conductivity of the extreme point of specific heat, which indicated that the heat transfer coefficient increased and the heat transfer process was enhanced in the critical region. In the monotonically decreasing region of specific heat, methane was completely transformed into supercritical fluid. The specific heat and thermal methane were both reduced and the viscosity tended to be stable, which made the surface heat transfer coefficient decreased continuously. Especially under the condition of low mass flow rate, the surface heat transfer coefficient was further reduced. Therefore, the phenomenon of heat transfer deterioration occurred when the methane was completely transformed into supercritical fluid

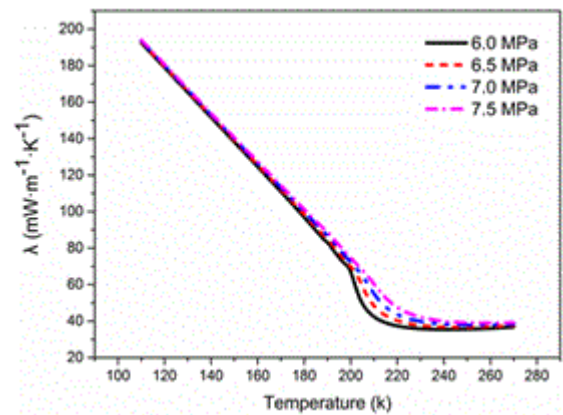
in the second half of the heat exchange tube. When the pressure was greater than 7.0 MPa, the increase of specific heat in the critical region decreased significantly, which made the increasing trend of surface heat transfer coefficient unobvious near the extreme point of specific heat and the extreme point of surface heat transfer coefficient disappeared. Zhou [17] studied the influences of mass flow rate on the heat transfer of supercritical LNG in the horizontal pipe and found that the maximum point of surface heat transfer coefficient occurred in the critical region, but the phenomenon of heat transfer deterioration in the second half of the heat exchange tube was not found under the condition of low mass flow rate. Li et al. [7] studied the characteristics of the flow and heat transfer process of the supercritical LNG in tube. The result that the maximum point of surface heat transfer coefficient occurred in the critical region was successfully predicted by numerical simulation and Dittus-Boelter formula, however, the phenomenon of heat transfer deterioration in the second half of the heat exchange tube was still not found under the condition of low mass flow rate. The above analysis and research showed that the heat transfer process in the tube can be enhanced in the critical region when the operating pressure was less than 7.0 MPa. The flow velocity increased with increase of the mass flow rate, which resulted in the increase of the disturbance of fluid. The thermal boundary layer of the fluid and the velocity boundary layer became thin, which was conducive to the convective heat transfer. Therefore, increasing the inlet mass flow rate of LNG made the surface heat transfer coefficient at the same position of the tube significantly improved. The position of heat transfer deterioration went backwards, and the range of heat transfer deterioration became smaller. Wang et al. [18] found that the increase of mass flow rate of LNG can make the surface heat transfer coefficient increased by analyzing the heat transfer process of supercritical LNG in the IFV. Du et al. [19] obtained the same conclusion as Wang by the numerical simulation of cooling heat transfer to supercritical methane in vertical circular tube. Therefore, it was suggested that the mass flow rate should be improved appropriately to increase the surface heat transfer coefficient and enhance the heat transfer process. Meanwhile, the range of heat transfer deterioration became smaller, and the phenomenon of heat transfer deterioration was improve.

The change of the specific heat under different operating pressures was the most significant near the extreme point of specific heat of methane, as

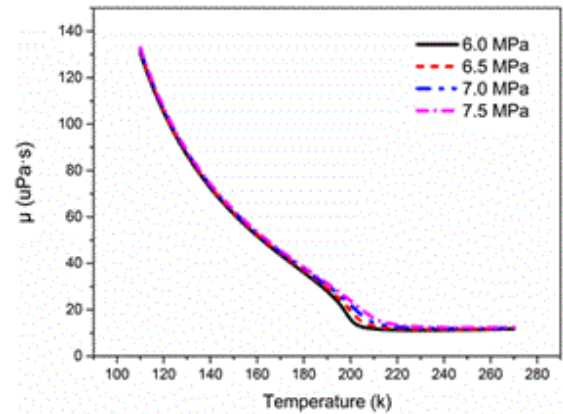
shown in Fig. 9. Thus, near the extreme point of specific heat, surface heat transfer coefficient was mainly affected by specific heat. The specific heat near the extreme point decreased sharply with the increase of operating pressure, which led to the decrease of surface heat transfer coefficient. In the region away from the extreme point of specific heat, the physical properties of methane under different operating pressures were very close, as shown in Fig. 9(a-c).



(a) Specific heat



(b) Thermal conductivity



(c) Viscosity

Fig. 9. Physical properties of methane under different pressures.

Therefore, the change of the operating pressure had little effect on the surface heat transfer

coefficient under the same mass flow rate. Because of the differences of the surface heat transfer coefficient under different operating pressures near the extreme point of specific heat, the average surface heat transfer coefficient was decreased with the increase of operating pressure. Pu [1] also found that the surface heat transfer coefficient decreased with the increase of operating pressure by the thermal performance analysis of IFV for LNG. However, Jin [11] obtained the opposite conclusion that the surface heat transfer coefficient increased with the increase of operating pressure. The reason why Jin got the opposite conclusion might be because of the difference of the heat exchange environment outside the heat exchange tube. Jin studied the flow and heat transfer process of the supercritical LNG in the submerged-combustion vaporizer, whose heat exchange environment outside the heat exchange tube is water bath environment, but the heat exchange environment in this paper is saturated propane steam. Thus, the difference of the heat exchange environment outside the heat exchange tube resulted in the different change laws of surface heat transfer coefficient inside the heat exchange tube.

Due to the limitation of the length of this paper, only the part of straight tube of the heat exchange tube was studied. The flow and heat transfer process of LNG in the elbow part will be further analyzed in the follow-up work.

CONCLUSIONS

In this paper, the flow and heat transfer process of LNG in the IFV condenser was analysed by numerical simulation. The effects of inlet mass flow rate and operating pressure on the flow and heat transfer process were studied respectively. The following conclusions are obtained:

1) The heat transfer process of LNG can be enhanced in the critical region when the operating pressure was less than 7.0 MPa, but it was not conducive for LNG to convective heat transfer in supercritical state. It appeared the phenomenon of heat transfer deterioration in the second half of the heat exchange tube especially under the condition of low mass flow rate.

2) Increased mass flow rate can enhance heat transfer, which effectively improved the phenomenon of heat transfer deterioration. The average surface heat transfer coefficient was improved by 13.56%, which was caused by the increase of the average mass flow rate of 0.01kg/s.

3) Increased operating pressure made the average surface heat transfer coefficient lower, and the average surface heat transfer coefficient was

decreased by 1%, which was caused by the increase of the average operating pressure of 0.5 MPa.

4) When the operating pressure was greater than 7.0 MPa, the phenomenon of heat transfer enhancement in the critical region disappeared, and the surface heat transfer coefficient decreased continuously. It was suggested that the IFV condenser should be operated under the pressure of less than 7.0 MPa.

Acknowledgements: This research was supported by the National high-tech. industrial development project plan (No. 2015-1409).

REFERENCES

1. P. Liang, Q. Zhiguo, B. Yuheng. *Applied Thermal Engineering No 1*, **15**, 564 (2014).
2. L. Fengxia, D. Yuqiang, W. Wei. *China Petroleum Process and Petrochemical Technology*, **15**(1), 564 (2013).
3. L.Ho-Saene, Y. Jung-In, K. Jae-Dol. *Applied Thermal Engineering*, **26**(10), 1054 (2006).
4. S. Yang, J. Xin, L. Wensheng. *Journal of Chemical Industry and Engineering*, **66**(S2), 62 (2015).
5. S. M. Liao, T. S. Zhao. *A Process in Computational Fluid Dynamics*, **2**(2), 144 (2002).
6. Y. Chuanyong, X. Jinliang. *International Journal of Heat and Mass Transfer*, **64**, 212 (2013).
7. L. Zhongzhen, G. Shaolong, T. Wenquan. *Journal of Engineering Thermophysics*, **34**(12), 2314(2013).
8. Y. Shiming, T. Wenquan. *Heat Transfer*. Fourth Edition. High. Education Press, Beijing, 2006.
9. C. Shuangshunag, J. Xin, L. Wensheng. *Refrigeration Technology*, **42**(12), 66(2014).
10. S. Haifeng. *The Calculation and Numerical Simulation of Heat Transfer Regarding Submerged Combustion Vaporizer for LNG*, Beijing University of Civil Engineering and Architecture, Beijing, 2014.
11. J. Shuwu. *Study of Flow and Heat Transfer Characteristics for Transcritical LNG Inner Tube*, Dalian University of Technology, Dalian, 2015.
12. K. Long. *Engineering Fluid Mechanics*. China Power Press, Beijing, 2014.
13. Y. Guojie. *Numerical Simulation of LNG Submerged-Combustion Vaporizer*, Dalian University of Technology, Dalian, 2009.
14. D. Xinghua. *Numerical Simulation of Fluid Flow and Heat Transfer in LNG Submerged-Combustion Vaporizer*, Dalian University of Technology, Dalian, 2007.
15. L. Jun. *The Analysis of Numerical Simulation Method on the Heat Transfer about Supercritical Water in the Vertical Pipe*, Harbin Institute of Technology, Harbin, 2013.
16. J. Bingbing, C. Jinping. *ANSYS ICEM CFD with Detailed Examples of Mesh Technology*. China Water & Power Press, Beijing, 2012.
17. Z. Zhaoyong. *Study of Heat Transfer Characteristics of Methane/Hydrogen Mixture at Supercritical*

- Pressure, Shanghai Jiaotong University, Shanghai, 2014.
18. W. Bojie, K. Yiwu, Q. Chao. *Journal of Chemical Industry and Engineering*, **66**(S2), 220 (2015).
19. D. Zhongxuan, L. Wensheng, G. Anzhong. *Journal of Chemical Industry and Engineering Suppl.*, **66**, 63 (2009).

Laboratory study of compatibility and interaction of scale inhibitor with oilfield chemicals for ASP flooding chain

K. Sun^{1,2}, B. Wang^{1*}, X. Sui¹, S. Feng¹, D. Yuan¹, J. Li¹, C. Liu¹, H. Li¹

¹ College of Chemistry & Chemical Engineering, Northeast Petroleum University, Daqing 163318, Heilongjiang, China

² College of Mechanical & Electronic Information, China University of Geosciences, Wuhan 430074, China

Received February 12, 2016; Revised December 26, 2016

The application of alkaline-surfactant-polymer (ASP) flooding has successfully enhanced oil recovery up to 20% in Daqing oilfields. Most notably, there is a significant obstacle on the scaling deposition along the produced fluid gathering and transportation chain. Firstly exemplified by the scaling of an ASP flooding zone in Daqing oilfield, newly designed and synthesized scaling inhibitors were investigated on the compatibility with the ASP chemicals and treatment agents. By a series of lab studies, the compatibility and interaction of scaling inhibitor with the chemical agents, including surfactant, polymer, defoamer, demulsifier and anti-deposition agent, are clearly exhibited. But the demulsifier changes in slight range. Based the data, the performance and mechanism of the interaction on the chemicals using in the produced fluid treatment are proposed and discussed. In addition, the strategy of chemicals usage, including the injection mode and amount, is suitably specified and adapted for the ASP flooding chain.

Keywords: Compatibility; Enhanced oil recovery; Oilfield chemical; Scale Inhibitor.

INTRODUCTION

Many ASP flooding technologies have successfully and successively been studied and applied to Daqing oilfield [1-2]. Four pilot tests were conducted in order to further enhance oil recovery and collect technical and practical experiences for extending the ASP pilot. It has been revealed that the ASP floods can successfully enhance oil recovery up to 20% in Daqing oilfields [3-4]. With the succession of the ASP flooding, significant obstacles were found during the production of the ASP pilots. Most notably, there is the scaling of produced fluid treatment chain [5]. It is the presence of the scaling deposition that gives rise to numerous problems. The formations of mineral scale deposits upon tubing, casing, perforations, and even the formation face itself, can constrict fluid flow of the treatment chain and thereby curtail the production rate of oil wells.

Oilfield chemicals were injected to an oil chain at different positions from the production to transportation. All the varied sectors in oil production generally were seeking chemicals dependently to assist in special operations, for drilling wells, for producing oil or transporting oil through pipeline. The oil chemicals were used for many purposes such as the defoaming, demulsifying, anti-depositing and scale inhibiting by an addition of varying amounts. The point has generally been accepted that it is not possible for

efficient and cost-effective production of oil without the use of suitable chemicals. So as to a good solution of the scaling deposition, the chemicals were used for in the ASP flooding chain. In the present ASP case, three types of chemicals exist in the produced fluids operation chain composed of the residual flooding chemicals, such as alkaline, surfactant and polymer. Over the last several years, the chemical treatment usages, such as defoamer, demulsifier, scale inhibitor and anti-deposition agent, have increased in the variety and amount, which is apparent in the ASP flooding. The flooding is characterized with produced fluid containing the concentrated silicon ions originated from concentrated alkaline and high viscosity caused from viscous polymer [6]. Generally, the highly concentrated alkaline is pumped in the well in the process of ASP flooding. The strong alkaline causticizes some materials in the oil reservoir. The scaling material is formed in all the touching sectors. This scale is deposited in/on the well or transportation system, resulting in a critical stop of the operation. Additionally, the properties of the produced fluid could be affected by the flooding agents on the same system. This introduces two primary concerns: the difficulty in silicon scale deposition, and the difficulty in demulsification for oil/water separation [6-9].

A present trend can be indicated that the increase in chemicals is due to the fact that oilfields are entering a high scaling operation and increasing requirements for oil treatment and water treatment. The efficient ASP flooding production generally relies on the adaptability and adoption of specific

To whom all correspondence should be sent:
E-mail: wangbaohui60@163.com

chemicals to prevent scale deposition, corrosion, and foaming. Consequently, many works has been done for the application of treatment chemicals for the oil region and ASP flooding chain. In Daqing oilfield, many treatment chemicals have been investigated and developed for the efficient and cost-effective treatment of ASP produced fluid in ASP flooding [7-9]. As a case, the development of the scale inhibitor used in ASP flooding has gone through the single dose to the compounded mixture and from water-suitable agents to especially Si-adapted chemicals [6-9].

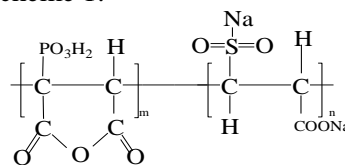
While the performance test is an important step in selecting appropriate chemicals in field applications, the compatibility of the chemicals with the other chemical materials used in the same operation system is critical to performing chemical treatment program. Extensive chemical formulation, laboratory test, and field verification are required to ensure that operation chemicals will compatible with chemicals system adopted to oil/water separation, oil processing and water treatment. In ASP flooding applications, particularly for the developing agents whose performances are not readily accessible without aid of the historical experiences, the compatibility of chemical system with any scale inhibitor is a key part of the effective flow process. Until now, the systematical study on the chemical compatibility has not reported for the ASP flooding chain of Daqing oilfield. This paper focused on compatibility of a developing scale inhibitor, typically applied to the ASP flooding pilot test in Daqing oilfield, with chemical system materials such as the residual chemicals, defoamer, demulsifier and anti-deposition agent. A comprehensive study of scale inhibitor -chemicals interaction and mechanism was implemented and discussed. These compatibility data can enhance the selection process for existing production, optimize material selection, design in the development stage for new chemicals, and facilitate formulation of new products.

EXPERIMENTAL SECTION

Formula and structure of ASP treatment chemicals

Recently, main types of scale inhibitors, such as phosphonate, polyphosphonate, aminopoly-carboxylate and surfactant agent, have been used for an efficient operation in the water flooding and polymer flooding. The current tendency is to research and develop the phosphonate-based polymer with varied functional groups. For meeting the unique requirements presented by the ASP flooding and the environment, a new type of scale

inhibitor has been designed and developed in this study. The formula and structure is schematically shown in scheme 1.



Scheme 1. Formula and structure of the scale inhibitor

The scale inhibitor, consisting of phosphonate, sulfonate and carboxylate groups on the long carbon bone, is a polymer. The soluble Ca, Mg and Ba ions in the ASP fluid can be stoichiometrically chelated by functional groups on the chain to prevent soluble silicon ion from the codeposition.

The defoamer, demulsifier and anti -deposition agent have effectively been adapted and adopted to this flooding treatment system. The compositions are simply illustrated as follows:

Defoamer-Fluorine-grafted polysiloxane (oil soluble);

Demulsifier-Phenolic resin-EO-PO polymer (oil soluble);

Anti-deposition agent-Long carbon chain grafted by phosphonate, sulfonate and carboxylate group;

Polymer-Polyacrylamide, M.W. 2500x104;

Surfactant-Long-chain alkylbenzene sulfonate.

All the chemicals were provided by the oilfield. The chemicals were used in the lab as received without further modification and purification.

Produced water and preparation in experiments

The specific produced fluids employed in the experiment was sampled from a pilot zone of the ASP flooding in Daqing oilfield. Based on the compositions of the produced fluid, the produced water was simulated with the original ion concentrations of 50 ppm Ca^{2+} (Mg^{2+}), 133 ppm CO_3^{2-} , 3184 ppm HCO_3^- and appropriate silicon ion.

Measurement of performance of the scaling inhibitor

The performance of the scaling inhibitor was indicated by an efficiency of the scale inhibiting. According on a standard of the PetroChina Company, the efficiency is evaluated by shown as:

$$E = (C_2 - C_1) / (C_0 - C_1) \times 100\%$$

Where, C_0 is Ca^{2+} concentration of the initial solution, mg/L or ppm; C_1 is Ca^{2+} concentration of the equilibrated solution without adding the scale inhibitor, mg/L or ppm; C_2 is Ca^{2+} concentration of the equilibrated solution with adding the scale inhibitor, mg/L or ppm.

RESULTS AND DISCUSSION

Analysis of produced fluid in ASP flooding system

In the manifold system of the ASP produced fluid, first newly developed scale inhibitor as shown in scheme 1 was injected to individual well, which was transported to a gathering center through mixed flow lines. Then defoamer and demulsifier were added to the system for easy separation of oil and water. The oil stream was inputted to oil processing sector and the water stream was treated by injection of anti-deposition agent. The scale inhibitor entirely got through the gathering and transportation system on the chain. In consequence, the scale inhibitor encountered in the ASP chemicals, defoamer, demulsifier and anti-deposition agent existing in the system. The scale inhibitor will interact with three agents. This is the starting point and final objective for this study.

Effect of polymer on performance of the scale inhibitor

By setting temperature at 50°C, putting 20 ppm scaling inhibitor into the simulated produced water solutions with 50, 100, 200, 300, 400 and 500 ppm polymer, the results of the PAM-effect on the efficiency are shown in Fig.1.

As shown in Fig.1, the efficiency of scaling inhibitor was decreased as the PAM concentration was increased. It means that the PAM polymer can affect the inhibition process. Due to the amount of residual polymer in the solution, the viscosity is increased and the solution flow gets worse. The scaling inhibitor could not be well distributed in the solution for catching the scaling cations. So, the cations can readily be combined with the anions to form the scale sediment.

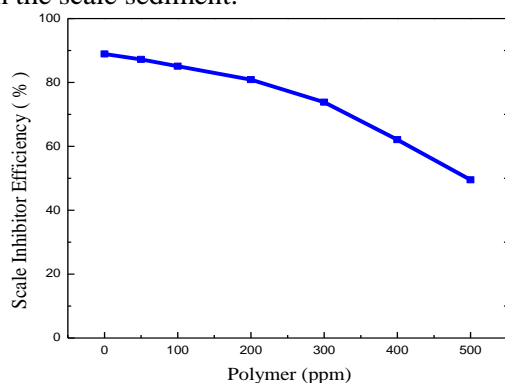


Fig. 1. Effect of polymer on performance of the scale inhibitor

Effect of surfactant on performance of the scale inhibitor

For testing the effect of surfactant on the scaling

inhibitor, 20 ppm of the scale inhibitor was added into the simulated produced water solutions with 50, 100, 150, 200 ppm of surfactant in 50°C. The results are shown as in Fig.2.

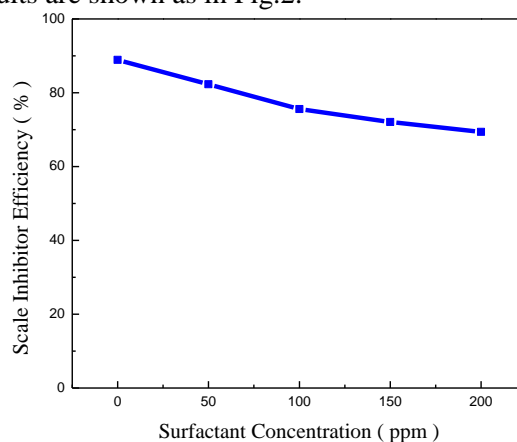


Fig. 2. Effect of surfactant on performance of the scale inhibitor

As indicated in Fig.2, the addition of the surfactant leads to a decrease of the efficiency. Even with the low concentration, the surfactant got worse than the no-adding solution. It is considered to be caused by the surfactant absorption closely with the scaling inhibitor. If the surfactant molecular is absorbed on the long chain of scaling inhibitor molecular, the steric hindrance will get increasing, and the big steric hindrance will get Ca^{2+} difficultly combined with scale inhibitor. As the result, the scale inhibitor efficiency is decreased.

Effect of demulsifier on performance of the scale inhibitor

As shown in Fig.3, 20 ppm of scaling inhibitor was adding into the simulated produced water solutions with 0, 5, 10, 20, 30 and 50 ppm of demulsifier for keeping for 24 hrs in 50°C.

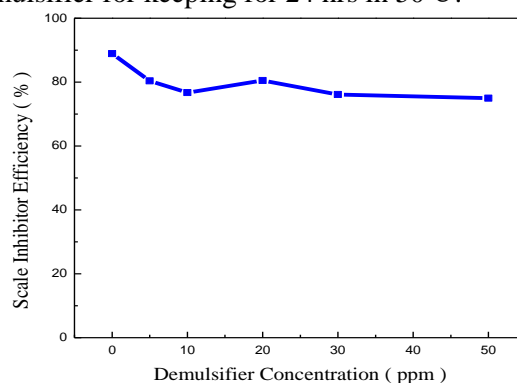


Fig. 3. Effect of demulsifier on performance of the scale inhibitor

As shown in Fig.3, the percentage of the inhibition was slightly decreased. Specifically speaking, the demulsifier makes inhibition

percentage decrease on the small range. This means the appropriate compatibility is presented by two agents by the wide concentrations in this condition.

Effect of defoamer on performance of the scale inhibitor

Firstly by putting 20 ppm of the scale inhibitor into the simulated produced water solutions with 0, 15, 25, 35, 45 and 100 ppm of defoamer in 50°C, then the test for the effect of defoamer on the efficiency was performed. The results are shown as Fig.4.

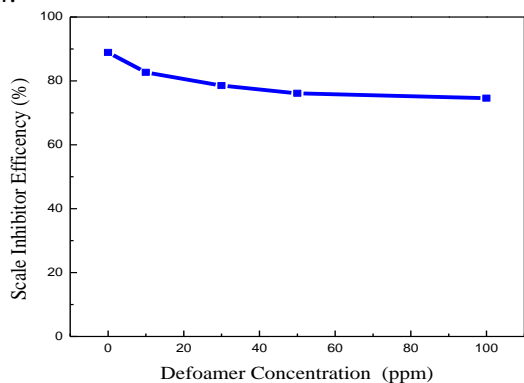


Fig. 4. Effect of defoamer on performance of the scale inhibitor

As demonstrated in Fig.4, the efficiency of the scaling inhibition was decreased with increasing the defoamer concentration. It implies that the addition of defoamer agent will have an impact on the inhibition percentage. If firstly adding the scaling inhibitor (without defoamer), the agent will be complexed efficiently with the Ca²⁺ ions. But the inhibition efficiency was slowly decreased when the defoamer concentration is increasingly added.

The results show the incompatibility of the scale inhibitor with the defoamer, resulting in decreasing the anti-scaling performance in existence of two agents under the condition.

Effect of anti-deposition agent on performance of the scale inhibitor

For testing the influence of anti-deposition agent on the scaling inhibitor, 20 ppm of the scale inhibitor was added into the simulated produced water solutions with 0, 10, 20, 30, 60, 90 ppm of anti-deposition agent in 50°C.

As shown in Fig.5, the results display that the addition of the anti-deposition made the efficiency slightly increasing. Even in very low concentration, the anti-deposition made better than the original solution. The profile of the anti-deposition-scale inhibitor curve exhibits the good compatibility of the scale inhibitor with the anti-deposition agent for leading to lifting scaling performance in existence of two agents under the condition.

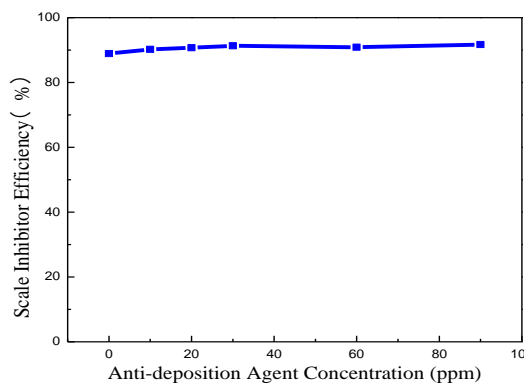


Fig. 5. Effect of anti-deposition agent on performance of the scale inhibitor

Comprehensive mechanism of compatibility and interaction between scale inhibitor and chemicals

Oilfield scaling. Generally, oilfield scales are formed by inorganic crystalline deposits that originates from the precipitation of solids in the reservoir and production system. The scale deposition results from changes in the ionic composition, pH, pressure and temperature of the reservoir and production. Common scaling compounds are calcium carbonate, barium sulphate and their complexes. The most common remediation is against the formation with chemical scale inhibitor in a “squeeze” treatment when the formation of sulphate or carbonate scale becomes a problem in produced fluids [9].

ASP flooding scaling mechanism. The formation of scaling in ASP flooding chain is very complicated. The scaling characteristics of the system consisting of Ca-Mg-Ba-Si in ASP flooding were presented by our previous paper [10]. It is different from water and polymer flooding by high Si and surfactant concentration. The dissolution of reservoir minerals by the strong alkaline enables the soluble Ca-Mg-Ba-Si materials into the reservoir fluid, which causes a serious scaling while occurring in changes of pressure, temperature, unstable thermodynamics and chemical incompatibility [11]. The scales in ASP flooding chain are mainly composed of carbonate and silicate. The CaCO₃/MgCO₃ particles serve as a grain for the precipitation while the silicon gel acts on a binder for coalescence of small particles. Silicon ion promotes the deposition of Ca(Mg)CO₃ particles. In this course, the inhibition of CaCO₃/MgCO₃ formation plays an important role in the control of the scaling.

The scaling formation ASP flooding is built by three steps: (1) soluble Ca-Mg-Ba ions plus Si ions from reservoir water and minerals in high solubility; (2) with lowering the solubility in change of temperature and pressure, molecule bond and

arrangement to form minicrystals, and begin to granulating; (3) lots of crystals to congregate, deposit and cause the scaling promoted by silicon ions.

ASP flooding scaling inhibiting mechanism. Phosphonate, sulfonate and carboxylate groups were one of the most common types of nonpolymeric or multipolymeric scale inhibitors, which have been used in the operation of the water and polymer flooding. In our case, phosphonate, sulfonate and carboxylate group were embedded in the scale inhibitor chain for ASP flooding. The groups are known to serve as the strong adsorbing scale inhibitor onto carbonates. The scale inhibitor is capable to chelate Ca-Mg-Ba ions to keep them soluble and to prevent carbonate from the deposition. Meanwhile, the silicon gel is prohibited from the codeposition.

Scale inhibitor-chemicals interaction and mechanism. The chemical compositions, as shown in section 2.1, reveal that the used chemicals are not able to undergo a chemical reaction between chemicals. It should be expected that interactive chemical reactions can not occur in the condition. Therefore, other types of interactions will be proposed as follows.

Scale inhibitor-demulsifier interaction. The demulsifier, existing in the chain, can be ionized while dissolved in the produced water. The scale inhibitor molecules are absorbed on the ionized demulsifiers. In this case, the scale inhibitor chains are entangled and lose the capability of chelating scaling ions. A liquid crystal phase will be formed to reduce the reverse action while adding high amounts of the demulsifier. In consequence, the inhibition percentage is slightly decreased, and then keeps flat in the curve.

Scale inhibitor-defoamer interaction. Hydrogen ions can be released while the defoamers are dissolved in the oil-water emulsion. The molecule chains of the defoamer are negatively charged, resulting in absorbing the scale inhibitor molecules and suspended solids. In this case, the scale inhibitor loses the positive function and the solid aggregation accelerates the scaling. In consequence, the inhibition percentage is sharply decreased, and gets worse with increasing the defoamer concentration.

Scale inhibitor-anti-deposition agent interaction. As shown in scheme 1, the anti-deposition agent consists of grafted phosphonate, sulfonate and carboxylate groups. The groups are known to be the strongly effective scale inhibitor like the scale inhibitor. So, the anti-deposition agent displays a positive compatibility with enhancement of the

scale inhibition.

For the detailed solution, our ongoing studies are being directed toward probing and proving this interaction and mechanism.

CONCLUSION

The study reports the compatibility and mechanism of the scale inhibitor combined with chemicals along the ASP flooding chain. The summary is listed as follows.

(1) The test of scale inhibitor exhibits that the scaling efficiency is decreased as the surfactant and polymer concentration are increased. That means the ASP chemicals will affect the inhibition percentage.

(2) The anti-deposition agent appears in positive compatibility while the negative effect of the demulsifier and defoamer on the scale inhibitor. But the action of the demulsifier changes in slight range.

(3) The interactive mechanism is attributed in the ionization of the demulsifiers, hydrogen ionization of the defoamers and effective functionalization of the anti-deposition agent.

(4) For the strategy of chemical usage, the adding sequence and dosage can be suitably specified and adopted for the ASP flooding chain by using the lab data.

Acknowledgements: For the financial support, we are grateful to the National Nature Science Foundation P.R. China (Project No. 21376049) and the PetroChina Daqing Oilfield.

REFERENCES

1. H. Pu, Q. Xu, *SPE*, **15**, 118746 (2009).
2. S. Gao, Q. Gao, *SPE*, **11**, 127714 (2010).
3. D. Wang, J. Cheng, Q. Li, L. Li, C. Zhao, J.Hong, *SPE*, **25**, 57304 (1999).
4. Y. Zhu, Q. Hou, W. Liu, D. Ma, *SPE*, **14**, 151285 (2012).
5. J. Cheng, W. Zhou, Y. Zhang, G. Xu, C. Ren, Z. Peng, W. Bai, Z. Zhang, X. Wang, H. Fu, Q. Wang, X. Kong, L. Shi, *SPE*, **19**, 144826 (2011).
6. D. Liu, J. Li, T. Li, Y. Zhen, X. Zhang, W. Wang, *Acta Petrolei Sinica*, **28**, 139 (2007).
7. Y. Wang, J. Liu, B. Liu, Y. Liu, H. Wang, G. Chen, *SPE*, **26**, 87469 (2004).
8. Q. Jia, B. Zhou, R. Zhang, Z. Chen, Y. Zhou, *SPE*, **30**, 74675 (2002).
9. Chen, A. Neville, M. Yuan, *J. Pet. Sci. Eng.*, **46**, 185 (2005).
10. Q. Gao, H. Qian, Z. Hou, L. Tang, *Oilfield Chem.*, **29**, 94 (2012).
11. J. Moghadasi, H. Müller-Steinhagen, M. Jamialahmadi, A. Sharif, *J. Pet. Sci. Eng.*, **43**, 201 (2004).

A feasibility study on heavy oil exploration by in-situ electric heating

Y. Hao*

China University of Geosciences, Beijing 100083

Received February 12, 2016; Revised December 26, 2016

There are many problems on the current exploration technologies of heavy oil, thus finally it often fails to enhance the oil recovery ratio. Based on analyses on the current problems, in-situ electric heating under the exploration well is proposed to eliminate the problem from other improved exploration technologies, e.g. small influence zone and low recovery. The physical model of heating heavy oil is established in this study based on the obtained weight-loss ratio under different temperatures from thermogravimetric tests, which is further used to simulate the in-situ temperature distribution of heavy oil. Production of crude oil from reservoir as well as electric energy to heat the reservoir under different temperatures is calculated according to the formula of weight-loss. Given the different saturation degrees of oil, the internal rate of return and the net present value methods are adopted to evaluate the economic feasibility of oil exploration by in-situ electric heating. Results indicate that fluid is required during the in-situ heating otherwise no heating effect is anticipated. The in-situ oil heating is very efficient as most of heavy oil can be recovered within the first three days. After that the recovery reduces significantly. It is not technically feasible for our domestic heavy oil reservoir to carry out recovery by in-situ electric heating given the current saturation degree and price of oil as the consumption in power is huge.

Keywords: Heavy Oil; in-situ heating; temperature distribution; weight-loss; feasibility; economic evaluation.

INTRODUCTION

Current exploration techniques worldwide on heavy oil can be classified into three types, e.g. thermal recovery, cold production and the compound production. Thermal recovery represents the use of heating on oil reservoir to reduce the viscosity of oil, even to decompose the heavy oil so as to enhance its mobility, including steam huff and puff, steam flooding, hot water flooding, Combustion of oil and in-situ electric heating (use of electricity, microwave and electromagnetism), etc. Cold production is to reduce the viscosity through changing the structure or composition in heavy oil, including chemical viscosity reducing method, carbon dioxide injection method, micro-organic method, magnetic viscosity reducing method, sound wave viscosity reducing method and etc. Combined technique is the comprehensive combination of both technologies associated with higher recovery ratio than the use of single technique. The steam flooding and steam huff and puff are commonly used in China with the mature technique. Problems occurring in the current exploration methods include: (a) the energy consumption is huge during the heating process for methods like steam huff and puff, steam flooding and hot water flooding. Even though the thermal insulation measure is taken, the base temperature is

no more than 350°C; (b) formation combustion, oil is hard to control and the combustion consumes plenty of resources; (c) for the cold production it is difficult for the injected fluid to contact well with heavy oil due to the existence of underground high permeable channel such that the influence zone is limited and the recovery is hard to be enhanced. (d) Methods like magnetic viscosity reducing or sound wave viscosity reducing take some effects but unable to realize high efficient recovery. The in-situ electric heating (including use of electricity, and electromagnetism) heats the reservoir directly, preventing the energy loss during hot fluid injection. By this method the temperature of reservoir can be increased to over 1000°C and under control. The heavy oil with reduced viscosity can be further completely decomposed into hydrocarbon fluids with coke remained, which prevents the resource loss as well as treatment after coke production on the ground due to the entry of oxygen in the combustion method. More importantly, the reservoir can be directly heated through the conduction and convection so that problems like small influence zone and low recovery in the other techniques can be finally resolved.

The in-situ electric heating has been currently applied on oil shale[2] recovery with the heating temperature of radiator of 343.3°C. Temperature of 371°C was reported by Yaqing Fan[3] for this application. Electric heating model on oil sands has been established by B.C.W. MCGEE[4] to simulate

* To whom all correspondence should be sent:
E-mail: yanghao@cugb.edu.cn

the heating mechanism on the asphalt of oil sands with the maximum temperature of 220°C, which validates the feasibility of electric heating on the recovery of oil sands. J.Y. Yuan [5] studied the electric heating process with the maximum temperature of 263°C at SAGD/VAPEX and carried out economic assessment. Comparatively only 150°C was achieved by B.C.W. McGee [6]. In the in-situ upgrading project (IUP) Deming Mao [7] reported the temperature of 350°C from the multiphase flow in the production well. R.S. Kasevich [8] studied the electromagnetic mechanism but only heating temperature of 200°C was achieved. Y. REN [9] conducted TGA (Thermo Gravimetric Analyzer) analysis on heavy oil and asphalts by heating them to 750°C at 10°C/min and found that the temperature to complete decompose them in nitrogen was 425°C within the range of 374°C to 519°C. TGA analysis by Zhao Fajun [10] indicated that under 300°C no obvious pyrolysis was observed; from 300°C to 430°C, slow production of volatile materials was observed; the pyrolysis mainly occurred within 430°C to 550°C with the peak ranging 470°C to 480°C. The above indicates that the temperature range to activate TG (thermogravimetry) has not been reached by the current in-situ heating on heavy oil, oil shale and oil sand, e.g. the current heating temperature is not capable to fully decompose heavy oil, oil shale and oil sand thus the heating temperature shall be raised. But a question is raised: Is it economically feasible to carry out in-situ recovery?

This paper focuses on heavy oil. Firstly the weight-loss rate of heavy oil under different temperatures was obtained through TGAs and the physical model of electric heating on heavy oil was established. Secondly after simulation on the distribution of temperatures from in-situ heating of heavy oil, oil productions as well as profits from reservoir under different temperatures were calculated according to the curve-fitted weight-loss formula. Then the electric cost is obtained based on the calculated energy. The IRR (internal rate of return) method and NPV (net present value) method were adopted finally to assess the feasibility of recovery by in-situ electric heating on heavy oil.

TGA ANALYSIS ON HEAVY OIL

Testing apparatus and procedure

The process as well as the influencing factors of thermal decomposition and weight loss is studied in this paper by TGA method. The TGA apparatus of DTG-1 from Beijing Hengjiu scientific and

equipment Ltd is adopted in laboratory experiments. Specifications are: a) heating rate of 0.1 ~ 80°C/min, b) accuracy of ±0.1°C, c) temperature range from indoor temperature to 1150°C, d) measuring capacity of 1mg~300mg, up to maximum 5g, e) resolution of 0.1µg, f) no shielding gas and g) natural cooling.

The heavy oil sample was taken from reservoir in Liaoning province, China. The sample was solid under normal temperature (30°C) and the heating rate was 10°C/min in nitrogen.

Testing program

The TGA apparatus adopted is automatically controlled by program specified as:

a) Activate the main switch and turn on the thermal balance; put the crucible into the heating chamber and measure its weight by the built-in balance; then take out the crucible and put in heavy oil, measure the total weight of the crucible plus the shale oil then the initial weight of oil can be determined from the total weight minus the weight of crucible;

b) Activate the control program, set the heating rate and termination temperature following the testing requirement, then put the crucible with heavy oil in the TGA chamber;

c) Turn on the heating unit of the TG, vary temperatures within the chamber by the built-in PID; the change in weight of heavy oil along with the variation in temperatures can be automatically recorded by the program;

d) When the temperature rose to the termination target, experiment was ended automatically and testing files were generated which include the weight loss curve and relevant data.

EXPERIMENTAL RESULTS

a. TGA tests

As seen from Figure 1 and 2, the normal steam temperature for steam huff and puff (steam flooding) is within 473.15K to 573.15K.

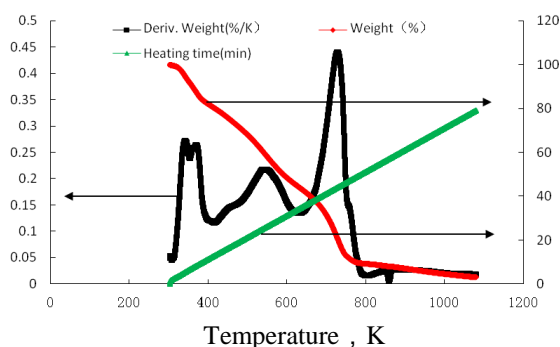


Fig. 1. Process of TGA tests.

The mass of heavy oil remained at 72.5% ~ 52.5%, rate of thermal weight loss 27.5% ~ 47.5%. Specifically the rate was respectively 80% and 90% for temperature at 728.15K and 773.15K. If the temperature kept rising, the increase in the rate became slow and meaningless, which however consumed huge energy. The peak weight loss occurred within 723.15K to 773.15K, e.g. good thermal decomposition occurred beyond the temperature of 773.15K. The curve-fitted accumulated rate of weight loss (η) is expressed as

$$\begin{aligned} \eta = & 3.181010980284 \times 10^{-17} T^6 - \\ & 1.05679123568331 \times 10^{-13} T^5 \\ & + 1.33690015495866 \times 10^{-10} T^4 \\ & - 8.31027615576241 \times 10^{-8} T^3 \\ & + 2.75887986536105 \times 10^{-5} T^2 \\ & - 3.22429179914252 \times 10^{-3} T - 1.2 \times 10^{-1} \\ R^2 = & 0.999717007448145 \end{aligned}$$

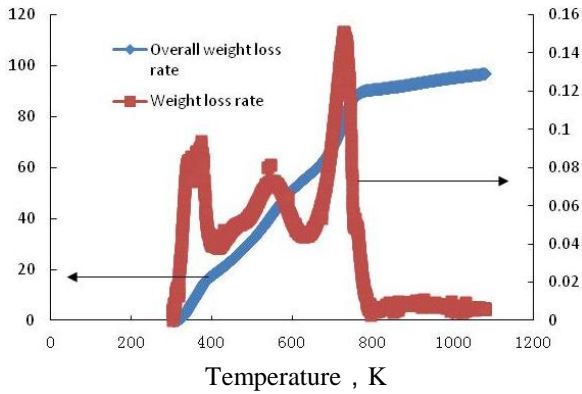


Fig. 2. Curve of Weight variations of heavy oil in TGA tests.

b. Decomposition of heavy oil

The heavy oil mainly consists of alkane, arene and asphaltene, etc. It is a particle composition of sulfur, nitrogen and oxygen. Decomposition of heavy oil experiences the following steps as[11]:

Thermal decomposition: $C_xH_y \rightarrow$ light hydrocarbon

Reconstitution of steam: $C_xH_y + 2xH_2O \rightarrow xCO_2 + (2x+y/2)H_2$

Transformation of water and gas: $CO + H_2O \rightarrow CO_2 + H_2$

Desulfuration: $C_xH_y S_2 + H_2O/H_2 \rightarrow H_2S +$ light hydrocarbon.

PHYSICAL MODELING

A cube was built with side length of 10m to represent the reservoir of heavy oil. A horizontal injection well and a horizontal recovery well is set at 3m height and 8.5m height along the central axis. Diameter of the two wells amounts to 216mm and length 9m. Upper and lower layers of the reservoir

are other stratum. The lower horizontal well is by fluid injection and in-situ electric heating. Increase in fluid temperature is realized by lower-access heating apparatus. The temperature of 873.15K can be maintained by adjustment of power and voltage. The upper horizontal well is coverage well.

The base depth of the reservoir is 2000m, temperature 353.15K, temperature gradient 3K/100m. The distributions^[12] of initial temperatures are defined by:

$$T_o = -0.03 * z + 353.15 \quad (1)$$

where z is the thickness of the reservoir within 0m~10m; If the normal pressure system is assumed, the distribution^[12] of initial pressure is described by

$$P_o = 9800 * (2000 - z) \quad (2)$$

The uneven heating resulted to the change in fluid density of the porous media thus the effect of buoyancy is considered, which expresses[12] as:

$$F = 1000 * 9.8 * \beta * (T - T_o) \quad (3)$$

where β is the expansive coefficient of fluid, 1/K and 0.04342 is adopted in this study; T_o is the initial temperature of stratum, K; T is the temperature of the reservoir; K is the instant temperature during heating.

NUMERICAL MODELING[12]

The Brinkman equation and heat transmission equation for porous media are adopted to simulate the heating transmission and fluid flow, incorporated by flow velocity.

Fluid flow equation:

$$\begin{cases} \frac{\mu}{K} u + \nabla P - \nabla \cdot \frac{\mu}{\varepsilon} (\nabla u + (\nabla u)^T) = \rho g \beta (T - T_c) \\ \nabla \cdot u = 0 \end{cases} \quad (4)$$

Heat transmission of porous media:

$$\begin{cases} (\rho C_p)_{eq} \frac{\partial T}{\partial t} + \rho C_p u \cdot \nabla T = \nabla \cdot (k_{eq} \nabla T) + Q_1 \\ k_{eq} = \theta_p k_p + (1 - \theta_p) k \\ (\rho C_p)_{eq} = \theta_p \rho_p C_{p,p} + (1 - \theta_p) \rho C_p \end{cases} \quad (5)$$

Heating transmission of fluid:

$$(\rho C_p)_{eq} \frac{\partial T}{\partial t} + \rho C_p u \cdot \nabla T = \nabla \cdot (k_{eq} \nabla T) + Q_2 \quad (6)$$

where T is the temperature of oil shale reservoir during heating, K; C_p is the specific heat at constant temperature, $J \cdot kg^{-1} \cdot K^{-1}$; K is the permeability of the porous media, m^2 ; Q_1 is the absorbed energy, J; Q_2 is the absorbed energy by water, J; ρ is the fluid density under the reference temperature T_c , kg/m^3 ; μ is the effective dynamic viscosity, $Pa \cdot s^{-1}$; u is the

expansive coefficient of fluid, $m \cdot s^{-1}$; β is the coefficient of volumetric thermal expansion, K^{-1} ; ε is the porosity of the media; ∇ is the Laplace operator $\nabla = \frac{\partial}{\partial x} i + \frac{\partial}{\partial y} j + \frac{\partial}{\partial z} k$; k_{ep} is the general thermal conductivity; k is the effective thermal conductivity, $W \cdot m^{-1} \cdot K^{-1}$; k_p is the heat transmission coefficient of solid; θ_p is the temperature without unit as $\theta = \frac{T - T_C}{T_H - T_C}$ in which T_H is the temperature at injection, T_C is the reference temperature, K. The model specification is in table 1.

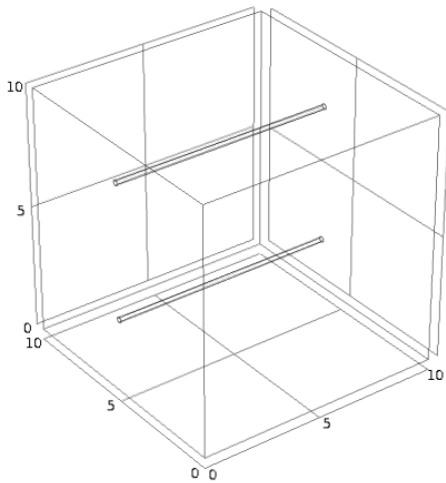


Fig. 3. Physical model of heating on heavy oil reservoir

TEMPERATURE DISTRIBUTIONS AFTER HEATING ON HEAVY OIL

The characteristics of temperature distributions for heavy oil within the reservoir are studied through injecting fluid into the stratum by radiator.

Table 1. Model specification

Reservoir of heavy oil		Water		Heavy oil	
Porosity	0.25	Fluid density, g/cm^3	1	Fluid density, g/cm^3	0.9
Permeability, m^2	$2e^{-13}$	Viscosity, $mPa \cdot s$	10^{-3}	Viscosity, $mPa \cdot s$	1000
Thermal conductivity, $W/(m \cdot K)$	2	Thermal conductivity, $W/(m \cdot K)$	0.58	Thermal conductivity, $W/(m \cdot K)$	0.1
Density, g/cm^3	2.5	Atmospheric heat capacity, $J/(kg \cdot K)$	4200	Atmospheric heat capacity, $J/(kg \cdot K)$	5000
Specific heat capacity, $J/(kg \cdot K)$	1812	Specific heat ratio	1	Saturation degree of oil	$So(0-1)$

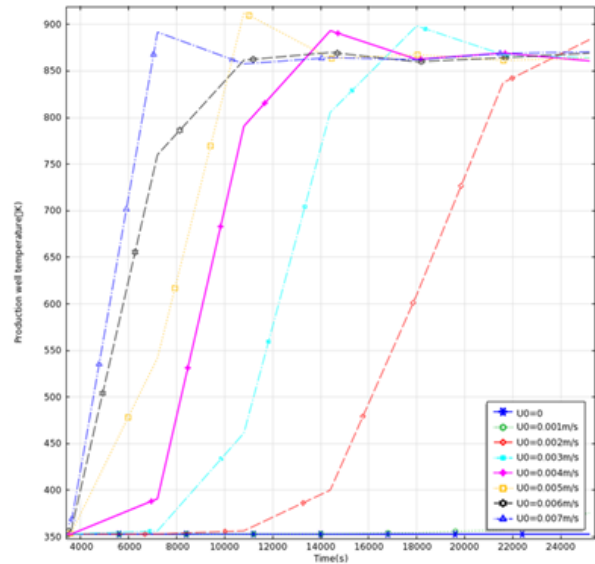


Fig. 4. Temperatures of production well given different injecting rates.

Optimization of injecting rate

At the oil stratum, the effect of water injection velocity (U_0) on the pressure at the entrance was studied. As seen from Figure 4, along with the increase in injection rate, temperature at the recovery well increased significantly; at the velocity of 0, little change in temperature was observed, e.g. heating only took effect once the fluid was injected to the stratum. It can be seen from Figure 5 that, with the increase in injection rate, oil pressure at the entrance increased. Given the pressure of about 20MPa, rate of $3 \times 10^{-3} m/s$ was adopted to prevent cracking of the reservoir as well as ensure the injection. The pressure amounted to 28MPa at this injection rate.

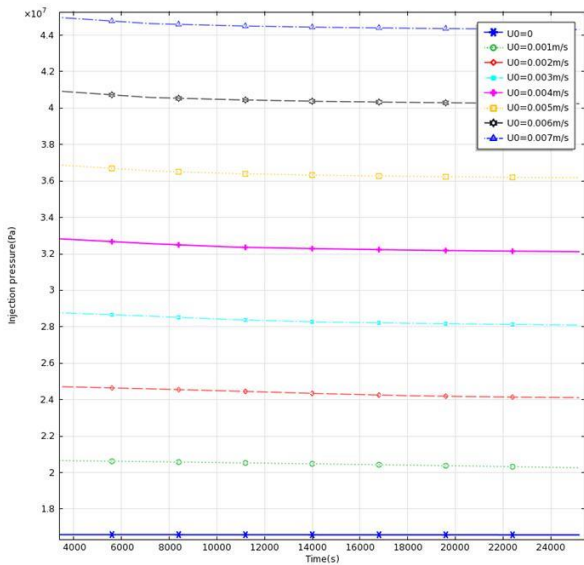


Fig. 5. Injecting pressures given different injecting rates.

Characteristics of temperature distributions for heavy oil after electric heating

Given the rate of $3 \times 10^{-3} \text{m/s}$, difference in recovery pressure amounted to 3MPa. Figure 6 presents the distribution of temperatures at the injection times of 0, 5d, and 10d, respectively. Subsequent results are calculated based on this injection rate and pressure difference. As seen from Figure 6, it only took a short time before the heavy oil reached the temperature for decomposition, which indicates positive heating effect.

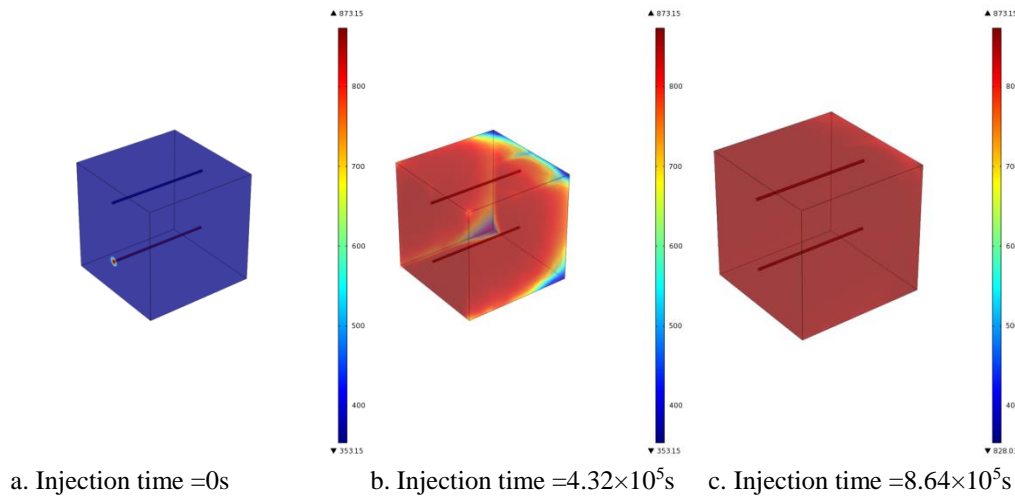


Fig. 6. Thermal distributions under different heating durations

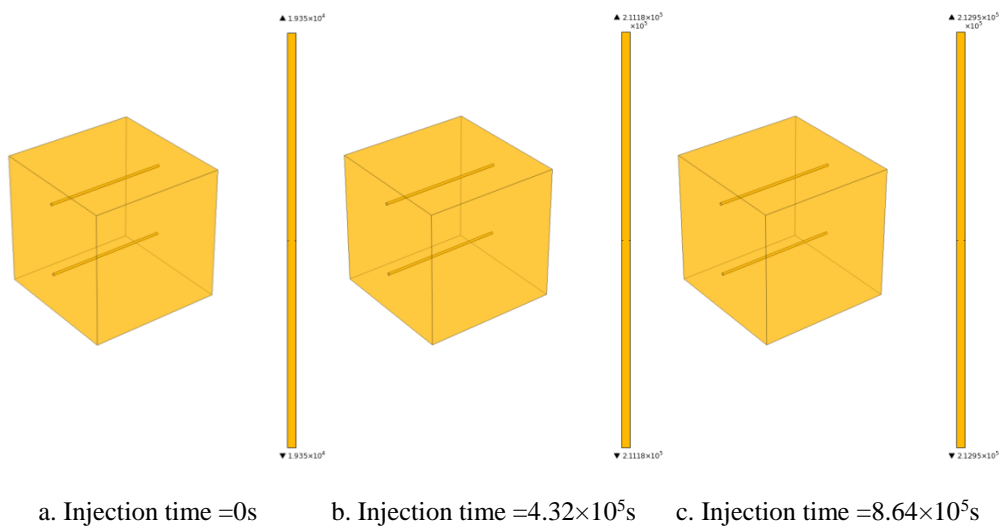


Fig. 7. Accumulated productions under different heating durations.

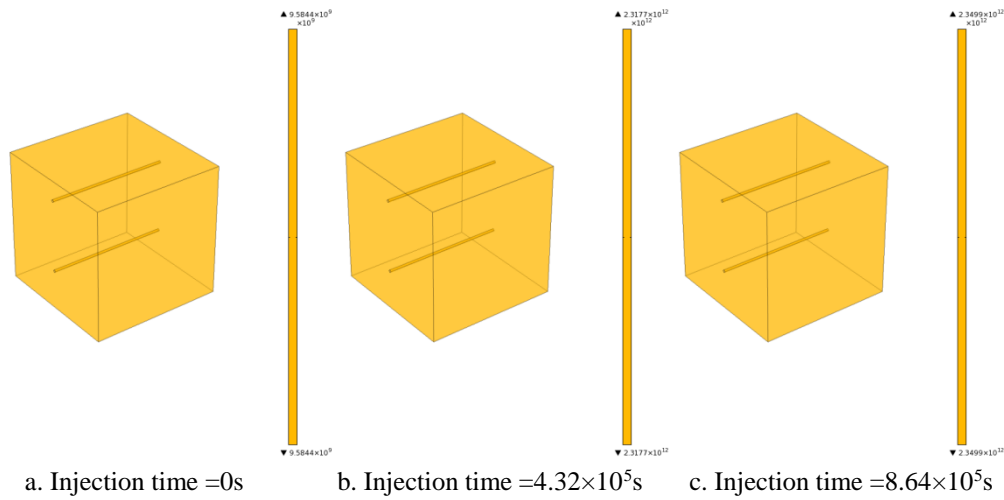


Fig. 8. Required energy absorbed for temperature increase under different heating durations

Table 2. Production of oil gas under different heating durations.

		Duration ($\times 10^4$ s)										
		0*	8.64	17.28	25.92	34.56	43.2	51.84	60.48	69.12	77.76	86.4
Accumulative recovery, t		19.35	155.87	186.32	201.28	208.42	211.18	212.33	212.76	212.9	212.93	212.95
	Stage recovery, t	19.35	136.52	30.45	14.96	7.14	2.76	1.15	0.43	0.14	0.03	0.02

*The oil gas mass denotes the required mass at time ‘0’ for the radiator to increase the temperature to the target one (873.15K).

Table 3. Required energy for the increase of temperature

		Time($\times 10^4$ s)										
		0*	8.64	17.28	25.92	34.56	43.2	51.84	60.48	69.12	77.76	86.4
Accumulative energy, 10^3 kWh		2.66	457.33	558.25	608.06	633.11	643.81	649.22	651.58	652.47	652.61	652.75
	Stage energy, 10^3 kWh	2.66	454.67	100.92	49.81	25.06	10.69	5.42	2.36	0.89	0.14	0.14

*: The energy denotes the required energy at time ‘0’ for the radiator to increase the temperature to the target one (873.15K).

Application of TGA analysis

To incorporate the fitted accumulative weight-loss rate into the reservoir under different temperatures, the recovery mass at different temperatures, namely the production of oil gas, can be calculated.

The oil and gas mass after weight loss is defined by

$$W = 0.9 \times 10^3 \times \iiint \phi \eta s_o d_v \quad (11)$$

where the density of oil is 900 kg/m^3 , porosity Φ of 0.25, and oil saturate s_o of 100%. The unit of W is kg.

As seen from Figure 7 and Table 2, the gas recovery at the target temperature of the radiator (873.15K at time of 0) is small. The recovery

increase quickly at the stage of constant temperature, e.g. the maximum recovery was obtained on the first day then the recovery decreased significantly and finally the recovery tended to be 0. Equipment to carry out in-situ electric heating can be reused due to the heating efficiency to reach the design temperature in a short time. Equipment for ground treatment of oil, gas and water shall also be reused to enhance the efficiency and reduce the production cost

Required energy of heavy oil to increase temperature through absorption

Based on the specific heat capacity to calculate the energy as

$$Q = cm\Delta T \quad (12)$$

The energy J required to heat the stratum to certain temperature is defined by

$$Q = 1812 \times 0.75 \times 2500 \times \iiint (T - T_o) dv + 5000 \times 0.25 \times So \times 900 \times \iiint (T - T_o) dv + 4200 \times 0.25 \times (1 - So) \times 1000 \times \iiint (T - T_o) dv \quad (13)$$

It can be seen from Figure 8 and Table 3 that the energy required for the temperature increase of the reservoir is the highest at the initial stage and reduces significantly, which finally tends to be 0.

ECONOMICAL ASSESSMENTS

The combination of internal rate of return (IRR) and the net present value (NPV) is adopted to assess the economic feasibility of heavy oil recovery.

The NPV is defined by:

$$\sum_{t=0}^n (CI - CO)_t (1 + IRR)^{-t} = NPV \quad (14)$$

where IRR is the internal rate of return; $(1+IRR)^{-t}$ is the present value at year t; n is the life time of the investment, year; CI is the incoming cash; CO is the outgoing cash; NPV is the net present value. When NPV is 0, the equation is transformed to the equation of IRR.

$(CI-CO)_t$ is the net cash income at year t. CI is the incoming cash, for instance the sale income of crude oil; CO is the outgoing cash, such as drilling, equipment, materials, fuels, salaries, depreciation, water and gas injection, underground mining, management, maintenance, repair, tax, treatment of water, gas and oil ,marketing, financial expense, etc. Based on the above calculated annual CI and CO, the net cash flow is calculated. Only if the calculated IRR is higher than the bank interest, economic benefit can be acquired in heavy oil recovery. Basically the IRR of 10% is adopted to evaluate the feasibility of a project.

Given the existing well net,100 thousand is required to establish the production line of in-situ electric heating assuming the daily expense of 10 thousand. Based on assumed price of heavy oil (93.7 USD per barrel), density (0.9g/cm³) and every ton of crude oil equivalent to 7 barrels, the price of every ton of oil is 700USD, equivalent to 4 thousand RMB per ton given the exchange rate of 6.1. Separate IRR and NPV for oil with different

saturation degrees can be obtained based on the recovery of heavy oil minus the expense and consumed electric charge (unit of 1RMB/kWh) within a certain period. Figure 9 presents the total recovery of oil gas and consumed electric charge for different recovery durations.

It is seen from Figure 9 that the recovery and electric charge mainly occur at the 1st to 3rd day after the start of heating then decrease quickly till very close to 0;the higher the oil saturation degree, more total recovery of oil gas can be produced with also the higher electric charge. The little difference between the total recovery and the electric consumption indicates the high electric cost. No economic benefit is expected if the drilling expense and ground separation expense for gas, oil and water are considered in in-situ electric heating.

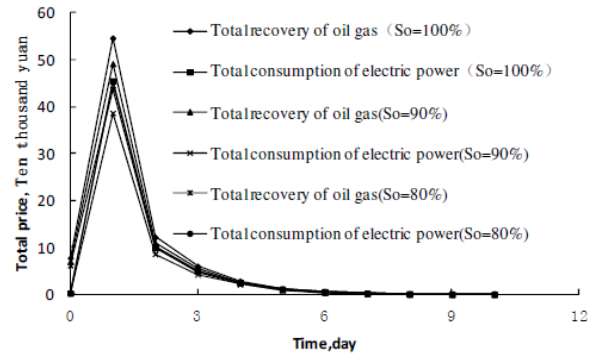


Fig. 9. Total recovery of oil gas and consumed electricity value at different time.

From Table 4 it can be seen that the higher IRR and NPV are associated with higher oil saturation (>90%), whereas for oil saturation of 80%, the NPV flows are all minus which indicates for oil with this saturation degree, no economic benefit is expected by electric heating. Since our current heavy oil reservoirs have been in the post-stage of development and the saturation degree only ranges 20% to 50%, no economic feasibility is expected once this technique is adopted.

Given the oil saturation degree lower than 20%, the required minimum oil price by electric heating on heavy oil reservoir is calculated.

In Table 5 when the NPV is 0, for the acquisition of 10% IRR, equation 14 is incorporated to calculate the oil price, namely 424USD/barrel, which indicates that for oil with 20% saturation degree, it is not economically feasible to carry out in-situ electric heating.

Table 4. Economic comparison among oil with various saturation degrees.

Saturation degree		Duration, day										
		0	1	2	3	4	5	6	7	8	9	10
100%	NPV*	-2.5	4.9	5.8	5.8	5.3	4.7	4.1	3.6	3.1	2.7	2.3
	IRR		2.223	2.351	2.351	2.345	2.342	2.341	2.34	2.34	2.34	2.34
90%	NPV*	-3.3	5.3	6.5	6.6	6.2	5.6	5.0	4.5	4.0	3.6	3.2
	IRR		1.881	2.019	2.024	2.018	2.015	2.013	2.013	2.013	2.013	2.013
80%	NPV*	-4.1	-6.5	-7.6	-8.4	-9.3	-10.0	-10.7	-11.2	-11.7	-12.1	-12.5

NPV*: that with IRR of 10%

Table 5. Production simulation by in-situ electric heating in heavy oil with 20% saturation degree

	Duration, day											
	0	1	2	3	4	5	6	7	8	9	10	
Recovery, ton	3.9	27.3	6.1	3.0	1.4	0.6	0.2	0.1	0.0	0.0	0.0	
Consumed power, kWh	2627.0	448650.8	99583.3	49111.1	24722.2	10555.6	5361.1	2305.6	888.9	138.9	166.7	
Total oil production, 10k	6.97	49.15	10.96	5.39	2.57	1.00	0.42	0.15	0.05	0.01	0.01	
Amount of consumption, 10k	0.26	44.87	9.96	4.91	2.47	1.06	0.54	0.23	0.09	0.01	0.02	
NPV*, 10k	-3.3	0.0	0.0	-0.3	-1.0	-1.6	-2.2	-2.8	-3.3	-3.7	-4.1	

NPV*: that with IRR of 10%

CONCLUSION

a. Put forward a new method of in-situ electric heating, simulation pointed out that in-situ electric heating should be injected into fluids, otherwise little heating effect is expected; recovery of heavy oil is mainly observed on the first 3 days, then decreases quickly and finally tends to be 0. In theory, in-situ electric heating can fundamentally solve the problem of heavy oil exploitation.

b. Simulated the economy feasibility of in-situ electric heating, under the reservoir conditions and prices, in-situ electric heating is not workable.

c. Heavy oil exploitation need to research and development more convenient and more efficient techniques.

Acknowledgement: This research was supported by NSFC project "Study on the evolution mechanism of composite materials with high temperature-high pressure-low elasticity modulus", No.51474192; and Basic research funding of central universities, No.2-9-2015-067.

REFERENCES

1. K. Yang, X.D. F.C. Tang-Liu, *Chemical Engineering of Oil & Gas*, **40**(5), 499 (2011).
2. T.D. Fowler; H.J. Vinegar, In: Oil Shale ICP-Colorado Field Pilots, (SPE Western Regional Meeting, San Jose, California, 24-26 March 2009), 2009, SPE 121164
3. Y. Fan; L. Durlofsky; H.A. Tchelepi, *SPE Journal*, 368 (2010).
4. B.C.W. McGee; F.E. Vermeulen, *Journal of Canadian Petroleum Technology*, **46**(1), 28 (2007).
5. J.Y. Yuan, H. Huang, R. Mintz, X. Wang, C. Jossy, C. Tunney, In: Wet Electric Heating for Starting Up SAGD/VAPEX[J]. (Canadian International Petroleum Conference, Calgary, Alberta, 8-10 June 2004), 2004, PETSOC-2004-130.
6. B.C.W. McGee; R.D. Donaldson, In: Heat Transfer Fundamentals for Electro-thermal Heating of Oil Reservoirs, (Canadian International Petroleum Conference, Calgary, Alberta, 16-18 June 2009), 2009, PETSOC-2009-204.
7. D. Mao, A. Harvey, In: Transient-Nonisothermal-Multiphase-Wellbore-Model Development With Phase Change and Its Application to Producer Wells, (SPE Annual Technical Conference and Exhibition, Denver, Colorado, USA, 30 October-2 November 2011), 2011, SPE 146318.
8. R.S. Kasevich, S.L. Price, D.L. Faust, M.F. Fontaine, In: Pilot Testing of a Radio Frequency Heating System for Enhanced Oil Recovery From Diatomaceous Earth, (SPE Annual Technical Conference and Exhibition, 25-28 September, 1994, New Orleans, Louisiana), 1994, SPE 28619.
9. Y. Ren, N.P. Freitag, N. Mahinpey, *Journal of Canadian Petroleum Technology*, **46**(4), 47 (2007).
10. F.J. Zhao, Study on mechanism and application of viscosity reduction through underground reconstitution of heavy oil [D]. Daqing Petroleum Institute, Daqing, Heilongjiang, 2008.
11. J.F. Du, J.Y. Cui, A.M. Lv, *Journal of China University of Petroleum (Edition of Natural Science)*, **34**(4), 99 (2010).
12. Y. Hao, D. Yunxing, *Petroleum Science and Engineering*, **122**, 304 (2014).

Metabolomics studies of chronic atrophic gastritis cold and heat syndrome

M.L. Wang^{1,*}, C.L. Zheng^{2,*}, Y.W. Zhou^{2,#}, T.G. Liu³, Y.B. Li³, H. Xie³, Y. Chang⁴, W.C. Liu³,
G.G. Chen³, X.L. Sun³, Y.H. Zhao^{5,*}, Z.H. Li^{6,*}

¹ Beijing Jiangong Hospital, Beijing 100054, China

² Beijing Gulou Hospital of Traditional Chinese Medicine, Beijing 100009, China

³ Beijing University of Chinese Medicine, Beijing 100029, China

⁴ Beijing Research Center of Urban System Engineering, Beijing 100037, China

⁵ School of Traditional Chinese Medicine, Capital Medical University, Beijing 100069, China

⁶ Dongzhimen Hospital, Beijing University of Chinese Medicine, Beijing 100007, China

Received December 12, 2014; Revised February 26, 2016

The objective of this work is to study the specific plasma metabolites of chronic atrophic gastritis cold and heat syndrome, and search the relevance pattern with cold-heat syndrome. Collect general data and blood samples of chronic atrophic gastritis cold-heat syndrome patients through clinical cross-sectional investigation, and resort GC-MS analytic technique to analyze the patient's metabolites and change of corresponding metabolites spectrum group. Then use many kinds of data-mining methods to discuss the corresponding relation between cold-heat syndrome and specific metabolites. The true positive rate of this decision tree modeling is 81.5 %, which is established by compounds whose retention time are 33.16, 21.83, 33.26, 34.69. chronic atrophic gastritis cold and heat syndrome will produce specific metabolites that may provide an objective basis for judging cold-heat syndrome. Accordingly, new ideas and methods are provided for pattern identification of traditional Chinese medicine (TCM) and deep research on symptoms.

Keywords: chronic atrophic gastritis, cold syndrome, heat syndrome, metabolomics, data mining

INTRODUCTION

Chronic atrophic gastritis is a chronic disease with atrophy of the stomach mucosa, leading to loss of gastric glandular cells, incrustation of mucosa muscle layer and their eventual replacement by intestinal and fibrous tissues. CAG is listed as the stomach precancerous disease or precancerous condition, and on its basis concomitant with intestinal metaplasia (IM) and hyperplasia (Dys) that regarded as gastric cancer and precancerous lesion of gastric cancer (PLGC). In China, as working pressure increases and life pace becomes faster, the incidence of chronic atrophic gastritis increased year by year, which has a serious impact on people's life quality. Traditional Chinese medicine has accumulated rich experience in the thousands of years of clinical practice. Traditional Chinese Medicine provided a complementary and alternative therapeutic regimen to treating CAG. It uses a holistic concept to balance whole body, being different to western medicine whose treatment of chronic atrophic gastritis.

TCM has a history of more than 2000 years to fight with CAG. Chronic atrophic gastritis, according to its symptoms and signs, can be assigned to "gastric stuffiness", "stomach duct pain". Its syndrome differentiation can be basically divided

into stomach cold and stomach heat. Syndrome differentiation is premise of treatment (diagnosis, prescription and drugs) whose accuracy is the key to clinical effect. In recent decades, people kept looking for the objective index of syndrome in order to reveal its essence, from multilevel aspect such as physiological, biochemical, immunity, cell pathology, ultrastructure, genomics and proteomics. However, the research results indicate that characteristic of the indicators is not manifest that it is difficult to find the specific indicators, while many of the chosen indicators are difficult to promote in clinical applications [1].

It is obvious that the specific indicator of "syndrome" is more likely the changes of a group of indicators, not just one or two "golden indicators". But by using the traditional method cannot find a group of specific indicators. And previous studies only associate the results with syndrome, lacking correlation analysis between the changes of characteristic indicators and classical metabolic pathway, so that making it difficult to clarify the nature of syndrome and its evolutionary mechanism. Therefore, the exploration of syndrome related metabolites group is undoubtedly significant to solve the key problem of syndrome biological basis.

With life science having entered post genomics era in nowadays, metabolomics technology not only overcomes genomics, proteomics and other technical limitation, but also possesses enormous

* To whom all correspondence should be sent:

E-mail: athena1231@126.com; lzhh3610@sina.com

advantage on holistically discerning the whole life process and dynamic change through the metabolic contour analysis [2,3,4], which fit close the holism traditional Chinese medicine emphasizes. Thereby, it provides new thinking and methods for syndrome research.

At present, cold syndrome and heat syndrome of chronic atrophic gastritis has made some progress on biology basic research. For instance, the researchers found the stomach heat syndrome patients, compared with stomach cold syndrome patients, PGE₂ and 6-keto-PGF_{1α} content in their gastric juice has a more obvious increase. Gastric heat syndrome patients appear more obvious congestion edema because of gastric mucosa vessels hemangiectasis and blood flow increase. In addition, scholars have found in the gastric juices of the stomach cold and heat syndrome, the Na⁺ concentration change is closely related to gastric mucosal barrier [5,6].

Li Shao and some people studied the "cold syndrome" and "heat syndrome" on molecular basis in neuroendocrine immune system, thought that "cold syndrome" may relate to hormone while "heat syndrome" may possibly relate to immune factor. The two relate each other by neurotransmitter, preliminary reveals the molecular pathways of cold and heat syndrome in rheumatoid arthritis, so that confirms the objective existence of cold and heat syndrome [7].

Therefore, this research will take chronic atrophic gastritis cold and heat syndrome as object, give the patients' organizations metabolite spectral analysis to get "syndrome-related metabolic spectrum group", combine data-mining method that is suitable for TCM syndrome data characteristics to find out specific signature metabolites, use bioinformatics methods to analyze the function of the biomarkers to preliminary reveal microscopic metabolites and disease and syndrome association laws, and reflect CAG cold and heat syndrome connotation by stomach tissue signature metabolic product in order to achieve objectification of syndrome differentiation and treatment.

MATERIALS AND METHODS

Standard of Diagnosis

CAG cold and heat syndrome disease and syndrome diagnostic standard basis

1) CAG Diagnosis Standard

New classification of chronic gastritis - Sydney system and revised Sydney system (1997)

*Endoscopic classification of CAG (national gastritis forum amendment, 1983)

2) Syndrome Diagnostic Standard

CAG syndrome differentiation standard refers to deficiency syndrome differentiation of TCM reference standard in 1986 and TCM diagnostics and relevant reports [8,9,10].

Stomach cold syndrome: main syndrome (1) stomach duct pain with heat preference, the pain will release when get heat; (2) watery stool; (3) stomach duct distention and fullness, obvious abdominal distension after noon; (4) pale or blue tongue body, white and moist tongue fur. Minor syndrome (1) exhausted; (2) sunken and fine pulse or slow pulse; (3) chills and cold limbs. People with three main syndromes and more than one minor syndrome belong to stomach cold syndrome.

Stomach heat syndrome: main syndrome (1) red tongue, yellow or less tongue fur; (2) pyrosis or stomach duct distention and fullness; (3) dry stool; (4), dry mouth, bitter taste in the mouth; (5) swift digestion with rapid hungering. Minor syndrome (1) noisy stomach or acid regurgitation; (2) slippery and string like pulse or rapid pulse. People with two main syndromes (the first one is requisite) and more than one minor syndrome belong to stomach heat syndrome.

Inclusion Criteria (satisfy all the following items)

- accord with CAG diagnosis standard and TCM syndrome diagnostic standard;
- check to confirm diagnosis within a month before the inclusion experiment;
- agree to sign the informed consent;
- between 20 to 65 years old.

Exclusion Criterion

- patients with peptic ulcer, gastric mucosal dysplasia or pathological diagnosis of suspected malignant;
- patients with heart, brain, liver, kidney and hematopoietic system serious primary diseases, or mental problems;
- women with pregnancy or prepare to pregnant, breastfeeding women;
- allergic constitution and allergy to a variety of drugs;
- CAG heat and cold syndrome mingled with other syndromes.

Reagent and Instruments

MSTFA+1% TMCS (USA Pierce) , methoxamine hydrochloride (98% pure, Sigma-Aldrich) ; alkane standard solutions (C8-C40, Sigma-Aldrich) ; pyridines (≥99.8%GC, Sigma-Aldrich) ; 1,2-13C₂ tetradecanoic acid (USA Isotec) ; methanol (pure chromatography, USA TEDIA) ;

methyristearic acid (Sigma-Aldrich) ; normal heptane (pure chromatography, Germany Merck)

GCMS solution V2.5 workstation, NIST lines library ; High speed low temperature centrifuge (sigma company, 3k18) ; low speed centrifuge (Shanghai Precise Operation Instrument Factory 80 -2) ; turbine mixer (Shanghai Xing Hang Industrial Company, TM-1).

Metabolomics Organization Sample Preparation and Extraction

All differentiations of the cases were taken by two attending physicians or higher position in the project team. Eligible people signed informed consent, and then fasted for 12 hours. When using electronic gastroscope (Olympus GIF - XQ260), take 2 biopsy blocks at sinuses ventriculi greater curvature or the same place of lesser curvature that 2~3cm from pylorus. One was sent for pathological examination; another was preserved in - 80 centigrade. The histopathological diagnosis consulted Chinese chronic gastritis consensus [11] and a person was designate to do pathological diagnosis. In *Helicobacter pylori* inspection WS was used for dyeing.

Take 20 mg tissue in 37 centigrade water bath to thaw for 15 minutes, add 800 μ L single phase extraction liquid that containing myristate (2.5 μ L/ml) with stable isotope as internal label (water: methanol = 1:4), then grid. Vortex oscillate the mixture for 3 minutes then oximate in 20centigrade for 16 hours; Add 30 μ g BSTFA and vortex oscillate it for 3 minutes then derivative in 20 centigrade for 1 hour. Finally add 30 μ l external labeled stearic acid heptane fluid (30 μ g/ml), then vortex 3 minutes. What is acquired is the sample.

GC-MS Analysis

Gas phase condition: split ratio is 2:1; sample quantity is 0.5 μ l. Injection port temperature: 280centigrade; Interface temperature: 250 centigrade. Temperature program: 80centigrade, keep 2 minutes. Rise to 140centigrade at the speed of 10 centigrade /min, then rise to 240 centigrade at the speed of 4 centigrade/min, and then rise to 280 centigrade at the speed of 10centigrade/ min, and keep 3 minutes. Ion source temperature: 200 centigrade. Carrier gas: high-purity helium. Mass spectra conditions: carrier gas flow rate 1.0mL/min. Ionization mode: EI, electron energy is 70eV. Scanning range: 50~800m/z. According to the retention time of each peak in the GC-MS total ion chromatogram choose common peak, and obtain the peak area data of each peak and internal labeled

peak, then use relative peak area (ratio with internal labeled peak) to represent the relative content of the metabolites.

Precision experiment: Take the same sample for 6 times continuously sampling and calculate the relative standard deviation (RSD) of the relative peak area.

Metabolite identification: Use NIST mass spectrum database to identify common endogenous metabolites. The identification result that matching degree > 80% is regarded as credible material.

Training

Project principal investigators provide professional training to the clinical centers before clinic, so that the researchers can fully understand clinical survey plan and its various standard operating procedures.

Qualifications of Principal Investigator

Investigator should have qualification above attending doctor, and relative fixed. The diagnosis of western medicine and TCM syndrome should be at least completed by an associate chief physician and a resident physician together, and clinical case report form to be filled by attending physician or above title.

Statistical Method

Use SPSS21.0 statistical software to carry on the calculation and adopt t-test, nonparametric test as analysis methods. Discrepancy $P < 0.05$ is regarded statistical significant.

Data mining and processing methods: Respectively use principal component analysis (PCA), cluster analysis and decision tree method to screen statistically significant characteristic metabolites that come from t-test and nonparametric test analysis in order to get CAG cold and heat syndrome classification model.

RESULTS

General Information

This experiment altogether collected 92 cases, 16 shedding cases, 23 eliminating cases. All cases come from inpatients of Dongzhimen hospital. Collection time is from 2012 to 2015. 28 cold syndrome cases, 25 heat syndrome cases; 15 male cases and 13 female cases in cold syndrome group, with an average age of 47; 13 male cases and 12 female cases in heat syndrome group, with an average age of 44 The gender, age baseline level of the two groups was consistent ($P > 0.05$); medical history and symptoms integral have no statistical difference. All selected people have signed informed consent, and by the

Ethics Committee of the Third Hospital of Peking University.

Characteristic Metabolites Screening Results

Extract 160 metabolites from 53 cases of chronic atrophic gastritis by NMR method. Various compounds account for different proportions in different patients. Table 1 lists 33 kinds of characteristic metabolite that frequency exceeds 50%.

Screening Results of Indicators Associated with Cold Syndrome and Heat Syndrome

Do t-test the above 33 kinds of compound to find specific ones. Results: three compounds that retention times are 21.83, 33.16, and 33.26 have significant difference ($P < 0.05$).

PCA and OPLS Pattern Recognition

Figure 1A and B shows the score diagram of principal component analysis (PCA) and orthogonal

signal correction partial least squares (OPLS) pattern recognition. In the scored diagrams PC1 and PC2 indicate the first and the second principal components of main components, and reflects the distribution of cold syndrome and heat syndrome samples in the coordinate system that composed by PC1 and PC2. As can be seen from the diagram, CAG cold syndrome group and heat syndrome group can be better separated with the help of pattern recognition by PCA method (Fig. 1 A), each of the two samples has an outlier beyond 95% range (elliptical area in the figure).

Corresponding to score diagrams, the load diagram shows detected variable distribution. It is easy to identify the difference between the two groups of metabolites from NMR analysis, through the load diagram. as shown in Figure 1B: 33.26、33.16、21.83.

Table 1. List of 33 kinds of characteristic metabolite that frequency exceeds 50%.

retention time (s)	frequency (number of times)	rate (%)	retention time (s)	frequency (number of times)	rate (%)
18.79	47	0.88679	31.95	40	0.75472
33.16	46	0.86792	34.69	40	0.75472
9.19	45	0.84906	25.15	38	0.71698
10.9	45	0.84906	28.15	38	0.71698
12.5	44	0.83019	21.34	37	0.69811
21.72	44	0.83019	21.83	37	0.69811
33.78	43	0.81132	33.26	37	0.69811
8.73	42	0.79245	16.01	36	0.67925
10.14	42	0.79245	20.56	36	0.67925
14.77	42	0.79245	22.49	36	0.67925
23.53	42	0.79245	17.45	32	0.60377
19.79	41	0.77358	19.33	32	0.60377
24.15	41	0.77358	14.03	30	0.56604
7.56	40	0.75472	8.01	29	0.54717
9.61	40	0.75472	17.58	28	0.5283
11.98	40	0.75472	32.08	27	0.50943
15.29	40	0.75472			

Table 2. Evaluation Form of CAG Cold and Heat Syndrome Judgment Model Based on Decision Tree

Category	Actual number of samples	Discernible number of samples	Negative detection accuracy (%)	Positive detection accuracy (%)	Detection accuracy (%)
Heat syndrome	36	25	18.5	81.5	81.5
Cold syndrome	40	28			

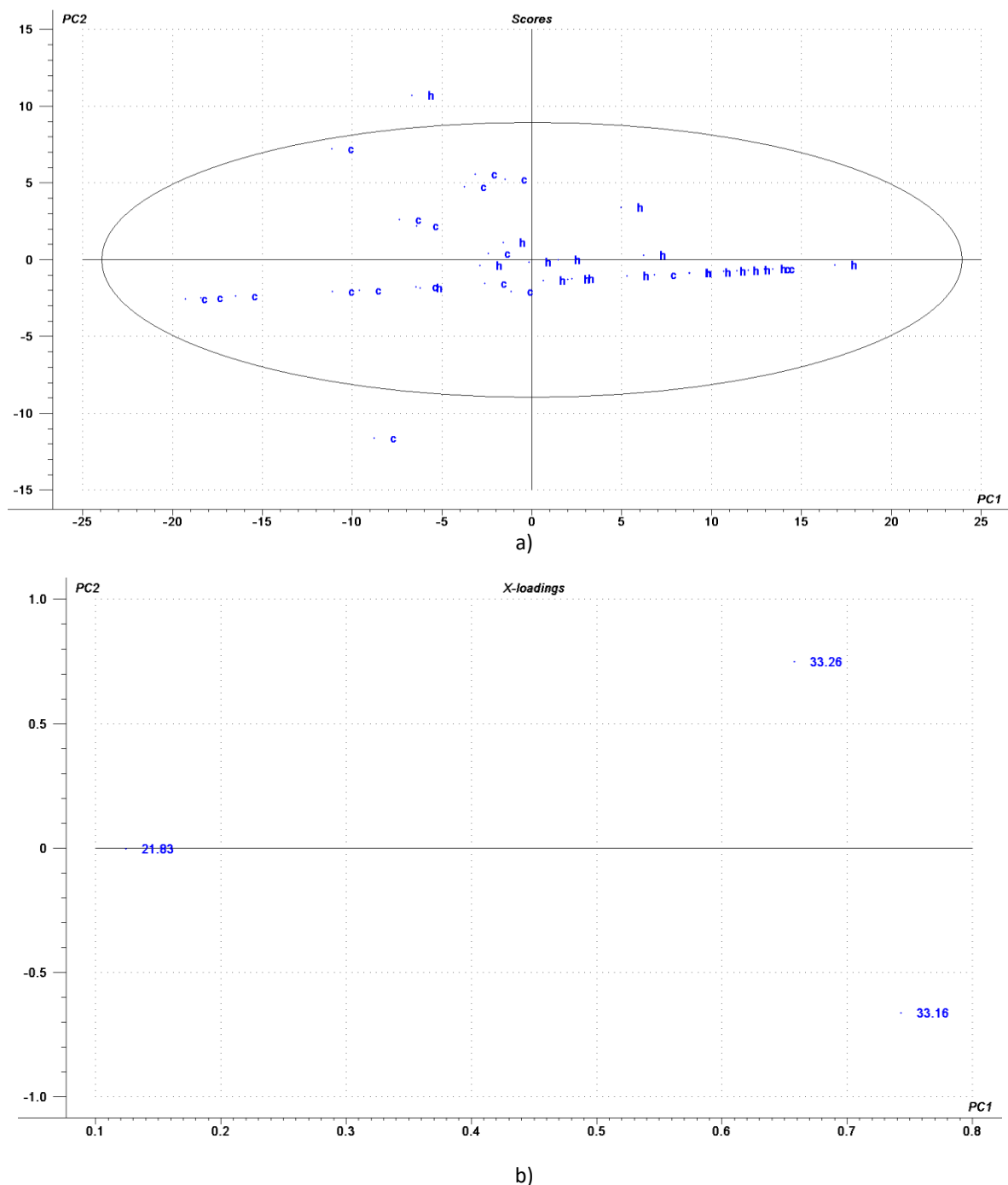


Fig. 1. a)PCA pattern recognition scoring diagram of CAG cold and heat syndrome; b) OPLS pattern recognition load diagram of CAG cold and heat syndrome.

Cluster Analysis

Take the characteristic metabolites screened out by T-test as variables to do cluster analysis on CAG cold and heat syndrome. The result is as shown in Figure 2.

Establishment of CAG Cold and Heat Syndrome Decision Tree Model

Adopt the significant compounds from T-test analysis as independent variables, and take "whether it is heat syndrome or not" as a dependent variable

into the decision tree model screening. Adopt Weka3.5.5J48 decision tree method to dig diagnostic rules, finally get decision tree classification model of CAG cold syndrome and heat syndrome.

There are five leaf nodes in the cold and heat syndrome decision tree classification model, and "TRUE" is on behalf of "heat syndrome" while "FALSE" is on behalf of "the cold syndrome. The number in parentheses represents the retention time of the compound. The model contains four kinds of compounds and their expression time was

33.16,21.83,33.26,34.69, which can be seen from Figure 3.

Evaluation of CAG Cold and Heat Syndrome Decision Tree Model

The testing accuracy of CAG cold and heat syndrome decision tree model is 81.5 %; Negative detection accuracy is 18.5 % and positive detection accuracy is 81.5 %.

Determine the Specific Metabolites

According to the retention time of the above-mentioned specific metabolites, find their corresponding possible metabolites from the information list of the metabolites, as shown in Figure 4A, 4B, 4C, 4D.

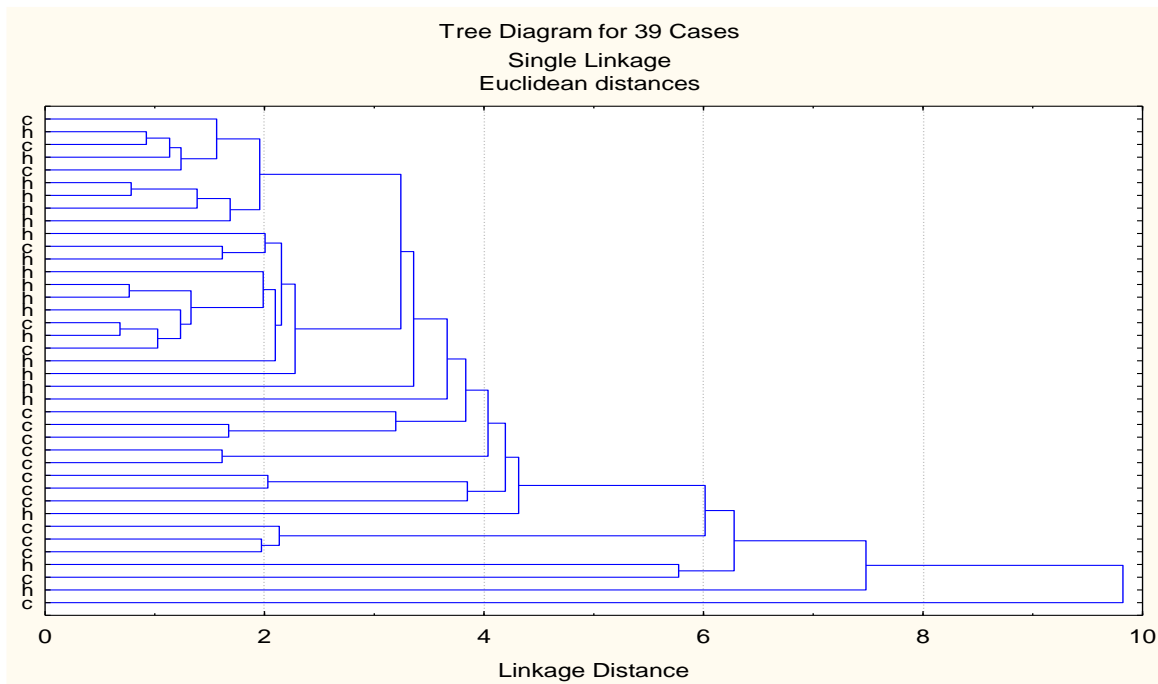


Fig. 2. CAG cold syndrome and heat syndrome clustering analysis based on two characteristic metabolites

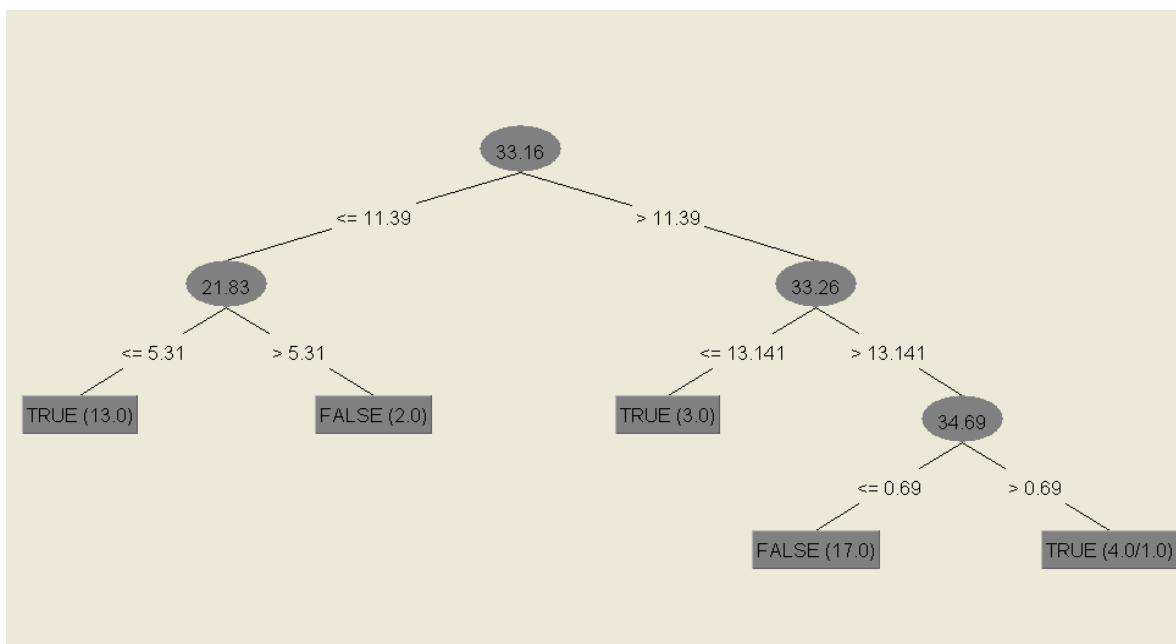


Fig. 3. CAG Cold and Heat Syndrome Judgment Schematic Diagram Based on the Decision Tree Method.

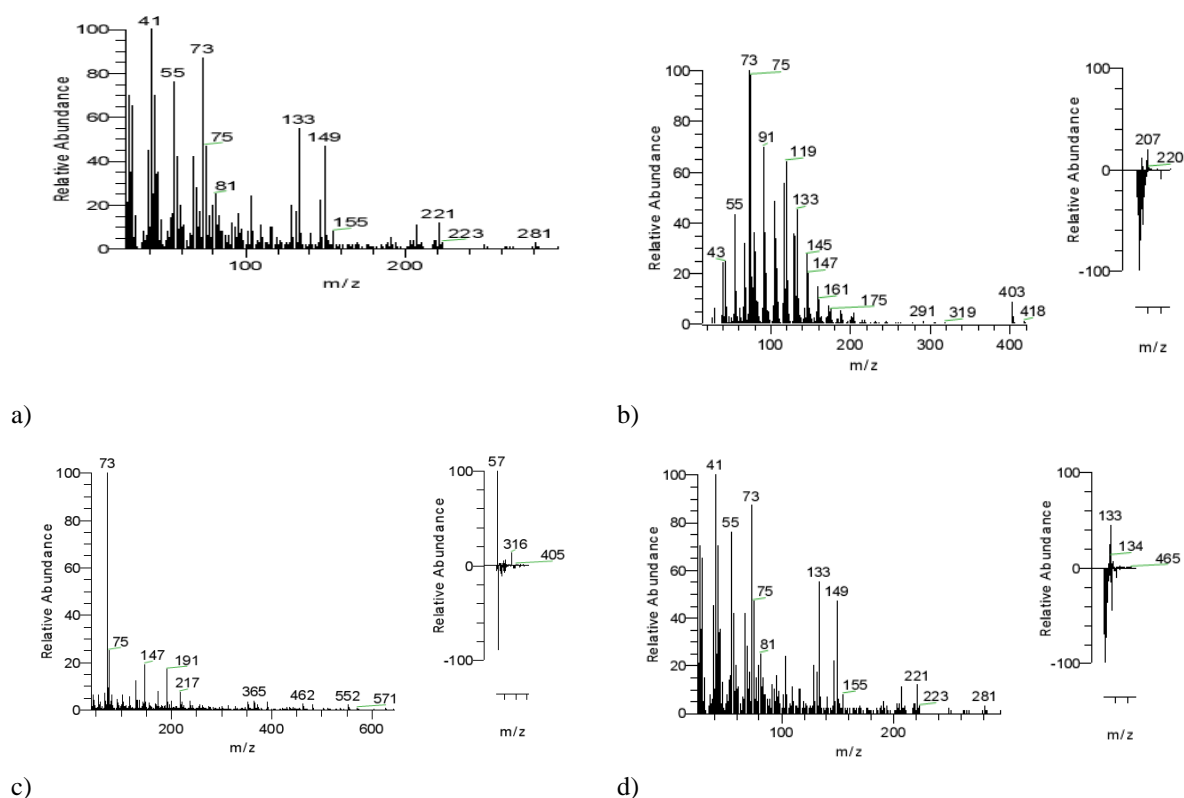


Fig. 4. a) 21.83; b) 33.16; c) 33.26; d) 34.69.

DISCUSSION

"Syndrome" is the starting point and the core of treatment based on syndrome differentiation. Syndrome refers to the synthetic reaction occurs when relationship between internal and external environment and all the systems disturb under the pathogenic factor function. It is a comprehensive diagnostic concept reflects the pathological elements of the etiology, pathogenesis, disease location, and disease potential at a certain stage. Because of syndrome holistic, dynamic, same syndrome existing in the different diseases and same disease belonging to different syndromes, and other characteristics, it is not possible to use a single indicator for qualitative, quantitative and positioning instructions. Accordingly, syndrome objective research uses comprehensive index and selects nonspecific index for specific combination to establish comprehensive, qualitative, quantitative, and positioning indicators which can reflects the nature of syndrome and distinguishes it from other syndromes. It is enormously significant on assisting the four methods of diagnosis and determining the syndrome diagnosis. Metabolomics possesses the "crowd", "group", "spectrum" integrated analysis function that can reflect and solve these problems. It is able to test the blood or urine of patients at different times, analyze its metabolites, and determine syndrome corresponding metabolites, in

order to provide a basis for objectification of syndrome differentiation and treatment [12].

This research used NMR technology to acquire CAG cold and heat syndrome metabolites, and analyzed CAG cold and heat syndromes' metabolomics product by principal component analysis, decision tree method and cluster analysis, preliminary got specific metabolite associated with CAG cold and heat syndrome and formed five judging ways of cold and heat syndrome with the decision tree model composed by 21.83、33.16、33.26、34.69, and the judgment accuracy was 81.5 %, and formed a clear, intuitive CAG cold and heat syndrome judgment model that may become the objective basis of CAG cold and heat syndrome differentiation and treatment. Therefore, the application that base on characteristics and advantages of metabonomics and combine data mining technology may provide new method for objective and dynamic observation of TCM syndrome.

Acknowledgements: This research is supported by Project of Beijing University of Chinese Medicine (2015-JYB-JSMS012), National Natural Science Foundation (No. 81574102) and Planned Project on Beijing Traditional Chinese Medicine "inheritance of 3 + 3 program" of Delu Tian and Beijing Nova Program (No : xx2013032) .

REFERENCES

1. W.F. Zhu, *Beijing: People's Medical Publishing House*, **6**, 2 (2008).
2. X.Z. Yan, J.Y. Zhao, S.Q. Peng, M.Y. Liao, *J Magn Reson*, **21**(2), 263 (2004)..
3. H. Zhu, H.R. Tang, X. Zhang, M.L. Liu, *Chem Bull*, **69**, 1 (2006).
4. J. LI, X.J. Wu, L.X. Liu, Y.J. Yuan, *Acta Pharm Sin*, **41**(1), 47 (2006).
5. Y. Guan, G. Liang, G.B. Martin, *BMC Genomics*, **18**(1), 64 (2017)
6. M. Ghoneum, M. Matsuura, M. Braga, *Int J Oncol*, **33**(3), 533 (2008).
7. S. Li, Z.Q. Zhang, L.J. Wu, X.G. Zhang, Y.D. Li, Y.Y. Wang, *IET System Biology*, **1**(1), 51 (2007).
8. Wu X. Wu, Y. Song, W. Liu, *Cell Death Discov*, **30**, 3 (2017).
9. T.T. Deng, *Shanghai Sci Tec Publishers*, 97 (1984).
10. N.H. Pang, Z.X. Fan, S.L. Niu, *Chinese J Integr Tradit Wes Med*, **7**(11), 652 (1987).
11. Z.Y. Hu, *Gastroenterology*, **11**(11), 674 (2006).
12. S.Y. Sun, L. Jin, *Chinese J Inf TCM*, **15**(4), 3 (2008).

Protective effect of huangjingzanyu capsule on cyclophosphamide-induced oligoasthenozoospermia in rats

C.L. Zheng^{1,2}, Q. Wang^{1#}, Y.W. Zhou², M. Jiang³, B. Zhu¹, J. Yan¹, Y. Tang¹, J.Z. Li¹, J. Wang¹, Y. F. Zheng^{1*}

¹Beijing University of Chinese Medicine, Beijing 100029, China

²Beijing Gulou Hospital of Traditional Chinese Medicine, Beijing 100009, China

³Third Affiliated Hospital, Beijing University of Chinese Medicine, Beijing 100029, China

Received December 12, 2015; Revised February 26, 2016

To investigate the protective effect of Huangjingzanyu Capsule on cyclophosphamide-induced oligoasthenozoospermia model in rats. Testicular damage was induced by cyclophosphamide to make the oligoasthenozoospermia model. The expression of testis-related genes in mRNA and protein level was detected by RT-PCR and Western-blot, and the histopathological changes of the testes were analyzed. Huangjingzanyu Capsule increased Bcl-2 protein and mRNA in testis of the rat ($P < 0.05$), and decreased the expression of Bax and Caspase3 protein and mRNA ($P < 0.05$). The pathological changes of testicular tissue injury of Huangjingzanyu Capsule group were significantly improved compared with cyclophosphamide group ($P < 0.05$). Huangjingzanyu Capsule has a protective effect on cyclophosphamide-induced testis injury in rats, and its mechanism is related to improving the expression of Bcl-2 protein and mRNA in testes and decreasing the expression of Bax, Caspase3 protein and mRNA

Keywords: Huangjingzanyu Capsule; Oligoasthenozoospermia; Mechanism of action

INTRODUCTION

Huangjingzanyu Capsule as the first specialized spermatogenic prescription for the treatment of male infertility, made by lifetime professor Wang Qi of Beijing University of Chinese Medicine, who is one of the founders of TCM andrology. Previous studies have found that Huangjingzanyu Capsule has a better therapeutic effect on oligoasthenozoospermia, but its molecular mechanism is unclear. In this study, cyclophosphamide was used to prepare the oligospermia model and analyze histopathological damage of the testis through detecting the protective effect of Huangjingzanyu Capsule on testis by RT-PCR and Western blot.

MATERIALS AND METHODS

Main experimental equipment

Western Blot electrophoresis apparatus (Bio-Rad); Genequant spectrophotometer (GE company); Nanodrop High-precision nucleic acid spectrophotometer (Thermo Fisher); ABI 7500 real-time fluorescence quantitative PCR instrument (Life); optical microscope: Japan Olympus company, product model: BX50; transmission electron microscope: Japan JEOL company, product model: JEM-1230.

Main Chinese patent medicine and drugs

Huangjingzanyu Capsule: Shanghai New Asia Pharmaceutical Hanjiang Co. Limited, lot number: 120603; Levocarnitine: Northeast Pharmaceutical Group Shenyang First Pharmaceutical Co., Ltd., lot number: 121001; Cyclophosphamide (CP): Shanxi Pude Pharmaceutical Co., Ltd., lot number: 04121003. The Chinese patent medicine and drugs above is suspended in 0.5% CMC in reserve before use.

Main reagents

Complete Protease Inhibitor Cocktail Tablets (Roche); ECL developing solution (Perkin-Elmer Life Sciences); PVDF film (MerckMillipore company); Trizol (Life Invitrogen company); 2X Mltra SYBR Mixture (CW0958) (Beijing Kangwei Century Co., Ltd.); Mixture (Promega company); DEPC (sigma company); Caspase-3 antibody (sc-7148, Santa Cruz); BAX (B-9) antibody (sc-7480, Santa Cruz); BCL-2 antibody (sc-7382, Santa Cruz); β -actin antibody (Tianjin Sungene Biotech); protein marker (Thermo Scientific).

Experimental methods

1. Grouping and administration methods: A total of 40 SD rats were randomly divided into four groups: normal group, model group, Huangjingzanyu Capsule group, and Levocarnitine control group, with 10 rats in each group. The rats were given adaptive feeding for three days. Normal

* To whom all correspondence should be sent:
E-mail: yanfei_z@163.com

group (NS): equal volume of normal saline instead of CP was given by intraperitoneal injection for five days, and normal saline was given by gastric perfusion from the sixth day for two weeks. Continuous gastric perfusion for 2 weeks. Model group (CP): CP of 35mg / kg was given by intraperitoneal injection for 5 days, and normal saline was given by gastric perfusion from the 6th day for two weeks. Huangjingzanyu Capsule group (HJZYC): CP of 35mg / kg was given by intraperitoneal injection for five days, and Huangjingzanyu Capsules of 1.24g / kg · d were given by gastric perfusion from the sixth day for two weeks. Levocarnitine group (Levocarnitine): CP 35mg/kg was given by intraperitoneal injection for five days, and Levocarnitine of 2.1ml / kg · d was given by gastric perfusion from the sixth day for two weeks. After 24 hours of the last administration, all the rats were anesthetized with chloral hydrate, and the testes and epididymis were quickly removed refrigerated in -80°C environment.

2. Real-time PCR was used to detect the contents of Caspase-3, Bcl-2 and Bax in testes.

3. Western Blot was used to detect the expression of Caspase-3, Bcl-2 and Bax in the testis.

4. Pathological detection of testicular tissue.

Six rats in each group were taken out, and their left testicular tissue was given HE staining for histopathological examination with light microscope. The spermatogenic cell lesions in

testicular seminiferous tubules were main observed and semi-quantitative Grading scale (Table 1) for testicular lesions was made. Two rats in each group were randomly selected to take two to three pieces of testicular tissue (about 0.5mm) to perform transmission electron microscopy.

Statistical methods

All measurement data were expressed as mean ± standard deviation ($\bar{x} \pm s$). Nonparametric rank sum test was used to compare the testicular lesions between each two groups, and statistics software SPSS 20.0 was used to perform T test with $P < 0.05$ meaning statistical significance between each group.

RESULTS

Caspase-3, Bcl-2 and Bax protein, expression results of mRNA

The results showed that the expression level of Caspase-3 protein and mRNA in the testicular tissue of model group was significantly higher than that of the normal group ($P < 0.05$). The expression level of Caspase-3 protein and mRNA in Huangjingzanyu Capsule group and Western medicine control group was significantly lower than that in model group ($P < 0.05$), suggesting that Huangjingzanyu Capsule and Levocarnitine had the effect on reducing the expression of Caspase-3 protein and mRNA. (seen in Figure 1 and Figure 2).

Table 1. Testicular grading criteria

Score	Pathological grading	Testicular lesions
0	-	Testicular seminiferous tubules were normal without obvious lesions.
1	+	Spermatogenic cells arranged disorder in testicular individual seminiferous tubule, part of the cell being swelling, degenerated, and sperm cells decreased.
2	++	Many spermatogenic tubules in testes underwent mildly atrophy, spermatogenic cells arranged in disorder, cell swelled and degenerated, and sperm cells significantly reduced.

Table 2. Changes of testicular lesion of each group.

Group	Lesion degree			Average rank
	-	+	++	
NS	6	0	0	8.50
CP	0	3	3	30.40#
HJZYC	4	1	1	13.80*
Levocarnitine	2	3	1	17.50*

Note: Compared with model group, * $P < 0.05$; Compared with normal group, # $P < 0.05$

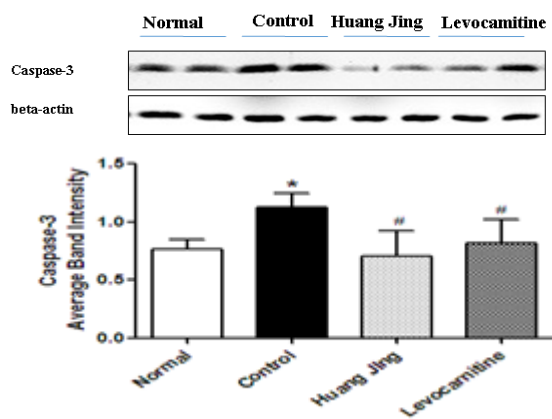


Fig. 1. Effect of Huangjingzanyu Capsule on the expression of Caspase - 3 protein in testicular tissue of Rats. Note: Compared with normal group, * $P < 0.05$; Compared with model group, # $P < 0.05$.

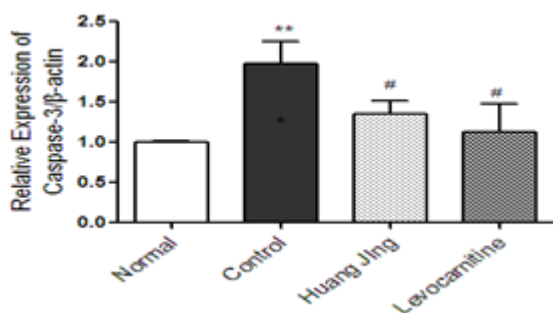


Fig. 2. Effect of Huangjingzanyu Capsule on the expression of Caspase - 3 mRNA in testicular tissue of Rats. Note: Compared with normal group, * $P < 0.05$; Compared with model group, # $P < 0.05$.

For the expression of Bcl-2 protein, the expression level of Bcl-2 protein and mRNA in the testis of CP group was significantly lower than that of NS group ($P < 0.05$). The expression level of Bcl-2 protein and mRNA in HJZYC group and levocarnitine group was significantly higher than that in CP group ($P < 0.05$), suggesting that Huangjingzanyu Capsule and Levocarnitine had the effect on increasing the expression of Caspase-3 protein and mRNA. While the expression level of Bax protein and mRNA in the testicular tissue of CP group was significantly higher than that in NS group ($P < 0.05$). The expression level of Bax protein and mRNA in HJZYC group and levocarnitine group was significantly lower than that in CP group ($P < 0.05$), suggesting that Huangjingzanyu Capsule and Levocarnitine all had the effect on reducing the expression of Bax protein and mRNA. (seen in Figure 3 and Figure 4).

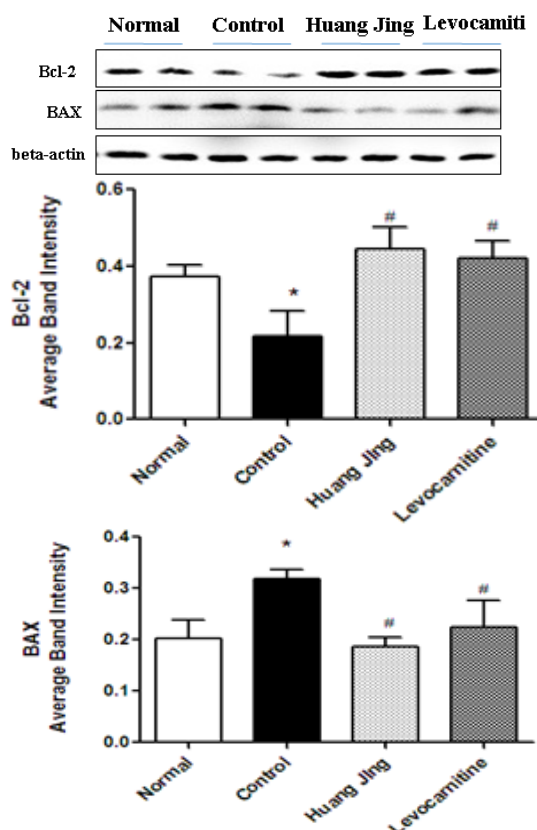


Fig. 3. Effect of Huangjingzanyu Capsule on the expression of Bcl-2 and Bax protein in testicular tissue of Rats. Note: Compared with NS, * $P < 0.05$; Compared with CP, # $P < 0.05$.

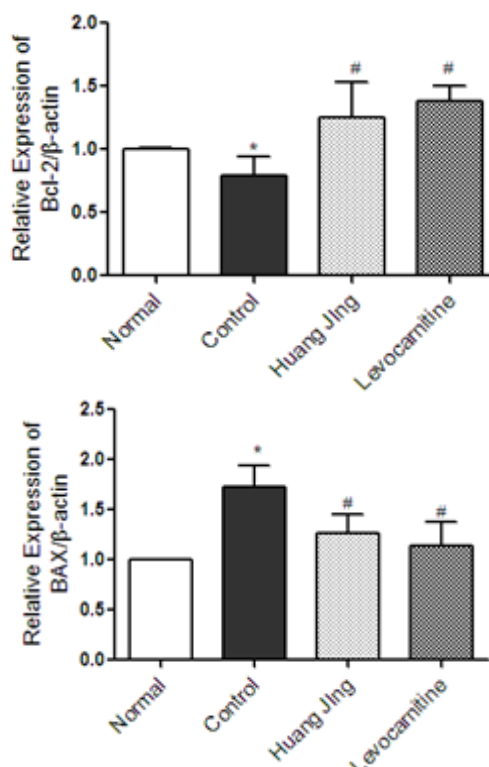


Fig. 4. Effect of Huangjingzanyu Capsule on the expression of Bcl-2 and Bax mRNA in testicular tissue of Rats. Note: Compared with NS, * $P < 0.05$; Compared with CP, # $P < 0.05$.

Histopathological changes of the testis

After the model was established, the testicular lesions of CP group were more serious than those of NS group ($P < 0.05$). After medication intervention, HJZYC group and Levocarnitine group improved significantly ($P < 0.05$). (more details seen in Table 2, Figure 5 - Figure 8)

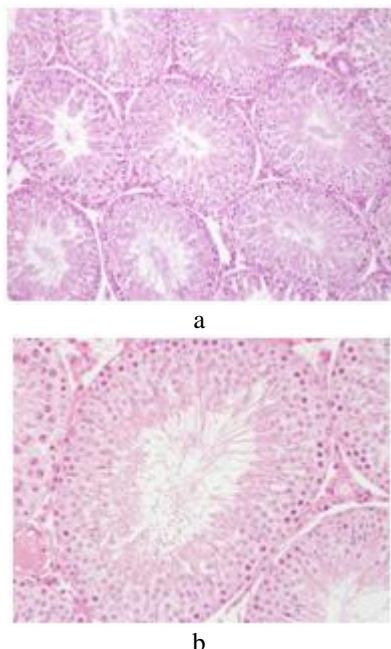


Fig. 5. Pathological section of rat testis in NS group: a) Pathological section of rat testis in NS group (HE×200); b) Pathological section of rat testis in NS group (HE×400)

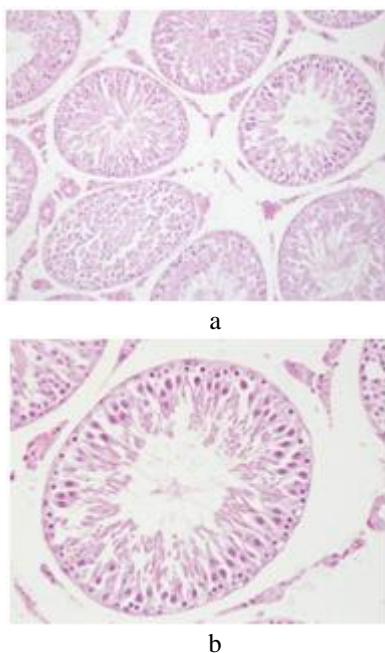


Fig. 6. Pathological section of rat testis in CP group: a) Pathological section of rat testis in CP group (HE×200); b) Pathological section of rat testis in CP group (HE×400)

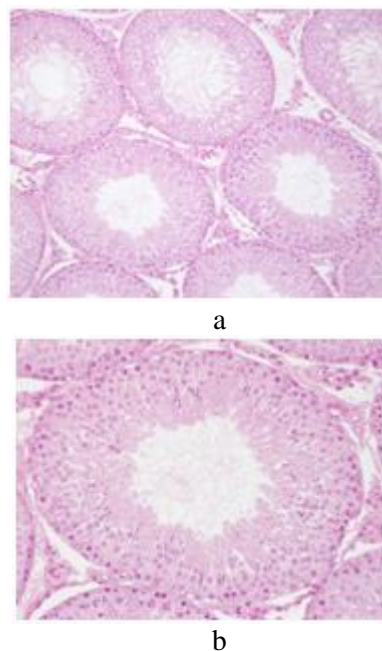


Fig. 7. Pathological section of rat testis in HJZYC group: a) Pathological section of rat testis in HJZYC group (HE×200); b) Pathological section of rat testis in HJZYC group (HE×400)

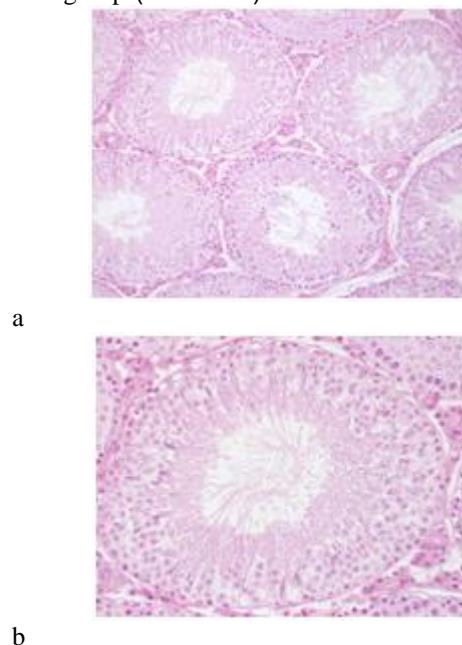


Fig. 8. Pathological section of rat testis in Levocarnitine group: a) Pathological section of rat testis in Levocarnitine group (HE×200); b) Pathological section of rat testis in Levocarnitine group (HE×400)

Changes of ultrastructure of testicular tissue

Spermatogenic cells and supporting cells were observed in the epithelium of seminiferous tubules in NS group. All levels of structure of Sperm cells were normal, and a lot of sperms were formed in the lumen. Cell membrane is smooth and complete with the existence of mitochondria and lysosomes. The mitochondria were round or rod with tubular ridge.

Supporting cell base was close to the basement membrane with oval nuclear, notch, and significant nucleolus (Figure 9). In the CP group, the basal membrane of the seminiferous tubule was irregular with widened gap or even local avulsion, defect, and fracture. The junction between supporting cell and spermatogonia widened and vacuolized. Mitochondria swelled showing polymorphic change with common ring and dumbbell shapes, and disappearance or vacuolization of mitochondrial ridges. Muscle-like cell shrunk with long oval shape (Figure 10). After the intervention of Huangjingzanyu Capsule, the base of the supporting cells was close to the basement membrane. The mitochondria of the spermatogenic cells and supporting cells were slightly swollen. The ridge of mitochondria ruptured slightly and partially vacuolated, but the whole condition was improved compared with the CP group (Figure 11) After the intervention of the Levocarnitine group, the support cells were round with marked nucleolus, and mitochondria and lysosomes were seen in the cytoplasm. The mitochondria were elliptic or round, slightly swollen, and some mitochondria decreased and vacuolated. The microtubule sperm tail was seen of "9 +2" structure (Figure 12).

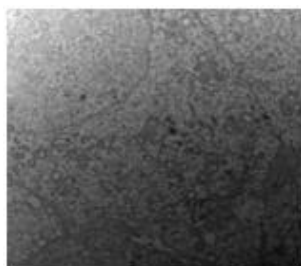


Fig. 9. Ultrastructure of NS group, $\times 12000$

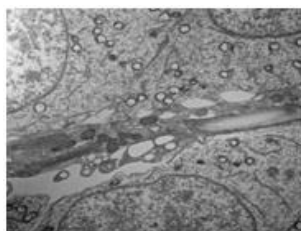


Fig. 10. Ultrastructure of CP group, $\times 8000$

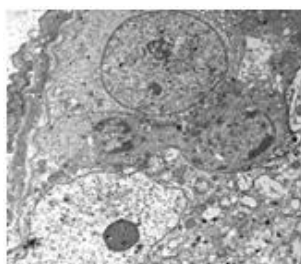


Fig. 11. Ultrastructure of HJZYC group, $\times 8000$

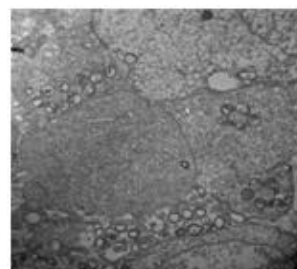


Fig. 12. Ultrastructure of Levocarnitine, $\times 8000$

DISCUSSION

The normal process of spermatogenesis requires the maintenance of the balance between cell proliferation and differentiation and apoptosis. Studies have shown that in the process of spermatogenesis, the body removes spermatogenic cells that are damaged or the chromosomes in them are abnormal through the germ cell apoptosis to strictly control the optimal number of spermatogenic cells and supporting cells and to ensure the normal number and quality of sperm differentiation and maturity [1]. The conditions such as environmental factors, living habits, pathological factors, physical and chemical factors, reproductive system infections, chronic inflammation, varicocele and other reasons can cause deterioration of testicular spermatogenic, and adverse effects of the testicular germ cell apoptosis or apoptosis-related genes[2], leading to spermatogenesis damage and the increase of all levels of apoptosis of spermatogenic cells (including sperm), resulting in sperm production increase, quality decrease, apoptosis index increase, and as an important result of less weak spermatogenesis [3], which is the important pathological step and mechanism of oligoasthenozoospermia. Studies show that 75% of the sperms die through apoptosis [4]. The mechanism of apoptosis during spermatogenesis has become one of the hotspots in the research of testicular biology [5].

So far, three apoptosis pathways have been identified: the death receptor pathway, the endoplasmic reticulum signaling pathway, and the mitochondrial pathway [8]. In mitochondrial pathway, cells are exposed to DNA damage, hypoxia, drug action and etc., and the mitochondrial permeability changes, membrane potential decrease and cytochrome C release, which activates Caspase-9 and Caspase-3 leading to apoptosis. Bcl-2 family is the main regulatory gene to prevent apoptosis cascade reaction process, through the regulation of transport and membrane permeability of endoplasmic reticulum nuclear matter inside and outside to prevent the release of cytochrome c. Bcl-

2 protein is a kind of membrane integral protein. The quantitative results show that the expression of Bcl-2 protein decreases with the increase of apoptosis rate in normal testis cells of rats. Bcl-2 gene family includes two major categories: genes that inhibits apoptosis such as Bcl-2 and genes that promotes apoptosis such as Bax. Bax is located in the cytoplasm and is activated by the apoptotic signal. Bax can form dimer or multimerize and insert into the mitochondrial membrane, leading to the decrease of mitochondrial membrane potential and the release of cytochrome c. The equilibrium state of intracellular Bcl-2 and Bax determines whether the cell ultimately survives or dies [9]. Studies have reported that when spermatogenic cells of kidney-yang deficiency rats undergo apoptosis, at the same time, Bax gene expression increases and Bcl-2 gene expression decreases, in order to promote spermatogenic cell apoptosis [10]. Chinese medicinal Shengjing Decoction can significantly improve the ratio of Bcl-2 / Bax, inhibit spermatogenic cell apoptosis, and promote cell proliferation [11].

This study has found that, after CP modeling, the expression of Bcl-2 protein and mRNA of testicular tissue in CP rats decreases, while the expression of Bax, Caspase3 protein and mRNA increases, indicating that CP can cause testicular spermatogenic dysfunction through apoptosis, and then result in less weak Spermatogenesis. After the intervention of Huangjingzanyu Capsule and Levocarnitine, the expression of Bcl-2 protein and mRNA in the testicular tissue of rats increases significantly, and the expression of Bax and Caspase3 protein and mRNA decreased significantly, suggesting that through increasing significantly the expression of Bcl-2 protein and mRNA, Huangjingzanyu Capsule can decrease the expression of pro-apoptotic gene Bax protein and mRNA to inhibit the apoptosis of spermatogenic cells, and significantly reduce the activity of Caspase-3, a public apoptotic factor, which plays a pivotal role in the apoptosis process to inhibit spermatogenic cell apoptosis, promote sperm production, and improve semen quality.

CONCLUSION

In HJZYC group and levocarnitine group the expression level of Bcl-2 protein and mRNA of

testicular tissue of rats increases, while the expression level of Bax, Caspase3 protein and mRNA decreases. The degree of testicular pathological damage in CP group is significantly higher than that in NS group ($P < 0.05$), indicating that the modeling is successful, and the gap between support cells and spermatogonia widens, breaks and ruptures. Mitochondria swells or vacuolizes. After the intervention of Huangjingzanyu Capsule, the condition improves significantly. the seminiferous tubule epithelium does not change significantly. There are more spermatogenic cells and they arrange more regularly. Testicular stroma is denser, and the stromal cells arrange more evenly. Mitochondria in spermatogenic and supporting cells are slightly swollen, and mitochondrial ridge is slightly ruptured and partially vacuolated, but the overall condition improved compared with CP group.

Acknowledgements: This Research was supported by Fundamental Research Project of Beijing University of Chinese Medicine(NO.2015-JYB-JSMS010) and National Natural Science Foundation Project (NO. 81503584).

REFERENCES

- 1.R.J. Blanco, G.C. Martinez, *Cell Prolif*, **29**(1), 13 (1996).
- 2.E. Pishavar, M. Shafiei, S. Mehri, *Drug Chem Toxicol*, **18** (2017).
- 3.M.Wu, C. Pan, Z. Chen, *Environ Sci Pollut Res Int*, **12** (2017).
- 4.D.T. Carrell, B.R. Emery, S. Hammoud, *Hum Reprod Update*, **13**(3), 313 (2007).
- 5.Y.F. Wang, *The Sixth National Conference of Reproductive Medicine Special Issue*, (2012).
- 6.X.W. Cao, C.Y. Li, C.W. Yuan, *Chinese J Sex Sci*, **20**(2), 51 (2011).
- 7.Q. Michele, M.B. Rosiane, C. Carla, *Eur J Obstet Gynecol Reprod Biol*, **167**, 47 (2013).
- 8.D.A. Ferrington, T.N. Tran, L. Kathleen, *Exp Eye Res*, **83**, 638 (2006).
- 9.M. Ghoneum, M. Matsuura, M. Braga, *Int J Oncol*, **33**(3), 533 (2008).
- 10.X. Li, J. Li, G.W. Fu, *Chengde Med Coll*, **2**, 118 (2007).
- 11.J. Mohammadian, M. Sabzichi, O. Molavi, *Asian Pac J Cancer Prev*, **17**, 11 (2016).
- 12.L. Wang, D.Chen, Z. Min, *Zhongguo Zhong Xi Yi Jie He Za Zhi*, **34**(5), 602(2014).

Cyclical variations of a HCCI engine fueled with n-butanol

G.Q. Lin*, G. Li, C. Zhang, Y. Shen, Q. Lv

School of Automobile, Chang'an University, Xi'an, China

Received February 12, 2015; Revised December 26, 2016

The 2nd cylinder of a water-cooled, naturally aspirated double-cylinders diesel engine was modified to operate on HCCI combustion mode. By changing intake temperature, mixture concentration and engine speed, the effects of parameter variation on cyclical variations of an HCCI engine fueled with n-butanol were investigated in this study. The results show that the peak cylinder pressure (P_{\max}) rises as the intake temperature or engine speed increases while reduces as the excess air ratio (λ) increases. The coefficient of variations for P_{\max} ($COV_{P_{\max}}$) is minimized at high intake temperature, low λ or high engine speed, which are 1.32%, 1.53% and 1.45%, respectively. Therefore, the optimal parameters may be obtained to improve the combustion stability of HCCI engines.

Keywords: HCCI, n-butanol, intake temperature, excess air ratio, cyclical variations

INTRODUCTION

Homogeneous charge compression ignition (HCCI) combustion is a new combustion mode, which compresses the premixed homogeneous air-fuel mixture until its automatic ignition near top dead center (TDC). This combustion mode combines the advantages of compression ignition engine and spark ignition engine [1]. In HCCI engines, the each point of premixed air-fuel mixture in combustion chamber is ignited simultaneously and the heat is released rapidly, close to the ideal constant volume combustion [2]. These contribute to the high thermal efficiency. Moreover, the HCCI engine may run with the lean homogeneous air-fuel mixture. This results in the low-temperature combustion, which subsequently produces low NO_x and less soot due to the temperature of combustion area in HCCI engine lower than compression ignition engines and spark ignition engines.

However, the combustion process of HCCI engines is instability because of misfire and knock so as to cause the HCCI engine operate within a relatively small range of speed and load. The combustion stability of HCCI engine is mainly controlled by chemical kinetics and influenced by various parameters [3]. The experimental research of the cyclical variations of HCCI engine conducted by Mauya et al under a fixed speed showed that the coefficient of variations (COV) increase as the intake temperature rises and the λ decreases [4]. Li et al conducted an experimental study on a single cylinder diesel engine to investigate the effects of

parameters such as compression ratio and inject pressure on cyclical variations of HCCI engine. They found that the cyclical variation is significantly influenced by ignition timing and retarded the ignition timing can lead to an increase of cyclical variations [5]. Xue et al investigated the cyclical variations of HCCI engine by changing the parameters such as intake temperature and mixture concentration and point out that the optimal intake temperature and mixture concentration may be obtained to ensure the combustion stability of HCCI engines [6].

As a potential renewable alternative fuel, the energy density and cetane number of n-butanol are higher than alcohol fuel (such as methanol and ethanol), which can meet the performance requirement of compression ignition engine [7]. Furthermore, the n-butanol is oxygenated fuel and has high latent heat of vaporization, which may reduce the cylinder temperature and improve the NO_x and soot emission of diesel engines. Therefore, an experiment on the influence of the various parameters such as intake temperature, mixture concentration and engine speed on the cyclical variations of HCCI engine fueled with n-butanol is investigated in this study. The aim of this research is to explore the cyclical variations of HCCI engine and provide the basis for the intake temperature, mixture concentration and engine speed optimization in an HCCI engine.

EXPERIMENTAL SETUP

Experimental apparatus

To evaluate the cyclical variation of HCCI engine, a modified double-cylinder, four-stroke, water-cooled, naturally aspirated and direct-injection engine is used in this study. The

* To whom all correspondence should be sent:

E-mail: lgq@chd.edu.cn

engine specifications are given in Table 1. Engine loads and speeds are controlled by an eddy current engine dynamometer (CW25, Cama, Luoyang, China) of 25 kW.

To operate the test engine on HCCI combustion mode, a few modifications are made for the test engine. Fig.1 shows the schematic diagram of experimental apparatus used in this study. Among them, the 1st cylinder is kept on its original combustion mode, but the 2nd cylinder is converted into HCCI combustion mode. The control system of intake temperature, installed in the 2nd cylinder, is used to control the 2nd cylinder intake temperature.

And the corresponding concentration homogeneous mixture is provided to the cylinder by PFI fuel injection system. The in-cylinder pressure is measured by a piezo-electric type pressure sensor (6052A, Kistler) installed on the 2nd cylinder and is amplified by a charge amplifier (5019, Kistler). The pressure data are taken over 150 cycles and acquired by a combustion analyzer (Kibox 283A, Kistler). The $COV_{P_{max}}$ is calculated based on the cylinder pressure.

Table 1. Specifications of test engine.

Model	CT2100Q
Combustion chamber shape	ω
Cylinder	100×105
Displacement(L)	1,65
Compression ratio	17:1
Intake valve opening angle	17°CA
Intake valve closing angle	43°CA
Exhaust valve opening angle	47°CA
Exhaust valve closing angle	17°CA

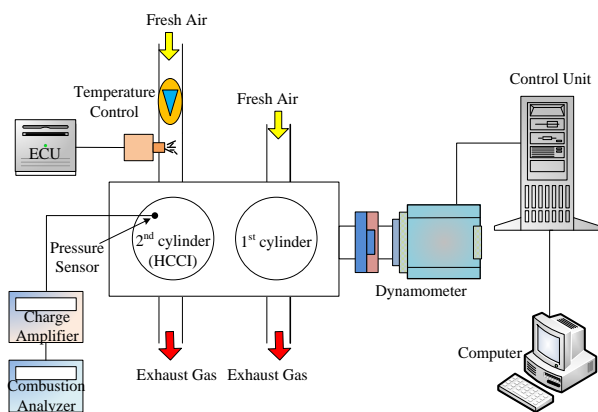


Fig.1 Schematic diagram of experimental apparatus.

Experimental procedure

Before the start of experiment, the 1st cylinder is started with diesel firstly, which drives the test one for warm-up until the coolant and lubricating oil temperature reached about 80°C. Then, the engine

is adjusted to the test conditions: to stop diesel fuel to the 1st cylinder, meanwhile start the 2nd one for HCCI combustion and record cylinder pressure data. The steady state tests are repeated at least twice to ensure that the results are repeatable within the experimental uncertainties.

Data processing

The cyclical variations are the parameters which may characterize the combustion stability of each cycle [6]. The combustion stability, fuel economy and emission can improve by reducing the cyclical variations of cylinder pressure. This paper uses the coefficient of variations for P_{max} ($COV_{P_{max}}$) to evaluate the cyclical variations of HCCI combustion. And its calculation formula is

$$COV_{P_{max}} = \frac{\delta_{P_{max}}}{\bar{P}_{max}} \times 100\% \quad (1)$$

Where, $\delta_{P_{max}}$ is the standard deviation of P_{max} , and \bar{P}_{max} is the average value of P_{max} in 60 continuous cycles.

RESULTS AND DISCUSSION

Effect of intake temperature on $COV_{P_{max}}$

Fig. 2 shows the $COV_{P_{max}}$ of HCCI engine fueled with n-butanol under different intake temperature at engine speed of 1000 r/min and λ of 2.5, respectively. It is shown that the peak cylinder pressure increases while the $COV_{P_{max}}$ decreases as the intake temperature rises. This is reasonable because the rise of intake temperature leads to increase the temperature of compression process, raise the activation energy of fuel mixture, and intensify the molecular motion of fuel mixture. These contribute to the more effective collision between fuel mixtures molecular, which subsequently enhance the combustion intensity and increase the quantity of heat release. Meantime, high intake temperature may promote the breaking of chemical bond and produce massive free radical, which can promote the chain reaction and accelerate the combustion rate, reduce the combustion duration and make the distribution of peak cylinder pressure centralized.

Effect of mixture concentration on $COV_{P_{max}}$

Fig. 3 shows the $COV_{P_{max}}$ of HCCI engine fueled with n-butanol under different mixture concentration at engine speed of 1000 r/min and intake temperature of 140°C, respectively. The mixture concentration is expressed by excess air ratio λ , shown in the figure, and the mixture becomes lean with the increase of λ . It is observed that the peak cylinder pressure increases and

$COV_{P_{max}}$ decreases as the λ reduces. It is considered that the ignite temperature is significantly influenced by mixture concentration. As the λ reduces, the fuel in per unit air-fuel mixture increases and the ignite temperature reduces; in this case, the air-fuel mixture is ignited more easily, leading to a stronger combustion and more heat release. Moreover, the mixture concentration is a key parameter to affect the formation of free radical. The rate of free radical production increases under the condition of lower λ , which may intensify the chemical reaction rate, enhance combustion intensity, reduce combustion duration and reduce the $COV_{P_{max}}$.

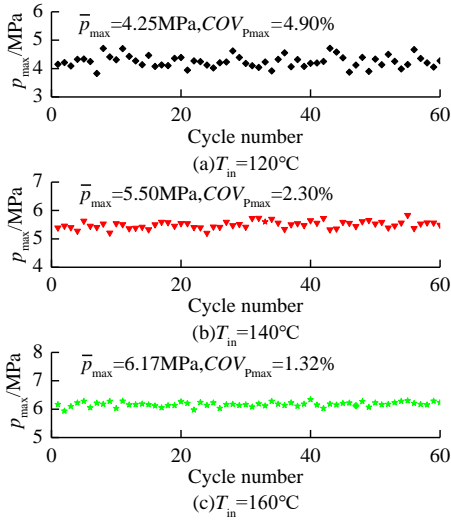


Fig. 2. The $COV_{P_{max}}$ of HCCI engine for various intake temperature.

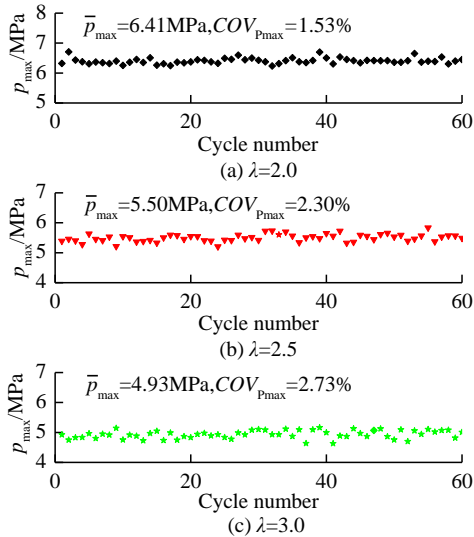


Fig. 3. The $COV_{P_{max}}$ of HCCI engine for various λ

Effect of engine speed on $COV_{P_{max}}$

Fig. 4 shows the $COV_{P_{max}}$ of HCCI engine fueled with n-butanol under different engine speed at intake temperature of $140^{\circ}C$ and λ of 2.5, respectively. It is found that the peak cylinder

pressure increases as $COV_{P_{max}}$ decreases with the increase of engine speed. The in-cylinder air motion is strengthened as engine speed increases.

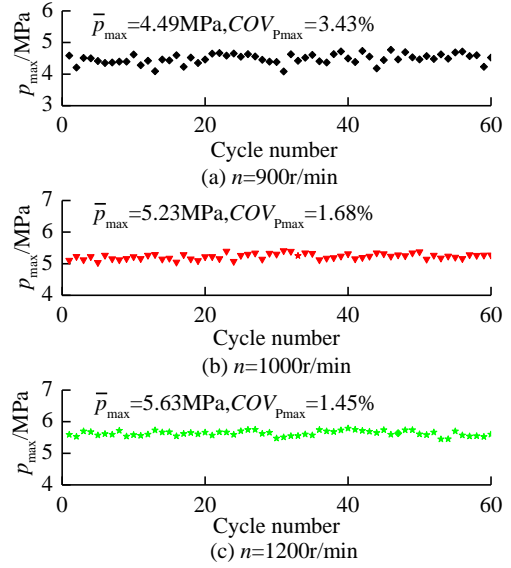


Fig. 4. The $COV_{P_{max}}$ of HCCI engine for various engine speeds

Consequently, it causes the air-fuel mixture more homogeneous, the effective collision between fuel molecules more frequently. Moreover, it is also possible that the heat loss reduces and thermal load rises as the engine speed increases, which may improve the temperature of air-fuel mixture and promote the formation of free radical. All these lead to promote auto-ignition, intensify combustion and increase the quantity of heat release. In addition, the strength of in-cylinder air motion and increase of air-fuel temperature are contribute to increase the heat release and improve the combustion condition so as to make the distribution of peak cylinder pressure centralized and improve the combustion stability.

CONCLUSIONS

- (1) The P_{max} increases as the intake temperature rises. The $COV_{P_{max}}$ is minimized at the intake temperature of $140^{\circ}C$, and this temperature is the optimal.
- (2) The higher P_{max} and lower $COV_{P_{max}}$ may be obtained at rich mixture, and this means that the combustion stability may be improved by the rich mixture.
- (3) The P_{max} increases as the engine speed rises. Under the condition of higher engine speed, the lower $COV_{P_{max}}$ may be obtained at relatively lower intake temperature.
- (4) The higher engine speed and richer mixture accomplish with relatively higher intake temperature may be a potential tool to improve the

cyclical variations of HCCI engines.

Acknowledgements: This work was supported by the project of Natural Science Foundation of Shaanxi Province [Grant NO. 2012JQ7031], the Special Fund for Basic Scientific Research of Central Colleges, Chang'an University [NO. 2013G1502063 and 2014G1221018], Doctor Postgraduate Technical Project of Chang'an University [No.2014G5220007], the transportation research project of Shaanxi Provincial Department of transportation [No.16-36K]. The authors are grateful for their financial supports.

REFERENCES

1. C. Zhang, H. Wu, *International Journal of Hydrogen Energy*, **37**, 4467 (2012).
2. M.-B. Liu, B.-Q. He, H. Zhao, *Energy*, **85**, 296 (2015).
3. H. Xie, B.-Q. He, Y. Zhang, T. Chen, H. Zhao, *Journal of Combustion and Technology*, **12**, 5 (2006).
4. R.K. Maurya, A. K. Agaewal, *Applied Energy*, **89**, 228 (2012).
5. H.L. Li, W. Stuart Neill, H. Guo, W. Chippior, *Journal of Energy Resources Technology*, **134**, 1 (2012).
6. L. Xue, C.-H. Zhang, J. Wang, *Journal of Chang'an University (Natural Science Edition)*, **34**(6), 157 (2014).
7. U. Ahmet, *Energy Conversion and Management*, **98**, 199, (2015).

Purify processing and utilization of mine water

S. Aijun, W. Shiwen*, Z. Liya

Hebei GEO University, China

Received February 12, 2016; Revised December 26, 2016

China is a large country of coal production. During the coal mining process, massive mine drainage has caused not only the waste of groundwater resource, but also environmental pollution. On the other hand, mining production and life supply water is very scarce. According to the mine water features, majority of mine drainage water belongs to the mine water containing suspended solids, the mine water needs to be necessarily purified before used. What the purification mainly eliminates is the suspended solids. In this paper, the methods and technological processes about mine water purification are discussed, such as coagulation, sedimentation, filtration and disinfection. Different ways of methods and technological processes have to be chosen according to different characteristics of water quality. Finally, examples on purification and utilization of mine water, such as Pingdingshan Coal Group Company, Wannian Coal Mine of Fengfeng Group Limited Company and Tangshan Coal Mine of Kailuan Group Company, are shown to prove the obvious social, economic and environmental benefits of mining water purification and utilization.

Keywords: mine water, purification, turbidity.

INTRODUCTION

China is a large country of coal production, raw coal production amounted to 10.79×10^8 t in 1990, and reached 21.1×10^8 t in 2005. It ranked the first in the world for many years [1]. Coal is the main energy source of China, accounting for over 70% of our one-time energy consumption. Chinese coal mainly comes from underground mining, accounting for about 97% of the overall coal production. As coal beds generally buried below the underground aquifers, in the coal mining process, people must discharge massive water inflow to ensure the mine safety. According to incomplete statistics, the drainage of whole national coal mine is approximately 22×10^8 t per year, and the average drainage is about 4 m^3 per 1t coal, but the utilization ratio is less than 20% [2-4]. The great massive mine drainage has caused not only the serious waste of groundwater resource, but also environmental pollution, on the other hand, mining production and life supply water is very scarce. In the mine area, industrial and agricultural supply water is also very scarce, a lot of mine drainage makes the contradictions between drainage and water supply more serious, and accelerated water crisis. As for the coal industry, 70% of the mining area in China faces water shortage, where 40% belongs to serious water shortage, and life supply water of many mining areas is very shortage [5].

With the economic and social development and the exploitation of coal resource, the contradiction between mine drainage and industrial, agricultural, life supply water also will become more and more highlight. Strengthening the new technique research and utilization of mine water purification can mitigate the water crisis, promote the economical continual development and protect ecological environment and so on.

Mine Water Quality Features

According to the mine water quality features, it can be generally divided into the following types [6]: (1) clean mine water; (2) mine water containing suspended solids; (3) high mineralization mine water; (4) acid mine water; (5) mine water containing special pollutants. In North China, most mine drainage belongs to mine water containing suspended solids.

Mine water containing suspended solids is the mine water in which the content of suspended solids (commonly expressed by SS) cannot be dissolved is very high. The general content of suspended solids is 100~500mg/L, sometimes over 1000mg/L. Therefore, the turbidity of mine water is about 100~300 degree. The suspended solids in the mine water are mainly come from coal fine, rock dust as exploitation activity generate into the mine water. Therefore, the mine water color shows dark, the sensory situation is very bad.

Under normal circumstances, mine water generally stay in the mine water storage for a period of time (generally 4~8 h), so larger pieces of coal granule, rock granule and other solid

* To whom all correspondence should be sent:
E-mail: wsw84946108@163.com

particles can be naturally deposited at the bottom of the water storage. Then, the drainage equipment pumps the mine water in the water storage to the ground. So the size of the suspended solids pumped to the ground is generally small, the diameters of majority particles are below 50 μ m, moreover, the density of suspended particles are also small, the average density is 1.2~1.3g/cm³, so its subsidence speed is very slow.

Another water quality feature of mine water containing suspended solids is that the bacteriological content is very high. Bacteriological indicators such as the total bacteria amount exceed the standard seriously, the colon bacillus often exceed the standard several times, or even thousands of times. This phenomenon is caused mainly by living, production activities under the mine well.

Mine water, especially the karst water, the original water is generally high quality groundwater, and belongs to HCO₃ or HCO₃-SO₄ - type water. The mineralization degree of water is generally smaller than 1g/L. The total hardness is smaller than 25 German degrees. As the result of exploitation, the wall rock groundwater with massive mine dusts, stives, and rock debris pellet in different size flowing into the mine system, made the water quality bad; especially make the suspended content rise, the reproduction of the bacterium and the mildew increase quickly. The water is turbid and the feeling and seeing state is bad. Therefore, mine water needs to be carried on essential purification before used[7].

New Purification About Mine Water

Purification methods

All impurities in mine water may be divided into 3 kinds: suspended, colloid and solute. The main objects which the purification needs to remove are the suspended and the colloid impurity, which are the main reasons of leading to water turbidity.

The principal characteristic about suspended solids is that they often present in suspended state in dynamic water. But they may be separated in the hydrostatic water, light matters will float up, and heavy ones will sink down. The principal characteristic about colloid grain is that it is quite stable in the water, it will not naturally subside after a long time even several years. When light illuminates, it is scattered and causes turbid. According to the characteristics of the suspended and the colloids, the main methods of the purification for living water are coagulation, sedimentation, filtering and disinfection.

(1) Coagulation, it is an extremely important aspect in the water purification technology. In the process of purify the turbid water, it needs to add the coagulants. The principles of select the coagulants are they can produce large, heavy, strong vitriol flower, the effect of purifying water is good, and it has no bad influence to the water quality. Moreover, the price is cheap and the source of goods is sufficient. Simultaneously, we should select the coagulant according to the water quality characteristic and the water temperature of the water source and so on. The commonly used coagulants may be divided into two kinds. One kind is the aluminum salt coagulants, another is the molysite coagulants, such as aluminum sulfate (Al₂SO₄·18H₂O), iron trichloride (FeCl₃·6H₂O), ferrous sulfate (FeSO₄·7H₂O), polymerization aluminum chloride, and organic high molecular polymer flocculants. Among them, aluminum sulfate is the most widespread coagulant at present, and the second is the polymerization aluminum chloride.

The mixing process is to let the medicament solution disperse into the water rapidly and evenly. The coagulant selected should be mixed evenly with the original water in a short time, and enables the whole colloid impurity in the water to react with the medicament. At present, two methods are mainly used in majority water factories: the water pump mix and the pipeline mix. After a instant mix of water and the medicament, some tiny vitriol flowers can appear. In order to sink rapidly, they must be agglomerated into large sizes (0.6~1.0mm), and close-grained, not frangibility. But in the coagulation stage, water turbulent motion intensely; the vitriol flower is difficult to become big. However, the work of reaction stage is that: the vitriol flowers condense to large vitriol flower pellets with size 0.6~1.0 mm in the slow water current of the reaction basin after certain time in order to sink fast in the sedimentation basin. There are many types of reaction basins. The commonly used are the clapboard reaction basin of advection type and vertical mobility type, the reaction basin of whirlpool type, the machinery reaction basin and the table-flap reaction basin.

(2) Sedimentation: the colloid impurity condenses to bigger vitriol flower granules in the water after adding the coagulant into the original water passing through mix reaction, the next is that they will be removed in the sedimentation basin. At present, the commonly used sedimentation pools are the sedimentation basin of advection type, the sedimentation basin of radial flow type, the sedimentation basin of sloping plate or of sloping

tube. Among those, the sloping plate and sloping tube sedimentation basin are more widely used.

(3) Filtration, one part of particles whose size are big or easily to be sank have been removed after the coagulation and the sedimentation of the original water, and turbidity of the water reduces by 100~150 approximately. But in order to enhance the water quality further, and make the turbidity to fulfill the drinking water standard, the method of filtration is also needed to get rid of the tiny impurity particle and parts of bacteria. The most commonly used filtration basins are the ordinary quick filtration basin, the siphon filtration basin, the non-valve filtration basin, the motion flushing cover filtration basin, and the pressure filtration basin. The filtration basin can clarify the water mainly depends on the filtration materials including quartz sand and anthracite grain. In addition, the plastic bead, the ceramsite, the magnetite grain are also used.

(4) Disinfection, disinfection is essential to prevent the spread of disease through drinking water in the treatment of domestic drinking water. Disinfection aims to eliminate the pathogenic effect of pathogenic microorganisms. Pathogenic organisms include bacteria, viruses and so on. The disinfecting methods of water may be divided into the physical disinfection and the chemical disinfection. The physical method includes the heating method, the ultraviolet radiation method, and the ultrasonic wave method. The chemistry method includes the chlorining method (or adding bleaching powder), the ozone method, the heavy metal ion method, or other oxidant method and so on. At present, the chlorining method is the most common one. The water after disinfecting can be transported into the pipe network for the users.

In addition, softening processing or desalination processing and so on are often needed according to the needs of the industrial use of water.

The technical process of purification

According to the hygienic standard requirement of domestic drinking water, the choice of the technical process of purification mainly depends on water quality characteristic of water source. Therefore, we have to conduct full investigation of the water quality of water source, then we can decide reasonable purification method and the technical process.

When the mine water wants to be used as the water source of domestic drinking water, we generally use the purification process shown in Figure. 1. Firstly, we add the coagulant in the water, and

make them mixed rapidly and fully after the agitation of water pump impeller. Then they grow gradually into the flocculent deposit material (flocculating constituent or vitriol flower) in the reaction basin. After getting rid of the vitriol flower in the sedimentation basin and in the filtration basin, we add the chlorine into the clear water to disinfect, then the water will be supplied to the users.

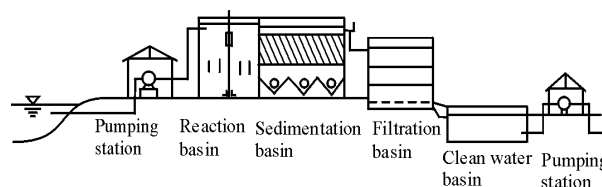


Fig. 1. Schematic diagram showing the purification.

If the mine water turbidity is low (frequently below 100o), the water added medicament can be directly filtered without coagulating sedimentation, this can omit the reaction basin and the sedimentation basin. After adding the chlorine disinfecting of the filtrated water, the pumping station transports the water into the pipe network. Its process is shown in Figure. 2.

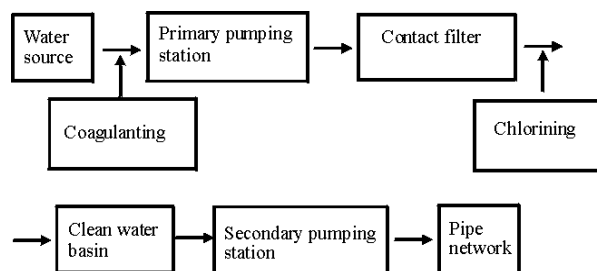


Fig. 2. Purification process of low-turbidity water.

For high turbidity water, in order to save the coagulant and achieve the anticipated effect, we can use the natural sedimentation method before the coagulating sedimentation. A lot of massive silts can be precipitated from the original water before future purification. The process of purification is shown in Figure. 3. According to practical experience, the common process of purification at present is:

coagulation→sedimentation→filtration→disinfect on.

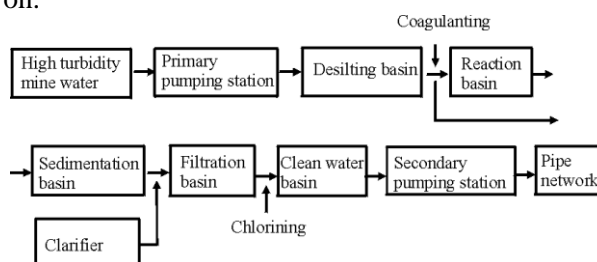


Fig. 3. Purification process of high-turbidity water.

APPLICATIONS

Pingdingshan Coal Group Company in Henan has accumulated rich experience in the term of water purification processing, and created a path of converting mine water into resource. Since 1977, Pingdingshan Coal Group Company built the first mine water purification factory, the company has built 16 mine water purification factories so far. Over 38 000 000 m³ mine water after purification reached “sanitary standard for drinking water” every year. The water becomes the main water source of production and living water, it also made the farmers nearby use the tap water. The main structures of water processing company include sand basin, reaction basin, sedimentation basin, filtration basin, and clean water basin. The water after processing can be directly supplied to the users. It has solved the water shortage problem of the mine area. The water is black before disposed, the suspended content is more than 200mg/L, and the turbidity is 150~300 degree. The sensory characteristic target of the purified mine water after disposed is good, the suspended solids may be eliminated, the water turbidity can achieve 3.50~6.50, the bacterium indexes of water fulfill the “sanitary standard for drinking water”.

Wannian Coal Mine of Fengfeng Group Limited Company, the purification plant was designed by Wuhan Design Institute of Coal Mine, and the invested over 0.7 million yuan. The designed purification mine water is 5200 m³/d, and it was operated in 1985. The main buildings are sewage regulating basin, pumping station, response basin, filtration basin, disinfection room, water storage, clean water basin and so on. The main technological processes are shown in Figure. 4. The water after purification passed the analysis of the water quality, and conforms to “sanitary standard for drinking water”. The cost of processing water is 1.5 yuan per ton at present.

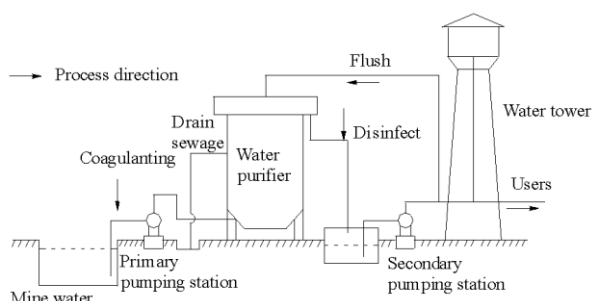


Fig. 4. Purification process of the mine water in Wannian Coal Mine

Tangshan Coal Mine subordinated to Kairuan Group Company invested 12.4 million yuan to construct mine water purification factory in 1992.

The designed capacity of water purification is 15000 m³/d. After purification, the turbidity of the mine water is less than 1 degree, conforming to “sanitary standard for drinking water”. By the end of 2004, the mine water processed had accumulate to 5860×10⁴ m³. While reducing the costs of drainage sewage and pumping groundwater resource for the enterprise, it also created tremendous social, economic and environmental benefits. Currently, the number of water-using households is over 10000. Taking the benefit of 2004 as example, the total annual production of purified water is 366.9×10⁴ m³, the cost is 1.32 yuan per ton, however, the cost of pumping underground water is 2.12 yuan per ton, thus, we can save 2.9352 million yuan.

For small type of supplying water (≤60m³/h), the integrative water purifier may be directly used. Now, a lot of coal mines in China use the integrative water purifiers to purify the mine water containing suspended solids. It was a small water purification device developed in 1980s in our country focused with reaction, sedimentation and filtration. It has advantages of small volume, small land occupation and convenient transportation. The integrative water purifier can be divided into the hydro-cycle type and the coagulation-sedimentation type. Now the coal mine enterprises mainly use the purifier of hydro-cycle type to purify the mine water. The processes of using the water purifier to purify the mine water are shown in Figure. 5.

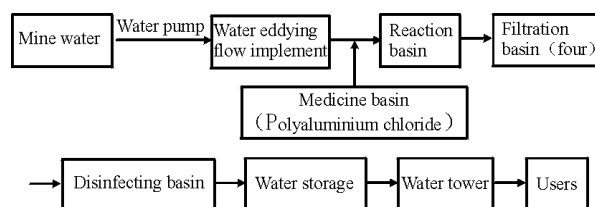


Fig. 5. Purification process of the integrative water purifier.

CONCLUSION

China is a large country of coal production. In the coal mining process, we must discharge massive mine water to ensure the production security. The great massive mine drainage has caused not only the waste of groundwater resource, but also environmental pollution. On the other hand, the industrial and agricultural water in the mining areas is extremely scarce, domestic water in many mining areas is also extremely shortage. Strengthening the research on the new techniques and utilization of mine water purification can mitigate the water crisis, promote

the economical sustainable development, and protect ecological environment.

From the mine water features, majority of mine drainage water belongs to the mine water containing the suspended solids. The mine water needs to be necessarily purified before used. Purification mainly eliminated the suspended and colloid impurity. The common methods of handle the mine water for drinking are coagulation, sedimentation, filtering and disinfection. At present, many coal mines use the small type water purification device (integrative water purifier), which contains reaction, sedimentation and filtration to process the mine water, obtaining the good effect. The water purification plants of Pingdingshan Coal Group Company, Wannian Coal Mine of Fengfeng Group Limited Company and Tangshan Coal Mine of Kailuan Group Company, not only solved the problem of the mine production and domestic water, but also have reduced the costs of drainage sewage and pumping groundwater resource for enterprises, they also created

tremendous social, economic and environmental benefits.

REFERENCES

1. W.R. Hu, Technologies of coal mine water and purification and utilization of waste water. Coal Industry Publishing House, Beijing, China, 1998.
2. J.L. Li, J. Jiang, Y.B. Wang, *Energy Environmental Protection*, **18**(1), 20 (2004).
3. A.J. Shao, X.D. Wang, T.S. Shao, *Hydrogeology and Engineering Geology*, **1**, 46 (1997).
4. A.J. Shao, F.W. Zhang, T.S. Shao, T.S. Liu, Coal mine groundwater, Geological Publishing House, Beijing, China, 2005.
5. L.P. Xiao, B. Liang J.Z. Di, *Journal of Liaoning Technical University*, **22**(6), 862 (2003).
6. M.Z. Chen, Z.Q. Huang, M.X. Zhang, et al., *Coal Science and Technology*, **28**(4), 25 (1996).
7. Z.M. Cao, L. Gao, G. Cui, Y.Z. Liu, L.R. Zhou, H.G. Niu, C.Y. Yu, J.D. Wei, A set of technologies and equipment for mine water purification and resource. Coal Industry Publishing House, Beijing, China, 2004.

Effect of NO oxidation to NO₂ from diesel engine over Mn-Ce/ γ -Al₂O₃ catalyst

L. L. Lei*, J. C. Yin, B. Zhang, P. Wang

School of Automotive and Traffic Engineering, Jiangsu University, Zhenjiang 212013, China

Received February 12, 2016; Revised December 26, 2016

A series of Mn-Ce/ γ -Al₂O₃ catalysts were prepared by loading different amounts MnO_x-CeO_x on the sol-gel synthesized γ -Al₂O₃ mixed oxides. The activities of the catalysts for NO oxidation to NO₂ were evaluated in 500ppm NO and 10% O₂ (N₂ balance) based upon the simulation experiment. The results showed that NO conversion rate raised with the increase of the temperature, which reached up to the peak value at 300°C and reduced with the further increase in temperature. The steady time for the volume fraction and NO₂ was reduced with the increase of temperature. All the 6Mn10Ce/ γ -Al₂O₃, 8Mn10Ce/ γ -Al₂O₃ and 10Mn10Ce/ γ -Al₂O₃ exhibited high catalytic oxidation of NO to NO₂, and NO conversion reached up to above 60%. Among all the catalysts, 6Mn10Ce/ γ -Al₂O₃ catalyst showed the highest catalytic activity with 44% of NO conversion at the temperature below 200°C, which indicated that 6Mn10Ce/ γ -Al₂O₃ catalyst was benefit for oxidation NO to NO₂ at low temperature.

Key words: Diesel engine, NO oxidation, MnO_x-CeO_x, simulation experiment

1 INTRODUCTION

Nitrogen Oxides (NO_x) emitted by automobiles often appears as a major source of air pollution, which is considered to be hazardous to environment and human health due to the formation of fine particles, ozone smog, acid rain and eutrophication [1,2]. NO_x storage/reduction (NSR) is currently regarded as one of the most practical technologies for lean-burn gasoline and diesel vehicles and has also been extensively studied for NO_x removal [3,4]. NSR catalysts are generally comprised of precious metals, NO_x storage components and support metal oxides working under lean/rich conditions. Compared with NO as primarily components of NO_x, NSR trapping materials more effectively sorb NO₂, or NO₂ may be the required intermediate compound for NO_x sorption. Then oxidation of NO to NO₂ will result in more efficient for NO_x removal.

In general, Pt has been recognized as the best active catalyst for NO oxidation, while Pt-group metals are expensive and suffered by sulfate poisoning referring to sulfate oxidation with oxygen on the surface of the catalyst. Replace Pt with alternative materials or reduce loading of Pt with monolayer catalysts and electrocatalysts have attracted more concern to reduce the cost of catalysts in recent years [5,6,7,8].

MnO_x based oxides present high active catalytic for NO_x removal [9,10,11]. Mn/TiO₂ and Mn/ZrO₂ mixed oxides showed high oxidation of NO, which the peak value could reach up to 59% at 298°C and 78% at 270°C respectively [12]. It was found that CeO_x metal oxides could storage Oxygen

through the transfer between Ce³⁺ and Ce⁴⁺, which was benefit for improving the catalytic activity at low temperature [13,14,15,16]. Mn-Ce mixed oxides showed higher NO oxidation that was about 3-10 times more than that of with CeO₂ and MnO_x at 200°C, indicating the interaction between Mn and Ce would enhance the oxidation activity of catalysts at low temperature [17].

In order to fully study the mechanism of NO oxidation to NO₂ over Mn-Ce mixed oxides catalysts, this report prepared a series of xMnyCe/ γ -Al₂O₃ (x=4,6,8,10. y=10) catalysts by a sol-gel deposition method. The activities for NO oxidation to NO₂ were measured based upon the fixed bed reactor by simulation test, and the effect of temperatures on NO oxidation over Mn-Ce catalysts were also investigated to reveal the evolution process between NO and NO₂.

MATERIALS AND METHODS

Catalyst Preparation

Mn-Ce mixed oxides catalysts were synthesized by a sol-gel method. Ce(NO₃)₃·6H₂O, C₄H₆MnO₄·4H₂O and γ -Al₂O₃ were dissolved in the solution containing deionized water, citric acid and polyethylene glycol, forming homogenous and transparent solution. After continuously stirring at 80°C until transparent gel was obtained, then dried at 110°C for 24h and then decomposed at 300°C for 1 h and calcined at 500°C for 5h under static air in a muffle to obtain the fresh catalyst samples.

* To whom all correspondence should be sent:
E-mail yutian820817@126.com

Catalyst characterization

X-ray diffraction patterns used to investigate the phase structure and phase composition of catalysts were measured on a Bruker D8 ADVANCE X-ray diffractometer with a Ni-filtered Cu K α ($\lambda = 0.154068$ nm) radiation source at 40 kV and 40 mA. The catalyst samples were scanned at 2θ ranging from 20° to 80° with a scanning velocity of 7°min^{-1} .

Catalytic Measurements

The catalytic test were carried out in a continuous fixed-bed quartz tubular microreactor with an inside diameter of 10 mm at atmospheric pressure, as shown in Figure 1. The oxidation of NO to NO₂ activity was measured at the temperatures in the range of 150-450°C. 0.3ml catalyst powder was packed in the reactor bed. The reactant gas mixture (500ppm NO, 10%O₂,N₂ balance) was fed to the reactor with a total flow rate of 100ml/min, corresponding to a gas hour space velocity (GHSV) of 50000h^{-1} . NO and NO₂ concentration were analyzed by a Thermo 42iHL NO_x gas analyzer (America). The NO conversion (X_{NO}) is defined as:

$$X_{\text{NO}} = \frac{\text{NO}_{2\text{ out}}}{\text{NO}_{\text{ in}}} \times 100\%$$

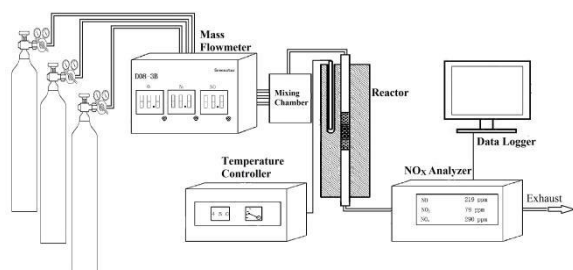


Fig. 1. Schematic diagram of catalyst activity test

RESULTS AND DISCUSSION

XRD Analysis

The XRD pattern of $x\text{Mn}10\text{Ce}/\gamma\text{-Al}_2\text{O}_3$ ($x=4,6,8,10$) catalysts are shown in Figure 2. As can be seen in Figure 2, all the samples exhibit characteristic peaks of $\gamma\text{-Al}_2\text{O}_3$ (JCPDS:PDF 48-0366). The main diffraction peaks at $2\theta=28.5^\circ$, 33.1° , 47.5° and 56.3° , attributed to the (111), (200), (220) and (311) planes of cubic fluorite CeO₂ (JCPDS:PDF 43-1002) [18]. Other two diffraction peaks at $2\theta=31.8^\circ$ and 56.3° (which are overlapped with the peaks of CeO₂) are identified as the phase of MnO₂ (JCPDS:PDF 65-7467). According to Scherrer's formula, the crystalline size of CeO₂ is calculated as 26 nm. Moreover, the diffraction peaks of CeO₂ shifted to lower

degrees, and the main reason is that a part of Ce⁴⁺ ions are replaced by Mn⁴⁺ and Mn³⁺ to form solid solution, which is benefit for oxygen vacancies forming and then improve the active catalytic of catalysts.

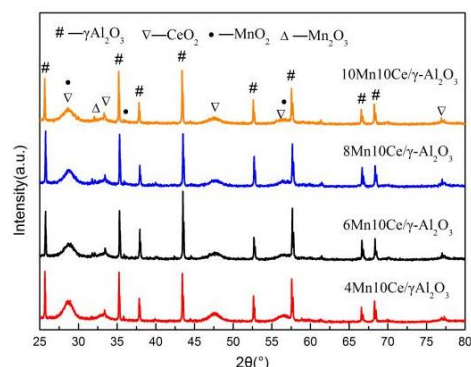


Fig. 2. XRD pattern of $x\text{Mn}10\text{CeO}/\gamma\text{-Al}_2\text{O}_3$ catalysts

Oxidation activity

NO and NO₂ concentration as a function of time at the temperature ranging from 150°C to 450°C over $x\text{Mn}10\text{Ce}/\gamma\text{-Al}_2\text{O}_3$ ($x=4,6,8,10$) catalysts are shown in Figure 3. It can be found that NO₂ concentration first sharp increases and then reduces with the rise of temperature. In the range of 150°C to 300°C, the stabilized NO₂ concentration increases as the temperature is increased and reaches up to the most high value at 300°C. With the further increase in temperature, NO₂ concentration decrease occurs. The time that from reaction began to NO₂ concentration got stabilized decreases as the temperature increases in the range of 150°C to 450°C. Among all the catalysts, the stabilized times for 6Mn10Ce/ $\gamma\text{-Al}_2\text{O}_3$ and 8Mn10Ce/ $\gamma\text{-Al}_2\text{O}_3$ catalysts are significantly shorter than that of 4Mn10Ce/ $\gamma\text{-Al}_2\text{O}_3$ and 10Mn10Ce/ $\gamma\text{-Al}_2\text{O}_3$ catalysts, which indicates that 6Mn10Ce/ $\gamma\text{-Al}_2\text{O}_3$ and 8Mn10Ce/ $\gamma\text{-Al}_2\text{O}_3$ catalysts have better oxidation catalytic. The stabilized time of NO₂ over 6Mn10Ce/ $\gamma\text{-Al}_2\text{O}_3$ catalyst is shorter than that of 8Mn10Ce/ $\gamma\text{-Al}_2\text{O}_3$ catalyst below 200°C, while the later will get more shorter above 250°C.

NO conversion as a function of temperature over $x\text{Mn}10\text{Ce}/\gamma\text{-Al}_2\text{O}_3$ ($x=4,6,8,10$) catalysts is shown in Fig.4. It can clearly be found that NO conversion presents the trend of increasing gradually and then reducing as the rise of temperature. Compared with 4Mn10Ce/ $\gamma\text{-Al}_2\text{O}_3$ catalyst, 6Mn10Ce/ $\gamma\text{-Al}_2\text{O}_3$, 8Mn10Ce/ $\gamma\text{-Al}_2\text{O}_3$ and 10Mn10Ce/ $\gamma\text{-Al}_2\text{O}_3$ catalysts shows obviously higher catalytic activity for oxidation NO to NO₂, especially at the temperature below 300°C.

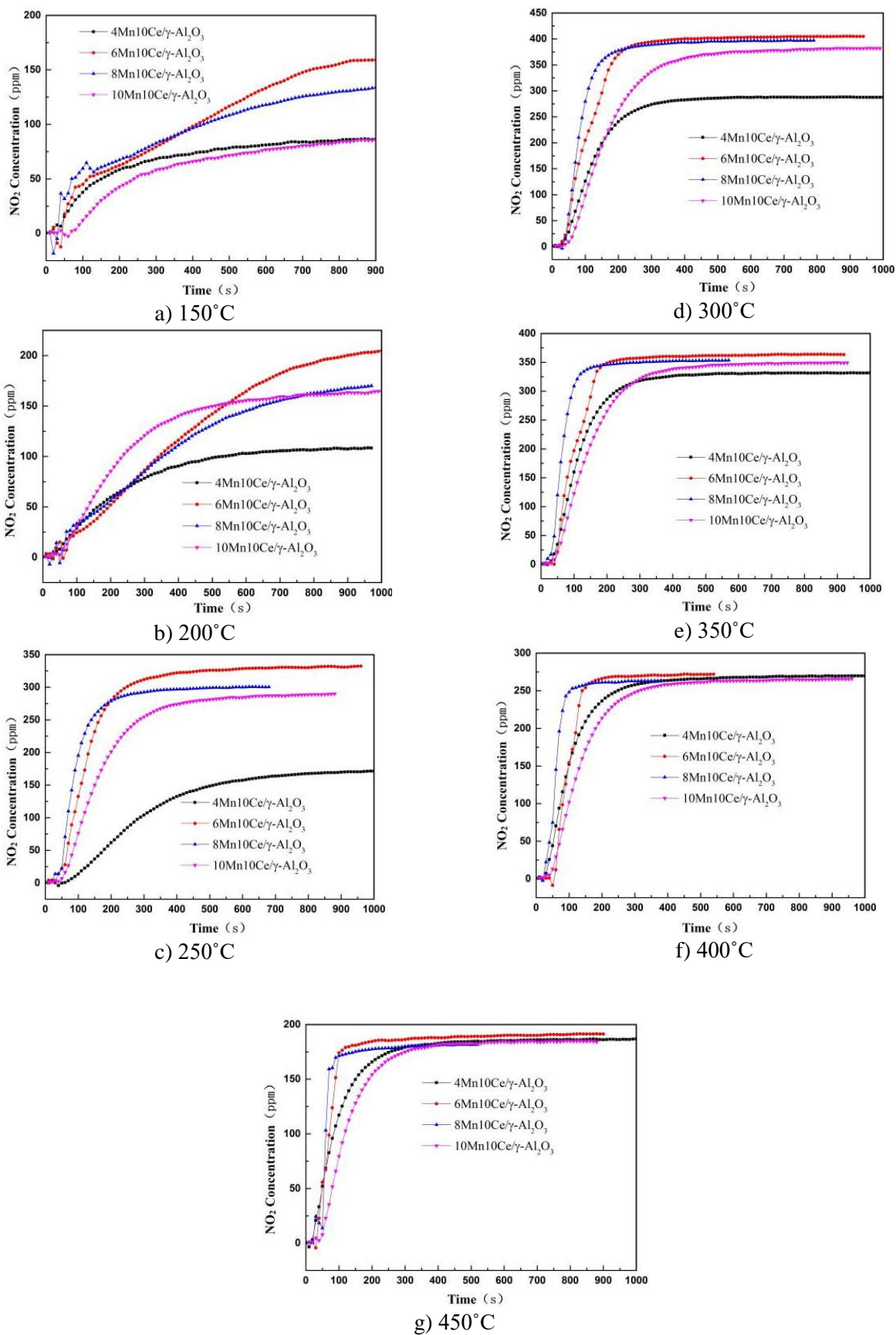


Fig. 3. NO and NO₂ concentration as the function of time over xMn10Ce/ γ -Al₂O₃(x=4,6,8,10) catalysts at different temperature

For example, NO conversion reaches up to 22% at 200°C over 4Mn10Ce/ γ -Al₂O₃ catalyst, while more than 44%, 35% and 33% NO conversion are achieved over the other three catalysts respectively. It is interesting to find that NO conversion over different catalyst get closer in the range of 400°C to 450°C, and that means the key important effect on catalytic activity is the temperature at that range but not the molar ratio of Mn/Ce in catalysts. All the catalysts show the best NO conversion at 300°C except for example, NO conversion can reach up to 83% over 6Mn10Ce/ γ -Al₂O₃ catalyst. It is also important to note that NO conversion decreases with the further increase of the temperature. The main reason is that NO oxidation to NO₂ is an exothermic reversible reaction and is limited by the thermodynamic equilibrium at high temperatures, and NO₂ can dissociate into NO and O₂ if it comes in contact with the Mn-Ce mixed oxidation catalyst at high temperature, as like that in the range of 400°C to 450°C.

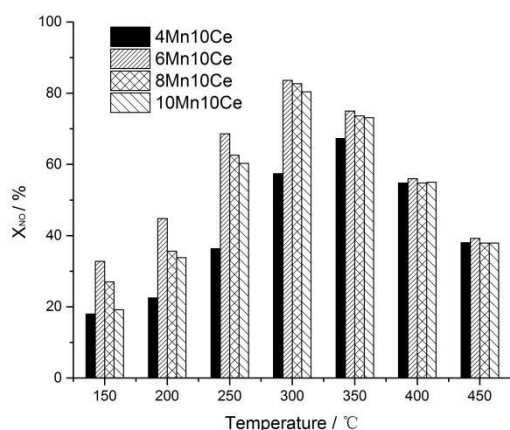


Fig. 4. NO conversion as the function of temperature over xMn10Ce/ γ -Al₂O₃ (x=4,6,8,10) catalysts.

CONCLUSION

1. Mn in the xMn10Ce/ γ -Al₂O₃ (x=4,6,8,10) catalysts is mainly in the form of MnO₂ and Mn₂O₃. And part of the Ce⁴⁺ ions will be replaced by Mn cation upon the incorporation of Mn⁴⁺ and Mn³⁺ cation into the CeO₂ lattice, which can lead to form more oxygen vacancies and then improve the NO to NO₂ oxidation activity of Mn-Ce mixed oxides catalysts.

2. The reaction time of stabilized NO₂ concentration will reduced gradually as the temperature increase. Among all the xMn10Ce/ γ -Al₂O₃ catalysts, NO₂ concentration up to the steady value after sharp increase is the shortest under the treatment of 6Mn10Ce/ γ -Al₂O₃ catalyst below 200°C, while the strong activity for the NO oxidation could be observed over 6Mn10Ce/ γ -Al₂O₃ catalyst

above 250°C.

3. NO conversion presents first increase and then decrease trend as the rise of temperature. All the xMn10Ce/ γ -Al₂O₃ catalysts show the most high oxidation catalytic at 300°C except the 4Mn10Ce/ γ -Al₂O₃ catalyst. Among the xMn10Ce/ γ -Al₂O₃ catalysts, 6Mn10Ce/ γ -Al₂O₃ shows the best oxidation activity for NO converting to NO₂. The high temperature is benefit for improving the oxidation activity of xMn10Ce/ γ -Al₂O₃ catalysts, while it will also lead to NO₂ dissociate into NO and then reduce the NO conversion.

Acknowledgments: Financial support of this paper was provided by The National Natural Science Found (51206068), Natural Science Foundation of Jiangsu Province (BK2015040369) and State Key Laboratory of Engines, Tianjin university (K15-07).

REFERENCES

1. F. Cao, J. Xiang, S. Su, P.Y. Wang, S. Hu, L.S. Sun, *Fuel Processing Technology*, **135**, 66 (2015).
2. P.S. Monks, C. Granier, S. Fuzzi, A. Stohl, M.L. Williams, H. Akimoto, M. Amann, A. Baklanov, *Atmos. Environ.*, **43**, 5268 (2009).
3. P.R. Maria, N. Isabella, T. Enrico, *Top Catal.*, **56**, 109 (2013).
4. Z.B. Wu, N. Tang, L. Xiao, *Journal of Colloid and Interface Science*, **352**, 143(2010).
5. C.G. Visconti, L. Lietti, F. Manenti, D. Marco, C.Michele, P. Sauro, F. Pio, *Topics in Catalysis*, **56**, 311(2013).
6. J. Li, A. Kumar, K. Kamasamudram, N. Currier, *Catalysis Today*, **258**, 169 (2015).
7. M. Sasaki, K. Suzuki, A. Sultana, M. Hanede, H. Hamada, *Topics in Catalysis*, **56**, 205 (2013).
8. K. Hauff, U. Tuttlies, G. Eigenberger, U. Nieken, *Applied Catalysis B Environmental*, **123-124**, 2095 (2012).
9. M.Q. Shen, Z. Zhao, J.H. Chen, Y.G. Su, J. Wang, *Journal of Rare Earths*, **31**, 119 (2013).
10. K. Li, X.L. Tang, H.H. Yi, P. Ning, D.J. Kang, C. Wang, *Chemical Engineering Journal*, **192**, 99 (2012).
11. D. Dimitrios, I. Theophilos, *Applied Catalysis B: Environmental*, **84**, 303 (2008).
12. B.H. Zhao, R. Rui, X.D. Wu, D. Weng, X.Y. Wu, C.Y. Huang, *Catalysis Communications*, **56**, 36 (2014).
13. A. Idriss, G.H. Noelia, B.L. Agustin, G.G. Avelina, *Applied Surface Science*, **256**, 7706 (2010).
14. S. Liu, X.D. Wu, D. Weng, M. L. H.R. Lee, *Chemical Engineering Journal*, **203**, 25 (2012).
15. X.H. Li, S.L. Zhang, Y. Jia, X.X. Liu, Q. Zhong, *Journal of Natural Gas and Chemistry*, **21**, 17(2012).
16. D. Shang, Q. Zhong, W. Cai, *Applied Surface Science*, **325**, 211 (2015).
17. G.S. Qi, W. Li, *Catalysis Today*, **258**, 205 (2015).
18. Z.Q. Zou, M. Meng, L.H. Guo, Y.Q. Zha, *J Hazard Mater*, **163**, 835 (2009)

Serum metallomics study on patients with osteoarthritis based on ICP-MS technique

S. Wang¹, F. Li¹, J. Rong¹, S. Tang², H. Jiang¹, H. Jin¹, J. Zhu³, Y. Gao⁴, D. Wang³, S. Tao¹
X. Ren^{1*}

¹Department of orthopedic surgery, The 2nd Affiliated Hospital, Harbin Medical University, Harbin, Heilongjiang, China

²Department of Health Statistics, Public Health College, Jinzhou Medical University, Jinzhou, Liaoning, China

³Department of Nutrition and Food Hygiene, Public Health College, Harbin Medical University, Harbin, Heilongjiang, China

⁴Department of Endemic disease research center, Harbin Medical University, Harbin, Heilongjiang, China

Received February 12, 2016; Revised December 26, 2016

The aim of the present study was to analyze the distribution of 21 metallic elements in patients with osteoarthritis from different ethnic nationalities and to examine their mechanisms of action in the development of osteoarthritis. Guolu Prefecture of Qinghai Province, Altay City of Xinjiang Uygur Autonomous Region, and Hulunbeier City of Inner Mongolia Autonomous Region were selected for random surveys of five ethnic groups, including Han, Tibetan, Mongolian, Kazakh, and Russian. Inductively coupled plasma mass spectrometry was used to test 21 metallic elements in the serum, including lithium, magnesium, aluminum, calcium, titanium, vanadium, chromium, manganese, iron, cobalt, nickel, copper, zinc, arsenic, selenium, strontium, molybdenum, cadmium, barium, thallium, and lead. Enzyme-linked immunoassay was used to detect human selenoprotein 1, human selenoprotein P, calcitonin, parathyroid hormone, and alkaline phosphatase in the serum. A two independent samples *t* test and χ^2 test were adopted for comparative statistical analysis; the Mann-Whitney U test and partial least squares (PLS-DA) were used for discriminant analysis of metal content. Of the 21 metals, six (Ti, V, Ni, As, Mo, and Tl) were not detected in the serum of osteoarthritis patients and 15 elements were detected, of which the contents of 11 elements differed significantly ($P < 0.05$) among the nationalities. Multidimensional statistics and one-dimensional statistical analysis showed that there was a significant difference ($P < 0.05$) in the serum contents of lithium, selenium, and strontium between osteoarthritis patients from different regions, different ethnic groups, and those of the control group; body hormones corresponding to the three elements were highly correlated with protein detection. Metallic element distribution and content in the serum differed among osteoarthritis patients of different nationalities. Variations in the contents of lithium, selenium, and strontium were correlated with protein metabolism, which may be related to the occurrence and development of osteoarthritis.

Keywords: Osteoarthritis, inductively coupled plasma mass spectrometry, metallic element, metallomics

INTRODUCTION

Osteoarthritis (OA) is a chronic degenerative bone disease characterized by biochemical and metabolic abnormalities of the articular cartilage, degeneration, injury, and cartilaginous hyperplasia that occurs mainly in the elderly. In the United States, OA ranks second in incidence among the population over 50 [1]; among the population over 65 with imaging abnormalities, the incidence of osteoarthritis is approximately 70% [2]. In China, where the population over 60 exceeds 330 million, there are approximately 90 million patients with OA, of which 55% are older than 60 years and 80% are older than 70 years [3]. In recent years, these figures have grown substantially, which may be related to bad habits, incorrect diet, general weight gain, drug abuse, excessive exercise, and other factors. Several theories have been proposed to explain the etiology of OA, including the intraosseous hypertension theory, cytokines and growth factor theory, cartilage

degradation theory, and immune response theory. Research into the etiology of OA has been performed using genomics, proteomics, metallomics, and related disciplines.

Genomics, which uses genome-wide association studies as an effective tool to identify disease-causing genes, is widely used to examine the genetic characteristics of OA. Proteomics analyzes complex gene interactions, gene expression related to cell internal activity and the environment, as well as the dynamic process of protein processing after translation. Metallomics [4], which studies metal-related molecular mechanisms in the organism and the metal ions and metal complexes within cells and tissues, uses inductively coupled plasma mass spectrometry (ICP-MS) and inductively coupled plasma atomic emission spectrometry (ICP-AES) to analyze the metallome and for morphological analysis [5]. Metallomics analyzes the metallic element content and distribution in biological fluids, cells, and organs, identifies metal proteins and metal enzymes, and studies the associations between

* To whom correspondence should be sent:
E-mail chinarenxg@126.com

metallic elements and biological molecules. It describes the metallic element enrichment process, metabolism, and biological functions in OA patients, and reveals possible relations between alterations in metallic element metabolism and OA pathogenesis.

In the present study, metal metabolomics technology was used to test 21 metallic elements [lithium (Li), magnesium (Mg), aluminum (Al), calcium (Ca), titanium (Ti), vanadium (the V), chromium (Cr), manganese (Mn), iron (Fe), cobalt (Co), nickel (Ni), copper (Cu), zinc (Zn), arsenic (As), selenium (Se), strontium (Sr), molybdenum (Mo), cadmium (Cd), barium (Ba), thallium (Tl), and lead (Pb)] and related metalloproteins in the serum of osteoarthritis patients from five Chinese ethnic nationalities (Han, Tibetan, Mongolian, Kazakh and Russian) to explore the distribution of metallic elements in OA patients from different ethnic nationalities and its impact on osteoarthritis occurrence and development. Metallic elements with potential relevance to OA were identified and the underlying mechanisms were explored to provide a scientific basis for early prevention, early diagnosis, and early treatment of OA.

MATERIALS AND METHODS

Plasma

A questionnaire was designed based on the control study survey method of epidemiological populations. Guolu Prefecture of Qinghai Province, Altay City of Xinjiang Uygur Autonomous Region, and Hulunbeier City of Inner Mongolia Autonomous Region were selected as survey areas to investigate patients among a population of over 40 OA patients. Patients were diagnosed according to the 1995 OA diagnostic criteria of the American College of Rheumatology, as well as orthopedist examination, X-ray images, and film-reading in patients from the following five nationalities: Chinese, Tibetan, Mongolian, Kazakh, and Russian. A total of 563 OA patients were screened and confirmed (132 Han, 136 Tibetans, 111 Mongolians, 125 Kazakh, and 59 Russian). A total of 555 patients from the case group and healthy volunteers (149 Han, 112 Tibetans, 93 Mongolians, 129 Kazakh, 72 Russian) were used as the control group. All subjects signed an informed consent and voluntarily participated and exited, as well as agreeing to a questionnaire and disease-related laboratory inspection.

Reagents and instruments

The instruments used were an Agilent-7700x inductively coupled plasma mass spectrometer (Agilent-7700x ICP-MS, Agilent Technologies Inc.),

IA-89 inductively coupled plasma mass spectrometer autosampler (Agilent Technologies Co., Ltd.), U410 type -80°C ultra-low temperature freezer (NBS company, US), A10-type Milli-Q ultrapure water machine (Merck Millipore Santa Clara, USA), and 10mL PTFE digestion tubes (homemade). A human selenoprotein 1 (SEP1) enzyme-linked immunosorbent assay (ELISA) kit and human selenoprotein P (SEP-P) ELISA kit (Boster Bioengineering) were also used.

Nitric acid (excellent pure), hydrogen peroxide (excellent pure), tuning solution (Agilent Technologies Co., Ltd.), multi element internal standard mixing solution (Agilent Technologies Co., Ltd.), and mixed standard solution with 21 elements (Li, Mg, Al, Ca, Ti, V, Cr, Mn, Fe, Co, Ni, Cu, Zn, As, Se, Sr, Mo, Cd, Ba, Tl, and Pb; U.S. Inorganic Ventures Corporation) were used. For the preparation of all standard solutions and samples, Milli-Q purified deionized water (> 18MΩ.cm) was used.

With the three mass number elements Li⁴⁵, Sr⁸⁸, and Tl²⁰⁹, P / A factor tuning of ICP-MS was performed to eliminate the effects of fluctuations in operating conditions. ICP-MS conditions were optimized as follows: the plasma work coil RF power (W) was set at 1550, the carrier gas flow rate (L/min) was 1.03, sampling depth (mm) was 7.9, sample lifting speed (rps) was 0.1, and the voltages for extraction taper hole 1, extraction taper hole 2, bias, lens, and octupole bias were 4.7 V, (-)200 V, (-)100 V, 7.4 V, and 8V, respectively.

Standard curve generation

The multi-element mixed standard solution (Ca: 1000μg/mL, Mg: 500μg/mL, Li, Al, Ti, V, Cr, Mn, Fe, Co, Ni, Cu, Zn, As, Se, Sr, Mo, Cd, Ba, Tl, and Pb: 10μg/mL) (5mL) was placed in a 50mL volumetric flask meter and the volume was adjusted to 50mL with ultrapure water, obtaining an intermediate stock solution. Aliquots of the intermediate stock solution of 0.5, 1, 2, 4, and 5mL were diluted to 50mL with ultrapure water, thus obtaining a standard series with concentrations of Li, Al, Ti, V, Cr, Mn, Fe, Co, Ni, Cu, Zn, As, Se, Sr, Mo, Cd, Ba, Tl, and Pb of 10, 20, 40, 80, and 100μg/L. With Bi²⁰⁹, Lu¹⁷⁵, Tb¹⁵⁹, Rh¹⁰³, Ge⁷², Sc⁴⁵, Li⁶ as internal standards, measurements were performed under optimal conditions using the above instrument.

Sample preparation and determination

Sterile vacuum negative pressure anticoagulation blood vessels were used to collect morning fasting venous blood from all study subjects. After centrifugation at 3000×g for 10 min, the upper

yellow translucent liquid was extracted to obtain the plasma sample, which was placed in EP0.5mL frozen sample tubes and stored at -80°C for metallomics analysis. The frozen plasma sample was removed from the -80°C refrigerator and thawed at room temperature. Plasma samples were shaken and blended for 30s with a vortex shaker. Then, 0.2mL of plasma sample was added to 10mL PTFE digestion tube with 0.3mL HNO_3 and 0.3mL H_2O_2 digestion liquid. The sample digestion tube was tightly sealed, placed in an oven at 130°C for 2h until the solution was clear and transparent. Then, the solution was removed, cooled, and transferred to 5-mL quantitative flasks. After adjusting the volume to the scale with Milli-Q purified deionized water, the solution was transferred to the ICP-MS autosampler, which then automatically determined the 21 elements of Li, Mg, Al, Ca, Ti, V, Cr, Mn, Fe, Co, Ni, Cu, Zn, As, Se, Sr, Mo, Cd, Ba, Tl, and Pb.

For ELISA, plasma was vortexed at $3000\times g$ for 10 min to remove particulates and metalloproteinase selenoprotein 1 (SEP-1), selenoprotein P (SEP-P), calcitonin (CT), parathyroid hormone (PTH), and alkaline phosphatase (ALP) were detected following kit instructions. The standard solution was diluted, and each empty sample volume was $50\mu\text{L}$; blank and sample wells were respectively set, wherein sample and enzyme labeled reagent were not added to the blank control well. For sample testing, a volume of $40\mu\text{L}$ was first added and then $10\mu\text{L}$ of the sample to be tested was added. After incubation at 37°C for 30min, the reaction well was washed and $50\mu\text{L}$ enzyme labeled reagent was added and incubated at 37°C for 30min. After washing, reagent A and B, each $50\mu\text{L}$, were successively added, followed by 15min coloration away from light at 37°C . A total of $50\mu\text{L}$ stop solution was added immediately to terminate the reaction. UV-visible spectrophotometer was selected for empty air zero adjustment, with OD value measured at 450nm. A standard curve was generated and the content of different metalloenzymes in serum was calculated.

Statistical analysis

Data were expressed as the mean \pm standard deviation. Three statistical software programs were used for data analysis, namely Epidata3.1, SPSS17.0 and SIMCA-P12.0. For comparisons between two groups, $p < 0.05$ was considered statistically significant. The Mann-Whitney U test and partial

least squares (PLS-DA) discriminant analysis were used to analyze metal content.

One-way ANOVA was used to analyze differences between mean values between groups, namely multiple comparisons of mean value. Patients with OA were classified according to ethnic nationality, and the least significant difference (LSD) method was adopted to analyze metallic element distribution in the serum of patients from various ethnic groups.

A two independent samples t test and χ^2 test were used for comparative statistical analysis.

RESULTS

The internal standards method was used to eliminate interference. The mass number of the internal standard elements (Bi^{209} , Lu^{175} , Tb^{159} , Rh^{103} , Ge^{72} , Sc^{45} , and Li^6) was between 7 and 209, including all mass numbers of elements to be tested (Figure 1). Fluctuations of the internal standard curve throughout the experiment were within the allowable range, except a greater fluctuation due to one argon replacement in the experiment.

ICP-MS was performed with wide linear range, generally in the linear dynamic range of nine orders of magnitude. Taking the content of each trace element in the serum into account, $0\text{--}10\mu\text{g/mL}$ was chosen for Ca and Mg in the standard curve range, whereas $0\text{--}100\text{ng/mL}$ was used for other elements. The correlation coefficients and quantitative detection limits of the 21 elements within the scope of the standard curve working range are shown in Table 1. The majority of correlation coefficients of the 21 trace elements were >0.999 ; the correlation coefficient of zinc was 0.9961. The quantitative detection limit was $0.0026\text{--}5.04\mu\text{g/L}$.

Day and inter-day reproducibility experiments were performed for the same mixed serum samples as shown in Figure 2 to examine the accuracy of the determination method for the elements to be tested. The results revealed that inter-day relative standard deviation (RSD%) of all elements to be tested was higher than the one day RSD%, indicating that the analysis of samples should be completed in a short time to ensure accurate testing. On the other hand, the RSD% of five elements (Al, Ca, Fe, Cu, and Zn) was generally higher than that of other elements, indicating that environmental factors may interfere with the analysis

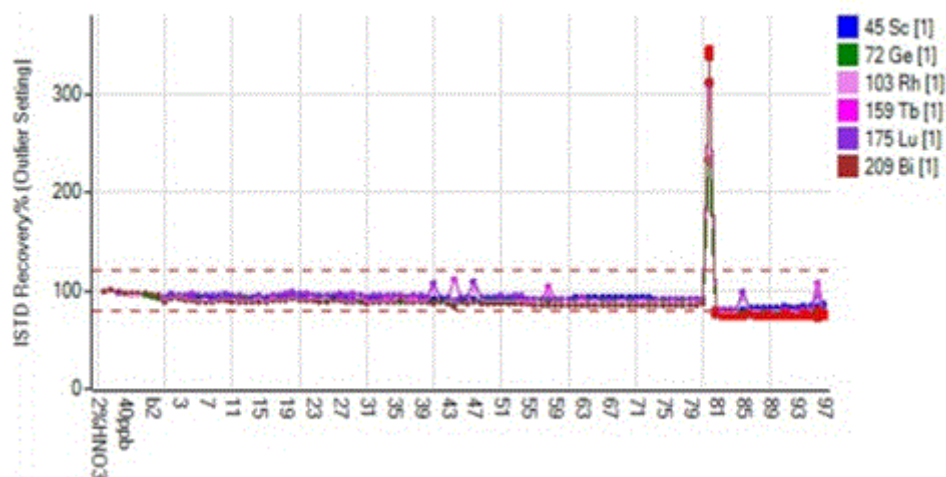


Fig.1. Results of internal standard of ICP-MS.

Table 1. Detection limit and correlation coefficient of 21 types of elements in plasma samples

	R	DI (μg/L)		R	DI(μg/L)
Li	0.9998	0.9	Cu	0.9999	1.3
Mg	0.9998	6	Zn	0.9961	0.8
Al	0.9994	8	As	0.9995	6
Ca	0.9998	50	Se	0.9998	1.3
Ti	0.9998	1.5	Sr	0.9995	0.3
V	0.9998	0.05	Mo	0.9997	0.1
Cr	0.9999	0.2	Cd	0.9999	0.07
Mn	0.9998	0.1	Ba	0.9993	0.7
Fe	0.9992	6	Tl	0.9991	0.03
Co	0.9999	0.08	Pb	0.9991	0.4
Ni	0.9994	2			

(1) R, correlation coefficient;(2)DI, detection limit.

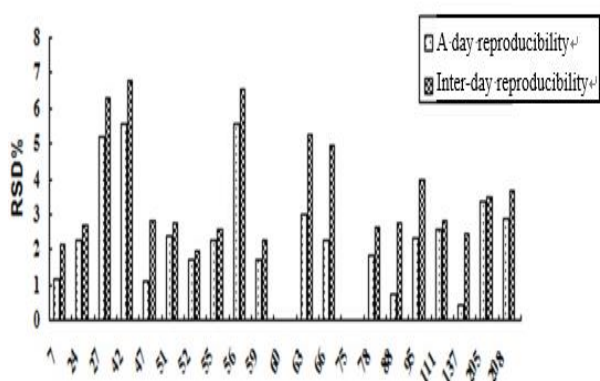


Fig. 2. Results of one day or inter-day reproducibility in 21 elements.

The content of the 21 elements (Li, Mg, Al, Ca, Ti, V, Cr, Mn, Fe, Co, Ni, Cu, Zn, As, Se, Sr, Mo, Cd, Ba, Tl, and Pb) was measured in the serum of patients and healthy controls and the results were shown in Table 2. Six elements (Ti, V, Ni, As, Mo, and Tl) were below the quantitative detection limit of the method; the other 15 elements were detected. There were significant differences ($P < 0.05$) in five elements (Li, Cu, Se, Sr, and Ba) between the OA case group and healthy control group. Se, Sr, and Ba contents were lower, whereas Li and Cu were higher in the serum of OA patients than in controls.

Figure 3 shows the serum sample ICP-MS mass spectrum of an OA patient and a healthy control. In

Figure 4, the abscissa shows the m/z detecting metallic element and the ordinate shows the count value per second (CPS). Because there were marked differences in the contents of the 21 metallic elements tested in the serum, it was difficult to determine the CPS value of all metallic elements. Therefore, the CPS in Figure 4 is shown in proportion to 1×10^4 (the CPS of some elements is beyond the ordinate range). General differences between the OA group and HC group were identified in the 21 elements tested; however, this did not represent statistically significant differences between the two groups. Therefore, multi-dimensional statistical analysis was needed.

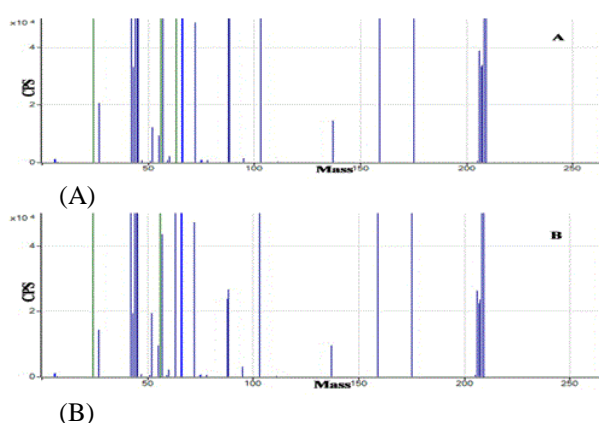


Fig.3. Serum ICP-MS spectrum of OA patients and healthy controls. (A) OA patient sample map; (B) healthy control sample map.

One-way ANOVA was used to analyze the distribution of trace elements in the serum of patients from the five ethnic nationalities (Table 3). Eleven elements (Mg, Ca, Cr, Mn, Fe, Co, Cu, Se, Sr, Cd, and Ba) were significantly affected by nationality. The LSD method for multiple comparisons showed that for magnesium, there were significant differences ($P < 0.001$) between Han and Tibetan, Mongolian and Tibetan, Kazakh and Tibetan, and Russian and Tibetan; for calcium, there was a significant difference ($P < 0.001$) between Han and Mongolian; for chromium, manganese, iron, and cobalt, there were significant differences ($P < 0.05$) between Kazakh and Han, Tibetan, Mongolian and Russian; for copper, there were significant differences ($P < 0.001$) between Kazakh and Han, Tibetan, Mongolian and Russian, and significant differences ($P < 0.001$) between Russian and Han, Tibetan and Kazakh; for selenium, there were significant differences ($P < 0.001$) between Han and Tibetan, Mongolian, and Kazakh, significant differences ($P < 0.001$) between Tibetan and other ethnic groups, significant differences ($P < 0.001$) between Mongolian and other ethnic groups,

significant differences ($P < 0.001$) between Kazakh and other ethnic groups, and significant differences ($P < 0.001$) between Russian and Tibetan, Mongolian, and Kazakh; for strontium, there were significant differences ($P < 0.001$) between Han and other ethnic groups, significant differences between Tibetan and other ethnic groups, significant differences ($P < 0.001$) between Mongolian and other ethnic groups, significant differences ($P < 0.001$) between Kazakh and Han, Tibetan, Mongolian, and significant differences ($P < 0.001$) between Russian and Han, Tibetan, and Mongolian; for cadmium, there were significant differences ($P < 0.001$) between Mongolian and other ethnic groups; for barium, there were significant differences ($P < 0.05$) between Mongolian and Han, Kazakh, and Russian, and significant differences ($P < 0.05$) between Russian and Han, Tibetan, and Mongolian.

Figures 4, 5, 6, 7, and 8 show the results of the statistical analysis of multidimensional data. The PLS-DA shot chart (Figures 4A and 5A) shows that the established PLS-DA model can completely separate the case group from the control group, indicating that the established PLS-DA model has good reliability and predictability. The chart (Figures 6A, 7A and 8A) shows that the boundary of the OA group and HC group is not obvious, although differences between the two groups were detected. The PLS-DA shot chart shows differences in content distribution *in vivo* of metallic elements in the OA group and HC group of different ethnic groups.

The load diagram can intuitively reflect the contribution of each element to the model. The corresponding positions of the 21 metallic elements to be tested are shown on the diagram. If the position of an element is on the same side as the position shown by OA, it means that there is a relatively high concentration of the element in the OA group, which can be considered as a risk factor for OA.

By contrast, if the element is on the opposite side of OA, there is a relatively high concentration of the element in the HC group, which can be considered as a protective factor against OA occurrence and development. The PLS-DA shot chart shows that (Figure 4B) for the Han population, the concentrations of lithium and barium are high in the serum of the OA group, which can be considered as a risk factor for OA. The concentrations of selenium and strontium are high in the serum of the HC group, which can be considered as a protective factor against OA. Figure 5B shows that for the Tibetan population, lithium and magnesium are high in the serum of the OA group and considered a risk factor, whereas selenium and strontium are high in the HC group and considered a protective factor against OA.

Figure 6B shows that for the Mongolian population, lithium is high in the OA group and considered as a risk factor, whereas selenium and strontium are high in the HC group and considered as a protective factor against OA.

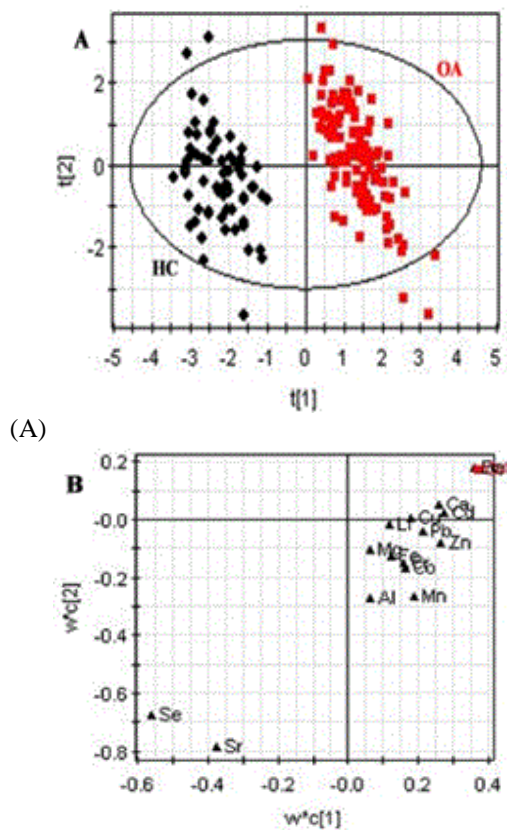


Fig.4. Partial least squares discriminant analysis model diagram of serum metallic element spectra discrimination of the Han OA case group and control group.(A) Shot chart; (B) load diagram.

Figure 7B shows that for the Kazakh population, lithium and calcium are high in the OA group and considered as a risk factor, whereas selenium and strontium are high in the HC group and considered as a protective factor against OA. Figure 8B shows that for the Russian population, lithium is high in the OA group and considered as a risk factor for OA, whereas selenium and strontium are high the HC group and considered as a protective factor against OA. The above results reveal that among the three elements lithium, selenium, and strontium, Li was always on the same side with OA, while Se and Sr were always on the opposite of OA

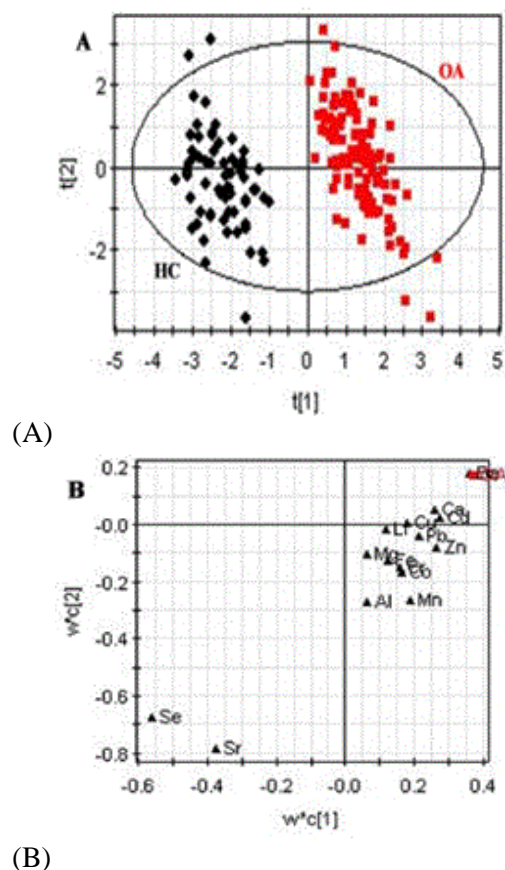


Fig.4. Partial least squares discriminant analysis model diagram of serum metallic element spectra discrimination of the Han OA case group and control group.(A) Shot chart; (B) load diagram.

By contrast, if the element is on the opposite side of OA, there is a relatively high concentration of the element in the HC group, which can be considered as a protective factor against OA occurrence and development. The PLS-DA shot chart shows that (Figure 4B) for the Han population, the concentrations of lithium and barium are high in the serum of the OA group, which can be considered as a risk factor for OA. The concentrations of selenium and strontium are high in the serum of the HC group, which can be considered as a protective factor against OA.

VIP was used as a selection indicator of the multi-dimensional model for different elements. According to the experimental value, $VIP > 1.0$ was used as the selection criterion of the model contribution variable. The PLS-DA model short chart and VIP value analysis provided preliminary data on the contribution of each element to the model and their relative concentration distribution among groups.

Table 2. Results of content determination of the 21 types of trace elements in OA and HC ($\bar{x}\pm s$)

	OA	HC	<i>p</i> -value*		OA	HC	<i>p</i> -value*
Li	145.5±77.8*	96.2±50.8	<0.05	Cu	1282±372*	1240±408	<0.05
Mg	23400±4625	22800±4525	n.s.	Zn	770±372	768±378	n.s.
Al	690±77	377±40	n.s.	As	—	—	—
Ca	104950±23750	104775±24350	n.s.	Se	73.2±28.5*	78.5±29.2	<0.001
Ti	—	—	—	Sr	64.0±33.5*	67.0±33.0	<0.05
V	—	—	—	Mo	—	—	—
Cr	202±104	328±154	n.s.	Cd	1.25±0.08	1.10±0.20	n.s.
Mn	32.0±26.0	39.5±32.5	n.s.	Ba	35.2±21.8*	38.5±31.2	<0.05
Fe	3530±940	4877±1430	n.s.	Tl	—	—	—
Co	2.40±1.02	3.40±1.48	n.s.	Pb	28.5±11.0	27.5±12.5	n.s.
Ni	—	—	—				

(1)*,µg/L;(2) -, not detected; (3)n.s., not significant.

Table 3. Results of content determination of the elements in different nationalities(\bar{x}).

	Han	Tibetan	Mongolian	Kazak	Russian	<i>p</i> -value*
Li	0.16	0.003	0.07	0.14	0.25	n.s.
Mg*	24.8	20.4	24.0	24.5	24.6	< 0.001
Al	1.64	0.19	0.13	0.41	0.32	n.s.
Ca*	100.49	89.70	94.15	105.23	106.58	<0.001
Cr*	0.04	0.005	0.01	0.76	0.20	< 0.001
Mn*	0.01	0.005	0.01	0.07	0.02	< 0.001
Fe*	1.79	1.90	1.46	2.71	2.84	< 0.001
Co*	0.0003	0.0003	0.0001	0.006	0.002	< 0.001
Cu*	1.21	1.15	1.23	1.46	1.34	< 0.001
Zn	0.64	0.67	0.59	0.64	0.61	n.s.
Se*	0.08	0.04	0.07	0.09	0.08	< 0.001
Sr*	0.07	0.03	0.06	0.08	0.08	< 0.001
Cd*	0.001	0.0004	0.001	0.001	0.0003	< 0.05
Ba*	0.03	0.03	0.03	0.04	0.04	< 0.05
Pb	0.02	0.01	0.02	0.01	0.02	n.s.

(1)*,mg/L;(2)n.s., not significant.

Table 4. The potential differences of elemental analysis with VIP > 1.0 and $P < 0.05$ in the cases and the control group of different ethnic groups

		VIP	P			VIP	P
Han	Li*	1.47	0.020	Kazakh	Li*	1.01	0.034
	Se*	2.19	0.000		Se*	1.19	0.002
	Sr*	1.02	0.035		Sr*	1.78	0.025
	Ba	1.24	0.044		Ca	1.65	0.019
Tibetan	Li*	1.08	0.017	Russian	Li	1.06	0.044
	Se*	1.59	0.000		Se*	1.19	0.001
	Sr*	1.14	0.000		Sr	1.78	0.027
	Mg	1.81	0.046				
	Zn	1.29	0.038				
Mongolian	Li*	1.39	0.041				
	Se*	1.69	0.000				
	Sr*	1.32	0.007				

DISCUSSION

Metallic element balance is indispensable to maintain human health. The development and progression of many diseases are associated with abnormal metallic elements. The metallic element content in the body is closely related to factors such as the geographical environment, lifestyle, and dietary structure. In recent years, studies on the correlation between trace elements and OA mostly focused on copper, selenium, zinc and iron[6-8].

The content and mechanism of trace elements in the plasma of patients with OA are less studied. In this paper, an epidemiological survey was performed on OA patients of five ethnic nationalities, namely Han, Tibetan, Mongolian, Kazakh and Russian, to analyze 21 metallic elements in the serum of OA patients. The results showed differences in the content of 11 metallic elements (Mg, Ca, Cr, Mn, Fe, Co, Cu, Se, Sr, Cd, and Ba) in the serum of different ethnic groups, with significant differences between

the OA group and HC groups ($p < 0.05$) in three elements, namely Li, Se, and Sr in various ethnic groups.

Lithium can promote osteoblast differentiation *in vitro*, while it can promote bone regeneration *in vivo*[9]. Oral administration of lithium for bipolar disorder has been used in the clinic for more than 50 years[10]. Epidemiological studies have shown that for patients taking lithium, fracture risk is significantly reduced[11]. In the present study, the lithium content in OA patients' serum was higher than that in the healthy control group, which is consistent with Krachler's results [12]. Despite some research on lithium toxicity[13] and physiological and biochemical effects, such as the roles of lithium in reproduction and growth[14], endocrine function [15-16] and enzyme activity[17], the significance of increased lithium in the serum of OA patients has not been reported previously. However, increased lithium may not be the direct cause of OA, since according to test results; lithium concentration in the

serum of OA patients is still far below toxic levels. Lithium chloride can increase osteoporotic bone mass in senile and ovariectomized animals, and also result in increased bone mineral density in normal animals. The literature shows that lithium is involved in the clinical manufacture of bone models, indicating that this element exerts certain effects on bone growth and development. The present results showed that lithium content in the serum of the case group did not reach toxic levels. We suspect that increased lithium affects bone growth and development, leading to the occurrence of osteoarthritis.

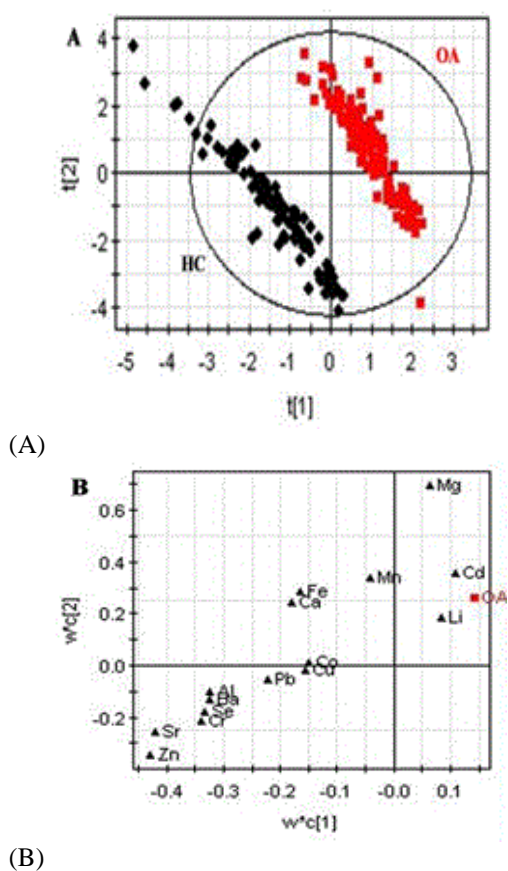


Fig.5.Partial least squares discriminant analysis model diagram of serum metallic element spectra discrimination of the Tibetan OA case group and control group.(A) Shot chart; (B) load diagram.

Selenium is an essential trace nutrient for the body. Its physiological functions as antioxidant, and in eliminating free radicals and enhancing immunity play an important role in health maintenance. Therefore, selenium has a high value in health care in terms of physical activity and disease prevention and treatment[18].

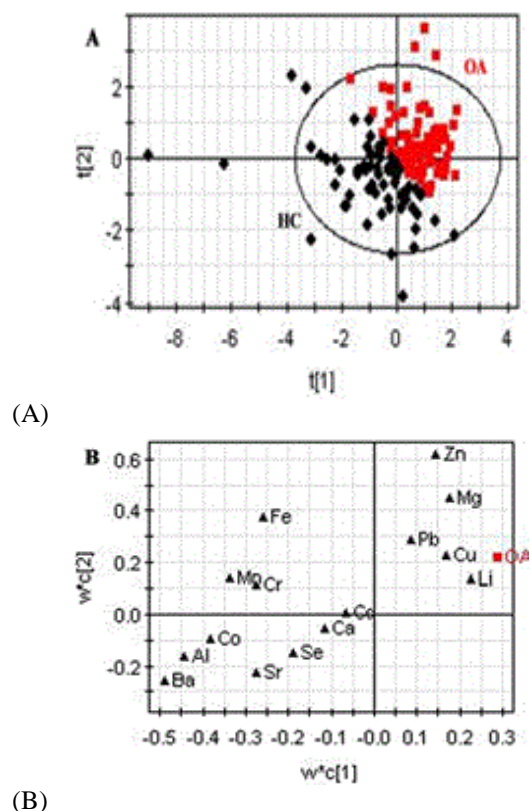


Fig.6. Partial least squares discriminant analysis model diagram of serum metallic element spectra discrimination of the Mongolian OA case group and control group.(A) Shot chart; (B) load diagram.

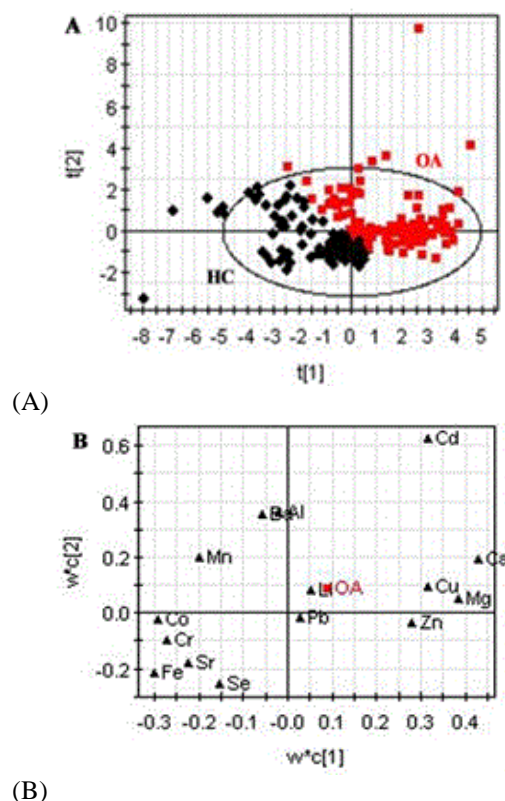


Fig.7.Partial least squares discriminant analysis model diagram of serum metallic element spectra discrimination of the Kazakh OA case group and control group.(A) Shot chart; (B)load diagram.

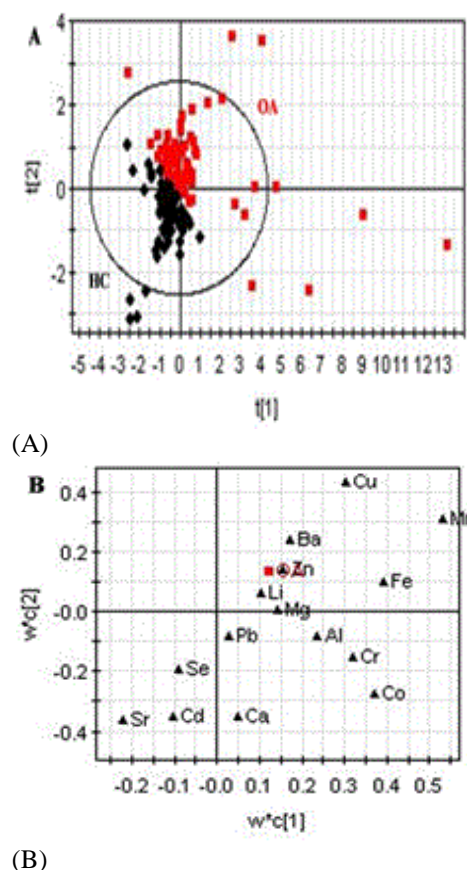


Fig.8. Partial least squares discriminant analysis model diagram of serum metallic element spectra discrimination of the Russian OA case group and control group. (A) Shot chart; (B) load diagram.

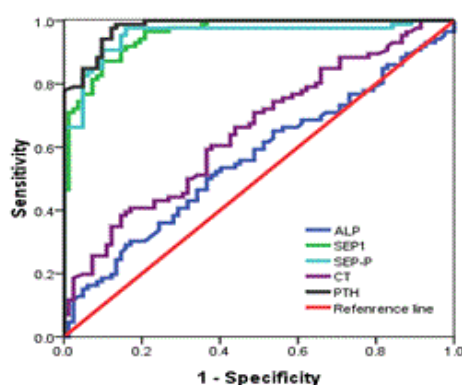


Fig.9. Receiver operating characteristic curve analysis of metalloproteinase of the case and control groups.

A large number of domestic and foreign clinical trials demonstrated that selenium deficiency in the human body can result in organ dysfunction, leading to many serious diseases. More than 40 countries around the world are in selenium deficiency areas, China's hundreds of millions of people are at selenium deficiency or low selenium regions, and these areas feature very high incidence of cancer, liver disease, and cardiovascular disease[19]. In this study, selenium content in the serum of OA patients was significantly lower than that in the healthy

control group. The results show that the selenium content in the serum of OA patients was lower than the normal level; therefore, selenium cannot play a protective role, resulting in the development and progression of the disease. Human selenoprotein 1 and human selenoprotein P were further detected in an attempt to explore effect of selenium content reduction on OA occurrence and development.

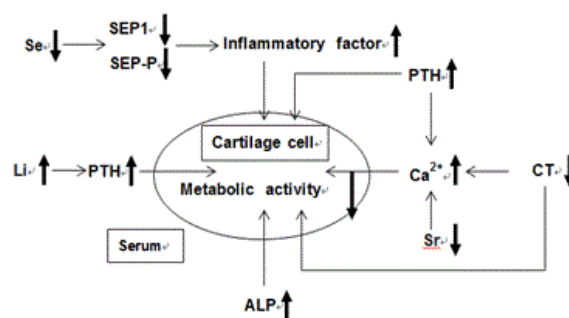


Fig.10. Relation between metal metabolic disorder and OA occurrence and development.

Strontium and calcium belong to the same family as essential trace elements for the human body and important components of bone, which can promote calcium absorption and osteoid formation, regulate metabolism of bone calcium, increase trabecular bone, and improve bone microstructure [20]. Strontium content in serum is 28–44ng/ml[20]. However, excessive strontium can replace calcium in bone tissue and interfere with calcium absorption and metabolism, leading to bone disease. In this study, the average strontium content in the serum of OA patients was 25.6ng/ml, which was significantly lower than that of normal people. The calcium content in serum was significantly higher than that of the control group, indicating that strontium content reduction affected calcium absorption, which might be one factor leading to OA occurrence. Therefore, strontium can be considered as one of the heavy metals potentially threatening human health.

The main reason why metallic element metabolic disorder *in vivo* can cause certain diseases is that metallic elements combine with metalloproteins, enzymes or other biological molecules containing metallic elements, resulting in biological effects. Therefore, in this paper, the biological effects of the three metallic elements lithium, strontium, and selenium on OA were further investigated. SEP1, SEP-P, CT, PTH and ALP contents in OA and HC serum were detected to understand how metallic elements affect OA (Figure 10). Increase in lithium can cause hyperparathyroidism, resulting in excessive secretion of PTH, while elevated PTH content affects the metabolic activity of cartilage cells, resulting in OA occurrence and development.

PTH detection and content determination indicated that PTH has a good ability to identify and diagnose OA and can be used as a sensitive and reliable serum biomarker of OA. Based on the analysis results, we speculate that selenium may cause OA development and progression by affecting selenoprotein metabolism. Selenoprotein is the main carrier for selenium, which refers to protein after peptide synthesis with selenium in the form of selenocysteine (Sec). Because of the active properties of Sec, it plays an important role in redox reactions[21]. SEP-P is the storage protein of blood selenium, which mainly exists in the serum[22]. A study found relevance between SEP-P and KBD, and the main clinical manifestation is bone and joint deformation[23-24]. Among KBD patients, SEP-P's mRNA expression was lower in patients than in controls[25-26]. The results of the present study showed that the selenoprotein content in the serum of osteoarthritis patients was significantly lower than that of the healthy control group, and selenium content in the serum was low. This indicated that the reduction in selenium content affected selenoprotein synthesis, which might be one factor leading to OA. In addition, selenoprotein content reduction in serum might be caused by its degradation, resulting in increased inflammatory factor content in damaged cartilage cells, leading to OA occurrence. Selenoprotein 1 and selenoprotein P detection and content determination indicated that the two metals have a good ability to identify and diagnose OA, which can be used as a sensitive and reliable serum biomarker of OA. Strontium promotes osteoblast growth and inhibits osteoclast activity[27], exerting positive effects on calcium absorption in bone tissue. In this study, strontium content was reduced, while there was no significant difference in calcium content, although it showed an increasing trend. Strontium reduction leads to decreased calcium absorption by cartilage cells and increased calcium content in serum. Both increased PTH and elevated calcitonin (CT) will affect the concentration of calcium ions in serum[28-29]. Increased blood calcium promotes osteogenic activity and new bone formation, causing OA. Metabolic disorders of PTH and CT will also affect the metabolism of cartilage cells, resulting in diseases. We found that the ALP content in the OA group was higher than that in the control group. ALP is mainly generated by cartilage cell secretion[30]. Its elevated level reflects metabolic changes. The elevated level of ALP may lead to metabolic imbalances in cartilage cells, leading to disease.

Metabolic disorders of the three metallic elements lithium, selenium, and strontium directly

affect the bioactivities of parathyroid hormone, human selenoprotein 1, and human selenoprotein P, which is inextricably linked to cartilage and subchondral bone protection and restoration in the early stage of OA. Hence, the three metallic elements lithium, selenium, and strontium may be important causes of OA.

Acknowledgements: We would like to thank the Guolu Prefecture of Qinghai Province, Altay City of Xinjiang Uygur Autonomous Region and Hulunbeier City of Inner Mongolia Autonomous Region who provided invaluable assistance in collecting samples. This work was supported by the National Natural Science Foundation of China and the Grant number is 81273193.

REFERENCES

1. C.Y. Wenham, P.G. Conaghan, *AgeAgeing*, **42**, 272 (2013).
2. W. Wei, W. Kun-zheng, D. Xiao-qian, P. Chuan-yi, W. Chun-sheng, S. Zhi-bin, M. Shu-qiang, *Journal of Medical Colleges of PLA*, **22**(3), 179 (2007).
3. C.G. Helmick, D.T. Felson, R.C. Lawrence, S. Gabriel, R. Hirsch, C.H. Kwoh, M.H. Liang, H.M. Kremers, M.D. May-es, P.A. Merkel, S.R. Pillemer, J.D. Reveille, J.H. Stone, *Arthritis Rheum*, **1**, 26 (2008).
4. H. Haraguchi, *J Anal At Spectrom*, **19**, 5 (2004).
5. A.R. Upton, C.A. Holding, A.A. Dharmapatni, D.R. Haynes, *Rheumatol Int.*, **32**, 535 (2012).
6. M. Yazar, S. Sarban, A. Kocyigit, D. Isikan, *Biol Trace Elem Res*, **106**, 123 (2005).
7. M. Krachler, W. Domej, *Bio Trace Elem Res*, **79**, 139 (2001).
8. M.W. Krachler, K. Domej, J. Irgolic, *Biol Trace Elem Res*, **75**, 253 (2000).
9. Y. Chen, H.C. Whetstone, A.C. Lin, P. Nadesan, Q. Wei, R. Poon, B.A. Alman, *PLoS Medicine*, **4**(7), e249 (2007).
10. C. Livingstone, H. Rampes, *J Psychopharmacol*, **20**, 317 (2006).
11. P. Vestergaard, L. Rejnmark, I. Mosekilde, *Calcif Tissue Int*, **77**, 1 (2005).
12. M. Krachler, W. Domej, *Biol Trace Elem Res*, **79**, 139 (2001).
13. L.S. Richman, A.L. Dzierba, K.A. Connolly, P.M. Bryan, S. Chandra, *J Pharm Pract*, **28**, 1 (2015).
14. M. Bauer, M. Adli, T. Bschor, M. Pilhatsch, A. Pfennig, J. Sasse, R. Schmid, U. Lewitzka, *Neuropsychobiology*, **62**, 36 (2010).
15. T.C. Oliveira, I.A.C. Neto, M.H. Aguiar-Oliveira, A.F. de Pereira, *Arq Bras Endocrinol Metabol*, **58**, 619 (2014).
16. L. Pesce, P. Kopp, *Int J Pediatr Endocrinol*, **2014**, 8 (2014).
17. P. Clément-Lacroix, M. Ai, F. Morvan, S. Roman-Roman, B. Vayssière, C. Belleville, K. Estrera, M.L. Warman, R. Baron, G. Rawadi, *National Academy of Sciences*, **102**, 17406 (2005).
18. K.G. Patel, P.C. Yadav, C.B. Pandya, H.N. Saiyed, *J Environ Bio I*, **25**(4), 413 (2004).

19. H.J. Zhuo, A.H. Smith, C. Steinmaaus, *Cancer Epidemiol Biomarkers Prev*, **13**, 771 (2004).
20. Y.Wu, S.M. Adeeb, M.J. Duke, D. Munoz-Paniague, M.R. Doschak. *Journal of pharmacy and pharmaceutical sciences*, **16**(1), 52 (2013).
21. X. Ma, X. Zhang, Y. Jia, S. Zu, S. Han, D. Xiao, H. Sun, Y. Wang, *Int Orthop*, **37**, 1399 (2013).
22. B. Hollenbach, N.G. Morgenthaler, J. Struck, C. Alonso, A. Bergmann, J. Kohrle, L. Schomburg, *J Trace Elem Med Biol*, **22**, 24 (2008).
23. L.C. Davies, E.J. Blain, S.J. Gilbert, B. Caterson, V.C. Duance, *Tissue Eng Part A*, **14**(7), 1251 (2008).
24. L.Y. Sun, F.G. Meng, Q. Li, Z.J. Zhao, C.Z. He, S.P. Wang, R.L. Sa, W.W. Man, L.H. Wang, *Osteoarthritis Cartilage*, **22**(12), 2033 (2014).
25. W.Y. Sun, X. Wang, X.Z. Zou, R.X. Song, X.H. Du, J. Hu, *Br J Nutr*, **104**, 1283 (2010).
26. E.L. Kuyinu, G. Narayanan, L.S. Nair, C.T. Laurencin, *J Orthop Surg Res*, **11**, 19 (2016).
27. C.R. Scanzello, S.R. Goldring, *Bone*, **51**, 249 (2012).
28. Y. Zhang, K. Kumagai, T. Saito, *J Orthop Surg Res*, **9**, 68 (2014).
29. F. Eckstein, W. Wirth, M.I. Hudelmaier, S. Maschek, W. Hitzl, B.T. Wyman, M. Nevitt, M.-P. Hellio, *ArthritisResTher*, **11**, R90 (2009).
30. M. Bellido, L. Lugo, J.A. Roman-Blas, S. Castañeda, J.R. Caeiro, S. Dapia, E. Calvo, R. Largo, G. Herrero-Beaumont, *Arthritis ResTher*; **12**, R152 (2010).

Coupled heat and mass transfer in annular adsorption bed

D. D. Gao, Y. X. Li, Z. X. Yuan*, S. W. Du

College of Environmental and Energy Engineering, Beijing University of Technology

Received February 12, 2016; Revised December 26, 2016

A numerical simulation has been conducted to investigate the heat and mass transfer in the adsorption process of an annular cavity bed. The silica gel and the water was taken as the working pair. The 2D model of the heat and mass transfer has been established for the adsorption problem. To clarify the cooling effect of different situations, the air cooling mode and the water cooling mode were considered to apply onto the bed. Based on the numerical results the change of the temperature and the vapor concentration of the bed was analyzed and discussed. The influence of the bed layer porosity and the evaporation temperature on the performance was examined too. The results have revealed that the bed temperature increased largely at the first 400 seconds of the adsorption time. This time corresponded to the rapid adsorption and the large amount of the heat generation. Beyond a summit, the temperature of the bed decreased gradually while the bed concentration kept increasing. The bed layer porosity affected the adsorption only in a small scale, while increasing the evaporation temperature promoted the adsorption largely.

Keywords: adsorption bed, heat and mass transfer, temperature, dynamic

AIMS AND BACKGROUND

Nowadays much attention in the world is being paid to the excessive energy consumption and the environment pollution. Many technologies have been proposed to conserve energy and to reduce the harm to the environment. Specially, utilizing the solar energy as the driving source of the refrigeration system has got the attention of the researchers. Compared to the conventional vapor-compressed refrigeration technique, the adsorption cooling system has the advantage of low grade demanding of the heat source, low noise, and less pollution to the environment [1,2]. Therefore, the related study on such a topic has drawn many researchers around the world [2,3].

In adsorption refrigeration system the adsorbent bed is the most important component. Its characteristic directly affects the performance of the system. Especially, for the solar-driven adsorption system, the performance of the bed is highly affected by the heat and mass transfer in the bed. The solar energy should be transferred into the bed quickly to cause the bed to desorb. On the other hand, the reaction heat in the adsorption process must be discharged out as soon as possible so that the material can fully adsorb the refrigerant vapor. Some measurements have been proposed in the literature to enhance the heat transfer in the bed. Groll reviewed [4] the typical beds in the

adsorption system, he emphasized the same importance of the heat transfer in both the external and the internal sides of the bed. Pons et al studied [5] the dynamic temperature change in the bed and demonstrated the impact of the flow-rate of the circulating fluid. The application of zeolite-active carbon compound in the tube bed could promote the heat transfer by absorbing the solar energy directly [6]. Using the zeolite-coated bed for a sorption air conditioning system, Restuccia et al investigated the optimum conditions to reach the most effective heat and mass transfer [7]. Heat pipes or optimized thermal loops may also improve the performance of a sorption system. A novel design of passive evaporation known as the rising film evaporation was reported in [8], in which the gravity heat pipe was employed to enhance the heat transfer in the evaporator. The author also emphasized the significance of the appropriate arrangement of the thermal fluid and the refrigerant vapor. Niazmand et al [9] conducted a research on the coupling heat and mass transfer in the evacuated tube bed with fins. The numerical results revealed that increasing the fin number and decreasing the bed height was both able to reduce the cycle time.

Considering the intrinsic feature of the coupled heat and mass transfer in the bed, it is necessary to take into account of both them together in the study, so that the mutually-affected mechanism can be clearly verified. For this purpose, the current study is focused on the investigation into the heat and mass transfer in an evacuated tube bed during the

* To whom all correspondence should be sent:

E-mail zxyuan@bjut.edu.cn

adsorption process. The numerical results of the temperature and the adsorption concentration of the bed will be presented and discussed. In addition, the effect of the material porosity and the evaporation temperature will also be paid attention.

PHYSICAL AND MATHEMATICAL MODEL

For simplification, the heat and mass transfer in the evacuated tube bed is reduced to be a 2-D axially symmetrical problem, as shown in Figure 1 and Figure 2. The outer alloy tube and the inner copper tube forms the annular adsorption bed. The silica gel is used as the adsorbent. Through the annular inlet at the left the water vapor flows into the bed. At the same time, the circulating fluid flows through the copper tube to keep the bed cooling down. In the desorption process, which is not involved in this study, the solar irradiation heats the alloy tube through the outmost glass tube. The bed is exposed to the solar radiation and the cooling channel is shut down. Beyond the critical pressure, the desorbed water vapor is delivered to the condenser and liquefied. As the first part of the study, the result here is only for the heat and mass transfer in the adsorption process. The large amount of the reaction heat during the adsorption is rejected by the cooling fluid of either the air or the water. No solar heat is put on the bed during the adsorption process.

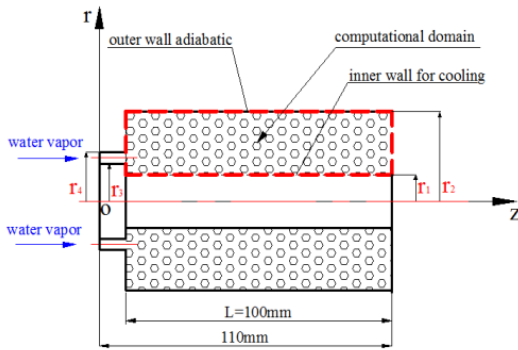


Fig.1. The two-dimensional model of the tube bed

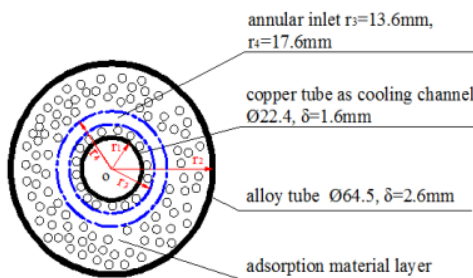


Fig.2. Cross-sectional schematic of the bed

In the numerical model the following assumptions are considered and followed, (a) The adsorbent particle is of the same size. The physical property of the bed material is isotropic, (b) All physical properties are constant and independent of the temperature and the concentration, and (c) The contact resistance between the adsorbent and the tube wall is neglected.

Energy Equation

In the energy equation the balance of the transient source term, the heat conduction, and the vapor convection are involved. The adsorption concentration q of the bed is taken as a heat source term [10]. The energy equation of the adsorption bed is as

$$\begin{aligned} (1-\varepsilon_i)\rho_s c_{ps} + \varepsilon_b \rho_g c_{pg} + (1-\varepsilon_i)\rho_s q c_{pw} \frac{\partial T_s}{\partial t} = \lambda_{\text{eff}} \left[\frac{1}{r} \frac{\partial}{\partial r} \left(r \frac{\partial T_s}{\partial r} \right) + \frac{\partial^2 T_s}{\partial z^2} \right] \\ - \frac{\partial}{\partial z} (\rho_g c_{pg} T_s u) + (1-\varepsilon_i)\rho_s \Delta H_{\text{ads}} \frac{\partial q}{\partial t} \end{aligned} \quad (1)$$

where, c_{ps} and c_{pg} is the specific heat of the adsorbent material and the refrigerant vapor, respectively. c_{pw} is the specific heat of the liquid refrigerant. u indicates the flowing velocity of the refrigerant vapor in the bed. λ_{eff} is the effective heat conductivity, which was determined by the weighted sum of the adsorbent's and the vapor's conductivity. ΔH_{ads} is the reaction heat of adsorption. The total porosity of the bed ε_i is determined by the weighted sum of the bed layer porosity ε_b and the particle porosity ε_p ,

$$\varepsilon_i = \varepsilon_b + (1-\varepsilon_b)\varepsilon_p \quad (2)$$

The boundary condition for the energy equation is

$$r = r_1, \quad -\lambda_{\text{eff}} \frac{\partial T(r, z)}{\partial r} \Big|_w = h(T_w - T_f) \quad (3)$$

$$r = r_2, \quad -\lambda_{\text{eff}} \frac{\partial T(r, z)}{\partial r} \Big|_w = 0 \quad (4)$$

$$r_1 < r < r_2, \quad \frac{\partial T_s}{\partial z} \Big|_{z=10} = \frac{\partial T_s}{\partial z} \Big|_{z=110} = 0 \quad (5)$$

Where h is the convective heat transfer coefficient between the coolant fluid and tube wall. Both the air and the water are taken as the coolant fluid. By the reference of the heat transfer handbook, we took $h = 6 \text{ W}/(\text{m}^2 \cdot \text{K})$ for the natural air convection, and $h = 500 \text{ W}/(\text{m}^2 \cdot \text{K})$ for the forced water convection. These two thermal boundary conditions will be the basis of the following comparison for the different cooling situation. In addition, the initial condition of the bed in the simulation is considered as

$$T(r, z, t) \Big|_{t=0} = 298 \text{ (K)} \quad (6)$$

The property of the type-A silica gel was adopted in the simulation. The diameter of the silica gel particle was taken as $d = 1.0\text{mm}$. The other properties of the silica gel are listed in Table 1.

Mass Equation

The mass equation describes the transient equivalence between the vapor convection and the vapor mass change in the pores of the bed

$$\frac{\partial(\varepsilon_t \rho_g)}{\partial t} + \nabla(\rho_g \bar{u}) = S_m \quad (7)$$

The source term S_m reflects the change of the adsorption concentration per unit time. It takes a negative value in the adsorption process and a positive value in the desorption process. The S_m term can be determined directly by the change of the concentration with the time

$$S_m = -(1 - \varepsilon_t) \rho_s \frac{\partial q}{\partial t} \quad (8)$$

Velocity Equation

For the hydrodynamic problem in a porous media where the effective porosity is not very high, the Darcy's law of the hydromechanics is applied. The Darcy's law describes the relation of the fluid velocity and the pressure gradient. Provided that the viscosity of the fluid μ and the apparent permeability K_{app} of the material is known, the velocity u has the relation to the pressure p as

$$u = -\frac{K_{app}}{\mu} \frac{\partial p}{\partial z} \quad (9)$$

The corresponding boundary condition for the current problem is

$$\left. \frac{\partial p}{\partial z} \right|_{z=110} = 0$$

$$p|_{z=10} = p_e \quad (10)$$

The initial pressure of the bed is assumed as $p = 0$.

The apparent permeability K_{app} is related to the intrinsic permeability of the material K and the physical property of the fluid [11,12]

$$K_{app} = K + \frac{\varepsilon_p \mu}{\tau p} D_g \quad (11)$$

Where τ is the collision factor and D_g is the diffusivity of the fluid. According to the theory of the transport phenomena, K is determined by the particle size d and the bed layer porosity ε_b , and is calculated by the semi-empirical Blake-Kozeny formula

$$K = \frac{\varepsilon_b^3 d^2}{150(1 - \varepsilon_b)^2} \quad (12)$$

The diffusivity D_g of the refrigerant vapor in

Eq.(11) is determined by the formula [13,14]

$$D_g = 1/(1/D_m + 1/D_k) \quad (13)$$

where D_m and D_k is the molecular diffusivity and the Knudsen diffusivity respectively

$$D_m = 0.02628 \frac{\sqrt{T^3/M}}{p\sigma^2\Omega} \quad (14)$$

$$D_k = \frac{2 \times 10^5 r_p}{3} \left(\frac{8RT}{\pi M} \right)^{1/2} \quad (15)$$

In Eq.(14) and (15), M is the molecular mass of the vapor. R is the universal ideal gas constant. σ is the collision diameter for the Lennard-Jones potential, and Ω is the collision integral. r_p denotes the radius of the adsorbent particle.

Adsorption Equation

The current adsorption problem is a typical non-equilibrium process. Based on the reaction kinetics theory, Sakoda and Suzuki studied the adsorption dynamics in the silica gel-water system. They argued that the adsorption rate was strongly influenced by the surface diffusion of the adsorbent particle [15]. To reflect the feature of the actual non-equilibrium in the adsorption process, they took into account the effect of the surface diffusion into the adsorption rate, and proposed the dynamic model as

$$\frac{\partial q}{\partial t} = \frac{15D_{so} \exp(-E_a/RT)}{r_p^2} (q^* - q) \quad (16)$$

The initial condition is $q = 0$ for $t = 0$, and D_{so} is the surface diffusivity of the material. q^* is the equilibrium concentration that is determined by the modified Dubinin-Astakhov equation

$$q^* = k(p_e/p_s)^{\frac{1}{n}} \quad (17)$$

k and n are constants related to the working pair. For the silica gel - water system, $k = 0.346 \text{ g}_w/\text{g}_s$ and $n = 1.6$. p_e is the evaporation pressure, and p_s is the saturation vapor pressure corresponding to the bed temperature T_s . In the numerical simulation, we adopted the empirical Antoine formula to determine the relationship of the saturation pressure and the temperature of water [16,17]

$$\lg p = A - B/(T + C) \quad (18)$$

$A = 8.10765$, $B = 1750.29$, $C = 235$, for $T = 0 \sim 60 \text{ }^\circ\text{C}$, and $A = 7.96681$, $B = 1668.21$, $C = 228$, for $T = 60 \sim 150 \text{ }^\circ\text{C}$.

It needs to note that the unit of the pressure in Eq.(18) is in mmHg.

Table 1. Physical properties of type A silica gel[10].

Average pore size (nm)	Specific surface (m ² /g)	Pore volume (ml/g)	Specific heat c_{ps} (kJ/(kg·K))	Thermal conductivity λ_s (W/(m·K))	Bulk density ρ_s (kg/m ³)	True density (kg/m ³)	Apparent density (/kg/m ³)
2.0-3.0	650-800	0.35-0.45	0.92	0.175	790	2200	1170

Table 2. The parameter values for the numerical model

Parameter	Symbol	Value	Unit
Initial inlet pressure	p_0	1703.5	Pa
Surface diffusion coefficient	D_{so}	2.54×10^{-4}	m ² /s
Activation energy of surface diffusion [18]	E_a	4.2×10^4	J/mol
Universal gas constant ¹⁸	R	8.314	J/(mol·K)
Specific gas constant for water vapor	R_g	461.5	J/(kg·K)
Adsorption heat of silica gel [13]	ΔH_{ads}	2560	kJ/kg
Particle density of silica gel	ρ_s	790	kg/m ³
Thermal conductivity of silica gel	λ_s	0.175	W/(m·K)
Specific heats of silica gel	c_{ps}	0.920	kJ/(kg·K)
Particle porosity of silica gel [10]	ε_p	0.42	—
Bed porosity [10]	ε_b	0.37	—
Specific heat of water vapor	c_{pg}	1.874	kJ/(kg·K)
Specific heat of water	c_{pw}	4.187	kJ/(kg·K)
Molecular weight of water	M	18	g/mol
Viscosity of water vapor	μ	9.06×10^{-6}	N·s/m ²
Thermal conductivity of water vapor [19]	λ_g	0.0196	W/(m·K)
Collision factor [13]	τ	3	—
Collision diameter for Lennard-Jones potential [13]	σ	2.641	Å
Collision integral [12]	Ω	2.236	—
Evaporation temperature	T_e	288	K

Table 3. Converged temperature of the monitored points for different grid system, water cooling condition at $T_f = 298K$, $h = 500$ W/(m²·K)

Grid number	T_A (K)	T_C (K)	T_D (K)
14500	307.69	308.04	318.31
25737	307.38	307.64	318.30
57500	307.30	307.67	318.23
103193	307.44	307.83	318.25

NUMERICAL METHOD

The numerical simulation to the current problem was conducted by using the FLUENT software. The GAMGIT program involved in the software package was used to generate the grid system. In advance of the simulation, the parameters that are involved in the equations above must be preset. By reference of the open literature that was related to the dynamic adsorption problem, the corresponding parameters were adopted and listed in Table 2.

In a simulation it is necessary to check the grid-independence of the numerical domain prior to the formal calculation. The appropriate grid system guarantees the convergence of the iteration and the accuracy of the numerical result. For this purpose, a preliminary study was conducted for the water cooling case. In the process of the iteration the

temperature, the pressure and the adsorption concentration of the bed were monitored. The monitored points are denoted by A, B, C, and D as shown in Figure 3, which coordinator value is as A(30, 15.6), B(50, 15.6), C(70, 15.6) and D(50, 27.6) respectively.

In the preliminary simulation, the temperature of point A, C and D was monitored for the different grid system. The checked result is presented in Table 3. With the grid number increasing from 14500 to 103193, the temperature changed not very much. The changing range of the temperature was in between 0.08K and 0.40K, with the maximum for point C and the minimum for point D. Therefore it was considered that the grid number in the range above did not affect the numerical accuracy too much, and then the grid number of 25737 was adopted in the formal study.

Table 4. Relation of the evaporation temperature to the pressure.

T (°C)	5	8	12	15
p_s (Pa)	871.5	1072.1	1401.5	1703.5

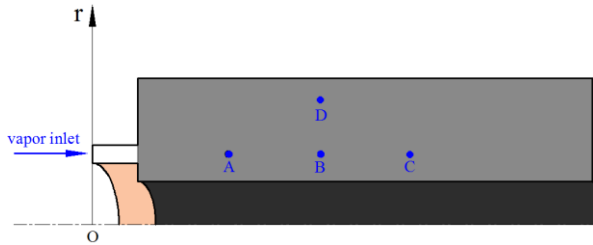


Fig.3. The numerical domain and the monitored points position.

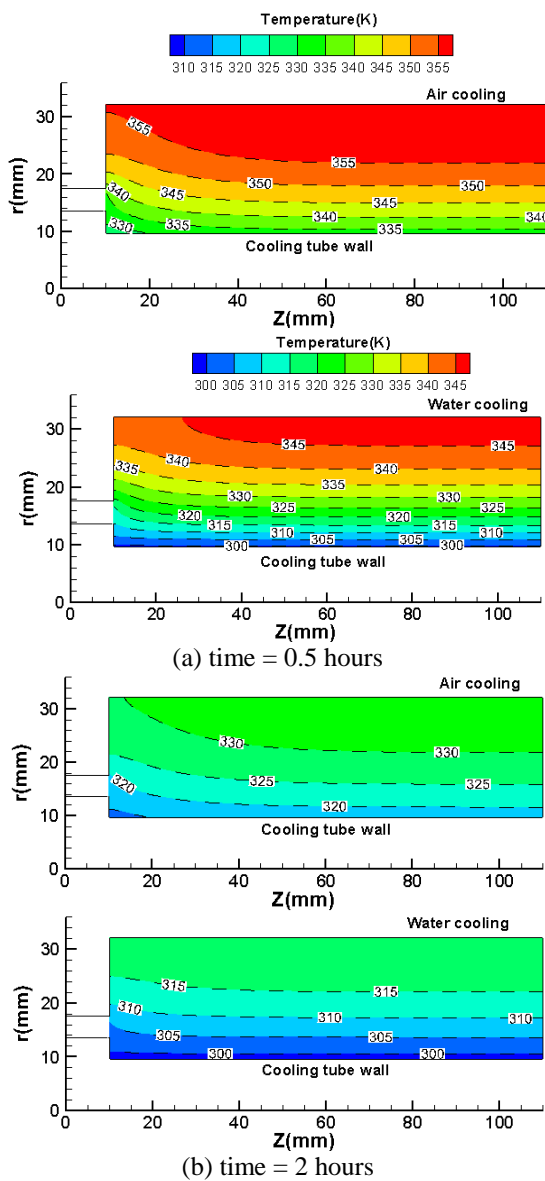


Fig. 4. Comparison of the temperature field for the air cooling and the water cooling, as adsorption time was 0.5 hour and 2 hours, respectively.

RESULTS AND DISCUSSION

Temperature and Concentration Field

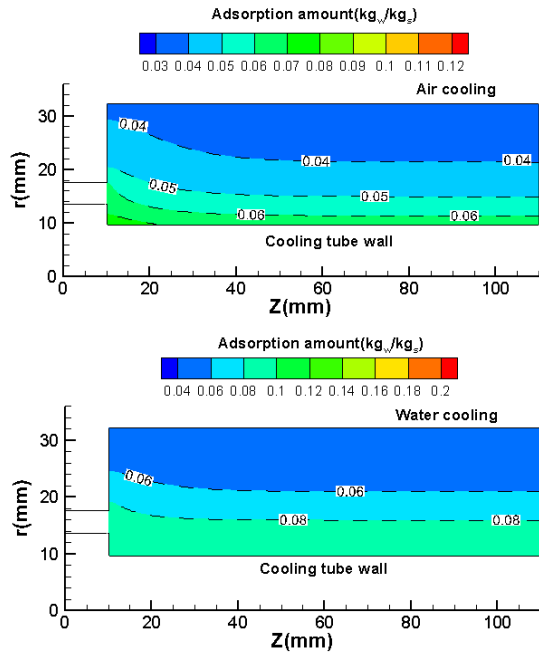
To analyze the distribution of the temperature, two sets of the temperature field of the bed at different time were presented in Figure 4. Figure 4 (a) and (b) is for the $t = 0.5$ hours and for the $t = 2$ hours of the adsorption time respectively. Obviously, the bed temperature distributed much more evenly at $t = 2$ hours as compared to that at time = 0.5 hours. After one and a half hours adsorption, the non-uniformity degree of the temperature had decreased from 25K to 15K for the air cooling, and from 45K to 15K for the water cooling. It is seen from the figure that the temperature changes more seriously along the radial direction rather than the axial direction. This tells us that the heat transfer was mainly towards the radial direction. As to the effect of the cooling mode, the cold area reflects the difference. In comparison, the cold area of the water-cooling patterns is clearly larger than that of the air cooling patterns. This demonstrates that the water cooling mode is better than the air cooling mode. The cooling effectiveness of the bed is very important in view of the sufficient adsorption of the material. The lower temperature promotes the adsorption while the high temperature frustrates the adsorption.

The corresponding concentration field to the above temperature field is shown in Figure 5. Different from the less-changing temperature field with the time, here the gradient of the concentration became greater with the time as comparing Figure 5 (b) to Figure 5 (a). This just reflected the effect of the temperature on the adsorption process. The inner cold area of the bed near the cooling tube wall tended to adsorb more strongly than the outer area. On the other hand, the adsorption difference resulted from the cooling mode is obvious. The high cooling strength of the water helped to improve the adsorption in the bed. Though the isosteric values in Figure 5(a) was not very different for the air cooling mode and for the water cooling mode, their difference in Figure 5(b) was as great as almost two times. The water cooling mode had the great advantage and should be taken into account in practical engineering.

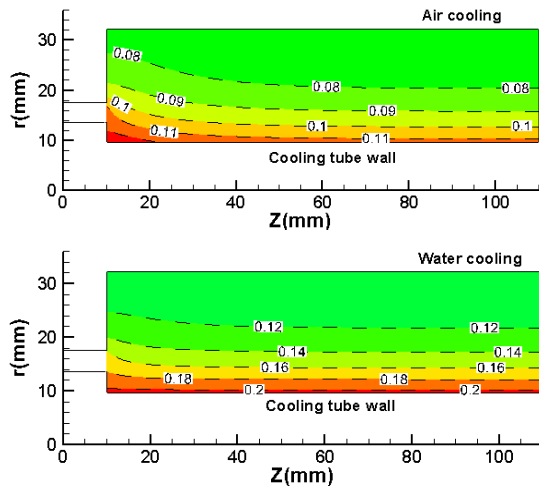
Dynamic Change of Temperature and Concentration

On the basis of the distribution field discussed above, it is necessary to delve into the temporal evolution of the temperature in the bed. In Figure 3 four points A, B, C, and D were taken to monitor

the change of the bed parameters. The dynamic response of the temperature and the concentration of the monitored points are shown in Figure 6 and Figure 7.



(a) time = 0.5 hours



(b) time = 2 hours

Fig. 5. Comparison of the concentration field for the air cooling and the water cooling mode, as adsorption time was 0.5 hour and 2 hours, respectively.

The temperature summit in Figure 6 is considered to be resulted from the unmatched heat dispersion between the adsorption heat generation and the poor capability of the conductivity of the adsorbent material. The large amount of reaction heat resulted from the adsorption at the beginning period could not be transferred effectively by the bed and then caused the sharply rising of the temperature. To distinguish the temperature difference of the monitored points,

a local enlarged view has been inserted into Figure 6. It is clear that the temperature curve of point D was different from the others. With the farthest distance to the cooling tube wall, the point D was of the greater thermal resistance. Therefore point D was subjected to the poorest cooling effect among the monitored points. The maximum temperature difference between point D and the others has reached 28K. The difference between the other three points was much less. A careful survey to the enlarged view revealed that the temperature of point A was the lowest.

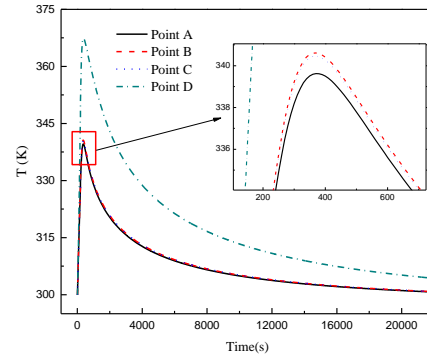


Fig.6. Dynamic change of the temperature of the monitored points for water cooling mode

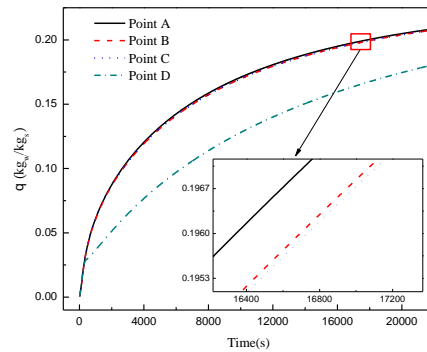


Fig. 7. Dynamic change of the concentration of the monitored points for water cooling mode

The change of the concentration is presented in Figure 7. After a rapid increasing at the beginning time, the adsorption rate tended to slow down gradually. A feature needs to pay attention is the sharp turning of the curve of point D. Approximately at time = 300 s, the adsorption rate of point D dropped down suddenly, and then the curve began to separate from the others. This feature can be interpreted from the relationship of the heat transfer ability and the mass transfer ability of the material. With higher diffusivity of the material than the conductivity, all points got a chance to adsorb quickly at the beginning. But with the proceeding of the adsorption, the inferior position of point D occurred right away because of the poor heat dissipation to the coolant fluid. The

bad cooling effect of point D frustrated its effective adsorption further more. As to point A, B, and C, not much difference was detected because they all share the same radial coordinate value.

Effect of Cooling Mode on Bed Performance

Different cooling conditions will result in the different performance of the bed. With the air cooling mode and the water cooling mode, the numerical simulation has presented the variation of the bulk average temperature and the average adsorption concentration of the bed, as shown in Figure 8 and Figure 9.

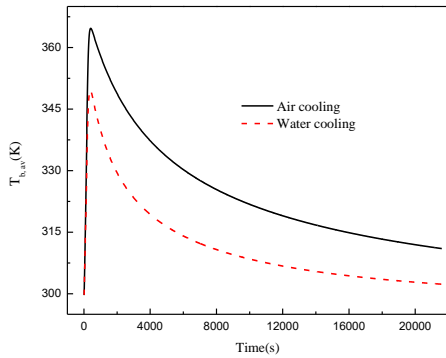


Fig. 8. Variation of the average temperature with the time.

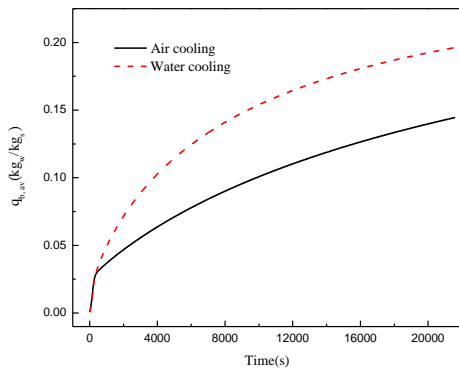


Fig. 9. Variation of the average concentration with the time.

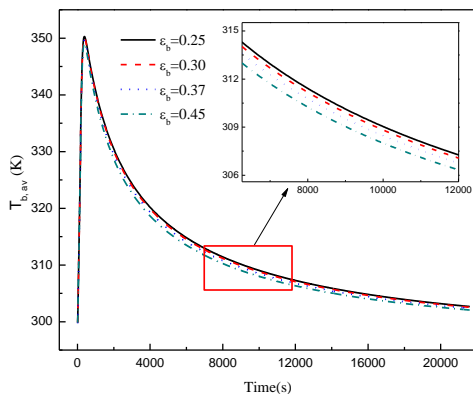


Fig.10. Porosity effect on the temperature change of the bed, for water cooling mode.

The variation of the bulk average temperature is similar to that of the monitored point in Figure 6. In Figure 8 the average temperature reached the maximum of 364.7K after 410s for the air cooling condition, and 349.6K after 380s for water cooling condition. The difference of the dynamic temperature for the two cooling modes is obviously. With less difference before the summit, the average temperature of the bed for the water cooling mode decreased faster than that of the air cooling mode. The maximum difference of the temperature for them was as much as 19.3K.

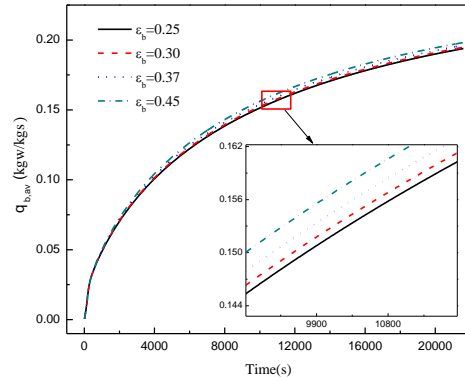


Fig. 11. Porosity effect on the concentration change of the bed, for water cooling mode.

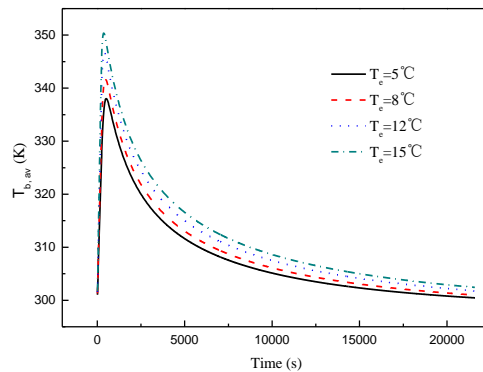


Fig. 12. Effect of the evaporation temperature on the bed temperature, for water cooling mode.

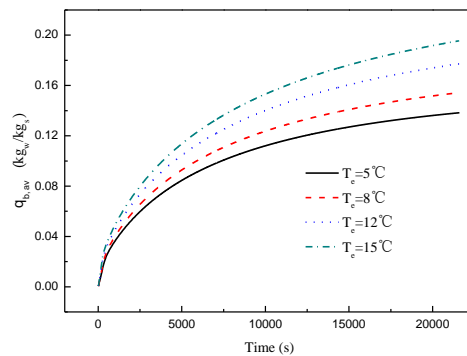


Fig.13. Effect of the evaporation temperature on the average concentration of the bed, for water cooling mode.

The bulk averaged concentration of the bed is presented in Figure 9. The figure shows the different tendency of the average concentration for the two cooling modes. The water cooling mode generates a smoothly increasing profile of the $q_{b,av}$, while the increasing of the concentration of the air cooling mode slowed down after a time period. The maximum difference of the concentration for the two cooling modes has reached 26.4%. The causation of this phenomenon is similar to what is mentioned in the discussion of Figure 7. After the transient effective adsorption at the beginning time, the good cooling way of the water mode tended to keep the bed in a sustainable good work state, while the air cooling mode does not have such ability because of the less cooling effect. Usually the power output of the refrigeration machine depends mainly on the adsorption amount per unit time, so the appropriate cooling way is highly appreciated.

Effect of Porosity of Adsorbent on Bed Performance

As aforementioned the total porosity of the bed consists of the particle porosity ε_p and the bed layer porosity ε_b . The ε_p is an intrinsic attribute of the adsorption material, which is determined by the product type, but the ε_b is changeable with the compactness of the bed. Leong et al [20] once conducted a study of the compressing effect of the adsorbent particle on the heat and mass transfer of the bed. Their result suggested that although the compacted bed improved the heat transfer, the decreased bed porosity affected the adsorption inversely. With the bed porosity decreasing, the mass transfer resistance increased, which would hinder the adsorption of the bed.

In the current study the bed porosity ε_b was considered as a variable. In the range of ε_b from 0.25 to 0.45, the effect of the bed porosity was numerically identified. The related variation of the $T_{b,av}$ and $q_{b,av}$ with the time is as shown in Figure 10 and Figure 11. It is seen that the effect of the bed porosity on the performance is not seriously. The maximum temperature difference for the different porosities was only about 1.8K, and the maximum concentration difference was about 2.2%. In addition, the result of the porosity effect was consistent with the conclusion of the study by Leong et al in [20]. The higher porosity did lower the average temperature of the bed to some extent, and promoted the adsorption slightly.

Effect of Evaporation Temperature on Bed Performance

The pressure of the refrigerant vapor is another significant factor to influence the adsorption. The

equilibrium concentration of the adsorbent material usually increases with the pressure and decreases with the temperature. On the other hand, the influence of the two elements is not in the same level. In the current study, a series of simulation has been performed on the effect of the inlet pressure of the refrigerant vapor. The numerical condition was the same as presented in Table 2 with the water cooling mode. Four pressure values were adopted, and their relation to the evaporation temperature is as shown in Table 4. The p_s is the saturation pressure at the given temperature. Figure 12 presented the change of the bed temperature $T_{b,av}$ at different evaporation temperatures. As seen in the figure, the bed temperature increased largely with the evaporation temperature. Increasing the evaporation temperature implies improving the inlet pressure of the vapor into the bed. The higher pressure upgraded the driving force of the adsorption. The improved adsorption generated more reaction heat and resulted in the temperature rising up quickly.

The effect of the evaporation temperature on the bed concentration is presented in Figure 13. Obviously, the evaporation temperature affected the bed concentration more strongly than the bed porosity, as shown in Figure 11. The maximum difference of the $q_{b,av}$ for $T_e = 5^\circ\text{C}$ and 15°C has reached as much as 67.7%. If we relate the $q_{b,av}$ curve to the $T_{b,av}$ curve in Figure 12, an interesting relationship is revealed. Corresponding to the shooting up of the temperature curve at the beginning time, the concentration curve increased fast too. To the declining temperature beyond the summit, the concentration curve tended to be flat. The higher temperature profile corresponded to the higher concentration profile. This feature is just the reverse to the relation of the $T_{b,av}$ and the $q_{b,av}$ discussed above about the effect of the cooling mode and the bed porosity. The high temperature of the bed itself frustrated the adsorption, while the high temperature of the evaporator helped to promote the adsorption. This reflects the difference of the adsorption driving potential from the outside and the inside of the adsorbent particle.

CONCLUSIONS

Based on the established model of the annular bed, the numerical simulation was performed on the characteristics of the adsorption process. The results revealed that the heat and mass transfer in the bed was highly coupled and affected each other. The temperature distribution of the bed was the integrated result of the adsorption and the cooling mode. The bed temperature also reacts against the

adsorption strongly. For the annular bed with the internal cooling tube, the water cooling mode resulted in a much better adsorption performance than the air cooling mode. At the beginning time the adsorption happened in a high rate, and a large amount of the reaction heat was generated. The heat generation resulted in a rapid rise of the temperature within the first 400 seconds or so. After reaching the summit, the bed temperature declined gradually. Correspondingly, the adsorption experienced a process from fast to slowing down.

Further study revealed that the higher bed porosity tended to reduce the mass transfer resistance and to improve the adsorption slightly. On the other hand, increasing the inlet vapor pressure of the bed promoted the adsorption in large scale. In general, applying the effective cooling mode, optimizing the bed structure, and reducing the heat and mass transfer resistance, are considered as the effective ways to improve the performance of the adsorption bed.

NOMENCLATURE

c_{ps}	[J/(kg·K)]	specific heat of silica gel
c_{pg}	[J/(kg·K)]	specific heat of refrigerant vapor
c_{pw}	[J/(kg·K)]	specific heat of refrigerant liquid
d	[m]	particle diameter
D_g	[m ² /s]	diffusivity of refrigerant vapor
D_k	[m ² /s]	Knudsen diffusivity of the material
D_m	[m ² /s]	molecular diffusivity of the material
D_{so}	[m ² /s]	surface diffusion coefficient
E_a	[J/mol]	diffusional activation energy
h	[W/(m ² ·K)]	convective heat transfer coefficient
K	[m ²]	intrinsic permeability of porous material
K_{app}	[m ²]	apparent permeability of porous material
k	[-]	constant in Eq.(17)
M	[g/mol]	molecular mass
n	[-]	constant in Eq.(17)
p	[Pa]	pressure
$p_{b,av}$	[Pa]	average pressure of adsorbent bed
p_s	[Pa]	saturated vapor pressure
q	[kg _w /kg _s]	adsorption concentration
q^*	[kg _w /kg _s]	equilibrium adsorption concentration
$q_{b,av}$	[kg _w /kg _s]	average adsorption capacity of bed
R	[J/(mol·K)]	universal ideal gas constant
r	[mm]	radial coordination
r_1	[mm]	radius of the cooling tube
r_2	[mm]	radius of the solar-absorbing alloy tube
r_p	[m]	radius of adsorbent particle
S_m	[kg/(m ³ ·s)]	mass source term in Eq.(7)
T	[K]	temperature
$T_{b,av}$	[K]	average temperature of adsorbent bed
T_e	[K]	evaporation temperature
T_f	[K]	temperature of the cooling fluid
T_s	[K]	temperature of the adsorbent
T_w	[K]	wall temperature of the cooling tube
T_0	[K]	initial temperature of the bed
t	[s]	time
u	[m/s]	velocity
Greek symbol		
μ	[N·s/m ²]	dynamic viscosity
ρ_g	[kg/m ³]	density of water vapor
ρ_s	[kg/m ³]	density of adsorbent
ΔH_{ads}	[kJ/kg]	heat generation of adsorption
ε_b	[-]	bed layer porosity
ε_p	[-]	particle porosity
ε_t	[-]	total porosity
τ	[-]	collision factor
σ	[Å]	collision diameter for Lennard-Jones potential
Ω	[-]	collision integral
λ_{eff}	[W/(m·K)]	effective thermal conductivity
λ_g	[W/(m·K)]	thermal conductivity of water vapor
λ_s	[W/(m·K)]	thermal conductivity of adsorbent

Acknowledgements: This research work was sponsored by the National Natural Science Foundation of China (Grant No. 51276005) and the National Key Basic Research Program of China (No.2015CB251303).

REFERENCES

1. W. Gazda, J. Koziol, *Appl. Energy*, **101**, 49 (2013).
2. H.Z. Hassan, A.A. Mohamad, R. Bennacer, *Energy*, **36**, 530 (2011).
3. R.Z. Wang, *Renewable Sustainable Energy Rev*, **5**, 1 (2001).
4. M. Groll, *Heat Recovery Syst. CHP*, **13**, 341 (1993).
5. M. Pons, D. Laurent, F. Meunier, *Appl. Therm Eng*, **16**, 395 (1996).
6. Z.Y. Liu, Y.Z. Lu, J.X. Zhao, *Sol. Energy Mater. Sol. Cells*, **52**, 45 (1998).
7. G. Restuccia, A. Freni, G. Maggio, *Appl. Therm. Eng*, **22**, 619 (2002).
8. R.Z. Wang, Z.Z. Xia, L.W. Wang, Z.S. Lu, S.L. Li, T.X. Li, J.Y. Wu, S. He, *Energy*, **36**, 5425 (2011).
9. H. Niazmand, I. Dabzadeh, *Int. J. Refrig*, **35**, 581 (2012).
10. H.T. Chua, K.C. Ng, W. Wang, C. Yap, X.L. Wang, *Int. J. of Heat Mass Transfer*, **47**, 659 (2004).
11. K.C. Leong, Y. Liu, *Int. J. of Heat Mass Transfer*, **47**, 4761 (2004).
12. R.B. Bird, W.E. Stewart, E.N. Lightfoot, *Transport Phenomena*, Wiley, New York, 1960.
13. H. Demir, M. Mobedi, S. Ülkü, *Int Commun Heat Mass Transfer*, **36**, 372 (2009).
14. D.M. Ruthven, *Principles of adsorption and adsorption processes*, John Wiley & Sons, New York, 1984, p. 124
15. A. Sakoda, M. Suzuki, *J. Chem. Eng. Jpn*, **17**, 52 (1984).
16. R.C. Reid, J.M. Prausnitz, T.K. Sherwood, *The properties of gases and liquids*, fourth ed., McGraw-Hill, New York, 1987.
17. A. Senol, *J. Chem. Thermodyn*, **67**, 28 (2013).
18. J. Di, J.Y. Wu, Z.Z. Xia, R.Z. Wang, *Theoretical Int. J. Refrig*, **30**, 515 (2007).
19. İ. Solmuş, D. Andrew, S. Rees, C. Yamali, D. Baker, B. Kaftanoğlu, *Int. J. Refrig*, **35**, 652 (2012).
20. K.C. Leong, Y. Liu, *Appl. Therm. Eng*, **24**, 2359(2004).

Establishment of detection method for the biological activity of Lumbrokinase

X.W. Huang¹, X.H. Li¹, X. Pan³, Y.L. Yan¹, D.Y. Xu¹, Q. Gao¹, L.C. Cui¹, Y. Pan², C.L. Zhou³,
S.Y. Yang³, M.H. Duan^{1*}, X. B. Qu^{1*}

¹Changchun University of Chinese Medicine

²Training Corps Three of the Aeronautical University

³Training Corps One of the Aeronautical University

Received December 12, 2015; Revised February 26, 2016

Lumbrokinase methodology validation research method for the determination of biological .Methods: In pharmacopoeia streptokinase biological activity determination method is improved, the preparation of agarose - fibrin plate, making standard curve. Results: More standard Lumbrokinase biological activity determination methods Conclusions: This method is more easy and accurate determination of Lumbrokinase activity of biology

Keywords: Lumbrokinase; Biological activity; Determination methods ; Validation

INTRODUCTION

Introduction to Earthworm

Shizhen Li, in his book "Compendium of Materia Medica" has documented in detail the morphology, behaviours, and medicinal value of the earthworms, he called it the "Earth Dragon". The earthworms have also been included by the "Shen Nong's Herbal Classic" as one of the collection of 67 animal-based remedies. It can be used for the treatment of urinary obstruction [1], fever, irritability, amenorrhea, convulsions, cough, asthma, physical disability, high blood pressure, nephritis, calculus formation, congenital epilepsy, pneumonia, arthralgia, rheumatism, jaundice, convulsions in children, and many other diseases.

Introduction to Lumbrokinase

Lumbrokinase is one of the biologically active ingredients in the earthworms. It has the ability to directly digest fibrin and activate the plasminogen, thus indirectly causing a fibrinolytic effect. Since Mihara et al. purified a fraction of proteins from the crude extracts of the earthworms with plasmin activity in 1983, lumbrokinase have subsequently been marketed as a thrombolytic drugs [2] in Korea and China. The Biophysics Centre of Chinese Academy of Sciences have developed the lumbrokinase in the form of a capsule, and have used it as a new generation of oral thrombolytic drug for the treatment of various diseases related to thrombosis in clinical trials.

EXPERIMENTAL METHOD

Materials

Plasminogen (bovine serum) (9IU/bottle)	Chinese National Institutes for Food and Drug Control
Thrombin (840IU/bottle)	Chinese National Institutes for Food and Drug Control
Lumbrokinase (26000U/tube)	Chinese Centre for Pharmaceutical and Biological Product Control
Agarose	BIOWEST
Fibrinogen	YINGBIOTECH
Sodium chloride physiological solution	Shandong Qidu Pharmaceutical Co., Ltd.

Principle behind the Determination of Lumbrokinase Biological Activity

The formation of Lumbrokinase-plasminogen complex [3] can activate the plasminogen into the biologically active plasmin, which can degrade the fibrin into water-soluble fibrin protein fragments. The formation of thrombolytic zone on top of the fibrin plate can be used as a quantitative measure of biological activity for the lumbrokinase.

Preliminary Establishment of Biological Activity Determination

A total of 125 mg of agarose was precisely weighed, and dissolved in 23 ml of sodium chloride physiological solution, this is followed by boiling of the solution to fully dissolve the agarose. The solution was incubate at 55-60oC by keeping the tube balanced in a water bath. 14 µl of 100IU/ml thrombin solution, 280 µl of 3IU/ml plasminogen, and 2.2 ml of 6 mg/ml fibrinogen was added to the

* To whom all correspondence should be sent:
E-mail quxiaobo0504@hotmail.com

molten agarose, with constant agitation to obtain a homogenised mixture. The molten agarose was immediately poured into an 8-cm diameter petri dish. The petri dish was left on a horizontal surface until fully solidified, stored at 4°C for at least 30 minutes (should be used within two days). In the petri dish containing the fibrin, 2-mm diameter wells were punched out, and 10 µl of the test solution and the standard solution was added to each well. A total of two wells were prepared for each dilution. The petri plates were incubated for 24 hours at 37°C in an incubator. The longitudinal and horizontal diameters of the thrombolytic zone were measured to obtain a mean value. The diameters of the thrombolytic zones were plotted against the concentration of the serially diluted standard solution to form a linear regression curve demonstrating their biological activity [4]. By using the linear regression equations, the biological activity of the test sample can be determined based on the average zone diameters.

Validation of the Lumbrokinase Biological Activity Detection Method

Preparation of the Fibrin Plates

1. Exploration of optimum preparation of fibrinogen solution.

A total of 66mg of fibrinogen and 11ml of sodium chloride physiological solution were incubated at 37°C in a water bath for 15 minutes. The sodium chloride physiological solution was then added to the fibrinogen. To fully dissolve the fibrinogen, the solution was incubated at 37°C in a water bath for a further 30 minutes before use. The condition of the solution was observed and recorded.

After the fibrinogen solution preparation was complete, the solution was removed from water bath and placed on the bench with the room temperature set to about 12°C for the preparation of fibrin plate. The condition of the solution was observed and recorded [5].

2. Configuration of the Timing and Handling of Agarose Swelling.

A total of 125 mg of agarose was added to the 23 ml of sodium chloride physiological solution and boiled. After boiling, the duration of time required for the agarose solution to clear and become fully dissolved was observed and recorded. The agarose solution was then incubated at 55-60°C in a water bath. The condition of the agarose solution was observed and recorded to determine if the volume of the solution is affected by the boiling process.

3. Optimisation of the Amount of Thrombin required.

Three fibrin plates were prepared according to the preliminary method established for the detection of biological activity. The amounts of thrombin added to each plate were 14 µl, 28 µl and 30 µl respectively, while other variables remained unchanged. The plates were incubated at 37°C for 24 hours in an incubator, and the turbidity of the fibrin was observed to determine the optimum amount of thrombin that need to be used.

4. Optimisation of the Amount of Fibrinogen required.

Three fibrin plates was prepared according to the preliminary method established earlier in the study, the amount of fibrinogen added to each plate were 2.2 ml, 4.4 ml and 6.6 ml respectively, while other variables remain unchanged. The plates were incubated at 37°C for 24 hours in an incubator, and the turbidity of the fibrin was observed to determine the optimum amount of fibrinogen that need to be used.

5. Optimisation of the Plasminogen Quantity required.

Three fibrin plates was prepared according to the preliminary method established earlier in the study, the amount of plasminogen added to each plate were 280 µl, 500 µl and 560 µl respectively, while other variables were kept constant, the plates were incubated at 37°C for 24 hours in an incubator, and the turbidity of the fibrin was observed to determine the optimum amount of plasminogen that need to be used.

6. Plating Method (e.g., prevention of the formation of bubbles).

A total of 125 mg of agarose was added to 23 ml of sodium chloride physiological solution and boiled. After boiling, the agarose solution was incubated at 55-60°C in a water bath. The molten agarose was subsequently added with 14 µl of 100IU/ml thrombin solution, 280 µl of 3IU/ml plasminogen, and 2.2 ml of 6 mg/ml fibrinogen with constant agitation. The homogenised agarose solution was immediately poured into the 8-cm diameter of petri dish. The method of how the solution should be poured and the timing of pouring were optimised.

7. Establishment of Detection Method for the Lumbrokinase Biological Activity.

A total of 125 mg of agarose was dissolved in 23 ml of sodium chloride physiological solution, and the solution was boiled to fully dissolve the agarose. It is then incubated at 55-60°C in a water bath. The molten agarose was subsequently added with 42 µl of 100IU/ml thrombin solution, 500 µl of

3IU/ml plasminogen, and 6.6 ml of 6 mg/ml fibrinogen with constant agitation. The homogenised mixture of molten agarose was immediately poured into the 8-cm diameter petri dish. The petri dish was left on a horizontal surface until the solution has fully solidified; followed by incubation at 40°C for 30 minutes.

Validation of Method

1. Correlation Study – Plot Standard Curve from the Standard Solutions

The serially diluted standard solutions: 4000IU/ml, 3000IU/ml, 2000IU/ml, 1000IU/ml and 500IU/ml were added at 10µl per well to the 2-mm diameter wells in the fibrin plate. The plates were incubated at 37°C for 24 hours in an incubator. The vertical and horizontal diameters of the thrombolytic zones were measured [6] to obtain the mean value. The biological activity of the standard solution at various concentrations was plotted against the diameters of the fibrinolytic zones using linear regression to obtain the corresponding linear regression equation.

The procedure of the above-described method was repeated three times to obtain the mean value.

2. Reproducibility and Intermediate Precision Study.

Two technicians were assigned to determine the titre of the given lumbrokinase sample according to the titration method using the test solution (4000IU/ml of lumbrokinase), the test was repeated 6 times by each technician and the results were recorded [7]. The six data sets were compared and the average values were calculated; followed by the calculation of the RSD (relative standard deviation) value of reproducibility. The test results of the two technicians were compared to obtain the mean value from the 12 sets of data, followed by the calculation of RSD values of the intermediate precision.

CONCLUSION

Optimisation of Fibrin Plate Preparation

1. Result of Fibrinogen Solution Preparation.

After the fibrinogen solution preparation was completed [8], the solution was removed from the water bath and placed on the bench with the room temperature set to about 12 °C. Flocculent precipitant was observed in the fibrinogen solution, and resulting fibrin plate was also cloudy and non-homogeneous, with some precipitation. After analysis, the reason for the fibrinogen precipitation observed was a decrease in the solubility of fibrinogen caused by a drop in temperature.

Therefore, the fibrinogen should be maintained at 37°C prior to the mixing of solutions to produce a homogeneous fibrin plate.



Fig. 1. Precipitation of fibrinogen.



Fig. 2. Uneven cloudy plate.

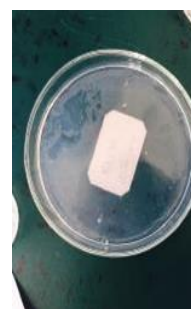


Fig. 3. Homogeneous cloudy plate.

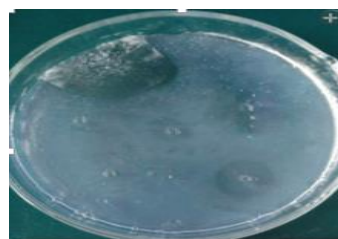


Fig. 4. Molten agarose failed to fully cover the plate due to reduced volume.

2. Result for Timing and Handling of Agarose Swelling Configuration.

A total of 125 mg of agarose was dissolved in 23 ml of sodium chloride physiological solution prior to being boiled. Our observation found that the agarose solution was clear when boiled for 10 minutes [9]. The molten agarose was cooled down to a homogenised temperature by incubating at 55-60°C in a water bath. Our observations suggest that

the volume of the solution was reduced after the boiling process, which might have been caused by the evaporation of water from the solution during the process of boiling. Therefore, we sealed the flask with cling film to reduce the evaporation of water and maintain the volume of solution.

3. Result for Optimisation of the Amount of Thrombin required.

The amount of thrombin best added to the fibrin plate was 28 μ l based on the turbidity of fibrin plate from the optimization process.

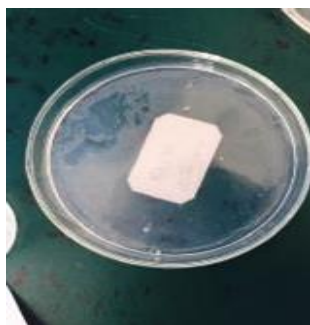


Fig. 5. 28 μ l of thrombin.

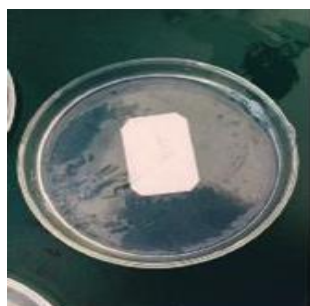


Fig. 6. 14 μ l of thrombin.



Fig. 7. 4.4ml of fibrinogen.

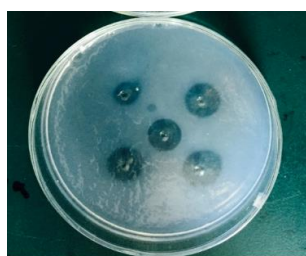


Fig. 8. 6.6ml of fibrinogen.

4. Result for Optimisation of the Amount of Fibrinogen required.

The amount of fibrinogen best added was 6.6ml based on the turbidity of fibrin plate from the optimization process.

5. Result for Optimisation of the Quantity of Plasminogen required.

The amount of Plasminogen [10] best added was 500 μ l based on the turbidity of the fibrin plate, as well as the budgetary consideration on efficient usage of Plasminogen.



Fig. 9. 280 μ l of plasminogen.



Fig. 10. 500 μ l of plasminogen.

6. Result of the Plating Method (e.g., how to prevent formation of bubbles).

The solution should be adherently poured into the plate, accompanied with shaking to ensure the full coverage of the agarose solution. Adherent pouring can reduce the formation of bubbles, and the timing of the pouring should be fast to prevent the agarose from solidifying before being poured to the plates.

7. Result of Standard Curve from the Standard Solutions.

The equation of linear regression for the biological activity of lumbrokinase was obtained by plotting the diameter of the resolving zone against

the concentration of the serially diluted standard solution [11].

8. Result for the Reproducibility and Intermediate Precision of experiment.

Records of experimental implementation and conclusion (Table 3)

Conclusion: The RSD values of the reproducibility and intermediate precision were less than 2%. Hence, the experiment was valid.



Fig. 11. 560µl of plasminogen.

Table 1. Result for Optimisation of Fibrin Plate Preparation.

Optimised Variables	Results
Fibrinogen solution	Pre-mixed solution of fibrinogen should be maintained at 37°C
Timing and handling of agarose swelling	Swelling time of 10min, seal the container with cling film
Amount of thrombin	28 µl of thrombin
Amount of fibrinogen	28 µl of thrombin
Amount of plasminogen	6.6 ml of fibrinogen
Plate (e.g., prevent formation of bubbles)	The solution should be poured adherently with shaking

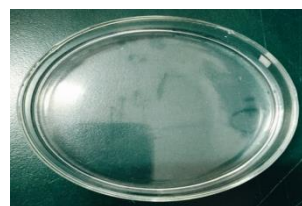


Fig. 12. No bubble formation on the fibrin plate

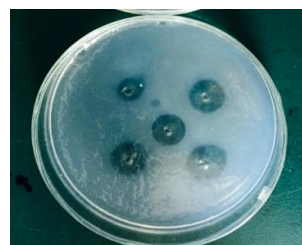


Fig. 13. Determination of lumbrokinase biological activity by measuring thrombolytic zones.

Table 3. Result for the reproducibility and intermediate precision of experiment.

Replicate	Test result 1	Test result 2
1	1.78	1.76
2	1.75	1.75
3	1.77	1.75
4	1.73	1.73
5	1.72	1.76
6	1.76	1.73
Mean value (u)	1.7517	1.7467
RSD value of repeatability (%)	1.3225	0.7822
Overall mean value (u)		1.7492
RSD value of intermediate precision (%)		1.0473

Table 2. Data sheet for the standard curve of lumbrokinase biological activity

Replicate	4000 IU/ml	3000 IU/ml	2000 IU/ml	1000 IU/ml	500 IU/ml
1	1.73 cm	1.51 cm	1.30 cm	1.01 cm	0.78 cm
2	1.73 cm	1.51 cm	1.31 cm	0.98 cm	0.80 cm
3	1.76 cm	1.49 cm	1.29 cm	1.01 cm	0.82 cm
Average value	1.74 cm	1.50 cm	1.30 cm	1.00 cm	0.80 cm

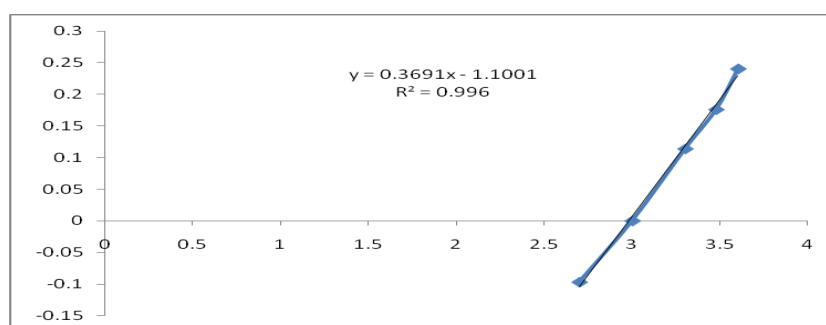


Fig. 14. Standard curve of the lumbrokinase biological activity.

DISCUSSION

1. Due to the limitation of resources in our laboratory and a lack of appropriate well puncher, needle and syringe was used in place of the appropriate well puncher [12]. Thus, extra care had to be taken using the appropriate technique during well punching to ensure removal of excessive gel using the syringe needle and prevent damage to the well.

2. The fibrin plates must be re-stored at -20°C immediately after sample loading [13] to prevent subsequent experiment being affected due to the change in temperature.

3. The fibrin plate must be incubated for 24 hours to avoid results being affected by different duration of incubation [14].

4. The diameter of the thrombolytic zone must be measured immediately after incubation [15] to prevent the results being affected by the change in temperature.

REFERENCES

1. S.P. Teotia, F.L. Duley, T.M. McCalla, *Neb. Agric. Exp. Sta. Res. Bull.*, **165**(1), 20 (1950).
2. C.L. Huang, X.P. Zhang, *J. Ecol.*, **24**(12), 1466 (2005).
3. C.S. Teng, B.C. Zhang, Z.H. Sun, *A.H. Agri. Sci.*, **33**(5), 906 (2005).
4. J.N. Zhang, B. Hu, S.Y. Li, *Feed Chi.*, **17**, 45 (2008).
5. F.C. Xu, X.Y. G, *Sou. Chi. Agri. Uni.: Nat. Sci. Ed.*, **22**(3), 86(2001).
6. X.L. Zhen, B.Y. Zhang, X.X. Mai, A.X. Li, Z.X. Zhang, *J. S.X. Med. Col.*, **26**(2), 81 (1995).
7. S.Z. Zhang, Q. Tian, Y.R. Li, F.K. Zhang, *J. 4th Mili. Med. Uni.*, **14**(5), 350 (1993).
8. S. Tsunoda, *Antican. Res.*, **17**(5A), 33 (1997).
9. H. Mihara, H.A. Sumi, *Jpn Physiol*, **41**(3), 461 (1991).
10. Y.C. Zhou, H. Zhu, R.R. Chen, Q. Hao, *J. Biochemi. Biophys.*, **22**(5), 469 (1990).
11. G.B. Song, Q.Y. Li, W.H. Xia, *Ani. Sin.*, **42**(2), 146 (1996).
12. N.L. Cheng, B. Niu, G.P. Zheng, F. Cheng, *Chi. J. Integr. Med.*, **S1**, 86 (1995).
13. Y. Gao, H. Zhang, J. Zhang, Y. Zuo, *Tradi. Chi. Med. Pat. Prescri.*, **31**(1), 18 (2009).
14. N.W. Yu, J. Liu, J.F. Wu, W. Wen, *Chi. Med.*, **4**(3), 169 (2009).
15. T. Astrup, S. Muhertz, *Arch Biochem Biophys*, **40**, 346 (1992).

Application of fuzzy comprehensive evaluation method in water quality evaluation

Y. Luo^{1,2}, Z.J. Yang^{1,2*}, Y. Dong³

¹College of Mechanical Engineering, Taiyuan University of Technology, Taiyuan, 030024, China

²Coal Mine Fully Mechanized Equipment Key Laboratory of Shanxi Province, Taiyuan, 030024, China

³School of Construction Engineering, Yulin University Yulin, Shanxi 719000

Received December 12, 2015; Revised February 26, 2016

Based on the fuzzy transformation principle and principle of maximum degree of membership, the comprehensive evaluation on the monitoring data of Weihe Tongguan drawbridge section in 2015-2016 is conducted by using the fuzzy comprehensive evaluation method. The results show that the water quality pollution levels of this section in 4 seasons of spring, summer, autumn and winter are Class V (seriously polluted), Class I (unpolluted), Class IV (heavily polluted) and Class V (seriously polluted) respectively. Compared with the traditional method of single factor assessment, this method can reflect the water quality more comprehensively and reasonably.

Keywords: fuzzy mathematics; comprehensive evaluation method; Weihe River; water quality evaluation

INTRODUCTION

The comprehensive evaluation of water quality is the basic work of water pollution control [1-3], it is an important reference for governance decision-making [4], therefore, it is important to select a suitable evaluation method [5-7]. The severity of water pollution is fuzzy concept [8,9], and the water quality assessment according to water quality standards is a typical fuzzy pattern recognition problem [10-13]. For fuzzy comprehensive evaluation, the selection of evaluation factor set, the establish of evaluation set and the calculation of weight depend on the characteristics of the statistical data [14-16]. The choice of the combination operator of fuzzy transformation and the principle of judgment are closely related to the error of the fuzzy evaluation model [17,18], around the contents, a lot of literatures have carried on the research [19-23]. The comprehensive evaluations of the Weihe River water quality are carried on in the article, the detailed process of establishing factor set, evaluation [24-27] set, weight, compound operation operator and judgment principle [28-32] is given, make use of the data of the Weihe river water quality in the Tongguan hanging bridge section during 2015-2016, the fuzzy comprehensive [33-35] evaluation of the water pollution in the four seasons of the year is carried out, the results provide a basis for the Weihe River water pollution control and governance [36]. This evaluation method has the universal

significance to the environment pollution statistical data analysis.

EXPERIMENT PART

Overview of contaminated area

The Weihe River is 818 kilometers in length, with a drainage area of 13.43 million square kilometers. The Weihe River Tongguan hanging bridge section is the control station of running into the Yellow River. In recent years, a large sum of industrial wastewater and domestic sewage directly or only after a simple treatment into the Weihe River, excessive discharge of sewage and unreasonable discharge of water cause great damage to the ecological environment. At present, the Weihe River water pollution is serious, and basically lost the ecological function. Therefore, it is of great practical value to make a correct evaluation of the present situation of Weihe River water quality.

Water quality monitoring data

The content of pH, DO, COD_{Mn} and NH₃-N in the Weihe river Tongguan hanging bridge section from March 2015 to February 2016 were collected, The data were averaged over every seasons of the year (the first quarter : 3-5 months; the second quarter: 6-8 months; third quarter: 9-11 months; fourth quarter: 12-February the following year), shown in Table 1.

* To whom all correspondence should be sent:

E-mail: yangzhaojian@tyut.edu.cn

Table 1. Water quality monitoring data

Time	pH	DO/ ($\text{mg} \cdot \text{L}^{-1}$)	COD _{Mn} / ($\text{mg} \cdot \text{L}^{-1}$)	NH ₃ - N/ ($\text{mg} \cdot \text{L}^{-1}$)
First quarter	8.07	4.64	8.32	2.04
Second quarter	8.02	4.78	7.95	0.80
Third quarter	7.87	5.01	7.56	0.96
Fourth quarter	7.78	5.60	7.21	1.37

Table 2. The changing data of BOD₅ and DO.

Time /d	-2	-1	0	1	2	3	4	5	6	7	8	9
DO	7.8	7.7	7.8	4.2	3.6	3.5	4.2	5.5	7.1	8.2	8.0	7.9
BOD ₅	3.8	3.9	19.5	16.0	12.5	9.8	6.1	4.9	4.2	3.9	3.9	3.8

Table 3. The commonly used fuzzy synthesizing operators

Detail	Operator			
	$M(\wedge, V)$	$M(\cdot, V)$	$M(\wedge, \oplus)$	$M(\wedge, V)$
Reflects weight	Not obvious	Obvious	Not obvious	Obvious
Integrated degree	Weak	Weak	Strong	Strong
R information utilization	Insufficiency	Insufficiency	More sufficiency	sufficiency
Type	Dominant- factor	Dominant- factor	Weighted average	Weighted average

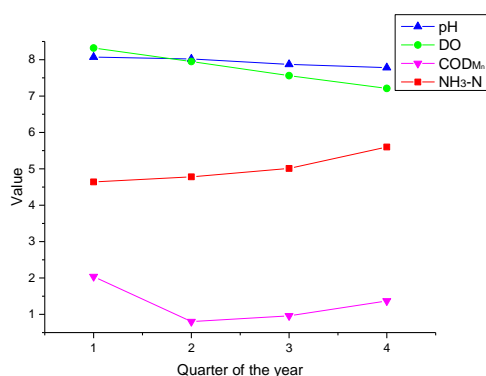


Fig. 1. he changing curve of Water quality monitoring data.

A contaminant zone real-time tracking data

The Table 2 data shows the tracking observations of organic contaminants in a contaminated zone in September 2015. According to Table 2, Fig. 2 is drawn, from the curves, the changes of BOD₅ and DO are observed during biodegradation.

As can be seen from Fig.2, the BOD₅ of the uncontaminated water bodies fluctuates between 3.5 and 4 $\text{mg} \cdot \text{L}^{-1}$, the dissolved oxygen(DO) varies from 7.5 to 8 $\text{mg} \cdot \text{L}^{-1}$. the DO of contaminated water bodies has a large decline in the initial 1~2

days, the content of DO in 2 ~ 6 days is relatively gentle , and the DO content is low, the content of DO in 6 ~ 8 days is relatively gentle increase slowly with a less increment; The biochemical demanded oxygen BOD₅ of polluted water increase rapidly in the initial 1~2 days, the peak value of BOD₅ reaches 19.5 $\text{mg} \cdot \text{L}^{-1}$, and then decreases with a larger amplitude, after about 4 to 5 days, the amplitude is small, and gradually approach the same biochemical demanded oxygen BOD₅ of clean water.

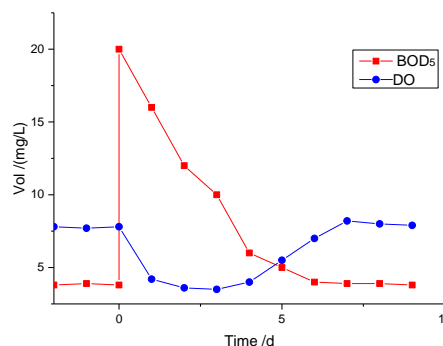


Fig. 2. The variation of BOD₅ and DO with time.

RESULTS AND DISCUSSION

Data processing algorithm

The fuzzy comprehensive evaluation method is adopted in the monitoring data processing. Based on the establishment of evaluation factors, factor rating criteria and weight value, the membership function of each factor to the corresponding water quality level was established, And then put the measured values into the corresponding membership function, after fuzzy transformation and integrated operations, get the comprehensive membership degree, and finally determine the water quality level. Generally need the following steps:

- Set the factor set, $U = \{U_1, U_2, \dots, U_3\}$, U represents the set of evaluation factors;
- Establish evaluation set, $V = \{V_1, V_2, \dots, V_3\}$, V Represents the set of corresponding rating criteria;
- Make sure membership function. The semi - trapezoid distribution in fuzzy mathematics is used to determine membership function. The indexes which smaller value is better, use Equation 1 for processing; The indexes which large value are better, use Equation 2 for processing.

$$u(x) = \begin{cases} 0 & x \geq a_2 \\ \frac{a_2-x}{a_2-a_1} & a_1 < x < a_2 \\ 1 & x \leq a_1 \end{cases} \quad (1)$$

$$u(x) = \begin{cases} 1 & x \geq a_1 \\ \frac{x-a_2}{a_1-a_2} & a_2 < x < a_1 \\ 0 & x \leq a_2 \end{cases} \quad (2)$$

- Establish the fuzzy relation matrix

Put the measured value into the determined membership function, calculate the membership degree of the i factor to the j -th level, get the fuzzy relation matrix R :

$$R = \begin{bmatrix} r_{11} & r_{12} & \dots & r_{1j} \\ r_{21} & r_{22} & \dots & r_{2j} \\ \vdots & \vdots & \ddots & \vdots \\ r_{i1} & r_{i2} & \dots & r_{ij} \end{bmatrix} \quad (3)$$

- Calculate the weight vector of the evaluation factors.

Because the evaluation factors have different effects on water quality, they should be given a different weight. The factors which smaller value are better, use Equation 4 for calculating the corresponding weight; The factors which large value are better, use Equation 5 for obtaining the weight; the weight factor calculation of the value of Ph adopts the Equation 6.

$$P_i = \frac{C_i}{S_2} \quad (4)$$

$$P_i = \frac{S_1}{C_i} \quad (5)$$

$$P_i = \frac{C_i-6}{9-6} \quad (6)$$

Where, C_i is the measured concentration of the i evaluation factor; S_1 is the minimum value of the multi-level concentration standard value of the i evaluation factor; S_2 is the maximum value of the multi-level concentration standard value of the i evaluation factor.

In order to facilitate the operation, normalize the weight value P_i of each evaluation factor, obtain the weighting set $W = \{W_1, W_2, \dots, W_i\}$.

- Factor set judgment

The fuzzy synthesizing operators which are commonly used in environmental chemistry are as follows:

$$\textcircled{1} M(\wedge, \vee) \quad (7)$$

$$b_j = \bigvee_{i=1}^m (a_i \wedge r_{ij}) = \max_{1 \leq i \leq m} \{ \min(a_i, r_{ij}) \}, j = 1, 2, \dots, n$$

$$\textcircled{2} M(\bullet, \vee)$$

$$b_j = \bigvee_{i=1}^m (a_i, r_{ij}) = \max_{1 \leq i \leq m} \{ a_i, r_{ij} \}, j = 1, 2, \dots, n \quad (8)$$

$$\textcircled{3} M(\wedge, \oplus)$$

$$b_j = \min \left\{ 1, \sum_{i=1}^m \min(a_i, r_{ij}) \right\}, j = 1, 2, \dots, n \quad (9)$$

$$\textcircled{4} M(\bullet, \oplus)$$

$$b_j = \min \left(1, \sum_{i=1}^m a_i r_{ij} \right), j = 1, 2, \dots, n \quad (10)$$

The features of the commonly used fuzzy synthesizing operators are summarized as shown in Table 3:

The weighting set W is compound operation with the fuzzy evaluation matrix R :

$$B = W \cdot R = \{W_1, W_2, \dots, W_i\} \cdot$$

$$\begin{bmatrix} r_{11} & r_{12} & \dots & r_{1j} \\ r_{21} & r_{22} & \dots & r_{2j} \\ \vdots & \vdots & \ddots & \vdots \\ r_{i1} & r_{i2} & \dots & r_{ij} \end{bmatrix} \quad (11)$$

- Processing method of fuzzy comprehensive evaluation vector $B = (b_1, b_2, \dots, b_n)$

The processing of fuzzy comprehensive evaluation vector $B = (b_1, b_2, \dots, b_n)$ often uses the following two methods in environmental chemistry:

1. The principle of maximum membership
If the fuzzy comprehensive evaluation result vector meet the Equation 12):

$$\exists b_r = \max_{1 \leq j \leq n} (b_j) \quad (12)$$

The evaluated object belongs to the r -th class as a

whole.

2. Weighted average principle

Think a level as a relative position, make it continuous. In order to be able to quantitative processing, use "1,2,3, ..., m" to express the level, calling them as the rank, then the rank of each level is summed with the corresponding component in B, so as to obtain the relative position of the object to be evaluated, which is expressed as follows:

$$A = \frac{\sum_{j=1}^n b_j^k \cdot j}{\sum_{j=1}^n b_j^k} \tag{13}$$

Where, k is the undetermined coefficient (k = 1 or 2), the purpose is to control the role of the larger b_j. When k → ∞, the weighted average principle is the principle of maximum membership.

Fuzzy comprehensive evaluation of monitoring data

- Set up the factor set and evaluation set

The values of pH, dissolved oxygen (DO), permanganate index (COD_{Mn}) and ammonia nitrogen (NH₃ - N) in Table 1 were selected as the evaluation factors, establish the factor set U = {pH, DO, COD_{Mn}, NH₃ - N} ; Select the "Surface Water Environmental Quality Standard" (GB 3838-2002) as the evaluation criteria, in the standard of GB 3838-2002, the water quality was divided into five grades: 1-uncontaminated, 2-light pollution, 3-medium pollution, 4-heavy pollution, 5-severe contamination, as is shown at the Table 4.

Table 4. The evaluation factors and evaluation criteria.

evaluation factors	1	2	3	4	5
The value of pH	6~9	6~9	6~9	6~9	6~9
DO/ (mg · L ⁻¹)	7.5	6	5	3	2
COD _{Mn} / (mg · L ⁻¹)	2	4	6	10	12
NH ₃ - N/ (mg · L ⁻¹)	0.15	0.5	1.0	1.5	2.0

- Make sure the Membership function and the fuzzy relation matrix

According to the Table 2, the membership function of each level is determined by the "semi - trapezoidal formula". For the smaller values of the COD_{Mn} and the NH₃ - N denote the better the water quality, the membership function should be selected partial small semi-trapezoidal function, as is shown

from Equation 14.

$$u(x) \begin{cases} u_i(x) = \begin{cases} 0 & x \geq a_2 \\ \frac{a_2-x}{a_2-a_1} & a_1 < x < a_2 \\ 1 & x \leq a_1 \end{cases}, i = 1 \\ u_i(x) = \begin{cases} 0 & x \geq a_{i+1}, x \leq a_{i-1} \\ \frac{x-a_{i-1}}{a_i-a_{i-1}} & a_{i-1} < x < a_i \\ \frac{a_{i+1}-x}{a_{i+1}-a_i} & a_i \leq x \leq a_{i+1} \end{cases}, i = 2 \sim n - 1 \\ u_i(x) = \begin{cases} 1 & x \geq a_n \\ \frac{x-a_{n-1}}{a_n-a_{n-1}} & a_{n-1} < x < a_n \\ 0 & x \leq a_{n-1} \end{cases}, i = n \end{cases} \tag{14}$$

For the larger values of the DO denote the better the water quality, the membership function should be selected partial larger semi-trapezoidal function, as is shown from Equation 15.

$$u(x) \begin{cases} u_i(x) = \begin{cases} 0 & x \leq a_{i+1}, x \geq a_{i-1} \\ \frac{x-a_{i+1}}{a_i-a_{i+1}} & a_{i+1} < x < a_i \\ \frac{a_{i-1}-x}{a_{i-1}-a_i} & a_i \leq x \leq a_{i-1} \end{cases}, i = 2 \sim n - 1 \\ u_i(x) = \begin{cases} 0 & x \geq a_{n-1} \\ \frac{x-a_n}{a_{n-1}-a_n} & a_n < x < a_{n-1} \\ 1 & x \leq a_n \end{cases}, i = n \end{cases} \tag{15}$$

Where, x is the measured concentration of an evaluation factor; a_i is the i-level water quality standards.

Put the measured value into the corresponding membership function, get the fuzzy relation matrix of four quarters of the year:

$$R_1 = \begin{bmatrix} 1 & 0 & 0 & 0 & 0 \\ 0 & 0 & 0.82 & 0.18 & 0 \\ 0 & 0 & 0.42 & 0.58 & 0 \\ 0 & 0 & 0 & 0 & 1 \end{bmatrix} \tag{16}$$

$$R_1 = \begin{bmatrix} 1 & 0 & 0 & 0 & 0 \\ 0 & 0 & 0.89 & 0.11 & 0 \\ 0 & 0 & 0.51 & 0.49 & 0 \\ 0 & 0.40 & 0.60 & 0 & 0 \end{bmatrix} \tag{17}$$

$$R_1 = \begin{bmatrix} 1 & 0 & 0 & 0 & 0 \\ 0 & 0.01 & 0.99 & 0 & 0 \\ 0 & 0 & 0.61 & 0.39 & 0 \\ 0 & 0.08 & 0.92 & 0 & 0 \end{bmatrix} \tag{18}$$

$$R_1 = \begin{bmatrix} 1 & 0 & 0 & 0 & 0 \\ 0 & 0.60 & 0.40 & 0 & 0 \\ 0 & 0 & 0.70 & 0.30 & 0 \\ 0 & 0 & 0.26 & 0.74 & 0 \end{bmatrix} \tag{19}$$

- Calculate the weight vector of the evaluation factors

The weight vector calculation of the evaluation of COD_{Mn} and NH₃-N use the equation 4, the weight vector calculation of the evaluation of DO use the equation 5, the weight vector calculation of the evaluation of pH use the equation 5, Normalize the weight calculation, the calculation results in Table 5.

- Water pollution comprehensive evaluation results

Through fuzzy comprehensive operation, according to the principle of maximum membership, it can be determined water qualities of the Weihe River Tongguan hanging bridge section of the four quarter from March 2015 to February 2016. The results are shown in Table 6.

Table 5. The normalized results of the weights.

evaluation factors	First quarter		Second quarter		Third quarter		Fourth quarter	
	P ₁	W ₁	P ₂	W ₂	P ₃	W ₃	P ₄	W ₄
pH	0.6900	0.2559	0.6733	0.3330	0.6233	0.3106	0.5933	0.2804
DO/ (mg · L ⁻¹)	0.4310	0.1599	0.4184	0.2070	0.3992	0.1990	0.3571	0.1687
COD _{Mn} / (mg · L ⁻¹)	0.5547	0.2058	0.5300	0.2622	0.5040	0.2512	0.4807	0.2274
NH ₃ - N/ (mg · L ⁻¹)	1.0200	0.3784	0.4000	0.1978	0.4800	0.2392	0.6850	0.3237
$\sum P_i$	2.6957	1.0000	2.0217	1.0000	2.0065	1.0000	2.1161	1.0000

Table 6. The comprehensive evaluation of Weihe River water quality

Time	I	II	III	IV	V	Fuzzy	Single factor
						Evaluation	evaluation
First quarter	0.2559	0.0000	0.2058	0.2058	0.3784	V	V
Second quarter	0.3330	0.1978	0.2622	0.2622	0.0000	I	IV
Third quarter	0.3106	0.0800	0.2512	0.2512	0.0000	I	IV
Fourthquarter	0.2804	0.1687	0.2600	0.3237	0.0000	IV	IV

CONCLUSIONS

Based on the data of the the Weihe river water quality during 2015-2016, use the fuzzy comprehensive evaluation in the purpose of making an assessment on the water quality in the Weihe River Tongguan hanging bridge section, The evaluation results shows the following contents:

- During 2015-2016, in the Tongguan hanging bridge section, the water quality grades of the four quarters are as follows: in the first quarter, the water pollution is V, it is severe contamination; in the second quarter and the third quarter, the water pollution is I, it is un-pollution; in the fourth quarter, the water pollution is IV, it is heavy pollution, compared with the same period during 2014-2015, the water quality has been significantly improved, But in the first and the fourth quarters , the pollution situation is still more serious, Caused a significant impact on the water quality safety.

- As can be seen from the results of the weight calculation, in the Tongguan hanging bridge section, The main pollutants in the first quarter were NH₃ - N and COD_{Mn}; The main pollutants in the second quarter were COD_{Mn} and DO; The main pollutants in the third quarter were COD_{Mn} and NH₃ - N; The

main pollutants in the fourth quarter were NH₃ - N and COD_{Mn}, the different distribution information of major pollutants at different quarters Contribute to the upstream pollution control of major sources of pollution and downstream water purification.

- The analysis of the experimental results verify that Fuzzy comprehensive evaluation method can be used for water quality evaluation which is more reasonable than traditional one-factor evaluation. In terms of the algorithm, the improvement of weight operator and compound operator can help to reduce the error of the evaluation model.

Acknowledgements: This study was financially supported by the Shanxi major science and technology projects (grant no. 20111101040), the Youth science and technology research foundation of Shanxi Province (grant no. 201601 D021084).

REFERENCES

1. K.O. Adebowale, F.O. Agunbiade, B.I. Olu-Owolabi *Chem Ecol*, **24**(4), 269 (2008).
2. V. Adriaenssens, B. De Baets, P.L.M. Goethals, N. De Pauw, *Sci Total Environ*, **319**, 1 (2004).
3. F.O. Agunbiade, A.T. Fawale, *Int J Environ Sci Technol*, **6**(2), 267 (2009).

4. F.O. Agunbiade, A.A. Awe, K.O. Adebowale, *Toxicol Environ Chem*, **93**(10), 1856 (2011).
5. F.O. Agunbiade, B.I. Olu-Owolabi, K.O. Adebowale, *Environ Monit Assess*, **184**(1), 89 (2012).
6. O.A. Akintola, A.Y. Sangodoyin, F.O. Agunbiade, *Water Pract Technol*, **8**(2), 244 (2013).
7. O. Akoto, G. Darko, M.A. Nkansah, *Int J Environ Res*, **5**(4), 847 (2011).
8. P. Mitchell, Guidelines for quality assurance and quality control in surface water quality programs in Alberta, W0603, Alberta Environment, 2006, p.67.
9. B. Alo, B. Orgu, A. Abayomi, *Eur J Sci Res*, **40**(2), 279 (2010).
10. APHA, Standard methods for the examination of water and wastewater, 19th edn. APHA, Washington, DC, 1995.
11. T.Y. Fu, Z.H. Zou, X.J. Wang, *Acta Scientiae Circumstantiae*, **34**(2), 473 (2014).
12. P.G.C. Campbell, In: Metal speciation and bioavailability in aquatic systems, A Tessier, D.R. Turner (eds), Wiley, New York, 1996, p. 45.
13. N.B. Chang, H.W. Chen, S.K. Ning, *J Environ Manag*, **63**, 293 (2001).
14. J. Ellith, M.A. Burgman, H. Regan, *Ecol Model*, **157**, 313 (2002).
15. M. Enea, G. Salemi, *Ecol Model*, **135**, 131 (2001).
16. J.N. Houser, W.B. Richardson, *Hydrobiologia*, **640**, 71 (2010).
17. J.G. Jabbra, N.W. Jabbra (eds) Challenging environmental issues: middle eastern perspectives, Brill, Leiden, 1997, p 101.
18. P.E. John-De-Zuane, Handbook of drinking water quality: standards and control, Wiley, New York, 1990.
19. K.S. Low, G.K. Lee, S.C. Liew, *Process Biochem*, **36**, 59 (2000).
20. R.S. Lu, S.L. Lo, *Water Res*, **36**, 2265 (2002).
21. T.E. McKone, A.W. Deshpande, *Environ Sci Tech*, **39**, 42A (2005).
22. W. Ocampo-Duque, N. Ferre´-Huguet, J.L. Domingo, M. Schuhmacher, *Environ Int*, **32**, 733 (2006).
23. G. Onkal-Engin, I. Demir, H. Hiz, *Atmos Environ*, **38**, 3809 (2004).
24. A. Plazinska, In: Microbiological quality of rainwater in selected Indigenous communities in central Australia. Rainwater: quality issuesq (Proc. 10th international rainwater catchment systems conference Germany, 2001), 2001, p. 129.
25. K. Sadegh-Zadeh, *Artif Intell Med*, **21**, 1 (2001).
26. E. Sazakli, A. Alexopoulos, M. Leotsinidis, *Water Res*, **41**(9), 2039 (2007).
27. G. Shen, Y. Lu, M. Wang, Y. Sun, *J Environ Manag*, **76**, 355 (2005).
28. W. Silvert, *Ecol Model*, **130**, 111 (2000).
29. T. Thomas, *Waterlines*, **18**(3), 7 (2000).
30. USEPA, Water quality standards handbook, 2nd edn. EPA-823-B-93-002 and EPA-823-B-94-006. Office of Water, Washington, DC, USA, 1993.
31. L.P. Yang, K. Mei, X.M. Liu, *Environmental Science and Pollution Research*, **20**, 5341 (2013).
32. World Health Organization, Guidelines for drinking water quality, 3rd edn, vol 1., RecommendationsWorld Health Organization, Geneva, 2004.
33. S. Yadav, P. Kumar, *Air Qual Atmos Health*, **7**(4), 559 (2014).
34. L.A. Zadeh, *Inform Control*, **8**, 338 (1965).
35. X. Ban, Q.Z. Wu, B.Z. Pan, *Environmental Monitoring and Assessment*, **186**, 4237 (2014).
36. H.M. Bu, X. Tan, S.Y. Li, *Environmental Earth Sciences*, **60**, 1631 (2010).

Low carbon logistics distribution route optimization research based on improved ant colony algorithm

T. Fei, L. Zhang*

Information Engineering College, Tianjin University of Commerce, Tianjin 300134, China

Received February 25, 2016; Revised November 12, 2016

Because of global warming, the fog weather and other pollution problems, and the increasing deterioration of environment and energy, the low carbon issues become more and more popular in the whole world. Since most carbon pollutions are produced by logistics industry, low carbon is the inevitable trend for logistics industry. In this paper, starting from the actual requirements of low carbon logistics, microscopic quantitative analysis was used for low carbon logistics. The minimum cost of carbon emissions model with considering the cost of carbon emissions were established to find the reasonable distribution routes to achieve energy conservation and emissions reduction based on the solution of chaos ant colony algorithm. According to the simulation of MATLAB, chaos ant colony algorithm had a better effectiveness than the basic ant colony algorithm on the issue of low carbon logistics distribution route optimization.

Keywords: Low carbon logistics, distribution, route optimization, chaos, ant colony algorithm.

AIMS AND BACKGROUND

Because of global warming, the fog weather and other pollution problems, and the increasing deterioration of environment and energy, the low carbon issues become more and more popular in the whole world. Since most carbon pollutions are produced by logistics industry, low carbon is the inevitable trend for logistics industry. The so-called low carbon logistics focuses on the low energy consumption, low pollution and low emissions in logistics process with the utilization of the technologies of energy efficiency, reusable energy and greenhouse gas emissions reduction to reduce the carbon emissions in the logistics, cut down the pollution produced by logistics activities, and improve the efficiency of logistics resources utilization [1]. To achieve low carbon logistics, it should meet two requirements. On one hand, use a variety of low carbon technologies to reduce carbon emissions in the process of transportation. On the other hand, optimize the logistics system by planning reasonable logistics routes, improve logistics efficiency, reduce waste of resources, and make full use of logistics resources [2].

With development of low carbon logistics, more and more scholars become curious about this issue. It mainly includes: the connotation, characteristics and development of low carbon logistics mode and direction of analysis [3-5]; low carbon logistics development are faced with the problem and countermeasure research [6-8]; low carbon logistics system construction of research [9-10]; research of

low carbon logistics distribution network optimization [11]. However, all the above researches are concentrated on the low carbon logistics macro qualitative studies, which lack microscopic quantitative researches.

In this paper, starting from the actual requirements of low carbon logistics, microscopic quantitative analysis was used for low carbon logistics. The minimum cost of carbon emissions model with considering the cost of carbon emissions were established to find the reasonable distribution routes to achieve energy conservation and emissions reduction based on the solution of chaos ant colony algorithm. According to the simulation of MATLAB, chaos ant colony algorithm had a better effectiveness than the basic ant colony algorithm on the issue of low carbon logistics distribution route optimization.

EXPERIMENTAL

DISTRIBUTION OPTIMIZATION MODEL OF MINIMUM COST OF CARBON EMISSIONS

Low carbon logistics is a kind of low energy cost and low pollution logistics whose goal is to achieve the highest efficiency of logistics with the lowest greenhouse gas emissions [12]. Relevant data shows that thermal power emission, vehicle exhaust emissions, and construction are the main sources of carbon dioxide emissions. Bearing the social goods transportation, storage, packaging, processing, distribution, loading, unloading and other services, logistics has become the big one for the carbon emissions. Looking for the reasonable distribution route to reduce carbon emissions is particularly important. The reduction in carbon

* To whom all correspondence should be sent:

E-mail: zhangliyi@tjcu.edu.cn

emissions model reflects the reduction of carbon emissions cost. Therefore, this paper established low carbon logistics distribution route optimization model to achieve the minimizing carbon emissions.

As the vehicles pickup or delivery goods in the different order crossing all customers, the car load changes. With the increase of vehicle load, the unit distance fuel consumption rises, leading to the increase of carbon emissions cost [13]. With the increase of vehicle transport distance, carbon emissions cost will also increase. Thus, the cost of carbon emissions is not only has relationship with transport distance, but also related to the vehicles' load.

The unit distance fuel consumption $\varepsilon(q)$ has a linear relationship with the total weight of the vehicles q_{sum} , which is:

$$\varepsilon(q) = \delta q_{sum} + b = \delta(q + q_0) + b \quad (1)$$

Where, $\varepsilon(q)$ is the unit distance fuel consumption, δ is relationship factor between the unit distance fuel consumption and vehicles' weight, q_{sum} is the total weight of the vehicles including vehicle loading weight q and vehicle's weight q_0 .

When vehicles are full, the unit distance fuel consumption is ε^* , which is:

$$\varepsilon^* = \delta(Q + q_0) + b \quad (2)$$

Where, ε^* is the unit distance fuel consumption when vehicles are full, Q is the vehicles' maximum load.

When vehicles are empty, the unit distance fuel consumption is ε_0 , which is:

$$\varepsilon_0 = \delta q_0 + b \quad (3)$$

From formula (2) and formula (3), we can get:

$$\delta = \frac{\varepsilon^* - \varepsilon_0}{Q} \quad (4)$$

Bring formula (4) into formula (1), the unit distance fuel consumption $\varepsilon(q)$ is as:

$$\begin{aligned} \varepsilon(q) &= \delta q_{sum} + b = \delta(q + q_0) + b = \\ &= \delta q + (\delta q_0 + b) = \frac{\varepsilon^* - \varepsilon_0}{Q} q + \varepsilon_0 \end{aligned} \quad (5)$$

Thus, the carbon emissions cost $CO_2(q_{ij})$ of the goods with the weight q_i from customer i to customer j is as:

$$CO_2(q_{ij}) = c_3 \eta_0 \varepsilon(q_i) d_{ij} = c_3 \eta_0 \left(\frac{\varepsilon^* - \varepsilon_0}{Q} q_i + \varepsilon_0 \right) d_{ij} \quad (6)$$

Where, c_3 is the unit carbon emissions cost, η_0 is the carbon emissions factor, d_{ij} is the distance from customer i to customer j , $\eta_0 \varepsilon(q_i)$ is the carbon emissions of the goods with the weight q_i from customer i to customer j .

For the convenience of model establishment, assume that there is only one distribution center whose location is known. All the vehicles starts from the distribution center, and return to distribution center after delivery. The vehicles' load is known. The location and the demand of customer are known. One vehicle is for one customer.

According to the above assumption, establish the minimizing carbon emissions cost model:

$$\begin{aligned} \min CO_2 &= \sum_{i=0}^L \sum_{j=0}^L \sum_{k=1}^{m'} c_3 \eta_0 \varepsilon(q_i) x_{ijk} = \\ &= \sum_{i=0}^L \sum_{j=0}^L \sum_{k=1}^{m'} c_3 \eta_0 \varepsilon(q_i) d_{ij} x_{ijk} \\ &= \sum_{i=0}^L \sum_{j=0}^L \sum_{k=1}^{m'} c_3 \eta_0 \left(\frac{\varepsilon^* - \varepsilon_0}{Q} q_i + \varepsilon_0 \right) d_{ij} x_{ijk} \quad (7) \\ &= \sum_{i=0}^L \sum_{j=0}^L \sum_{k=1}^{m'} c_3 \eta_0 \varepsilon_0 d_{ij} x_{ijk} + \\ &+ \sum_{i=0}^L \sum_{j=0}^L \sum_{k=1}^{m'} c_3 \eta_0 \frac{\varepsilon^* - \varepsilon_0}{Q} q_i d_{ij} x_{ijk} \end{aligned}$$

Where, L is the number of customers, m' is the number of vehicles, q_i is the demand of the i customer, Q is the maximum load of the vehicles, k is the vehicle's number.

The number of distribution center is 0. The numbers of customers are 1, 2, 3 ... L . Define variables x_{ijk} and y_{ki} as:

$$x_{ijk} = \begin{cases} 1, & \text{vehicle } k \text{ from } i \text{ to } j \\ 0, & \text{others} \end{cases} \quad (8)$$

$$y_{ki} = \begin{cases} 1, & \text{is service by vehicle } k \\ 0, & \text{others} \end{cases} \quad (9)$$

$$\sum_{i=0}^L q_i y_{ki} \leq Q \quad k \in [1, m'] \quad (10)$$

$$\sum_{k=1}^{m'} y_{ki} = 1 \quad i \in [0, L], k \in [1, m'] \quad (11)$$

$$\sum_{i=0}^L \sum_{k=1}^{m'} x_{ijk} = 1 \quad j \in [0, L], k \in [1, m'] \quad (12)$$

$$\sum_{j=0}^L \sum_{k=1}^{m'} x_{ijk} = 1 \quad i \in [0, L], k \in [1, m'] \quad (13)$$

$$\sum_{i=0}^L \sum_{k=1}^{m'} x_{0ik} = \sum_{j=0}^L \sum_{k=1}^{m'} x_{j0k} \quad (14)$$

Formula (7) is the objective function. The first part is the carbon emissions cost caused by the vehicle's weight. The second part is the carbon emissions cost caused by the vehicle's load. Formula (10) shows the sum of customers' demand cannot be greater than the maximum load of vehicles. Formula (11), (12), (13) show one vehicles is for one customer. Formula (14) shows vehicles starts from distribution center, and then return to distribution center.

ANT COLONY ALGORITHM (ACA)

Assume that there are n cities. The distance between any two cities i and j is d_{ij} ($i, j = 1, 2, \dots, n$). $b_i(t)$ is the number of ants at time t at city i . $m = \sum_{i=1}^n b_i(t)$ is the total number of ants. $\tau_{ij}(t)$ is the pheromone at time t on the line ij . At time $t = 0$, every path has the same pheromone strength. $\Delta\tau_{ij}(t) = 0$.

With time passing by, the new pheromone is added, and old pheromones evaporate. ρ is the pheromone volatilization coefficient which indicates pheromones volatile speed. When all the ants accomplish one travel, pheromone on every path is:

$$\tau_{ij}(t+1) = (1 - \rho)\tau_{ij}(t) + \Delta\tau_{ij}(t) \quad (15)$$

$$\Delta\tau_{ij}(t) = \sum_{k=1}^m \Delta\tau_{ij}^k(t) \quad (16)$$

$\Delta\tau_{ij}(t)$ is the pheromone increment on the path ij . At the beginning, $\Delta\tau_{ij}(0) = 0$. $\Delta\tau_{ij}^k(t)$ is the pheromone released by ant k on the path ij , which is determined by the ants performance.

$$\Delta\tau_{ij}^k(t) = \begin{cases} Q/L_k & \text{section k of ants pass edge ij in the course of this tour} \\ 0 & \text{else} \end{cases} \quad (17)$$

Where, Q is constant, L_k is the path length of the ant k . The transition probability of ant k from city i to city j is:

$$P_{ij}^k = \begin{cases} \frac{[\tau_{ij}(t)]^\alpha \cdot [\eta_{ij}(t)]^\beta}{\sum_{s \in allowed_k} [\tau_{is}(t)]^\alpha \cdot [\eta_{is}(t)]^\beta} & j \in allowed_k \\ 0 & others \end{cases} \quad (18)$$

Where, $allowed_k = (1, 2, \dots, n) - tabu_k$ indicates the city collection ant k can choose currently. $tabu_k$ ($k = 1, 2, \dots, m$) is the taboo table of ant k , which indicates the cities ant k has passed by to show the memory of ants. $\eta_{ij}(t)$ is prior knowledge visibility. In the TSP problem, it is the heuristic information from one city moved to another city, which generally is $\eta_{ij}(t) = 1/d_{ij}$. α is the importance of the residual information on the path ij . β is the importance of the heuristic information.

The basic ant colony algorithm to achieving process is [14]: m ants start from one certain city at the same time to choose the next city based on formula (18), which indicates that ants prefer visit the path with higher intensity of pheromone. The passed cities will be put into $tabu_k$. After all ants finishing one travel, renew the pheromone on each path based on Formula (15) to Formula (17). Repeat the above processes until termination condition is established.

CHAOS ANT COLONY ALGORITHM (CACA)

Chaos is a kind of movement form of nonlinear dynamic system under certain conditions, which is a random behavior when the system is in a non-equilibrium process [15]. Chaos is produced by some fixed rules which is often nonlinear, simple and without any random factors. Chaos movements are seemingly random, but it consists of delicate internal structures with the characteristics of universality, randomness, etc, which can repeatedly traverse all state according to its own law within a certain range. Due to the periodicity of chaotic movement, chaos can be served as a local search method to improve other optimization algorithm's global convergence.

In ant colony algorithm, since the ant foraging behavior has the chaos characteristics, apply the periodicity and random characteristics into ant colony algorithm to improve the ant colony algorithm to have a wider search range and a faster

search speed, therefore it forms a new search algorithm, chaos ant colony algorithm. Chaos ant colony algorithm is based on the basic ant colony algorithm introducing the chaos initialization and chaos disturbance to get a better optimization effect.

In the early stages of the basic ant colony algorithm, since ants leave the same pheromones on each path, the first ants process foraging behavior with the same probability. Such optimization is not only inefficient, but also difficult to find the global optimization. If the initial pheromone values in the basic ant colony algorithm are given according to the amount of chaos, the pheromone will be different on each path. Ants can select the optimal path based on the amount of pheromone to improve the efficiency of optimization. For chaos initialization, it generally chooses typical chaotic systems, Logistics mapping, as chaotic variables [16]:

$$Z_{ij}(t+1) = \mu Z_{ij}(t) [1 - Z_{ij}(t)] \quad (19)$$

Where, μ is control parameter whose value is [3.56,4] [17]. When the Logistics mapping is completely in chaos, $\mu = 4$ and $0 \leq Z_{ij}(0) \leq 1$. Use the permutation method in the literature [18] to process a whole arrangement to make each chaotic quantity correspond with an initial pheromone value.

Set a given cost in the basic ant colony algorithm, which can avoid unnecessary search by poor solution, therefore, to improve the search efficiency and convergence speed. When update the pheromone, introduce chaos disturbance to improve ants' periodicity to help ants get the better optimal solution and avoid falling into local optimum. The formulas with pheromone updating by chaos disturbance are as:

$$\tau_{ij}(t+1) = (1 - \rho)\tau_{ij}(t) + \Delta\tau_{ij}(t) + q_1 Z_{ij}(t) \quad (20)$$

Where, $Z_{ij}(t)$ is chaotic variable from the iteration of formula (19), q_1 is its coefficient.

STEPS OF MODEL SOLUTION

(1) Regarding $NC=0$ (NC is iteration), the load of vehicles is 0, proceed parameters initialization and chaos initialization.

(2) Put m ants at the distribution center.

(3) Based on the transition probability from (18), choose and move the ants to the next city j , and add j to $tabu_k$ at the same time. Check whether

the vehicles' load is larger than the maximum load. If so, return to distribution center.

(4) Check whether $tabu_k$ is full. If not, return to (3). Otherwise, go on (5).

(5) Calculate the target function (minimum carbon emissions cost or target evaluation function value). Record the best solution currently

(6) When the best solution is less than one certain value, update the chaotic pheromone based on formula (20).

(7) If $NC < NC_{max}$, then $NC = NC + 1$, empty $tabu_k$, and go back to Step2. If $NC = NC_{max}$, end.

RESULTS AND DISCUSSION

Assume the distribution center has 18 customers whose coordinate is (42,50). Table 1 is the demand of each customer. Table 2 is the coordinate of each customer. The maximum load of each vehicle is 5 tons. In the simulation, set $c_0 = 0, c_1 = 1, c_2 = \infty$. The unit distance fuel cost of empty car and full car are $\varepsilon_0 = 1$ and $\varepsilon^* = 2$. The unit carbon emissions cost is $c_3 = 0.3$. The emission factor is $\eta = 2.61$ [19]. The distances between each customer and distribution center can be calculated by formula (21). The delivery car can be calculated by formula (22).

$$d_{ij} = \sqrt{(x_i - x_j)^2 + (y_i - y_j)^2} \quad (21)$$

$$m' = \left\lceil \frac{\sum_{i=1}^L g_i}{\lambda q} \right\rceil + 1 \quad (22)$$

Since the total demand of each customer is 16.2 tons. According to formula (22), if $\lambda = 0.98$, the number of vehicles is:

$$m' = \left\lceil \frac{16.2}{0.98 \times 5} \right\rceil + 1 = 4 \quad (23)$$

Where, $\lceil \cdot \rceil$ indicate get the integer. $\lambda \in (0,1)$, which can be adjusted by the complexity of loading and constraint. Generally, the more complex the loading is, the less λ is. Otherwise, the λ is bigger [20].

Table 1. Demand of Customer.

Customer	1	2	3	4	5	6	7	8	9
Demand	0.3	0.5	1.0	1.3	0.9	1.2	1.5	0.4	1.5
Customer	10	11	12	13	14	15	16	17	18
Demand	0.2	0.4	1.0	1.1	1.3	1.5	1.0	0.5	0.6

Table 2. Coordinate of Customer.

Customer	1	2	3	4	5	6	7	8	9
X	16	25	10	60	33	18	20	50	58
Y	32	50	40	65	63	22	60	25	20
Customer	10	11	12	13	14	15	16	17	18
X	70	48	25	38	12	20	15	22	52
Y	23	30	42	62	12	18	65	27	52

Table 3. The results basic ant colony algorithm (minimum carbon emissions cost)

NO.	1	2	3	4	5	6	7	8	9	10	Ave
Carbon emissions cost	483.7	536.7	564.1	564.1	465.6	545.6	485.5	487	492	479.1	500.49
Vehicles	4	4	4	4	4	4	4	4	4	4	4
End iteration	96	67	56	63	79	62	151	71	51	47	74.3
Deviations	18.1	71.7	98.5	98.5	0	80	19.9	21.4	26.4	13.5	44.8

Table 4. The results chaos ant colony algorithm (minimum carbon emissions cost)

NO.	1	2	3	4	5	6	7	8	9	10	Ave
Carbon emissions cost	439.5	497	474.5	456.5	415.8	490.5	455.1	456.5	455.4	448.9	458.97
Vehicles	4	4	4	4	4	4	4	4	4	4	4
End iteration	20	85	32	14	56	36	54	16	76	20	40.9
Deviations	23.7	81.2	58.7	40.7	0	74.7	39.3	40.7	39.6	33.1	43.17

Table 3 is the 10 results by using the basic ant colony algorithm to solve the minimum carbon emissions cost model. Table 4 is the 10 results by using the chaos ant colony algorithm to solve the minimum carbon emissions cost model. Comparing Table 3 with Table 4 we can find:

(1) Carbon emissions cost: the minimum carbon emissions cost of basic ant colony algorithm is 465.6, the cost of chaos ant colony algorithm is 415.8. The chaos ant colony algorithm saves 10.6% of minimum carbon emissions cost comparing with basic ant colony algorithm. The average carbon emissions cost of basic ant colony algorithm is 500.49. The average cost of chaos ant colony algorithm is 458.97. For the average distribution cost, the chaos ant colony algorithm saves 8.2% comparing with basic ant colony algorithm. Thus, for the solution of minimum carbon emissions cost

distribution model, chaos ant colony algorithm can find the path with less carbon emissions cost, which is better for environmental protection.

(2) The number of final generation: the average number of final generation of basic ant colony algorithm is 74.3. The average number of final generation of chaos ant colony algorithm is 40.9. From the average number of final generation, we can find the chaos ant colony algorithm has a better convergence.

(3) The difference with minimum carbon emissions cost. The average difference between basic ant colony algorithm and minimum carbon emissions cost is 44.8. The average difference between chaos ant colony algorithm and minimum carbon emissions cost is 43.17. From the difference with minimum carbon emissions cost, we can find

the chaos ant colony algorithm is more stable in the process of search minimum carbon emissions.

Figure 1 is the optimization curves of minimum carbon emissions cost. From the figure, we can find chaos ant colony algorithm has a better effectiveness in the process of searching minimum carbon emissions cost. Comparing with basic ant colony algorithm, it can find the lower carbon emissions cost with a faster convergence speed. Figure 2 is distribution path of basic ant colony based on the minimum carbon emissions cost model. Figure 3 is distribution path of chaos ant colony based on the minimum carbon emissions cost model.

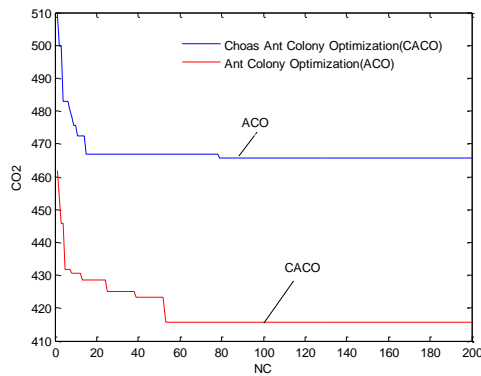


Fig. 1. Optimization curve

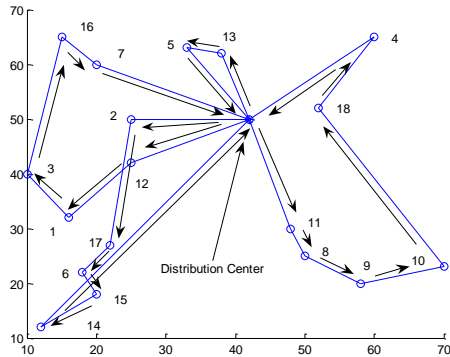


Fig.2. Distribution Path of ACA

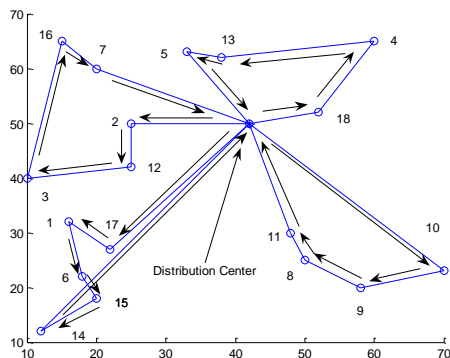


Fig. 3. Distribution Path of CACA

CONCLUSIONS

This paper introduced the low carbon logistics distribution path optimization models, including minimum carbon emissions cost model. Use chaos ant colony algorithm, the new mixed algorithm, to solve the two models to prove its effectiveness through simulation. But this is the preliminary research on the low carbon logistics distribution route optimization problem. It is the exploration stage for low carbon logistics distribution route optimization model. The models are established based on the ideal situation without consideration of many complex factors and real situations in the constraints of the models. In future study, it still needs to optimize the model to make the model more accord with the actual needs. Although there have been some algorithm researches, they are limited to chaos ant colony algorithm, the certain kind of algorithm to solve the optimization model. In the future research, it needs to develop solutions of different intelligent algorithm models to find the more suitable intelligent algorithm for models' solutions.

REFERENCES

1. X. Xu, *Com. Research*, **4**, 183 (2011).
2. M. Baiyu, *Jiangsu Com. Forum*, **7**, 70 (2012).
3. Z. Dajun, *Mana. Journal*, **25**, 161 (2013).
4. Z. Peng, *Chinese chain*, **9**, 26 (2013).
5. W. Yan, L. Zuoju, *The com. era*, **14**, 32 (2010).
6. W. Lei, *Econo.Problems*, **10**, 72 (2012).
7. Z. Xinhong, *Railway Pur. and Log.*, **5**, 49 (2011).
8. Z. Songling, *Logistics Sci-Tech*, **10**, 60 (2012).
9. H. Yunchao, S. Jingcheng, H. Ailing, *Logistics Tech.*, **31**(8), 56 (2012).
10. X. Xu, *Comm. Times*, **10**, 23 (2011).
11. Z. Li, *China Pop.*, **23**(7), 78 (2013).
12. H. Hua, *ICEEE*, 635 (2010).
13. S. Qin, Research on Fuel Consumption Minimized Vehicle Routing Problem. Master's thesis of Tsinghua University, 2011.
14. Y. Le, P. Zhen, *Logistics Tech.*, **27**(11), 84 (2008).
15. M. Dorigo, *IEEE Transactions on Evolutionary Computation*, **1**(1), 53 (1997).
16. L. Ning, Research of Hybrid optimization based on chaos optimization algorithm, Master paper, Zhongnan university, 2004.
17. G. Shang, *Sys. Engi. & Prac.*, **8**(9), 100 (2005).
18. G. Shang, Y. Jinyu, *Pattern Reco. and Artificial Intel.*, **19**(2), 266 (2006).
19. L. Pin, *Application Research of Com.*, **30**(10), 2977 (2013).
20. L. Cheng, C. Zhiya, F. Daixi, *Sys. Engi.*, **23**(10), 7 (2005).

Sorbent concentration effect on the adsorption of Pb(II) on Fe₃O₄@Mg₂Al-EDTA LDH in aqueous solution

L.-X. Zhao^{1,*}, M.-C. Jiang², L.-Y. Luan¹, Q. Li¹, J. Zhang¹

¹ Analysis and Test Center, Shandong Academy of Sciences, Jinan 250014, P. R. China

² Huadian Electric Power Research Institute, Shandong Branch, Jinan 250014, P. R. China

Received February 12, 2016; Revised December 26, 2016

The adsorption of Pb(II) onto Fe₃O₄@Mg₂Al-EDTA LDH as a function of Fe₃O₄@Mg₂Al-EDTA LDH concentration was studied, and a sorbent concentration effect (*C_s*-effect), namely, adsorption isotherm declines as sorbent concentration (*C_s*) increases, was observed. The experimental data were fitted to the adsorption models including the classic Freundlich model and the surface component activity (SCA) model. The results show that the the Freundlich-SCA equation can adequately describe the *C_s*-effect observed in the batch adsorption tests. In other words, their intrinsic parameters simulated from the experimental data are independent of *C_s* value. In this case, the values of parameters obtained at given *C_s* values can used to predict the adsorption behavior for any *C_s* values.

Key words: Sorbent concentration effect, Freundlich equation, surface component activity model.

INTRODUCTION

In studies of adsorption at the solid-liquid interface, an anomalous phenomenon of “sorbent concentration effect” [1] or “solids effect” [2, 3] (*C_s*-effect), namely, adsorption isotherm declines as sorbent concentration increases, has been observed since the 1980s. Thermodynamically, the adsorption equilibrium constant (or equilibrium partition coefficient) for a given adsorption reaction under constant temperature, pressure, and medium composition (e.g., pH, ionic strength) should be independent of both adsorbate and sorbent concentrations [4]. So, the classic adsorption model cannot explain this anomalous phenomenon because it was derived on the assumption that the adsorption equilibrium constant is independent of the sorbent concentration (*C_s*).

In fact, there has been controversy about the reasons for the *C_s*-effect over the last thirty years. Some researchers [5-8] have attributed the *C_s*-effect to a variety of experimental artifacts, while other researchers [1, 4, 9-15] believed that the *C_s*-effect is a constancy phenomenon based on thermodynamic principles although many artifacts may cause a pseudo *C_s*-effect. Because the substances for which adsorption isotherm apparently declined with increasing *C_s* include inorganic and organic adsorbates in freshwater and marine sediments, quarts, clays and clays minerals, and digested sewage sludge, it seems unlikely that experimental artifacts could explain widespread agreement of a *C_s*-effect for so diverse a set of adsorbates, adsorbents, and investigators [16]. Thus, it can be concluded that the *C_s*-effect is an experimental fact indeed, not an artifact, and there should be a

universal reason that causes the *C_s*-effect although it is still not clear now.

In this study, the sorption of Pb(II) on Fe₃O₄@Mg₂Al-EDTA LDH in aqueous solution was investigated at various *C_s* values. The Freundlich-SCA equation derived from the surface component activity (SCA) model [17-19] was examined for describing the *C_s*-effect observed in the batch adsorption tests.

MATERIALS AND METHODS

Materials

All chemicals used in this work were of analytical grade. Ultra pure water was used in all cases.

Magnetic nanoparticles were prepared by dissolving 0.01 mol of FeCl₂·4H₂O and 0.02 mol of FeCl₃·6H₂O in water solution under stirring at 65°C, and 20 wt% of NH₃·H₂O were added dropwise together at a constant pH value of 10-11. The obtained material (Fe₃O₄) was recovered, washed several times with deionized water until the pH was neutral. The obtained Fe₃O₄ was preserved as suspension.

Fe₃O₄@Mg₂Al-EDTA LDH with a Mg²⁺/Al³⁺ molar ratio of 2:1 was prepared by co-precipitation. An aqueous solution containing 0.1 mol Mg(NO₃)₂·6H₂O and 0.1 mol Al(NO₃)₃·9H₂O was added dropwise to Fe₃O₄ solution with Fe/Mg molar ratio equal to 0.02, under vigorous stirring. During the synthesis, the temperature was maintained at 65°C and pH at 11-12 by the simultaneous addition of EDTA-Na₂ ammonia solution with EDTA-Na₂/Al molar ratio equal to 1. The reaction mixtures were aged for 45 min in mother solution at room

temperature and then filtered, washed with deionized water until the pH was neutral. The filter cakes were further hydrothermally treated at 80°C for 24 h. The sols were dried, triturated and sieved to collect the particles of <74 μm in diameter.

Magnetic Fe₃O₄@Mg₂Al-EDTA LDH was characterized by XRD. The magnetization curves were obtained at ambient temperature by vibrating sample magnetometry (VSM, JDM-13) (Fig. 1).

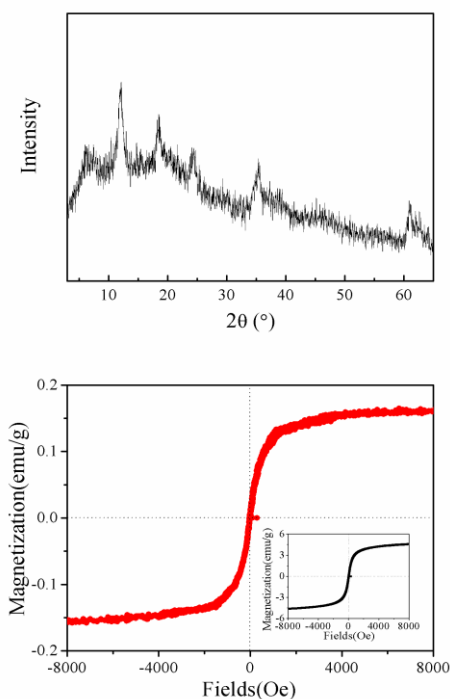


Fig. 1. XRD pattern and magnetization curves of Fe₃O₄@Mg₂Al-EDTA LDH sample and the inset is the magnetization curve of Fe₃O₄

Adsorption experiments

Adsorption tests of Pb(II) on Fe₃O₄@Mg₂Al-EDTA LDH sample were carried out by batch equilibration technique [20-22]. Solutions with various concentrations (0-800 mg/L) of Pb(II) were prepared in 0.01 mol/L of NaNO₃ with Pb(NO₃)₂, and the pH values of the solutions were adjusted to 5.0 with 0.1 mol/L HNO₃ and NaOH solutions. Known masses of Fe₃O₄@Mg₂Al-EDTA LDH samples were mixed with Pb(II) solutions of various initial concentrations in polyethylene centrifugal tubes. The centrifugal tubes were put into a thermostatic water bath shaker at 25±0.2°C for 24 h. Then the suspensions were centrifuged at a speed of 4000 r/min for 5 min. The Pb(II) equilibrium concentrations in the supernatants were determined by flame atomic absorption spectrometry (TAS-990, Beijing Purkinje General Instrument Co., Ltd.). The

equilibrium adsorption amounts were calculated using the following equation:

$$\Gamma_e = \frac{(C_0 - C_e)V}{m} \quad (1)$$

where C_0 (mg/L) and C_e (mg/L) are the initial and the remaining (equilibrium) concentration respectively, Γ_e (mg/g) is the equilibrium adsorption amount, V (mL) is the volume of the suspension and m (g) is the mass of the Fe₃O₄@Mg₂Al-EDTA LDH sample.

RESULTS AND DISCUSSION

Fig. 2(a) shows the adsorption isotherms of Pb(II) on Fe₃O₄@Mg₂Al-EDTA LDH at different Fe₃O₄@Mg₂Al-EDTA LDH concentrations. As can be seen, the adsorption isotherms decline significantly as the sorbent concentrations increase. This phenomenon accords with the law which is described by a C_s -effect. The applicability of current theories to predict the C_s -effect phenomenon was examined as following.

Classical Freundlich equation

As we know, Langmuir model was developed on the basis of the thermodynamic equilibrium theory while Freundlich model was originally an empirical equation. However, it was found that Freundlich equation could be thermodynamically derived based on assuming that the adsorption sites of sorbent are of different energies and the adsorption of sorbate on the sites having same energy level obeys Langmuir equation [23].

Classical Freundlich equation is represented as [23, 24]:

$$\Gamma_e = K_F C_e^{n_F} \quad (2)$$

where Γ_e is equilibrium adsorption amount, C_e is equilibrium concentration, K_F and n_F are Freundlich constants.

The Eq. (2) can be expressed by the following linear form:

$$\lg \Gamma_e = \lg K_F + n \lg C_e \quad (3)$$

The adsorption data of Pb(II) on Fe₃O₄@Mg₂Al-EDTA LDH were fitted with the Freundlich equation (see Fig.2). It was found that Freundlich equation can adequately describe the adsorption equilibrium for a given C_s value, and all the correlation coefficients (R^2) are greater than 0.98. The fitted Freundlich parameters, K_F and n_F , for various C_s values are presented in Table 1. This dependence of the Freundlich parameters on C_s showed that the classical Freundlich model cannot predict the C_s -effect. That is to say, using the Freundlich parameters obtained with given C_s values to predict the adsorption behavior of

adsorbate at other C_s values will be inaccurate.

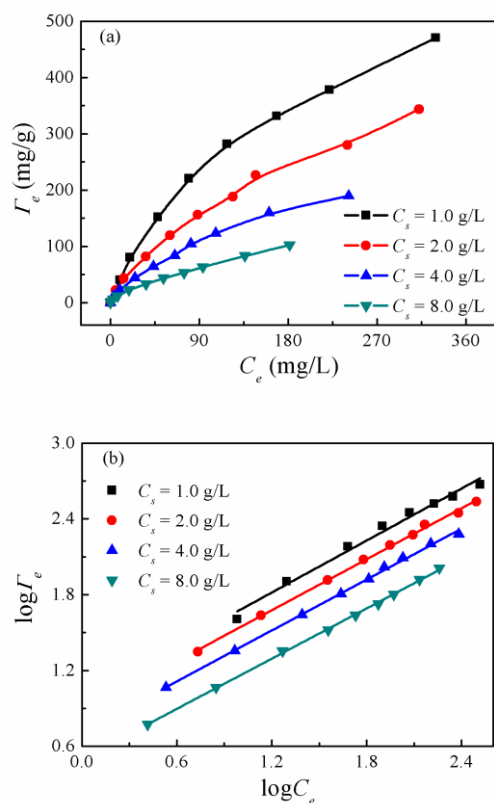


Fig. 2. Adsorption isotherms (a) and linear correlation plots for the classical Freundlich equation (b) at different sorbent concentrations

Table 1 Parameters of the classical Freundlich equation at different sorbent concentrations

C _s (g/L)	n _F	K _F	R ²
1.0	0.686	9.877	0.985
2.0	0.673	7.400	0.998
4.0	0.671	5.319	0.998
8.0	0.663	3.154	0.999

The fact that Freundlich equation can adequately describe the adsorption behavior for a given C_s value indicates that Freundlich equation is available for the real adsorption systems studied. Therefore, the deviation of the prediction of Freundlich equation from the experimental data for different C_s values should be because the effect of C_s on adsorption was not accounted for in the derivation process of the classical Freundlich equation.

Examining using the Freundlich-SCA equation

Considering the deviation of a real adsorption system from an ideal one, we proposed a alternative model, surface component activity (SCA) model [17-19]. It suggests that (1) the surface of the sorbent is uniform, that is, all the adsorption sites are equivalent; (2) all adsorption occurs through the same mechanism; (3) at the maximum adsorption, only a monolayer is formed; (4) the molecular size

of solute and solvent are similar; (5) surface component (adsorption site or adsorbed solute) activity coefficient is not equal to unity because of the deviation of a real adsorption system from a ideal one. A C_s-dependent Freundlich equation (or Freundlich-SCA equation) can be derived as following,

$$\Gamma_e = K_S \cdot f_{H_2O}^s \cdot C_e^{n_S} \quad (4)$$

The linear form of Eq. (4) is

$$\lg \left(\frac{\Gamma_e}{f_{H_2O}^s} \right) = n_S \lg C_e + \lg K_S \quad (5)$$

The coefficients, n_S and K_S, of a given system are independent of sorbent concentration.

The C_s-dependent function of f_{H₂O}^s is an exponential form,

$$f_{H_2O}^s = \exp(-\gamma C_s^\alpha) \quad (6)$$

where γ and α are empirical constants. Then,

$$K_F = K_S \exp(-\gamma C_s^\alpha) \quad (7)$$

Thus, the C_s-dependent function of f_{H₂O}^s can be estimated from the relationship between the experimental measured K_F values and C_s values.

The change of the K_F with C_s for the adsorption system was fitted to Eq. (7) using a non-linear least-squares method (Excel Solver) (see Fig.3), and the best-fit values of the empirical constants, γ and α, are 0.449 and 0.626.

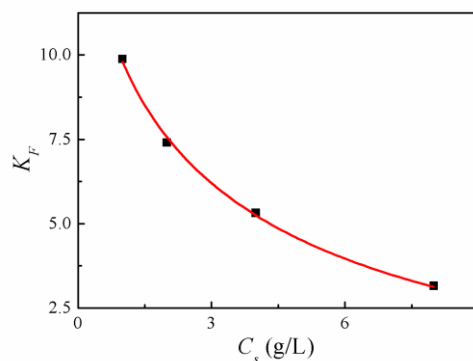


Fig. 3. Relationship between K_F and C_s

Using the simulated γ and α values, the normalized non-linear plot of (Γ_e / f_{H₂O}^s) vs. C_e for the studied system was obtained (see Fig.4(a)). A unique curve independent of C_s was obtained from experimental data. Fig.4(b) presents the normalized plot of lg(Γ_e / f_{H₂O}^s) vs. lgC_e. As can be seen, a unique fairly straight line for various C_s values was obtained. The K_S and n_S values obtained from the slope and intercept of the linear plot are 0.677 and 17.9. The correlation coefficients (R²) of

the non-linear and linear plots are higher than 0.98, indicating that the Freundlich-SCA equation can adequately describe the C_s -effect observed in the studied system.

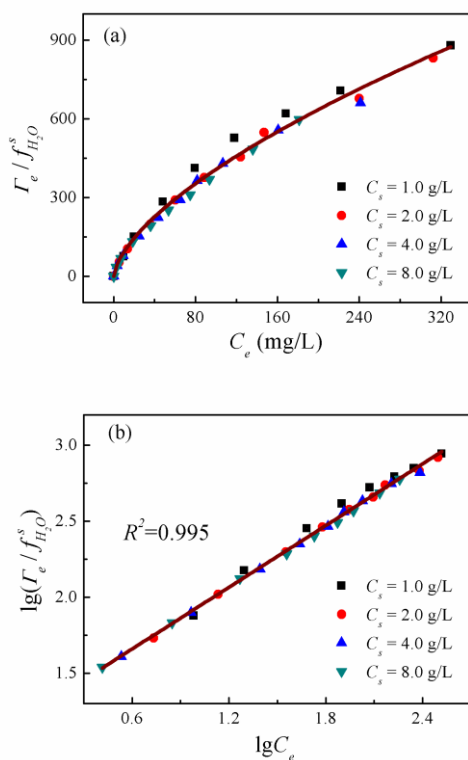


Fig. 4 The Freundlich-type MEA isotherm (a) and linear correlation plot of the Freundlich-type MEA model (b)

CONCLUSION

The adsorption of Pb(II) onto Fe₃O₄@Mg₂Al-EDTA LDH in the studied conditions is subject to the C_s -effect in which the adsorption isotherm declines as the sorbent concentration increases. The above fitting result of the adsorption data with Freundlich-SCA equation shows that Freundlich-SCA equation can be used to describe the C_s -effect observed in the batch adsorption tests. In this case, the values of parameters obtained at given C_s values can be used to predict the adsorption behavior for any C_s values.

The SCA model supposes that it is the interaction between the sorbent particles that induces the deviation of a real adsorption system from an ideal one, just as the deviation of a real solution from an ideal one. With increasing the C_s value, the interaction between the sorbent particles strengthens, resulting in the decrease of the effective adsorption site density, therefore, the adsorption isotherms decline.

REFERENCES

1. T.C. Voice, W. Weber, *J. Environ. Sci. Technol.*, **19**, 789 (1985).
2. D.J. O'Connor, J.P. Connolly, *Water Res.*, **14**, 1517 (1980).
3. T.C. Voice, C.P. Rice, W.J. Weber, *Environ. Sci. Technol.*, **17**, 513 (1983).
4. G. Pan, P.S. Liss, *J. Colloid Interface Sci.*, **201**, 71 (1998).
5. P.M. Gschwend, S.C. Wu, *Environ. Sci. Technol.*, **19**, 90 (1985).
6. M.A. Cohen-Stuart, J.M. Scheutjens, G. Fleer, *J. Polymer Sci.: Polymer Physics Ed.*, **18**, 559 (1980).
7. U.P. Nyffeler, Y.H. Li, P.H. Santschi, *Geochim. Cosmochim. Acta*, **48**, 1513 (1984).
8. D. Grolimund, M. Borkovec, P. Federer, H. Sticher, *Environ. Sci. Technol.*, **29**, 2317 (1995).
9. D.M. DiToro, J.D. Mahony, P.R. Kirchgraber, A.L. O'Byrne, L.R. Pasquale, D.C. Piccirilli, *Environ. Sci. Technol.*, **20**, 55 (1986).
10. G. Pan, P.S. Liss, M.D. Krom, *Colloids Surf. A*, **151**, 127 (1999).
11. A.K. Helmy, E.A. Ferreiro, S.G. Bussetti, *J. Colloid Interf. Sci.*, **225**, 398 (2000).
12. T.W. Chang, M.K. Wang, *Chemosphere.*, **48**, 419 (2002).
13. X.F. Wu, Y.L. Hu, F. Zhao, Z.Z. Huang, D. Lei, *J. Environ. Sci.*, **18**, 1167 (2006).
14. H. J. Lu, M.T. Luan, J.L. Zhang, Y.X. Yu, *J. China Univ. Min. Technol.*, **18**, 125 (2008).
15. H.D. Utomo, K.A. Hunter, *Bioresour. Technol.*, **101**, 1482 (2010).
16. P.J. McKinley, E.A. Jenne, *Environ. Sci. Technol.*, **25**, 2082 (1991).
17. L.X. Zhao, W.G. Hou, *Colloids Surf. A*, **396**, 29 (2012).
18. L.X. Zhao, S.E. Song, N. Du, W.G. Hou, *Acta Physico-Chimica Sinica.*, **28**, 2905 (2012).
19. L.X. Zhao, S.E. Song, N. Du, W. G. Hou, *Colloid Polymer Sci.*, **291**, 541 (2013).
20. M.C. Hermosin, L. Pavlovic, M.A. Ulibarri, J. Cornejo, *Water Res.*, **30**, 171 (1995).
21. L. Ma, R.K. Xu, J. Jiang, *J. Environ. Sci.*, **22**, 689 (2010).
22. P. Ding, K.L. Huang, H. Yang, G.Y. Li, Y.F. Liu, *J. Cent. South Univ. Technol.*, **17**, 277 (2010).
23. C.H. Sheindorf, M. Rebhun, M. Sheintuch, *J. Colloid Interf. Sci.*, **79**, 136 (1981).
24. T. Santhi, S. Manonmani, T. Smitha, *Int. J. Eng. Sci. Technol.*, **2**, 287 (2010).

Research and application of anti-leakage drilling fluid

Y. Hao

China University of Geosciences (Beijing), Beijing 100083, China

Received February 25, 2016; Revised November 12, 2016

Micro-foam drilling fluid can effectively lower the pressure of liquid columns and seal the reservoir space in a good way. Through the strict control of water loss and enhancement of sealing, it can effectively reduce the damages to reservoir strata. The technical research is carried out towards the geological conditions and reservoir characteristics of K Oil Field. The research starts from the two aspects--cementing fluid design and cementing construction process design. And design the low-density anti-leakage slurry system meeting the requirements on the on-site construction, which is micro-foam drilling fluid. This system boasts the features of great rheological and thickening performance, high compressive strength, strong anti-leakage and channeling prevention ability. This technology has been applied to three wells for trial in K Oil Field. The process of cementing construction is smooth and with no leakage. The percent of pass for the cementing quality reaches 100%, the high-quality rate reaches 80%, and rate of the cement returning height during the well cementation reaching the standard is 100%, and test results are good. It has reached the anticipated objective of the project.

Keywords: Micro-foam drilling fluid; Anti-Leakage; Optimal selection of the Formula; Foam performance; Field application.

INTRODUCTION

As for the Jurassic oil deposits of the main development layers of K Oil Field, the values of the current formation pressure are only 2.9MPa and 3.2MPa. The pressure maintenance levels are only 48.3% and 53.3% of the original formation pressure (6.0MPa). The pressure in the local areas is only 1.5MPa and the pressure maintenance level is only 25%. At present, the actually measured pressure coefficients of Jurassic reservoir layers have decreased to the range between 0.32 and 0.93. The formation deficit is serious. The oil deposits in cretaceous system and Jurassic system of K Oil Field belong to the oil deposits with bottom water. The formation permeability and connectivity are relatively good. The strata are loose and the loading capacity declines. The formation porosity is relatively large. K Oil Field belongs to typical low-pressure oil reservoir easy to leak. During the process of development, it is quite easy to pollute the reservoirs. During the process of drilling operation, under the influence of differential pressure, the drilling fluid may permeate into the reservoirs; and under the influence of extremely high differential pressure, the malignant leakage may be aroused, thus making a large amount of drilling fluid and solid contents enter the reservoir pores, which will result in severe contamination. The protection of low-pressure reservoirs usually starts from the reduction of differential pressure of the operations in the well bottom and the

improvement of the operation fluids and underlying compatibility [1]. It is to reduce the differential pressure of operations in the well bottom, reduce the risks of leakage, and decrease the entry of the external fluid into the formation. When the entry of the external fluid is inevitable during the development of low-pressure reservoirs, it needs to improve the operational fluids and underlying compatibility, to reduce the pollution to the oil reservoirs. The micro-foam drilling fluid has distinctive low-density effects and foam plugging effect [2~4]. It is the drilling fluid system applicable to the development and protection of low-pressure reservoirs. It can save time and equipments so that bring benefits [5]. Considering the geological conditions and reservoir characteristics of K Oil Field, it chooses micro-foam drilling fluid and optimizes the drilling fluid. The test of the micro-foam drilling fluid in K Oil Field has obtained good effects.

THE STABILITY AND THE MECHANISM OF MICRO-FOAM DRILLING FLUID

The stability of Micro-Foam

The factors influencing the stability of the micro-foam drilling fluid are divided into internal cause and external cause, Internal cause is mostly drainage of liquid film and diffusion function of gas through the liquid film; The external cause includes temperature, pressure and the intrusion of outside materials and so on [6~7].

In terms of the micro-foam, is not irreplaceable

* To whom all correspondence should be sent:

E-mail: yanghao@cugb.edu.cn

by ordinary foams [8]. due to the differences between it and the ordinary foams in microstructure, the main factor causing the burst of micro-bubbles is the action of gravity [9]. The fluid descends due to its own gravity, which makes the liquid films become thinner and thinner and finally leads to the burst of the bubbles; therefore, the properties of the liquid films are the main factor influencing the stability of the foam. Besides, when the external conditions including temperature and pressure change or the foam is shocked or vibrated by the external forces, it will accelerate the process of rupture.

Action Mechanism of the Micro-Foam Drilling Fluid

Firstly, low-density effect. When the density of the micro-foam drilling fluid is lower than the ordinary water-based drilling fluid, the fluid column pressure at the well bottom can be effectively lowered, the water loss can be reduced, the leakage can be decreased, the pollution can be lessened and the reservoirs can be protected.

Secondly, Jamin Effect [10]. During the permeation of micro-foam into the strata, the micro-foam is captured in the pore throat. The superimposition of Jamin Effect largely increases the resistance of the foam drilling fluid to flow into the strata, and prevent the further permeating or draining of the drilling fluid to the strata.

Thirdly, the mechanism to resist the pressure transmission. The foams in the micro-foam drilling fluid can resist the transmission of the fluid column pressure of the drilling fluid to the strata, thus slowing down the increase of the formation pore pressure.

OPTIMAL SELECTION OF THE FOAMING AGENT AND THE FOAM STABILIZER

Optimal Selection of the Foaming Agent

Compared to the ordinary foam drilling fluid, the micro-foam drilling fluid proposes stricter requirements on the foaming agent. It requires the foaming agent in use to boast relatively high foaming ability, but not generate too many bubbles. The generated bubbles must be tiny and even, and have good stability; meanwhile it shall possess relatively good resistance to salt, calcium and temperature.

Tilt-pour method is the method commonly used to evaluate the foaming performance in production and experiments. This method is relatively convenient and accurate. The equipment adopted is Ross-Miles Foaming Apparatus, which is shown in the following figure 1.

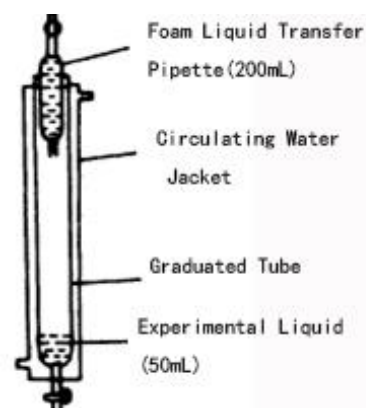


Fig. 1. Ross-Miles foaming apparatus.

The tilt-pour method is applied to evaluate many kinds of foaming agents. The added volume is all 0.4% and the results are shown in Table 1.

Table 1. The Evaluation of the Foaming Agent.

Title	Foaming Height (mm)	Half-Life Period (min)
ASB	178	45
DSB	168	51
F871	358	133
JP-2	308	109
SJ-6	188	131
TSB-2	264	134

From the experimental data it is known that the foaming agents F871, JP-2, SJ-6 and TSB-2 all have great foaming ability, and their half-life period is relatively long. They are all relatively good foaming agents.

Table 2. The Evaluation of the Foam Stabilizer.

Foam Stabilizer	Added Volume (%)	Foaming Height (mm)	Half-Life Period (min)
CMC	0.5	502	196
HEC	0.5	352	183
XC	0.5	410	245
PAC	0.5	321	246
XC+PAC	0.25+0.25	378	286

The Evaluation of the Foam-Stabilizer

Through the theoretical research and the mechanism analysis, the evaluation test has been conducted on the foam stabilizing effects of the treating agent of the drilling fluid. 0.5% TSB-2 is taken as the foaming agent of the test. The results of the test are shown in Table 2.

The experimental data suggest that PAC, XC and CMC are all the great foam stabilizers. The foam fluid made by them is high in foaming volume and great in stability.

THE RESEARCH OF THE MICRO-FOAM DRILLING FLUID FORMULA AND ITS PERFORMANCE EVALUATION

The Research of the Formula

The micro-foam drilling fluid is the multi-phase disperse system with the phases of gas, liquid and solid. Its stability depends on the stable existence of the micro-foam as well as the stability of the drilling fluid system; while the stability of the micro-bubbles mainly depends on the stability of the liquid foams; meanwhile, it renders the liquid films with relatively low liquid drainage rate [11]; therefore when selecting the base mud of the micro-foam drilling liquid, the base mud shall satisfy the following conditions: firstly, appropriate solid contents; secondly, a certain liquid viscosity; thirdly, the stable drilling fluid performance.

Flow Pattern Adjustment.

Formula 1:

4% bentonite+0.2%Na₂CO₃+0.1%NaOH+0.1% XC+0.5%Na-HPAN +0.3%CMC +0.1%PAC+2%SMP-II+0.25% TSB-2

Formula 2:

4% bentonite+0.2%Na₂CO₃+0.1%NaOH+0.2% XC+0.5%Na-HPAN +0.3%CMC +0.1%PAC+2%SMP-II+0.25% TSB-2

Formula 3:

4% bentonite+0.2%Na₂CO₃+0.1%NaOH+0.1% XC+0.5%Na-HPAN +0.3%CMC +0.3%PAC+2%SMP-II+0.25% TSB-2

Formula 4:

4% bentonite+0.2%Na₂CO₃+0.1%NaOH+0.2% XC+0.5%Na-HPAN +0.3%CMC

+0.2%PAC+2%SMP-II+0.25%TSB-2

The results of the test are shown in Table 3.

The optimal selection of the inhibitor

The adding of the inhibitor of inorganic salts, may affect the stability of micro-foam liquid films in the micro-foam drilling liquid [12], thus lowering the stability of the micro-foam drilling fluid system. The test evaluates the inhibitory effects of the commonly-used polymer inhibitors on the clay expansion.

The study shows that compared to K-PAM and FA367, the inhibitory effects of tackifying inhibitor YFKN on the mudstone dispersion are more significant. Its compatibility with the micro-foam drilling fluid system is good and there are no adverse effects on the stability of the micro-foam.

According to above test results and analysis, the micro-foam drilling fluid system is to choose the one with appropriate base fluid viscosity, good foaming ability, strong anti-pollution capacity, and inhibiting ability to the shale, which is easy to prepare and can totally meet the requirements on the on-site construction. The finally determined formula of micro-foam drilling fluid is listed below:

4% bentonite+0.2%Na₂CO₃+0.1-0.2%NaOH+0.1-0.3%XC+0.5-1%Na-HPAN+0.2-0.5%YFKN+0.3-0.5%CMC+0.1-0.3%PAC+2-3%SMP-II+0.2-0.5%TSB-2.

The performance evaluation of the drilling fluid

Temperature Resistance Test

The 1st Formula +0.2%YFKN is selected to conduct the aging tests at different temperatures, and the test results are shown in Table 5.

Table 3. The Performance test of the drilling fluid.

Formula	Density (g/cm ³)	Plastic Viscosity (mPa•s)	Yield Point (Pa)	Yield Point and Plastic Viscosity Ratio	FLAPI (mL)
1	0.71	20	11	0.55	4.5
2	0.71	19	10.5	0.55	4.5
3	0.74	24	18.5	0.77	3.5
4	0.73	21	14.5	0.69	4.1

Table 4. Drilling fluid performance table.

Density (g/cm ³)	Viscosity (s)	FLAPI (mL)	Mud Cake (mm)	pH Value	Sand Content (%)	FLHTHP (mL)	Static Shear Force (Pa)		Plastic Viscosity (mpa•s)	Yield Point (Pa)
							Initial Shear	Final Shear		
0.8-1.0	45-80	< 5	< 0.5	8-9	< 0.3	< 15	1-3	2-6	10-25	8-15

Table 5. Temperature Resistance Test

Temperature	Density (g/cm ³)	Plastic Viscosity (mPa.s)	Performance Dynamic Shear Force (Pa)	Yield Point and Plastic Viscosity Ratio	Filter Loss (mL)
20°C	0.725	21	15	0.71	4.1
80°C /8h	0.775	24	17	0.71	3.9
100 ° C /8h	0.779	22	15	0.70	4.1
120 ° C /8h	0.808	24	16	0.68	4.5
130°C /8h	0.824	21	14	0.67	5.5

Table 6. Physical properties of the cores of the oil reservoir for the dynamic experiment.

No.	Length(cm)	Diameter (cm)	Porosity(%)	Permeability (10 ⁻³ μm ²)	Phase Reversal Permeability (10 ⁻³ μm ²)	Recovery Value (%)
1	5.75	2.18	13.6	11.66	10.7	91.8
2	5.49	2.17	14.7	17.65	16.0	90.1

The test results show that the rise of the temperature plays a certain role on the stability of the micro-foam, but the influence is not huge. With the rise of the temperature, the base liquid tends to be sparse, the half-life period becomes shorter and the filter loss volume is slightly increased. However, during the on-site construction, according to the actual situations, with the changes of the well temperature, it shall appropriately adjust the viscosity of the base liquid, increase the volume of the film stabilizer, and choose the appropriate micro-foam liquid formula.

Anti-Pollution Capacity

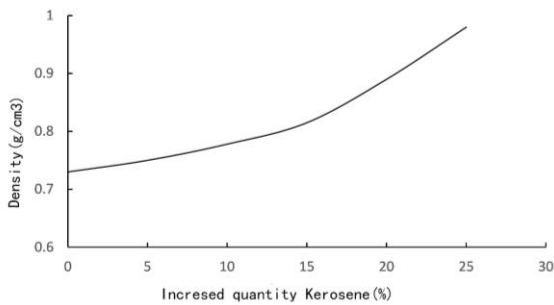


Fig. 2. The density fluctuation curve chart with the increase of the quantity of kerosene.

The influence of kerosene on micro-foam drilling fluid is expressed as: with the increase of the quantity of kerosene, the foaming ability of the foaming agent presents the declining trend but its density is on the rise. When the oil reservoir is discovered during the on-site drilling, it shall increase the quantity of the foaming agent, so as to increase the stability of the micro-foam drilling fluid.

Density Characteristics

Low density is one of the outstanding characteristics of the foam drilling fluid^[13], as for which, there are a large quantity of gas. Under the influence of the factors like temperature and pressure, the variation range of density is large. The method generally used to express the fluid density in the two phases of solid and liquid as well as the gas density cannot describe the density fluctuation rules of the micro-foam drilling liquid; therefore the relation among the density, pressure and temperature of micro-foam drilling fluid shall be rendered by the experimental method.

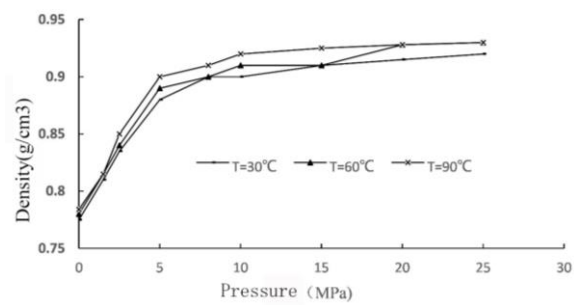


Fig. 3. Temperature-pressure-density curve of the micro-foam drilling fluid.

From the above figure, it can be seen that the influence of pressure on the density of the micro-foam drilling fluid is relatively huge, but the influence of temperature on it is relatively small; among which, before 5MPa, the change rate of the density curve is relatively high, while after 5MPa, the change rate of the density is relatively low. Density slightly increases with the rise of the temperature, but the increasing rate is relatively small.

Protective Effects on Reservoir

The micro-foam drilling fluid is applied to conduct the pollution evaluation experiment towards the sandstone cores in the reservoirs of two blocks. The results are shown in Table 6.

From the test data, it can be seen that the recovery value of the micro-foam drilling fluid permeability rate is above 90%, and it has relatively good protective effects on the oil reservoir.

FIELD APPLICATION

According to the stratigraphic characteristics of K Oil Field, the characteristics of micro-foam drilling fluid and the domestic application conditions, the corresponding technical measures are formulated, to guarantee the smooth implementation of the construction.

Site operation.

K1 Well is a vertical well with one opening and three spuddings. The design well depth is 1350m. According to the design, surface drilling can reach the depth of 30m. The micro-foam drilling fluid can be tested in the well section below 374m of the 2nd spudding. Attention shall be paid to the lower reservoir leakage and actions shall be taken to prevent the lower reservoir leakage. The construction difficulty of this well lies in that there are the lower Jurassic reservoir belongs to abnormal low-pressure reservoir. The difference of pressure coefficients is large and the leakage risk is huge. The density of the drilling fluid decreases from 1.20g/cm³ to 1.10g/cm³. The blistering is smooth, and the micro-foam in the drilling fluid is tiny and uniform with good foam stabilizing effects. During the operations of drilling, pipe trip, wireline logging, well clearing, casing and well cementing, the downhole conditions are all normal and have realized the anticipated leakage-proof effects of micro-foam.

K2 well is a vertical well with one opening and three spuddings. The design well depth is 1350m. According to the design, the 2nd spudding drilling can reach the depth of 375m. The micro-foam drilling fluid can be tested in the well section below 400m of the 3rd spudding. Actions shall be taken to prevent the lower reservoir leakage., it is required to implement the 3rd spudding at the drilling well fluid density of 1.17g/cm³, and then adopt the micro-foam technique to prevent the leakage. During the construction, the minimum density of the drilling fluid can reach 1.12g/cm³, which can successfully prevent the well leakage.

K3H well is a horizontal well with one opening

and three spuddings. The design well depth is 1655m. The 2nd spudding drilling can reach the depth of 375m. The micro-foam drilling fluid can be tested in the 3rd spudding. Actions shall be taken to prevent the lower reservoir leakage. In the position at the well depth of 1354.81m, the vertical depth is 1252.54m. Compared to the adjacent wells, the gas cap of the gas reservoir may exist in the vertical depth of 1252.54m. It shall not directly adopt the low-density drilling fluid in the 3rd spudding. The oil gas indication shows when drilling to the well depth of 1351.48m; however when the pump is stopped, there is no overflow by the observation, and it begins to test the micro-foam drilling fluid. The density of the 3rd drilling fluid of well decreases from 1.19g/cm³ to 1.12g/cm³. When the drilling is completed, the density of the drilling fluid is 1.12g/cm³, the signals of the directional instrument are normal, and the well leakage is successfully prevented.

Application Effects

The performance of the micro-foam drilling fluid is stable, and the decreased density range is approximately 0.08g/cm³. The performance of the drilling fluid is stable. The correlation data of the low-density microsphere drilling fluid and the polymer drilling fluid are listed in Table 7.

The density of the micro-foam drilling fluid is lower than the conventional water-base drilling fluid, and equal to the low-density microsphere drilling fluid. The filter loss of the drilling fluid is low, and can reduce the damages to the strata. The viscosity shear force is high and the rock-carrying ability is strong, which can effectively get rid of the rock debris at the well bottom. The solid content is low, which makes it easy to control the rheological property. There is no need to use the air compressor and other gas injection equipment or nitrogen generator, and it can be used in a recycled manner.

The test of the micro-foam drilling fluid in K Oil Field has obtained good effects and is successful in the leakage prevention of the low-pressure strata. The statistics of the relevant data are listed in Table 8.

In the well section with high pressure and low pressure in the same formation, that the micro-foam enters the formation and blocks the pores can effectively prevent the leakage of the low-pressure formation. The minimum drilling density is decreased to 0.10 g/cm³, which prevents the well leakage.

Through the survey of the perforation and oil extraction in the test wells of K1 well and K2 well, the correlation data are listed in Table 9.

Table 7. The comparison between the performances of different drilling fluids.

Drilling Fluid System	Density (g/cm ³)	Viscosity (s)	API Filter Loss (mL)	Plastic Viscosity (mPa.s)	Yield Point (Pa)	Solid Content (%)
Micro-foam	0.80-1.0	45~55	4~5	15~25	8~12	1~5
Low-Density Microsphere	0.86~1.0	40~50	5~8	10~20	5~10	10~20
Polymer	1.02~1.09	40~45	5~8	10~15	5~8	1~5

Table 8. The statistical table of the test conditions of the micro-foam drilling fluid.

No.	Well No	Well Section of Application (m)	Formation Pressure Coefficient	Density of the Drilling Fluid (g/cm ³)	Leakage (m ³)
1	K1	374~1355	0.83~0.95	1.10~1.20	0
2	K2	375~1350	0.85~0.92	1.12~1.17	0
3	K3H	375~1657	0.87~0.97	1.12~1.19	0

Table 9. The comparison between the test well and the well in oil production data.

No.	Well No	Test Well/Contrast Well	Daily Oil Production Volume (m ³ /d)	Number of Perforation	Production Volume Per Hole (m ³ /d)	Improvement Rate (%)
1	K1	Test Well	23.5	176	0.132	29.4
	K4	Contrast Well	17.8	177	0.102	
2	K2	Test Well	27.5	244	0.116	81.3
	K5	Contrast Well	16.2	265	0.064	

Compared to the adjacent wells, the daily oil production volume of K1 well is larger than that of the K4 by 5.7m³, and the daily oil production volume of K2 well is larger than that of the K5 well by 11.3m³. The average oil production volume per hole improves by 29.4% and 81.3% respectively, which suggests that the protective effect of the micro-foam drilling fluid system on the low-pressure reservoirs is significant, which is conducive to improving the recovery efficiency of single well.

CONCLUSIONS AND SUGGESTIONS

1. Firstly, the micro-foam drilling fluid has the property of low density, and its performance is stable during drilling, which solves the well leakage problem encountered in the low-pressure reservoir drilling previously and avoids the damages to reservoir caused by leakage;

2. Secondly, the micro-foam drilling fluid can effectively protect the low-pressure reservoir, facilitate the fluid's flow-back and improve the recovery efficiency;

3. Thirdly, the micro-foam drilling fluid has

relatively strong carrying capacity. It is normal to see the rock debris flowing out of the wellhead during drilling, which satisfies the requirements on geological mudlogging and drilling engineering;

4. Fourthly, a new drilling fluid system has been provided to the drilling construction on the low-pressure oil reservoirs. The on-site application suggests that the leakage-proof effects of the micro-foam drilling fluid are good, and the protective effect on the reservoir is significant. It is worthy of popularization and application.

Acknowledgement: This research was supported by NSFC project "Study on the evolution mechanism of composite materials with high temperature-high pressure-low elasticity modulus", No. 51474192; and Basic research funding of central universities, No. 2652015067.

REFERENCES

1. L.J. Hua, *Journal of Inner Mongolia petrochemical*, **16**, 106 (2013).
2. S. G. Jun, *Science and technology innovation and application*, **27**, 79 (2014).
3. W.H. Jun, Z.J. Zheng, X. Hua, X.B. Ru, *Oil drilling*

- technology*, **05**, 88 (2007).
4. C.D. Ivan, F.B. Growcock, J.E. Friedheim, SPE Annual Technical Conference and Exhibition, San Antonio, Texas, 29 September–2 October 2002, SPE 77445
 5. A. Belkin, M.O. Irving, B. Connor, M. Fosdick, T.L. Hoff, F.B. Growcock, SPE Annual Technical Conference and Exhibition, 9-12 October, 2005, Dallas, SPE-96145-MS
 6. W.G. Quan, S.Y. Xue, L.J. Xin, S.L. Wei, *Journal of drilling technology and practices*, **06**, 75 (2010).
 7. L. Qian, *Journal of Science&Technology Vision*, **28**, 245 (2015).
 8. C.C. White, A.P. Chesters, C.D. Ivan, S. Maikranz, R. Nouris, *World Oil*, **224**(10), 37 (2003).
 9. N. Bjorndalen, E. Kuru, *Petroleum Society of Canada*, **47**, 6 (2006).
 10. Z.X. Qin, W.Y. Chi, *Journal of synthetic material ageing and applications*, **42**, 28 (2013).
 11. F.B. Growcock, A. Belkin, M. Fosdick, M.O. Irving, B. Connor, T. Brookey, *SPE Drill. Complet.* **22** (2), 74 (2007).
 12. C.H. Bo, *Journal of Inner Mongolia*, **02**, 39 (2015).
 13. F.B. Growcock, G.A. Simon, A.B. Rea, R. Leonard, S.E. Noello, R. Castellan, IADC/SPE Drilling Conference, Dallas, March 2-4, 2004, IADC/SPE 87134
 14. J. Montilva, C.D. Ivan, J. Friedheim, R. Bayter, Offshore Technology Conference, Houston, May 6-9, 2002, OTC 14278
 15. A.B. Rea, E.C. Alvis, B.P. Paiuk, J.M. Climaco, M. Vallejo, E. Leon, J. Inojosa, SPE Latin American and Caribbean Petroleum Engineering Conference, 27-30 April, 2003, Port-of-Spain, Trinidad and Tobago, SPE-81082-MS

BULGARIAN CHEMICAL COMMUNICATIONS

Instructions about Preparation of Manuscripts

General remarks: Manuscripts are submitted in English by e-mail or by mail (in duplicate). The text must be typed double-spaced, on A4 format paper using Times New Roman font size 12, normal character spacing. The manuscript should not exceed 15 pages (about 3500 words), including photographs, tables, drawings, formulae, etc. Authors are requested to use margins of 3 cm on all sides. For mail submission hard copies, made by a clearly legible duplication process, are requested. Manuscripts should be subdivided into labelled sections, e.g. **Introduction, Experimental, Results and Discussion**, etc.

The title page comprises headline, author's names and affiliations, abstract and key words.

Attention is drawn to the following:

a) **The title** of the manuscript should reflect concisely the purpose and findings of the work. Abbreviations, symbols, chemical formulas, references and footnotes should be avoided. If indispensable, abbreviations and formulas should be given in parentheses immediately after the respective full form.

b) **The author's** first and middle name initials, and family name in full should be given, followed by the address (or addresses) of the contributing laboratory (laboratories). **The affiliation** of the author(s) should be listed in detail (no abbreviations!). The author to whom correspondence and/or inquiries should be sent should be indicated by asterisk (*).

The abstract should be self-explanatory and intelligible without any references to the text and containing not more than 250 words. It should be followed by key words (not more than six).

References should be numbered sequentially in the order, in which they are cited in the text. The numbers in the text should be enclosed in brackets [2], [5, 6], [9–12], etc., set on the text line. References, typed with double spacing, are to be listed in numerical order on a separate sheet. All references are to be given in Latin letters. The names of the authors are given without inversion. Titles of journals must be abbreviated according to Chemical Abstracts and given in italics, the volume is typed in bold, the initial page is given and the year in parentheses. Attention is drawn to the following conventions:

a) The names of all authors of a certain publications should be given. The use of “*et al.*” in

the list of references is not acceptable.

b) Only the initials of the first and middle names should be given.

In the manuscripts, the reference to author(s) of cited works should be made without giving initials, e.g. “Bush and Smith [7] pioneered...”. If the reference carries the names of three or more authors it should be quoted as “Bush *et al.* [7]”, if Bush is the first author, or as “Bush and co-workers [7]”, if Bush is the senior author.

Footnotes should be reduced to a minimum. Each footnote should be typed double-spaced at the bottom of the page, on which its subject is first mentioned.

Tables are numbered with Arabic numerals on the left-hand top. Each table should be referred to in the text. Column headings should be as short as possible but they must define units unambiguously. The units are to be separated from the preceding symbols by a comma or brackets.

Note: The following format should be used when figures, equations, etc. are referred to the text (followed by the respective numbers): Fig., Eqns., Table, Scheme.

Schemes and figures. Each manuscript (hard copy) should contain or be accompanied by the respective illustrative material as well as by the respective figure captions in a separate file (sheet). As far as presentation of units is concerned, SI units are to be used. However, some non-SI units are also acceptable, such as °C, ml, l, etc.

The author(s) name(s), the title of the manuscript, the number of drawings, photographs, diagrams, etc., should be written in black pencil on the back of the illustrative material (hard copies) in accordance with the list enclosed. Avoid using more than 6 (12 for reviews, respectively) figures in the manuscript. Since most of the illustrative materials are to be presented as 8-cm wide pictures, attention should be paid that all axis titles, numerals, legend(s) and texts are legible.

The authors are asked to submit **the final text** (after the manuscript has been accepted for publication) in electronic form either by e-mail or mail on a 3.5” diskette (CD) using a PC Word-processor. The main text, list of references, tables and figure captions should be saved in separate files (as *.rtf or *.doc) with clearly identifiable file names. It is essential that the name and version of

the word-processing program and the format of the text files is clearly indicated. It is recommended that the pictures are presented in *.tif, *.jpg, *.cdr or *.bmp format, the equations are written using "Equation Editor" and chemical reaction schemes are written using ISIS Draw or ChemDraw programme.

The authors are required to submit the final text with a list of three individuals and their e-mail addresses that can be considered by the Editors as potential reviewers. Please, note that the reviewers should be outside the authors' own institution or organization. The Editorial Board of the journal is not obliged to accept these proposals.

EXAMPLES FOR PRESENTATION OF REFERENCES

REFERENCES

1. D. S. Newsome, *Catal. Rev.–Sci. Eng.*, **21**, 275 (1980).
2. C.-H. Lin, C.-Y. Hsu, *J. Chem. Soc. Chem. Commun.*, 1479 (1992).
3. R. G. Parr, W. Yang, *Density Functional Theory of Atoms and Molecules*, Oxford Univ. Press, New York, 1989.
4. V. Ponec, G. C. Bond, *Catalysis by Metals and Alloys* (Stud. Surf. Sci. Catal., vol. 95), Elsevier, Amsterdam, 1995.
5. G. Kadinov, S. Todorova, A. Palazov, in: *New Frontiers in Catalysis* (Proc. 10th Int. Congr. Catal., Budapest, 1992), L. Guzzi, F. Solymosi, P. Tetenyi (eds.), Akademiai Kiado, Budapest, 1993, Part C, p. 2817.
6. G. L. C. Maire, F. Garin, in: *Catalysis. Science and Technology*, J. R. Anderson, M. Boudart (eds), vol. 6, Springer-Verlag, Berlin, 1984, p. 161.
7. D. Pocknell, *GB Patent 2 207 355* (1949).
8. G. Angelov, PhD Thesis, UCTM, Sofia, 2001.
9. JCPDS International Center for Diffraction Data, Power Diffraction File, Swarthmore, PA, 1991.
10. *CA* **127**, 184 762q (1998).
11. P. Hou, H. Wise, *J. Catal.*, in press.
12. M. Sinev, private communication.
13. <http://www.chemweb.com/alchem/articles/1051611477211.html>.

CONTENTS

<i>M. Mohamadzadeh, M. Homae, E. Pazira</i> , Modeling desalinization to reclamation of saline-sodic soils	5
<i>M. Sasani, S. Khoramnejadian, R. Safari</i> , Anthracene biodegradation by <i>Pseudomonas aeruginosa</i> isolated from Babolrood River estuary in Mazandaran province	14
<i>A. Mohammadi, M.R. Baneshi, T. Khalili</i> , Choline reduces the hepatocyte nuclear factor-4 α (HNF-4 α) in HepG2 cells	20
<i>M.F. Abari, S. M. Zarandi, N. Mansouri</i> , Assessment of the contributions of the highest NO ₂ concentrations by industrial sources using AERMOD dispersion model	25
<i>A. Sahraei, H. Kargar, M. Hakimi</i> , Applications and attributes of nickel (II) schiff base complexes derived of phenylenediamine	33
<i>E. Mirzakhani, F. Mortazaeinezhad, A. Tahmorespour, H. Radnezhad</i> , Potential of phytoremediation for the removal of petroleum hydrocarbons in contaminated soils associated with <i>Rhodococcus erythropolis</i> ...	44
<i>A. Mohammadi, M. R. Baneshi, T. Khalili</i> , Effects of choline, TMA, and TMAO on the expression of flavin-containing monooxygenases 3 and 5 in mice	52
<i>L. Chu, J. Wang, F. Wang, M. Chen, Z. Liu</i> , Prokaryotic pico- and nanoplankton community structure in the hypersaline lakes of the Qaidam Basin	60
<i>Li Yajie</i> , Study on gas recognition and determination based on gas sensors	69
<i>M. Tian, Y.J. Xu</i> , Preparation of acrylamide/2-ethylhexyl acrylate copolymer and calculation of monomer reactivity ratios	74
<i>H. Liu, W. Liu, Y. Cui</i> , Quantitative analysis of the relationship between permeability and microstructure of solidified dredger fill	79
<i>X. Wang, Y. Lu, R. Zhu, Q. Fu, W. Zhong</i> , Study of hydraulic performance and pressure pulsation characteristics of the grinder pump in case of clogging	87
<i>M. Li, Y. Song, F.Chen</i> , Analysis on stability of slope in a typical cold region based on thermo-mechanical coupling	96
<i>L.-Y. Luan, L.-H. Wang, L.-X. Zhao, Z.-H. Wang, J. Li, D.-J. Sun</i> , Direct synthesis of Mg/Al layered double hydroxide films with different oriented hexagonal platelets via vapor phase transport and hot water treatment	104
<i>Z. Yong, Z. Liyi, W. Li, H. Jianfeng, B. Zhe</i> , Chemical gas leakage source determination using distributed EM algorithm with Gaussian mixture model	108
<i>B. Yang, Q. Li, Y. Wu, G. Tian, M. Dong, F. Yin, X. Zhao, Y. Wang, W. Xiao, W. Zhang, X Cui</i> , Spatial dynamics of bacterial communities in rural household biogas digesters in different climatic regions of Yunnan plateau, China	117
<i>Y. Shouguang, X. Wenjie, Y. Yong, Z. Lianwei</i> , Numerical simulation analysis of flow and heat transfer of supercritical LNG in the IFV condenser	123
<i>K. Sun, B. Wang, X. Sui, S. Feng, D. Yuan, J. Li, C. Liu, H. Li</i> , Tin electrodeposition in the presence of <i>Linseed</i> essential oil	131
<i>Y. Hao</i> , A feasibility study on heavy oil exploration by in-situ electric heating	136
<i>M.L. Wang, C.L. Zheng, Y.W. Zhou, T.G. Liu, Y.B. Li, H. Xie, Y. Chang, W.C. Liu, G.G. Chen, X.L. Sun, Y.H. Zhao, Z.H. Li</i> , Metabolomics studies of chronic atrophic gastritis cold and heat syndrome	144
<i>C.L. Zheng, Q. Wang, Y.W. Zhou, M. Jiang, B. Zhu, J. Yan, Y. Tang, J.Z. Li, J. Wang, Y. F. Zheng</i> , Protective effect of huangjingzanyu capsule on cyclophosphamide-induced oligoasthenozoospermia in rats	152
<i>G.Q. Lin, G. Li, C. Zhang, Y. Shen, Q. Lv, G.Q. Lin*, G. Li, C. Zhang, Y. Shen, Q. Lv</i>	158
<i>S. Aijun, W. Shiwen, Z. Liya</i> , Purify processing and utilization of mine water	162
<i>L. L. Lei, J. C. Yin, B. Zhang, P. Wang</i> , Effect of NO oxidation to NO ₂ from diesel engine over Mn-Ce/ γ -Al ₂ O ₃ catalyst.....	167
<i>S. Wang, F. Li, J. Rong, S. Tang, H. Jiang, H. Jin, J. Zhu, Y. Gao, D. Wang, S. Tao, X. Ren</i> , Serum metallomics study on patients with osteoarthritis based on ICP-MS technique	171
<i>D. D. Gao, Y. X. Li, Z. X. Yuan, S. W. Du</i> , Coupled heat and mass transfer in annular adsorption bed	183
<i>X.W. Huang, X.H. Li, X. Pan, Y.L. Yan, D.Y. Xu, Q. Gao, L.C. Cui, Y. Pan, C.L. Zhou, S.Y. Yang, M.H. Duan, X. B. Qu</i> , Establishment of detection method for the biological activity of Lumbrokinase	193
<i>Y. Luo, Z.J. Yang, Y. Dong</i> , Application of fuzzy comprehensive evaluation method in water quality evaluation ..	199
<i>T. Fei, L. Zhang</i> , Low carbon logistics distribution route optimization research based on improved ant colony algorithm	205
<i>L.-X. Zhao, M.-C. Jiang, L.-Y. Luan, Q. Li, J. Zhang</i> , Sorbent concentration effect on the adsorption of Pb(II) on Fe ₃ O ₄ @Mg ₂ Al-EDTA LDH in aqueous solution	211
<i>Y. Hao</i> , Research and application of anti-leakage drilling fluid	215
INSTRUCTIONS TO THE AUTHORS	222